“Germanium-based multiferroic compounds with melilite structure”

Von der Fakultät für Georessourcen und Materialtechnik der
Rheinisch-Westfälischen Technischen Hochschule Aachen

zur Erlangung des akademischen Grades eines

Doktors der Naturwissenschaften

genehmigte Dissertation

vorgelegt von

Henrik Friedrich Thoma, M. Sc.

Berichter: Univ.-Prof. Dr. rer. nat. Georg Roth
Univ.-Prof. Dr. Peter Böni

Tag der mündlichen Prüfung: 17.10.2023

Abstract

This work is dedicated to the detailed investigation of the atomic and magnetic structure in a selection of germanium-based melilite-type compounds, namely $Ba_2TGe_2O_7$ (T = Cu, Co and Mn) and the $Ba_2Cu_{1-x}Mn_xGe_2O_7$ solid solution series. These materials gained high interest in the current condensed matter research as they revealed a strong magnetoelectric coupling that could not be explained by the conventional models of spin-driven multiferroicity. Inspired by their peculiar magnetoelectric effects, new mechanisms have recently been proposed, which might be of high potential for spintronic applications.

Detailed structural parameters of the $Ba_2Cu_{1-x}Mn_xGe_2O_7$ solid solution series are provided as a function of the concentration x by X-ray and neutron powder diffraction on a series of recently synthesized polycrystalline compounds. Moreover, spurious phases are identified and characterized. Additional heat capacity measurements reveal the emergence of two distinct low-temperature magnetic phases for the Cu-rich and Mn-rich compounds, separated by a critical concentration of $x \approx 0.57$. The macroscopic properties of these phases and their evolution with applied magnetic field are mapped out by magnetization measurements. The magnetic ground state in $Ba_2Cu_{1-x}Mn_xGe_2O_7$ is identified and specified by high-resolution neutron powder diffraction, disclosing an antiferromagnetic cone-like structure for the Cu-rich and a commensurate antiferromagnetic structure for the Mn-rich phase.

A comprehensive study of the magnetic structure in $Ba_2TGe_2O_7$ (T = Cu, Co and Mn) single crystals is provided by polarized neutron diffraction. For this study, the flipping ratio setup of the POLI instrument at the Heinz Maier-Leibnitz Zentrum in Garching, Germany, is extended for a new high-field magnet with a dedicated supermirror bender. This setup is numerically optimized and the neutron polarization confirmed to be above 99%. Corresponding flipping ratios are measured on the $Ba_2TGe_2O_7$ single crystals in the para- and antiferromagnetic phases, revealing precise values for the ordered and field-induced magnetic moments, the susceptibility tensors and local anisotropies. Based on these results and a careful symmetry analysis, the sign of the Dzyaloshinskii-Moriya interaction vector in T = Cu and Co is reported for the first time. Additional spherical neutron polarimetry on $Ba_2CoGe_2O_7$ confirms $P2'_12_12'$ as the magnetic space group of the ground state and demonstrates the high sensitivity of the remanent domain configuration on applied magnetic fields.

In the context of this thesis, an advanced maximum entropy approach for the reconstruction of magnetization densities from polarized neutron diffraction data was developed and implemented in a new software tool. Applied to $Ba_2TGe_2O_7$, it provides aspherical density shapes for the transition metal ions that directly relate to their $3d$ orbital configuration resulting from crystal field effects. This is confirmed by multipole expansion, revealing orbital populations close to the expected values.

Zusammenfassung

Diese Arbeit widmet sich der detaillierten Untersuchung der atomaren und magnetischen Struktur in einer Auswahl von Germanium-basierten Melilithen, darunter $Ba_2TGe_2O_7$ (T = Cu, Co und Mn) Kristalle und $Ba_2Cu_{1-x}Mn_xGe_2O_7$ Mischverbindungen. Diese Materialien beeindrucken durch ihre starke magnetoelektrische Kopplung, welche nicht mit den herkömmlichen multiferroischen Modellen vereinbar ist. Inspiriert von diesen neuartigen Effekten wurden neue Mechanismen in der Literatur vorgeschlagen, die für spintronische Anwendungen von großem Interesse sein könnten.

Detaillierte Strukturparameter der $Ba_2Cu_{1-x}Mn_xGe_2O_7$ Mischverbindungen werden in Abhängigkeit von x durch Röntgen- und Neutronenpulverdiffraktion an einer Reihe von erst kürzlich synthetisierten polykristallinen Verbindungen ermittelt. Darüber hinaus werden Fremdphasen identifiziert und charakterisiert. Zusätzliche Wärmekapazitätsmessungen signalisieren zwei unterschiedliche magnetische Phasen für die Cu- und Mn-reichen Verbindungen, getrennt durch eine kritische Konzentration $x \approx 0,57$. Die makroskopischen Eigenschaften dieser Phasen und ihre Abhängigkeit vom angelegten Magnetfeld werden durch Magnetisierungsmessungen untersucht. Hochauflösende Neutronendiffraktion identifiziert den magnetische Grundzustand in $Ba_2Cu_{1-x}Mn_xGe_2O_7$ als eine antiferromagnetische, kegelförmige Struktur für die Cu-reiche und eine kommensurable antiferromagnetische Struktur für die Mn-reiche Phase.

Polarisierte Neutronendiffraktion ermöglicht zudem eine umfassende Untersuchung der magnetischen Struktur in $Ba_2TGe_2O_7$ (T = Cu, Co und Mn) Einkristallen. Diesbezüglich wird das Flipping Ratio Setup des Instruments POLI am Heinz Maier-Leibnitz Zentrum in Garching, Deutschland, um einen Hochfeldmagneten und einen Supermirror Polarisator erweitert. Für das durch numerische Simulationen optimierte Setup wird eine Neutronen Polarisation von über 99% nachgewiesen. Flipping Ratio Messungen an den $Ba_2TGe_2O_7$ Einkristallen in den para- und antiferromagnetischen Phasen ergeben präzise Werte für die geordneten und feldinduzierten magnetischen Momente sowie für Suszeptibilitätstensoren und lokale Anisotropien. Anhand dieser Ergebnisse und einer detaillierten Symmetry Analyse wird zudem das Vorzeichen des Dzyaloshinskii-Moriya Vektors in T = Cu und Co zum ersten Mal bestimmt. Außerdem wird $P2_1'2_12'$ als magnetische Raumgruppe des Grundzustands in $Ba_2CoGe_2O_7$ bestätigt und die hohe Empfindlichkeit der remanenten Domänenkonfiguration auf Magnetfelder dargelegt.

Zudem wurde im Rahmen dieser Arbeit eine verbesserte Maximum-Entropie Methode zur Rekonstruktion von Magnetisierungsdichten aus polarisierten Neutronendiffraktionsdaten entwickelt und in ein neues Software-Tool implementiert. Angewandt auf $Ba_2TGe_2O_7$ ergeben sich asphärische Dichten für die Metallionen, die sich direkt auf die Struktur ihrer $3d$ Orbitale und somit auf Kristallfeldeffekte zurückführen lässt. Multipolentwicklung bestätigt dies und liefert eine Besetzung der Orbitale nahe der Erwartung.

Contents

1. Introduction

The melilite group refers classically to the binary solid solution series between gehlenite ($Ca_2Al_2SiO_7$) and åkermanite ($Ca_2MgSi_2O_7$), which is naturally formed by igneous activities or in thermally metamorphosed limestone [1]. Interestingly, very pure melilites were also found in Ca-Al-rich inclusions in meteorites and their precisely known temperature-composition relationship can be used as a diagnostic and informative tool to understand the formation and evolution of one of the oldest materials of our solar system [2, 3]. In 1930, the basic tetragonal crystal structure of an intermediate melilite was first solved by Warren [4] and the space group determined to be $P\bar{4}2_1m$. The melilite structure is characterized by layers of corner-sharing (Si,Mg,Al)O_4 tetrahedrons connected together by Ca atoms accommodated in a distorted eight-coordinated antiprismatic polyhedron [5]. The tetrahedral layers are arranged as Si_2O_7 dimers linked by tetrahedrally coordinated (Mg, Al). In the following years, this structure could be evidenced in further materials of general stoichiometry $A_2TB_2O_7$ with a large, monovalent to trivalent cation A (e.g. Ca, Ba, Na, Sr) and small, divalent to quadrivalent cations B (e.g. Si, Ge) and T (e.g. transition metals), forming the rich class of the melilite-type compounds [5, 6].

Due to their layered noncentrosymmetric structure and the high variability of the atomic compositions, a wide range of novel and complex physical effects could be evidenced in melilite-type compounds. Already in 1968, Alam *et al.* [7] could achieve laser action in neodymium doped $Ba_2MgGe_2O_7$ at room-temperature (RT) and therefore initiated the detailed studies of their nonlinear optical and lasing properties [8]. Especially the occurrence of stimulated Raman scattering in some compounds of the melilite-type group (e.g. $Ca_2ZnSi_2O_7$ [9], $Sr_2MgGe_2O_7$ [10] and $Ba_2MgGe_2O_7$ [11]) promotes them as potential candidates for the realization of efficient Raman laser converters allowing the generation of new laser wavelengths, which is of high interest for the application in modern laser physics [12].

1.1. Magnetic properties of melilites

Besides their exceptional optical properties, the melilite-type compounds can host magnetic ions (e.g. Cu, Co, Mn) at the T site, leading to a broad range of magnetic structures [13]. As the magnetic T ions form a square-planar arrangement in the tetrahedral layers separated by the large A cations, the intralayer interactions are considered to be stronger than the interlayer ones, which may result in a low-dimensional magnetic behavior. Thus, they might serve as model compounds for a 2D square lattice Heisenberg antiferromagnet [14, 15] and the existence of a Higgs mode in the excitation spectrum is predicted [16]. Additional to the symmetric exchange, the antisymmetric Dzyaloshinskii-Moriya

interaction (DMI) is allowed by the noncentrosymmetric melilite structure [17–20] with an uniform in-plane and and alternating out-of-plane component [21, 22]. This DMI became of particular interest in current condensed matter research as it is present in a wide range of complex magnetic materials like multiferroics [23], topological insulators [24] and antiferromagnetic (AFM) spin wave field-effect transistors [25]. Moreover, it is the driving force to stabilize various novel topological non-collinear magnetic structures, such as spin spirals [26], magnetic skyrmions [27], or magnetic soliton lattices [28]. The DMI is commonly attributed to relativistic spin-orbit coupling (SOC) in conjunction with a broken inversion symmetry [17–20]. Typically, T = Co magnetic melilite-type compounds are ordered antiferromagnetically in the ab plane with a ferromagnetic (FM) stacking in the c direction (e.g. $Ba_2CoGe_2O_7$ [29, 30], $Sr_2CoGe_2O_7$ [14], $Ca_2CoSi_2O_7$ [31, 32]). In this magnetic moment configuration, the alternating out-of-plane component of the DMI may introduce an in-plane canting in the otherwise collinear AFM structure, leading to a spontaneous weak ferromagnetic (WFM) moment in all three example compounds [14, 29, 31]. In contrast, melilites with T = Mn typically have an AFM order in both the ab plane and the c direction (e.g. $Ba_2MnGe_2O_7$ [15], $Sr_2MnGe_2O_7$ [14]). Although the DMI might introduce an in-plane canting as well, no macroscopic WFM moment is observed in these compounds due to the AFM stacking. For T = Fe, the adopted magnetic structure depends on the selected alkali earth metal B such that $Ba_2FeGe_2O_7$ orders Co-like, whereas $Sr_2FeGe_2O_7$ orders Mn-like [33]. By substituting the A site with a rare-earth metal or the B site with a transition metal (TM), a ferrimagnetic ordering between Eu^{2+} and Mn^{2+} in $Eu_2MnSi_2O_7$ or a spin-glass behavior in $Ba_2Fe_2GeO_7$ could be evidenced, respectively [34, 35].

Additional to these almost collinear magnetic structures, an AFM spin spiral structure with a field-induced incommensurate to commensurate (I/C) phase transition was observed in $Ba_2CuGe_2O_7$, stabilized by a competition between the uniform in-plane component of the DMI and the isotropic exchange [36]. This unconventional compound has incited great interest in the literature as it is one of the rare materials where spiral spin textures and weak ferromagnetism are predicted to coexist and it could support a stable skyrmion phase [37]. Skyrmions are non-trivial topologically stable magnetic structures that are promising candidates as information carriers for future ultrahigh-density storage and logic devices [38–42].

1.2. Multiferroic properties of melilites

The broad scientific interest in the melilite-type compounds was again enhanced in 2008 by the discovery of the appearance of ferroelectricity and a strong magnetoelectric coupling below the AFM ordering temperature in $Ba_2CoGe_2O_7$ [43]. The magnetoelectric effect, a phenomenon that describes the mutual control of the magnetization by electric field and the polarization by magnetic field, was already predicted at the end of the nineteenth century by Curie [44] and first theoretically addressed by Landau and Lifshitz [45] and Dzyaloshinskii [46]. Especially for the application in spintronics, multiferroics, defined as materials hosting more than one ferroic property like ferroelectricity,

ferromagnetism or ferroelasticity in the same phase, provide the fundamental functionality for the development of next-generation devices with minimal energy dissipation [47, 48]. These ferroic properties are strongly coupled to the materials symmetry such that magnetism and ferroelectricity require a broken time and spatial inversion symmetry, respectively. Thus for multiferroic magnetoelectrics, which are both ferromagnetic and ferroelectric in a single phase, the two symmetries must be simultaneously broken [49, 50]. Unfortunately, the interference between ferroelectricity and magnetism is usually small as their microscopic mechanisms are quite different: Whereas ferroelectrics are mostly TM oxides with empty d shells in a covalent bonding, magnetic materials favour partially filled d shells leading to uncompensated spins available for the magnetic ordering [23, 50]. Therefore, classical magnetoelectrics like $BiMnO_3$ and $BiFeO_3$ are essentially ferroelectrics with additional magnetic ions slightly influencing the dielectric constant upon their ordering at low temperatures [51–53].

This changed with the discovery of the giant magnetoelectric effect in orthorhombic $TbMnO_3$ caused by a magnetic-field-induced electric polarization flop [54]. In $TbMnO_3$ and other so-called spin-driven ferroelectrics, the magnetic structure breaks the inversion symmetry of the system and ferroelectricity appears as accidental by-product, leading to an intrinsically strong coupling of the two effects [23]. Therefore, systems with complex inversion symmetry breaking magnetic structures have attracted renewed interest as promising candidates for new magnetoelectrics. Two different types of spin-driven magnetoelectric responses were initially found: First, in chiral spin structures resulting from competing exchange interactions, a ferroelectric polarisation was observed perpendicular to the propagation vector and the spin rotation axis [55]. Typical examples are geometrically frustrated magnets including the orthorhombic perovskite type rare-earth manganites $RMnO_3$ ($R = Tb_{1-x}Dy_x$ [54, 56–58], $Eu_{1-x}Y_x$ [59, 60]), the quasi-one-dimensional chain cuprates (e.g. $CuCl_2$ [61], $CuBr_2$ [62], $LiCu_2O_2$ [63], $LiCuVO_4$ [64]) and the orthorhombic Kagomé staircase structured $Ni_3V_2O_8$ [65, 66]. This phenomena can be microscopically explained by the spin current or the inverse DMI mechanism of multiferroicity, both predicting an electric polarization $\mathbf{P} \propto \sum_{ij} \mathbf{e}_{ij} \times (\mathbf{S}_i \times \mathbf{S}_j)$ for neighboring spins $\mathbf{S}_i$ and $\mathbf{S}_j$ connected by a unit vector $\mathbf{e}_{ij}$ [67]. Whereas the ferroelectic polarization in the spin current model arises from the spin chirality of a cluster configuration with two octahedrally coordinated TM ions with one of the ligands at their middle point, the polarization in the inverse DMI mechanism can be attributed to a slight shift of these central anions from the midpoints to increase the DMI energy, and thus producing local electric polarizations that do eventually not cancel out [68, 69]. As second type, a spin-driven ferroelectric polarization was found in collinear frustrated magnetic structures like in orthorhombic perovskite type small-rare-earth-ion manganites $RMnO_3$ (R = Y [70], Tm[71], Ho, Er, Yb, $Y_{1-x}Lu_x$ [72]), synthesized under high pressure [72], or in $Ca_3Co_{1.04}Mn_{0.96}O_6$ and $GdFeO_3$ hosting chains of alternating magnetic ion types [73, 74]. The spin-driven magnetoelectricity in these compounds can be microscopically attributed to the so-called exchange striction mechanism, which is driven by the symmetric exchange interaction $\propto J\mathbf{S}_1 \cdot \mathbf{S}_2$ between the two magnetic atoms with spins $\mathbf{S}_i$. As the exchange constant J strongly depends on the bond distance between the magnetic atoms or on the position of a mediating anion, this coupling can induce a displacement

modulation in the lattice based on the scalar product of the spins to maximize the energy gain [47, 75]. However, the energy scale for such a lattice modulation, which might lead to a ferroelectic polarization $\mathbf{P} \propto \sum_{ij} \mathbf{\Pi}_{ij} (\mathbf{S}_i \cdot \mathbf{S}_j)$ along a specific crystallographic direction $\mathbf{\Pi}_{ij}$, is usually larger than the contribution of the symmetric exchange. For this reason, exchange striction occurs only in a limited number of cases. In particular, the energy gain by the anion displacement might only be efficient if the initial bond is already bent as the symmetry of J for a straight bond leads to an only small energy contribution for its displacement [67]. A typical example for spin-driven ferroelectricity by exchange striction can be found in the Ising spin chain with up-up-down-down magnetic structure. By alternating displacements of the magnetic atoms, energetically favoured pairs with parallel spins are formed that break the lattice inversion symmetry and may induce a ferroelectric polarization along the bond direction if the ionic order of the magnetic atoms is alternating as well [73]. Interestingly, both exchange striction and spin-current mechanism might coexist in the orthorhombic rare-earth manganese oxides $R\mathrm{Mn_2O_5}$ (R = Yb [76], Tm [77, 78], Er [79], Y [80], Tb [81], Dy, Ho [82]), demonstrating a rich and complex variety of magnetoelectric properties [67, 83].

As the noncentrosymmetric melilite structure lacks intrinsically an inversion center and can host several types of magnetic structures, it contains promising characteristics towards spin-driven multiferroicity. And indeed, many magnetic melilite-type compounds (e.g. $\mathrm{Ca_2CoSi_2O_7}$ [84], $\mathrm{Ba_2CoGe_2O_7}$ [43], $\mathrm{Sr_2CoSi_2O_7}$ [85], $\mathrm{Ba_2MnGe_2O_7}$ [86], $\mathrm{Ba_2CuGe_2O_7}$ [87]) show a substantial coupling between magnetic and electric degrees of freedom. Whereas the ferroelectric polarization of the helical domains in spin-spiral $\mathrm{Ba_2CuGe_2O_7}$ can be well explained by the spin current model, for example, the multiferroicity of $\mathrm{Ba_2CoGe_2O_7}$ is clearly distinguished as the electric polarization does not flop sharply but instead rotates gradually by applying magnetic fields [43]. As this intriguing magnetoelectric effect could not be explained by the spin current or exchange striction model, new mechanisms were proposed.

The first mechanism to explain this novel electrical response is the *spin-dependent p-d hybridization model*, originally proposed to explain the multiferroicity observed in the 120° spin structured delafossite compounds $\mathrm{Cu(Fe,Al)O_2}$ [88]. It attributes the ferroelectric polarization to spin-orbit interactions between the metal and its ligands. The resulting spin-driven polarization is given by $\mathbf{P} \propto \sum_i \mathbf{e}_i (\mathbf{S} \cdot \mathbf{e}_i)^2$ with $\mathbf{e}_i$ the connection vector between the metal with spin $\mathbf{S}$ and its i^{th} ligand. This model reproduces well the observed gradual rotation of the polarization with field and was later extended for antiferroelectric coupling effects to explain the sharp polarization decrease in the low field region [89, 90].

As second model, a contribution to the ferroelectric polarization from a *spontaneous toroidic effect mechanism* was proposed by Toledano *et al.* [91]. It was shown that a spontaneous toroidal moment is allowed parallel or antiparallel to the AFM moment in $\mathrm{Ba_2CoGe_2O_7}$. By applying electric or magnetic fields perpendicular to the total toroidal moment, additional polarization and magnetization components can arise. As further toroidal moments can be induced by electric and magnetic fields via the electrotoroidal and magnetotoroidal tensors or by applying both fields non-collinear to each other, this results in a complex magnetoelectric coupling, which allows to describe the specific

magnetoelectric properties observed in $Ba_2CoGe_2O_7$. Microscopically, these toroidal contributions can be attributed to single ion effects [91].

As third mechanism, a *spin-nematic interaction model* was considered by Soda *et al.* [92]. The spin-nematic operator, defined as a symmetric rank two tensor of local spin operators, represents a magnetic ordering invariant to time reversal and is equivalent to an electric polarization due to the lack of inversion symmetry in the point group of the CoO_4 tetrahedron. The exchange between these quadrupolar spin-nematic operators, which can be traced back to electrostatic intersite polarization interactions, represents a rotational symmetry breaking two-ion anisotropy. These spin-nematic interactions of antiferronematic type explain consistently the experimentally observed magnetic fourfold in-plane anisotropy in both the neutron spectrum and the bulk magnetic susceptibility and the almost vanishing ferroelectric polarization along the z direction in zero magnetic field [92, 93].

Finally, *Jahn-Teller (JT) distortions* are proposed as a novel source of multiferroicity by Barone *et al.* [94]. For JT-active TM ions in the tetrahedral environment provided by the melilite-type structure, polar JT distortions may locally develop and lead to antiferro-, ferro- or ferrielectric phases. As these polar JT distortions can be realized in the presence of a magnetic phase, an intrinsic magnetoelectric coupling might emerge [94].

The strong multiferroicity observed in many melilite-type compounds may also drastically influence their optical properties, leading to remarkable phenomena. For example, in multiferroic $(Ca,Sr)_2CoSi_2O_7$ and $Ba_2CoGe_2O_7$ four-coloured magnetoelectric spin-wave excitations were found [95]. This quadrochroism, i.e. different absorption coefficients for all four combinations of the propagation and polarization directions of a light beam, can be used to realize one-way transparency, which is reversible by external magnetic fields. Thus, these compounds may give the unique opportunity to fabricate magnetically controllable optical-diodes, which could open up new horizons in photonics [95–97].

1.3. Goals and experimental methods of this study

As the unconventional multiferroicity in the melilite-type compounds is of spin-driven origin, a precise knowledge of the adopted magnetic structure and its evolution with temperature and applied magnetic field is crucial. Thus, the primary goal of this work is to provide a systematic and detailed study focused on the magnetic ordering processes in the different germanium-based melilites $Ba_2TGe_2O_7$ (T = Cu, Co, Mn) in order to get a deeper insight into the exceptional details of the realized magnetic structures and the possible mechanisms of the magnetoelectric coupling in these intriguing materials. For this purpose, single crystals of the three pure compounds and polycrystals of the $Ba_2Cu_{1-x}Mn_xGe_2O_7$ solid solution series were provided by collaborators at the Department of Physics, University of Salerno, Italy, the RIKEN Center for Emergent Matter Science (CEMS) in Wako, Japan, and the Department of Physics, Technical University of Munich (TUM), Germany [98]. As this comparably small group of materials

has the same melilite-type chemical cell but hosts a wide range of novel and extraordinary magnetic, electric and optical properties depending on the selected TM ion T [15, 36, 86, 95–97], outlined in more detail in Chap. 2, they provide a structurally simple but physically interesting playground to study the underlying magnetic interactions, their interplay with applied magnetic fields and their connection to the proposed models of multiferroicity.

Although different experimental techniques are considered within this work to achieve the main goal of a proper and comprehensive analysis of the magnetic properties, the primary one is neutron diffraction as it is a powerful and outstanding tool to simultaneously probe both the nuclear and magnetic structure at the unit cell (UC) level. The theoretical principles and the different experimental methods of this technique are discussed in Chap. 3. In particular, polarized neutron diffraction (PND) is introduced as a unique approach to reveal precise and exclusive information about the magnetic structure, even for very small magnetic moments. As this work is closely linked to the polarized neutron single crystal diffractometer POLI at the Heinz Maier-Leibnitz Zentrum (MLZ) in Garching, Germany, it additionally aims at extending the PND capabilities of this instrument and advancing the PND technique in general. In this frame, a generally applicable and straightforward approach to determine the absolute sign of the DMI vector by PND is established in Chap. 4 and supplemented by a corresponding symmetry analysis of the $Ba_2TGe_2O_7$ compounds. As new instrumental developments at POLI, the implementation of a suitable software for ^{3}He spin polarisation monitoring and the extension of the available PND instrument options are approached. For the latter, the objective is the design and commissioning of an upgraded high-field PND setup option utilizing a newly acquired 8 T superconducting magnet with asymmetric field geometry and a polarizing Fe/Si supermirror bender. These instrumental ambitions are addressed in Chap. 5.

For this work's systematic study of the germanium-based melilites, the first goal is a comprehensive investigation of the newly synthesized polycrystalline samples of the $Ba_2Cu_{1-x}Mn_xGe_2O_7$ solid solution series. This goal can be divided into three steps. As there is a lack of atomic information on these mixed samples, the first one is a detailed structural characterization. For this purpose, high-resolution neutron and laboratory X-ray powder diffraction measurements are conducted in Sec. 7.2 to evaluate the crystal quality, detect potential impurities and precisely determine composition dependent lattice and atomic parameters. The next step is the characterization of the macroscopic magnetic properties and outlining the composition dependent magnetic phase diagram for the $Ba_2Cu_{1-x}Mn_xGe_2O_7$ compounds. This is achieved by temperature-dependent heat capacity (HC) and macroscopic magnetization measurements in Sec. 7.3, providing valuable information about the magnetic ordering type, the existence of (weak) FM contributions and the magnetic phase boundaries. To finalize this study, the last step is the identification of the microscopic magnetic orderings in the individual phases. This goal is addressed by low temperature neutron powder diffraction (PD), revealing two considerably different magnetic structures for the Cu- and Mn-rich compounds in Secs. 7.4 and 7.5, respectively.

For the three pure $Ba_2TGe_2O_7$ (T = Cu, Co, Mn) compounds, the lattice and atomic

parameters have been largely settled and the incommensurate magnetic structure of $Ba_2CuGe_2O_7$ has already been exhaustively studied in the literature. Thus, this work focuses mostly on the field-induced structures in the paramagnetic (PM) and the commensurate WFM phases of all three compounds as they have drawn hardly any consideration in previous studies. Using the flipping ratio (FR) method, described in detail in Sec. 3.3.1 and denoting PND in high applied magnetic fields, several goals are addressed. First, FR in the PM phase of all three $Ba_2TGe_2O_7$ compounds is utilized to reveal precise values for the magnitude and directions of the field-induced magnetic moments, the susceptibility tensors and the magnetic form factors, providing a valuable insight into the microscopic magnetic properties of the different TM ions and anisotropy effects. The results are presented and discussed in Secs. 6.2.2, 7.4.1 and 7.5.1 for T = Co, Cu and Mn, respectively. Second, the low temperature commensurate WFM phases in $Ba_2CoGe_2O_7$ and at high field in $Ba_2CuGe_2O_7$ are studied by the FR method in Secs. 6.3.2 and 7.4.2. This provides access to the microscopic details of both the field-induced FM and ordered AFM structure. In combination with the DMI symmetry analysis in Chap. 4, these details are used in Secs. 6.3.3 and 7.4.3 to determine for the first time by PND the absolute sign of the DMI vector parameter in $Ba_2CuGe_2O_7$ and $Ba_2CoGe_2O_7$, respectively. As last objective, the WFM ground state of $Ba_2CoGe_2O_7$ is addressed by zero-field spherical neutron polarimetry (SNP) in Sec. 6.4. This study discloses the highly sensitive magnetic field dependency of the AFM domain distribution and answers conclusively the long standing question of the true magnetic ground state symmetry in $Ba_2CoGe_2O_7$.

The final and most delicate goal of this work aims for the development and implementation of a novel maximum entropy approach that overcomes the classical limitation to collinear magnetic moments and centrosymmetric structures for the reconstruction of magnetization densities from PND data. This novel approach, which is mathematically elaborated in Chap. 3, demonstrates its proper functioning by the application to the PND data of the noncentrosymmetric melilite-type $Ba_2TGe_2O_7$ compounds in Chap. 8. The revealed peculiar magnetization density shapes for the three $Ba_2TGe_2O_7$ compounds are directly related to their respective electronic configuration and provide an astonishing insight into the connection between the magnetization and the unpaired electron density. Thus, this novel maximum entropy approach could open up new and advanced perspectives and applications for PND in general.

2. The family of $Ba_2TGe_2O_7$

A major subgroup of the melilite-type compounds is formed by the barium germanates with general stoichiometry $Ba_2TGe_2O_7$. Many members of this family were successfully synthesized as single crystals with the $P\bar{4}2_1m$ melilite structure (e.g. T = Co, Cu, Fe, Mg, Mn, Zn [15, 99–102]). However, the focus within this work is on the magnetic T = Cu, Co and Mn compounds, exhibiting remarkable optical, magnetic and multiferroic properties [86, 95].

2.1. Atomic structure

The atomic arrangement of the melilite structure in the tetragonal unit cell (UC) of $Ba_2TGe_2O_7$ is illustrated in Fig. 2.1. It is composed of layers of corner sharing TO_4 and GeO_4 tetrahedrons (blue and green in Fig. 2.1), separated by layers of Ba atoms (gray spheres in Fig. 2.1). Within the tetrahedral layers, two GeO_4 tetrahedrons with the Ge atom at the 4e Wyckoff position are linked together by the oxygen atom at

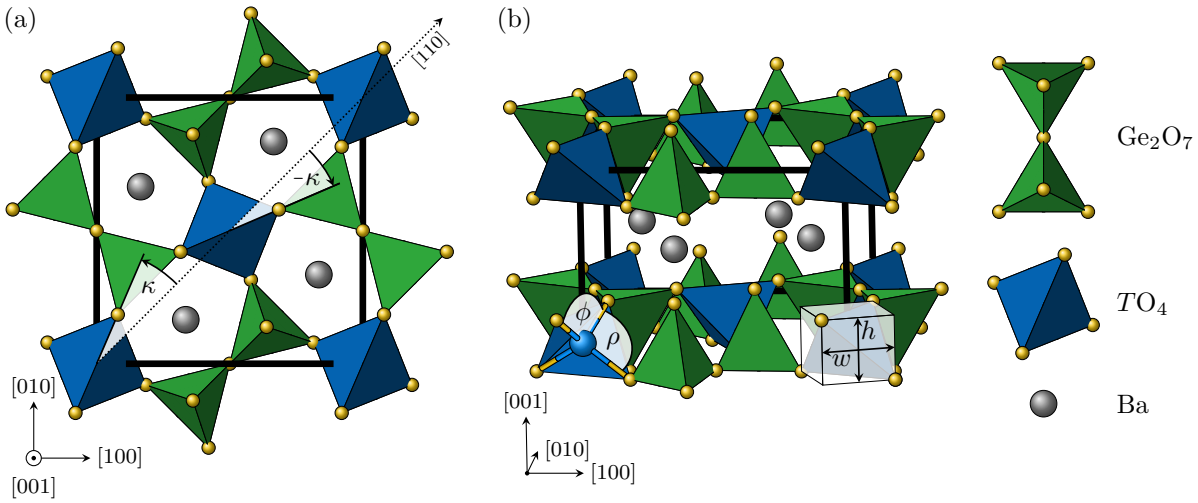

Figure 2.1.: The atomic arrangement in the UC of $Ba_2TGe_2O_7$ having the $P\bar{4}2_1m$ melilite structure. The germanium and cobalt atoms are located in the center of the blue and green tetrahedrons, respectively. The oxygen atoms are shown as yellow spheres. The barium atoms, which are located between two TO_4/Ge_2O_7 layers, are shown as gray spheres. Panel (a) provides a top view of the UC and displays the alternating deviation angle κ of the TO_4 tetrahedron. In panel (b), a perspective view of the UC illustrates the layered arrangement of the melilite structure. In addition, the bond angles ϕ and ρ characterizing the deformation of the TO_4 tetrahedron with height h and width w are defined. The compound specific values for the angles and the h/w compression are given in Table 2.1.

Table 2.1.: Literature values for lattice parameters and specific bond lengths and angles in $Ba_2TGe_2O_7$ with T = Cu, Co and Mn at RT. The shown angles are defined in Fig. 2.1 and $d_{T\text{-O}}$ denotes the T-O distance. In addition, the compression $c_t = 1 - h/w$ is listed, which is defined by the height h and the width w of the TO_4 tetrahedron illustrated in Fig. 2.1(b). For T = Co and Mn, the angles, distance and compression are calculated from the atomic positions as they are not directly provided by the authors.

	$Ba_2CuGe_2O_7$	$Ba_2CoGe_2O_7$	$Ba_2MnGe_2O_7$
a [Å]	8.466	8.392(1)	8.509(2)
c [Å]	5.445	5.561(1)	5.529(5)
κ [deg]	20.0(3)	21.71(2)	22.59(3)
ϕ [deg]	123.6(4)	116.67(6)	116.41(8)
ρ [deg]	102.9(3)	106.00(3)	106.11(4)
$d_{T\text{-O}}$ [Å]	1.95(1)	1.9825(7)	2.05(1)
c_t [%]	24(1)	12.77(7)	12.3(1)
Ref.	[103]	[104]	[105]

the $2c$ position to form Ge_2O_7 dimers as clearly visible in Fig. 2.1(a). These dimers are connected by the TO_4 tetrahedrons with the T atom at the $2b$ and the oxygen atom at the $8f$ positions. This leads to an alternating left and right twist of the two nonequivalent TO_4 tetrahedrons in the UC, visible in Fig. 2.1(a) by a deviation angle κ of the upper-lying oxygen bond from the [110] direction. The precise atomic positions at room-temperature (RT) for T = Cu, Co and Mn are listed in Refs. [103], [104] and [105], respectively. Using these values, the angle κ can be calculated for all three compositions and is listed in Table 2.1 together with the tetragonal lattice parameters and further details on the TO_4 tetrahedron. The angle κ is increasing with larger T-O bond distance $d_{T\text{-O}}$ from Cu to Mn, which can be attributed to differences in the ionic radii [105].

The deformation of the TO_4 tetrahedron, which plays an important role for the multiferroicity in the novel spin-dependent p-d hybridization model as recently demonstrated in high-pressure experiments by Nakajima *et al.* [106], is characterized by the O-T-O bond angles ϕ and ρ defined in Fig. 2.1(b) and listed in Table 2.1. These angles are related to the ratio between the height h and and width w of the tetrahedron, indicated also in Fig. 2.1(b). For a regular tetrahedron with $h/w = 1$, both angles ϕ and ρ would approach a value of around 109.5°. For the T = Co and Mn compounds, almost equal values of around $\phi \approx 116.5°$ and $\rho \approx 106.0°$ are observed, leading to an overall compression $c_t = 1 - h/w$ of around 12.5% for the TO_4 tetrahedron in c direction. Barone *et al.* [94] relate this compression to the quasilayered structure of the melilites. For T = Cu, a significantly larger degree of tetrahedral compression with around 25% is observed, which can be attributed to an enhancement by the Jahn-Teller (JT) active properties of Cu compared to Co and Mn, discussed in the next section [105].

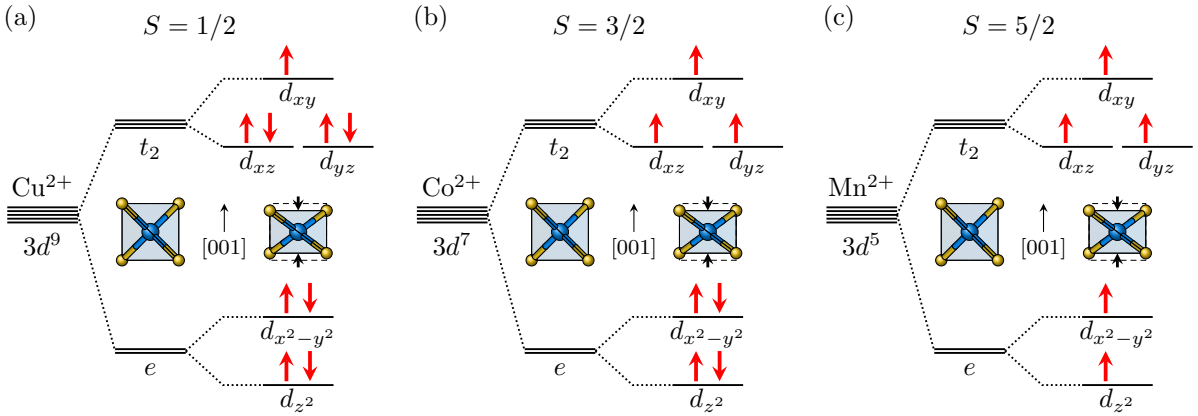

Figure 2.2.: Electronic structure of the $3d$ levels for the T^{2+} ions in $Ba_2TGe_2O_7$ with (a) T = Cu, (b) T = Co and (c) T = Mn. The tetrahedral environment induces a crystal-field splitting of the $3d$ orbitals in triply degenerated t_2 states and doubly degenerated e states. A compression of the ideal tetrahedron lifts this degeneracy almost completely. The expected spin configurations for the individual $3d$ orbitals in the distorted tetrahedral environment are discussed in the text and shown by the red arrows. In addition, the total spin S is listed.

2.2. Magnetic structure

In the melilite structure, the magnetic transition metal (TM) ion has an oxidation state of +2 and is situated in a tetrahedral environment; thus, the electronic $3d$ levels are split into triply degenerated t_2 states and lower lying doubly degenerated e states. If the tetrahedral compression along the c axis is considered, the degeneracy is further lifted such that the t_2 states split into the higher lying d_{xy} orbital and the degenerate, lower lying d_{xz} and d_{yz} orbitals. For the e states in the distorted tetrahedron, the $d_{x^2-y^2}$ orbital has a higher energy than the d_{z^2} orbital [107]. Assuming a weak crystal-field splitting by the tetrahedral environment compared to the energy gain associated with the first Hund's rule originating from intra-atomic coulomb interactions, a high spin configuration as shown in Fig. 2.2 can be deduced with spin quantum number $S = 1/2$, $3/2$ and $5/2$ for T = Cu, Co and Mn, respectively. Notably, only the electron configuration of the Cu^{2+} ion in Fig. 2.2(a) has an unequal filling of the higher and lower lying t_2 orbitals, and thus can be considered as JT active [108]. This JT effect in the Cu^{2+} electronic configuration clearly favours the previously discussed tetrahedral compression as the distortion-induced energy gain of the completely filled d_{xz} and d_{yz} orbitals exceeds the energy increase of the half filled d_{xy} orbital [107].

Starting from the electronic configuration, the atom's magnetism is driven by the unpaired electrons, which occupy states with orbital momenta $\mathbf{l}_i$ and spins $\mathbf{s}_i$. For the light TM atoms, Coulomb interactions between the electrons are more important than spin-orbit coupling (SOC) for a single electron, and thus the effective magnetic moment m_{eff} per ion can be well described by the Russell-Saunders coupling [109]. In this approach, the total orbital ($\mathbf{L} = \sum_i \mathbf{l}_i$) and spin ($\mathbf{S} = \sum_i \mathbf{s}_i$) angular momentum are given by the sum over the individual electrons and finally couple to the atoms total angular momentum $\mathbf{J} = \mathbf{L} + \mathbf{S}$. This $\mathbf{J}$ is connected to an effective magnetic moment

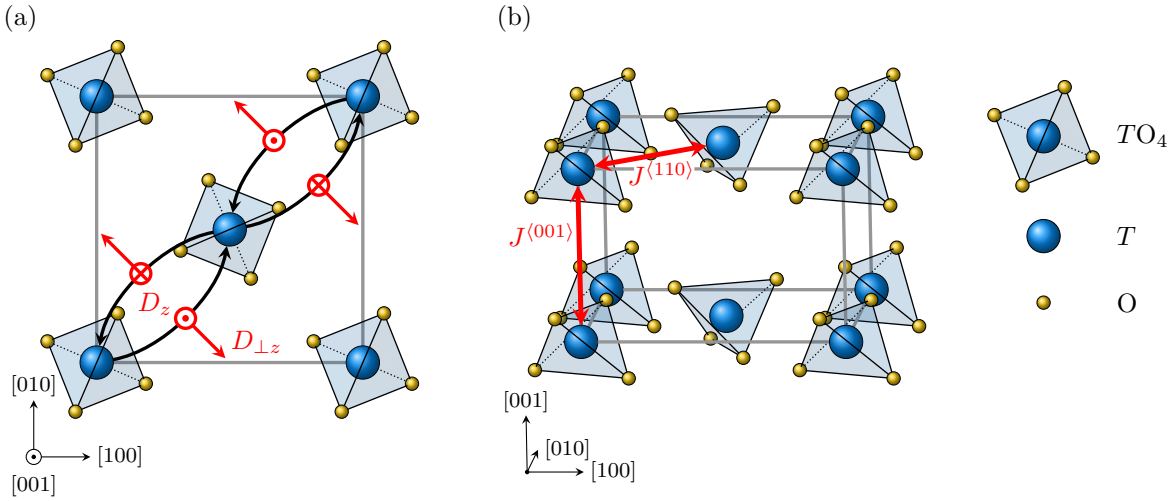

Figure 2.3.: Visualization of the potential exchange interactions between nearest neighboring TM ions (blue spheres), located in the distorted tetrahedral environment of $Ba_2TGe_2O_7$. (a) Arrangement of the in-plane ($D_{\perp z}$) and out-of-plane (D_z) Dzyaloshinskii-Moriya interaction (DMI) vector component for a bonding direction as indicated by the curved black arrows. (b) Intra-plane ($J^{\langle 110\rangle}$) and inter-plane ($J^{\langle 001\rangle}$) symmetric exchange couplings indicated by the red arrows.

given by

$$m_{\text{eff}} = \underbrace{\left(\frac{3}{2} + \frac{S(S+1) - L(L+1)}{2J(J+1)}\right)}_{g_J} \sqrt{J(J+1)}\mu_B \tag{2.1}$$

with g_J the Landé g-factor, μ_B the Bohr magneton and S, L and J the spin, orbit and total angular momentum quantum number [109]. As the only degenerate orbitals d_{xz} and d_{yz} in the compressed tetrahedral environment are both either partially or fully occupied for the three electron configurations of Cu^{2+}, Co^{2+} and Mn^{2+} depicted in Fig. 2.2, the orbital angular momenta are typically assumed to be quenched ($L = 0$). Thus, a spin-only effective magnetic moment of $m_{\text{eff}} = g_e\mu_B\sqrt{S(S+1)} = 1.73\,\mu_B$ for Cu, $3.87\,\mu_B$ for Co and $5.92\,\mu_B$ for Mn is expected assuming the free electron spin g-factor of $g_e \simeq 2.0023$.

To describe the emergence of long range magnetic order at low temperatures, various exchange interactions need to be considered. First, the classical symmetric exchange $\propto \mathbf{S}_1 \cdot \mathbf{S}_2$ between nearest neighboring T atoms in the diagonal $\langle 110\rangle$ and vertical $\langle 001\rangle$ directions with exchange constants $J^{\langle 110\rangle}$ (intra-plane) and $J^{\langle 001\rangle}$ (inter-plane), respectively [86]. These symmetric exchange paths are illustrate in Fig. 2.3(b). Although the intra-plane nearest neighbor (NN) distance $d^{\langle 110\rangle}$ is slightly larger than the inter-plane distance $d^{\langle 001\rangle}$ ($d^{\langle 110\rangle}/d^{\langle 001\rangle}$ is around 1.10 for Cu, 1.07 for Co and 1.09 for Mn), $J^{\langle 110\rangle}$ is expected to be significantly larger than $J^{\langle 001\rangle}$ as the magnetic square lattice layers are separated by the large Ba atoms in c direction [14, 15]. A positive or negative sign of the exchange constant results in an antiferromagnetic (AFM) or ferromagnetic (FM) coupling, respectively. Note that Zheludev *et al.* [29] proposed to additionally split the intra-plane exchange contribution into $J_{\parallel z}^{\langle 110\rangle} S_{i,z}S_{j,z}$ and $J_{\perp z}^{\langle 110\rangle}(S_{i,x}S_{j,x} + S_{i,y}S_{j,y})$ to ac-

count for anisotropies induced by the complex crystal-field level scheme resulting from SOC. Within this work, the index x, y and z refers to the component in the crystal a, b and c direction, if not stated otherwise. Although this approach of splitting the intra-plane contribution was adapted in several reports on $Ba_2CoGe_2O_7$ and related compounds (see Refs. [90, 92, 110–114]), it is important to emphasize that it is a phenomenological approach based on effective spins and with hidden microscopic meaning [29]. A general review on the usage of effective spins in Co^{2+} systems is provided by Piwowarska *et al.* [115]. A further discussion on anisotropies resulting from crystal field effects combined with SOC within a single TM ion can be found below.

As second interaction, the antisymmetric DMI $\propto \mathbf{S}_1 \times \mathbf{S}_2$ with vectorial exchange constant $\mathbf{D}$ is allowed due to a lack of inversion symmetry between neighboring T ions. The DMI vector parameter $\mathbf{D}$ is restricted by the local symmetry to the plane perpendicular to the bonding direction. Following one of these diagonal bonding directions, the DMI has a uniform in-plane component $D_{\perp z}$ and an alternating out-of-plane component D_z. As the DMI is antisymmetric, the sign of $\mathbf{D}$ changes if the bonding direction is reversed. This situation is visualized in Fig. 2.3(a) for bonds in [110] direction. A detailed symmetry analysis of $\mathbf{D}$ and its full pattern in the UC are developed in Sec. 4.2. As the D_z component induces an alternating canting in otherwise collinear magnetic structures, this out-of-plane DMI component can be associated with the emergence of a weak ferromagnetic (WFM) moment in the ab-plane. In contrast, the in-plane component $D_{\perp z}$ favours a uniform canting, which may stabilize helical spin structures in the (110) or $(1\bar{1}0)$ plane.

In addition, a single ion anisotropy (SIA) $\propto S_z^2$ with anisotropy constant Λ and a Zeeman contribution $\propto \mathbf{S}^\mathsf{T}\mathcal{G}\mathbf{B}$ might be present. For the first term, $\Lambda < 0$ indicates an easy-axis and $\Lambda > 0$ an easy-plane type magnetic anisotropy, which is usually driven by crystal field effects and SOC [116]. The latter term describes the potential magnetic energy of the ion's magnetic moment in an applied external magnetic magnetic field $\mathbf{B}$. In general, the relation of the ion's effective spin $\mathbf{S}$ to this magnetic moment can be described by the g-tensor $\mathcal{G}$ and might be anisotropic if SOC is present. In the compressed tetrahedral environment, $\mathcal{G}$ is restricted to two principal values $g_{\perp z}$ and $g_{\parallel z}$ by symmetry [111]. Note that these anisotropic contributions may directly affect the magnetic susceptibility tensor χ that connects the applied magnetic field $\mathbf{B}$ with the induced magnetization $\mathbf{m} = \chi\mathbf{B}$ in both the paramagnetic (PM) and ordered state. This susceptibility tensor is generally symmetric ($\chi_{ij} = \chi_{ji}$) and restricted to $\chi_{11} = \chi_{22}$ and $\chi_{12} = \chi_{13} = \chi_{23} = 0$ for the melilite-type compounds with space group $P\bar{4}2_1m$. For this reason, the anisotropy is reflected by the ratio χ_{11}/χ_{33}.

Combining the discussed magnetic interactions and contributions, the effective spin Hamiltonian can be expressed as

$$\mathcal{H} = \sum_{\substack{NN \\ \langle 110 \rangle}} \Big(\underbrace{J^{\langle 110 \rangle} \mathbf{S}_i \cdot \mathbf{S}_j}_{\substack{\text{intra-plane} \\ \text{exchange}}} + \underbrace{\mathbf{D} \cdot (\mathbf{S}_i \times \mathbf{S}_j)}_{\text{DMI}} \Big) + \sum_{\substack{NN \\ \langle 001 \rangle}} \underbrace{J^{\langle 001 \rangle} \mathbf{S}_i \cdot \mathbf{S}_j}_{\substack{\text{inter-plane} \\ \text{exchange}}} + \sum_i \Big(\underbrace{\Lambda S_{i,z}^2}_{\text{SIA}} - \underbrace{\mu_B \mathbf{S}_i^\mathsf{T} \mathcal{G} \mathbf{B}}_{\text{Zeeman}} \Big) \quad (2.2)$$

with the sums over the NNs j for atom i in $\langle 110 \rangle$ and $\langle 001 \rangle$ directions. Depending on the TM ion T in $Ba_2TGe_2O_7$, different exchange types are dominant, and thus various

magnetic structures are realized and outlined in the following for T = Cu, Co and Mn.

2.2.1. Helimagnetism in $Ba_2CuGe_2O_7$

In $Ba_2CuGe_2O_7$, the Cu^{2+} ion contains only one unpaired $3d$ electron ($S = 1/2$) in the d_{xy} orbital (see Fig. 2.2). Thus, the SIA is expected to be negligibly small [116, 117]. In contrast, the g-tensor can have anisotropic components $g_{\perp z}$ and $g_{\parallel z}$ that are different from the free electron g-value. As SOC mixes the singly occupied d_{xy} orbital with the completely occupied d_{xz}, d_{yz} and $d_{x^2-y^2}$ orbitals, first-order perturbation theory of the spin-½ system provides an admixture of exited states to the ground-state wavefunctions. By applying a magnetic field, the operator-based Zeeman Hamiltonian $\propto (\hat{\mathbf{L}} + g_e\hat{\mathbf{S}}) \cdot \mathbf{B}$ lifts the degeneracy of these wavefunctions by a field direction dependent Zeeman energy, which can be expressed in terms of the effective spin Hamiltonian (see Eq. (2.2)) by the anisotropic g-tensor components [118]. Electron spin resonance (ESR) spectroscopy revealed values of $g_{\perp z} = 2.044$ and $g_{\parallel z} = 2.474$ in $Ba_2CuGe_2O_7$, corresponding well to the results of Cu^{2+} ions in other compounds with compressed tetrahedral environments [119, 120]. This easy-axis type anisotropy in the g-tensor with $g_{\perp z}/g_{\parallel z} \approx 0.83$ is also reflected in the susceptibility tensor as demonstrated by Zheludev *et al.* [119] with magnetization measurements at 2 K resulting in $\chi_{11}/\chi_{33} \approx 0.70$ for $B > 3$ T.

For the magnetic ground state in $Ba_2CuGe_2O_7$, an AFM spin spiral structure was identified in zero magnetic field below an ordering temperature of around 3.26 K using neutron diffraction [117]. This incommensurate magnetic structure can be described by an AFM cycloid with propagation vector $\boldsymbol{\tau}$ in [110] direction and spins confined to the $(1\bar{1}0)$ plane as illustrated in Fig. 2.4(a). It is stabilized by the competition between the AFM isotropic exchange $J^{\langle 110\rangle} > 0$ and the in-plane DMI $D_{\perp z}$ for nearest neighboring Cu^{2+} ions. This competition results in a uniform canting [36]

$$\phi = \tan^{-1}\left(\frac{D_{\perp z}}{J^{\langle 110\rangle}}\right) \tag{2.3}$$

of neighboring AFM spins in propagation direction as shown in Fig. 2.4(a). For Cu-bonds in $[1\bar{1}0]$ direction, which is perpendicular to the helical spin plane, only the isotropic exchange is active forming collinear AFM spin planes (light blue planes with uniform ϕ in Fig. 2.4(a)). Due to the tetragonal symmetry, a second equivalent magnetic domain with propagation direction $[1\bar{1}0]$ and spin rotation plane (110) is present in zero magnetic field, resulting in four magnetic satellites at $(h \pm \zeta, k \pm \zeta, l)$ and $(h \pm \zeta, k \mp \zeta, l)$ for $h+k$-odd Bragg reflections. The incommensurability parameter $\zeta \approx 0.0273$ is directly related to the rotation angle of the AFM cycloid, which is determined to be $\phi = 2\pi\zeta \approx 9.83°$ [121].

In c-direction, a FM stacking of the AFM spin spiral structure was observed, revealing a negative $J^{\langle 001\rangle}$ exchange constant. This could be confirmed by inelastic neutron scattering measurements of the spin wave dispersion relation, determining $J^{\langle 001\rangle} = -0.013(1)$ meV and $J^{\langle 110\rangle} = 0.482(3)$ meV [122]. The high $|J^{\langle 001\rangle}/J^{\langle 001\rangle}| = 37(3)$ ratio suggests a strong 2D character of the magnetic system, which is further endorsed by the

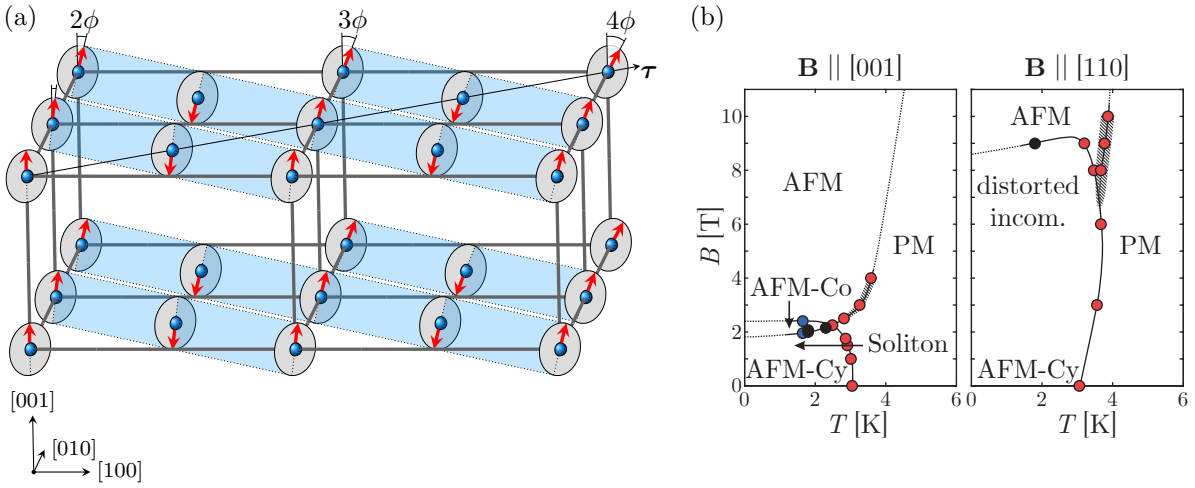

Figure 2.4.: (a) Zero-field AFM spin spiral structure in $Ba_2CuGe_2O_7$ with magnetic propagation vector $\boldsymbol{\tau}$ in [110] direction and a $(1\bar{1}0)$ helical spin plane. Collinear spins with the same rotation angle ϕ form AFM planes which are indicated in light blue. (b) Field-temperature phase diagram of $Ba_2CuGe_2O_7$ for out-of-plane (left panel) and in-plane (right panel) magnetic fields, modified from Ref. [126]. Blue points are from neutron diffraction, black points from magnetic susceptibility and red points from heat capacity. The almost AFM cycloidal phase is denoted as AFM-Cy, the AFM cone phase as AFM-Co, the commensurate AFM phase as AFM and the PM phase as PM. For in-plane fields, the AFM cycloidal phase transforms with increasing field strength to a distorted incommensurate structure and for out-of-plane fields to a soliton lattice as discussed in the text.

2D-like critical exponent $\beta \approx 0.15$ in Ref. [117]. Utilizing Eq. (2.3), the magnitude of $D_{\perp z}$ can be estimated to be 0.0835(5) meV.

Interestingly, weak higher-order harmonics of 3ζ could be evidenced in $Ba_2CuGe_2O_7$ by zero-field neutron diffraction, indicating a slight distortion of the ideal AFM cycloid structure [123]. This distortion was attributed to an additional KSEA interaction $(2J^{\langle 110\rangle})^{-1}(\mathbf{S}_i \cdot \mathbf{D}_{\perp z})(\mathbf{S}_j \cdot \mathbf{D}_{\perp z})$, first introduced by **K**aplan, **S**hekhtman, **E**ntin-Wohlman and **A**harony [124, 125], creating an easy-axis type two-ion anisotropy exactly compensating the easy-plane anisotropy of strength $D^2/2J$ induced by the DMI, and thus restoring the local $O(3)$ symmetry of the Heisenberg Hamiltonian [121]. This additional anisotropy acts as an effective magnetic field along the [001]-direction and forces the local AFM spins to the tetragonal plane. Thus, a slower spin rotation for regions with AFM spins almost in the ab plane and a faster spin rotation for regions with AFM spins almost along c direction becomes energetically favourable, finally leading to the observed distortion and the appearance of odd higher-order harmonics [123].

Moreover, it was theoretically predicted by Bogdanov *et al.* [37] that the alternating out-of-plane component D_z, which favours an in-plane canting of the AFM spins close to the ab plane, might induce a WFM sinusoidal structure perpendicular to the helical plane with the same periodicity as the AFM spin spiral. The presence of such an incommensurate FM structure would cause satellites at $(h\pm\zeta, k\mp\zeta, l)$ and $(h\pm\zeta, k\pm\zeta, l)$ for $h+k$-even Bragg reflections. And indeed, Mühlbauer *et al.* [127] could evidence these four FM satellites centered around the Γ point by small angle neutron scattering.

Applying a magnetic field to this non-planar, slightly distorted AFM spin spiral structure in $Ba_2CuGe_2O_7$ reveals a rather complex phase diagram as illustrated in Fig. 2.4(b). For small in-plane magnetic fields (right panel of Fig. 2.4(b)), the degeneracy between the two magnetic domains observed in zero field is lifted, as the domain with spin rotation plane normal to the field direction is energetically favoured by the Zeeman effect. As a result, the intensities of the $(h \pm \zeta, k \mp \zeta, l)$ magnetic satellites increase whereas the intensities of the $(h \pm \zeta, k \pm \zeta, l)$ satellites decrease for an applied magnetic field in [110] direction. To reach a single domain state, it is already sufficient to either field-cool the sample in fields as small as 10 mT or apply magnetic fields above 0.3 T below the magnetic transition [126, 128]. With an increasing applied field strength, the entire spin rotation plane is aligned perpendicular to the in-plane magnetic field direction. This continuous spin plane rotation, saturating at around 1 T, is accompanied by a change in the propagation vector $\boldsymbol{\tau}$, such that equal angles are formed by the normal of the spin plane and $\boldsymbol{\tau}$ with the a axis of the crystal, denoted as 'bisection rule' by Zheludev *et al.* [128]. For even higher fields, the cycloidal spin structure transforms into a strongly distorted incommensurate phase, characterized by the emergence of higher-order harmonics. Interestingly, also even multiples of ζ appear, which might be attributed to the interaction of the magnetic field with the WFM sinusoidal structure perpendicular to the helical plane. As this interaction favours energetically only the half of the period with WFM moments parallel to the applied field, it might induce asymmetric distortions that give rise to the observed even-order harmonics [126]. For a critical in-plane field of around 9 T, an incommensurate to commensurate (I/C) transition is observed. The resulting commensurate high-field structure is characterized by an AFM arrangement in the tetragonal plane that is stacked ferromagnetically in c direction. Experimentally, it is evidenced by the vanishing of the incommensurate satellites and the appearance of magnetic intensity at the commensurate $h + k$-odd reflections [126].

If an external magnetic field is applied in [001] direction (left panel of Fig. 2.4(b)), it aligns with the effective magnetic field caused by the KSEA interaction, and thus strengthens its effects. This results in a gradual increase in the distortion of the spiral spin structure, visible by an increased weight of the 3ζ harmonics and a decrease of the incommensurability parameter ζ [121]. With increasing field-induced anisotropy, the cycloid is distorted towards a soliton lattice, which is illustrated in Fig. 2.5(a). This spin structure has almost commensurate AFM regions (central part of Fig. 2.5(a) with slowly increasing rotation angle ϕ) that are regularly separated by AFM Néel-type domain walls (outer parts in Fig. 2.5(a) with quickly changing rotation angle ϕ). If the applied magnetic field contains a small in-plane component, one of the two magnetic domains is selected as discussed before. Above a critical field of around 1.95 T, the plane of spin rotation is no longer conserved and an AFM cone structure as visualized in Fig. 2.5(b) emerges. This phase is characterized by a commensurate in-plane AFM moment combined with a conical AFM spin component with rotation plane and in-plane propagation vector $\boldsymbol{\tau}$ perpendicular to the commensurate AFM moment. This leads to a nutation of the AFM spins around the commensurate AFM direction forming a cone-like AFM structure [129]. An in-plane component of the applied magnetic field aligns the direction of the commensurate in-plane AFM moment perpendicular and thus

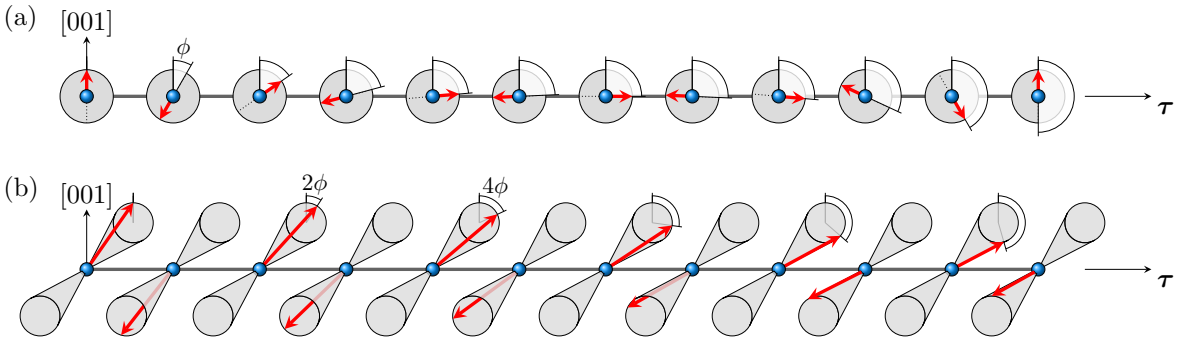

Figure 2.5.: Illustration of (a) the magnetic soliton lattice and (b) the AFM cycloidal structure that are proposed as incommensurate magnetic structures in $Ba_2CuGe_2O_7$ for an applied magnetic field close to the [001] direction by Mühlbauer *et al.* [129].

the propagation vector parallel to it. Therefore, incommensurate magnetic reflections at $(h \pm \zeta, k \pm \zeta, l)$ and commensurate magnetic intensities at (hkl) with $h + k$-odd are observed for an in-plane component of the magnetic field in [110] direction. Notably, these commensurate and incommensurate intensities in the AFM cone phase are clearly distinct from the purely incommensurate intensities at $(h \pm \zeta, k \mp \zeta, l)$ observable in the AFM cycloid phase with corresponding field direction. For an almost perfect alignment of the applied magnetic field in [001] direction (misalignment $\leq 5°$), a small discontinuity in the incommensurability parameter ζ at the phase transition from the cycloidal to the conical phase is observed, whereas for higher misalignment angles (e.g. 15°) this transition is rather continuous. Moreover, no higher-order harmonics like 3ζ are observed in the AFM cone phase for a proper alignment between the applied magnetic field and the [001] direction, which might indicate that the external field causes a canting of the commensurate AFM component out of the *ab* plane rather than a distortion of the cycloidal component. For higher misalignment angles, higher-order harmonics (primarily 2ζ) are again observed, which might be attributed to a distortion induced by the interaction between the magnetic field and WFM moments induced by the alternating D_z component [126, 129, 130]. At even higher fields of around 2.4 T, the I/C transition finally takes place, experimentally evidenced by vanishing incommensurate reflections [129].

2.2.2. Weak ferromagnetic structure in $Ba_2CoGe_2O_7$

The Co^{2+} ion in $Ba_2CoGe_2O_7$ has three unpaired electrons ($S = 3/2$) in the t_2 orbitals (see Fig. 2.2), and thus a considerable SIA is expected [99]. Indeed, a strong easy-plane anisotropy was found in $Ba_2CoGe_2O_7$, which forces the spins to the tetragonal plane [111, 135]. In contrast to $Ba_2CuGe_2O_7$, this prevents the formation of any incommensurate helical state as favoured by the uniform in-plane DMI component. Consequently, a commensurate AFM structure (i.e. $J^{\langle 110 \rangle} > 0$) below $T_N = 6.7$ K with magnetic moments confined to the *ab* plane and FM stacking in *c* direction (i.e. $J^{\langle 001 \rangle} < 0$) was observed as magnetic ground state by neutron diffraction [29]. By terahertz absorption experiments, Miyahara and Furukawa [135] estimated the NN in-plane exchange constants by $J^{\langle 110 \rangle} =$

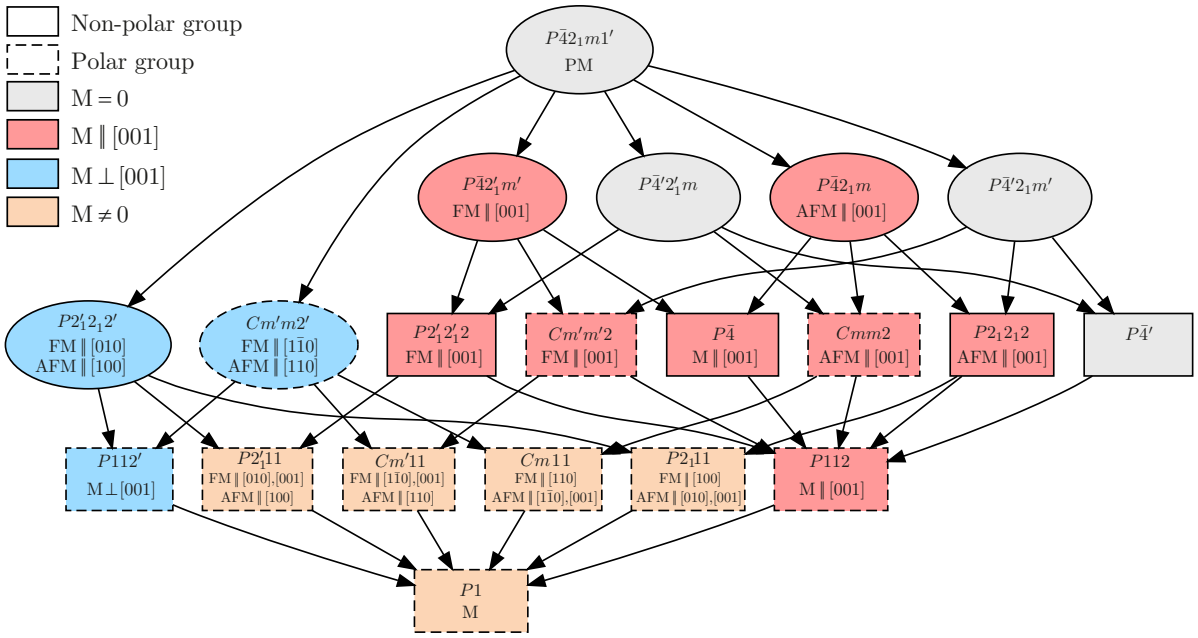

Figure 2.6.: Graph of all possible magnetic space groups in Belov-Neronova-Smirnova (BNS) notation [131, 132] for a magnetic ordering resulting from the $P\bar{4}2_1m1'$ symmetry of the PM structure and a zero propagation vector. The k-maximal magnetic groups (i.e. the groups with the highest magnetic symmetry) are elliptically framed. Magnetic space groups that do not allow a magnetic ordering for the Co^{2+} ions are marked in grey. The groups that allow a magnetic order in the tetragonal plane, along the c direction or in all three dimensions are highlighted in blue, red or orange, respectively. Restrictions on the magnetic ordering type in the high-symmetry directions are additionally listed. M denotes an arbitrary magnetic ordering type that is potentially limited to a plane or direction. Polar magnetic space groups, which leave at least one line of points unmoved, may allow a ferroelectric polarization and are indicated by a dashed frame. The graph was modified from the Graphviz [133] output of the k-SUBGROUPSMAG program from the Bilbao Crystallographic Server [134].

0.175 meV, $|D_z| = 0.007$ meV and $\Lambda = 1.4$ meV. As SOC mixes the singly occupied t_2 orbitals with the completely occupied e orbitals in the electronic configuration of $Ba_2CoGe_2O_7$, an admixture of higher-order states to the ground-state wavefunction is expected, leading to anisotropic g-tensor components as discussed for $Ba_2CuGe_2O_7$ in the previous section [136]. This was confirmed by ESR studies in Ref. [111], revealing $g_{\perp z} = 2.3$ and $g_{\parallel z} = 2.1$, which are close to the results in the related $Sr_2CoGe_2O_7$ compound with $g_{\perp z} = 2.28$ and $g_{\parallel z} = 2.23$ [114]. This easy-plane anisotropy in the g-tensor and the $\Lambda > 0$ is also reflected in the susceptibility tensor of $Ba_2CoGe_2O_7$ with a ratio of around $\chi_{11}/\chi_{33} \approx 2$ as shown by magnetization measurements in Ref. [43, 99].

To identify the magnetic ground state symmetry of $Ba_2CoGe_2O_7$, an overview of all possible magnetic space groups resulting from the parent symmetry $P\bar{4}2_1m1'$ is given in Fig. 2.6. As an in-plane AFM order of the Co moments was experimentally evidenced, all magnetic space groups that allow only a magnetic ordering in [001] direction (red in Fig. 2.6) or no magnetic ordering at all (gray in Fig. 2.6) can be excluded as ground states. Therefore, only the two high-symmetry magnetic space groups $P2_1'2_12'$ and $Cm'm2'$ can be identified as potential candidates with AFM spins along the high-symmetry [100]

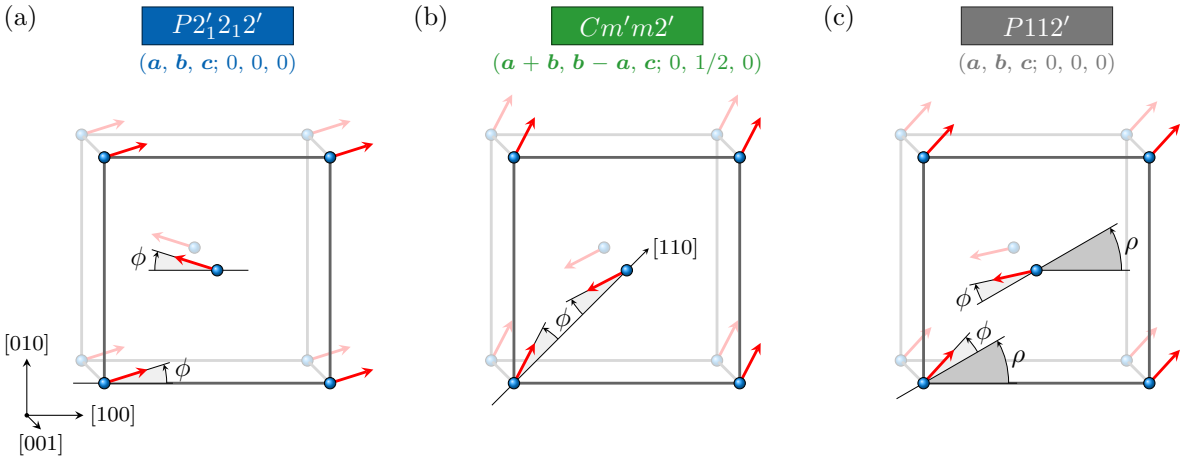

Figure 2.7.: Possible magnetic ground state symmetries and their basic spin configuration for the $P\bar{4}2_1m$ parent space group and an in-plane AFM structure with zero propagation vector. The high-symmetry configurations (a) $P2'_12_12'$ and (b) $Cm'm2'$ have an AFM moment in the lattice and diagonal direction, respectively. The (c) $P112'$ configuration breaks both the mirror planes and the screw axes of the parent space group, resulting in an AFM moment in an arbitrary in-plane direction enclosing an angle ρ with the a axis. All three symmetries exclude magnetic moments in c direction but allow an spontaneous WFM moment perpendicular to the AFM moment, resulting in an in-plane canting ϕ of the AFM spins. Below the BNS label, the lattice vector transformation and origin shift from the setting of the parent group to the standard setting of the magnetic space group is given.

and [110] directions, respectively. For a more general alignment of the AFM spins in the ab plane, characterized by the angle ρ between the a axis and the direction of the AFM moments, the corresponding magnetic space group is $P112'$. Although all three magnetic symmetries (blue in Fig. 2.6) prohibit any magnetic moment in the c direction, they allow a spontaneous WFM moment perpendicular to the primary AFM moment direction that might be induced by a canting ϕ of the AFM spins through the alternating D_z component. These basic spin configurations for each magnetic space group are illustrated in Fig. 2.7 and discussed in more detail in appendix A.3. The low symmetry groups, which allow an additional magnetic moment in c direction (orange in Fig. 2.6), may be excluded as no experimental evidence for a magnetic ordering in [001] direction is reported.

As the emergence of the commensurate Néel-type order breaks the four-fold inversion axis of the parent space group $P\bar{4}2_1m$, four tetragonal (90°) magnetic domains are expected. A second set of four tetragonal domains with inverted angle ρ occurs in $P112'$ as all mirror planes and screw axes of $P\bar{4}2_1m$ are additionally broken. However, all magnetic domains have the same canting direction ϕ, and thus the same alignment of the WFM to AFM moment (i.e. a uniform vector product of the WFM and AFM moment). This ensures that the DMI energy caused by the alternating D_z component is conserved between the domains, as discussed in more detail in Sec. 6.4.1. Notably, the symmetry breaking of the magnetic structure at low temperature may also indicate a symmetry lowering of the nuclear structure to the respective orthorhombic $P2_12_12$ or $Cmm2$ space group as the magnetic structure generally follows the crystal symmetry [137]. However

at RT, Sazonov *et al.* [104] ruled out a tetragonal-to-orthorhombic symmetry lowering by a precise multiple diffraction study using long and short wavelength neutrons. At low temperature, Hutanu *et al.* [30] demonstrated in a detailed neutron diffraction study that the orthorhombic distortions at 2 K, if present, are extremely small and the average crystal structure can be equally well described by the tetragonal parent structure. In addition, no indication of a structural phase transition at T_N was found by neutron diffraction or infrared phonon mode analysis in Ref. [30]; thus, only the melilite-type tetragonal space group $P\bar{4}2_1m$, which is generally accepted as the nuclear symmetry for the $Ba_2TGe_2O_7$ compounds in the literature [86], is used as the symmetry of the nuclear structure throughout this work.

By magnetization measurements, an in-plane WFM moment of around $0.009\,\mu_B/Co^{2+}$ was reported in Ref. [43]. This is over two orders of magnitude smaller than the ordered AFM moment of around $2.8\,\mu_B$ determined by neutron diffraction, leading to an only slight canting of around $\phi = 0.18°$ [30, 112]. The field-induced magnetization at $T = 4$ K starts to saturate for in-plane fields above 15 T, whereas for magnetic fields in c direction no saturation could be observed up to the maximal measured field of 32 T, indicating again a strong easy-plane anisotropy. The onset of the saturation for in-plane fields of 15 T is accompanied by a clear peak and followed by a sudden drop in the susceptibility, indicating a field-induced magnetic transition from the canted AFM to a fully collinear FM state [112].

As the three potential magnetic ground states shown in Fig. 2.7 are indistinguishable by conventional neutron diffraction in zero magnetic field due to equally populated tetragonal domains, a polarized neutron study has been performed by Hutanu *et al.* [112]. This study indicates $Cm'm2'$ (shown in Fig. 2.7(b)) as the most probable one. However, this conclusion was drawn based on spherical neutron polarimetry (SNP) measurements of a single (102) reflection (denoted as (112) in the C centered UC setting used in Ref. [112]) and the presence of superstructure reflections, which would indicate the previously addressed tetragonal-to-orthorhombic symmetry lowering but were later on attributed to multiple scattering (see Ref. [104]). Thus, a more detailed consideration of the true magnetic ground state in $Ba_2CoGe_2O_7$ is required.

2.2.3. Canted antiferromagnetic structure in $Ba_2MnGe_2O_7$

Like in $Ba_2CoGe_2O_7$, a finite SIA term is expected in $Ba_2MnGe_2O_7$ due to the high-spin configuration of the Mn^{2+} ion with one unpaired electron in each of the $3d$ orbitals ($S = 5/2$). This suggests again a commensurate AFM structure as magnetic ground state rather than a transverse helical spin structure as found in $Ba_2CuGe_2O_7$ [86]. This was confirmed by neutron diffraction in Ref. [15], revealing an in-plane AFM structure (i.e. $J^{\langle 110\rangle} > 0$) below $T_N = 4.0$ K with $\boldsymbol{\tau} = (00\frac{1}{2})$ and thus an additional AFM stacking in [001] direction (i.e. $J^{\langle 001\rangle} > 0$), doubling the UC along c. The value of the exchange parameters were determined to be $J^{\langle 110\rangle} = 27.8(3)\,\mu$eV and $J^{\langle 001\rangle} = 1.0(1)\,\mu$eV, emphasizing the 2D character of the magnetic system [15]. In addition, the SIA was quantified as $\Lambda \approx 2.2\,\mu$eV [138]. Comparing the energy of this easy-plane anisotropy to the symmetric exchange yields in a ratio of $\Lambda/J^{\langle 110\rangle} \approx 0.1$, which is two orders of magnitude

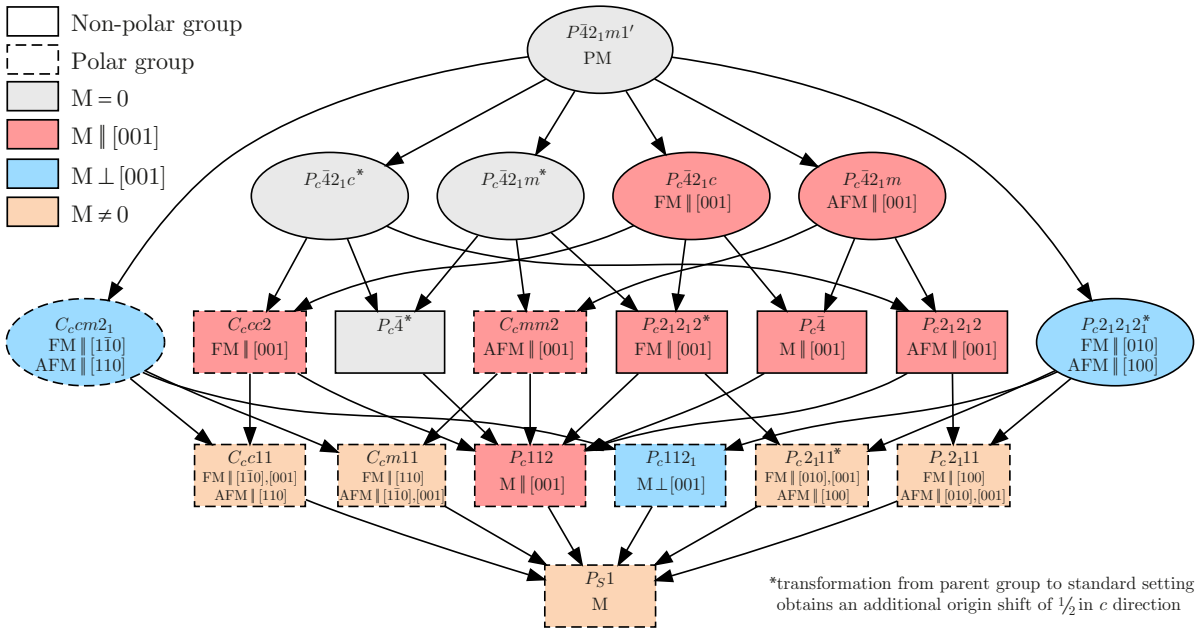

Figure 2.8.: Graph of all possible magnetic space groups in BNS notation for a magnetic ordering resulting from the $P\bar{4}2_1m1'$ symmetry of the PM structure and a $\boldsymbol{\tau} = (00\frac{1}{2})$ propagation vector. The k-maximal magnetic groups (i.e. the groups with the highest magnetic symmetry) are elliptically framed. Magnetic space groups that do not allow a magnetic ordering for the Mn^{2+} ions are marked in grey. The groups that allow a magnetic order in the tetragonal plane, along the c direction or in all three dimensions are highlighted in blue, red or orange, respectively. Restrictions on the magnetic ordering type in the high-symmetry directions are additionally listed. M denotes an arbitrary magnetic ordering type that is potentially limited to a plane or direction. Polar magnetic space groups, which leave at least one line of points unmoved, may allow a ferroelectric polarization and are indicated by a dashed frame. The graph was modified from the Graphviz [133] output of the k-SUBGROUPSMAG program from the Bilbao Crystallographic Server [134].

weaker than in $Ba_2CoGe_2O_7$ with $\Lambda/J^{\langle 110\rangle} \approx 10$. As there is a large energy difference between the exited states and the high-spin ground state of the Mn^{2+} ion, the deviation of the g-tensor components from the free electron value, scaling reciprocal with this energy difference, is expected to be small [136]. This is confirmed by ESR measurements providing $g_{\perp z} = 2.005$ and $g_{\parallel z} = 2.002$ [15]. This very weak in-plane anisotropy in both the SIA and the g-tensor is also reflected in an almost negligible anisotropy of around $\chi_{11}/\chi_{33} = 1.02$ in the susceptibility tensor at 10 K, evident from magnetization measurements by Masuda *et al.* [15].

The possible space groups for the magnetic ground state that are consistent with the parent symmetry $P\bar{4}2_1m1'$ and a $\boldsymbol{\tau} = (00\frac{1}{2})$ propagation vector are shown in Fig. 2.8 and discussed in more detail in appendix A.4. The experimentally observed in-plane AFM structure rules out all magnetic space groups that forbid a magnetic ordering (gray in Fig. 2.8) or allow it exclusively in c direction (red in Fig. 2.8). Thus, only two high-symmetry magnetic space groups remain as potential candidates for the ground state symmetry, namely $P_c2_12_12_1$ and C_ccm2_1, which allow an AFM moment in the [100] and [110] direction, respectively. For a more general alignment of the AFM spins

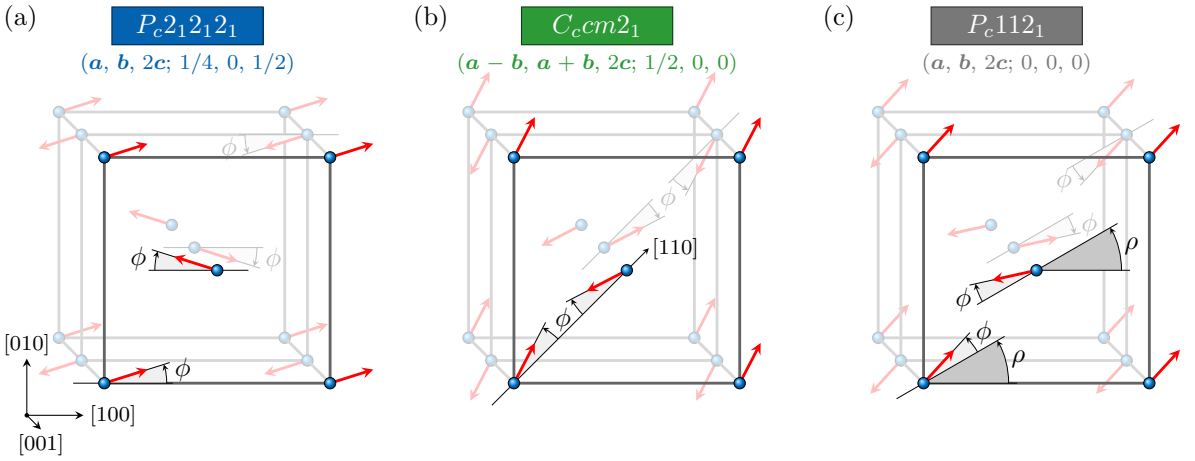

Figure 2.9.: Possible magnetic ground state symmetries and their basic spin configuration for the $P\bar{4}2_1m$ parent space group and an in-plane AFM order with $\boldsymbol{\tau} = (00\frac{1}{2})$ propagation vector, doubling the UC in c direction. The high-symmetry configurations (a) $P2'_12_12'$ and (b) $Cm'm2'$ have an AFM moment in the lattice and diagonal directions, respectively. The lower symmetry (c) $P112'$ configuration has an AFM moment in an arbitrary in-plane direction enclosing an angle ρ with the a axis. All three groups exclude magnetic moments in c direction but allow an spontaneous WFM moment perpendicular to the direction of the AFM order, resulting in an in-plane canting ϕ of the AFM spins. The magnetic moments of NNs in c direction is exactly reversed, as expected by $\boldsymbol{\tau} = (00\frac{1}{2})$. Below the BNS label, the lattice vector transformation and origin shift from the setting of the parent group to the standard setting of the magnetic space group is given.

in the ab plane, characterized by the angle ρ between the a axis and the direction of the AFM moment, the corresponding magnetic space group is P_c112_1. For all three magnetic space groups, an in-plane WFM moment is allowed perpendicular to the direction of the AFM moment, leading to a canting ϕ of the spins. The basic spin configuration for each magnetic space group is shown in Fig. 2.9. As the coupling in c-direction is purely AFM, the direction of the WFM moment reverses between neighboring magnetic planes (clearly indicated by inverted phi directions in Fig. 2.8). Therefore, the local WFM moments are microscopically canceled out and cannot be observed in magnetization measurements. No experimental evidence for a magnetic ordering in [001] direction is reported. For this reason, the remaining low symmetry magnetic space groups that allow an additional magnetic moment in c direction (orange in Fig. 2.8) may be excluded.

The magnetic structure below the Néel temperature breaks the four-fold inversion axis of the parent space group, like in $Ba_2CoGe_2O_7$. Thus, four tetragonal magnetic domains are expected for $P_c2_12_12_1$ and C_ccm2_1 and an additional set of four tetragonal domains with inverted ρ for the even lower symmetry P_c112_1. Again, the three potential magnetic ground states are indistinguishable by conventional neutron diffraction in zero magnetic field due to equally populated magnetic domains. However, the magnitude of the ordered AFM moment was determined to be 4.66(6) μ_B/Mn by neutron diffraction [15]. As the measurement was carried out at a cold neutron triple axis spectrometer (HQR at JRR-3M, Japan), the experimental conditions, in particular the covered q-range, might not have been ideal for a proper magnetic structure determination. In addition, only very

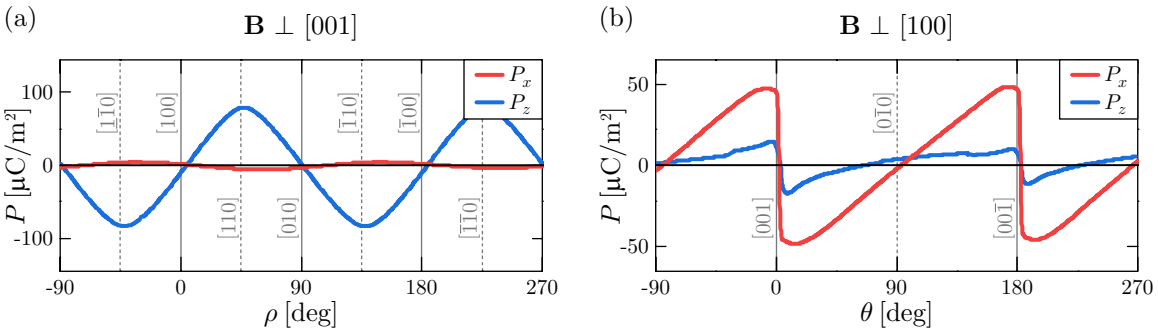

Figure 2.10.: Variation of the electric polarization components for a rotation of the applied magnetic field **B** of (a) 1 T in the (001) plane and (b) 5 T in the (100) plane. The measurement was performed in the AFM phase at 2.0 K. The angle enclosed by the field direction and the [100] and [001] axis are denoted as ρ and θ, respectively. High-symmetry directions of the magnetic field are indicated by gray lines and labeled accordingly. The figures are taken and modified from Ref. [89].

little information about the experimental procedure and and no refinement details are given by Masuda *et al.* [15]. Therefore, a more comprehensive study might be required to reliably determine the ordered magnetic moment.

Magnetization measurements showed a clear saturation of the induced magnetic moment for in-plane fields above 8.2 T in the AFM state at 1.8 K. Like in $Ba_2CoGe_2O_7$, this saturation is accompanied by a sharp peak and followed by a sudden drop in the susceptibility, which might be attributed to a magnetic transition from a strongly canted AFM to a field-induced FM state [86].

2.3. Emergence of multiferroicity

In $Ba_2CoGe_2O_7$, the appearance of ferroelectricity below the magnetic ordering temperature of 6.7 K was first discovered by Yi *et al.* [43]. They reported a ferroelectric polarization **P** of around 11 μC/m^2 along the [001] direction. With an applied magnetic field in c direction, the magnitude of **P** increased significantly and its direction rotated towards the ab plane. In a more detailed study by Murakawa *et al.* [89], the x and z components of the electric polarization were systematically measured for a rotation of the applied magnetic field in the (001) and (100) planes and are shown in Fig. 2.10. For an in-plane field rotation with angle ρ enclosed by the field direction and the a axis, an approximate sine law dependency of P_z on 2ρ could be observed (visible in Fig. 2.10(a)). In addition, a weak P_x component was found, which might result from an imperfect alignment of the magnetic field in the (001) plane. For a field rotation in the (100) plane with θ denoting the angle between the field direction and the c axis, a discontinuous electric polarization is observed with jumps at $\theta = 0°$ and 180° (clear to see in Fig. 2.10(b)). As discussed by Perez-Mato and Ribeiro [139], both dependencies can be understood solely from magnetic symmetry arguments.

If a weak anisotropy in the ab plane is assumed, an in-plane magnetic field ($\theta = 90°$) aligns the WFM moment parallel to the field direction and the AFM moment

perpendicular to it. Thus, the adopted magnetic space group is expected to change as a function of the field angle ρ. For magnetic fields in lattice directions ($\rho = 0°$, 90°, 180° and 270°), the equivalent magnetic space groups $P2_1'2_12'$ or $P2_12_1'2'$ are realized. As they do not have a polar point group (see Fig. 2.6), no ferroelectricity is expected. And indeed, these directions correspond to the nodes of P_z in Fig. 2.10(a). In contrast, for diagonal ($Cm'm2'$ or $Cmm'2'$) or arbitrary ($P112'$) in-plane fields, the magnetic point group is polar along the c direction, which allows a spontaneous P_z component. The magnitude of P_z can be estimated by considering the lowest order symmetry-allowed coupling term responsible for the spontaneous polarization, resulting in $P_z \propto m_x^{\mathrm{AFM}} m_y^{\mathrm{AFM}}$, and for the linear magnetoelectric response, leading to $P_z \propto (m_y^{\mathrm{FM}} m_y^{\mathrm{AFM}} - m_x^{\mathrm{FM}} m_x^{\mathrm{AFM}})$. The FM and AFM vectors are defined as $\mathbf{m}^{\mathrm{FM}} = (\mathbf{m}_1 + \mathbf{m}_2)/2$ and $\mathbf{m}^{\mathrm{AFM}} = (\mathbf{m}_1 - \mathbf{m}_2)/2$, with $\mathbf{m}_1$ and $\mathbf{m}_2$ denoting the magnetic moments associated with the TM ions located at the (000) and ($\frac{1}{2}\frac{1}{2}0$) positions ($\mathbf{r}_1$ and $\mathbf{r}_c$ in Fig. 4.1(b) in Sec. 4.2). As the direction of the AFM and the induced FM moment are determined by the applied magnetic magnetic field, their amplitudes can be estimated for in-plane magnetic fields ($\theta = 90°$) by $\mathbf{m}^{\mathrm{AFM}} \propto (\sin(\rho), -\cos(\rho), 0)^{\mathsf{T}}$ and $\mathbf{m}^{\mathrm{FM}} \propto (\cos(\rho), \sin(\rho), 0)^{\mathsf{T}}$. This finally predicts a variation $P_z \propto \sin(2\rho)$ as observed in Fig. 2.10(a) [139].

For magnetic field angles of $\theta = 90°$ and 270° in the (100) plane ($\rho = 90°$), the non-polar magnetic space group $P2_1'2_12'$ is realized, visible again as nodes in P_z and P_x in Fig. 2.10(b). For any other θ value, an additional magnetization $m_z^{\mathrm{FM}} \propto \cos(\theta)$ along c direction is induced that further reduces the symmetry to $P2_1'11$ (see Fig. 2.6). This magnetic space group is polar along a, and thus allows a polarization component P_x. From the lowest order symmetry-allowed coupling term, its magnitude can be estimated as $P_x \propto m_x^{\mathrm{AFM}} m_z^{\mathrm{FM}}$. Note that the magnitude of the m_x^{AFM} component is expected to be constant for all θ values. However, as the in-plane field component $B_y \propto \sin(\theta)$, which aligns the WFM moment parallel and the AFM moment perpendicular to it, switches sign for θ larger or smaller than 0°, m_x^{AFM} is also expected to change its sign accordingly. Thus, the in-plane polarization is predicted to be $P_x \propto \cos(\theta)$ for $-180° < \theta < 0°$ and $P_x \propto -\cos(\theta)$ for $0° < \theta < 180°$ with discontinuities at $\theta = 0°$ and 180° [139]. This agrees well with the observed response of the P_x component shown in Fig. 2.10(b). Note that the non-zero P_z in Fig. 2.10(b) is attributed to an imperfect alignment of the applied magnetic field with the (100) plane by Murakawa *et al.* [89]. The deformation of the ideal cos-dependency of P_x towards a rather linear response between the discontinuities results from to the strong easy-plane anisotropy in $Ba_2CoGe_2O_7$ (see Sec. 2.2.2). This anisotropy causes a gradual increase of the field-induced canting of the AFM moments for magnetic fields closer to the ab-plane (θ almost $\pm 90°$), and thus reduces the magnitude of m_x^{AFM}, which is directly proportional to P_x.

In addition to these symmetry forced magnetoelectric effects, Murakawa *et al.* [89] report a highly non-linear dependence of P_z on the magnitude B of the applied magnetic field in [110] direction, including also a change of sign at higher fields. This peculiar behaviour of P_z, which is similarly present in both $Ba_2CoGe_2O_7$ and $Ba_2MnGe_2O_7$ (see Fig. 2.11), cannot be directly predicted by symmetry arguments and may originate from one or more of the different proposed atomic mechanisms [139]. These proposals will be discussed in what follows.

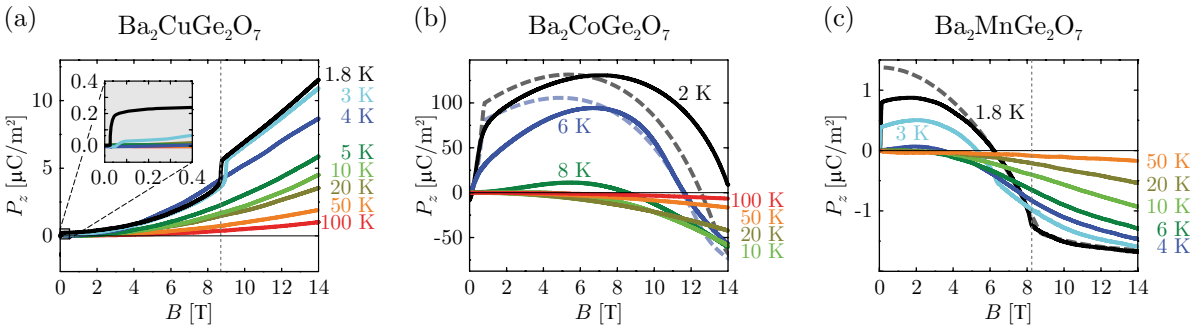

Figure 2.11.: Variation of the electric polarization P_z for an in-plane magnetic field in [110] direction at different temperatures in $Ba_2TGe_2O_7$ with TM ion (a) Cu, (b) Co and (c) Mn. The vertical dashed gray lines indicate the critical fields for (a) the I/C phase transition and (c) the canted AFM to field-induced FM transition at temperatures of 1.8 K. The inset in (a) shows the P_z contribution in the AFM cycloid phase by helical domain alignment in the small field region. The dashed lines in (b) are taken from Ref. [90] and originate from finite-T calculations at $T = 2$ K and 6 T assuming a spin-induced electric polarization as in the p-d hybridization model combined with an antiferroelectric coupling (more detailed in Sec. 2.3.1). In (c), the dashed line is taken from Ref. [86] and calculated from the p-d hybridization model in mean-field approximation for $T = 1.8$ K. The measured polarizations (solid lines) are taken from Ref. [86].

2.3.1. Spin-dependent *p-d* hybridization model

The formalism for the spin-dependent p-d hybridization model was originally derived by Jia *et al.* [140, 141] for TM–ligand–TM clusters and introduced to explain the multiferroicity in the delafossite compounds $Cu(Fe,Al)O_2$ [88]. Based on spin-orbit interactions within the partially filled t_2 orbitals of a TM ion, the t_2 degeneracy can be lifted and an additional energy shift to the p levels of its surrounding ligand is induced. This energy difference scales with the spin component S_e of the TM ion in bonding direction $\mathbf{e}$ and modifies the degree of hybridization with its ligand, which causes a variation in the ionic charge $\propto S_e^2$ at the ligand position [88]. As a result, a spin-driven local electronic polarization $P \propto S_e^2$ arises in bonding direction between the TM ion and its ligand [141]. Particularly for TM ions in noncentrosymmetric environments (e.g. tetrahedral), these local electronic polarizations may not cancel out macroscopically and form a ferroelectric polarization $\mathbf{P}$, which can be generally expressed as

$$\mathbf{P} \propto \sum_i \mathbf{e}_i \left(\mathbf{S} \cdot \mathbf{e}_i\right)^2 \tag{2.4}$$

with $\mathbf{e}_i$ the connection vector between the TM ion with spin $\mathbf{S}$ and its i^{th} ligand.

Applying (2.4) to the case of $Ba_2CoGe_2O_7$, the p-d hybridization model predicts for a magnetic field applied in the ab plane, enclosing an angle ρ with the a axis and introducing a canting ϕ of the AFM spins in field direction, an electric polarization along the c direction with magnitude

$$P_z^{\mathbf{B}\perp[001]} \propto \sin(2\rho)\cos(2\kappa - 2\phi), \tag{2.5}$$

where κ is the deviation angle of the CoO_4 tetrahedron as illustrated in Fig. 2.1(a). This dependency reproduces well the experimentally observed sine law behaviour of P_z

on 2ρ shown in Fig. 2.10(a) and is consistent with the previously discussed symmetry arguments provided by Perez-Mato and Ribeiro [139]. Furthermore, the in-plane polarization P_x is predicted to cancel out in the p-d hybridization model for $\mathbf{B} \perp [001]$ as expected from the measurement results shown in Fig. 2.10(a).

For fields in the (100) plane, the AFM moment is aligned along the [100] direction and reverses its direction as the field passes the z axis. Using the p-d hybridization model, an electric polarization

$$P_x^{\mathbf{B}\perp[100]} \propto \begin{cases} \sin(2\kappa)\cos(\theta)\sin(2\phi) - A(\kappa,\theta,\phi) & \text{for } -180° < \theta < 0° \\ -\sin(2\kappa)\cos(\theta)\sin(2\phi) - A(\kappa,\theta,\phi) & \text{for } 0° < \theta < 180° \end{cases} \tag{2.6}$$

is predicted in a direction with ϕ the canting angle of the AFM moment in field direction and θ the field angle to the c axis. The additional contribution $A(\kappa,\theta_H,\phi) = \cos(2\kappa)\sin(2\theta)\sin^2(\phi)$ can be neglected for magnetic fields close to the lattice directions ($\sin(2\theta) \to 0$) and for a weak canting ($\sin^2(\phi) \to 0$) and thus small fields. The primary contribution to this discontinuous sine law dependency is again in agreement with the symmetry considerations provided by Perez-Mato and Ribeiro [139] and the experimental results shown in Fig. 2.10(b). Note that the canting angle ϕ depends also on θ if there is an anisotropy in the susceptibility tensor. This gives an additional dependency of $\tan(\phi) \propto \sqrt{1 + (\chi_{11}/\chi_{33} - 1)\cos^2(\theta)}$ to Eq. (2.6) and is particularly important for $Ba_2CoGe_2O_7$ with $(\chi_{11}/\chi_{33} - 1) \approx 1$. As discussed before, this variation in the canting angle is noticeable in Fig. 2.10(b) by the distortion of the expected $P_x^{\mathbf{B}\perp[100]} \propto \cos(\theta)$ towards a somewhat linear behavior on θ. This distortion is further enhanced by the additional $A(\kappa,\theta,\phi)$ contribution, not disclosed by the symmetry considerations discussed before.

Because Eq. (2.5) depends also on the field-induced canting angle ϕ, it can be utilized to predict P_z in $Ba_2CoGe_2O_7$ as function of the field strength in [110] direction ($\rho = 45°$). For very small magnetic fields, a gradual increase of P_z is expected until it reaches its maxima for $\phi = \kappa \approx 22°$. For even higher fields, a sign change in P_z is expected at $\phi = \kappa + 45°$. Finally, the electric polarization saturates at $\phi = 90°$, which corresponds to a pure FM spin state. This predicted behaviour for $Ba_2CoGe_2O_7$ is consistent with the experimental observation shown in Fig. 2.11(b). However, towards very low fields in the AFM phase a sharp drop in P_z is clearly visible in Fig. 2.11(b). To account for this effect, Murakawa *et al.* [86] proposed a multidomain state that minimizes the electrostatic potential whereas Romhányi *et al.* [90] suggested to include an antiferroelectric coupling term $\propto K_z P_{i,z} P_{j,z}$ between the nearest neighboring Co sites i and j with coupling constant $K_z > 0$ in the Hamiltonian. This anisotropic contribution is allowed by the symmetry and might arise due to lattice effects. It energetically favours $P2'_12_12'$ as ground state and leads to a two domain, canted ferrimagnetic spin configuration for small fields up to around 1 T in [110] direction. As $P2'_12_12'$ does not allow a ferroelectric polarization, its field-induced deformation to the ferrimagnetic state with polar $P112'$ symmetry is accompanied by a steep increase in P_z [90]. The predicted P_z behaviour for magnetic fields applied in the [110] direction assuming a spin-induced electric polarization as in the p-d hybridization model combined with an antiferroelectric coupling for

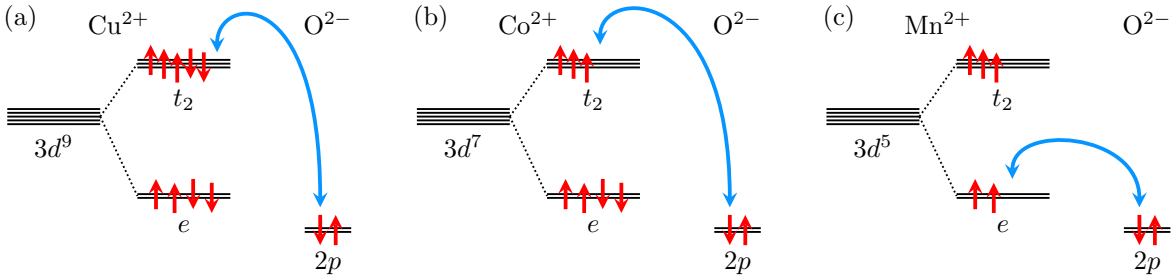

Figure 2.12.: Schematic illustration of the hybridization (blue arrow) between the TM ion's d orbitals, split into t_2 and e levels, and the ligand's p orbitals in $Ba_2TGe_2O_7$ with T = (a) Cu^{2+}, (b) Co^{2+} and (c) Mn^{2+}. The figure is modified from Ref. [86].

$T = 2\,\mathrm{K}$ and $6\,\mathrm{K}$ is shown in Fig. 2.11(b) by dashed lines. Clear to see is the calculated drop of P_z for fields below $1\,\mathrm{T}$ due to the antiferroelectric coupling, reproducing the main characteristics of the experimental findings.

Applying the p-d hybridization model to the AFM structure in $Ba_2MnGe_2O_7$ with $\boldsymbol{\tau} = (00\frac{1}{2})$, Murakawa *et al.* [86] derived an electric polarization of

$$P_z^{\mathbf{B}\perp[001]} \propto \sin(2\rho_H)\cos(2\kappa)\cos(2\phi) \tag{2.7}$$

in c direction for fields in the (100) plane. Considering the magnetic field-induced transition to a FM spin arrangement at around $8.2\,\mathrm{T}$, the calculated polarization variation in mean-field approximation for $1.8\,\mathrm{K}$ is shown in Fig. 2.11(c) by a dashed line. It reproduces roughly the experimental findings but shows clear discrepancies at small fields [86]. The calculation might be improved by considering an antiferroelectric coupling as in Ref. [90] for $Ba_2CoGe_2O_7$.

In $Ba_2CuGe_2O_7$, the spiral spin structure is associated with an electric polarization in c direction according to the spin-current or the inverse DMI model with $\mathbf{P} \propto \sum_{ij} \mathbf{e}_{ij} \times (\mathbf{S}_i \times \mathbf{S}_j)$ for neighboring spins $\mathbf{S}_i$ and $\mathbf{S}_j$ connected by a unit vector $\mathbf{e}_{ij}$ [55, 67–69]. A brief outline of these two conventional mechanisms and their microscopic origin is given in Sec. 1.2 and the DMI is generally discussed in Chap. 4. As the two helical domains in $Ba_2CuGe_2O_7$ with (110) and $(1\bar{1}0)$ spin rotation plane have an oppositely signed electric polarization, P_z chancels out in zero field due to equally distributed domains. For small fields in the [110] direction, the degeneracy is lifted and a single domain state emerges, leading to the sharp increase of P_z visible in the inset of Fig. 2.11(a) [87]. However, for fields above the I/C transition at around $8.7\,\mathrm{T}$, $Ba_2CuGe_2O_7$ has a commensurate spin structure similar to the one in $Ba_2CoGe_2O_7$, and thus possesses according to the p-d hybridization model a distinct electric polarization. This is consistent with the discontinuous jump in P_z observed at the I/C transition in Fig. 2.11(a).

In the PM state, the p-d hybridization model predicts an electric polarization $P_z = A_z \sin(2\kappa + 2\rho_H)(m^{\mathrm{FM}}/m_S)^2$ for fields in the (001) plane with coupling constant A_z and high-field saturated magnetization m_S. As the field-induced magnetization m^{FM} is almost linear with the applied magnetic field below its saturation, the p-d hybridization model reproduced well the smooth B^2 dependency of P_z observed for all three compounds in Fig. 2.11 in the PM state. Note that the value of the coupling constant A_z, which is

determined by the degree of hybridization and the charge transfer energy between the TM ion's d and the ligand's p orbital as well as the spin-orbit interaction energy [141], is similar for Cu ($A_z^{\mathrm{Cu}} \approx 24\,\mu\mathrm{C/m^2}$) and Co ($A_z^{\mathrm{Co}} \approx 46\,\mu\mathrm{C/m^2}$) at 50 K, whereas the one for Mn ($A_z^{\mathrm{Mn}} \approx 0.50\,\mu\mathrm{C/m^2}$) is almost two orders of magnitude smaller [86]. The origin of this large difference can be found in the electronic configuration. For Cu and Co, the p-d hybridization is dominantly between the partially filled t_2 and the ligand p orbitals as schematically shown in Figs. 2.12(a) and 2.12(b). As discussed before, this hybridization is strongly influenced by the active SOC in the t_2 orbitals that lifts their degeneracy. In contrast for Mn, the hybridization with the ligand's p orbitals are mediated by the lower lying, non-degenerate e orbitals with quenched orbital momenta as illustrated in Fig. 2.12(c). Thus, the hybridization is only influenced by an effective spin-orbit interaction resulting form perturbation processes with the higher-lying t_2 levels, clearly reducing the magnitude of A_z in Mn as experimentally observed [86].

2.3.2. Spontaneous toroidic effect mechanism

Alternatively to the p-d hybridization model, Toledano *et al.* [91] proposed a spontaneous toroidic effect mechanism as origin for the magnetoelectric effects in $Ba_2CoGe_2O_7$. Compared to the electric dipole, which is symmetric under time reversal and antisymmetric under spatial inversion, and the magnetic dipole, which is antisymmetric under time reversal and symmetric under spatial inversion, the (polar) toroidal moment addressed in Ref. [91] is antisymmetric under both symmetries. Thus, the existence of a macroscopic toroidal moment requires at least a broken inversion symmetry, which is fulfilled by the noncentrosymmetric $P\bar{4}2_1m$ melilite-type structure in the $Ba_2TGe_2O_7$ compounds (see Sec. 2.1). The toroidal dipole moment, which is the so-called anapole and reflects the toroidal multipole of lowest order, corresponds to a ring-shaped magnetic field and is often depicted in a classical example as the field of a solenoid bent into a torus or in a quantum-mechanical example as a head-to-tail arrangement of spins forming a vortex [142]. However, also AFM structures may have a toroidal moment if they break the time and space reversal symmetry [143].

Analyzing the free energy of the $Cm'm2'$ magnetic space group in the $Ba_2TGe_2O_7$ compounds, Toledano *et al.* [91] found symmetry invariant $(\mathbf{T} \times \mathbf{m}^{\mathrm{FM}}) \cdot \mathbf{P}$ and $(\mathbf{T} \times \mathbf{P}) \cdot \mathbf{m}^{\mathrm{FM}}$ terms including a toroidal moment $\mathbf{T}$. These mixed vector products lead to by third rank tensors μ and λ interconnected values for the spontaneous polarization $\mathbf{P}^{\mathrm{S}} = \mu(\mathbf{T}^{\mathrm{S}} \times \mathbf{m}^{\mathrm{WFM}})$ pointing in c direction, the in-plane WFM moment $\mathbf{m}^{\mathrm{WFM}} = \lambda(\mathbf{P}^{\mathrm{S}} \times \mathbf{T}^{\mathrm{S}})$ and the spontaneous toroidal moment $\mathbf{T}^{\mathrm{S}}$, which is allowed by the polar $Cm'm2'$ magnetic space group collinear to the AFM ordering direction. Note that $\mathbf{T}^{\mathrm{S}}$ has the same symmetry as the AFM order parameter and can be considered as bilinearly coupled to it. The basic orientations of these components are illustrated in Fig. 2.13 for all four tetragonal domains of $Cm'm2'$. For applied electric $\mathbf{E}$ and magnetic $\mathbf{B}$ fields, the total polarization, magnetization and toroidal moment are given by [91]

$$\mathbf{P} = \mathbf{P}^{\mathrm{S}} + \epsilon\mathbf{E} + \alpha\mathbf{B} + \sigma^{B}(\mathbf{T} \times \mathbf{B}) \tag{2.8}$$

$$\mathbf{m}^{\mathrm{FM}} = \mathbf{m}^{\mathrm{WFM}} + \chi\mathbf{B} + \beta\mathbf{E} + \sigma^{E}(\mathbf{T} \times \mathbf{E}) \tag{2.9}$$

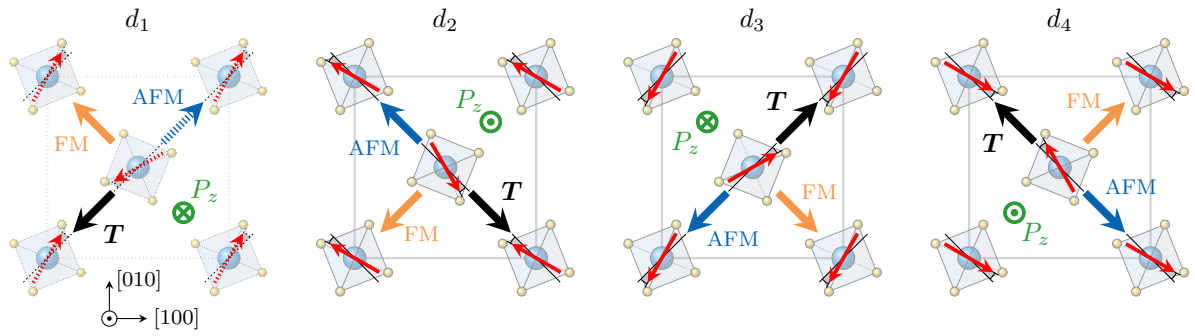

Figure 2.13.: The basic orientation of the magnetization (FM), the AFM ordering direction (AFM), the toroidal moment ($\mathbf{T}$) and the electric polarization ($\mathbf{P}$) for the four tetragonal domains d_i of the $Cm'm2'$ magnetic space group in multiferroic $Ba_2CoGe_2O_7$. Red arrows indicate the magnetic moments of the individual Co atoms. The figure is based on Fig. 1 in Ref. [91]; however, corrected for an inconsistent definition of the AFM vector.

$$\mathbf{T} = \mathbf{T}^{\mathrm{s}} \qquad + \kappa^{E}\mathbf{e} + \kappa^{B}\mathbf{B} + \sigma^{EB}\left(\mathbf{E}\times\mathbf{B}\right) \tag{2.10}$$

with Greek letters denoting second rank tensors expect for σ^B, σ^E and σ^{EB}, which are of third rank. This set of equations provides the basis for the interpretation of the peculiar magnetoelectric effects reported in $Ba_2CoGe_2O_7$ (e.g. in Ref. [43, 89]) by the spontaneous toroidic effect mechanism.

For applied magnetic fields in [001] direction, Eq. (2.8) predicts an induced in-plane polarization

$$P_{\tilde{x}} = \left(\alpha_{13} + T^{\mathrm{S}}_{\tilde{y}}\left(\chi_{33} + \sigma^{B}_{123}\right)\right) B_{\tilde{z}} \tag{2.11}$$

in the orthorhombic setting $\tilde{x} \parallel [1\bar{1}0]$, $\tilde{y} \parallel [110]$ and $\tilde{z} \parallel [001]$. This linear dependence on $B_{\tilde{z}}$ agrees well with the behaviour of the P_x component reported in Ref. [43], showing a steady increase for applied fields in c direction and a sign reversal upon reversing the field direction. Interestingly, Toledano *et al.* [91] account the sharp increase of P_x upon cooling below T_N in a constant field reported in Ref. [43] to a substantial toroidal contribution ($T^{\mathrm{S}}_{\tilde{y}}\sigma^{B}_{123}B_{\tilde{z}}$), which is assumed to vary critically as $(T_N - T)^{\frac{3}{2}}$) compared to the magnetoelectric contribution ($\alpha_{13}B_{\tilde{z}}$) and the field-induced magnetization ($\chi_{33}B_{\tilde{z}}$) both varying as $(T_N - T)^{\frac{1}{2}}$. However, fitting the data of Ref. [43] to a power law $(T_N - T)^{\beta}$ reveals a critical exponent β of around 0.2, which might be rather contradictory to a large toroidal contribution with $\beta \approx \frac{3}{2}$. Moreover, Toledano *et al.* [91] predict from the spontaneous toroidic effect mechanism for an applied magnetic field in [001] direction a z component of the electric polarization given by

$$P_{\tilde{z}} = P^{\mathrm{S}}_{\tilde{z}} + \left(\chi_{23}T^{\mathrm{S}}_{\tilde{x}} - \chi_{13}T^{\mathrm{S}}_{\tilde{y}}\right) B_{\tilde{z}}. \tag{2.12}$$

Although this is consistent with the measured finite P_z at zero field that increases with applied field in Ref. [43], it does not recover its non-linear shape and the symmetric behaviour for a field inversion (i.e. $P_z(B_z) = P_z(-B_z)$). To overcome this issue, Toledano *et al.* [91] propose to consider higher-order contributions like $\propto B^2_{\tilde{z}}$.

For magnetic fields in the [110] direction, the electric polarization in z direction can be calculated from Eq. (2.8) as

$$P_{\tilde{z}} = \frac{1}{2}\left(\alpha_{31} + \sigma^{B}_{321}T^{\mathrm{S}}_{\tilde{y}} + \sigma^{B}_{312}T^{\mathrm{S}}_{\tilde{x}}\right)B_{\tilde{y}}, \tag{2.13}$$

with $P_{\tilde{z}}(B_{\tilde{y}}) = -P_{\tilde{z}}(B_{\tilde{x}})$, reproducing well the reported sign change in P_z for an in-plane field rotation of 90° in Ref. [89]. If the additional higher-order invariant $(\mathbf{T}^{\mathrm{S}}\cdot\mathbf{B})(\mathbf{T}^{\mathrm{S}}\times\mathbf{B})$ is included in Eq. (2.8), Eq. (2.13) will be expanded by a contribution $\propto B^2_{\tilde{y}}$, which may lead to an extremum in $P_{\tilde{z}}$ for a critical field $B^{\mathrm{c}}_{\tilde{y}}$ and to a sign change for $2B^{\mathrm{c}}_{\tilde{y}}$. Such a behaviour recovers the main characteristics of the experimental findings in Ref. [89] shown in Fig. 2.11(b).

Finally, by analyzing the spontaneous polarization calculated from the equilibrium values of the four order parameters, representing the in-plane components of the FM and AFM moments, Toledano *et al.* [91] conclude that the spontaneous FM and AFM contributions result from single-ion effects and the symmetric part of the exchange coupling between the Co spins, whereas the spontaneous toroidal contribution reflects only single-ion effects.

2.3.3. Spin-nematic interaction model

By inelastic neutron scattering and magnetic susceptibility measurements, Soda *et al.* [92] found evidence for the presence of a four-fold in-plane anisotropy in $Ba_2CoGe_2O_7$. This behaviour cannot be explained by the previously discussed effective spin Hamiltonian in Eq. (2.2), including the conventional mechanisms of anisotropy such as SIA $\propto \Lambda S_z^2$. Even the phenomenological splitting of the symmetric intra-plane exchange contributions $\propto J^{\langle 110\rangle}\mathbf{S}_i\mathbf{S}_j$ into in-plane $\propto J^{\langle 110\rangle}_{\perp z}(S_{i,x}S_{j,x} + S_{i,y}S_{j,y})$ and out-of-plane $\propto J^{\langle 110\rangle}_{\parallel z}S_{i,z}S_{j,z}$ components, addressed in Sec. 2.2, does not cause such behaviour. Thus, Soda *et al.* [92] identified in a phenomenological approach spin-nematic interactions as the origin of the in-plane anisotropy since they represent the lowest order two-ion anisotropy that breaks the rotational symmetry. The spin-nematic operator, whose microscopic origin remains hidden in Ref. [92], is a rank two symmetric tensor of local spin operators S with general formula $O_{\alpha\beta} = S_\alpha S_\beta + S_\beta S_\alpha$. In this regards, α and β refer to axes of the local coordinate system XYZ, which is defined in $Ba_2CoGe_2O_7$ by the alignment of the respective CoO_4 tetrahedron as illustrated in Fig. 2.14(a). For a spin $\mathbf{S}$ in the local $\alpha\beta$ plane, enclosing an angle ϕ_S with the α axis, the expectation value of the spin-nematic operator is given by $\langle O_{\alpha\beta}\rangle \propto \sin(2\phi_S)$. This quadrupolar characteristic of $\langle O_{\alpha\beta}\rangle$ is illustrated in Fig. 2.14(b) and 2.14(c).

As the point group symmetry $\bar{4}2m$ of the TO_4 tetrahedron in the melilite structure lacks an inversion center, the spin-nematic operator is equivalent to a local polarization $\mathbf{P}$ with components $P_X \propto O_{YZ}$, $P_Y \propto O_{ZX}$ and $P_Z \propto O_{XY}$. For spins $\mathbf{S}_i \perp [001]$ at Co site i, only O_{XY} is finite and a local polarization $P_{i,z} \propto \sin(2\rho_i - 2\kappa_i)$ occurs, where ρ_i is the rotation angle of $\mathbf{S}_i$ from the a axis and κ_i the tetrahedral deviation defined in Fig. 2.14(a). For a general in-plane alignment of the Co spins in $Ba_2CoGe_2O_7$, characterized by an AFM moment enclosing an angle ρ with the a axis and a canting ϕ as shown in Fig.

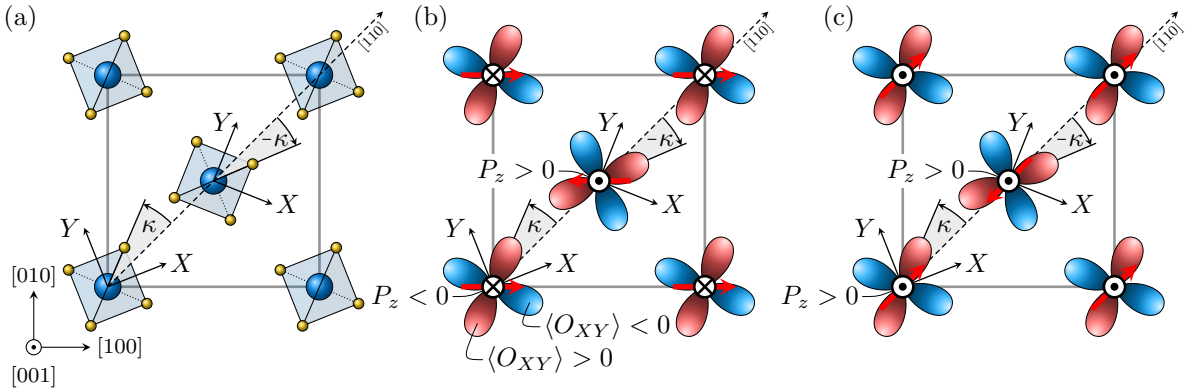

Figure 2.14.: (a) Definition of the local XYZ coordinate system in the CoO_4 tetrahedron, distorted for an alternating angle $\kappa \approx 22°$ [104] in [110] direction. The local Z axis is parallel to the tetragonal c direction. (b),(c) Quadrupolar structure of the expectation value of the spin-nematic operator O_{XY}. The magnitude of $\langle O_{XY} \rangle$ for a spin in the local XY plane is given by the size of the lobe in the corresponding direction (maximized and minimized for local $\langle 110 \rangle_{XYZ}$ and $\langle 100 \rangle_{XYZ}$ directions, respectively) whereas the sign is reflected by the color (red for $\langle O_{XY} \rangle >$ and blue for $\langle O_{XY} \rangle < 0$). For AFM moments in the [100] direction in (b), $\langle O_{XY} \rangle$ has different signs for the two Co sites, and thus an antiferroelectric state emerges with local polarizations $P_z \propto O_{XY}$. Accordingly, a ferroelectric state is present in (c) with AFM moments in the [110] direction, resulting in same signed $\langle O_{XY} \rangle$ [92].

2.7(c), the summation of these local polarizations leads to a ferroelectric polarization $P_z \propto \sin(2\rho)\cos(2\kappa - 2\phi)$, which is consistent with Eq. (2.5) for the p-d hybridization model.

The spin-nematic interaction, which becomes equivalent to the inter-site interaction of the electric polarization suggested in Ref. [90] as extension to the p-d hybridization model, leads to an additional contribution

$$\mathcal{H}_P = \sum_{n.n.\,\langle 110 \rangle} J_P P_{i,z} P_{j,z} = \sum_{n.n.\,\langle 110 \rangle} J_O O_{XY,i} O_{XY,j} \tag{2.14}$$

to the Hamiltonian with same signed J_P and J_O exchange constants. This contribution causes $\langle 110 \rangle$ and $\langle 100 \rangle$ easy axes for a ferro- ($J_O < 0$) and antiferro-type ($J_O > 0$) spin-nematic interaction, corresponding to a ferroelectric ($J_P < 0$) and antiferroelectric ($J_P > 0$) coupling, respectively. The antiferroelectric and ferroelectric states with AFM order in [100] and [110] direction are illustrated in Fig. 2.14(b) and 2.14(c). As Soda *et al.* [92] could experimentally evidence $\langle 100 \rangle$ easy-axes, they conclude about the antiferro-type of the spin-nematic interaction and determine the magnitude $J_O = 0.198\,\mu$eV of the interaction constant by fitting the anisotropy gap occurring in the inelastic neutron scattering spectrum. Moreover, Soda *et al.* [144] could demonstrate by neutron diffraction that an applied electric field in c direction during the cooling rotates the AFM direction with increasing field strength from $\langle 100 \rangle$ to $\langle 110 \rangle$, which is consistent with the spin-nematic model as the ferroelectric state is favoured by the external field.

2.3.4. Jahn-Teller distortion model

Finally, Barone *et al.* [94] proposed the emergence of an electric polarization in the melilite structure based on JT distortions. Analyzing the local symmetry of the TO_4 tetrahedron and the level structure of the $3d$ orbitals in the compressed tetrahedral environment (see Fig. 2.2), they showed that a set of four different distortion modes may locally develop. Driven by the lack of inversion symmetry, one of these JT modes is polar such that its distortions induce a local electric polarization at the TM ion site. Density functional theory (DFT) calculations in Ref. [94] suggest that these local electric polarizations prefer an antiferroelectric ordering to minimize asymmetric distortions of the Ge_2O_7 dimers by the JT modes, which is in agreement with the theoretical considerations by Romhányi *et al.* [90] discussed in Sec. 2.3.1. Moreover, a close connection between the JT modes and the spin-dependent p-d hybridization mechanism is predicted as the distortions can affect the spin-dependent modulation of charge density and vice versa. This might realize an intrinsically large magnetoelectric coupling in the melilites

Table 2.2.: Overview of the multiferroic models and their prediction for the magnetic field-induced electronic polarization in $Ba_2CoGe_2O_7$. For the general expression of the models, $\mathbf{P}^{\mathrm{S}}$ denotes the spontaneous electric polarization whereas $\mathbf{P}^{B}$ is the field-induced one. The local XYZ system for the spin-nematic model is defined in Fig. 2.14(a). For the prediction of P_z in $Ba_2CoGe_2O_7$, the magnetic in-plane field encloses an angle ρ with the a axis and induces a canting ϕ of the AFM spins. The angle κ denotes the deviation of the CoO_4 tetrahedron from the [110] direction as illustrated in Fig. 2.1(a). For P_x, the field angle to the c direction is θ and the upper and lower signs refer to $\theta \in (0, \pi)$ and $\theta \in (-\pi, 0)$, respectively. For the spontaneous toroidic effect mechanism in Ref. [91], predictions of P_z and P_x are only elaborated for particular field directions and c denotes a scale factor. Note that in the tetrahedral environment of $Ba_2TGe_2O_7$, the general expression of the p-d hybridization and spin-nematic interaction model are equivalent such that the predictions on $\mathbf{P}$ are the same.

Model	General expression	P_z for $\mathbf{B} \perp [001]$	P_x for $\mathbf{B} \perp [100]$
Symmetry analysis [139]	$P_z^{\mathrm{S}} \propto m_x^{\mathrm{AFM}} m_y^{\mathrm{AFM}}$ $P_x^{B} \propto m_x^{\mathrm{AFM}} m_z^{\mathrm{FM}}$ $P_z^{B} \propto (m_y^{\mathrm{FM}} m_y^{\mathrm{AFM}} - m_x^{\mathrm{FM}} m_x^{\mathrm{AFM}})$	$\propto \sin(2\rho)$	$\propto \pm\cos(\theta)$
p-d hybridization [86]	$\mathbf{P} \propto \sum_i \mathbf{e}_i (\mathbf{S} \cdot \mathbf{e}_i)^2$	$\propto \sin(2\rho)\cos(2\kappa - 2\phi)$	$\propto \begin{pmatrix} \pm\sin(2\kappa)\cos(\theta)\sin(2\phi) \\ -\cos(2\kappa)\sin(2\theta)\sin^2(\phi) \end{pmatrix}$
Spontaneous toroidic effect [91]	$\mathbf{P}^{\mathrm{S}} = \mu(\mathbf{T}^{\mathrm{S}} \times \mathbf{m}^{\mathrm{WFM}})$ $\mathbf{P}^{B} = \begin{pmatrix} \epsilon\mathbf{E} + \alpha\mathbf{B} \\ +\sigma^{B}(\mathbf{T} \times \mathbf{B}) \end{pmatrix}$	$\propto \begin{cases} B + cB^2 & \rho = \frac{\pi}{4} \\ -B - cB^2 & \rho = \frac{3\pi}{4} \end{cases}$	$\propto B$ for $\theta = 0$
Spin-nematic interaction [92]	$P_X \propto S_Y S_Z + S_Z S_Y$ $P_Y \propto S_Z S_X + S_X S_Z$ $P_Z \propto S_X S_Y + S_Y S_X$	$\propto \sin(2\rho)\cos(2\kappa - 2\phi)$	$\propto \begin{pmatrix} \pm\sin(2\kappa)\cos(\theta)\sin(2\phi) \\ -\cos(2\kappa)\sin(2\theta)\sin^2(\phi) \end{pmatrix}$
Inverse DMI [67]	$\mathbf{P} \propto \sum_{ij} \mathbf{e}_{ij} \times (\mathbf{S}_i \times \mathbf{S}_j)$	0	0

[94]. As the JT modes lift the degeneracy between the d_{xz} and d_{yz} orbitals, they are only active for melilites with TM ions that have an odd number of total electrons in the d_{xz} and d_{yz} orbitals, like Ni^{2+} ($3d^8$) or V^{2+} ($3d^3$) [94]. However, this is not the case for the TM ions of Cu, Co and Mn (see Fig. 2.2) such that a significant electric polarization from polar JT distortions is not expected to arise in the $Ba_2TGe_2O_7$ compounds studied within this work. Thus, we refer for further details, discussions and applications of the JT distortion model to Ref. [94].

2.3.5. Overview of the models' electric polarization

To conclude the introduction to the proposed models of multiferroicity for the melilite-type compounds, the basic predictions for the spontaneous and field-induced electric polarization, particularly for the $Ba_2CoGe_2O_7$ compound, are summarized in Table 2.2. Note that the JT distortion model is not listed as it is not expected to be present in to the studied compounds within this work (see discussion above). For completeness, the expression of the inverse DMI model, briefly introduced in Sec. 1.2, is listed as well. However, this conventional model is only applicable to the incommensurate magnetic order in $Ba_2CuGe_2O_7$ (see Sec. 2.2.1), which is not in the focus of this work.

2.4. The $Ba_2Cu_{1-x}Mn_xGe_2O_7$ solid solution series

The $Ba_2Cu_{1-x}Mn_xGe_2O_7$ solid solution series provides a structurally simple but physically highly interesting playground to study the various interactions present in the melilite-type compounds. In particular, the anisotropic effects resulting from the SOC and the crystal field effects proved to be of significant importance for the magnetic ordering but have a clearly different characteristic for the two TM ions, as discussed in detail in Secs. 2.2.1 and 2.2.3. Based on the electronic configuration of the Cu^{2+} ion in the tetrahedral environment, the SIA is expected to be negligibly small and an incommensurate AFM spin spiral ground state structure emerges, which is ferromagnetically coupled in c direction ($J^{\langle 001\rangle} < 0$) and primarily formed by the competition between the symmetric intra-plane interaction ($J^{\langle 110\rangle} > 0$) and the uniform in-plane DMI component $D_{\perp z}$ [36, 117, 121, 122]. The magnetic field-induced behaviour displays, however, a sizable easy-axis type anisotropy in the g-tensor. In contrast for the Mn^{2+} ion, only a very weak easy-plane type g-tensor anisotropy is found but a finite SIA is expected to be present, leading to a commensurate in-plane AFM structure ($J^{\langle 110\rangle} > 0$) that is antiferromagnetically coupled in c direction ($J^{\langle 001\rangle} > 0$, $\boldsymbol{\tau} = (00\frac{1}{2})$) and slightly canted by the alternating out-of-plane DMI component D_z [15, 86]. Given these significant differences, it is extremely interesting to clear how these differently signed and sized coupling effects compete in the mixed compounds of the $Ba_2Cu_{1-x}Mn_xGe_2O_7$ solid solution series and might help to better understand the basic interactions. Furthermore, it might provide a deeper insight into the spin-driven multiferroicity, which is attributed to the spin current mechanism for the incommensurate magnetic structure in $T = Cu$ [87] and to the novel p-d hybridization mechanism for the commensurate magnetic structure in $T = Mn$ [86].

Finally, this unique interplay of the different mechanisms in the $Ba_2Cu_{1-x}Mn_xGe_2O_7$ solid solution series might lead to the emergence of some new and interesting magnetic, multiferroic or quantum-critical properties.

So far, only the successful synthesis and structural characterization of polycrystalline samples is reported in the literature for the $Ba_2Cu_{1-x}Mn_xGe_2O_7$ solid solution series [98]. However, for the $Ba_2Cu_{1-x}Co_xGe_2O_7$ solid solution series, Sato *et al.* [99] performed magnetization measurements on polycrystalline samples. With these measurements, they could demonstrate the presence of a WFM moment for $x \geq 0.10\%$, which indicates that already a small Co concentration is sufficient to break the spiral AFM state and replace it by the commensurate AFM structure characteristic for $Ba_2CoGe_2O_7$.

3. Neutron Diffraction: Theory and Methods

In a quantum mechanical description, the elastic scattering process of neutrons from an initial momentum state $|\mathbf{k}_i\rangle$ to the final momentum state $|\mathbf{k}_f\rangle$ on a general potential $V(\mathbf{r})$ can be described by *Fermis Golden rule*, leading to an experimentally measurable differential scattering cross-section of [145]

$$\frac{\mathrm{d}\sigma}{\mathrm{d}\Omega} = \left(\frac{m_N}{2\pi\hbar^2}\right)^2 |\langle \mathbf{k}_f|V(\mathbf{r})|\mathbf{k}_i\rangle|^2. \tag{3.1}$$

As neutrons can be approximated by plane waves with propagation vector $\mathbf{k}$, the transition matrix element $\langle \mathbf{k}_f|V(\mathbf{r})|\mathbf{k}_i\rangle$ is given by the Fourier transformation

$$\langle \mathbf{k}_f|V(\mathbf{r})|\mathbf{k}_i\rangle \propto \int V(\mathbf{r}) e^{-i\mathbf{q}\cdot\mathbf{r}}\,\mathrm{d}\mathbf{r} \tag{3.2}$$

with the scattering vector $\mathbf{q} = \mathbf{k}_f - \mathbf{k}_i$. Note that in X-ray diffraction, $\mathbf{q}$ is usually defined as $\mathbf{k}_i - \mathbf{k}_f$ resulting in the the complex conjugate of the scattering matrix element, which is decisive for defining the handedness of chiral structures (see Sec. 3.3.2, in particular Eq. (3.32)). For scattering on the periodic potential of a lattice, a finite scattering amplitude is only observed if $\mathbf{q}$ is a reciprocal lattice vector. In this case, the Fourier transformation can be reduced to an integral over the UC

$$\langle \mathbf{k}_f|V(\mathbf{r})|\mathbf{k}_i\rangle \propto \sqrt{\frac{N_{\mathrm{UC}}}{V_{\mathrm{UC}}}} \underbrace{\int_{\mathrm{UC}} V(\mathbf{r}) e^{-i\mathbf{q}\cdot\mathbf{r}}\,\mathrm{d}\mathbf{r}}_{F}\,. \tag{3.3}$$

This integral is denoted as structure factor F and scaled by the number N_{UC} of UCs in the crystal and their volume V_{UC}.

For nuclear scattering, $V(\mathbf{r})$ is given by the sum of the scattering potentials of the individual atoms located at $\mathbf{r}_j$ in the UC. As the range of the nuclear interaction, defined by the size of the nucleus ($\sim 10^{-15}\,\mathrm{m}$), is clearly smaller than the neutron wavelength ($\sim 10^{-10}\,\mathrm{m}$), these individual potentials can be approximated by Fermi pseudo potentials, reducing the interaction to Dirac delta functions $V_j(\mathbf{r}) \propto b_j\,\delta(\mathbf{r} - \mathbf{r}_j)$ with coherent scattering length b_j. Therefore, the nuclear structure factor N can be written as [145]

$$N(\mathbf{q}) = \sum_j b_j e^{-W_j(\mathbf{q})} e^{-i\mathbf{q}\cdot\mathbf{r}_j}. \tag{3.4}$$

The q-dependent influence of the atoms thermal displacements $\mathbf{u}_j(t)$ from the equilibrium position $\mathbf{r}_j$ is summarized in the Debye-Waller factor with $W_j \propto |\mathbf{q}|^2$. Usually, the Debye-Waller factor is expressed by the isotropic (U^{iso}) or anisotropic (U_{ij}) mean atomic displacement parameters of the crystal structure

$$W^{\text{iso}}(\mathbf{q}) = \frac{1}{2}U^{\text{iso}}|\mathbf{q}|^2 \qquad W^{\text{aniso}}(\mathbf{q}) = \frac{1}{2}\sum_{ij} h_i a_i^* U_{ij} h_j a_j^*, \tag{3.5}$$

where h_i are the Miller indices of $\mathbf{q}$ and a_i^* the magnitudes of the reciprocal lattice vectors $\mathbf{a}_i^*$, such that $\mathbf{q} = \sum_i h_i \mathbf{a}_i^*$ [146, 147].

For magnetic scattering, the potential $V(\mathbf{r})$ is given by the interaction between the dipole moment $\boldsymbol{\mu}_N$ of the neutron and the magnetization density $\mathbf{m}(\mathbf{r})$ of the unpaired electrons in the UC [148]. Note that only the magnetization perpendicular to the scattering vector $\mathbf{m}_{\perp\mathbf{q}} = \hat{\mathbf{q}} \times (\mathbf{m} \times \hat{\mathbf{q}})$ contributes, thus $V(\mathbf{r}) \propto \boldsymbol{\mu}_N \cdot \mathbf{m}_{\perp\mathbf{q}}(\mathbf{r})$. As the neutrons dipole moment is given by the Pauli spin operator $\hat{\boldsymbol{\sigma}}$, it can be extracted from the Fourier transformation in Eq. (3.3), resulting in a vectorial magnetic scattering factor $\mathbf{M}$, which can be written as [149]

$$\mathbf{M}(\mathbf{q}) = \left(\frac{\gamma_N r_0}{2\mu_B}\right) \int_{\text{UC}} \mathbf{m}_{\perp\mathbf{q}}(\mathbf{r}) e^{-i\mathbf{q}\cdot\mathbf{r}}\, \mathrm{d}\mathbf{r} \tag{3.6}$$

with conversion constant $\gamma_N r_0/2\mu_B \approx 2.695\,\text{fm}/\mu_B$ from magnetization to scattering length. In dipole approximation, the integral over the magnetization can be replaced by a sum of individual magnetic moments $\mathbf{m}_j$ of atoms j at $\mathbf{r}_j$ multiplied by a magnetic form factor $f_j(\mathbf{q})$, accounting for its spatial distribution, and the Debye-Waller factor. This reduces the magnetic scattering factor to

$$\mathbf{M}(\mathbf{q}) = \left(\frac{\gamma_N r_0}{2\mu_B}\right) \sum_j f_j(\mathbf{q}) (\mathbf{m}_j)_{\perp\mathbf{q}} e^{-W_j(\mathbf{q})} e^{-i\mathbf{q}\cdot\mathbf{r}_j}. \tag{3.7}$$

For spin-modulated structures with propagation vectors $\boldsymbol{\tau}_k$, the magnetic moment $\mathbf{m}_j$ is replaced in the magnetic scattering factor for a specific $\boldsymbol{\tau}_n$ by the complex Fourier coefficient $\mathbf{T}_{j,\boldsymbol{\tau}_n}$, which is given by the expansion of $\mathbf{m}_j$ in the modulations $\boldsymbol{\tau}_k$ as

$$\mathbf{m}_j = \frac{1}{2}\sum_k \mathbf{T}_{j,\boldsymbol{\tau}_k} e^{i\boldsymbol{\tau}_k\cdot\mathbf{r}_j} + \mathbf{T}^*_{j,\boldsymbol{\tau}_k} e^{-i\boldsymbol{\tau}_k\cdot\mathbf{r}_j} = \sum_k \mathrm{Re}\left[\mathbf{T}_{j,\boldsymbol{\tau}_k} e^{i\boldsymbol{\tau}_k\cdot\mathbf{r}_j}\right]. \tag{3.8}$$

If an isotropic distribution $\mathbf{m}(\mathbf{r}) = \mathbf{m}(|\mathbf{r}|)$ of the magnetization density is assumed, the dependency of the magnetic form factor on the direction of $\mathbf{q}$ can be dropped. The resulting $f_j(q)$, which depends only on the magnitude of the scattering vector $q = |\mathbf{q}|$, is usually approximated by

$$f(q) = \mathcal{J}_0(q) + \mathcal{J}_2(q)\left(\frac{2}{g_J} - 1\right) \tag{3.9}$$

using the Landé factor g_J, which is given in Eq. (2.1) and defined by the electronic configuration, and the orthogonal Bessel functions $\mathcal{J}_n$ with order n, defined by

$$\mathcal{J}_n(q) = 4\pi \int_0^\infty \mathcal{J}_n(q\,r)\rho(r)r^2\,\mathrm{d}r \tag{3.10}$$

with ρ the normalized density of the unpaired electrons averaged over all directions. For a more convenient application, Brown [150] provides empirical coefficients for an analytical approximation of $\mathcal{J}_0(q)$ and $\mathcal{J}_2(q)$ by

$$\mathcal{J}_0(q) = A\mathrm{e}^{-as^2} + B\mathrm{e}^{-bs^2} + C\mathrm{e}^{-cs^2} + D \tag{3.11}$$

$$\mathcal{J}_2(q) = s^2\left(A'\mathrm{e}^{-a's^2} + B'\mathrm{e}^{-b's^2} + C'\mathrm{e}^{-c's^2} + D'\right) \tag{3.12}$$

with $s = q/4\pi = \sin(\theta)/\lambda$. For quenched orbital momenta ($L = 0$), the approximation of the magnetic form factor depends only on $\mathcal{J}_0$ as $g_J = 2$.

3.1. Neutron spin and density matrix formalism

So far, only the scattering of one momentum state to another was considered. However, neutrons are spin-½ particles, and thus have an additional spin state $|\chi\rangle$. For a quantization axis z, which might be defined by a magnetic field, the spin state can be expressed as a superposition of the pure spin-up $|+\rangle$ and spin-down $|-\rangle$ states. The neutron spin $\mathbf{s}$ is connected to the spin state by the expectation value of Pauli spin operator $\hat{\boldsymbol{\sigma}}$

$$\langle \mathbf{s} \rangle = \frac{\hbar}{2}\left\langle \chi^\dagger \middle| \hat{\boldsymbol{\sigma}} \middle| \chi \right\rangle \tag{3.13}$$

with Planck constant $\hbar$ and spin matrices (see appendix B.1)

$$\hat{\sigma}_x\,|\pm\rangle = |\mp\rangle \qquad \hat{\sigma}_y\,|\pm\rangle = \pm i\,|\mp\rangle \qquad \hat{\sigma}_z\,|\pm\rangle = \pm\,|\pm\rangle\,. \tag{3.14}$$

To describe the polarization $\mathbf{P}$ of a neutron beam, which reflects a statistical ensemble of neutron spin states, the density matrix formalism [151, 152] can be used. It defines a new density operator $\hat{\rho}$, which can be expressed as the average dyadic product of the individual spin states $|\chi_i\rangle$ for the N_n neutrons in the beam [153]

$$\hat{\rho} = \frac{1}{N_n}\sum_i \left|\chi_i\middle\rangle\middle\langle\chi_i^\dagger\right| = \frac{1}{2}\left(\mathbb{1} + \mathbf{P}\cdot\hat{\boldsymbol{\sigma}}\right). \tag{3.15}$$

Within this formalism, the ensemble average of an operator $\hat{A}$, denoted as $\left\langle \hat{A} \right\rangle_{\hat{\rho}}$, can be written as

$$\left\langle \hat{A} \right\rangle_{\hat{\rho}} = \mathrm{Tr}\left(\hat{\rho}\hat{A}\right), \tag{3.16}$$

which leads to the useful identity $\mathbf{P} = \langle \hat{\boldsymbol{\sigma}} \rangle_{\hat{\rho}}$ for the incoming neutron beam polarization. This density matrix formalism is especially powerful to determine scattering

cross-sections. Investigating the transformation of the spin state by a general scattering matrix $\hat{V}$ in Born approximation, the density matrix $\hat{\rho}'$, describing the neutron beam after the scattering process, can be written as [154]

$$\hat{\rho}' = \hat{V}\hat{\rho}\hat{V}^\dagger. \tag{3.17}$$

The trace of $\hat{\rho}'$ recovers the total scattering cross-section $\sigma_{\hat{V},\mathbf{P}}$ on $\hat{V}$ for an incident polarization $\mathbf{P}$ of the beam (see appendix B.1)

$$\sigma_{\hat{V},\mathbf{P}} = \mathrm{Tr}\left(\hat{\rho}'\right) = \left\langle \hat{V}^\dagger\hat{V}\right\rangle_{\hat{\rho}} = \frac{1}{2}\left[\mathrm{Tr}\left(\hat{V}^\dagger\hat{V}\right) + \mathbf{P}\cdot\mathrm{Tr}\left(\hat{\boldsymbol{\sigma}}\hat{V}^\dagger\hat{V}\right)\right]. \tag{3.18}$$

Thus, the density matrix describing the neutron beam after the scattering process is scaled for its cross-section and can be written as

$$\hat{\rho}' = \frac{\sigma_{\hat{V},\mathbf{P}}}{2}\left(\mathbb{1} + \mathbf{P}^{\mathrm{sc}}\cdot\hat{\boldsymbol{\sigma}}\right), \tag{3.19}$$

with the final polarization $\mathbf{P}^{\mathrm{sc}}$ of the scatted beam. The evaluation of the ensemble average of $\hat{\boldsymbol{\sigma}}$ leads to the general formula for $\mathbf{P}^{\mathrm{sc}}$ based on the incoming neutron polarization $\mathbf{P}$ and the scattering matrix $\hat{V}$

$$\sigma_{\hat{V},\mathbf{P}}\mathbf{P}^{\mathrm{sc}} = \langle\hat{\boldsymbol{\sigma}}\rangle_{\hat{\rho}'} = \left\langle \hat{V}^\dagger\hat{\boldsymbol{\sigma}}\hat{V}\right\rangle_{\hat{\rho}} = \frac{1}{2}\left[\mathrm{Tr}\left(\hat{V}^\dagger\hat{\boldsymbol{\sigma}}\hat{V}\right) + \mathrm{Tr}\left(\mathbf{P}\cdot\hat{\boldsymbol{\sigma}}\hat{V}^\dagger\hat{\boldsymbol{\sigma}}\hat{V}\right)\right]. \tag{3.20}$$

For coherent elastic neutron scattering, the scattering matrix is given by

$$\hat{V} = N\mathbb{1} + \mathbf{M}\cdot\hat{\boldsymbol{\sigma}} \qquad\qquad \hat{V}^\dagger = N^*\mathbb{1} + \mathbf{M}^*\cdot\hat{\boldsymbol{\sigma}}, \tag{3.21}$$

with potentially complex nuclear and magnetic structure factors N and $\mathbf{M}$ defined in Eqs. (3.4) and (3.7), respectively. Note that the additional scale factor, accounting, e.g., for the crystal size, was dismissed for clarity. If this scattering matrix is plugged into Eqs. (3.18) and (3.20), the two master equations of polarized neutron diffraction (PND) are revealed, which were first derived by Blume [155] and Maleev *et al.* [156] and are capable of completely describing the coherent elastic neutron scattering process.

$$\begin{aligned}
\sigma_{\mathbf{P}} =& NN^* && \}\,\text{nuclear}\\
&+ \mathbf{M}\cdot\mathbf{M}^* && \}\,\text{magnetic}\\
&+ 2\mathbf{P}\cdot\mathrm{Re}[\mathbf{M}N^*] && \}\,\text{interference}\\
&- i\mathbf{P}\cdot(\mathbf{M}\times\mathbf{M}^*) && \}\,\text{chiral}
\end{aligned} \tag{3.22}$$

$$\begin{aligned}
\mathbf{P}^{\mathrm{sc}}\sigma_{\mathbf{P}} =& \mathbf{P}NN^* && \}\,\text{nuclear}\\
&- \mathbf{P}\left(\mathbf{M}\cdot\mathbf{M}^*\right) + 2\,\mathrm{Re}[\mathbf{M}\left(\mathbf{P}\cdot\mathbf{M}^*\right)] && \}\,\text{magnetic}\\
&+ 2\,\mathrm{Re}[\mathbf{M}N^*] + 2\mathbf{P}\times\mathrm{Im}[\mathbf{M}N^*] && \}\,\text{interference}\\
&+ i\left(\mathbf{M}\times\mathbf{M}^*\right) && \}\,\text{chiral}
\end{aligned} \tag{3.23}$$

The individual contributions from pure nuclear and magnetic scattering and the mixed interference terms are labeled. The chiral contribution can only be present in helical spin structures (i.e. spin structures with the same amplitude modulation $\boldsymbol{\tau}$ in at least two independent spin components with a finite phase shift $\phi \neq n\pi$ between them) and its sign defines the handedness of the spin spiral. Some properties of the Pauli spin matrices, useful to derive these equations, are listed in appendix B.1.

3.2. Non-polarized neutron diffraction

For an non-polarized neutron diffraction experiment, the measured intensity I for a Bragg reflection $\mathbf{q}$ is given by the total scattering cross-section in Eq. (3.22) with $\mathbf{P} = 0$, which yields

$$I \propto \sigma_{\mathbf{P}=0} = \underbrace{NN^*}_{\propto I^N} + \underbrace{\mathbf{M} \cdot \mathbf{M}^*}_{\propto I^M}. \tag{3.24}$$

Thus, the measured intensity can be separated into a pure nuclear (I^N) and magnetic (I^M) part. As both contributions scale with the square of the scattering factor, small magnetic contributions might be difficult to observe (e.g. if $|\mathbf{M}|$ is 10% of $|N|$, the magnetic contribution I^M is only 1% of I^N). Moreover, any phase information about N and $\mathbf{M}$ is lost and the the dependency of the scattered intensity on the direction of the magnetic moments $\mathbf{m}$ is only given by the projection perpendicular to $\mathbf{q}$ in Eq. (3.7). Thus, it might not be possible to distinguish between different magnetic moment arrangements by non-polarized neutron diffraction. For example in Sec. 4.2.2, the two magnetic moment configurations displayed in Figs. 4.2(a) and 4.2(b) corresponding to a negative and positive sign of the DMI in $Ba_2CoGe_2O_7$, respectively, are indistinguishable by non-polarized neutron diffraction as they differ only in the sign of the AFM moment. Likewise, it is impossible to distinguish between the two magnetic ground state symmetries $P2_1'2_12'$ and $Cm'm2'$ in $Ba_2CoGe_2O_7$ with equally populated tetragonal domains and AFM moments in the [100] and [110] directions as illustrated in Figs. 6.9(a) and 6.9(b), respectively. This issue is further discussed in Sec. 6.3.1 and Ref. [30].

3.2.1. Neutron single crystal diffraction (ND)

In non-polarized neutron single crystal diffraction (ND), the intensity of a preferably large set of Bragg reflections is collected. This allows to determine precise values for the atoms positions, the mean square displacements and the occupancies by least-square refinement. Moreover, ND can be effectively used to determine the magnitude of ordered magnetic moments and monitor their dependency on external properties like temperature, applied magnetic or electric fields and pressure. This works especially well for $\mathbf{t} \neq 0$ magnetic structures (e.g. incommensurate or AFM structures), where the nuclear and magnetic intensities occur on a separate type of reflection.

Typically, ND experiments are carried out at four-cycle instruments (e.g. HEiDi [157] at the Heinz Maier-Leibnitz Zentrum (MLZ), Germany, or D9 and D10 at the Institut Laue-Langevin (ILL), France). A photograph of the HEiDi diffractometer with labeled primary instrumental components is shown in Fig. 3.1(a). However, for very bulky sample environments, like large high-field cryomagnets or voluminous cryostats, also two-axis normal beam geometry instruments (e.g. POLI [159] at MLZ or D23 at ILL) might be used for ND. Notably, they require an additional correction for the intensity of out-of-plane reflections measured by rocking curves as the vertical sample rotation axis is not perfectly perpendicular to the scattering vector.

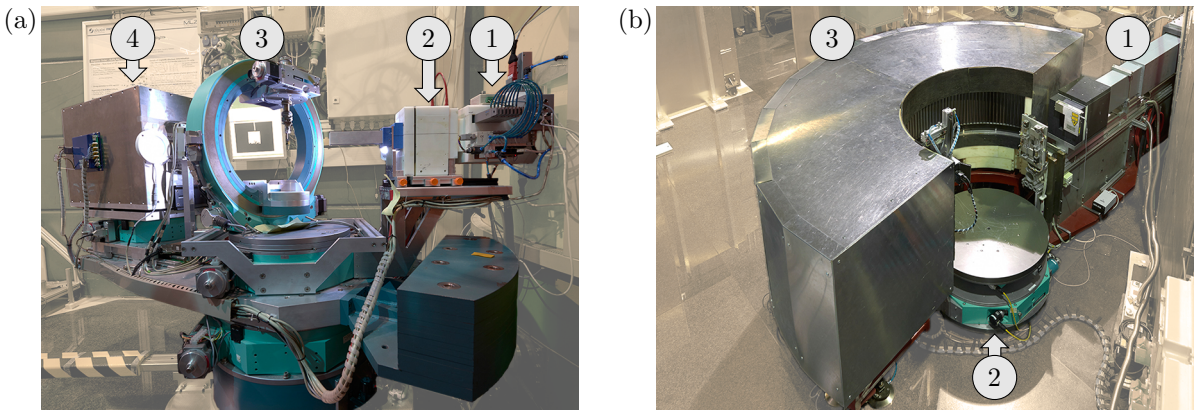

Figure 3.1.: Photograph of (a) the four-cycle neutron single crystal diffractometer HEiDi and (b) the neutron powder diffractometer SPODI, modified from Refs. [157] and [158], respectively. In (a), the monochromatic neutron beam is coming from the right side of the picture and first passes (1) optional resonance filters and (2) collimators before being scattered at the sample mounted to (3) the Eulerian cradle. Notably, the cradle can also host a compact cryostat or furnace, giving access to sample temperatures between 2 K and 500 K. The scattered neutron beam is counted in (4) the detector. In (b), the monochromatic neutron beam is also coming from the right side of the picture and is first shaped in (1) optional beam collimators before being scattered at the sample, which can be hosted in various sample environment devices supported by (2) the large sample table. The scattered neutrons are counted in the position sensitive ^{3}He detector covering an angular range of 160° horizontally and a height of 300 mm.

3.2.2. Neutron powder diffraction (PD)

As the powder sample is composed of many small single crystals with random orientation, the wave vectors $\mathbf{k}_f$ of the scattered neutrons lie for a fixed incoming wave vector $\mathbf{k}_i$ on a cone, which is known as the *Debye-Scherrer cone* [160]. Thus, so-called Debye rings are detected instead of individual Bragg reflections. Accordingly, the total scattering cross-section is calculated by averaging over all possible crystal orientations leading for a specific $\mathbf{q}$ to a sum of contributions from all reflections with the same value of $|\mathbf{q}|$ [145]. The measured powder pattern is typically analyzed by Rietveld refinement [161]. Within the pattern, the peak positions precisely define the lattice parameters whereas the peak intensities reflect the atomic and magnetic structure. The peak shape can additionally be used to conclude about the crystallinity and structural disorder or defects [162].

Assuming a completely random orientation of the large number of crystallites in a finely ground powder, the diffracted intensity is distributed evenly around the Debye rings. Therefore, it is sufficient to measure only a narrow region of the powder ring, as it is done in conventional neutron powder diffraction (PD) instruments (e.g. SPODI [158] at MLZ or D2B and D20 at ILL) by a cylindrical area detector placed around the sample position and covering a certain angular range of the diffracted beam (e.g. scattering angles from $2\theta = 0°$ up to 160° at SPODI). A photograph illustrating the primary components of the SPODI instrument is shown in Fig. 3.1(b). Although PD allows to determine the evolution of the nuclear and magnetic structure under various environmental conditions, different magnetic spin arrangements might be indistinguishable

due to the powder averaging. Notably, the application of directed external influences (e.g. uniaxial pressure and magnetic or electric fields) might break the assumption of completely randomized orientations of the crystallites. If X-rays are used instead of neutrons, the same experimental procedure as described above can be applied; however, the scattering cross-sections need to be modified accordingly. The resulting formalism for X-ray powder diffraction (XRD) is discussed in detail, e.g., in Ref. [163].

3.3. Polarized neutron diffraction (PND)

In a more classical approach compared to Sec. 3.1, the neutron beam polarisation can be treated as a vector $\mathbf{P} = P\hat{\mathbf{e}}_\mathbf{B}$ directed along a quantization axis $\hat{\mathbf{e}}_\mathbf{B}$ defined by an external magnetic field $\mathbf{B}$. The polarization value P is given by the number of the neutrons in the up (n^+) and down (n^-) state as

$$P = \frac{n^+ - n^-}{n^+ + n^-}. \tag{3.25}$$

If the magnetic field changes its direction suddenly, the neutron polarization $\mathbf{P}$ starts to precess around the new direction $\mathbf{B}'$ with Larmor frequency $f_L = -2913\frac{\mathrm{Hz}}{\mathrm{G}}B'$, where B' denotes the magnitude of the field. Taking into account the neutron velocity $v_N = 3956\,\frac{\mathrm{mÅ}}{\mathrm{s}}/\lambda$, this corresponds to a precession angle $\phi_L = 265\frac{\mathrm{deg}}{\mathrm{GÅm}}B'\lambda s$ over a distance s. Note that non-SI units $\mathrm{G} = 0.1\,\mathrm{mT}$ and $\mathrm{Å} = 0.1\,\mathrm{nm}$ are commonly used in neutron diffraction. As the neutron beam has a finite wavelength spread $\Delta\lambda/\lambda$, there is also a spread in ϕ_L. Although this effect is negligible for a single precession, it causes the polarization component perpendicular to $\mathbf{B}'$ to average out after many rotations. Thus, the new polarization $\mathbf{P}'$ in $\mathbf{B}'$ is given by the projection $P' = \mathbf{P} \cdot \hat{\mathbf{e}}_{\mathbf{B}'}$. In contrast, a sudden field change and a well defined Larmor precession over a short distance is used in spin flip devices (e.g. Mezei-type double coil flippers [164] or cryoflippers [165]) and precession coils [166] to modify the beam polarization. A spin flip denotes the reversal of the polarization state in regard to the quantization axis (i.e. $P' = -P$). However, if the angular rotation of the magnetic field is slow compared to the Larmor frequency ($\omega_B < \omega_L/10$), the precession allows the polarization to follow this so-called adiabatic field rotation. This is crucial for polarized neutron instrumentation as it allows to guide the beam polarization by only smoothly changing magnetic fields. If the strength of these guide fields is clearly larger than environmental stray fields at the instrument, they additionally suppress unwanted precessions of the neutron polarization.

In general, a neutron beam polarization can be created and analyzed by using dedicated polarizers, like FM single crystals [167], supermirrors [168] or ^{3}He spin filter cells (SFCs) [169]. Their basic functionality is briefly described in appendix B.2. By using different combinations of neutron polarizers with spin flippers or precession coils before and after the sample position, further scattering contributions in Eq. (3.22) and 3.23 are experimentally accessible, providing a more detailed insight into the nuclear and magnetic structure. In the following, two of the most common PND methods, namely the classical flipping ratio (FR) and the SNP technique, are briefly described and their scattering cross-sections developed.

3.3.1. Flipping ratio (FR) method

For the FR method, the sample is situated in a magnetic field, which serves as guide field for the neutron polarization; thus, $\mathbf{P}$ is parallel to the applied field direction. As small magnetic fields of a few Gauss are already sufficient to maintain the beam polarization, a wide range of magnetic field strengths are accessible to study the magnetic response of the investigated compound. For the FR method, only the incoming neutron beam is polarized with a value P given by the efficiency of the polarizer. In addition, a spin flipper is placed between the polarizer and the sample. As discussed above, this flipper can be used to reverse the polarization direction with an efficiency η^{SF}, leading to an incoming polarization $\mathbf{P}^- = -\eta^{\mathrm{SF}}\mathbf{P}^+$, where $\mathbf{P}^+$ denotes the polarization with deactivated spin flipper. Usually, this flipping efficiency is very close to one and can be neglected.

The measured intensities with deactivated (I^+) and activated (I^-) spin flipper are given by the total scattering cross-section $\sigma_{\mathbf{P}}$ defined in Eq. (3.22) with $\mathbf{P}^+$ and $\mathbf{P}^-$, respectively. These intensities are used to define the so-called asymmetry A, which is directly related to the nuclear and magnetic scattering factors as

$$A = \frac{I^+ - I^-}{I^+ + I^-} = P\frac{2\,\mathrm{Re}[\mathbf{M}_{\parallel\mathbf{B}}N^*] - i\,(\mathbf{M}\times\mathbf{M}^*)_{\parallel\mathbf{B}}}{NN^* + \mathbf{M}\cdot\mathbf{M}^*}. \tag{3.26}$$

Note that classically, the flipping ratio $R = I^+/I^-$ is used instead of the asymmetry A. Although they are basically equivalent (i.e. $R = (1+A)/(1-A)$), the R value is highly non-linear and asymmetric in the polarization dependent contributions. Thus, the asymmetry A is preferred in the following. For Eq. (3.26), a perfect flipping efficiency $\eta^{\mathrm{SF}} = 1$ is assumed. If this is not the case (i.e. $\eta^{\mathrm{SF}} < 1$), the measured asymmetry A has to be corrected by

$$A^{\mathrm{corr}} = \frac{2}{(1+\eta^{\mathrm{SF}}) - A(1-\eta^{\mathrm{SF}})}A. \tag{3.27}$$

The clear advantage of using asymmetries rather than intensities is that scaling effects, like the absorption at irregular crystal shapes and the Lorentz factor, which may strongly affect the measured absolute intensity, cancel out by forming the intensity ratio (see Sec. 3.4 for more details). This facilitates also the usage of large 2D detectors, as there is no need for complex geometrical corrections, which simply cancel out in A. For point detectors, it is usually sufficient to perform background-peak-background scans instead of measuring the full rocking curve. However, this requires high mechanical precision such that no discrepancy occurs in the sample positioning between the I^+ and I^- measurement, which may lead to distorted asymmetries.

For mixed nuclear magnetic reflections, which typically requires a zero magnetic propagation vector $\boldsymbol{\tau}$, the asymmetries are primarily defined by the interference term in the numerator of Eq. (3.26). As this term is linear in the magnetic scattering factor, FR measurements allow to extract even small magnetic contributions. In particular, the analysis of the measured asymmetries enables to precisely determine field-induced magnetic moment values, leading to detailed atomic site susceptibility tensors [170] and high-quality magnetic form factors [171, 172]. Since the interference term is given by

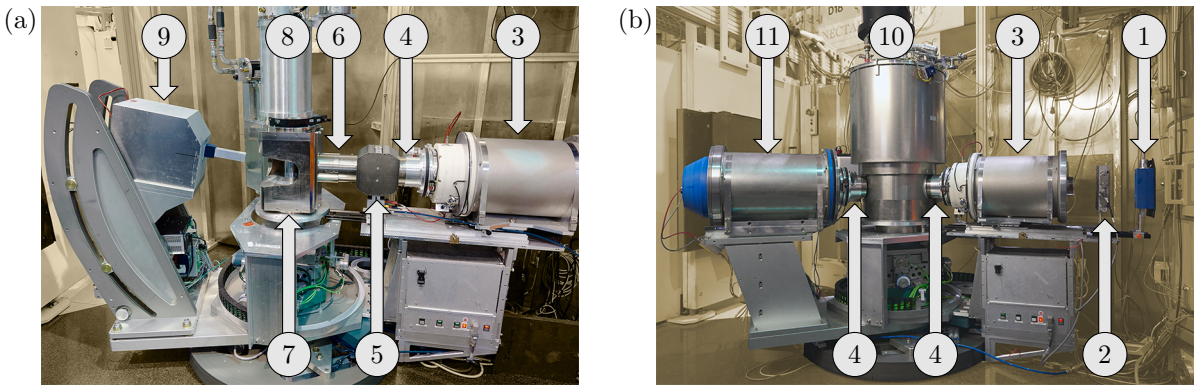

Figure 3.2.: Photograph of (a) the FR and (b) the SNP setup option for PND at POLI. For both setups, the monochromatic neutron beam is coming from the right side of the pictures and passes first (1) a neutron monitor and (2) motorized slits, which are not visible in (a). The neutron beam is polarized in (3) the polarizer hosting a ^{3}He SFC (see appendix B.2). At the exit of the polarizer, there is (4) a nutator (see Ref. [176]) attached, which allows to rotate the neutron polarization in the plane normal to the beam. However, for the FR setup in (a), this nutator is fixed such that the neutron polarization is directed vertically and flipped by (5) a passively shielded Mezei-type spin flipper (see Sec. 5.1.3). This flipper is connected by (6) shielded guide fields to (7) the superconducting 2.2 T magnet. The sample is located in (8) the cryostat, which is inserted into the magnet. The scattered neutrons are counted in (9) the detector with lifting mechanics, giving access to angles ν from $-5°$ to $30°$ below and above the instrumental plane, respectively. In contrast for the SNP setup option in (b), there is (10) a CryoPAD (see Ref. [177]) installed at the sample position, which provides a zero field chamber and has precession coils, which are used in combination with (4) the two nutators to select any axis for the neutron polarization and analysis. For this analysis, another ^{3}He SFC and a neutron detector are combined in (11) the Decpol (see Ref. [178]). Picture (a) is modified from Ref. [179].

the projection of $\mathbf{M}$ to the polarization axis defined by the magnetic field direction, the FR method provides an additional spatial resolution that can help to identify even complex magnetic moment arrangements. Finally, the phase shift between nuclear and magnetic structure factor is conserved by the interference term, which allows to extract the magnetization density distribution $\mathbf{m}(\mathbf{r})$ in the UC by inverse Fourier transformation [173], multipolar expansion [174] or maximum entropy reconstruction [175] (more detailed in Sec. 3.5). As $\mathbf{m}(\mathbf{r})$ is related to the density of the unpaired electrons, the basic motivation to reconstruct the magnetization density is to gain a better insight into the electronic structure by identifying aspherical density distributions [153]. In addition, this phase information may also help to distinguish between different magnetic moment arrangements as utilized, for example, in Secs. 6.3.3 and 7.4.3 to reveal the absolute sign of the DMI vector in $Ba_2CoGe_2O_7$ and $Ba_2CuGe_2O_7$, respectively.

Although Eq. (3.26) is valid for different magnetic field directions defining the polarization axis, a typical FR setup at a normal beam geometry instrument (e.g. POLI [179] at MLZ or D3 at ILL) utilizes large superconducting magnets providing a fixed high magnetic field along the vertical instrument axis. Therefore, different polarization axes might only be available by reorientation of the crystal. A photograph of the FR setup option at POLI, using a 2.2 T superconducting magnet with a symmetric field design as described in Ref. [179], is shown in Fig. 3.2(a).

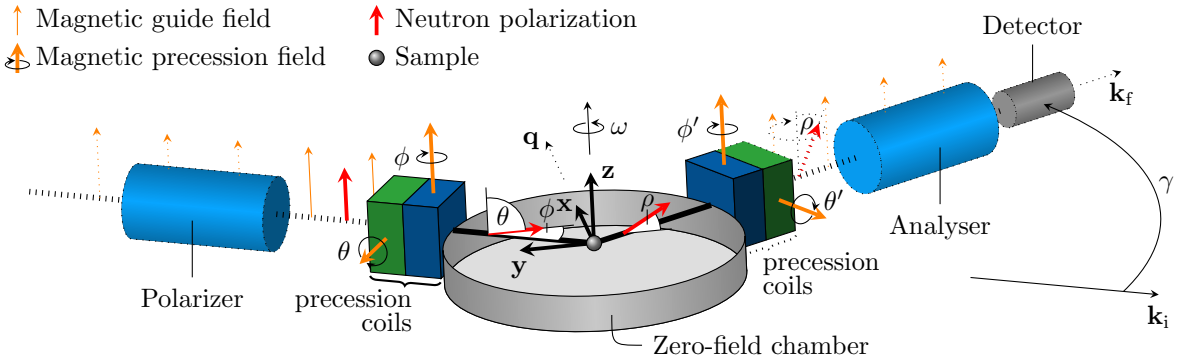

Figure 3.3.: Layout of a typical SNP instrument. The incoming monochromatic neutron beam from the left passes first a polarizer situated in a magnetic guide field. This leads to a neutron polarization $\mathbf{P}$ parallel to the field. Afterwards, precession coils are used to rotate the polarization in any desired direction. The polarization rotation angles θ and ϕ are selected by adjusting the magnitude and sign of the precession fields. Within this illustration, the angles θ and ϕ are chosen such that the incoming polarization $\mathbf{P}$ points in $-\mathbf{y}$ direction of the scattering reference system, defined as $\mathbf{x} \parallel \mathbf{q}$, $\mathbf{z} \parallel \mathbf{k}_i \times \mathbf{k}_f$ and $\mathbf{y} \parallel \mathbf{z} \times \mathbf{x}$ (thick black arrows). Directly after the precession coils, the neutron beam enters a zero-field chamber, which conserves $\mathbf{P}$ until the scattering at the sample. Within this illustration, the scattering process leads to a slight rotation of the neutron polarisation out of the instrumental plane, which can be caused by real and finite N and M_z values with $M_y = 0$. Consequently, the scattered polarization $\mathbf{P}^{\mathrm{sc}}$ encloses an angle ρ with the $-\mathbf{y}$ direction. Using a second set of precession coils at the exit of the zero-field chamber, any polarization direction $\mathbf{P}'$ can be rotated to the analysis direction defined by the subsequent guide field. After this rotation, the component of $\mathbf{P}^{\mathrm{sc}}$ that was perpendicular to $\mathbf{P}'$ will be perpendicular to the guide field as well, and thus averages out due to Larmor precession. This corresponds to the projection of $\mathbf{P}^{\mathrm{sc}}$ to $\mathbf{P}'$ for the analysis. Within this illustration, the angles ϕ' and θ' are chosen such that $-\mathbf{y}$ is rotated in analysis direction. Thus, the projection in the guide field of the analyser, indicated by the precessional motion of the rotated beam polarization, is given by $\mathbf{P}^{\mathrm{sc}} \cdot \mathbf{P}' = P\cos(\rho)$. The measured intensity in the detector is described by the cross-section $\sigma_{\mathbf{PP}'}$ ($\sigma_{\bar{y}\bar{y}}$ for this example) defined in Eq. (3.29) and listed in Table B.1 in the appendix.

3.3.2. Spherical neutron polarimetry (SNP)

A typical instrumental layout for SNP is illustrated and described in Fig. 3.3. The essential difference to the FR method is that the sample is placed in a zero-field chamber, which conserves the neutron beam polarization $\mathbf{P}$ and $\mathbf{P}^{\mathrm{sc}}$ (indicated by red arrows in Fig. 3.3) before and after the scattering process, respectively. Using a polarizer with efficiency P and a set of two precession coils (green and blue cuboids in Fig. 3.3), which have an abrupt transition to the zero-field chamber to conserve the spin direction, any axis can be selected for the incoming neutron polarization $\mathbf{P}$. Analogously, by using another set of two precession coils and an analyzer with efficiency P' after the sample, the scattered polarization $\mathbf{P}^{\mathrm{sc}}$ can be projected to any analysis axis $\mathbf{P}'$. Thus, the total scattering cross-section is given by

$$\sigma_{\mathbf{PP}'} = \frac{1 + \mathbf{P}' \cdot \mathbf{P}^{\mathrm{sc}}}{2} \sigma_{\mathbf{P}}. \tag{3.28}$$

Replacing $\mathbf{P}^{\mathrm{sc}}\sigma_{\mathbf{P}}$ by Eq. (3.23) and $\sigma_{\mathbf{P}}$ by Eq. (3.22) leads to the general connection between the scattered cross-section and the nuclear and magnetic structure factor for

an SNP measurement with arbitrary polarization and analysis direction given as

$$\begin{aligned}
\sigma_{\mathbf{PP}'} =& \frac{1+\mathbf{P}\cdot\mathbf{P}'}{2} NN^* && \} \text{ nuclear} \\
&+ \frac{1-\mathbf{P}\cdot\mathbf{P}'}{2} \mathbf{M}\cdot\mathbf{M}^* + \mathrm{Re}[(\mathbf{P}\cdot\mathbf{M})\left(\mathbf{P}'\cdot\mathbf{M}^*\right)] && \} \text{ magnetic} \\
&+ (\mathbf{P}+\mathbf{P}')\cdot\mathrm{Re}[\mathbf{M}N^*] - (\mathbf{P}\times\mathbf{P}')\cdot\mathrm{Im}[\mathbf{M}N^*] && \} \text{ interference} \\
&- \frac{i}{2}(\mathbf{P}-\mathbf{P}')\cdot(\mathbf{M}\times\mathbf{M}^*)\,. && \} \text{ chiral}
\end{aligned} \tag{3.29}$$

For improved clarity, one might introduce a new reference system for the scattering process with $\mathbf{x} \parallel \mathbf{q}$, $\mathbf{z} \parallel \mathbf{k}_i \times \mathbf{k}_f$ and $\mathbf{y}$ making up a right-handed set (illustrated by thick black arrows in Fig. 3.3). As $\mathbf{x}$ is chosen in direction of the scattering vector $\mathbf{q}$, the M_x component is zero. Thus, Eq. (3.29) can be written as

$$\begin{aligned}
\sigma_{\mathbf{PP}'} =& \frac{1+P_xP_x'+P_yP_y'+P_zP_z'}{2} NN^* \\
&+ \frac{1-P_xP_x'+P_yP_y'-P_zP_z'}{2} M_yM_y^* \\
&+ \frac{1-P_xP_x'-P_yP_y'+P_zP_z'}{2} M_zM_z^* \\
&+ \left(P_y+P_y'\right)\mathrm{Re}[M_yN^*] + \left(P_xP_z'-P_zP_x'\right)\mathrm{Im}[M_yN^*] \\
&+ \left(P_z+P_z'\right)\mathrm{Re}[M_zN^*] + \left(P_yP_x'-P_xP_y'\right)\mathrm{Im}[M_zN^*] \\
&+ \left(P_x-P_x'\right)\mathrm{Im}[M_yM_z^*] + \left(P_yP_z'+P_zP_y'\right)\mathrm{Re}[M_yM_z^*]
\end{aligned} \tag{3.30}$$

This equation provides a good overview of the information that are accessible with SNP. Although it is valid for an arbitrary polarization and analysis axis, $\mathbf{P}$ and $\mathbf{P}'$ are chosen in a typical SNP experiment to be parallel or antiparallel to one of the three axes of the reference system. These six independent directions ($\pm\mathbf{x}$, $\pm\mathbf{y}$, and $\pm\mathbf{z}$) for $\mathbf{P}$ and $\mathbf{P}'$ lead to a total of 36 possible scattering channels, which are listed in Table B.1 in the appendix.

To separate the individual contributions and to cancel out scaling effects of the absolute intensity (see discussion about the equivalent asymmetry in Sec. 3.3.1), the so-called polarization matrix $\mathcal{P}$ is used with elements

$$\mathcal{P}_{\mathbf{PP}'} = \frac{\sigma_{\mathbf{PP}'} - \sigma_{\mathbf{P-P}'}}{\sigma_{\mathbf{PP}'} + \sigma_{\mathbf{P-P}'}}, \tag{3.31}$$

resulting from the intensities measured with antiparallel analysis directions $\mathbf{P}'$ and $-\mathbf{P}'$. These nine matrix elements are given in appendix B.4. For incommensurate reflections (i.e. $N = 0$), the chiral ratio R^{ch} is additionally defined as

$$R^{\mathrm{ch}} = \frac{\sigma_{\mathbf{P-P}'} - \sigma_{\mathbf{-PP}'}}{\sigma_{\mathbf{P-P}'} + \sigma_{\mathbf{-PP}'}} = \frac{P+P'}{1+PP'} \underbrace{\frac{-i\,(\mathbf{M}\times\mathbf{M}^*)_{\parallel\mathbf{q}}}{\mathbf{M}\cdot\mathbf{M}^*}}_{\frac{2\,\mathrm{Im}[M_yM_z^*]}{M_yM_y^*+M_zM_z^*}}, \tag{3.32}$$

with $\mathbf{P}$ and $\mathbf{P}'$ parallel to $\mathbf{q}$. As this ratio is directly proportional to the chiral contribution, the experimentally measured sign of R^{ch} allows to determine the handedness of a magnetic structure [180]. The magnitude of R^{ch} denotes the eccentricity of the spiral structure projected to the plane perpendicular to $\mathbf{q}$. For the contribution of a single spin spiral in a single domain state, the projected spin spiral is circular for $|R^{\mathrm{ch}}| = 1$ and linear for $|R^{\mathrm{ch}}| = 0$, whereas it is elliptical for $0 < |R^{\mathrm{ch}}| < 1$. However, for equally populated left and right handed domains, the total chiral ratio cancels out although a spin spiral is present.

In general, SNP can be applied to determine precise magnetic moment values and directions [181], domain distributions [182] and magnetic form factors [183], in particular, for AFM and spin modulated structures. This might allow to solve even complex magnetic structures and can be combined with the variation of external parameters like pressure [184] or electric field [185, 186]. In addition, the sample may be cooled below the magnetic transition temperature in an applied magnetic field. This might result in a field-dependent spin alignment or domain imbalance even after removing the field for the SNP measurement [187].

Experimentally, the zero field chamber for SNP is realized by using either a mu-metal or a superconducting Meissner shielding, denoted as MuPAD [188] or CryoPAD [177], respectively. As both devices are rather voluminous and only allow the measurement of Bragg-reflections in the instrumental plane, the SNP option is typically offered by normal beam geometry instruments (e.g. POLI [176] at MLZ or D3 at ILL) or three-axis spectrometers (e.g. MIRA [189] at MLZ or IN20 at ILL). A photograph of the SNP setup option at POLI using the third generation CryoPAD device and a ^{3}He SFC polarizer and analyzer (see appendix B.2) is shown in Fig. 3.2(b).

3.4. Intensity corrections

So far, the theory of neutron scattering has been developed by assuming the kinematic theory of diffraction [145]. However, in a typical diffraction measurement, additional effects like absorption, structural and magnetic domains, multiple scattering, extinction and λ/n contamination can strongly influence the measured intensity. Therefore, additional correction parameters may be introduced.

3.4.1. Absorption

The absorption within the crystal is strongly correlated with the crystal shape and can clearly influence the total measured intensity of a specific reflection. For a regular crystal shape like a sphere or cylinder, the values of the q-dependent absorption correction factor $A(\mathbf{q})$ are tabulated or can be analytically approximated [190, 191]. For irregular shapes in contrast, the values of $A(\mathbf{q})$ are usually calculated by numerical integration over an approximated crystal shape [192]. As the absorption correction factor is assumed to be neutron polarization independent, it cancels out by forming the intensity ratio in polarized diffraction. However, for a proper refinement of non-polarized single crystal

diffraction data, the absorption correction is essential.

3.4.2. Influence of structural and magnetic domains

Assuming an incoherent superposition of the individual contributions from the domains d, the scattered intensity σ of the crystal is given by the sum of the individual scattered intensities σ_d weighted by their domain fraction c_d as

$$\sigma = \sum_d c_d \sigma_d. \tag{3.33}$$

Thus, domains need to be considered for both, polarized and non-polarized single crystal diffraction. Note that for PND an imbalance between magnetic domains with inverted sign of $\mathbf{M}$ is essential to access the scattering contributions linear in $\mathbf{M}$ (see interference terms in Eqs. (3.22) and (3.23)).

3.4.3. Multiple scattering

Multiple scattering for a reflection $\mathbf{q}$, also known as Renninger effect [193], occurs when the surface of the Ewald sphere simultaneously passes through another reciprocal lattice point $\mathbf{q}^{'}$, which implies that $\mathbf{q}^{''} = \mathbf{q} - \mathbf{q}^{'}$ is a reciprocal lattice point as well. Therefore, the scattering vector can also be expressed as $\mathbf{q} = \mathbf{q}^{'} + \mathbf{q}^{''}$, resulting in an additional contribution from the scattering first at $\mathbf{q}^{'}$ then at $\mathbf{q}^{''}$ and vice versa [194]. Multiple scattering affects both non-polarized and polarized diffraction and was found to be strong, e.g., in $Ba_2CoGe_2O_7$ [104]. Note that for PND, the incoming neutron polarization for the second scattering event is given by the scattered polarization from the first event, which may lead to a rather complex behaviour.

3.4.4. Extinction

Extinction describes the attenuation of the incident and the diffracted neutron beam by scattering in the crystal, leading to a reduction of the integrated intensity from the expected value of the kinematic theory [195]. In a perfect crystal, the neutron transmission is clearly reduced for those beam directions in which diffraction takes place, as some of the neutrons are redirected into the scattered beam. In particular for strong reflections, the lower lying layers of the crystal see a less intense neutron beam, and thus contribute less to the diffracted intensity. In contrast, for weak reflections, only a slight attenuation of the neutron beam takes place such that all layers of the crystal contribute almost equally. Moreover, multiple diffraction with $\pm\mathbf{q}$ might occur and cause destructive interference, reducing both the intensity of the diffracted and initial neutron beam. These effects in perfect crystals can be treated by the dynamical theory of diffraction and are known as *primary extinction* [196]. However, for an imperfect crystal, which might be modeled as a mosaic crystal composed of small but perfect crystallites, only small parts of the crystal are coherently aligned. For this reason, the primary extinction, occurring only within the small crystallites, becomes less important.

Nevertheless, lower parts of the crystal still see a reduced neutron beam due to diffraction on crystallites in the upper part. This effect, denoted as *secondary extinction*, depends again on the strength of the corresponding reflection but also on the mosaic spread of the crystal, describing the half width of the angular distribution of the crystallites orientation [197]. Notably, no destructive interference contributes to secondary extinction as the crystallites are incoherently aligned. Decisive for the extinction in general are the particle size and mosaic spread of the crystal combined with the neutron wavelength and the crystal dimensions [195–197].

A commonly used approximation for primary extinction in a perfect crystal and secondary extinction in a mosaic crystal is provided by Becker and Coppens [195]. The basic equations are summarized in appendix C and, for example, used in single crystal refinement programs like the Cambridge Crystallographic Subroutine Library (*CCSL*) [198] and *JANA2006* [199]. A compromise to treat both primary and secondary extinction simultaneously and to include anisotropy effects was found by the empirical model

$$y_\sigma = \left(\sqrt{1 + \frac{x\sigma\lambda^5}{4000 \sin(2\theta) \sin^2(\theta)}} \right)^{-1}, \tag{3.34}$$

with the neutron wavelength λ, the theoretical cross-section σ and the diffraction angle θ. As a result, the measured cross-section for a reflection $\mathbf{q}$ with Miller indices $\mathbf{h}$ is given by $\sigma^{\text{mes}} = y_\sigma \sigma$, where x is calculated from the extinction tensor $\mathcal{X}$ by projection on $\mathbf{h}$ as

$$x = \mathbf{h}^\mathsf{T} \mathcal{X} \mathbf{h} = \left[\begin{pmatrix} x_{11} & x_{12} & x_{13} \\ 0 & x_{22} & x_{23} \\ 0 & 0 & x_{33} \end{pmatrix} \cdot \mathbf{h} \right] \cdot \mathbf{h}. \tag{3.35}$$

The entries x_{ij} are determined by least-square refinement [200]. This extinction correction model is implemented in single crystal refinement programs like *Mag2Pol* [200], *FullProf* [201] and *SHELX* [202].

As the extinction correction is non-linear in the scattering cross-section, the total intensity in PND, which is given by $\sigma_{\mathbf{PP}'}$ for a polarization and analysis axis $\hat{\mathbf{P}}$ and $\hat{\mathbf{P}}'$ with efficiencies P and P' (see Eq. (3.29)), must be separated into the four basic scattering processes $\sigma_{\pm\hat{\mathbf{P}}\pm\hat{\mathbf{P}}'}$ and $\sigma_{\pm\hat{\mathbf{P}}\mp\hat{\mathbf{P}}'}$, denoted as $\sigma_{\pm\pm}$ and $\sigma_{\pm\mp}$, respectively. This results in

$$\sigma_{\mathbf{PP}'} = w_{++}\sigma_{++} + w_{+-}\sigma_{+-} + w_{-+}\sigma_{-+} + w_{--}\sigma_{--}, \tag{3.36}$$

with weighting factor $w_{\pm\pm} = (1 \pm P)(1 \pm P')/4$ and $w_{\pm\mp} = (1 \pm P)(1 \mp P')/4$. Thus, the measured cross-section that considers extinction is given by

$$\sigma^{\text{mes}}_{\mathbf{PP}'} = w_{++}y_{\sigma_{++}}\sigma_{++} + w_{+-}y_{\sigma_{+-}}\sigma_{+-} + w_{-+}y_{\sigma_{-+}}\sigma_{-+} + w_{--}y_{\sigma_{--}}\sigma_{--}. \tag{3.37}$$

This equation reflects the most general case as applied in SNP. For the FR method, the polarization can be set to $\hat{\mathbf{P}} = \hat{\mathbf{P}}' \parallel \mathbf{B}$ and $P' = 0$, and thus the four basic scattering cross-sections in Eq. (3.37) are written as

$$\begin{aligned} \sigma^{\text{FR}}_{\pm\pm} &= |N|^2 + \left|\hat{\mathbf{P}} \cdot \mathbf{M}\right|^2 \pm 2\hat{\mathbf{P}} \cdot \text{Re}[\mathbf{M}N^*] \\ \sigma^{\text{FR}}_{\pm\mp} &= |\mathbf{M}|^2 - \left|\hat{\mathbf{P}} \cdot \mathbf{M}\right|^2 \mp i\hat{\mathbf{P}} \cdot (\mathbf{M} \times \mathbf{M}^*) \end{aligned} \tag{3.38}$$

with weighting factors $w_{\pm\pm} = w_{\pm\mp} = (1 \pm P)/4$. This leads finally to the same FR extinction correction factors as presented in Ref. [200] and in the manual of *FullProf*. Note that an extinction correction for the general case of SNP is only implemented in *Mag2Pol*; however, its details are not reported in Ref. [200]. Thus, Eq. (3.37) proposes for the first time a specific formalism also applicable to the extinction correction in SNP.

3.4.5. Higher-order reflections

If there are λ/n contaminations in the neutron beam, which denote fractions c_n of neutrons with wavelengths λ/n, additional higher-order reflections with $\mathbf{q}_n = n\mathbf{q}$ might contribute to the scattered intensity. This may not only change the measured absolute intensity but also distort the polarization of the scattered beam, as the higher-order reflections usually have different N and $\mathbf{M}$. Although the λ/n contaminations could be considered during the structure refinement, they are especially difficult to treat in PND as the efficiency and transmission of polarizer and analyzer might be wavelength dependent as well (see SFC polarizer in appendix B.2).

3.5. Reconstruction of magnetization densities

Going back to Eq. (3.6) reveals that measurements of the magnetic scattering factors $\mathbf{M}$ provide direct information about the Fourier components $\mathbf{F}_\mathrm{M}$ of the magnetization density $\mathbf{m}(\mathbf{r})$ in the UC as

$$\mathbf{M} = \left(\frac{\gamma_N r_0}{2\mu_B}\right) \hat{\mathbf{q}} \times (\mathbf{F}_\mathrm{M} \times \hat{\mathbf{q}}) \tag{3.39}$$

with

$$\mathbf{F}_\mathrm{M} = \int_\mathrm{UC} \mathbf{m}(\mathbf{r}) e^{-i\mathbf{q}\cdot\mathbf{r}} \, \mathrm{d}\mathbf{r} \,. \tag{3.40}$$

As the measured intensity in a non-polarized neutron diffraction experiment depends on $|\mathbf{M}|^2$ (see Eq. (3.24)), typically all phase information on $\mathbf{F}_\mathrm{M}$ is lost. However, for PND measurements, some phase information on $\mathbf{F}_\mathrm{M}$ is conserved in the nuclear magnetic interference terms (see Eqs. (3.22) and (3.23)), which may be extracted if the atomic arrangement is well known. Thus, PND might allow to reconstruct the magnetization density in the UC, which provides an exceptional insight into the density distribution of the unpaired electrons [153].

3.5.1. Direct inverse Fourier transformation

The obvious choice for a reconstruction of $\mathbf{m}(\mathbf{r})$ is a Fourier inversion according to

$$\mathbf{m}(\mathbf{r}) = \frac{1}{V_\mathrm{UC}} \sum_{\mathbf{q}} \mathbf{F}_\mathrm{M} e^{i\mathbf{q}\cdot\mathbf{r}}, \tag{3.41}$$

which requires the precise knowledge of $\mathbf{F}_\mathrm{M}$ for all magnetic reflections $\mathbf{q}$. However, due to the projection of $\mathbf{F}_\mathrm{M}$ to the plane perpendicular to $\mathbf{q}$ in Eq. (3.39), a full knowledge about $\mathbf{F}_\mathrm{M}$ for each measured reflection is rare. One typical example for that $\mathbf{F}_\mathrm{M}$ can be directly calculated from the measurement is the reconstruction of field-induced magnetization densities in centrosymmetric structures by the FR method [203, 204]. This classical case is shortly summarized in appendix D.1.

As the experimentally accessible number of reflections is necessarily limited, not all Fourier coefficients $\mathbf{F}_\mathrm{M}$ can be determined. In addition, the measured intensities, and thus the determined Fourier coefficients, are polluted by noise. This can clearly affect the quality of the reconstructed magnetization density, which might suffer from heavy truncation and noise effects [175].

3.5.2. Conventional maximum entropy method

To overcome the issue of incomplete and noisy neutron diffraction data, Papoular and Gillon [175] suggested to use a maximum entropy method (MEM) for the reconstruction of magnetization densities. This Bayesian statistical technique is widely used to improve the image quality, for example, in (medical) tomography, astronomy, or general image processing [205, 206]. It can be applied to almost all reconstructions of an image from a discrete set of projection data. For the case of PND, the image is the magnetization density $\mathbf{m}_i$ in the UC at specific grid points $\mathbf{r}_i$ and the projections are the measured Fourier components $\mathbf{F}_k$ for reflections $\mathbf{q}_k$ [175].

According to the classical MEM algorithm of Skilling and Bryan [207], which was extended for sign-altering densities by Balandin and Kaneko [205] and requires a fixed magnetic moment direction such that the magnetization density and the Fourier components can be reduced to scalar values m_i and F_k, two main properties are defined. First, the entropy S for the $2N_i$ positive image points $f_i^\pm$ as

$$S = -\sum_i f_i^\pm \left(\log\left(\frac{f_i^\pm}{A} \right) - 1 \right), \tag{3.42}$$

such that the magnetization density at the UC grid point $\mathbf{r}_i$ is given by $m_i = f_i^+ - f_i^-$. The parameter A denotes the default value of $f_i^\pm$ that maximizes the entropy. As the image points will approach A if there are no data constraints, it can be considered as background and is typically selected below the significance of the expected density [207]. The second property is the quality of fit C as

$$C = \frac{1}{N_k} \sum_k \frac{(F_k^\mathrm{calc} - F_k^\mathrm{obs})^2}{(dF_k^\mathrm{obs})^2}, \tag{3.43}$$

with the calculated and measured Fourier components F_k^calc and F_k^obs for the N_k reflections. For the assumption of a commensurate structure, F_k^obs can be directly calculated from the measured asymmetry as demonstrated in appendix D.1 whereas F_k^calc can be defined from Eq. (3.40) by replacing the integral with a sum over the grid points $\mathbf{r}_i$ and

d$\mathbf{r}$ with V_{UC}/N_i. The residuals are weighted by dF_k^{obs}, denoting the uncertainty of the measurement result.

In an iterative process, the MEM selects the density with the highest entropy that is compatible with the data within a given precision, defined as upper limit C_{aim} for C. According to the general Bayes' theorem, the selected density has the highest intrinsic probability among all possible reconstructions sharing the same C_{aim} value [208]. As a result, $m(\mathbf{r}_i)$ is only non-zero at positions, which are clearly indicated in the measured data. Moreover, no assumptions are made about the not measured Fourier components and the experimental uncertainty is considered. Therefore, truncation and noise effects are reduced compared to the classical Fourier inversion [209]. The basic concept of the maximum entropy algorithm of Skilling and Bryan [207] is outlined in appendix D.2.

A conventional MEM algorithm is, for example, implemented in the *CCSL* software suit as *MENT* subroutine, initially designed for the reconstruction of nuclear densities from neutron powder and single crystal diffraction but extended for the reconstruction of magnetization densities from FR measurements [210]. Using the *ARRANGE* and *SORGAM* subroutines, the Fourier components F_k^{obs} are calculated for the measured reflections $\mathbf{q}_k$ and serve as input for *MENT*. Thus, this software can only treat centrosymmetric crystals and requires a fixed magnetic moment direction.

3.5.3. Advanced 3D maximum entropy method

A further improvement of the conventional MEM algorithm for the FR method was provided by Schleger *et al.* [211]. They could show that the method can also be applied if the measured projections are complex non-linear functions of the image points. With this generalization, they redefined the fit quality C on the residuals of the measured asymmetries A_k^{obs} (see Sec. 3.3.1) with experimental uncertainty dA_k^{obs} as

$$C = \frac{1}{N_k} \sum_k \frac{(A_k^{\mathrm{calc}} - A_k^{\mathrm{obs}})^2}{(dA_k^{\mathrm{obs}})^2}. \tag{3.44}$$

Consequently, the Fourier components F_k^{obs} must not be calculated explicitly from the measured FR data. For this reason, the density reconstruction in noncentrosymmetric crystals becomes available. Moreover, it is possible with this improved approach to apply corrections for extinction and λ/n contamination (see Sec. 3.4) by directly including it in the calculation of A_k^{calc}. Although Schleger *et al.* [211] implemented their results in a modified version of the *FORTRAN 77*-based *MEMSYS3* subroutine library, this version is not publicly available and still limited to the FR method with a collinear magnetization aligned along the applied magnetic field.

However, under the prerequisite of this possible non-linear extension in C, the formalism required for an advanced maximum entropy algorithm, capable of reconstructing a non-collinear magnetization density from a general PND measurement, can be derived. Within this novel approach, applicable for the first time not only to FR but also to SNP data, the calculation of the fit quality is based on the general scattering cross section for a polarized and analyzed neutron beam presented in Eq. (3.29). To overcome the

restriction of collinear aligned densities, a set of up to three orthonormal base vectors $\mathbf{b}_b$ is introduced such that the magnetization density at grid point $\mathbf{r_i}$ is given by $N_b \leq 3$ image points $f_{i,b}$ as

$$\mathbf{m}(\mathbf{r}_i) = \sum_b f_{i,b}\mathbf{b}_b = \mathcal{B}\mathbf{f}_i. \tag{3.45}$$

The columns of $\mathcal{B}$ are given by the N_b base vectors $\mathbf{b}_b$. With some effort, the general scattering cross section σ_k in Eq. (3.29) can be rearrange in terms of the image points $\mathbf{f}_i$ as

$$\sigma_k = u_k + \sum_i \mathbf{v}_{i,k} \cdot \mathbf{f}_i + \sum_{i,j} \mathbf{f}_j^{\mathsf{T}} \mathcal{W}_{i,j,k} \mathbf{f}_i \tag{3.46}$$

with u_k, $\mathbf{v}_{i,k}$ and $\mathcal{W}_{i,j,k}$ determined by the incoming polarization $\mathbf{P}_k$ and analysis axis $\mathbf{P}_k^{'}$ and explicitly given in appendix D.3. As a result, A_k^{calc} in Eq. (3.44) is given by

$$A_k^{\mathrm{calc}} = \frac{\sigma_k^+ - \sigma_k^-}{\sigma_k^+ + \sigma_k^-} \tag{3.47}$$

with $\sigma_k^{\pm}$ denoting the scattering cross section with and without spin flipping. Note that typically $\mathbf{P}_k^{\pm} = \pm\mathbf{P}_k$ and $\mathbf{P}_k^{'\pm} = 0$ for the FR method, whereas $\mathbf{P}_k^{\pm} = \mathbf{P}_k$ and $\mathbf{P}_k^{'\pm} = \pm\mathbf{P}_k^{'}$ for SNP (see Secs. 3.3.1 and 3.3.2).

To avoid distortions of the reconstructed density, the entropy S, which reflects the probability of the image, should be independent from the magnetization direction. Thus, the conventional definition in Eq. (3.42) is not directly applicable to the novel non-collinear case as the entropy would be maximized for magnetization directions along the base vectors even if the magnitude of the magnetization stays constant. A possible solution is the quadratic entropy definition available in the conventional *MEMSYS5* subroutine library [212]. However, this approach reduces the maximum entropy to a least squares, which is not intended. As an alternative, the image points f_i in the conventional entropy definition might be replaced by $|f_i| + A$, which allows positive and negative values for f_i and conserves the original behaviour of S as shown in appendix D.3. Without any data constraints, this approach maximizes the entropy by $f_i = 0$, correctly reproducing a vanishing density. This alternative entropy description can be straightforwardly extended to the non-collinear case such that S is finally given as

$$S = -\sum_i (|\mathbf{f}_i| + A)\left(\log\left(\frac{|\mathbf{f}_i| + A}{A}\right) - 1\right). \tag{3.48}$$

Note that $|\mathbf{m}(\mathbf{r}_i)| = |\mathbf{f}_i|$ holds due to the orthonormal choice of base $\mathcal{B}$. Although the partial derivatives of C and S with respect to the image points $f_{i,b}$, which are derived in appendix D.3, become considerably more complex, the same basic algorithm of Skilling and Bryan [207], outlined in appendix D.2, can be applied.

This novel approach is implemented in the graphical user interface (GUI) based **Adv**anced maximum **Ent**ropy (*AdvEnt*) software package, entirely written in *C++* for high performance and mainly based on the *Qt5* library. It is designed for multicore processing, significantly speeding up the iterative reconstruction process. The implementation of the basic MEM solver is based on the *C++* translation of the original

FORTRAN 77-based *MEMSYS* code, generously provided by Marsh [213] for public usage. As the software utilizes the general scattering cross section for a polarized and analyzed neutron beam in Eq. (3.29), it can treat both FR and SNP data with arbitrary polarization values and directions. Additional features like the usage of multiple datasets, symmetry constraints on the reconstructed density, magnetic domains and extinction corrections are implemented and automated. Moreover, an experimental approach to utilize directly the measured intensities in the calculation of C to enable also the inclusion of non-polarized data is provided but not yet thoroughly tested. The software is compiled using a static *QT5* version and thus available as standalone executable on *WINDOWS*.

For the practical usage of the new software employing the basic MEM algorithm of Skilling and Bryan [207], a proper selection of the control parameters C_{aim}, A and l_0, defined in Sec. D.2 and denoting the desired fit quality, the default value and the step size, respectively, is beneficial for a quick and stable convergence of the algorithm. The C_{aim} value directly influences the weighting between maximizing the fit quality and the entropy. For a too small C_{aim}, the measurement values are over-interpreted such that the background fluctuations and artifacts in the reconstructed densities clearly increase whereas for too large values of C_{aim}, the densities get less detailed and features, which might be clearly evident in the data, are blurred. Systematically comparing different values and combinations of the MEM parameters in various compounds, a C_{aim} of around 10% larger than C_{min}, the smallest C value that can be reached by a density reconstruction, proved to be a practical compromise. This C_{min} value provides a good measure for the systematic deviations in the combined FR datasets that are not considered in the uncertainty estimation and cannot be recovered by a physical density (e.g. uncertainties in the crystal orientations or an imperfect background correction resulting in inconsistent values for the same Bragg reflection measured in different FR datasets). For ideal datasets with an accurate uncertainty estimation, the C_{min} should be close or even below 1. An unusually large C_{min} value might hint at the selection of unsuitable symmetry restrictions or incorrect base vectors for the density reconstruction. In contrast, the choice of A and l_0 did not noticeably influence the final image but they define the convergence behaviour. Values of around $A = 0.01\,\mu_B/V_{\mathrm{UC}}\mathrm{T}$ and $l_0 = 1$ demonstrated a stable and reasonably fast convergence for all tested compounds. As convergence criteria, an image variation $|\mathrm{d}\mathbf{f}|/|\mathbf{f}| < 0.1\%$ with $|\mathbf{f}| = \sqrt{\sum_{i,b} f_{i,b}^2}$ proved to be reliable and resulted consistently in an angle $\phi < 1°$ enclosed between the gradients of S and C according to the definition in Eq. (D.17), which reflects a true maximum entropy solution for $\phi = 0$. The ϕ parameter itself showed a rather volatile behaviour and thus could not serve as a reliable convergence parameter. Owing to the parallel design of the *ADVENT* software, a reasonable fast iteration speed and a convergence within a couple of minutes could be reached on a Intel i7-7700K processor (four physical and eight virtual cores at 4.2 GHz) even for combined datasets with several thousand reflections and high-resolution grids. First applications of the new method and software to PND data on the $Ba_2TGe_2O_7$ ($T =$ Cu, Co and Mn) compounds are presented and discussed in Chap. 8.

3.5.4. Local susceptibility approach

During the completion of this work, another maximum entropy approach for the reconstruction of non-collinear magnetization densities was developed by Kibalin and Gukasov [214] using local susceptibilities. In the following, this approach is shortly introduced, discussed and compared to our method presented in the previous section. As starting point, Kibalin and Gukasov [214] partition the UC into atomic basins, defined as polyhedral regions of space closest to the corresponding atom. At grid points $\mathbf{r}_i$ in basins of non-magnetic atoms, the magnetization density $\mathbf{m}_i$ is assumed to be collinear to the applied magnetic field direction $\hat{\mathbf{B}}$ and given by $\mathbf{m}_i^{\mathbf{B}} = (f_i^+ - f_i^-)\hat{\mathbf{B}}$, with positive image points $f_i^{\pm}$ as discussed for the conventional MEM in Sec. 3.5.2. However, at grid points in the basins of magnetic atoms j, a normalized local susceptibility tensor χ_j is assumed and the magnetization density is given by $\mathbf{m}_i^{\chi} = f_i^{\chi}(\chi_j \hat{\mathbf{B}})$ with positive image points f_i^{χ}. The normalization of χ_j is such that the largest axis of the magnetic ellipsoid formed by the tensor is one; thus, defining only its shape but not its magnitude. The entries of these χ_j tensors are restricted by symmetry and might be related between different magnetic atoms j.

For the entropy S, Kibalin and Gukasov [214] reuse the concept of the two-channel entropy in Eq. (3.42) by extending the sum for the f_i^{χ} values. This definition allows them to introduce a more general approach that uses magnetic basins (partitions of the UC considering only magnetic atoms) and has both $\mathbf{m}_i^{\mathbf{B}}$ and $\mathbf{m}_i^{\chi}$ contributing to $\mathbf{m}_i$ at all $\mathbf{r}_i$. However, they dismiss this approach with reference to a strong increase in the calculation time and convergence issues in the reconstruction. In addition, it might be important to note that their proposed definition of S is not independent from the magnetization direction if $\mathbf{m}_i^{\mathbf{B}}$ and $\mathbf{m}_i^{\chi}$ are simultaneously active. According to the discussion in Sec. 3.5.3 and appendix D.3, this can cause artifacts and severe distortions in the reconstructed density and should be avoided. Nevertheless, their simplified approach of atomic basins using either $\mathbf{m}_i^{\mathbf{B}}$ or $\mathbf{m}_i^{\chi}$ exclusively does not have these issues. As fit quality C, a definition similar to Eq. (3.44) is applied, preventing the limitation to centrosymmetric structures.

The reconstruction algorithm is based on an iterative process that alternately repeats a least square refinement for χ_j and a maximum entropy calculation for the image points until convergence is reached. In that sense, it is not a pure maximum entropy approach but breaks down to a combination of the conventional MEM (see Sec. 3.5.2) with an additional and separated refinement of local susceptibilities. As a result, the reconstructed magnetization density is collinear within the atomic basins, which is typically sufficient to describe the field-induced magnetization density for most TM ion compounds in the PM phase. However, noncollinearities might emerge within these basins in more complex environments, like magnetically ordered phases or for rare-earth ions, that can not be recovered as demonstrated and discussed by the simulated magnetization density of $R_2Ti_2O_7$ ($R =$ Tb, Ho, Er, Yb) in Ref. [214]. In addition, discontinuities in the magnetization direction might appear at the boundaries of the basins and their software can only be applied to FR data. These essential limitations do not exist for our advanced MEM, presented in Sec. 3.5.3.

4. The Dzyaloshinskii-Moriya interaction (DMI)

The DMI was first introduced in the late fifties to explain a small canting of magnetic moments away from the perfect collinear AFM alignment as found in the classical weak ferromagnets α-Fe_2O_3, $MnCO_3$ and $CoCO_3$ [17–20]. Based on pure symmetry arguments, Dzyaloshinsky [18] could show that for an appropriate crystal symmetry an additional contribution

$$E^{\mathrm{DMI}} = \mathbf{D} \cdot (\mathbf{S}_A \times \mathbf{S}_B) \tag{4.1}$$

in the interaction between two AFM sublattices $\mathbf{S}_1$ and $\mathbf{S}_2$ is possible, which depends on the vector parameter $\mathbf{D}$ and favours a small canting of collinear spins [17, 18]. Shortly afterwards, Moriya [19] provided the microscopic mechanism of the DMI by including SOC in the theory of anisotropic superexchange, described by the formalism of Anderson [215]. For a sufficiently low crystal symmetry, requiring in particular a broken local inversion symmetry, the predominant term of this extended anisotropic superexchange interaction is linear in the SOC and has an antisymmetric form as given by Eq. (4.1) [19, 20].

The DMI reattained particular interest in current condensed matter research as it is present in a wide range of complex magnetic materials [23–25] and is the driving force to stabilize various novel topological non-collinear magnetic structures [26–28]. Especially for thin film systems, where a so-called interfacial DMI can be artificially induced by a local inversion symmetry breaking at the layer interface, the DMI induced magnetic structures provide promising characteristics towards novel spintronic devices [26].

Compared to the symmetric exchange energy, scaling with the scalar product $\mathbf{S}_1 \cdot \mathbf{S}_2$ of the two spins, the magnitude of the antisymmetric DMI is usually small, but its direction, as emphasized by Hu [216], is often a decisive factor in determining the system's chirality [217]. For example in ultrathin magnetic heterostructures with Néel-like domain wall spirals, the interfacial DMI sign is directly coupled to the direction to which a domain wall moves with current via the spin Hall torque [218–220]. In addition, the DMI sign has a fundamental impact on skyrmions, topologically stable magnetic structures that are promising candidates as information carriers for future ultrahigh-density storage and logic devices [38–42, 217]. By interface engineering, i.e. sandwiching the skyrmion carrying magnetic layer between two heavy-metal films characterized by interfacial DMI constants of opposite sign, a strong DMI was achieved to facilitate ultra-dense skyrmion packaging [221]. Furthermore, to realize a straight, longitudinal transmission of isolated magnetic skyrmions in thin films, which is essential for future skyrmionic devices, the skyrmion Hall effect, leading to a transverse motion, must be suppressed [222]. A recent

approach for such a suppression utilizes a fine-tuned mixture of interfacial and bulk DMIs, the latter classically arising from an inversion symmetry breaking in the atomic structure of the layer, causing an asymmetry in the spin-orbit-torque-induced skyrmion Hall angle for the two different skyrmion polarities [223]. In this regard, the sign of the bulk DMI determines the polarity of the straightly transmitted skyrmion.

However, using the DMI definition in Eq. (4.1), the sign of the vector parameter $\mathbf{D}$ can not be uniquely defined, since it depends on our choice which magnetic sublattice is A or B [224]. To resolve this issue, the global interaction vector between the sublattices is redefined on an atomic level by an antisymmetric $\mathbf{D}_{ij}$ for each magnetic moment pair $\mathbf{m}_i$, $\mathbf{m}_j$. This leads to a contribution of the DMI to the interaction energy of [225]

$$\Delta E = \sum_{i,j} \mathbf{D}_{ij} \cdot (\mathbf{m}_i \times \mathbf{m}_j)\,. \tag{4.2}$$

Since the vector parameter $\mathbf{D}_{ij}$ is antisymmetric (i.e. satisfies $\mathbf{D}_{ij} = -\mathbf{D}_{ji}$), Eq. (4.2) is kept invariant under any spin interchange, and thus can be used to define the sign of the DMI.

4.1. Symmetry-induced restrictions of the DMI vector

As already suggested by Dzyaloshinsky [18], the components of the DMI vectors $\mathbf{D}_{ij}$ are restricted by the local symmetry of the corresponding system. A general approach for the determination of these restrictions was recently developed by us and presented in Ref. [21]. This approach is briefly summarized in the following.

As the vector product $(\mathbf{m}_i \times \mathbf{m}_j)$ of the contributing moments transforms as an axial vector (see appendix A.1), the DMI vector parameter $\mathbf{D}$ may also be expected to transform as an axial vector such that the DMI energy remains invariant under any symmetry operation. This means, if two sites $\mathbf{r}_1$ and $\mathbf{r}_2$ are connected by the DMI vector $\mathbf{D}_{12}$, then the sites $\mathbf{r}_{S1}$ and $\mathbf{r}_{S2}$, resulting from $\mathbf{r}_1$ and $\mathbf{r}_2$ by symmetry operation $\mathcal{S}$, are connected by

$$\mathbf{D}_{S1\,S2} = \det(\mathcal{R})\,\mathcal{R}\mathbf{D}_{12}, \tag{4.3}$$

where $\mathcal{R}$ is the point group symmetry part of $\mathcal{S}$. This does not only relate the DMI vectors of symmetry equivalent site-pairs but also imposes symmetry restrictions on $\mathbf{D}_{12}$, if $\mathcal{S}$ interchanges $\mathbf{r}_1$ and $\mathbf{r}_2$ or leaves them unchanged. For an interchange of the two sites, e.g., by an inversion center between them, Eq. (4.3) can be reduced to $\mathbf{D}_{12} = -\det(\mathcal{R})\,\mathcal{R}\mathbf{D}_{12}$, utilizing the antisymmetric properties of $\mathbf{D}$. If the sites are unchanged by $\mathcal{S}$, like for a mirror plane including $\mathbf{r}_1$ and $\mathbf{r}_2$, Eq. (4.3) reduces to $\mathbf{D}_{12} = \det(\mathcal{R})\,\mathcal{R}\mathbf{D}_{12}$. These two relations can be used to reproduce the five basic symmetry restrictions on $\mathbf{D}$ found by Moriya [20], with $\mathbf{D}_{12}$ shortened as $\mathbf{D}$ and $\mathbf{d} = \mathbf{r}_2 - \mathbf{r}_1$ denoting the connection vector between $\mathbf{r}_1$ and $\mathbf{r}_2$ with central point $\mathbf{r}_c = (\mathbf{r}_1 + \mathbf{r}_2)/2$:

1. *When a center of inversion is located at* $\mathbf{r}_c$*, then* $\mathbf{D} = 0$*:*
   In this case, the point group symmetry is $\mathcal{R} = \bar{1}$ and the two sites are interchanged, thus $\mathbf{D} = -\det(\mathcal{R})\,\mathcal{R}\mathbf{D} = -\mathbf{D}$ and consequently $\mathbf{D} = 0$.

2. *When a mirror plane normal to* $\mathbf{d}$ *passes through* $\mathbf{r}_c$*, then* $\mathbf{D} \perp \mathbf{d}$*:*
   Without loss of generality, we assume $\mathbf{d} \parallel z$ and therefore $\mathcal{R} = m_z$. Since the mirror plane interchanges the two sites, $\mathbf{D} = -\det(\mathcal{R})\,\mathcal{R}\mathbf{D} = (D_x,\, D_y,\, -D_z)^\mathsf{T}$ and consequently $\mathbf{D} \perp z$, which is equivalent to $\mathbf{D} \perp \mathbf{d}$.

3. *When there is a mirror plane including both sites, then* $\mathbf{D} \parallel \mathbf{n}$*, with* $\mathbf{n}$ *the normal vector of the mirror plane:*
   Without loss of generality, we assume a mirror plane normal to the z axis and therefore $\mathcal{R} = m_z$. Since the mirror plane does not change the two sites, $\mathbf{D} = \det(\mathcal{R})\,\mathcal{R}\mathbf{D} = (-D_x,\, -D_y,\, D_z)^\mathsf{T}$ and consequently $\mathbf{D} \parallel z$, which is equivalent to $\mathbf{D} \parallel \mathbf{n}$.

4. *When a two-fold rotation axis is perpendicular to* $\mathbf{d}$ *and passes through* $\mathbf{r}_c$*, then* $\mathbf{D} \perp \mathbf{2}$*, with* $\mathbf{2}$ *the direction of the two-fold rotation axis:*
   Without loss of generality, we assume a two-fold rotation axis along the z axis and therefore $\mathcal{R} = 2_z$. Since the rotation axis interchanges the two sites, $\mathbf{D} = -\det(\mathcal{R})\,\mathcal{R}\mathbf{D} = (D_x,\, D_y,\, -D_z)^\mathsf{T}$ and consequently $\mathbf{D} \perp z$, which is equivalent to $\mathbf{D} \perp \mathbf{2}$.

5. *When there is an* n*-fold rotation axis* ($n \geq 2$) *along* $\mathbf{d}$*, then* $\mathbf{D} \parallel \mathbf{d}$*:*
   Without loss of generality, we assume $\mathbf{d}$ in z direction and therefore $\mathcal{R} = n_z$. Since this rotation axis leaves the two sites unchanged, $\mathbf{D} = \det(\mathcal{R})\,\mathcal{R}\mathbf{D} = (\cos(\frac{2\pi}{n})D_x - \sin(\frac{2\pi}{n})D_y,\, \cos(\frac{2\pi}{n})D_y + \sin(\frac{2\pi}{n})D_x,\, D_z)^\mathsf{T}$ and consequently $\mathbf{D} \parallel z$, which is equivalent to $\mathbf{D} \parallel \mathbf{d}$.

This consistency between the rules of Moriya [20] and Eq. (4.3) clearly proves that $\mathbf{D}$ transforms as an axial vector.

4.2. DMI symmetry analysis for the $Ba_2TGe_2O_7$ family

The symmetry elements of the nuclear space group $P\bar{4}2_1m$ are illustrated in Fig. 4.1(a). It is clear to see that mirror planes m (solid red lines in Fig. 4.1(a)) are located in the center between nearest neighboring magnetic atoms T. As the normals of these mirror planes are parallel to the connection vectors $\mathbf{d}_{ij} = \mathbf{r}_j - \mathbf{r}_i$, the second rule of Moriya [20] (see Sec. 4.1) can be applied, restricting the DMI vector $\mathbf{D}_{ij}$ to the plane perpendicular to $\mathbf{d}_{ij}$. Thus, the exemplary DMI vector parameter $\mathbf{D}_{1c}$ for the exchange between the magnetic ions at $\mathbf{r}_1$ and $\mathbf{r}_c$, with labels as defined in in Fig. 4.1(b) and connection vector $\mathbf{d}_{1c} \parallel [110]$, is given by $\mathbf{D}_{1c} = (D_x,\, -D_x,\, D_z)^\mathsf{T}$.

The four-fold inversion axis $\mathcal{S}_c^{\bar{4}}$ in the center of the UC transforms $\mathbf{r}_i$ to $\mathbf{r}_{i+1}$ with $\mathbf{r}_{4+1} = \mathbf{r}_1$, whereas $\mathbf{r}_c$ remains invariant. Thus, it can be used to define a connection between the individual DMI vectors in the UC by applying Eq. (4.3). The point group symmetry part of $\mathcal{S}_c^{\bar{4}}$ and its determinant are given by

$$\mathcal{R}_c^{\bar{4}} = \begin{pmatrix} 0 & 1 & 0 \\ -1 & 0 & 0 \\ 0 & 0 & -1 \end{pmatrix}, \quad \det\left(\mathcal{R}_c^{\bar{4}}\right) = -1. \tag{4.4}$$

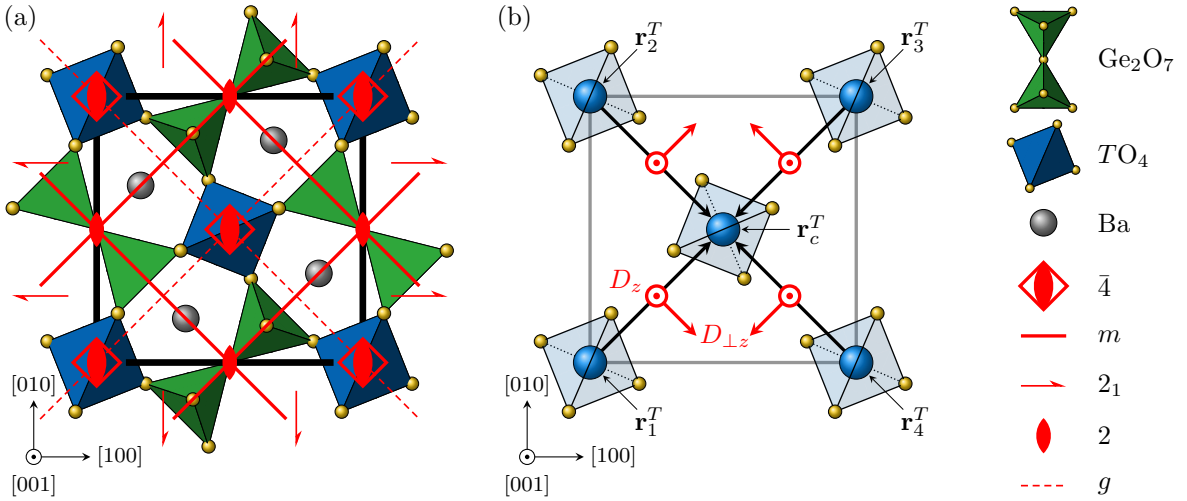

Figure 4.1.: (a) Top view of the UC of $Ba_2TGe_2O_7$ visualizing the symmetry elements of space group $P\bar{4}2_1m$. The generating symmetry operations are the four-fold inversion axes ($\bar{4}$) in [001] direction and the two-fold screw axes (2_1) in [100] and [010] direction. Corresponding expressions for these symmetry elements are provided in appendix A.2. In addition, the mirror planes (m) normal to the [110] and [1$\bar{1}$0] directions, the glide planes (g) normal to the [110] and [1$\bar{1}$0] directions and the two-fold rotation axes (2) in [001] direction, originating all from different combinations of the generators $\bar{4}$ and 2_1, are indicated. The resulting symmetry restricted arrangement of the DMI vector $\mathbf{D}$, developed in the text and separated into in-plane ($\mathbf{D}_{\perp z}$) and out-of-plane ($\mathbf{D}_z$) component, is shown in (b). The thick black arrows indicate the bonding direction for the DMI. Furthermore, the labels for the individual TM ions T, which are located at the corners ($\mathbf{r}_1^T$ to $\mathbf{r}_4^T$) and the center ($\mathbf{r}_c^T$) of the ab face, are defined.

Therefore, the DMI vectors $\mathbf{D}_{ij}$ can be written as

$$\mathbf{D}_{2c} = \det\left(\mathcal{R}_c^{\bar{4}}\right)\mathcal{R}_c^{\bar{4}}\mathbf{D}_{1c} = (D_x,\, D_x,\, D_z)^{\mathsf{T}} \tag{4.5}$$

$$\mathbf{D}_{3c} = \det\left(\mathcal{R}_c^{\bar{4}}\right)\mathcal{R}_c^{\bar{4}}\mathbf{D}_{2c} = (-D_x,\, D_x,\, D_z)^{\mathsf{T}} \tag{4.6}$$

$$\mathbf{D}_{4c} = \det\left(\mathcal{R}_c^{\bar{4}}\right)\mathcal{R}_c^{\bar{4}}\mathbf{D}_{3c} = (-D_x,\, -D_x,\, D_z)^{\mathsf{T}} \tag{4.7}$$

and are illustrated for D_x, $D_z > 0$ in Fig. 4.1(b), separated into the in-plane ($\mathbf{D}_{\perp z}$) and the out-of-plane component ($\mathbf{D}_z$). The sign of $\mathbf{D}$ reverses, if the exchange direction, indicated by the thick black arrows in Fig. 4.1(b), is inverted. Note that this DMI vector arrangement, which was first presented by us in Ref. [226], differs in the alignment of the in-plane component from that provided by Romhányi *et al.* [90]. The latter is, however, not consistent with the four-fold inversion symmetry.

4.2.1. DMI in $Ba_2CuGe_2O_7$

In $Ba_2CuGe_2O_7$, the ground state magnetic structure is an AFM spin spiral propagating in [110] or [1$\bar{1}$0] direction with spins confined to the (1$\bar{1}$0) or (110) plane, respectively (see Sec. 2.2.1 and Fig. 2.4(a)). As this helical order is stabilized by the in-plane DMI component $\mathbf{D}_{\perp z}$, the sign of D_x determines the rotation sense of the spiral. For $D_x > 0$,

the in-plane components $\mathbf{D}_{\perp z}$ are directed as illustrated in Fig. 4.1(b) and favour a right-handed spin rotation around the $[1\bar{1}0]$ and [110] direction for a propagation in [110] and $[1\bar{1}0]$ direction, respectively. In contrast, a left-handed spin rotation, as illustrated in Fig. 2.4(a), indicates $D_x < 0$.

The sense of the spin rotation is closely coupled to the sign of the ferroelectric polarization $\mathbf{P} \propto \sum_{ij} \mathbf{d}_{ij} \times (\mathbf{m}_i \times \mathbf{m}_j)$ predicted by the inverse DMI mechanism of multiferroicity for neighboring moments $\mathbf{m}_i$ and $\mathbf{m}_j$ with connection vector $\mathbf{d}_{ij}$ [67, 69]. To be energetically favoured by the DMI, $\mathbf{m}_i \times \mathbf{m}_j$ is expected to be antiparallel to $\mathbf{D}_{ij}$ (see Eq. (4.2)) and local polarizations $P_z \propto (\mathbf{d}_{ij} \times \mathbf{D}_{ij})_z$ may arise. Thus, the sign of P_z in $Ba_2CuGe_2O_7$ should be different for the AFM spin spirals propagating in [110] and $[1\bar{1}0]$ direction (clear to see in Fig. 4.1(b) as $(\mathbf{d}_{ic} \times \mathbf{D}_{ic\perp z})_z$ is positive for $i = 2, 4$ and negative for $i = 1, 3$). This predicted behaviour is confirmed by electric polarization measurements of Murakawa *et al.* [87] revealing a opposite signed P_z for magnetic fields in [110] ($P_z > 0$) and $[1\bar{1}0]$ ($P_z < 0$) direction, favouring a (110) and $(1\bar{1}0)$ spin rotation plane, respectively. Note that the previously mentioned different $\mathbf{D}_{\perp z}$ alignment proposed by Romhányi *et al.* [90] would lead to a same signed P_z for both spin rotation planes, which is contradictory to the experimental results, and thus can be excluded.

In this AFM spin spiral phase of $Ba_2CuGe_2O_7$, the D_z component of the DMI generates an additional in-plane canting of the AFM spins close to the *ab* plane resulting in an amplitude modulated WFM moment perpendicular to the spin rotation plane (see Sec. 2.2.1 and Ref. [227]). In this regard, the sign of the D_z component determines the phase shift between the AFM cycloid and the WFM modulation.

For high magnetic fields above the I/C transition, the adopted magnetic structure is similar to that found in $Ba_2CoGe_2O_7$; therefore, the same implications on the DMI as discussed in the next section apply.

4.2.2. DMI in $Ba_2CoGe_2O_7$

As presented in Sec. 2.2.2 and illustrated in Fig. 2.7, the magnetic moments in $Ba_2CoGe_2O_7$ are ordered antiferromagnetically in the *ab* plane. The magnetic sublattices denoted as *A* and *B* with magnetizations $\mathbf{m}_A$ and $\mathbf{m}_B$ are formed by the Co^{2+} ions at the corners ($\mathbf{r}_1$ to $\mathbf{r}_4$ in Fig. 4.1(b)) and the center ($\mathbf{r}_c$ in Fig. 4.1(b)) of the UC, respectively. Therefore, the total DMI energy between the four NN pairs in the UC can be written as

$$E_{\mathrm{UC}}^{\mathrm{DMI}} = \sum_{i=1}^{4} \mathbf{D}_{ic} \cdot (\mathbf{m}_A \times \mathbf{m}_B) = 4D_z \, (\mathbf{m}_A \times \mathbf{m}_B)_z \tag{4.8}$$

with the in-plane DMI components $\mathbf{D}_{\perp z}$ proportional to D_x averaging out [226]. The remaining out-of-plane component D_z favours a canting in the otherwise collinear AFM structure, leading to an in-plane WFM moment. According to the discussion in Sec. 2.3, this WFM moment can be aligned in the *ab* plane by an external magnetic field and the magnetic moments separated into FM and AFM parts that are given by

$$\underbrace{\mathbf{m}^{\mathrm{FM}} := \mathbf{m}_A^{\mathrm{FM}}}_{=\mathbf{m}_B^{\mathrm{FM}}} = \frac{\mathbf{m}_A + \mathbf{m}_B}{2} \quad \text{and} \quad \underbrace{\mathbf{m}^{\mathrm{AFM}} := \mathbf{m}_A^{\mathrm{AFM}}}_{=-\mathbf{m}_B^{\mathrm{AFM}}} = \frac{\mathbf{m}_A - \mathbf{m}_B}{2} \tag{4.9}$$

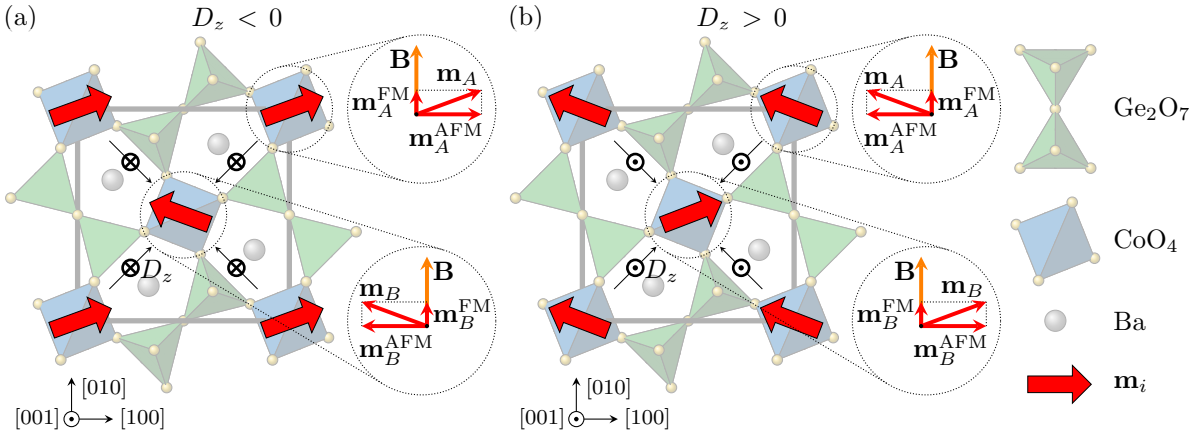

Figure 4.2.: Panels (a) and (b) show the two possible magnetic moment configurations in $Ba_2CoGe_2O_7$ stabilized depending on the sign of D_z by applying an external magnetic field **H** along the [010] direction and thus, aligning the WFM moment along **H**. The direction of the component $\mathbf{D}_z$ is illustrated by a crossed and dotted circle for pointing in and out of the paper plane, respectively, for a bonding directions as given by the thin black arrows. The figure was modified from Ref. [226]

as illustrated in Fig. 4.2 in the detailed view in the dotted circles. Using this separation, the DMI energy can be written as

$$E_{\mathrm{UC}}^{\mathrm{DMI}} = 4D_z \left(\mathbf{m}^{\mathrm{AFM}} \times \mathbf{m}^{\mathrm{FM}}\right)_z . \tag{4.10}$$

The macroscopically measurable $\mathbf{m}^{\mathrm{FM}}$ is given by the sum of the field aligned WFM and field-induced FM moment, and thus points in field direction. In contrast, $\mathbf{m}^{\mathrm{AFM}}$ is confined to the *ab* plane perpendicular to $\mathbf{m}^{\mathrm{FM}}$ (see Sec. 2.3) and the sign of the D_z component determines which of the two possible AFM arrangements is energetically favoured, i.e. minimizes Eq. (4.10). For an applied magnetic field along the [010] direction, this is illustrated in Figs. 4.2(a) and 4.2(b) for a negative and positive D_z component, respectively.

4.2.3. DMI in $Ba_2MnGe_2O_7$

In $Ba_2MnGe_2O_7$, the in-plane AFM structure, characterized by the D_z component as in $Ba_2CoGe_2O_7$, is additionally stacked antiferromagnetically in *c* direction (see Sec. 2.2.3 and Fig. 2.9). Therefore, the direction of both the AFM and WFM moment are reversed between neighboring tetrahedral layers. As a result, the overall WFM moment cancels out and is not macroscopically measurable. The sign of the D_z component determines for the inter-layer AFM ordering the phase shift between the AFM and WFM moments.

In contrast to $Ba_2CoGe_2O_7$, the application of an external in-plane magnetic field does not lift the degeneracy between 180° AFM domains in $Ba_2MnGe_2O_7$ since the overall WFM moment is compensated. In fact, an external magnetic field breaks the magnetic ground state symmetry as none of the three space groups suggested in Sec. 2.2.3, namely $C_c cm2_1$, $P_c2_12_12_1$ and P_c112_1, allows an field-induced FM moment.

4.3. Absolute DMI sign determination with PND

For a comprehensive understanding of the DMI and to validate numerical estimations, not only the value but also the sign of **D** needs to be carefully measured. For thin film interfacial DMI systems, where the sign of **D** is especially crucial for a proper sample design, Brillouin light scattering is considered to be one of the most reliable techniques to determine both its value and sign since it measures directly the non-reciprocal spin-wave dispersion [217, 228]. To define the DMI in bulk systems, polarized small-angle neutron scattering (SANS) or SNP are commonly used [180, 229, 230]. By measuring the chiral term of the magnetic scattering intensity (see Sec. 3.3.2), polarized SANS and SNP give direct access to the handedness of the spiral structure, which might be directly related to the DMI sign as discussed in Sec. 4.2.1. Therefore, SNP could be applied to the spiral phase of $Ba_2CuGe_2O_7$ to determine the D_x sign. However, these well-established measurement techniques are limited to helical spin structures only, and thus are not applicable to weak ferromagnets with $\boldsymbol{\tau} = 0$ like $Ba_2CoGe_2O_7$.

The issue of determining the DMI sign in classical WFM materials has been addressed by Dmitrienko *et al.* [231]. They used magnetic resonant X-ray scattering at a synchrotron source to determine the sign of the DMI in iron borate ($FeBO_3$). For this novel experimental technique, the interference of two scattering processes is required. First, magnetic X-ray scattering (see Ref. [232]) with an external magnetic field applied in various directions to vary the alignment of the system's magnetic moment, and second, resonant anomalous X-ray scattering (see Ref. [233]), involving only electric quadrupole events [231]. Combining the results of both measurements, they were able to relate the phase of the scattered waves from the magnetic and crystal structure, and thus determine the DMI sign in this compound. Although this method was applied to further weak ferromagnets with the same crystal symmetry as $FeBO_3$ (e.g. $MnCO_3$, $CoCO_3$, $NiCO_3$ [225, 234]), it is rather complex and difficult to interpret.

A direct and more elegant approach to determine the DMI sign for WFM compounds with $\boldsymbol{\tau} = 0$ is offered by PND. Since the sign of **D** is connected to a specific phase shift between the AFM and the atomic structure as discussed in Sec. 4.2.2 for $Ba_2CoGe_2O_7$, the phase-sensitive interference term in the scattering cross-section of PND can be used to distinguish between the possible magnetic moment configurations as illustrated in Fig. 4.2, and thus between a negative and positive sign of the DMI. Consequently, the experimental effort can be reduced to the measurement of a single asymmetry on a suitable mixed nuclear-magnetic Bragg reflection using the FR method described in Sec. 3.3.1. This advanced measurement technique, developed and presented in detail by us in Ref. [21], has been successfully applied to determine the DMI sign in the classical WFM compounds rhodochrosite ($MnCO_3$) and hematite (α-Fe_2O_3) with $R\bar{3}c$ symmetry as well as in the magnetocaloric, orthorhombic $HoFeO_3$ with $Pbnm$ symmetry [21, 235]. Within this work, it is additionally applied to $Ba_2CoGe_2O_7$ in Sec. 6.3.3 and to the commensurate phase of $Ba_2CuGe_2O_7$ in Sec. 7.4.3 to determine for the first time the D_z sign in these multiferroic materials directly by measurement. In $Ba_2MnGe_2O_7$, this novel PND approach cannot be applied as there is no AFM contribution to the mixed nuclear-magnetic Bragg reflections due to $\boldsymbol{\tau} = (00\frac{1}{2})$.

5. Instrumental development at POLI at MLZ

The **Pol**arization **I**nvestigator (POLI), located at the SR-9a beam tube on the hot source of the research neutron source Heinz Maier-Leibnitz (FRM II) in Garching, Germany, is a two-axes normal beam geometry single crystal diffractometer primarily dedicated to the investigation of magnetic structures by polarized neutrons [159]. POLI has two double focusing monochromators of Si-311 and Cu-220, providing a high neutron flux and resolution. As they can be operated at takeoff angles of 25° and 41°, neutron wavelengths of 0.55, 0.70, 0.90 and 1.15 Å are available. POLI is designed for the usage of bulky sample environments like high-field superconducting magnets or large cryostats. In addition, a polarizer and analyzer can be placed in the beam path before and after the sample such that PND becomes available. Three standard options for single crystal diffraction are routinely used at POLI:

The first option is the conventional ND mode (see Sec. 3.2.1). It provides the highest neutron flux at the sample position and a high q coverage can be achieved by using out-of-plane lifting mechanics for the single counter detector, giving access to out-of-plane angles of $-5° \leq \nu \leq 30°$ for the diffracted beam. For this option, extreme sample conditions like very low and high temperatures, electric and magnetic fields or high pressure are available.

Using a high-field magnet, which is coupled to a neutron polarizer and a spin flipper by dedicated guide fields, classical FR measurements (see Sec. 3.3.1) can be provided as second method at POLI. This option uses also the so-called lifting counter detector (see Fig. 3.2(a)), providing a high q coverage. In addition to applied magnetic fields, very low and high temperatures and the combination with electric fields or high pressure are available.

Using a third-generation CryoPAD [176] and dedicated ^{3}He SFC polarizers and analyzers, the third option at POLI is SNP (see Sec. 3.3.2). For this option, the accessible q range is limited to the instrumental plane as the Decpol, combining a neutron spin analyzer and detector (see Fig. 3.2(b)), has no out-of-plane lifting mechanics. In addition to low and high temperatures for the sample, electric fields or high pressure are optionally available.

In addition to these three standard options, custom-made setups are possible at POLI. For example, a uniaxial polarization analysis (PA) setup can be built by combining the FR setup with the Decpol of SNP. This PA setup was, e.g., successfully used to monitor magnetic domain distributions with applied magnetic fields in Hematite (α-Fe_2O_3) [179].

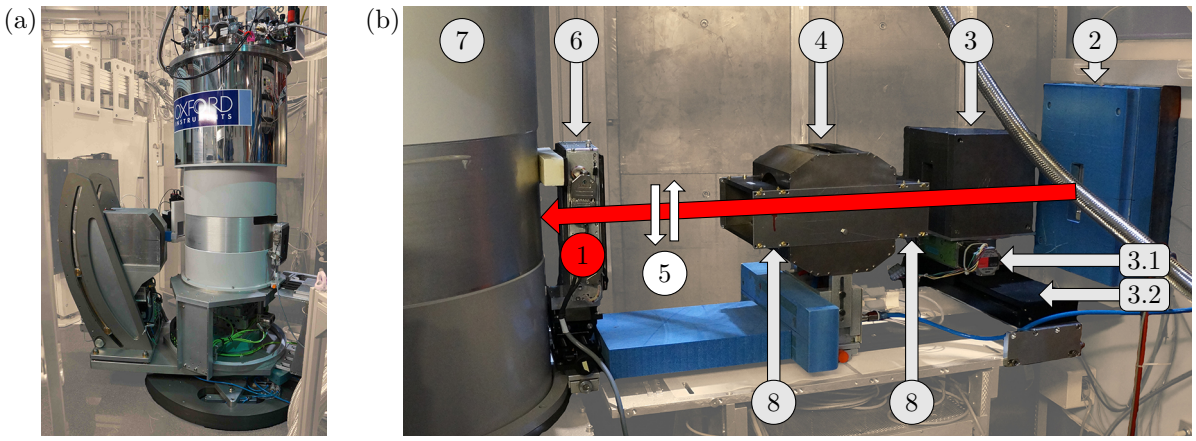

Figure 5.1.: Photograph of (a) the new 8 T split-coil superconducting oxford magnet mounted on the sample table of POLI and (b) the components of the FR setup. The non-polarized monochromatic neutron beam is coming from the right side of the picture and is indicated by (1) a red arrow. The incoming neutrons first pass (2) a monitor before being polarized by (3) the supermirror bender, which is equipped with a motorized (3.1) rotation and (3.2) translation stage. A shielded Mezei-type flipper (4) can be used to reverse the beam polarization as indicated by (5). The beam is shaped by (6) motorized slits before entering (7) the 8 T magnet. Additional guide fields (8) are provided by permanent magnets to adiabatically connect the vertical magnetic fields of bender, flipper and magnet. The figure is modified from Ref. [239].

5.1. Implementation of 8 T PND setup

The first PND setup for FR measurements on POLI was successfully implemented in 2018 using a compact high-T_c superconducting magnet and a ^{3}He SFC polarizer available from SNP [179, 236]. Although the good performance of the this setup was confirmed in a detailed characterization and by first scientific experiments [179, 236–238], the maximal available field of the used magnet is limited to 2.2 T. This is comparatively small and might be insufficient to study many topical magnetic materials with weak ordered magnetic moments or with field-induced effects that only occur at high fields. In particular for $Ba_2CuGe_2O_7$, a magnetic field of only 2.2 T is insufficient to reach the commensurate magnetic phase above the I/C transition (see Sec. 2.2.1), which is required to determine the D_z sign with PND (see Sec. 4.3).

5.1.1. New 8 T oxford magnet

To overcome the low-field limitations, a new 8 T split-coil superconducting magnet has been procured by Oxford Instruments [241] and implemented for non-polarized and polarized neutron diffraction on POLI. A photograph of this magnet mounted on the sample table of POLI is shown in Fig. 5.1(a). The magnet was designed to provide a large vertical access of $-5°$ to $25°$ to the diffracted beam, coinciding well with the available out-of-plane angle ν of the lifting counter detector (see Sec. 3.3.1). This ensures a high q coverage and a good spatial resolution also in the vertical crystal direction. Moreover, the magnet has as little as possible material in the beam path, which minimizes the

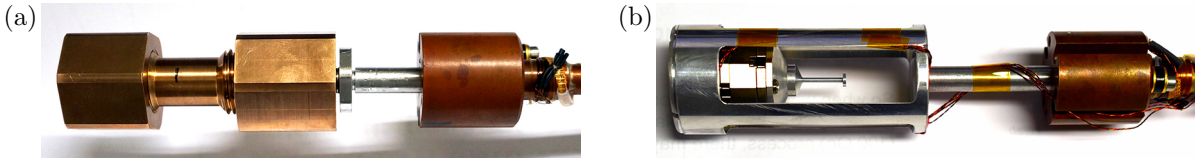

Figure 5.2.: (a) Exemplary $CoBe_2$ clamp cell, which is mounted to the sample rod and fits in the sample tube of the 8 T magnet, providing pressures of around 1 GPa [240]. (b) Sample holder with additional xy translation stage. As the translation is driven by two non-magnetic piezoelectric motors, it is functional even in high magnetic fields and at low temperatures. Thus, it allows an *in-situ* alignment of the sample in the rotation center of the sample rod during the experiment.

background scattering. A small dark angle of only 60° enables the usage in right- and left-handed scattering geometry. The magnet is equipped with a re-condensing liquid He cryostat, which allows to maintain a zero He boil-off rate at a constant sample temperature over a long time period. This clearly reduces the magnet's operational costs and maintenance effort. Using a dedicated low and high temperature sample rod, sample temperatures between 1.7 K and 800 K are available. The spacious sample tube with a diameter of 34 mm and a coil split of 56 mm provides a large sample volume, which can be used to insert, e.g., a pressure cell (see Fig. 5.2(a)) or a motorized xy translation stage for *in-situ* sample alignment (see Fig. 5.2(b)). The sample rod is additionally equipped with a motorized vertical translation, which allows a precise centering of the sample in the beam.

The vertical magnetic field of up to 8 T is produced by ten asymmetrically distributed superconducting coil packs in the central part of the magnet. They are enclosed by an additional set of two coils with inverted current direction to suppress the magnets stray field. This active shielding is necessary to not disturb other sensitive instruments in the close vicinity of POLI. The magnetic field strength as function of the radial distance from the sample position is illustrated in Fig. 5.3(a). An almost perfect agreement between the measured and the with *COMSOL Multiphysics* [242] simulated field map is observed. Due to the asymmetric field design, the zero field node, typically located at the transition from the main to the stray field (dashed black line labeled as (1) in Fig. 5.3), is shifted out of the beam path. As a result, the magnetic field rotates gradually from form $-z$ to $+z$ as indicated by the rotation angle $\theta_B = \arctan(B_z/|B_r|)$ in Fig. 5.3(b), with B_z and B_r the vertical and radial part of the magnetic field, respectively. Due to the high field strength at the transition (around 20% of the central field strength of the magnet), the rotation frequency of the magnetic field ω_B is even for short-wavelength neutrons slow compared to their Larmor frequency ω_L (see dashed gray line in Fig. 5.3(b) with $\omega_L/\omega_B \gg 10$, simulated for $\lambda = 0.55$ Å). Thus, the rotation can be considered as adiabatic and prevents a neutron depolarization (see Sec. 3.3). Also for smaller fields in the magnet, the simulation consistently showed $\omega_L/\omega_B \gg 10$ in the beam path.

The overall design of the magnet was optimized for the limited experimental space and maximal possible device weight available at POLI. The magnets control is fully implemented and automatized in the instrument control software *NICOS*. More technical details of the new magnet can be found in Ref. [239].

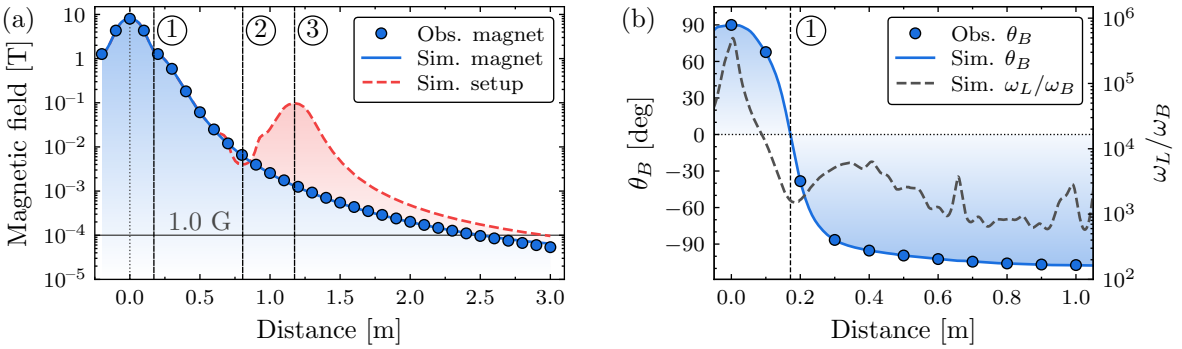

Figure 5.3.: (a) Simulated and observed magnetic field strength in the horizontal plane of the new 8 T magnet as function of the radial distance from its center at maximal field. Due to the active shielding of the stray field, it is reduced by an order of magnitude compared to the classical design and is below 25 G above a radial distance of 1 m. The dashed line at (1) indicates the transition from the main to the stray field. In addition, the simulated field strength along the neutron beam path of the full FR setup illustrated in Fig. 5.1(b) is shown as dashed red line. The central positions of the shielded flipper (2) and the supermirror bender hosted by permanent magnets (3) are indicated. (b) Simulated and observed field angle θ_B to the radial direction with (1) the transition from the main ($B_z > 0$) to the stray field ($B_z < 0$). As the field rotation ω_B is extended over a region of around 30 cm, it is slow compared to the Larmor frequency ω_L of $\lambda = 0.55$ Å neutrons. The ratio ω_L/ω_B is shown as dashed gray line and stays above 10^3 at the transition.

5.1.2. New Fe/Si supermirror bender

Although the new 8 T magnet is actively shielded, its stray field gradients are still too large to be used with the sensitive ^{3}He SFC polarizer of the previous setup in its close vicinity. This cannot be overcome by increasing the distance between the location of the SFC and the center of the magnet (around 1 m), as the available space in the beam path at POLI is strictly limited. Thus, a new solid-sate supermirror bender was developed and produced by the Neutron Optics Berlin [243] company. As the bender's magnetic field, generated by strong NdFeB-type permanent magnets, is around two orders of magnitude larger than the local magnet's stray field (see position (3) in Fig. 5.3(a)), the efficiency of the bender polarizer is expected to be undisturbed by the magnet. The direction of the bender's magnetic field is aligned with the stray field of the magnet, both pointing in vertical direction and serving as guide field for the neutron polarization.

The new bender consists of a C-shape bend stack of thin Si wafers that are coated on both sides with Fe/Si supermirrors ($m = 3$) and enclosed with a layer of Gd. The working principle of polarizing supermirrors is shortly outlined in appendix A.3. This supermirror coating allows neutrons with one spin component to travel inside the Si wafers by total reflection whereas the other spin component cannot follow the C-shape and is absorbed in the Gd, leading to a high neutron beam polarization. The bending radius and the large opening ($130 \times 42\,\mathrm{mm}^2$) of the new bender are optimized for the short neutron wavelength and large beam cross-section provided by the two double-focusing monochromators at POLI. The bender is encased in a Pb housing, absorbing the gamma radiation arising from the neutron absorption in the Gd layers. For a fast and straightforward alignment of the bender in the neutron beam, it is mounted on a

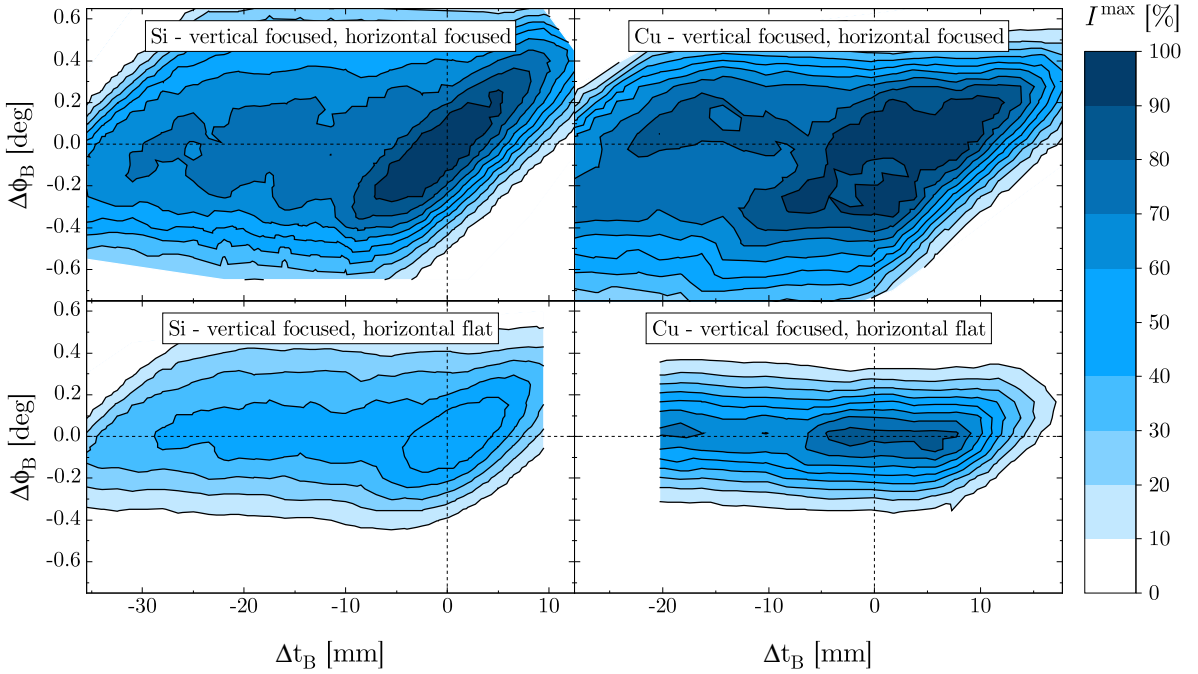

Figure 5.4.: The peak intensity $I^{\max}$ of the (111) reflection of a Heusler (Cu_2MnAl) single crystal at the sample position as function of the rotation and translation of the bender polarizer, which is shown as deviations Δt_B and $\Delta\phi_B$ from the optimized bender positions. These optimized positions provide the highest peak intensity in the double focusing configuration (top panels) for the Si-311 (left panels, $\lambda = 1.15\,\text{Å}$) and Cu-220 (right panels, $\lambda = 0.90\,\text{Å}$) monochromators, respectively, and were used for normalization of the intensity. Note that the maximal peak intensity for the Si monochromator is around 2.3 times higher than for Cu.

motorized rotation and translation stage (see positions (3.1) and (3.2) in Fig. 5.1(b)).

To characterize the transmission of the bender, the diffracted intensity of the (111) reflection of a Heusler (Cu_2MnAl) single crystal at the sample position was mapped out as function of the benders translation t_B and rotation angle ϕ_B. For each bender position, the reflection was precisely centered and a rocking curve collected. As background-peak-background measurements are typically performed in PND (see Sec. 3.3.1), the peak intensity $I^{\max}$ is taken as reference for the transmission rather than the integrated intensity. The observed peak intensity maps for different monochromator configurations are shown in Fig. 5.4. Clear to see is a somewhat inhomogeneous neutron transmission over the transversal bender cross section, which is maximized on the same side for all maps with an around 20% higher peak intensity. As the C-shaped bending of the Si wafers is achieved by squeezing them between convex and concave metal profiles, the higher transmission observed close to the convex profile might result from a more homogeneous bending. However, as the transversal bender size with 42 mm is clearly larger than the typical sample width of up to 10 mm at POLI, it is possible to use only the better performing side, indicated by the optimized bender position (intersection point of dashed lines in Fig. 5.4).

The diagonal distortion of the intensity map results from a rotation induced change in

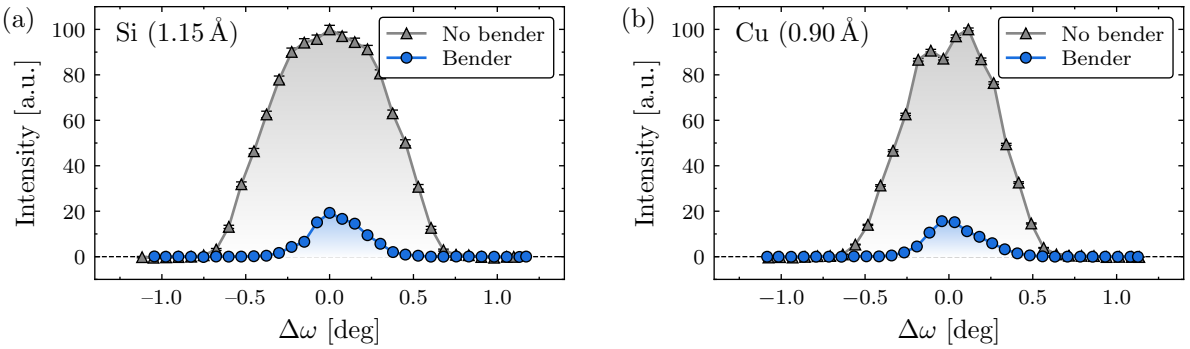

Figure 5.5.: Intensity of the (111) Heusler reflection with and without bender in the beam path. The intensity was corrected for the non-perfect polarizing efficiency of the Heusler crystal and the background as discussed in the text to display the diffracted intensity resulting from the correct spin component only. For the measurement, the double focusing configuration of the (a) Si and (b) Cu monochromator was used.

the illuminated portion of the bender, which can be compensated by a translation. As the horizontal divergence of the beam is clearly reduced for a horizontally flat monochromator (lower panels in Fig. 5.4), the rotational positioning of the bender is more selective and the maximal area becomes narrower. In addition, the maximal observed peak intensity is reduced to around 85% for Cu and to around 60% for Si if the horizontal focus is removed. The larger intensity gain with horizontal focusing for Si may be attributed to an increased mosaicity of the monochromator crystals, resulting from the mechanical stress of focusing that physically bends the Si slabs. In contrast, the horizontal focusing of the Cu monochromator is purely geometrical.

To determine the absolute transmission of the new solid state bender, the intensity of the (111) Heusler reflection was measured with and without bender in the beam path. As the magnetized Heusler single crystal has a non-perfect polarizing efficiency $P_{\mathrm{H}}^{\mathrm{Pol}} \approx -0.95$ (see appendix B.2), the scattering-cross section for the suppressed spin component contributes a fraction of $(1-|P_{\mathrm{H}}^{\mathrm{Pol}}|)/2$ to the total scattering-cross section of a non-polarized beam. Thus, the intensity measured without bender in the beam path must be scaled by $(1+|P_{\mathrm{H}}^{\mathrm{Pol}}|)/2$ to get the diffracted intensity resulting from the correct spin component only. For the measurement with bender, a fully polarized incoming neutron beam can be assumed due to the almost perfect polarizing efficiency ($P^{\mathrm{Pol}} > 0.99$) of the Bender discussed below. Thus, only the correct spin component is expected to be present in the beam and no correction of the scattered intensity from the Heusler crystal is required. The measured intensities, corrected for $P_{\mathrm{H}}^{\mathrm{Pol}}$ and the background, are shown in Figs. 5.5(a) and 5.5(b) for the Si and Cu monochromator, respectively. Comparing the maximal observed peak intensities, which is the relevant quantity for a typical PND measurement as discussed before, a transmission of 19.3(7)% for 1.15 Å and 15.6(3)% for 0.90 Å is determined for the correct spin component. Although the smaller value for the shorter wavelength is expected due to a reduced supermirror cutoff angle (see appendix B.2), the overall values are by a factor of around 1.5 lower than theoretically predicted based on the neutron absorption in the Si [239]. This might

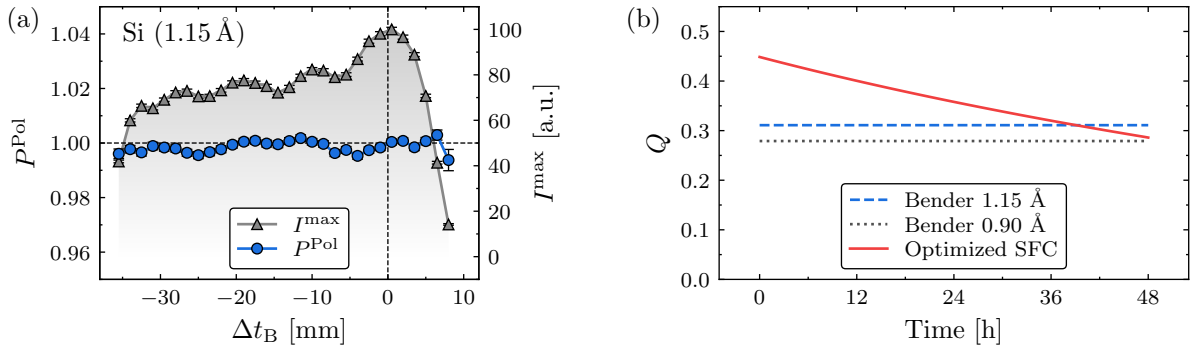

Figure 5.6.: (a) Polarization efficiency P^{Pol} of the new supermirror bender as function of its transversal position determined using a Heusler crystal analyzer and the double focused Si monochromator ($\lambda = 1.15\,\text{Å}$). In addition, the observed peak intensity $I^{\max}$ of the Heusler's (111) reflection is shown, corresponding to a cut along the horizontal dashed line in the upper left panel of Fig. 5.4. The vertical dashed line indicates the optimized bender translation value. (b) Calculated time dependence of the quality factor Q for the bender at 1.15 Å and 0.90 Å and an exemplary SFC. For the SFC, a ^{3}He starting polarization of 70%, a relaxation time of 100 h and optimized cell parameters (p[bar] l[cm] λ[Å] $\approx$ 26 [244]) were assumed.

be attributed to the potential bending-inhomogeneities identified in Fig. 5.4 or to the randomisation of the orientation of the single wavers to each other, which was selected to avoid substantial Bragg reflection in the bulk of the Si body as discussed in Ref. [239]. Comparing the integrated intensities, only very low transmission values of the correct spin component of 8.5(2)% for 1.15 Å and 9.05(7)% for 0.90 Å are observed. However, these values are not representative as the bender acts as an additional collimator for the incoming neutron beam, clearly reducing the full width at half maximum (FWHM) from 0.89(2)° to 0.35(2)° for 1.15 Å and from 0.66(1)° to 0.36(1)° for 0.90 Å, and thus also the integrated intensity as visible in Fig. 5.5. Nevertheless, the bender's collimation improves slightly the peak-to-background ratio.

In addition, the (111) reflection of a magnetized Heusler single crystal at the sample position can be used as analyzer for the polarization efficiency P^{Pol} of the new bender. In this configuration, the measured asymmetry A is given by the product of $P_{\mathrm{H}}^{\mathrm{Pol}}$, P^{Pol} and P_{T} with the latter being the polarized neutron spin transport efficiency accounting for all setup-related losses and the flipping efficiency. Typically P_{T} is assumed to be very close to one; therefore, P^{Pol} is given by the asymmetry normalized by $P_{\mathrm{H}}^{\mathrm{Pol}}$ of the Heusler crystal. The measured polarizing efficiency of the bender over its transversal cross-section is shown in Fig. 5.6(a) for the Si monochromator. Clear to see is a homogeneous $P^{\mathrm{Pol}} > 0.99$ over the full Δt_{B} range, indicating a high efficiency of the new supermirror bender at POLI. Similarly high and homogeneous values are found for the Cu monochromator, demonstrating no significant wavelength dependence in P^{Pol}.

The performance of a neutron polarizer is typically expressed by the quality factor $Q = P\sqrt{T}$ with the polarization efficiency P and the total transmission T for a non-polarized neutron beam [245]. This quantity allows to compare the new supermirror bender with the existing SFC polarizer at POLI. Using the previously determined values for P and T, the bender has a constant quality factor of around 0.31 for 1.15 Å and

(a) (b)

Figure 5.7.: (a) Original design of the shielded flipper developed for the previous FR setup using the 2.2 T magnet discussed in Ref. [179, 236]. Additional depolarization will occur on the edges denoted by the red arrows. (b) Modified design with additional polar pieces (orange) and permanent magnets (yellow) to avoid field vortexes by an extension of the guide field. The figure is taken from Ref. [239].

0.28 for 0.90 Å. In contrast, SFCs have a time dependent quality factor due to the relaxation of the ^{3}He polarization (see definition of P and T in appendix B.2). Using an optimized opacity and realistic values for the ^{3}He starting polarization and the relaxation time, the time dependence of Q for an exemplary SFC is shown in Fig. 5.6(b) over a typical usage period of 48 h. Particularly a freshly polarized SFC clearly outperforms the bender. However, considering the bender's reduced operational effort and the simplified data correction due to its constant performance, its extremely high polarizing efficiency, especially beneficial for strong magnetic signals [245], and its low sensitivity to external magnetic stray fields, the on average only around 14% lower quality factor for the bender at 1.15 Å compared to the SFC is an acceptable trade-off.

5.1.3. Adjustment of guide field construction and neutron flipper

To provide a high transport and flip efficiency for the neutron polarization, an attempt was made to reuse the existing guide field construction with Mezei-type flipper, originally developed for the 2.2 T magnet setup shown in Fig. 3.2(a), as linkage between the magnetic fields of the new supermirror bender polarizer and the 8 T magnet. This compact device was optimized for the short neutron wavelength and large beam cross-section at POLI and is presented in detail in Ref. [179, 236]. First test measurements showed a good transport efficiency for a non-focused neutron beam whereas a vertically focused beam suffered of considerable depolarization. Finite element simulations of the shielded flipper box in the new environment of the 8 T setup with *COMSOL Multiphysics* revealed stray fields between the polar plates (orange in Fig. 5.7(a)) and the shielding (dark gray in Fig. 5.7(a)), leading to inhomogeneities in the magnetic guide field as indicated by the red arrows in Fig. 5.7(a). As these inhomogeneities are located at the boundary of the in- and outlet of the flipper box, only a vertically focused beam passes through these regions and causes the observed partial depolarization.

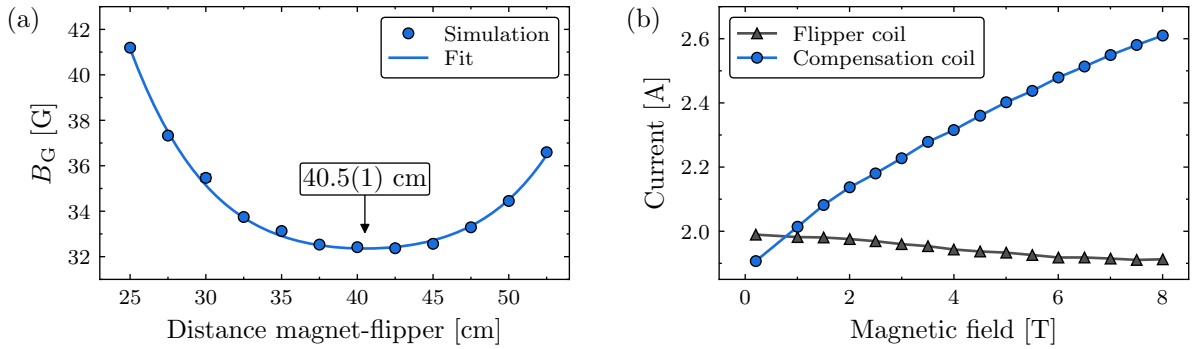

Figure 5.8.: (a) Numeric optimisation of the simulated guide field strength B_G at the center of the flipper as function of the distance between flipper box and magnet with a fixed bender distance of 80 cm from the magnet's surface. This fixed distance is determined by the strictly limited space in the beam path at POLI. For the simulation, the magnet was set to the highest available field of 8 T, representing the typical operation state and causing the most severe stray fields. (b) Experimentally calibrated currents in the coils of the Mezei-type flipper as function of the field in the magnet. The figure is modified from Ref. [239].

To overcome this issue, a dedicated extension of the flipper box, consisting of two sets of polar pieces connected by NdFeB-type permanent magnets, was designed, numerically optimized and built to link the guide field of the flipper to the fields of the magnet and the bender. This extension of the flipper box is illustrated in Fig. 5.7(b) and indicated in Fig. 5.1(b) as position (8). Using this modified version of the flipper box, no significant depolarization of the focused neutron beam could be evidenced as shown in Sec. 5.1.4.

In addition, the position of the flipper box in the beam path between magnet and bender was numerically optimized. As the performance of the used Mezei-type flipper is determined by the homogeneity of its guide field, the optimized position of the flipper box is found by minimizing the magnetic field gradients, and thus selecting the position with a minimal guide field strength B_G at the center of the flipper. The with *COMSOL Multiphysics* simulated values of B_G are shown as function of the distance d_F between flipper box and magnet in Fig. 5.8(a). By approximation with a fourth-order polynomial even in $(d_F - d_F^{opt})$, an optimal distance d_F^{opt} of around 40 cm was found.

Using the optimal flipper position, the currents of the Mezei-type flipper were successfully calibrated as function of the main field in the magnet. For each field value, The optimal compensation and flip currents were specified by maximizing the measured asymmetry for the (111) reflection of a Heusler single crystal at the sample position, indicating the highest possible flip efficiency. These optimized currents are shown in Fig. 5.8(b). Clear to see is an almost constant value for the flipper coil over the whole field region of the new magnet, which is expected as the required field for a π-flip of the polarization depends ideally only on the wavelength of the neutrons. In contrast, the current in the compensation coil, which suppresses the guide field, increases smoothly with the main field in the magnet. However, the reasonably small current variation below 1 A for the compensation coil over the complete field range indicates an effective screening of the stray field of the magnet by the flipper box. This is also visible in Fig. 5.3(a) where the magnetic field at (2) the central position of the flipper for the complete

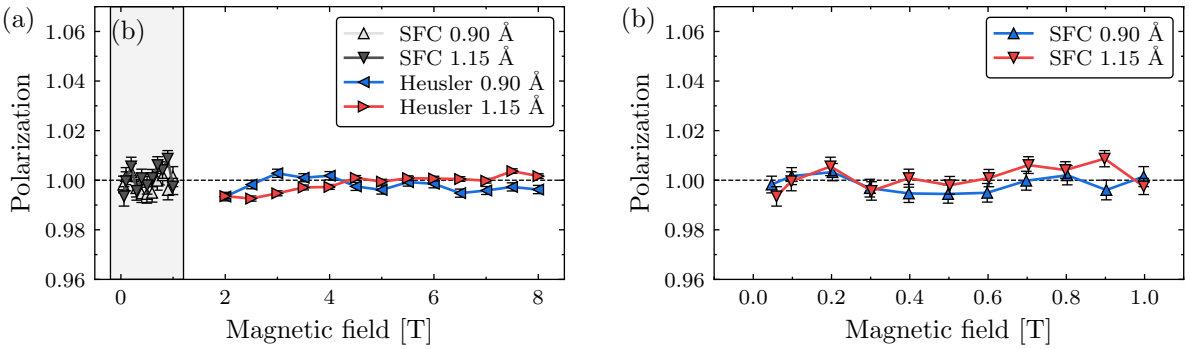

Figure 5.9.: Incoming neutron polarization at the sample position as function of the main field in the magnet. This polarization combines the polarization efficiency of the supermirror bender and the transport efficiency of the setup. It is calculated from the measured asymmetry by normalization with the efficiency of the analyzer. For the high-field region shown in (a), a magnetized Heusler single crystal was used as analyzer, whereas for the low field region, shown in detail in (b), a SFC was used. The monochromators were in a double-focusing configuration for both wavelengths.

setup (dashed red line) drops below the value expected from the magnet's stray field only (solid blue line), even in the additional presence of the strong field of the bender at (3). Overall, the observed smooth variations in both currents fulfill the expectations and allow a straightforward, reliable and highly efficient usage of the optimized flipper for all fields of the magnet.

5.1.4. Characterization

To demonstrate the reliability and high-performance of the new 8 T FR setup at POLI, the incoming neutron polarization at the sample position was analyzed for the entire available field region. For high fields, the (111) reflection of a fully magnetized Heusler single crystal at the sample position was used as analyzer. In this configuration, the measured asymmetry A is given by the product of $P_{\mathrm{H}}^{\mathrm{Pol}}$, P^{Pol} and P_{T}, as discussed in Sec. 5.1.2. For this reason, the neutron polarization $P = P^{\mathrm{Pol}} P_{\mathrm{T}}$ at the sample position can be calculated by the normalization of A with the Heusler analyzing efficiency $P_{\mathrm{H}}^{\mathrm{Pol}} \approx -0.95$ (see appendix B.2). A constant and high value of $P > 0.99$ is observed for both monochromators in the double focusing configuration, as clearly visible in Fig. 5.9(a).

As the full magnetization of the Heusler crystal, which is mandatory for its high analyzing efficiency, is only reached above 2 T, a SFC analyzer was used to determine the neutron polarization in the low-field region. With a non-magnetic Cu single crystal at the sample position, conserving the neutron spin state during the scattering process at the (220) Bragg reflection, the neutron polarization at the sample position can be analogously determined by normalizing the measured asymmetry with the time-dependent analyzing efficiency $P_{\mathrm{SFC}}^{\mathrm{Pol}}$ of the SFC, placed between sample and detector in the so-called Decpol available from SNP (see Sec. 3.3.2). Notably, this experimental configuration cannot be used at fields above 1 T as the stray fields of the magnet may depolarize the ^{3}He gas in the sensitive SFC. Nevertheless, the measurement results in Fig. 5.9(b)

confirm an accordingly high polarization value of $P > 0.99$ in the low field region for both monochromators.

Overall, the new FR option, consisting of the 8 T high-field magnet, the solid state supermirror bender and the Mezei-type flipper with dedicated guide field, could be successfully implemented at the single crystal diffractometer POLI. Prior to fabrication, all components were numerically simulated and optimized. In a dedicated test experiment, the constant and high polarizing, transport and flip efficiency of the new setup over the entire available field region could be demonstrated and is now available for the internal and external user community at POLI [239].

5.2. Implementation of NMR setup for SNP

For a proper analysis of FR and SNP data, the precise knowledge of the polarizer and analyzer efficiency is absolutely mandatory (see Sec. 3.3). This efficiency is constant for solid state polarizers, like polarizing supermirrors or single crystals, and thus, after a proper one-time characterization, easy to correct for. In contrast, the efficiency for ^{3}He SFCs is time dependent as it is based on the decaying spin polarization P^{He} of the ^{3}He gas (see Sec. B.2). Typically, the cell's ^{3}He starting polarization P_0^{He} and the relaxation time T_1 are determined by neutron transmission measurements during insertion and removal of the SFC. However, the cell parameters derived from only two transmission measurements showed to have in practice a rather high uncertainty [246].

To overcome this issue, it is possible to place a neutron monitor before and after the SFC in the beam path and constantly measure the cell's neutron transmission, and thus the P^{He} decay during the experiment [246]. Although this works considerably well for a SFC polarizing the incoming neutron beam, the transmission of an analyzing SFC after the sample depends additionally on the polarization of the scattered beam, which is, for example, for a magnetic sample typically unknown. Moreover, this transmission monitoring relies on a calibration of the monitor count rates during insertion and removal of the SFC, which may become invalid if the beam geometry (e.g. monochromator focusing or slits) is changed during the experiment.

Another possibility to monitor the ^{3}He polarization decay during the experiment is by nuclear magnetic resonance (NMR) spectroscopy. By an excitation pulse of an oscillating magnetic field, directed perpendicular to the environmental field $\mathbf{B}_{\mathrm{SFC}}$ of the SFC and with frequency close to the Larmor frequency $f_L^{\mathrm{He}} = 3.24341 \frac{\mathrm{kHz}}{\mathrm{G}} B_{\mathrm{SFC}}$ of the ^{3}He gas, a small portion of the ^{3}He spins are rotated towards the plane normal to $\mathbf{B}_{\mathrm{SFC}}$. The Larmor precession of these spins around the environmental field after the excitation pulse can be measured as a decaying sinusoidal signal induced in the pickup coil of an oscillating circuit. In this regard, the amplitude of the induced NMR signal is directly proportional to the polarization of the ^{3}He gas. Therefore, it can be used to monitor P^{He} independently of neutrons, which is especially attractive for SFC analyzers.

The necessary hardware and software components for a ^{3}He NMR spectrometer, including a circuit diagram and the signal processing and analysis strategy, are presented in detail in Ref. [247]. Based on this work, a dedicated NMR spectrometer has been

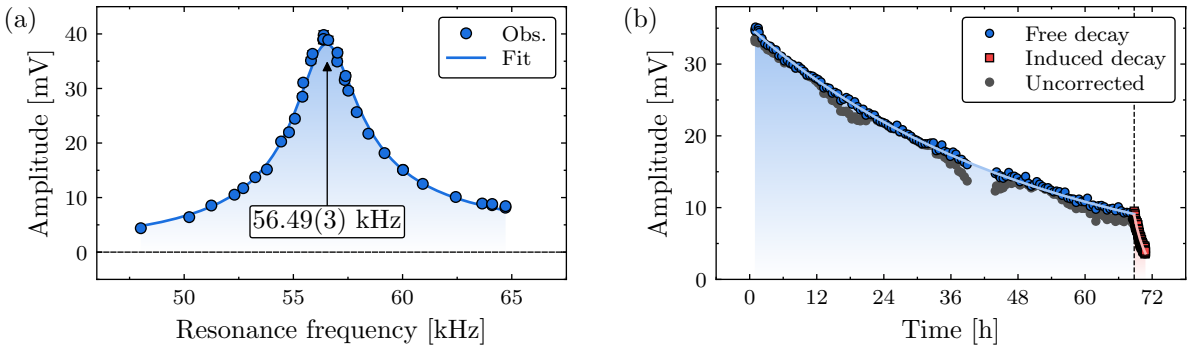

Figure 5.10.: (a) Amplitude of the NMR signal as function of the resonance frequency f_R of the oscillating circuit, fitted according to Eq. (5.1). (b) Time-dependent amplitude of the NMR signal as measured (dark gray) and corrected by Eq. (5.1) (blue circles and red squares). After around 68 h (vertical dashed line), the NMR pulse rate was significantly increased, leading to a faster depolarization of the ^{3}He gas. The results of the combined fit with an exponential decay function (solid line) are given in the text.

built in 2011 for the SNP setup at POLI to monitor the ^{3}He polarization in the SFC polarizer and analyzer. However, the associated NMR software was developed as standalone *LabView* program on *Windows*, which turned out to be difficult to integrate in the *Python*-based instrument control software *NICOS*. Therefore, the NMR software was converted from *LabView* to *Python* code within this work.

To support the NMR project, a scholarship for a twelve-week internship in the framework of the Baltic Science Network Mobility Programme for Research Internships (BARI) was successfully attracted from the German Academic Exchange Service (DAAD). The internship student, Avantika Arya Agrawal from the University of Tartu, Estonia, succeeded in transferring the *LabView* program to *Python* code, using the *PyDAQmx* library as interface between *Python* and the *NIDAQmx* driver for the National Instruments data acquisition (DAQ) card of the NMR setup. This *Python* library provides access the complete functionality of the DAQ driver and is compatible with the *Linux* operating system used for the standard device servers at MLZ. Within the conversion process, the digital signal processing and filtering procedures were optimized and extended for additional functionality, like automatic resonance frequency detection for the oscillating circuit. As the amplitude of the NMR signal is very sensitive to a mismatch between the frequency f_E of the excitation pulse and the Larmor frequency f_L, the measurement procedure was changed from a single f_E pulse to a scan in f_E, revealing high-precision values for the amplitude A and f_L by an approximation with a Gauss function.

As the received signal acts as a sinusoidal driving force for the RLC oscillating circuit with resonance frequency $f_R = (2\pi\sqrt{LC})^{-1}$, the measured amplitude A in the circuit can be identified with the commonly known response function for a driven damped harmonic oscillator

$$A \propto \frac{f_R^2}{\sqrt{(f_L\zeta)^2 + (f_R^2 - f_L^2)^2}} \tag{5.1}$$

with damping $\zeta \propto 1/\sqrt{C}$ in the parallel RLC circuit. In a calibration experiment, the internship student could carefully measure the amplitude A as a function of f_R by systematically changing the capacity C of the oscillating circuit. For this experiment, the SFC was placed in a magnetic cavity driven by permanent magnets, and thus providing a constant environmental field B_{SFC} and Larmor frequency f_L. The results are shown in Fig. 5.10(a) and can be well explained by Eq. (5.1). The corresponding fit reveals a Larmor frequency of $f_L = 56.49(3)\,\mathrm{kHz}$, precisely determining an environmental field of $B_{\mathrm{SFC}} = 17.4168(9)\,\mathrm{G}$.

In the second part of the test experiment, the internship student measured the amplitude of the NMR signal at regular intervals to determine the ^{3}He polarization decay with time. The results are shown in Fig. 5.10(b). For the measurement, a constant capacity was used, leading to a constant f_R of the circuit. Due to daily variations in the room temperature causing a deformation of the magnetic cavity, slight differences in the B_{SFC}, and thus in f_L, were observed. At around 42 h, these changes became so large that f_L left the f_E scan range and a precise amplitude determination was no longer possible. In the final version of the NMR software, this issue is overcome by an automatic adjustment of the f_E scan range. As both f_L and f_R are precisely known from the measurement, the calibrated Eq. (5.1) is automatically applied to normalize the amplitude of the raw NMR signal (dark gray points in Fig. 5.10(b)), resulting in a smooth and steady decrease of the amplitude, which is well described by an exponential decay (solid line in Fig. 5.10(b)). To separate the total ^{3}He polarization decay into the relaxation time T_1, combining cell surface, magnetic field gradient and dipole-dipole interaction effects [244], and the induced depolarization by each NMR measurement, the NMR pulse rate was increased by a factor of 81 after the dashed vertical line at around 68 h. A combined fit of the two regions yields a free cell relaxation time of $T_1 = 69.8(4)\,\mathrm{h}$ and an average ^{3}He depolarization of $\Delta P^{\mathrm{He}} = 0.00778(5)\%$ for each NMR pulse. This low ΔP^{He} is suitable for application, in particular as a rather low NMR pulse rate can be selected in practice. The somewhat short T_1 value can be attributed to sizable magnetic field gradients in the magnetic cavity driven by permanent magnets. Overall, these successful measurements demonstrate the reliability and good performance of the new NMR software at POLI.

Additional to the BARI internship, third-party funds were successfully attracted from the Helmholtz International Fellow Award for new hardware components, including two PCIe-6351 DAQ cards from National Instruments with accessories for rack mounting. Using these new hardware components and wrapping the newly developed NMR *Python* code as a TANGO device, a standardized Linux-based device server for the NMR setup was built. This ensures an easy integration in the NICOS instrument control software at POLI and provides portability between different TANGO-based MLZ instruments. This finalizes the successful commissioning of the new NMR software and setup, which is now ready to be used at POLI.

6. Magnetic structure of $Ba_2CoGe_2O_7$

One of the most prominent members of the barium germanates is $Ba_2CoGe_2O_7$, as it attracted significant scientific interest due to its intriguing optical and magnetoelectric properties, outlined in Sec. 2.2.2. Although the compound has been extensively studied in recent years, most of the research was focused on macroscopic phenomena, like the dependency of the optical properties, the magnetization and the electric polarization on external magnetic fields [43, 86, 89, 96, 99, 106, 135], whereas the microscopic structure is addressed only by a few authors.

A detailed structural study was performed by Hutanu *et al.* [30, 246] with X-ray and neutron single crystal diffraction, revealing precise values for the fractional atomic coordinates and the atomic displacement parameters at room and low temperature. As they found a set of superstructure reflections that are inconsistent with the melilite-type space group $P\bar{4}2_1m$, they initially suggested a symmetry lowering of the nuclear structure to either $P\bar{4}$ or $Cmm2$. In a subsequent study, however, they could show that these additional reflections are attributed to multiple diffraction, known as the Renninger effect [104].

As discussed in Sec. 2.2.2, the basic WFM structure of $Ba_2CoGe_2O_7$ was proposed by Sato *et al.* [99] from magnetization measurements and could be confirmed by Zheludev *et al.* [29] in a preliminary ND experiment with limited data quality. In a more detailed ND study by Hutanu *et al.* [30, 112], an ordered AFM moment of around 2.8 μ_B was found for the Co^{2+} ions. Using PND, the authors suggested $Cm'm2'$ as magnetic ground state symmetry. However, this was based on SNP measurements of only a single reflection and under the assumption of the disproved symmetry lowering outlined above. Moreover, only the local magnetic susceptibility for in-plane magnetic fields is reported by Hutanu *et al.* [112], providing no information about the the expected easy-plane anisotropy in the susceptibility tensor. Therefore, a more comprehensive and careful PND study of the magnetic structure in both the WFM and PM phase was performed and is presented within this chapter. Considering the symmetry analysis of the DMI vector in Sec. 4.2.2, the PND results in the WFM phase are additionally used in Sec. 6.3.3 to determine the absolute DMI sign in $Ba_2CoGe_2O_7$.

6.1. Single crystal sample and preparation

For the neutron diffraction experiments, a high-quality single crystal of $Ba_2CoGe_2O_7$ was used. The crystal, which was provided by the RIKEN Center for Emergent Matter Science (CEMS) in Wako, Japan, was grown by the floating-zone technique and has a cylindrical shape with around 6 mm in diameter and height. It was already used and

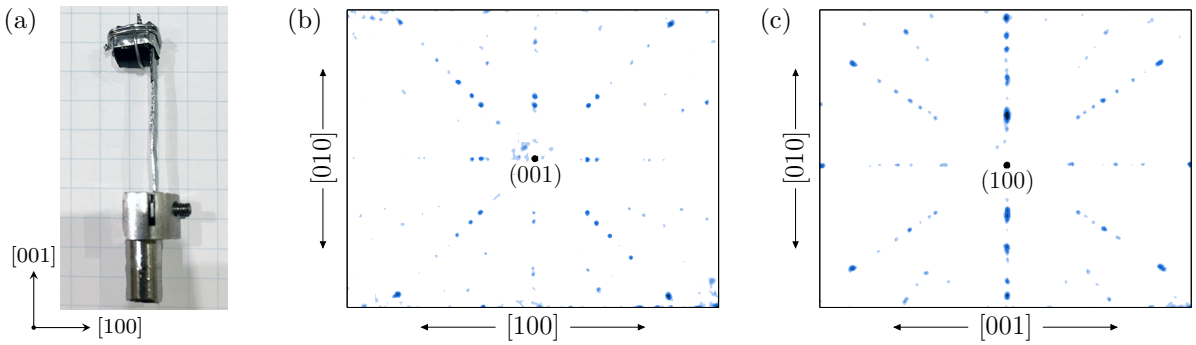

Figure 6.1.: (a) $Ba_2CoGe_2O_7$ single crystal sample used for the neutron diffraction measurements with the c direction vertical and the a direction to the right as indicated by the black arrows. (b,c) Neutron Laue images recorded with the single crystal shown in (a) with the crystalline (b) [001] and (c) [100] directions parallel to the incident neutron beam at the nLaue instrument at MLZ.

well characterized in previous studies (see [104] and references therein). A photograph of the crystal, mounted on an aluminum pin for an easy adjustment of the crystal orientation during the neutron experiment, is shown in Fig. 6.1(a). The orientations of the crystal directions were verified by neutron Laue diffraction at the nLaue instrument at the MLZ. Using a white thermal beam with a considerable intensity between 0.8 and 4 Å, this instrument records the Laue diffraction patterns in backscattering geometry on a $261 \times 200\,\mathrm{mm}^2$ sized detector with 2000×1598 pixels resolution and a variable distance from the sample. Two exemplary patterns, recorded during the alignment of the $Ba_2CoGe_2O_7$ sample, are shown in Figs. 6.1(b) and 6.1(c).

6.2. Paramagnetic structure

In the paramagnetic phase at $T = 10\,\mathrm{K}$, slightly above the magnetic ordering temperature of $T_N = 6.7\,\mathrm{K}$, detailed structural parameters are reported for $Ba_2CoGe_2O_7$ in Ref. [30]. For the crystal structure refinement, the authors used the well-known *MAGLSQ* program of *CCSL* [198] but dismissed extinction effects due to the short neutron wavelength of 0.87 Å used for the experiment. However, the subsequent neutron study in Ref. [176], which was performed at RT with an even shorter neutron wavelength of 0.79 Å, demonstrated the presence of a significant extinction effect, which was taken into account by a Becker-Coppens type 1 isotropic correction (see Sec. 3.4.4 and appendix C). Therefore, the nuclear structure data of Ref. [30] is revised using the novel *Mag2Pol* software, which provides a *SHELX*-like anisotropic extinction correction (see Sec. 3.4.4). This software is selected because it is currently the only GUI-based and actively maintained software that can treat all common types of non-polarized and polarized (FR and SNP) single crystal diffraction data. To validate the new software, the extinction-free refinement in Ref. [30] was reproduced. The results, presented in appendix F.1, are in agreement with the structural parameters obtained by the *CCSL* software.

Atom	x	y	z	U^{iso} [Å^2]
Ba	0.3348(2)	$0.5 - x$	0.4922(3)	0.0006(4)
Co	0	0	0	0.003(1)
Ge	0.1406(1)	$0.5 - x$	0.0404(2)	0.0020(3)
O1	0	0.5	0.1599(4)	0.0033(5)
O2	0.1384(2)	$0.5 - x$	0.7300(3)	0.0038(4)
O3	0.0793(1)	0.1848(1)	0.1883(2)	0.0039(3)
Extinction tensor:	$x_{11} = x_{22} = \frac{c^2}{a^2} x_{33} = 0.073(8)$			
	$x_{12} = x_{23} = x_{13} = 0$			

Table 6.1.: Structural parameters of $Ba_2CoGe_2O_7$ at 10.4 K refined within the space group $P\bar{4}2_1m$ from the HEiDi ND data presented in Ref. [30], assuming an isotropic extinction correction.

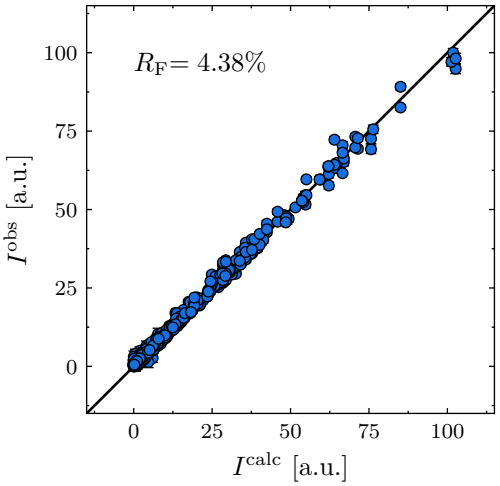

Figure 6.2.: Comparison between the calculated and observed integrated intensities in $Ba_2CoGe_2O_7$ at 10.4 K.

6.2.1. Crystal structure

To get precise values for the atomic positions, displacement parameters and extinction correction, the literature data, collected in the paramagnetic phase of $Ba_2CoGe_2O_7$ at 10.4 K by rocking curves with a neutron wavelength of 0.87 Å at the four-circle diffractometer HEiDi at the MLZ [30], is refined in the $P\bar{4}2_1m$ symmetry using the *Mag2Pol* software. he collected data consists of the integrated intensities of 528 Bragg reflections, from which eleven are excluded due to a negligible intensity that could not be properly separated from the background. The starting values of the structural parameters for the refinement are selected according to the results reported in Ref. [30]. To apply an isotropic extinction correction as in Refs. [104, 246], the components of the *SHELX*-like extinction tensor $\mathcal{X}$ are restricted to $x_{11} = x_{22} = \frac{c^2}{a^2} x_{33}$ and $x_{12} = x_{23} = x_{13} = 0$. This ensures that the extinction parameter x in Eq. (3.35) depends only on the magnitude of the scattering vector $\mathbf{q}$ and not its direction. The refinement results are listed in Table 6.1. As visible in Fig. 6.2, a good agreement between the calculated and observed intensities is achieved, which can be expressed as residual $R_F = 4.38\%$, calculated as

$$R_F = \frac{\sum_{\mathbf{q}} \left| F_N^{obs}(\mathbf{q}) - F_N^{calc}(\mathbf{q}) \right|}{\sum_{\mathbf{q}} |F_N^{obs}(\mathbf{q})|} \tag{6.1}$$

with F_N^{calc} and F_N^{obs} the calculated and observed nuclear scattering factors, respectively.

The refined structural parameters in Table 6.1 are consistent with the results of Hutanu *et al.* [30] (see Table F.1), but the fit quality is clearly improved due to the application of the isotropic extinction correction. The necessity of this correction becomes particularly apparent when the Hamilton test (see appendix E and Ref. [248]) is applied. Comparing the two refinements, a ratio of $\mathcal{R} = 1.11$ can be calculated for omitting the extinction

correction. As $\mathcal{R}_{1,499,0.005} = 1.008 \ll \mathcal{R}$, the necessity of this correction becomes evident at a significance level below 0.5% (i.e. with a probability of more than 99.5% it is correct to perform an extinction correction). This is consistent with the severe extinction effects for large $Ba_2CoGe_2O_7$ single crystals reported in Refs. [29, 176].

Using the full anisotropic extinction tensor, the residuals can be further reduced to $R_F = 4.10\%$. The refined extinction tensor components are given by $x_{11} = 0.021(7)$, $x_{22} = 0.10(1)$, $x_{33} = 0.17(2)$, $x_{12} = -0.15(1)$, $x_{23} = 0.03(3)$ and $x_{13} = 0.01(3)$, whereas the structural parameters do not change within their uncertainty compared to Table 6.1. Applying again the Hamilton test to the isotropic restriction of $\mathcal{X}$, a ratio of $\mathcal{R} = 1.22$ is calculated, providing a clear evidence for an anisotropic character of $\mathcal{X}$ at a significance level below 0.5%. Especially the considerable x_{12} value indicates a strong anisotropy, which may also be attributed to the irregular in-plane shape of the crystal, resulting from its cylinder axis in a direction (see Fig. 6.1).

6.2.2. Field-induced magnetic structure

To microscopically study the field-induced magnetic structure in the PM phase, polarized neutron FRs (see Sec. 3.3.1) were measured at 10 K in $Ba_2CoGe_2O_7$ on the VIP and Super-6T2 diffractometers at the Orphée reactor at the Laboratoire Léon Brillouin (LLB) in Saclay, France. Compared to the instrumental FR setup at POLI (see Sec. 5.1), VIP and Super-6T2 use Heusler single crystals as polarizers and VIP is additionally equipped with an area detector. The setups are presented in more detail in Refs. [249, 250]. The FR experiment was carried out in an applied external magnetic field of 5 and 6 T and with a neutron wavelength of 1.4 and 0.84 Å for Super-6T2 and VIP, respectively. For the measurements, the $Ba_2CoGe_2O_7$ single crystal presented in Sec. 6.1 was oriented with the [100], [210] and [001] direction almost parallel to the vertical axis of the instrument and thus to the field direction.

The 2D detector data from the FR measurements at VIP are reduced by a series of custom-made programs of the LLB, responsible for the integration, indexing and calculation of the asymmetry value [249, 250]. To automatize and simplify the reduction workflow, these LLB programs, written in *Fortran 90*, were embedded in a *Python* script. For the detection and integration of the Bragg spots in the 2D data, a minimal measurement accuracy of $I/dI > 50$ was selected, corresponding to a peak intensity I above around 2% of the maximal observed value. This proved to be a reasonable criteria to exclude spurious spots and very weak peaks that are often not properly separated from the background by the 2D integration algorithm and have a high uncertainty in the calculated asymmetry. For the measurements at Super-6T2, which were automatically integrated using the *Davinci* software [251], the 86 Bragg reflections with $I/dI > 50$ were analogously excluded as they showed similar difficulties in the peak-background separation and a high uncertainty in the calculated asymmetry. Thus, the asymmetry of in total 1905 Bragg reflections could be successfully reduced from the FR measurements at 10 K.

As the asymmetry depends mainly on the ratio between the nuclear and magnetic structure factor (see Eq. (3.26)), only the magnetic moments were refined from the

reduced FR datasets using *Mag2Pol* whereas the structural parameters (atomic positions, U^{iso} values and extinction parameters) were specified as presented in Table 6.1. Note that no significant change in the refined moments but a slight decline in the overall refinement quality could be registered if the anisotropic instead of the isotropic values for the extinction parameters were used, although the anisotropic character of the extinction correction was clearly evident in the non-polarized neutron data (see Sec. 6.2.1). As this might be connected to the somewhat different measurement techniques used for non-polarized and polarized diffraction, the better performing and less complex isotropic extinction model was selected for the FR data refinement. As the magnetic moments of the individual Co atoms in $Ba_2CoGe_2O_7$ can be separated into FM ($\mathbf{m}^{\text{FM}}$) and AFM ($\mathbf{m}^{\text{AFM}}$) contributions based on Eq. (4.9), the unrestricted refinement has in total six free magnetic moment components that are addressed in a field-dependent reference system with $\mathbf{x} \parallel \mathbf{B}$, $\mathbf{y} \parallel (\mathbf{c} \times \mathbf{x})$ and $\mathbf{z} \parallel (\mathbf{x} \times \mathbf{y})$, where $\mathbf{c}$ denotes the lattice [001] direction. Note that the field direction $\mathbf{B}$ is calculated from the experimental orientation matrix of the crystal. Due to the practical limitations in the alignment of the crystal orientation, $\mathbf{B}$ has for all FR measurements within this work, even for those with magnetic field in c direction, a finite in-plane component, which clearly defines the $\mathbf{y}$ axis of the reference system. For the restricted refinement, all the moments are assumed to point parallel to the field direction, and thus only m_x^{FM} is non-zero.

The results of the free and restricted magnetic moment refinement for the four different FR datasets are presented in Table 6.2. As the magnetic scattering factor $\mathbf{M}(\mathbf{q})$, defined in Eq. (3.7), is given by

$$\mathbf{M} \propto \mathbf{m}^{\text{FM}} \underbrace{\left(1 + e^{-i\pi(h+k)}\right)}_{=\begin{cases} 0 & h+k \text{ odd} \\ 2 & h+k \text{ even} \end{cases}} + \mathbf{m}^{\text{AFM}} \underbrace{\left(1 - e^{-i\pi(h+k)}\right)}_{=\begin{cases} 2 & h+k \text{ odd} \\ 0 & h+k \text{ even} \end{cases}} \tag{6.2}$$

in $Ba_2CoGe_2O_7$, $h+k$ even Bragg reflections are only sensitive to the FM moment and are thus denoted as FM-type reflections, whereas $h+k$ odd reflections, denoted as AFM-type, depend only on the AFM moment. This separation is also used to break down the total fit quality, indicated by χ_r^2 (last column of Table 6.2), into the individual ones $\tilde{\chi}_r^{2,\,\text{FM}}$ and $\tilde{\chi}_r^{2,\,\text{AFM}}$ (second last column) for FM- and AFM-type reflections, respectively. These fit qualities are based on the residuals in the asymmetry and calculated by

$$\chi_r^2 = \frac{1}{n-m} \sum_i^n \left(\frac{A^{\text{obs}}(\mathbf{q}_i) - A^{\text{calc}}(\mathbf{q}_i)}{dA^{\text{obs}}(\mathbf{q}_i)} \right)^2 \tag{6.3}$$

with n the number of the measured asymmetries and m the free refinement parameters. All refinements in Table 6.2 show a reasonable good fit quality, which is, however, slightly better for the 6 T datasets collected at VIP, indicated by smaller χ_r^2 values.

For the free magnetic moment refinements, a significant contribution is only observed in the m_x^{FM} component, which agrees with the expectation of an induced FM moment in field direction. Solely for the $\mathbf{B} \parallel [100]$ dataset, noticeable deviations from zero in

Table 6.2.: Overview of the results of the free and symmetry restricted magnetic moment refinement for the reduced FR datasets in $Ba_2CoGe_2O_7$ at 10 K. The used instrument for each dataset is specified in the first column. The components of the magnetization refer to the xyz directions defined in the text.

Magnetic field	Component	Restriction	m_x [μ_B]	m_y [μ_B]	m_z [μ_B]	$\tilde{\chi}^2_r$	χ^2_r
B ∥ [100], 5 T (Super-6T2)	$\mathbf{m}^{\mathrm{FM}}$	free	0.632(5)	0.10(6)	−0.14(4)	4.74	3.01
	$\mathbf{m}^{\mathrm{AFM}}$	free	0.02(2)	−0.09(7)	0.03(7)	0.80	
	$\mathbf{m}^{\mathrm{FM}}$	∥ **B**	0.630(5)	0	0	4.80	3.07
	$\mathbf{m}^{\mathrm{AFM}}$	= 0	0	0	0	0.88	
B ∥ [210], 6 T (VIP)	$\mathbf{m}^{\mathrm{FM}}$	free	0.719(6)	−0.02(3)	0.02(3)	3.42	2.57
	$\mathbf{m}^{\mathrm{AFM}}$	free	−0.014(8)	−0.07(3)	0.03(3)	1.81	
	$\mathbf{m}^{\mathrm{FM}}$	∥ **B**	0.720(6)	0	0	3.41	2.59
	$\mathbf{m}^{\mathrm{AFM}}$	= 0	0	0	0	1.85	
B ∥ [001], 5 T (Super-6T2)	$\mathbf{m}^{\mathrm{FM}}$	free	0.270(3)	−0.04(3)	−0.04(3)	5.08	4.07
	$\mathbf{m}^{\mathrm{AFM}}$	free	−0.00(1)	0.04(8)	0.01(9)	1.25	
	$\mathbf{m}^{\mathrm{FM}}$	∥ **B**	0.270(3)	0	0	5.19	4.09
	$\mathbf{m}^{\mathrm{AFM}}$	= 0	0	0	0	1.19	
B ∥ [001], 6 T (VIP)	$\mathbf{m}^{\mathrm{FM}}$	free	0.316(4)	−0.01(2)	−0.01(2)	2.10	1.74
	$\mathbf{m}^{\mathrm{AFM}}$	free	−0.006(6)	−0.00(2)	0.01(2)	1.39	
	$\mathbf{m}^{\mathrm{FM}}$	∥ **B**	0.316(4)	0	0	2.09	1.73
	$\mathbf{m}^{\mathrm{AFM}}$	= 0	0	0	0	1.38	

the remaining components are observed, which might be attributed to inaccuracies in the experimentally determined crystal orientation matrix defining the field direction, and thus the used xyz reference system. As a result, the restricted refinements, which allow only non-zero m_x^{FM} components, provide a similar fit quality and the same induced moments within the uncertainty.

The field-induced magnetic moments of the restricted refinement in Table 6.2 can be used to determine the symmetry-adapted magnetic susceptibility tensor χ, which is generally symmetric ($\chi_{ij} = \chi_{ji}$) and restricted to $\chi_{11} = \chi_{22}$ and $\chi_{12} = \chi_{13} = \chi_{23} = 0$ for space group $P\bar{4}2_1m$ as discussed in Sec. 2.2. Using a least squares refinement, the two independent tensor components are determined with values of $\chi_{11} = 0.123(2)\,\mu_B/\mathrm{T}$ and $\chi_{33} = 0.053(4)\,\mu_B/\mathrm{T}$ per Co atom, indicating a strong easy-plane anisotropy of $\chi_{11}/\chi_{33} = 2.3(2)$. Although the results are slightly lower than the expectations of around $\chi_{11} = 0.16\,\mu_B/\mathrm{T}$ and $\chi_{33} = 0.08\,\mu_B/\mathrm{T}$ from magnetization measurements at 10 K in a 0.2 T field [43], the expected in-plane anisotropy of around $\chi_{11}/\chi_{33} = 2$ (see Sec. 2.2.2) is clearly reproduced.

In our recent inelastic neutron study in $Ba_2CoGe_2O_7$ and in results derived from first-principles electronic structure calculations, there is some indication of a non-vanishing orbital Co moment [110, 252, 253], which may originate from the admixture of higher-order states due to SOC (see Sec. 2.2.2). This issue can also be addressed by polarized

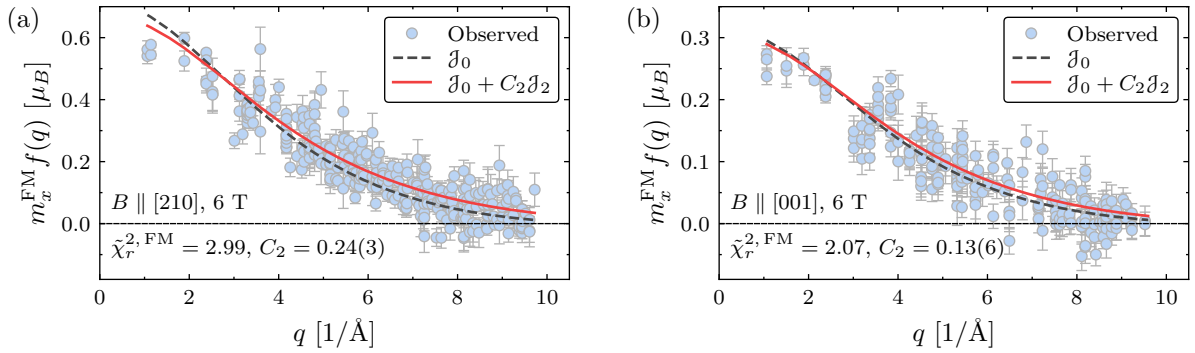

Figure 6.3.: Comparison between the magnetic form factors as function of q assuming a quenched (gray dashed line) and finite (red solid line) orbital magnetic moment for the refinement of the FR dataset with applied magnetic field in (a) [210] and (b) [001] direction. In addition, the fit quality of the FM-type reflections and the C_2 value are listed for the finite orbital moment refinement, whereas corresponding values for the quenched refinement can be found in Table 6.2. The observed magnetic scattering amplitudes (light blue points) are calculated directly from the measured asymmetries using $m_x^{\mathrm{FM}} f(q) = \frac{1}{2} F_{\mathrm{M}} e^{W(q)}$ with the magnetic Fourier coefficients $\mathbf{F}_{\mathrm{M}} = F_{\mathrm{M}}\hat{\mathbf{B}}$, which can be derived from Eqs. (3.39), (6.2) and (D.3) given that the magnetic moments of the Co atoms are equal and directed along the field ($\mathbf{m}_j = m_x^{\mathrm{FM}}\hat{\mathbf{B}}$). The observed magnetic scattering amplitudes with an uncertainty in the form factor above 0.1 were excluded from the figure for clarity.

neutron scattering, as the magnetic form factor is different for the spatially compact orbital (m_L) and the more extended spin (m_S) moments [254]. Analogously to Eq. (3.9), the magnetic form factor can thus be written in dipole approximation as

$$f(q) = \mathcal{J}_0(q) + C_2\mathcal{J}_2(q) \tag{6.4}$$

with $C_2 = m_L/m$ the ratio of the orbital to the total magnetic moment $m = m_S + m_L$. To investigate the presence of a finite orbital moment in $Ba_2CoGe_2O_7$, this C_2 parameter was additionally refined using the restricted model ($\mathbf{m} \parallel \mathbf{B}$) with isotropic extinction correction. The influence of the C_2 parameter is most prominent for high-q reflections; thus, only the FR datasets collected up to $q_{\max} \approx 10\,\text{Å}^{-1}$ at VIP allow for a proper C_2 refinement compared to the Super-6T2 datasets limited to $q_{\max} \approx 6.5\,\text{Å}^{-1}$ by the larger neutron wavelength of 1.4 Å. The refinement results for the measurements at VIP are shown in Fig. 6.3(a) and 6.3(b). They both provide a positive C_2 value, indicating a finite orbital moment parallel to the spin moment, which is in agreement with the predictions from the first-principles calculations [252, 253]. In particular for the measurement with $\mathbf{B} \parallel [210]$ shown in Fig. 6.3(a), the fit quality of the FM-type reflections improves considerably as indicated by the reduction of $\tilde{\chi}_r^{2,\mathrm{FM}}$ from 3.42 to 2.99. Moreover, a significant C_2 value is observed, which is somewhat close to the value of $C_2 \approx 0.15$ that can be derived from the calculations reported in Ref. [252]. Nevertheless, some of the the observed form factor values, calculated directly from the experimentally measured asymmetries and shown as blue points in Figs. 6.3(a) and 6.3(b), have a clear spread even for similar q values. This behaviour can not be explained by the simple form-factor approximation used for the refinements and indicates an additional dependency on the direction of $\mathbf{q}$, which may result from a non-spherical magnetization density. Using

multipolar refinements and the advanced 3D MEM (Sec. 3.5.3), these potentially non-spherical magnetization density distributions in $Ba_2CoGe_2O_7$ are investigated in more detail in Chap. 8 and compared to the ones found in $Ba_2CuGe_2O_7$ and $Ba_2MnGe_2O_7$.

6.3. Weak ferromagnetic structure

Below $T_N = 6.7\,\mathrm{K}$, $Ba_2CoGe_2O_7$ orders in a WFM structure as discussed in Sec. 2.2.2. This phase transition was shown to be purely magnetic by neutron diffraction and infrared phonon mode analysis [30]. Detailed structural parameters and an ordered moment of $2.9(1)\,\mu_B/Co^{2+}$ were found by Hutanu *et al.* [30] from non-polarized neutron diffraction. However, no extinction correction was taken into account and the refinement is thus revised in the following section. The extinction-free refinement is reproduced in appendix F.1 using *MAG2POL*, validating again the new software.

6.3.1. Crystal structure and ordered moment

The literature data from Ref. [30] was collected in the WFM phase of $Ba_2CoGe_2O_7$ at 2.2 K by rocking curves with a neutron wavelength of 0.87 Å at the four-circle diffractometer HEiDi at the MLZ. The collected data consists of the integrated intensities of 568 Bragg reflections, from which nine are excluded due to a negligible intensity that could not be properly separated from the background. The starting values of the refinement parameters are selected according to the results reported in Ref. [30] and an isotropic extinction correction is applied. For the refinement, the ordered AFM moment is selected to point in [100] direction with four equally populated, energetically equiva-

Atom	x	y	z	U^{iso} [Å^2]
Ba	0.3349(2)	$0.5 - x$	0.4928(4)	0.0022(4)
Co	0	0	0	0.003(1)
Ge	0.1407(1)	$0.5 - x$	0.0403(2)	0.0033(3)
O1	0	0.5	0.1596(5)	0.0058(6)
O2	0.1383(2)	$0.5 - x$	0.7298(3)	0.0051(4)
O3	0.0793(2)	0.1845(2)	0.1882(2)	0.0053(3)
Extinction tensor:	$x_{11} = x_{22} = \frac{c^2}{a^2} x_{33} = 0.08(1)$			
	$x_{12} = x_{23} = x_{13} = 0$			
Magnetic moment:	$m^{\mathrm{AFM}} = 2.6(2)\,\mu_B$			

Table 6.3.: Structural parameters of $Ba_2CoGe_2O_7$ at 2.2 K refined within the magnetic ground state $P2_1'2_12'$ from the HEiDi ND data presented in Ref. [30], assuming equally populated tetragonal domains and an isotropic extinction correction.

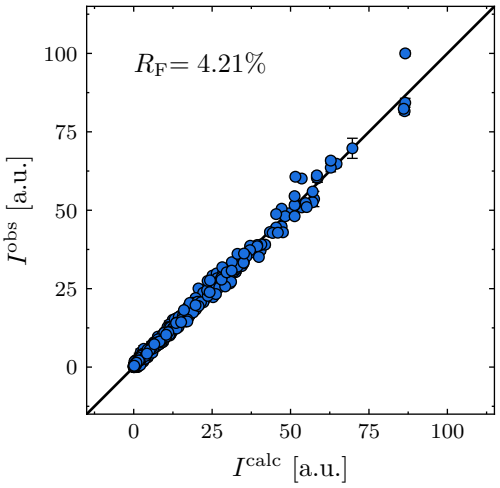

Figure 6.4.: Comparison between the calculated and observed integrated intensities in $Ba_2CoGe_2O_7$ at 2.2 K.

lent tetragonal domains, corresponding to the $P2'_12_12'$ ground state (see Sec. 2.2.2) and the results are listed in Table 6.3. Note that an alternative refinement in the $Cm'm2'$ or $P112'$ ground state with corresponding tetragonal magnetic domains provides the same results since the models are indistinguishable by non-polarized neutron diffraction [30]. As visible in Fig. 6.4, a good agreement between the calculated and observed intensities is achieved with residuals of $R_F = 4.21\%$. Compared to the extinction-free refinement in appendix F.1 with $R_F = 4.53\%$, the clearly reduced residuals demonstrate again the necessity of a proper extinction correction in $Ba_2CoGe_2O_7$. Applying the Hamilton test, a ratio of $\mathcal{R} = 1.08$ confirms this necessity at a significance level below 0.5%.

Refining the full anisotropic extinction tensor, components of $x_{11} = 0.07(1)$, $x_{22} = 0.00(3)$, $x_{33} = 0.42(4)$, $x_{12} = -0.23(2)$, $x_{23} = 0.02(6)$ and $x_{13} = 0.04(4)$ are determined and the fit quality is further improved by reducing the residuals to $R_F = 3.75\%$ without any significant change in the structural parameters or the magnitude of the ordered AFM moment compared to Table 6.3. As the application of the Hamilton test results in a ratio of $\mathcal{R} = 1.34$ for the anisotropic character of the extinction correction, which corresponds to a significance level clearly below 0.5%, the absolute necessity of a proper extinction correction for large $Ba_2CoGe_2O_7$ single crystals is emphasized again.

6.3.2. Field-induced magnetic structure

Applying even weak magnetic fields in the *ab* plane breaks the degeneracy between the four tetragonal domains, favouring those with WFM moment preferably parallel to the field direction [90]. For stronger magnetic fields above around 1 T, a saturated single AFM domain state is formed with the magnetic moments canted towards the field direction. Within this configuration, the AFM part is aligned in the *ab* plane perpendicular to the field direction ($[001] \perp \mathbf{m}^{\mathrm{AFM}} \perp \mathbf{B}$), whereas the FM part, composed of the intrinsic WFM ($m^{\mathrm{WFM}} \approx 0.009\,\mu_B/\mathrm{Co}^{2+}$) and the field-induced ($\mathbf{m}^B = \chi\mathbf{B}$) moment, is aligned with the field direction ($\mathbf{m}^{\mathrm{FM}} \parallel \mathbf{B}$) [89]. Thus, only non-zero m_x^{FM} and m_y^{AFM} components are expected in the field-dependent reference system introduced in Sec. 6.2.2.

To investigate the magnetic structure in high fields, polarized neutron FRs were measured in the WFM phase at 2 K in $Ba_2CoGe_2O_7$ on the VIP diffractometer using the same instrumental setup as in Sec. 6.2.2. The FR experiment was carried out in applied external magnetic fields of 1, 3 and 6 T oriented along the [100], [110] and [001] crystal directions. For the measurements with magnetic field almost parallel to the [001] direction, the small in-plane component $\mathbf{B}_{\perp[001]}$ of the field was aligned almost perfectly along [010]. Using the structural parameters and the isotropic extinction coefficients listed in Table 6.3, the *Mag2Pol* refinement of the AFM-type reflections results in a ordered AFM moment of around $m^{\mathrm{AFM}} \approx 1.8\,\mu_B/\mathrm{Co}^{2+}$ for all measured field directions and values, which is clearly lower than the expected value of around $2.6\,\mu_B/\mathrm{Co}^{2+}$ from the non-polarized measurements in Sec. 6.3.1. However, the refined AFM moment clearly increases if the highest intensity reflections are systematically removed from the refinement, which can be achieved by refining only the group of reflections with an intensity below a decreasing limit I^{limit}. This is exemplified by the gray triangles in Fig. 6.5(a) for the measurement with a field of 6 T applied along the [110] direction. As extinction

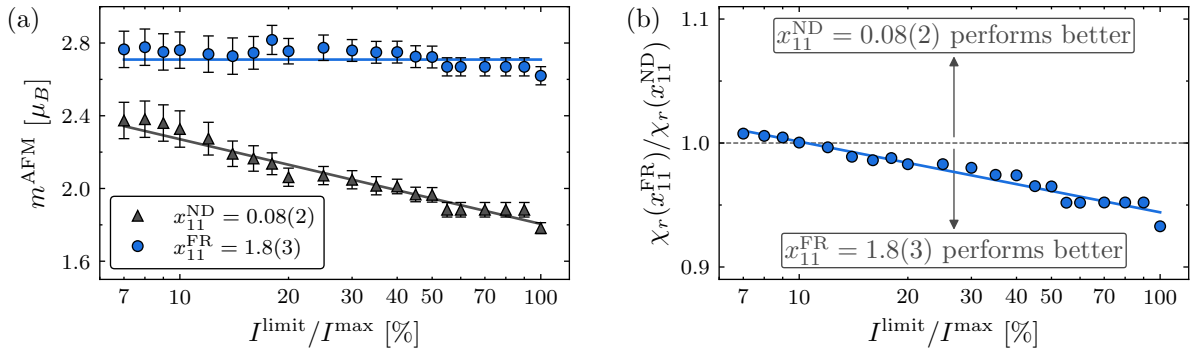

Figure 6.5.: (a) Refined AFM moment m^{AFM} for an applied magnetic field of 6 T along the [110] direction in $Ba_2CoGe_2O_7$ as function of the limit I^{limit}, restricting the refinement data to reflections with intensity $I < I^{\mathrm{limit}}$, and by using the extinction coefficient determined from the non-polarized (x_{11}^{ND}, gray triangles) and polarized (x_{11}^{FR}, blue circles) measurements. (b) The square root of the ratios between the respective fit qualities χ_r^2 using x_{11}^{ND} and x_{11}^{FR} as function of the limit I^{limit}. A ratio smaller than one indicate a better performance of the refinement using the larger extinction coefficient x_{11}^{FR}. The depicted lines are linear fits to the respective values and serve as a guide to the eye.

effects are particularly strong for high intensity reflections, this increasing behaviour of m^{AFM} on a decreasing I^{limit} clearly indicates an underestimation of the extinction coefficient. And indeed, refining the isotropic extinction parameter x_{11} additionally to the AFM moment for all FR datasets, an average value of $x_{11}^{\mathrm{FR}} = 1.8(3)$ is revealed. Note that a proper refinement of the full anisotropic extinction tensor was not possible from the FR measurement due to strong correlations arising between the individual coefficients. The significantly higher value of x_{11}^{FR} compared to $x_{11}^{\mathrm{ND}} = 0.08(2)$ from non-polarized neutron diffraction might be attributed to the strong spin flip diffraction, which results from the sizable magnetic scattering amplitude of the AFM structure in the nuclear-magnetic interference and causes an additional extinction contribution for FR measurements [197]. Moreover, neutron beam depolarization effects may occur for PND in large magnetically ordered crystals and lead to similar deviations in the measured asymmetry as by the extinction correction [255].

Using the determined $x_{11}^{\mathrm{FR}} = 1.8(3)$ isotropic extinction coefficient for the refinement of the AFM-type reflections, a high AFM moment of around $m^{\mathrm{AFM}} \approx 2.6\,\mu_B/\mathrm{Co}^{2+}$ is established, which is in agreement with the expectations from the non-polarized measurements. In addition, the AFM moment remains roughly constant if the highest intensity reflections are systematically removed from the refinement as shown in Fig. 6.5(a) by the blue circles, which is a more reasonable behaviour. Moreover, the refinements using x_{11}^{FR} instead of x_{11}^{ND} show an improved fit quality for high intensity reflections as illustrated in Fig. 6.5(b) by the reduced ratio of their respective χ_r^2 values for the exemplary FR dataset with a 6 T field in [110] direction. Only for the low intensity reflections ($I/I^{\mathrm{max}} < 15\%$), for which the extinction correction has little to no effect, similar χ_r^2 values are observed for both types of refinement.

The results of the magnetic moment refinements are listed in Table 6.4 for all nine datasets, which are reduced from the FR measurements at 2 K as described in Sec. 6.2.2 and contain the asymmetry of in total 6675 Bragg reflections. The refinements

Table 6.4.: Overview of the results of the restricted magnetic moment refinement for the reduced FR datasets with different field values and directions in $Ba_2CoGe_2O_7$ at 2 K. The components of the magnetization refer to the field-dependent xyz reference system defined in the text. The results of the free refinement with unrestricted FM and AFM moments are listed in Table F.3 in the appendix.

Magnetic field		m_x^{FM} [μ_B]	m_y^{AFM} [μ_B]	$\chi_r^{2,\,\mathrm{FM}}$	$\chi_r^{2,\,\mathrm{AFM}}$	χ_r^2
B ∥ [100]	1 T	0.150(6)	−2.56(3)	1.77	2.04	1.91
	3 T	0.425(7)	−2.58(4)	1.96	2.25	2.11
	6 T	0.93(1)	−2.46(6)	2.06	1.72	1.88
B ∥ [110]	1 T	0.134(7)	−2.60(4)	1.61	2.06	1.84
	3 T	0.420(8)	−2.68(5)	1.79	1.86	1.83
	6 T	0.931(9)	−2.63(5)	2.12	1.59	1.84
B ∥ [001]	1 T	0.074(6)	−1.92(3)	1.74	1.96	1.85
	3 T	0.211(7)	−2.39(4)	1.96	3.01	2.52
	6 T	0.415(7)	−2.66(5)	1.84	2.12	1.99

are based on the structural parameters from Table 6.3 and the isotropic extinction coefficient of $x_{11}^{\mathrm{FR}} = 1.8(3)$. In addition, a single domain state is assumed with magnetic moments restricted to $\mathbf{m}^{\mathrm{FM}} \parallel \mathbf{B}$ and $[001] \perp \mathbf{m}^{\mathrm{AFM}} \perp \mathbf{B}$, leading to the two non-zero refinement parameters m_x^{FM} and m_y^{AFM} in the field-dependent reference system as discussed above. The results for the free refinements with unrestricted FM and AFM moments are provided in Table F.3 in the appendix and show no major difference to the restricted results and a similar fit quality.

As expected from magnetization measurements, the refined FM moment (m_x^{FM} in Table 6.4) increases linearly with increasing field strength and shows a strong easy *ab* plane anisotropy [43]. By applying a least-squares refinement to the measured FM moments, the two independent components of the magnetic susceptibility tensor for the induced magnetic moment are determined to be $\chi_{11} = 0.151(3)\,\mu_B/\mathrm{T}$ and $\chi_{33} = 0.067(3)\,\mu_B/\mathrm{T}$ per Co atom. The good agreement between the refined FM moment ($m^{\mathrm{FM,\,ref}} = |m_x^{\mathrm{FM}}|$) and the one calculated from the susceptibility ($m^{\mathrm{FM,\,calc}} = |\chi\mathbf{B}|$) is illustrated in Fig. 6.6(a). Contributions from the intrinsic WFM moment are neglected as their small magnitude of around $0.009\,\mu_B/\mathrm{Co}$ is below the sensitivity of the measurement [43]. Like in the PM phase in Sec. 6.2.2, the refined susceptibility parameters are slightly smaller than the values of $\chi_{11} = 0.173\,\mu_B/\mathrm{T}$ and $\chi_{33} = 0.089\,\mu_B/\mathrm{T}$ reported from magnetization measurements but the observed in-plane anisotropy of $\chi_{11}/\chi_{33} = 2.3(1)$ is agreement with the literature value of around 2.2 [43].

For the ordered AFM moment, a consistently negative m_y^{AFM} component is observed, which allows to conclude about the absolute direction of the DMI vector in $Ba_2CoGe_2O_7$ as discussed in detail in Sec. 6.3.3. Combining the refined AFM moment with the field-induced magnetization yields the total ordered magnetic moment $\mathbf{m}^{\mathrm{tot}} = \mathbf{m}^{\mathrm{FM}} + \mathbf{m}^{\mathrm{AFM}}$ per Co atom. Its magnitude is shown in Fig. 6.6(b) as function of the strength of the in-plane component $\mathbf{B}_{\perp[001]}$ of the applied magnetic field. Clear to see is a saturation of the total moment for in-plane fields above 1 T. This is in excellent agreement with

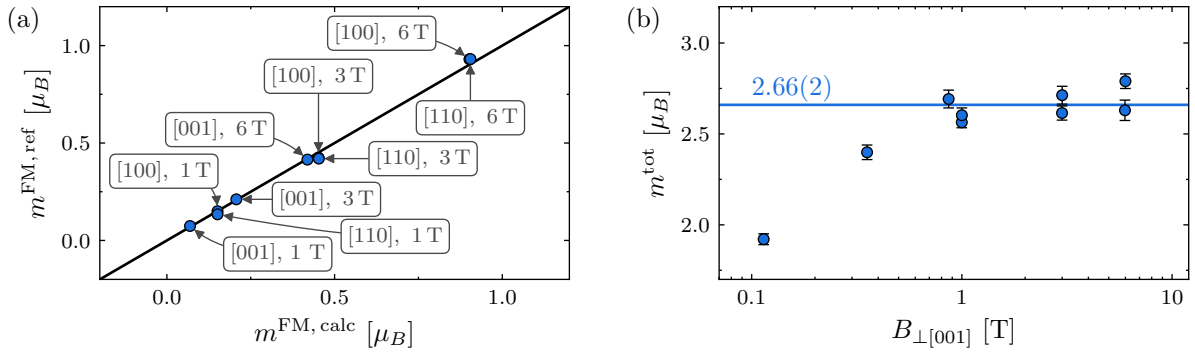

Figure 6.6.: (a) Comparison between the refined FM moment ($m^{\mathrm{FM,\,ref}}$), denoted in Table 6.4 as m_x^{FM}, and the calculated one ($m^{\mathrm{FM,\,calc}}$) from $\chi_{11} = 0.151(3)\,\mu_B/\mathrm{T}$ and $\chi_{33} = 0.067(3)\,\mu_B/\mathrm{T}$. Each point is labeled by its respective magnetic field direction and value. The uncertainty is smaller than the symbols. (b) The total refined magnetic moment as function of the strength of the in-plane component $\mathbf{B}_{\perp[001]}$ of the applied magnetic field. The line at $2.66(2)\,\mu_B$ indicates the average value of the saturated magnetization for fields above 1 T.

the expectation from field-dependent electric polarization measurements, predicting a multidomain state below fields of around 1 T [86, 90]. As a single domain state is assumed for the refinement, the presence of such a multidomain state will reduce the refined total moment towards lower fields accordingly. For the saturated magnetic moment values above 1 T, an average value of $2.66(2)\,\mu_B$ per Co atom is found, which is consistent with the results from the non-polarized neutron diffraction in Sec. 6.3.1. The low-field multidomain structure is investigated in more detail in Sec. 6.4.2.

Taking into account the susceptibility and the total ordered magnetic moment, the field-induced spin canting ϕ can be estimated as $\phi = \sin^{-1}(|\chi\mathbf{B}|/m^{\mathrm{tot}})$. This angle is a crucial parameter for the field-induced ferroelectric polarization according to the p-d hybridization and the spin-nematic interaction model as discussed in Secs. 2.3.1 and 2.3.3, respectively. Both mechanisms predict an electric polarization of $P_z^{[110]} \propto \cos(2\kappa - 2\phi)$ along the z axis for a field in the [110] direction and a negative m_y^{AFM} component (see Table 2.2). A distortion angle of $\kappa = 21.74(6)°$ for the CoO_4 tetrahedron (see Fig. 2.1) can be precisely determined from the structural parameters listed in Table 6.3. Using the refined values for χ and m^{tot}, the maximal $P_z^{[110]}$ with $\phi = \kappa$ is expected at 2 K for a field of $B_{\mathrm{max}} = \sin(\kappa)m^{\mathrm{tot}}/\chi_{11} = 6.6(2)$ T. This value is close to the experimental result of Murakawa *et al.* [86] shown in Fig. 2.11(b), having a maximal ferroelectric polarization at around 7 T in the [110] direction. This verifies that the ratio between the refined susceptibility and the total ordered magnetic moment is reasonable, although χ_{11} is smaller than expected from magnetization as discussed above. For $\phi = \kappa + 45°$, a sign change in $P_z^{[110]}$ is predicted by the two models. Using again the estimation of ϕ from the refined values, the sign change is expected at a magnetic field of $B_0 = 16.2(4)$ T. This value is higher than the experimental finding of around 14.5 T, which can be explained by an increase in the susceptibility for higher fields, which is not covered by our measurements limited to 6 T but clearly evident from a non-linear behavior of the field-induced magnetization shown up to 14 T in Ref. [86]. As this slight convex curvature of the

magnetization is centered at around 7 T, it might be attributed to the antiferroelectric coupling identified in Ref. [90], favouring a preferably small $|P_z^{[110]}|$ value. This coupling suppresses the field-induced spin canting, and thus the susceptibility, for $B < B_{\max}$ as $\partial|P_z^{[110]}|/\partial B > 0$ and enhances it for $B > B_{\max}$ as $\partial|P_z^{[110]}|/\partial B < 0$, leading to the observed convex curvature.

6.3.3. Absolute direction of the DMI vector

As the alignment of the AFM to WFM moment is determined by direction of the DMI vector $\mathbf{D}$, the precise magnetic moment values listed in Table 6.4 allow to conclude about the absolute sign of the D_z component. For the single domain state, which is reached for in-plane fields above 1 T (see Secs. 6.3.2 and 6.4.2), there are in general two magnetic moment configurations possible depending on the sign of D_z as discussed in Sec. 4.2.2 and illustrated in Fig. 4.2 for a magnetic field in [010] direction. Applying the field-dependent reference system, which is used for the magnetic moment refinement with only non-zero m_x^{FM} and m_y^{AFM} components, the DMI energy of $Ba_2CoGe_2O_7$ in Eq. (4.10) can be simplified to

$$E_{\mathrm{UC}}^{\mathrm{DMI}} = -4D_z m_y^{\mathrm{AFM}} \underbrace{m_x^{\mathrm{FM}}}_{>0} \underbrace{\sin(\theta)}_{\geq 0}, \tag{6.5}$$

with θ the angle enclosed by the field direction and the crystal [001] axis. As $\mathbf{m}^{\mathrm{FM}}$ is aligned in field direction and $\theta \in [0, \pi]$, both m_x^{FM} and $\sin(\theta)$ are positive. Thus, D_z and m_y^{AFM} must have the same sign in order to be energetically favorable ($E_{\mathrm{UC}}^{\mathrm{DMI}} < 0$). Comparing these conclusions with the refinement results listed in Table 6.4, the consistently positive m_x^{FM} satisfies the expectations. Note that a negative m_x^{FM} may indicate an error either in the assumed magnetic field or neutron polarization direction, and thus serves as a simple verification method for the refinement model. For the AFM moment, a consistently negative m_y^{AFM} is evident in Table 6.4, which unambiguously reveals for the first time a negative D_z sign in $Ba_2CoGe_2O_7$ directly from the measurement as reported by us in Ref. [226]. This negative sign is consistent with the results of Romhányi *et al.* [90], theoretically predicting $D_z < 0$ based the shape of the DMI sign dependent simulation of the field-induced ferroelectric polarization and its comparison with the measurement in Ref. [89]. Moreover, the consistency of the m_y^{AFM} sign for different field directions confirms the DMI as origin for the WFM canting. If the WFM canting would be caused by a local in-plane anisotropy due to crystal field effects of the Co atoms' tetrahedral environment, the canting direction, and thus the m_y^{AFM} sign, would reverse between fields applied in [100] and [110] direction, which is clearly not the case. Note that also a consistently negative m_y^{AFM} sign is found for the measurements with $\mathbf{B} \parallel [001]$ in Table 6.4. This is caused by the slight in-plane field component $\mathbf{B}_{\perp[001]}$, which results from a tilting of the applied magnetic field of $\theta \approx 7°$ towards the [010] direction that is considered in the definition of the xyz reference system for the refinement (see Sec. 6.2.2). As this $\mathbf{B}_{\perp[001]}$ aligns the WFM moment, Eq. (6.5) is also applicable to the measurements with $\mathbf{B} \parallel [001]$ and confirms again $D_z < 0$. However, as the magnitude of $\mathbf{B}_{\perp[001]}$ is

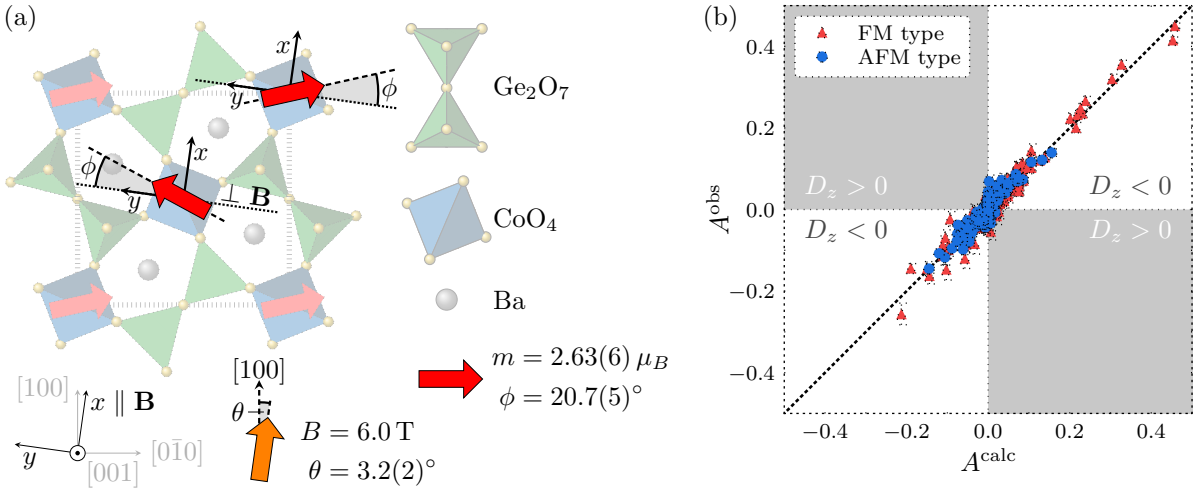

Figure 6.7.: Results of the magnetic moment refinement in $Ba_2CoGe_2O_7$ from Table 6.4 with an applied magnetic field of 6 T close to the [100] direction. The projection of the exact field direction (orange arrow) and the resulting magnetic moment configuration (red arrows) on the *ab* plane are visualized in (a). The in-plane tilt angle of the magnetic field is drawn exaggerated to be visible. In addition, the x, y and z directions of the field-dependent reference system used for the refinement are illustrated. The comparison between the observed and calculated asymmetry values, divided into FM- and AFM-type reflections, is shown in (b). The figure was modified from Ref. [226].

clearly below 1 T for the $\mathbf{B} \parallel [001]$ measurements with field strengths of 1 T and 3 T, no single domain state is achieved and the refined magnitude of m_y^{AFM} is slightly reduced as discussed in Secs. 6.3.2 and 6.4.2.

Visualizing the results of the magnetic moment refinement for the measurement with the magnetic field of 6 T in the [100] direction as in Fig. 6.7(a), the negative D_z sign can also be confirmed by graphical comparison with Fig. 4.2. Note that the UC shown in Fig. 6.7(a) is rotated by 90° compared to Fig. 4.2 to equalize the directions of the applied magnetic field. This rotation, however, does not affect the alignment of the AFM to WFM moment such that the magnetic moment configurations shown in Fig. 4.2 can still serve as reference for a positive or negative DMI sign. The good quality of the refinement is shown in Fig. 6.7(b) by comparing the measured and observed asymmetry values. As discussed in detail in Ref. [226], it is important to note that the sign of the asymmetry for an AFM-type reflection is directly related to the sign of m_y^{AFM}. This becomes apparent when applying the field-dependent reference system to Eq. (3.26), resulting in an asymmetry for the AFM-type reflections of

$$A^{\mathrm{AFM}} = -\frac{2aP\hat{q}_x\hat{q}_y \,\mathrm{Re}[N^*]}{|N|^2 + a^2\left(1-\hat{q}_y^2\right)\left(m_y^{\mathrm{AFM}}\right)^2} m_y^{\mathrm{AFM}}, \tag{6.6}$$

with the positive coefficient $a = \gamma_N r_0 \mu_B^{-1} f e^{-W}$, including the temperature and magnetic form factor of the Co atoms. Taking also into account the connection between the signs of D_z and m_y^{AFM} based on Eq. (6.5), the measured asymmetry for each AFM-type reflection directly reflects the sign of D_z. As the refined magnetic moment arrangement visualized

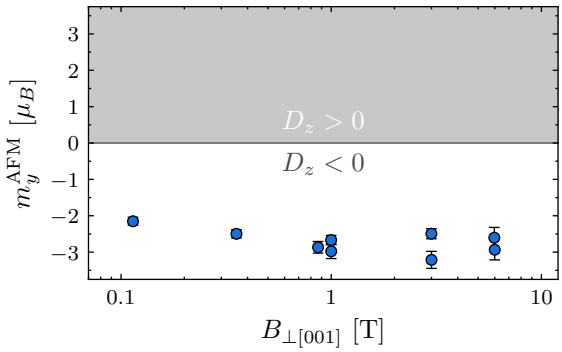

Figure 6.8.: AFM moment m_y^{AFM} directly calculated from the asymmetry values of the (121) reflection or equivalent for different magnetic field values and directions. The direction of the y axis in ab plane is shown in Fig. 6.7(a). The calculated magnetic moment values are shown as function of the in-plane component of the applied magnetic field, which saturates the single domain state. The figure was modified from Ref. [226].

in Fig. 6.7(a) refers to a negative D_z, the signs of A^{calc} in Fig. 6.7(b) for the AFM-type reflections are the ones expected for $D_z < 0$. If the sign of the observed asymmetry A^{obs} for an AFM-type reflection is consistent with the sign of A^{calc}, it reproduces $D_z < 0$ and will be located within the two white areas of Fig. 6.7(b). In contrast, if the sign of an observed AFM-type asymmetry A^{obs} is inconsistent with A^{calc} and thus suggests $D_z > 0$, it will be located within the two gray areas. Therefore, all the AFM-type asymmetries within the white areas in Fig. 6.7(b) confirm the negative D_z sign, whereas the values in the gray areas suggest a positive one. As all significant AFM-type asymmetries are within the white areas, $D_z < 0$ is clearly confirmed.

Using the direct relation between the sign of D_z and the asymmetry, it is in fact sufficient to measure a single strong AFM-type reflection by PND to unambiguously determine the DMI sign [21, 226]. This unique strength of PND is especially useful in compounds with a small accessible q-range or low counting rates, preventing large collections of data for a complete magnetic moment refinement. To illustrate this for the DMI sign in $Ba_2CoGe_2O_7$, only the asymmetry value of the strong AFM-type (121) reflection or its symmetry equivalent is taken from the FR measurement for the different magnetic field directions and values listed in Table 6.4. Solving Eq. (6.6) for the AFM moment, the expected values of m_y^{AFM} are directly calculated from the measured asymmetries using the structural parameters listen in Table 6.3. An extinction correction was dismissed as it may only influence the determined magnetic moment value but not its sign. The resulting m_y^{AFM} is shown in Fig. 6.8 as function of the in-plane component of the applied magnetic field. Like for the refined total magnetic moment in Fig. 6.6(b), a slight saturation behavior is observed at low fields, which can be attributed to the presence of multiple domains. The variation of the saturated AFM moment at higher fields may result from the missing extinction correction, which proved to be essential to get proper magnetic moment values (see Sec. 6.3.2). However, as m_y^{AFM} is clearly negative for all magnetic field values and directions in Fig. 6.8, it demonstrates that PND allows to unambiguously conclude from the asymmetry of a single AFM-type reflection about

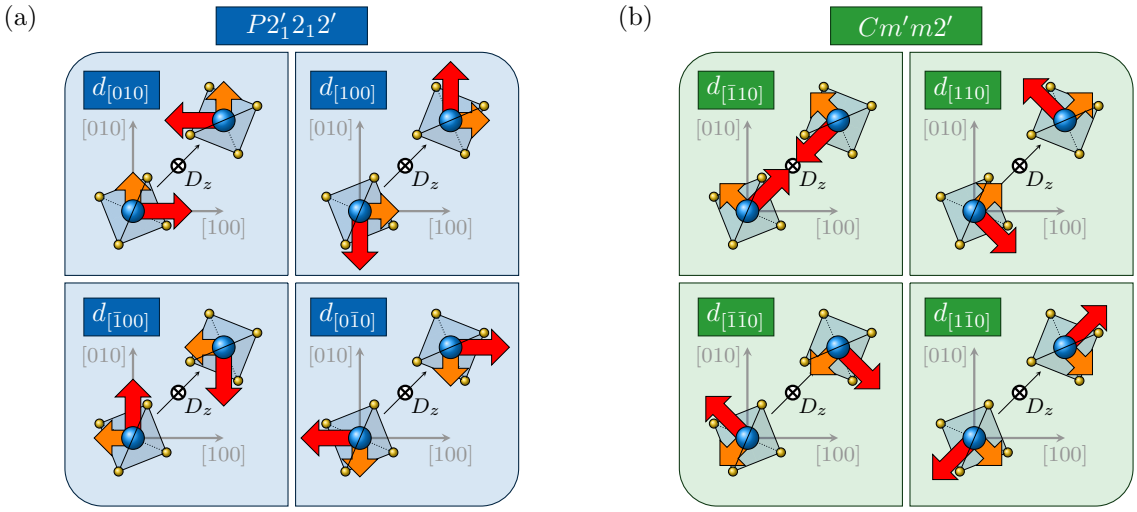

Figure 6.9.: Schematic view of the magnetic moment configurations for the four tetragonal domains in $Ba_2CoGe_2O_7$, assuming a (a) $P2_12_12'$ and (b) $Cm'm2'$ magnetic symmetry. The large red and short orange arrows denote the ordered AFM and WFM moments, respectively. The alignment of their directions is chosen to be energetically beneficial according to Eq. (4.10) with a negative D_z sign as determined by in Sec. 6.3.3. The labeling of the domains reflects the direction of the WFM moment.

the negative D_z sign in $Ba_2CoGe_2O_7$ based on Eq. (6.5).

6.4. Magnetic ground state structure

Starting from the paramagnetic $P\bar{4}2_1m1'$ symmetry and considering the in-plane alignment of the ordered magnetic moments in the WFM phase in $Ba_2CoGe_2O_7$, two magnetic space groups are identified in Sec. 2.2.2 as potential high-symmetry models for the magnetic ground state, namely $P2_12_12'$ with $\mathbf{m}^{\mathrm{AFM}} \parallel [100]$ and $Cm'm2'$ with $\mathbf{m}^{\mathrm{AFM}} \parallel [110]$. An illustration of their basic magnetic structure can be found in Fig. 2.7. Using PND, Hutanu *et al.* [112] suggested $Cm'm2'$ as the most probable ground state. However, this conclusion was drawn based on SNP measurements of a single AFM-type reflection and by considering a disproved symmetry lowering as discussed in more detail in Sec. 2.2.2. Moreover, a theoretical investigation of the field-dependent electric polarization in $Ba_2CoGe_2O_7$ by Romhányi *et al.* [90] leads to contrary results, suggesting $P2_12_12'$ as magnetic ground state due to an antiferroelectric in-plane coupling between the Co atoms, which favors an orientation of the AFM moments in [100] direction in weak fields. To resolve this uncertainty about the true magnetic ground state in $Ba_2CoGe_2O_7$, a detailed PND study was performed.

6.4.1. Magnetic domain structure

As shortly addressed in Sec. 2.2.2, four tetragonal domains are expected for the high-symmetry magnetic ground states due to a broken four-fold inversion axis of the parent structure. These four magnetic domains are depicted in Fig. 6.9(a) and 6.9(b) for the

Table 6.5.: Magnetic domain distributions and fit quality χ_r^2 resulting from the refinement of the AFM-type reflections assuming either a $P2_1'2_12'$ or $Cm'm2'$ magnetic symmetry and a total ordered moment of $2.66\,\mu_B$ per Co atom. The directions of the AFM and WFM moment for each domain are shown in Fig. 6.9(a) and 6.9(b). The direction of the in-plane field component is close to [010].

	$P2_1'2_12'$					$Cm'm2'$				
$B_{\perp[001]}$ [T]	$d_{[100]}$ [%]	$d_{[\bar{1}00]}$ [%]	$d_{[010]}$ [%]	$d_{[0\bar{1}0]}$ [%]	χ_r^2	$d_{[110]}$ [%]	$d_{[\bar{1}\bar{1}0]}$ [%]	$d_{[\bar{1}10]}$ [%]	$d_{[1\bar{1}0]}$ [%]	χ_r^2
0.114	15.2(8)	8.9(7)	75.9(8)	0.0(1)	1.89	54.5(7)	0.0(1)	45.5(7)	0.0(1)	2.04
0.354	6(1)	0(1)	93(1)	1(1)	2.90	55(1)	0(1)	45(1)	0(1)	5.01

$P2_1'2_12'$ and $Cm'm2'$ magnetic space groups, respectively. For $P2_1'2_12'$, the in-plane AFM moments, indicated as large red arrows in Fig. 6.9, are directed along the lattice directions, whereas for $Cm'm2'$, they are aligned with the diagonals. Resulting from the DMI induced canting of the ordered moment, an additional WFM moment, shown as a small orange arrow in Fig. 6.9, is expected perpendicular to the AFM moment for each magnetic domain. The directions of the WFM moments in Fig. 6.9 are selected for each domain such that the DMI energy given by Eq. (4.10) is minimized ($E_{\mathrm{UC}}^{\mathrm{DMI}} < 0$), assuming $D_z < 0$ as experimentally determined in Sec. 6.3.3. It is important to note that the application of a small magnetic in-plane field favors the domains with WFM moment preferably parallel to it.

6.4.2. Low field structure

To investigate the low-field multidomain magnetic structure in more detail, the refinement for the two datasets in Fig. 6.6(b) with an in-plane field clearly below 1 T is revised using a fixed total magnetic moment of $2.66\,\mu_B$ and a tetragonal AFM domain structure as expected for the high-symmetry $P2_1'2_12'$ and $Cm'm2'$ ground states illustrated in Fig. 6.9(a) and 6.9(b), respectively. For the two low-field datasets, the in-plane component $\mathbf{B}_{\perp[001]}$ of the applied magnetic field was directed along the [010] direction with a slight deviation of around 6.5° towards [100]. The refined domain distributions are listed in Table 6.5. Note that even a change of $\pm 0.1\,\mu_B$ in the fixed total AFM moment did not cause differences in the refinement results larger than their uncertainty.

Assuming the $P2_1'2_12'$ magnetic model, $d_{[010]}$ can be clearly identified as the primary domain. This agrees well with the expectations as the WFM moment of $d_{[010]}$ points in [010] direction and is thus energetically most favored by the applied magnetic field. With decreasing field, an increasing faction of the primary domain is distributed towards domains $d_{[100]}$ and $d_{[\bar{1}00]}$. As the WFM moments of these two domains are almost perpendicular to the applied magnetic field, they are the energetically most efficient domains to populate for a multidomain state. However, due to the small deviation of the in-plane component of the magnetic field towards [100], $d_{[100]}$ is energetically slightly more favored than $d_{[\bar{1}00]}$, leading to the somewhat larger fraction. For domain $d_{[0\bar{1}0]}$, a clear suppression is evident for all field values, which is in agreement with the expectation from its WFM moment antiparallel to the direction of the applied magnetic field.

For the refinement with the $Cm'm2'$ magnetic model, only domains $d_{[110]}$ and $d_{[\bar{1}10]}$ are populated and show a similar domain fraction. This distribution reflects well the energetically favorable alignment of their WFM moments to the applied field direction. The discussed deviation of the field towards [100] slightly prefers domain $d_{[110]}$ as observed. However, the domain distribution remains constant within its uncertainty for decreasing magnetic fields and this is clearly not expected for the formation of a multidomain state. In addition, the χ^2_r values are consistently higher for the $Cm'm2'$ refinement model, suggesting $P2'_12_12'$ as the true ground state symmetry. Nevertheless, the low field structure may not necessarily reflect the ground state, in particular as Romhányi *et al.* [90] proposed a somewhat different canted ferrimagnetic order for small magnetic fields parallel to the [110] direction. Therefore, a dedicated zero-field measurement is required to unambiguously select the correct ground state symmetry.

6.4.3. Field cooled magnetic structure and domain distribution

To precisely investigate the zero-field magnetic ground state in $Ba_2CoGe_2O_7$ at a temperature of around 2 K, detailed polarization matrices were measured by SNP at the D3 diffractometer at the Institut Laue-Langevin (ILL), France. The layout of the instrument is similar to that presented in Sec. 3.3.2, using a saturated Heusler (Cu_2MnAl) monochromator as polarizer, a ^{3}He SFC as analyzer and the CryoPAD [177] as neutron polarimeter. To induce an imbalance between the tetragonal domains, the $Ba_2CoGe_2O_7$ single crystal (see Sec. 6.1) was placed in a magnetic field of 0.1 T parallel to the [010] direction during the cooling process. This was achieved by mounting the crystal with its [010] direction vertical in a cryostat and inserting it in an external magnet outside of the CryoPAD for cooling. After reaching a sample temperature of around 2.3 K, which is clearly below T_N, the magnetic field was removed and the cryostat carefully installed in the CryoPAD for the zero-field SNP measurement, giving access to $(h0l)$-type Bragg reflections in the instrumental plane. This rather complex experimental procedure is necessary as the desired contributions from nuclear-magnetic interference in the measured cross-section (see Eq. (3.29)) would average out for equally populated domains. In the SNP experiment, the full positive $\mathcal{P}_{ij}$ and negative $\mathcal{P}_{\bar{i}j}$ polarization matrices, and thus all 36 different channels of SNP (see Table B.1), were collected for all available AFM-type Bragg reflections. The measured matrix elements were corrected for the finite efficiencies of the polarizer and analyzer. The additional collection of the purely nuclear (003) reflection served as reference for this correction.

For the magnetic moment refinement of the SNP data using *Mag2Pol*, the matrix elements of the six reflections with the lowest intensity are removed due to very high uncertainties. For the remaining 902 matrix elements, the magnitude of the AFM moment, the fractions of the four tetragonal domains and the isotropic extinction coefficient are refined using the structural parameters as listed in Table 6.3 and a $P2'_12_12'$ or $Cm'm2'$ magnetic moment model. The refinement results are shown in Fig. 6.10(a) and 6.10(b) for the $P2'_12_12'$ and $Cm'm2'$ models, respectively.

For the diagonal $\mathcal{P}_{xx}$ and $\mathcal{P}_{yy}$ elements of the purely magnetic (300) reflection, indicated by red triangular symbols in Fig. 6.10, a strong deviation from the calculated

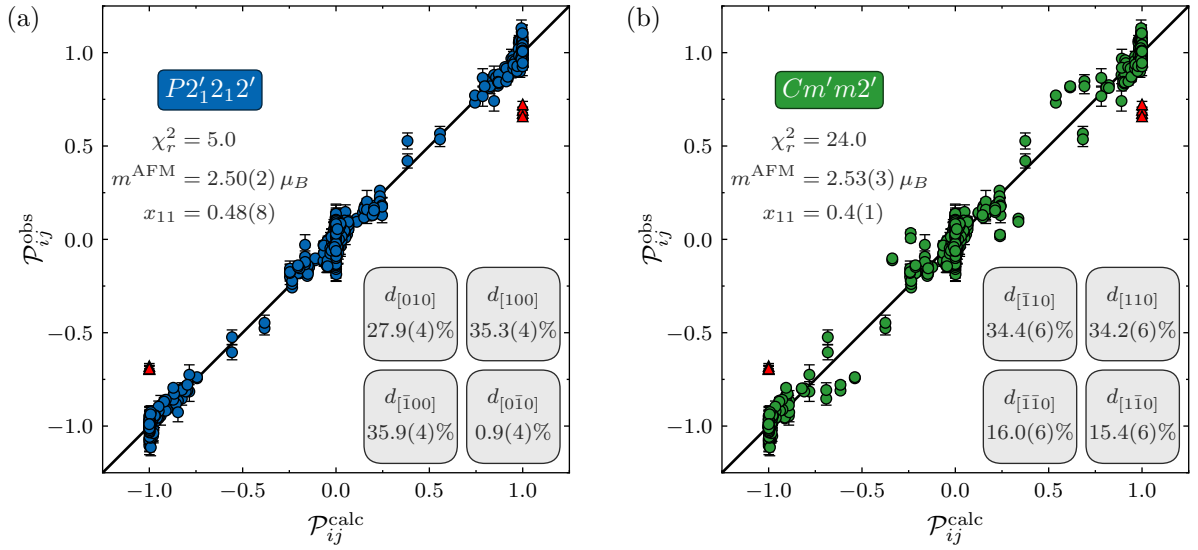

Figure 6.10.: Comparison between the observed and calculated polarization matrix elements $\mathcal{P}_{ij}$ for the AFM-type Bragg reflections collected by SNP on the $Ba_2CoGe_2O_7$ single crystal after magnetic field cooling in 0.1 T applied along the [010] direction. For the refinement, the magnetic moment directions were restricted as expected for the (a) $P2'_12_12'$ and (b) $Cm'm2'$ magnetic space groups with four tetragonal domains as illustrated in Fig. 6.9(a) and 6.9(b), respectively. The measured matrix elements of the (300) Bragg reflection (red triangles) are excluded from the refinement due to large contributions from multiple diffraction as discussed in the text. The resulting domain fractions, the ordered AFM moment, the fit quality χ^2_r and the isotropic extinction coefficient x_{11} are presented in the figure.

value is clearly visible for both models. This deviation can be attributed to an additional contribution from multiple diffraction, which was shown to be particularly strong for the (300) reflection by Sazonov *et al.* [104]. If the neutron polarization is assumed to remain almost constant for multiple diffraction, the additional intensity can be treated as a nuclear contribution N^{mult} that does not interfere with the Bragg scattering intensity. Thus, the diagonal matrix elements of the purely magnetic (300) reflection, which has only a non-zero M_z component in xyz scattering geometry due to $\mathbf{y} \perp \mathbf{m}^{\mathrm{AFM}}$, can be defined according to appendix B.4 as

$$\mathcal{P}_{xx} = \mathcal{P}_{yy} = \frac{\left|N^{\mathrm{mult}}\right|^2 - |M_z|^2}{\left|N^{\mathrm{mult}}\right|^2 + |M_z|^2} \qquad \mathcal{P}_{zz} = \frac{\left|N^{\mathrm{mult}}\right|^2 + |M_z|^2}{\left|N^{\mathrm{mult}}\right|^2 + |M_z|^2} = 1 \tag{6.7}$$

with $\mathcal{P}_{ii} = -\mathcal{P}_{\bar{i}\bar{i}}$. Comparing Eq. (6.7) with the average values of 0.95(1) for the $\mathcal{P}_{zz}$ and −0.68(1) for the $\mathcal{P}_{xx}$ and $\mathcal{P}_{yy}$ elements, a multiple diffraction contribution of around $N^{\mathrm{mult}} = 0.65(1)$ fm to the measured intensity of the (300) reflection can be estimated by calculating M_z based on the refinement results listed in Fig. 6.10(a). The small deviation of $\mathcal{P}_{zz}$ from 1 might be attributed to a slight dependency of the multiple diffraction intensity on the neutron polarization direction. Due to the strong distortion by multiple diffraction, the collected polarization matrix elements of the (300) reflection are excluded from the refinement.

Visually comparing the calculated and observed matrix elements in Fig. 6.10(a) and

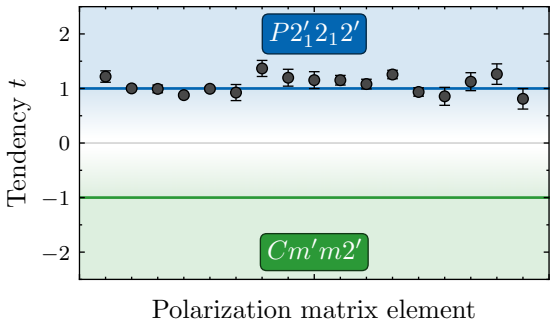

Figure 6.11.: Tendency t, defined in Eq. (6.8), for the 17 matrix elements with a difference between the calculated $\mathcal{P}_{ij}^{\text{calc}}$ values of the $P2_1'2_12'$ and $Cm'm2'$ model that is ten times larger than the measurement uncertainty $d\mathcal{P}_{ij}^{\text{obs}}$. A value of $t = 1$ denotes a perfect fit with the expected value from the $P2_1'2_12'$ model (blue line), whereas $t = -1$ suggests $Cm'm2'$ (green line).

6.10(b), the better agreement of the $P2_1'2_12'$ model (Fig. 6.10(a)) is clearly evident and quantified in a significantly reduced χ_r^2. To emphasise this even further, the matrix elements with a difference $\Delta\mathcal{P}_{ij}^{\text{calc}} = \mathcal{P}_{ij}^{P2_1'2_12'} - \mathcal{P}_{ij}^{Cm'm2'}$ between the calculated values for the two models that is ten times larger than the measurement uncertainty $d\mathcal{P}_{ij}^{\text{obs}}$ are separately inspected. For each of these elements, the tendency t is defined as

$$t_{ij} = \frac{\left(\mathcal{P}_{ij}^{\text{obs}} - \mathcal{P}_{ij}^{P2_1'2_12'}\right) + \left(\mathcal{P}_{ij}^{\text{obs}} - \mathcal{P}_{ij}^{Cm'm2'}\right)}{\Delta\mathcal{P}_{ij}^{\text{calc}}}. \tag{6.8}$$

The calculated value of t approaches 1 if the measured $\mathcal{P}_{ij}^{\text{obs}}$ reflects the expectations of the $P2_1'2_12'$ model and -1 for the $Cm'm2'$ model. The tendency values for these 17 highly sensitive polarization matrix elements are shown in Fig. 6.11. Clear to see is a consistent and explicit shift towards $t = 1$ that reliably identifies the $P2_1'2_12'$ symmetry as the zero-field magnetic ground state. This result is consistent with the conclusion in Ref. [90], which is based on a theoretical investigation of the field-dependent electric polarization in $Ba_2CoGe_2O_7$. Note that a similar analysis of four additional SNP datasets, two collected at D3 (ILL) and two at POLI (MLZ) with different values and directions for the applied magnetic field during the cooling, indicated also consistently $P2_1'2_12'$ as magnetic ground state of $Ba_2CoGe_2O_7$; however, the differences between the two models were most prominent for the presented measurement.

Considering the refined domain distribution for the $P2_1'2_12'$ model, almost equal and high populations of around 36% are observed for the $d_{[100]}$ and $d_{[\bar{1}00]}$ domains. The $d_{[010]}$ domain, which should be energetically most favored by the applied magnetic field in [010] direction during cooling, has a slightly lower value of around 28%. However, this is not surprising, as the FR measurement in Sec. 6.4.2 clearly showed a redistribution of the $d_{[010]}$ domain fraction to $d_{[100]}$ and $d_{[\bar{1}00]}$ for decreasing fields in [010] direction. For the present measurement, the field was completely removed, and thus the majority of the $d_{[010]}$ population redistributes to $d_{[100]}$ and $d_{[\bar{1}00]}$. The similar values for the two formed domains may reflect the almost perfect alignment of the applied magnetic field

with the crystal [010] direction. The clear suppression of the $d_{[0\bar{1}0]}$ can be attributed to its WFM moment antiparallel to the applied magnetic field. The domain fractions of the disproved $Cm'm2'$ model are listed for completeness in Fig. 6.10(b).

The refined magnetic moment value of $2.50(2)\,\mu_B$/Co for the $P2'_12_12'$ model is slightly lower than expected from FR and non-polarized measurements. However, for similar SNP measurements in $Ba_2CoGe_2O_7$ with other magnetic field orientations, like the one presented in Sec. 6.4.4 with $\mathbf{B} \parallel [\bar{1}20]$ and a somewhat higher ordered moment of $2.7(2)\,\mu_B$/Co, a better agreement with the FR results is found. Thus, the slight differences in the refined m^{AFM} value between the various measurements might be attributed to the influence of multiple diffraction and other effects connected to the crystal orientation. These effects can be particularly strong for some of the SNP measurements because only one reciprocal plane is available for each SNP dataset as the detector is limited to the instrumental plane (see Sec. 3.3.2). In contrast, several reciprocal planes are accessed in FR and non-polarized measurements such that some of the effects connected to the crystal orientation might average out. Moreover, the relative effect of multiple diffraction is in general different for the three experimental techniques. For example, the multiple diffraction contribution N^{mult} of the pure magnetic (300) reflection distorts the SNP elements $\mathcal{P}_{xx}$ and $\mathcal{P}_{yy}$ by more than 30% as discussed above, whereas it would only increase the non-polarized intensity by less than 20% and not affect the FR result at all since there is no interference of N^{mult} with the magnetic Bragg scattering. Moreover, the isotropic extinction parameter of the discussed SNP refinement ($x_{11}^{\mathrm{SNP}} = 0.48(8)$, see Fig. 6.10(a)) is clearly smaller than for the FR refinement ($x_{11}^{\mathrm{FR}} = 1.8(3)$, see Sec. 6.3.2). This difference in x_{11}, which can be attributed to the beneficial vertical alignment of the sample's cylindrical axis for the SNP measurement that leads to a regular and compact shape of the crystal in the instrumental plane, may also influence the refined m^{AFM} value. An attempt to refine an anisotropic extinction tensor from the SNP measurements proves to be unsuccessful due to the emergence of strong correlations between the refinement parameters.

6.4.4. Magnetic field switching of the domain distribution

To study the influence of the magnetic field that is applied during cooling on the remanent magnetic domain distribution, a experiment like in Sec. 6.4.3 was performed at the POLI diffractometer. The corresponding SNP setup, using ^{3}He SFCs as polarizer and analyzer and the third generation CryoPAD, is outlined in Sec. 3.3.2. For the experiment, the $Ba_2CoGe_2O_7$ single crystal sample was mounted with the $[\bar{1}20]$ direction vertical, giving access to $(2h\,hl)$ reflections in the instrumental plane. During cooling, the cryostat was placed in an external electromagnet, providing fields up to $\pm 750\,\mathrm{G}$ in vertical direction at the sample position. After reaching a temperature of around 3.7 K, which is clearly below T_N, the external field was switched off and the cryostat mounted in the CryoPAD for the SNP measurement. To monitor the remanent domain distribution in zero field, it is sufficient to collect the polarization matrix elements of a few AFM-type Bragg reflections with significant nuclear-magnetic interference contributions. Thus, only the (213) and $(21\bar{3})$ reflections were selected and the full negative

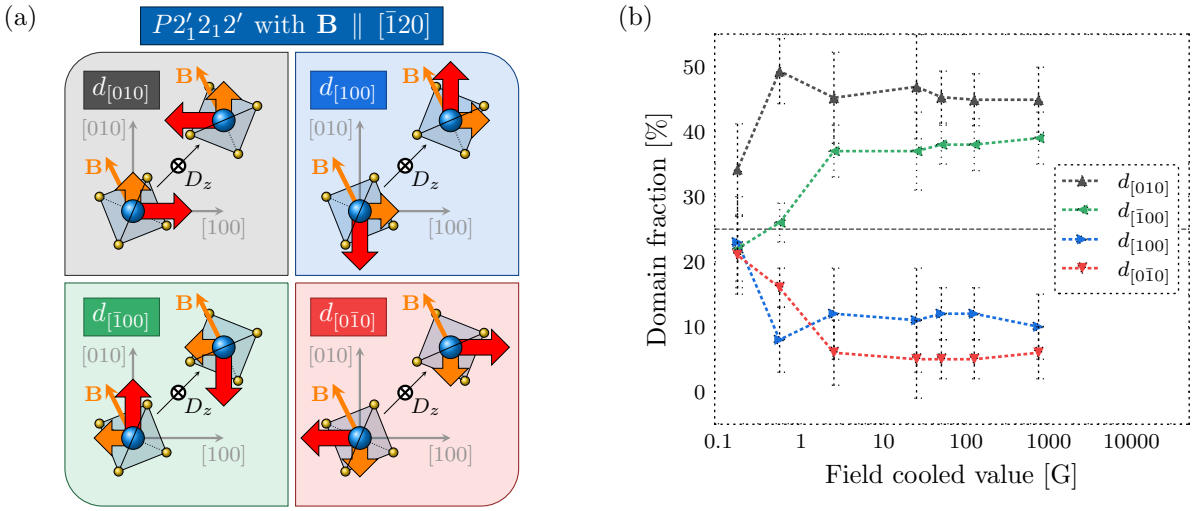

Figure 6.12.: (a) Schematic view of the magnetic moment configurations for the four tetragonal domains in $Ba_2CoGe_2O_7$, assuming a $P2_12_12'$ magnetic ground state symmetry, as illustrated in Fig. 6.9(a). In addition, the magnetic field direction $\mathbf{B} \parallel [\bar{1}20]$ for the field cooled SNP experiment at POLI is shown by a thin orange arrow. (b) Refined remanent domain distribution for the four tetragonal domains illustrated in (a) as function of the applied magnetic field value during cooling. The dashed line indicates a domain fraction of 25%, corresponding to the value adopted for an equal distribution. The coloring of the data symbols refers to the color of the domains in (a).

($\mathcal{P}_{\bar{i}j}$) and the diagonal entries of the positive polarization matrix ($\mathcal{P}_{ii}$) measured. After finishing the collection of data, the cryostat was removed from the CryoPAD and the sample heated again to around 100 K, clearly above T_N. Afterwards, the procedure was repeated with a different field cooled value. For the maximal available field of 750 G, a full datacollect was performed as reference. Its refinement in the $P2_12_12'$ model with $\chi^2_r = 5.5$ provides an ordered AFM moment of $2.7(2)\,\mu_B$/Co and an isotropic extinction parameter of $x_{11} = 8(5)$. These values serve as basis for the magnetic domain distribution refinement on the reduced datasets with only the two (213)-type reflections. Notably, a comparable refinement in the $Cm'm2'$ model provides a considerably worse fit quality as indicated by an increased $\chi^2_r = 6.5$, confirming again $P2_12_12'$ as the true ground state symmetry (see Sec. 6.4.3).

The WFM and AFM magnetic moment configurations for each of the domains in the $P2_12_12'$ magnetic model are illustrated in Fig. 6.12(a) in relation to the applied magnetic field direction $\mathbf{B} \parallel [\bar{1}20]$. The corresponding domain fractions, which are refined from the reduced datasets, are shown in Fig. 6.12(b) as function of the applied field during cooling. For the highest field of 750 G, domains $d_{[010]}$ and $d_{[\bar{1}00]}$ are clearly predominant with the former being slightly more pronounced. This is in agreement with the expectations from Fig. 6.12(a), showing a good and even better alignment between the WFM moment and the field direction for the $d_{[\bar{1}00]}$ and $d_{[010]}$ domains, respectively. In contrast, the WFM moments of domains $d_{[100]}$ and $d_{[0\bar{1}0]}$ are aligned opposite to the field direction, suggesting a suppression of the two domains, which is maximized for the latter one. This is clearly reflected in the refined domain populations with $d_{[100]}$ and $d_{[0\bar{1}0]}$ being suppressed below

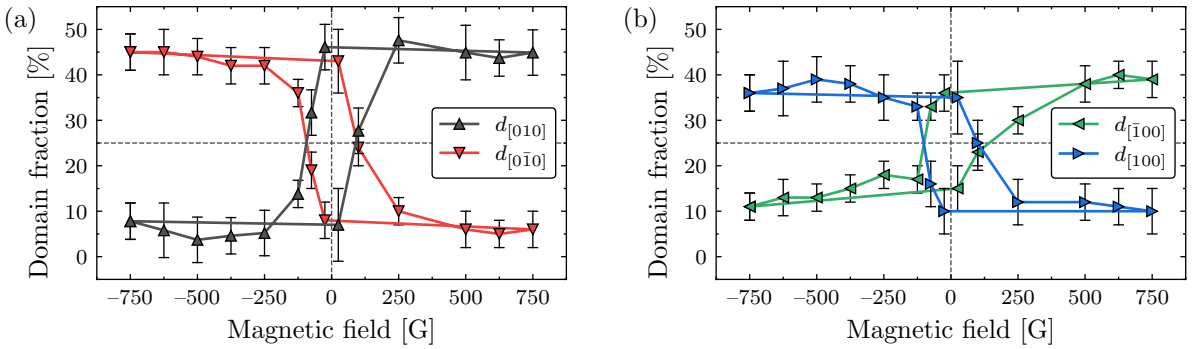

Figure 6.13.: Refined remanent magnetic domain distribution from zero-field SNP measurements as function of the externally applied magnetic field in the $[\bar{1}20]$ direction at 3.7 K. Prior to the application of the field, the domain distribution was saturated by field-cooling in an opposite directed magnetic field stronger than 1 G. The domain fractions for the two domains with WFM moment almost parallel or antiparallel to the field direction are shown in (a). The values for the other two domains with WFM moment almost perpendicular to the field are given in (b). The corresponding magnetic moment configurations of all four domains are illustrated Fig. 6.12(a), reflecting also the coloring of the symbols.

a fraction of around 10% at the highest field cooled value. This domain distribution remains almost constant for fields above around 1 G. Towards very weak fields, the domain fractions approach an almost equal distribution; however, the $d_{[100]}$ domain is still slightly favoured. This indicates that an applied magnetic field as small as 1 G during cooling is sufficient to cause a considerable imbalance between the magnetic domains. Notably, the actual magnetic moment configuration of the individual domains during the application of a magnetic field in the almost diagonal $[\bar{1}20]$ direction may be different from that shown in Fig. 6.12(a) due to a slight field-induced ferrimagnetic distortion discussed in Ref. [90]. However, for the remanent magnetic structure measured by SNP in zero field, no such distortion is expected.

In addition to the field cooled measurements, the influence of external fields on the remanent magnetic domain distribution is studied. Therefore, the sample was similarly cooled in an applied magnetic field lager than 1 G to saturate the magnetic domain distribution as shown in Fig. 6.12(b). However, after reaching 3.7 K, an opposite directed field was applied by switching the current in the electromagnet before the SNP measurement. This was repeated for different applied magnetic field values, leading to a hysteric behaviour of the refined domain fractions as shown in Figs. 6.13(a) and 6.13(b). For the smallest applied magnetic field of 25 G in the opposite direction, no clear change of the field cooled domain distribution is observed. However, if the applied field is increased to a value of around 100 G, the initial field cooled domain configuration vanishes completely and an equal distribution is observed. For even higher fields above around 250 G, an opposite domain configuration saturates, with the initially suppressed domains enhanced and vice versa. Thus, the field-induced imbalance between the magnetic domains is completely reversible and can be switched by an applied magnetic field of only 250 G.

6.5. Conclusions

The magnetic structures of $Ba_2CoGe_2O_7$ in the PM and WFM phase have been comprehensively studied by PND. Applying the FR method to the PM phase at 10 K, detailed values for the field-induced magnetization were found in Sec. 6.2. Combining these refinement results for different applied magnetic field values and directions, the local susceptibility tensor of the Co atoms was determined. Its coefficients display a strong in-plane anisotropy as expected from magnetization measurements in Ref. [43] and theoretical considerations in Sec. 2.2.2. Moreover, a detailed analysis of the magnetic form factor indicated a slight contribution from an orbital Co moment and a potentially non-spherical magnetization density distribution that is further examined in Chap. 8. The revealed orbital contribution supports recent reports in the literature [110, 252, 253] and might be further investigated by X-ray magnetic circular dichroism (XMCD) measurements in the near future; however, these experiments are beyond the scope of this thesis.

For the low-temperature WFM structure, the precise magnetic moment values and directions were determined by FR measurements at 2 K in Sec. 6.3. This allowed to provide accurate values for the ordered AFM moment and the local susceptibility in $Ba_2CoGe_2O_7$, which were successfully applied to the p-d hybridization and spin-nematic interaction model to reproduce the main features of the field-dependent ferroelectric polarization reported in the literature [86]. Based on the detailed symmetry analysis in Sec. 4.2.2, the DMI sign was unambiguously determined by the FR measurement and proves to be consistent with theoretical predictions in Ref. [90]. It was demonstrated that the newly established PND approach is efficient and straightforward to use and can be reduced to the measurement of a single suitable Bragg reflection. In the near future, the presented PND method may be applied to determine the sign of the DMI in many more WFM compounds and might serve as valuable reference to experimentally verify theoretical models and numerical simulations.

Carefully investigating the zero-field magnetic structure by SNP measurements at temperatures clearly below T_N in Sec. 6.4, the $P2'_12_12'$ magnetic model with the AFM moments parallel to the lattice directions was conclusively identified as the high-symmetry ground state in $Ba_2CoGe_2O_7$. Although this result contradicts the previous SNP analysis in Ref. [112], it coincides with the theoretical study in Ref. [90] that suggests an antiferroelectric coupling between the Co atoms. The exact definition of the magnetic ground state is of fundamental importance and interest, in particular, as the different multiferroic models strongly depend on the precise orientations of the magnetic moments. Finally, it was demonstrated that the remanent ground state magnetic domain distribution can be saturated by applied in-plane magnetic fields as small as 1 G during cooling and completely switched by fields above 250 G at 3.7 K. This particularly high sensitivity to low magnetic fields combined with the rich magnetoelectric properties of $Ba_2CoGe_2O_7$ might be an interesting starting point for further studies towards novel materials for spintronic applications.

7. The $Ba_2Cu_{1-x}Mn_xGe_2O_7$ solid solution series

Comparing the end members of the $Ba_2Cu_{1-x}Mn_xGe_2O_7$ solid solution series, clear differences in the structural and magnetic properties are found despite both having the same crystal symmetry $P\bar{4}2_1m$. Whereas $Ba_2CuGe_2O_7$ shows a strong compression of the TO_4 tetrahedron for all temperatures and an incommensurate AFM spin spiral structure below T_N, $Ba_2MnGe_2O_7$ orders in a slightly canted in-plane AFM structure, antiferromagnetically coupled in c direction. As discussed in Sec. 2.4, these differences can be attributed mainly to the nature of the two TM ions Cu^{2+} and Mn^{2+}. Thus, the $Ba_2Cu_{1-x}Mn_xGe_2O_7$ solid solution series is particularly interesting to study as it may shed light on the competing exchange interactions and might lead to the emergence of some new and exceptional magnetic, multiferroic or quantum-critical properties.

After Bogdanov *et al.* [37] predicted a stable skyrmion phase in $Ba_2CuGe_2O_7$, its magnetic phase diagram and incommensurate AFM cycloidal structure were investigated in detail by Mühlbauer *et al.* [39, 126, 127, 129] with macroscopic methods and neutron diffraction, whereas the remarkable magnetoelectric properties were comprehensively studied in Refs. [86, 87]. However, only rather imprecise structural parameters are reported in the literature by laboratory XRD (see Ref. [103]) and little attention was given to the high-field commensurate magnetic structure in $Ba_2CuGe_2O_7$. In particular, this high-field $\boldsymbol{\tau} = 0$ structure is interesting to study with PND as it gives access to mixed nuclear magnetic Bragg reflections like in $Ba_2CoGe_2O_7$. Performing dedicated FR measurement in the different phases of $Ba_2CuGe_2O_7$, a profound insight into the magnetic ordering on a microscopic level is provided within this chapter, which is also used in Sec. 7.4.3 to reveal the absolute DMI sign in $Ba_2CuGe_2O_7$.

For $Ba_2MnGe_2O_7$, the crystal structure and the magnetoelectric properties were substantially studied in Refs. [86, 105], whereas the low-temperature AFM structure was addressed solely by one inelastic neutron diffraction experiment in Ref. [15]. Although this inelastic study lead to precise values for the symmetric exchange constants and an estimate for the ordered magnetic moment, this estimate for m^{AFM} was based on the measurement of only 18 magnetic Bragg reflections. In addition, no further refinement details are provided, especially concerning a proper extinction correction, which proved to be essential in Sec. 6.3.1. Thus, a more comprehensive magnetic structure study on $Ba_2MnGe_2O_7$ using PD and PND is presented in this chapter.

For the mixed $Ba_2Cu_{1-x}Mn_xGe_2O_7$ compounds with a relative concentration $0 < x < 1$, no magnetic properties are reported in the literature yet. Thus, their magnetic phase diagram as function of composition, temperature and magnetic field is mapped out carefully using heat capacity (HC) and macroscopic magnetization measurements in

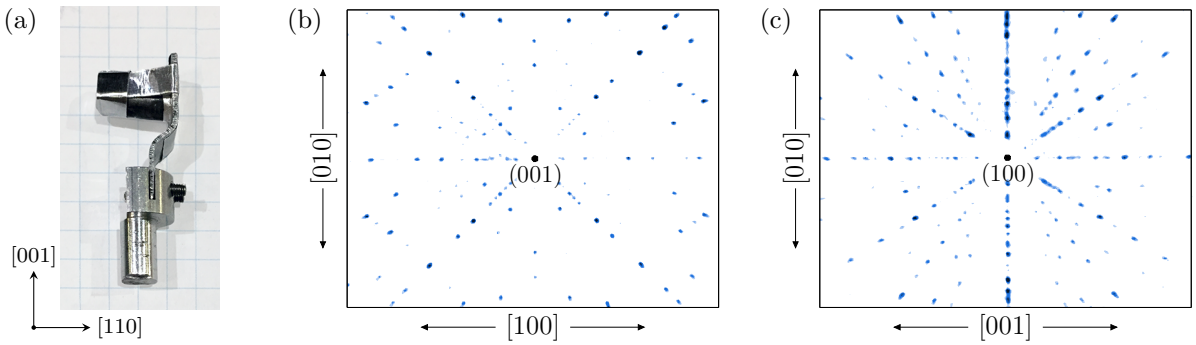

Figure 7.1.: (a) Cylindrical $Ba_2CuGe_2O_7$ single crystal sample used for the neutron diffraction measurements with the lattice directions as indicated by the black arrows. (b,c) Neutron Laue images of the $Ba_2CuGe_2O_7$ single crystal denoted as N27c recorded with the crystal (b) [001] and (c) [100] directions parallel to the incident neutron beam at the nLaue instrument at MLZ.

Sec. 7.3. The magnetically ordered structures at low temperature are characterized by high-resolution PD in Secs. 7.4.4 and 7.5.2. In addition, precise atomic and lattice parameters are provided in Sec. 7.2 by laboratory XRD and high-resolution PD.

7.1. Samples and preparation

To investigate the nuclear and magnetic structures in the $Ba_2Cu_{1-x}Mn_xGe_2O_7$ solid solution series, different single and polycrystalline samples are prepared for macroscopic measurements and neutron diffraction.

7.1.1. $Ba_2CuGe_2O_7$ single crystals

Grown by the floating zone technique, a set of high-quality $Ba_2CuGe_2O_7$ single crystals have been provided by the Department of Physics, University of Salerno, Italy. Details about the growing process and their characterization are given in Refs. [100, 256]. Using the neutron nLaue instrument at the MLZ (see Sec. 6.1), their good quality and monocrystalline structure could be confirmed. An exemplary neutron Laue image for the largest $Ba_2CuGe_2O_7$ single crystal denoted as N27c with a total mass of around 170 mg is shown in Figs. 7.1(b) and 7.1(c). This crystal was also used for some of the PND measurements presented in Sec. 7.4.

For macroscopic magnetization measurements (see Sec. 7.3.2), another $Ba_2CuGe_2O_7$ single crystal denoted as N21 with a mass of 38.1(1) mg was carefully oriented at the nLaue instrument. To facilitate the alignment of the irregularly shaped crystal during the macroscopic measurements, two quadratic glass plates (around $2 \times 2\,mm^2$, cut from a typical cover slip) were glued to the crystal such that their faces precisely represent the crystalline (100) and (001) planes, respectively. The edges of the plates were additionally aligned with the tetragonal lattice directions, providing a reliable reference for the crystal orientation.

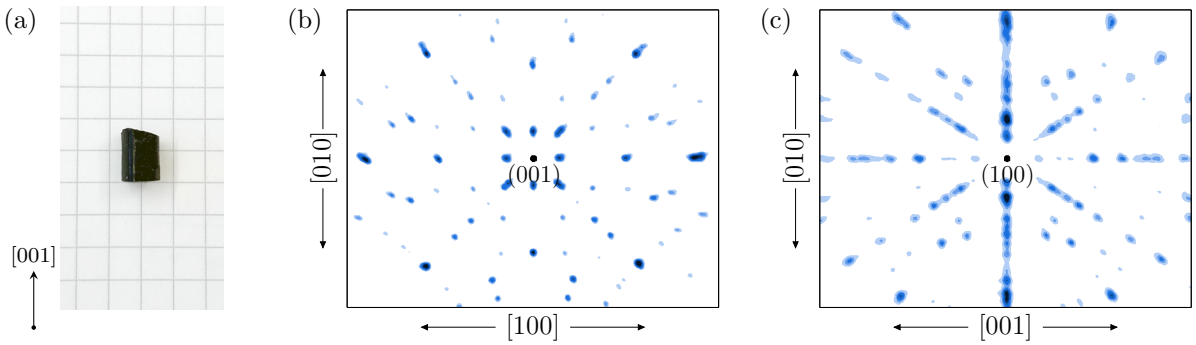

Figure 7.2.: (a) Cylindrical $Ba_2MnGe_2O_7$ single crystal sample used for the neutron diffraction measurements with the c direction vertical as indicated by the black arrow. (b,c) Neutron Laue images recorded with the single crystal shown in (a) with the crystalline (b) [001] and (c) [100] directions parallel to the incident neutron beam at the nLaue instrument at MLZ.

In addition, a large $Ba_2CuGe_2O_7$ single crystal was borrowed from the Department of Physics, Technical University of Munich (TUM), Germany, for PND experiments (see Sec. 7.4). The crystal has a cylindrical shape with around 5 mm in diameter and 12 mm in length. It was already used and well characterized in previous neutron diffraction experiments (see Ref. [127] and references therein). Details about its growing process are given in Ref. [126]. As visible in Fig. 7.1(a), the crystal was mounted to an aluminum sample holder for easy adjustment during the experiment.

7.1.2. $Ba_2MnGe_2O_7$ single crystals

Like for $Ba_2CuGe_2O_7$, a set of high-quality $Ba_2MnGe_2O_7$ single crystals have been grown by the Department of Physics, University of Salerno, Italy, using the floating zone technique. By neutron Laue diffraction at the nLaue instrument (MLZ), the good quality of the provided crystals could be confirmed. In addition, the $Ba_2MnGe_2O_7$ single crystal denoted as 3E with a mass of 10.3(1) mg was precisely oriented and prepared for macroscopic magnetization measurements (see Sec. 7.3.2). For this purpose, two quadratic glass plates with around $2 \times 2\,\mathrm{mm}^2$ in size were glued to the irregularly shaped crystal, representing the crystalline (100) and (001) planes, respectively. Again, the edges of the plates were aligned with the tetragonal lattice directions.

For the neutron diffraction measurements, a large $Ba_2MnGe_2O_7$ single crystal was provided by the International Graduate School of Arts and Sciences, Yokohama City University, Japan. This crystal has a cylindrical shape with around 6 mm in diameter and height and is shown in Fig. 7.2(a). It was already used and well characterized in previous neutron diffraction experiments (see Ref. [105] and references therein). Details about its growing process by the floating zone technique are provided in Ref. [15]. Two exemplary neutron Laue images recorded at the nLaue instrument at the MLZ are shown in Figs. 7.2(b) and 7.2(c). Compared to the Laue images of the small N27c $Ba_2CuGe_2O_7$ single crystal in Figs. 7.1(b) and 7.1(c) and the similarly sized $Ba_2CoGe_2O_7$ crystal in Figs. 6.1(b) and 6.1(c), clearly larger spots are observed for the $Ba_2MnGe_2O_7$ sample.

(a)

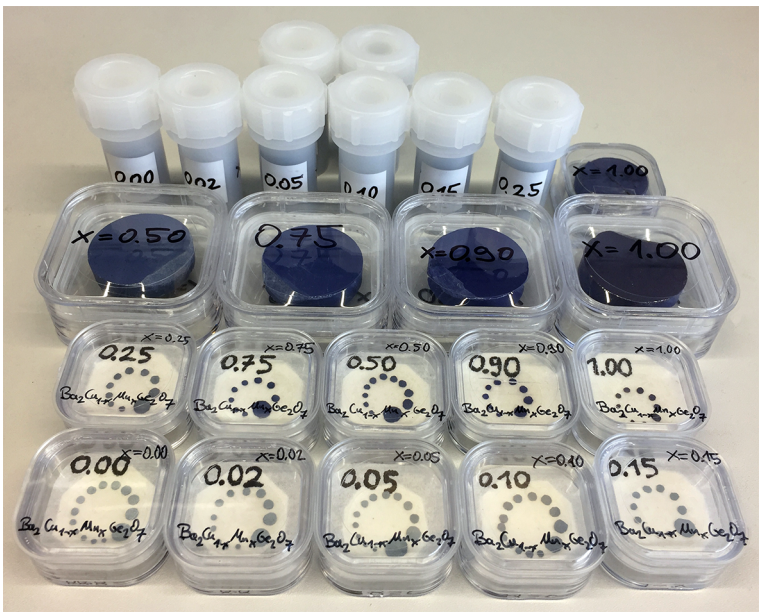

(b)

Figure 7.3.: (a) Selection of the available compounds of the $Ba_2Cu_{1-x}Mn_xGe_2O_7$ solid solution series as raw powder (large pellets for Mn-rich compounds and in the white laboratory bottles for the more brittle Cu-rich side) and pressed in thin pellets for HC measurements. (b) Manual press with 3 mm pressing die set for sample preparation.

This difference can be attributed to the strong mosaicity in this $Ba_2MnGe_2O_7$ crystal, which was estimated by a mosaic spread of $\nu = 1.6°$ and a mosaic block radius of $r = 400\,\mu m$ in Ref. [105] compared to the significantly smaller values of $\nu = 0°$ and $r = 15\,\mu m$ for the similarly sized $Ba_2CoGe_2O_7$ crystal in Ref. [104].

7.1.3. Mixed $Ba_2Cu_{1-x}Mn_xGe_2O_7$ powders

For the mixed $Ba_2Cu_{1-x}Mn_xGe_2O_7$ compounds, only polycrystalline powders are available. These powders have been synthesized as pressed pellets by the Department of Physics, University of Salerno, Italy, using a dedicated heating procedure, described in detail in Ref. [98]. By adjusting the stoichiometric ratio of the starting materials and optimizing the synthesis procedure, they could provide polycrystalline samples with $x = 0.00$, 0.01, 0.02, 0.05, 0.10, 0.15, 0.25, 0.38, 0.50, 0.63, 0.75, 0.90, 0.93, 0.97 and 1.00. For each compositions, a pellet with a mass of up to 15 g was synthesized. Some of these raw pellets are visible in the central area of the photograph in Fig. 7.3(a). For the Cu-rich side ($x < 0.5$), the pellets tend to be more brittle, and thus were broken into pieces and stored in the white laboratory bottles visible in the upper part of Fig. 7.3(a). For the magnetization and diffraction measurements, a portion of the raw pellets was ground using an agate mortar and pestle. In particular for neutron and X-ray powder diffraction, an extensive and careful grinding is essential to avoid texture effects.

In addition, some of the $Ba_2Cu_{1-x}Mn_xGe_2O_7$ powder was pressed in thin plates for HC measurements using a manual press with a 3 mm and 6 mm pressing die. A picture of the press is shown in Fig. 7.3(b). By manually cutting the plates, samples with various

(a) 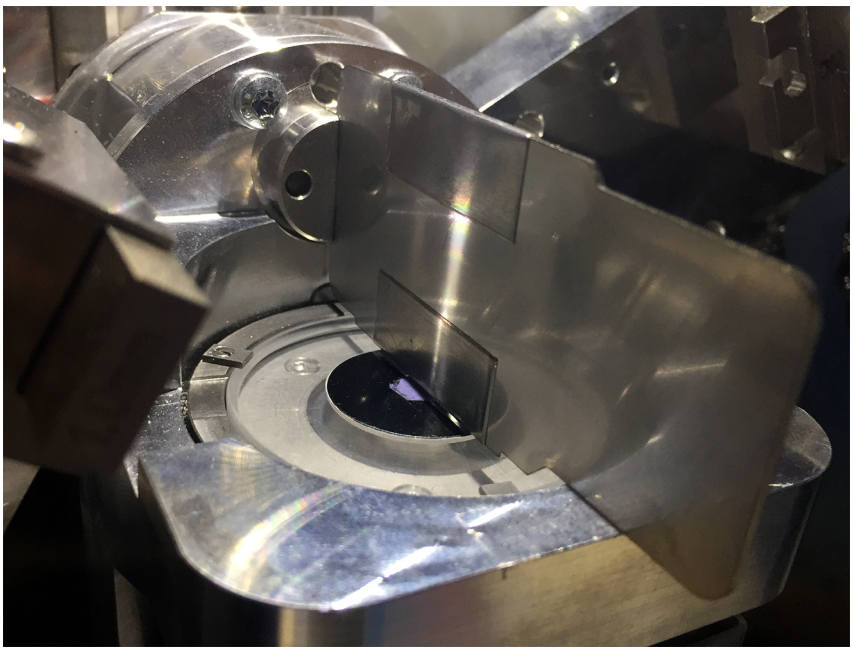 (b) 

Figure 7.4.: (a) View to the sample stage of the Bruker D2 PHASER used for the RT XRD. (b) Photograph of a 8 mm vanadium can that is filled with around 4.5 g of $Ba_2Cu_{1-x}Mn_xGe_2O_7$ powder, covering around 40 mm in height, and used for the PD measurements at SNS.

diameters were prepared as exemplified in the lower half of Fig. 7.3(a). The typical weight of a 3 mm diameter plate was around 5 mg.

7.2. Crystal structure

For a comprehensive analysis of the $Ba_2Cu_{1-x}Mn_xGe_2O_7$ solid solution series and as basis for a proper study of the magnetic structure, precise values for the lattice and the atomic parameters are essential. In particular, the oxygen position in the tetrahedral environment of the TM ion plays a key role in defining the magnetic and multiferroic properties as discussed in Sec. 2.3. Thus, RT XRD and low-temperature PD measurements (see Sec. 3.2.2) were performed on the $Ba_2Cu_{1-x}Mn_xGe_2O_7$ polycrystalline powders using the laboratory X-ray diffractometer Bruker D2 PHASER [257] at the outstation of the Jülich Center for Neutron Science (JCNS) in Garching, Germany, and the time-of-flight (TOF) neutron powder diffractometer POWGEN [258] at the Spallation Neutron Source (SNS) of the Oak Ridge National Laboratory (ORNL) in Oak Ridge, Tennessee, United States, respectively. For the XRD, finely ground $Ba_2Cu_{1-x}Mn_xGe_2O_7$ powder with a mass of around 100 mg was evenly distributed on a rotating low background Si sample holder as visible in the photograph in Fig. 7.4(a) and measured using an X-ray beam provided by a typical Cu anode with wavelengths of $\lambda_{K\alpha1} = 1.540562$ Å and $\lambda_{K\alpha2} = 1.544398$ Å in a ratio of $I_{K\alpha2}/I_{K\alpha1} = 0.497$. For the neutron measurements at POWGEN, around 5 g of $Ba_2Cu_{1-x}Mn_xGe_2O_7$ powder was filled into a 8 mm vanadium can as shown in Fig. 7.4(b) and mounted in an orange-type cryostat, which can reach sample temperatures

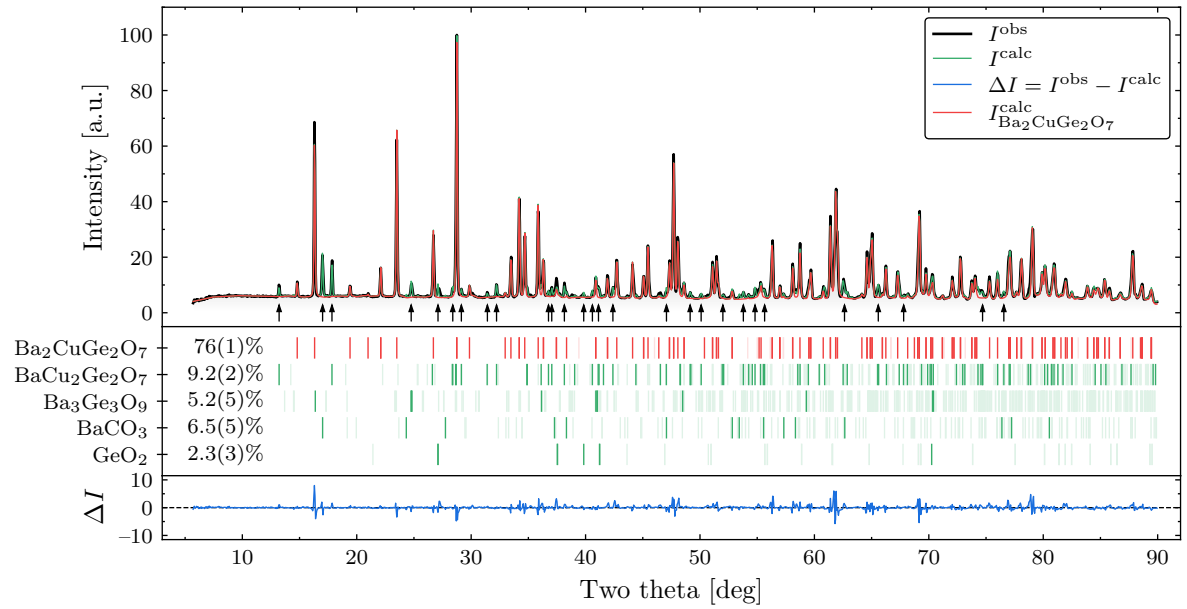

Figure 7.5.: PD pattern of $Ba_2CuGe_2O_7$ reduced from the TOF measurement at 10 K at POWGEN (SNS) with the center of the wavelength bandwidth at 2.665 Å. The observed and calculated intensities are shown by the black and green lines, respectively. For the Rietveld refinement, the contributions of four spurious phases are considered in addition to the $Ba_2CuGe_2O_7$ intensity (red line). Their compositions, phase fractions and expected peak positions (vertical lines) are given in the central area of the figure. The bold vertical lines indicate the positions of peaks with a relative intensity larger than 1% of the maximum intensity. Clearly visible peaks that cannot be indexed by the $Ba_2CuGe_2O_7$ structure are marked by small black arrows. The difference profile ΔI is shown as blue line.

of around 1.5 K. For the experiment, the instrument was driven in high-resolution mode with the center of the bandwidth chopper either at a wavelength of 1.500 Å or 2.665 Å. Using the *Mantid* software, the TOF data, collected with a 2D detector, was automatically combined, integrated and reduced as described in detail in Ref. [258]. For the usage in the refinement software, the d-spacing of the resulting diffraction pattern was converted into two theta values, assuming a wavelength of 1.54 Å and performing a third order spline interpolation in angular steps of 0.05° by the *interp1d* function of the *SciPy* package [259]. Complementary to the experiment at the SNS, the $Ba_2Cu_{0.25}Mn_{0.75}Ge_2O_7$ powder was also measured at the BT-1 high-resolution neutron powder diffractometer at the NIST Center for Neutron Research (NCNR) in Gaithersburg, Maryland, United States, using a ^{3}He sorption insert in the cryostat to reach very low sample temperatures of around 0.3 K. For the experiment, the polycrystalline powder was similarly filled into a 9.2 mm vanadium can and measured with a monochromatic neutron wavelength of 1.54 Å in steps of 0.05° in two theta.

7.2.1. Structure of $Ba_2CuGe_2O_7$

To provide precise structural parameters, the PD and XRD patterns collected at low temperature (10 K and 100 K) and RT (300 K) in the PM phase of $Ba_2CuGe_2O_7$ were

Table 7.1.: A selection of potential candidates for spurious phases in the polycrystalline $Ba_2CuGe_2O_7$ sample. For each compound, the crystal symmetry with reference and a potential occurrence is given. The starting oxides and mixed phases for the synthesis are taken from Ref. [100].

compound	crystal symmetry	Reference	occurrence
$BaCO_3$	$Pnma$	[263]	starting oxides
GeO_2	$P3_121$, $P4_2/mnm$	[264], [265]	
CuO	$C2/c$	[266]	
Al	$Fm\bar{3}m$		sample environment (e.g. cryostat)
V	$Im\bar{3}m$		sample can
SiO_2	$P3_121$	[264]	mortar
$BaGeO_3$	$P2_12_12_1$	[267]	mixed phases
$Ba_3Ge_3O_9$	$C12/c1$	[268]	
Ba_2CuO_3	$Immm$	[269]	
$BaCuO_2$	$Im\bar{3}m$	[270]	
$CuGeO_3$	$Pbmm$	[271]	
$BaCu_2Ge_2O_7$	$Pnma$	[272]	

refined using the *Jana2006* software. For the Rietveld refinement, a Pseudo-Voigt peak-shape function was assumed and a preferred orientation in the [001] direction according to the March-Dollase approach [260, 261] allowed. For the refinement of the X-ray data, additional parameters for the surface roughness of the sample according to Pitschke *et al.* [262] and for the shift of the diffraction pattern were considered.

The Rietveld refinement of the PD pattern collected at POWGEN with 5.28 g polycrystalline $Ba_2CuGe_2O_7$ powder at 10 K is shown in Fig. 7.5. The calculated intensity for the $Ba_2CuGe_2O_7$ structure (red line in Fig. 7.5) explains well the majority of the observed peaks (black line in Fig. 7.5). However, there are several clearly evident peaks, which cannot be explained by the $Ba_2CuGe_2O_7$ structure as their positions do clearly not match the $P\bar{4}2_1m$ symmetry. Note that these positions do also not fit to an orthorhombic distortion of the UC, addressed in Sec. 2.2.2. The most prominent non-matching peaks are marked by small black arrows in Fig. 7.5, whereas the expected peak positions for $Ba_2CuGe_2O_7$ are shown as red vertical lines. This clearly indicates the presence of at least one other spurious phase. Potential candidates for such phases are typically found in the synthesis, the sample preparation and the direct sample environment. A list of specific candidate materials and their crystal symmetry is given in Table 7.1. As discussed in more detail in Sec. 7.2.3, a combination of four different phases, namely $BaCu_2Ge_2O_7$, $Ba_3Ge_3O_9$, $BaCO_3$ and GeO_2 ($P3_121$ symmetry) was successfully identified as the best match for the spurious peaks and their lattice and atomic parameters are determined from a multi-pattern refinement. The peak positions and the phase fractions for these spurious phases are given in Fig. 7.5.

Taking the additional spurious phases into account, a good match between the calculated (green line in Fig. 7.5) and observed diffraction pattern is achieved, which can be

expressed by the (weighted) profile R-factors $R_p = 5.33\%$ and $R_{wp} = 8.13\%$, defined as

$$R_p = \frac{\sum_i \left| I_i^{\mathrm{obs}} - I_i^{\mathrm{calc}} \right|}{\sum_i I_i^{\mathrm{obs}}} \tag{7.1}$$

$$R_{wp} = \sqrt{\frac{\sum_i \left(I_i^{\mathrm{obs}} - I_i^{\mathrm{calc}} \right)^2 / \left(dI_i^{\mathrm{obs}} \right)^2}{\sum_i \left(I_i^{\mathrm{obs}} / dI_i^{\mathrm{obs}} \right)^2}} \tag{7.2}$$

for all profile points i. A visual inspection shows also no clear non-indexed peaks; however, the presence of further spurious phases cannot be entirely ruled out.

The precise lattice and atomic parameters for $Ba_2CuGe_2O_7$ resulting from the Rietveld refinement of the polycrystalline powder data collected at 10 K and 100 K with neutrons and at 300 K with X-rays are listed in Table 7.2. The corresponding powder profiles for the 100 K and 300 K refinements are shown in appendix G.1. Comparing the determined lattice constants, a slight thermal expansion of 0.043(2)% in c is found between 10 K and 100 K whereas the expansion of 0.001(2)% in a is at the accuracy limit of the measurement. Between 100 K and 300 K, an expansion of 0.066(2)% in a and 0.255(2)% in c could be determined. Although the total thermal expansion between 10 K and 300 K has with 0.067(2)% in a and 0.298(2)% in c a similar size as reported for the related $Ba_2MnGe_2O_7$ compound (0.13(3)% in a and 0.3(1)% in c [105]), the clearly larger differences between 100 K and 300 K may also be connected to the different diffraction methods used. In particular for the laboratory XRD at 300 K, an additional shift parameter was required to properly describe the pattern, which may lead to systematical uncertainties in a and c. Thus, the laboratory XRD results can be considered as less precise than the neutron results at 10 K and 100 K. This may also explain the slight differences to and between the reported RT values of $a = 8.466(1)$ Å and $c = 5.445(1)$ Å in Refs. [103, 273] and $a = 8.46023(5)$ Å and $c = 5.43962(4)$ Å in Ref. [100], all measured by laboratory XRD.

For the atomic positions and thus also for the CuO_4 tetrahedron, which is defined by the angles κ, ϕ and ρ, the Cu-O distance $d_{\mathrm{Cu\text{-}O}}$ and the compression c_{t} along [001] direction (see Fig. 2.1), no significant differences between the results at 10 K and 100 K are observed. These refined parameters are also consistent with the literature values reported in Ref. [103] but provide a higher precision. However, for the refinement of the XRD pattern at 300 K some clear discrepancies are found for the positions of the O atoms whereas the Ge and Ba positions are reproduced rather well. This may be attributed to the smaller contribution of the light O atoms compared to the heavy Ba and Ge atoms to the diffracted intensity and the rapidly decreasing atomic form factor in XRD, which is constant for neutrons (see Sec. 3.2). This leads finally to a lower sensitivity in the XRD data refinement at 300 K to the oxygen positions. In addition, the contributions from the multiple spurious phases were less pronounced and more difficult to separate from the primary $Ba_2Cu_{1-x}Mn_xGe_2O_7$ structure in the XRD data. For this reason, the refinement may not fully account for all spurious intensities, leading to distortions of the positional parameters. These inaccuracies affect also directly the determined properties of the CuO_4 tetrahedron at 300 K, which is defined by the O3 position. In particular for

Table 7.2.: Structural parameters of $Ba_2CuGe_2O_7$ determined by a Rietveld refinement of the PD and laboratory XRD data, considering the additional four spurious phases given in the text. The calculated and observed pattern for the refinement at 10 K are shown in Fig. 7.5. The powder diffraction patterns for the Rietveld refinements at 100 K and 300 K are presented in appendix G.1.

		10 K		100 K		300 K (XRD)	
a [Å]		8.45524(9)		8.4553(1)		8.4609(1)	
c [Å]		5.42636(8)		5.42869(9)		5.44253(9)	
		position	U^{iso} [Å^2]	position	U^{iso} [Å^2]	position	U^{iso} [Å^2]
Ba	x	0.3320(5)	0.000(1)	0.3317(5)	0.000(2)	0.3336(1)	0.0322(7)
	y	$0.5-x$		$0.5-x$		$0.5-x$	
	z	0.493(1)		0.494(1)		0.4916(4)	
Cu	x	0	0.006(1)	0	0.000(2)	0	0.034(1)
	y	0		0		0	
	z	0		0		0	
Ge	x	0.1384(4)	0.014(1)	0.1384(4)	0.009(1)	0.1379(2)	0.033(1)
	y	$0.5-x$		$0.5-x$		$0.5-x$	
	z	0.0299(7)		0.0295(8)		0.0278(6)	
O1	x	0	0.013(2)	0	0.008(2)	0	0.036(3)
	y	0.5		0.5		0.5	
	z	0.146(2)		0.148(2)		0.157(3)	
O2	x	0.1338(5)	0.002(2)	0.1341(5)	0.000(2)	0.142(1)	$U^{\text{iso}}_{\text{O1}}$
	y	$0.5-x$		$0.5-x$		$0.5-x$	
	z	0.7091(8)		0.7095(9)		0.719(2)	
O3	x	0.0810(5)	0.013(1)	0.0816(5)	0.009(1)	0.0980(9)	$U^{\text{iso}}_{\text{O1}}$
	y	0.1853(4)		0.1853(5)		0.173(1)	
	z	0.1712(9)		0.172(1)		0.174(2)	
κ [deg]		21.4(5)		21.2(5)		15(1)	
ϕ [deg]		123.0(2)		122.7(3)		121.2(5)	
ρ [deg]		103.2(2)		103.3(2)		104.0(4)	
$d_{\text{Cu-O}}$ [Å]		1.946(4)		1.951(4)		1.931(9)	
c_{t} [%]		23.1(5)		22.7(5)		20.2(9)	
R_p [%]		5.33		5.75		6.10	
R_{wp} [%]		8.13		8.59		8.41	

the deviation angle κ and the compression c_{t} of the tetrahedron clear deviations to the neutron results and larger uncertainties are found. This emphasizes the importance of a proper neutron diffraction experiment towards precise oxygen positions, which play a crucial role in the proposed multiferroic models (see Sec. 2.3).

In addition to the atomic positions, isotropic temperature factors U^{iso} are determined. It is important to note that the refinement of these values showed a somewhat strong correlation to the absolute level of the background at high two theta angles ($2\theta > 60°$)

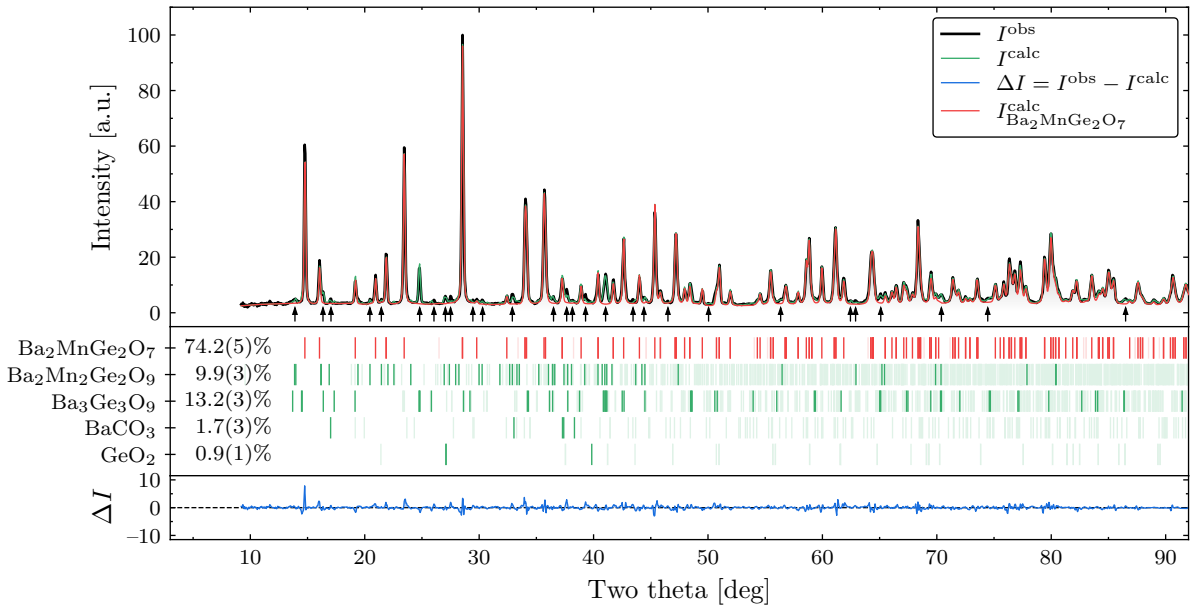

Figure 7.6.: Neutron powder diffraction pattern of $Ba_2MnGe_2O_7$ reduced from the TOF measurement at 10 K at POWGEN (SNS) with the center of the wavelength bandwidth at 1.500 Å. The full diffraction pattern is shown in Fig. G.3. As *Jana2006* has allocation problems if too many reflections are present, the intensities above around 135° had to be excluded from the refinement. The layout of the figure is analogous to that described in Fig. 7.5.

where many reflections overlap. Thus, the uncertainty of U^{iso} is clearly underestimated by the refinement results listed Table 7.2. By manually modifying the background level at high angles such that the refinement quality, indicated by R_p and R_{wp}, is not significantly changed, a more realistic uncertainty of around 0.005 Å^2 could be estimated for the refined U^{iso} values. Taking these increased uncertainties into account, the refinement shows comparable and and almost negligible U^{iso} values at 10 K and 100 K and as expected, consistently higher values at 300 K. For the refinement of the XRD pattern at 300 K, the U^{iso} values of the oxygen atoms had to be restricted to be equal to stabilize the refinement. An attempt to refine (partially) anisotropic temperature factors for the neutron diffraction patterns at 10 K and 100 K did not lead to a satisfactory convergence. In Ref. [103], no temperature factors are reported that could serve as reference.

7.2.2. Structure of $Ba_2MnGe_2O_7$

The neutron powder diffraction data collected at 10 K, 100 K and 300 K for the polycrystalline $Ba_2MnGe_2O_7$ samples was refined in the same way as for $Ba_2CuGe_2O_7$ in Sec. 7.2.1. The neutron diffraction pattern, measured at POWGEN with 5.30 g polycrystalline $Ba_2MnGe_2O_7$ powder at 10 K, and the corresponding Rietveld refinement are shown in Fig. 7.6 like for $Ba_2CuGe_2O_7$ in Fig. 7.5. Clear to see are again several peaks that are marked by small black arrows and cannot be properly indexed by the refined $Ba_2MnGe_2O_7$ structure with $P\bar{4}2_1m$ symmetry. This indicates again the presence of at least one spurious phase in the measured $Ba_2MnGe_2O_7$ sample. A selection of potential

Table 7.3.: A selection of potential candidates for spurious phases in the polycrystalline $Ba_2MnGe_2O_7$ sample. For each compound, the crystal symmetry with reference and a potential occurrence is given. The starting oxides and some mixed phases for the synthesis are taken from Ref. [100].

compound	crystal symmetry	Reference	occurrence
$BaCO_3$	$Pnma$	[263]	
GeO_2	$P3_121$, $P4_2/mnm$	[264], [265]	starting oxides
$MnCO_3$	$R\bar{3}c$	[274]	
Al	$Fm\bar{3}m$		sample environment (e.g. cryostat)
V	$Im\bar{3}m$		sample can
SiO_2	$P3_121$	[264]	mortar
$BaGeO_3$	$P2_12_12_1$	[267]	
$Ba_3Ge_3O_9$	$C12/c1$	[268]	
Ba_2MnO_3	$C1c1$	[275]	
$BaMnO_2$	$Pnma$	[276]	mixed phases
$MnGeO_3$	$Pbca$, $C12/c1$	[277]	
MnO	$Fm\bar{3}m$	[278]	
$Ba_2Mn_2Ge_2O_9$	$Pbca$	[279]*	

*Ge and Si based structures are assumed to be similar

candidates for additional phases are listed in Table 7.3. According to the discussion in Sec. 7.2.3, the spurious peaks can be attributed to a combination of four phases, namely $Ba_3Ge_3O_9$, $BaCO_3$, GeO_2 ($P3_121$ symmetry) and $Ba_2Mn_2Ge_2O_9$. Although the latter compound was also detected in Ref. [280], its structure has not been reported yet; thus, it is assumed to be similar to that of $Ba_2Mn_2Si_2O_9$ presented in Ref. [279]. The peak positions and the phase fractions of these spurious phases are given in Fig. 7.6. The calculated total intensity (green line in Fig. 7.6) reproduces well the measured diffraction pattern as demonstrated by the small residuals (blue line in Fig. 7.6) and quantified by the profile R-factors of $R_p = 5.07\%$ and $R_{wp} = 5.22\%$.

The detailed results of the Rietveld refinement for the $Ba_2MnGe_2O_7$ structure at 10 K, 100 K and 300 K, considering the identified spurious phases, are listed in Table 7.4. The corresponding powder profiles for the 100 K and 300 K refinements are shown in appendix G.2. The lattice parameters show a thermal expansion of 0.009(1)% in a and 0.026(2)% in c between 10 K and 100 K, which is slightly larger than for $Ba_2CuGe_2O_7$ in Sec. 7.2.1. A clearly stronger expansion of 0.085(3)% in a and 0.205(2)% in c is evident between 100 K and 300 K, which may, however, be partially attributed to the different diffraction methods used as discussed for $Ba_2CuGe_2O_7$ in Sec. 7.2.1. The total thermal expansion between 10 K and 300 K with 0.094(3)% in a and 0.231(4)% in c is in agreement with the results in Ref. [105] (0.13(3)% in a and 0.3(1)% in c) reported by neutron single crystal diffraction at the four-circle diffractometer HEiDi. In fact, also the absolute c values of 5.512(5) Å at 10 K and 5.529(5) Å at 100 K reported in Ref. [105] are consistent with the refinement results listed in Table 7.4. In contrast, the absolute a values are

Table 7.4.: Structural parameters of $Ba_2MnGe_2O_7$ determined by a Rietveld refinement of the PD and laboratory XRD data, considering the additional four spurious phases given in the text. The calculated and observed pattern for the refinement at 10 K are shown in Fig. 7.6. The powder diffraction patterns for the Rietveld refinements at 100 K and 300 K are presented in appendix G.2.

		10 K		100 K		300 K (XRD)	
a [Å]		8.47380(6)		8.47456(7)		8.4818(3)	
c [Å]		5.51722(6)		5.51865(7)		5.5300(2)	
		position	U^{iso} [Å^2]	position	U^{iso} [Å^2]	position	U^{iso} [Å^2]
Ba	x	0.3348(2)	0.0004(4)	0.3347(2)	0.0012(5)	0.3348(2)	0.028(1)
	y	$0.5-x$		$0.5-x$		$0.5-x$	
	z	0.4925(4)		0.4917(4)		0.4945(8)	
Mn	x	0	0.0048(7)	0	0.0060(9)	0	0.020(3)
	y	0		0		0	
	z	0		0		0	
Ge	x	0.1385(1)	0.0072(3)	0.1380(1)	0.0070(4)	0.1395(3)	0.024(2)
	y	$0.5-x$		$0.5-x$		$0.5-x$	
	z	0.0449(2)		0.0451(3)		0.033(1)	
O1	x	0	0.0059(5)	0	0.0062(7)	0	0.007(4)
	y	0.5		0.5		0.5	
	z	0.1629(5)		0.1613(5)		0.158(5)	
O2	x	0.1382(2)	0.0072(4)	0.1381(2)	0.0081(4)	0.137(1)	U^{iso}_{O1}
	y	$0.5-x$		$0.5-x$		$0.5-x$	
	z	0.7321(3)		0.7316(4)		0.722(3)	
O3	x	0.0770(2)	0.0081(3)	0.0767(3)	0.0084(3)	0.085(1)	U^{iso}_{O1}
	y	0.1904(2)		0.1904(2)		0.184(1)	
	z	0.1943(3)		0.1940(3)		0.202(2)	
κ [deg]		23.0(2)		23.1(2)		20(1)	
ϕ [deg]		116.74(8)		116.8(1)		114.0(6)	
ρ [deg]		105.96(7)		105.95(9)		107.2(6)	
$d_{Mn\text{-}O}$ [Å]		2.044(1)		2.043(2)		2.05(1)	
c_t [%]		12.9(1)		13.0(2)		8(1)	
R_p [%]		5.07		6.12		6.59	
R_{wp} [%]		5.22		6.09		8.50	

around 0.3% smaller than reported in Ref. [105] with 8.498(2) at 10 K and 8.509(2) at 100 K. This marginal difference might be connected to minor systematic uncertainties, for example, in the single crystal sample alignment in Ref. [105]. Moreover, the refined cell parameters at 300 K are consistent with the results presented in Ref. [98].

For the positional parameters of the atoms, there is no clear difference between 10 K and 100 K observed. This is in agreement with Ref. [105], reporting a negligible change in the atomic coordinates between room and low temperature. Thus, also the tetrahedral

parameters (κ, ϕ, ρ, $d_{\text{Mn-O}}$ and c_{t}, defined in Sec. 2.1) coincide for 10 K and 100 K within their uncertainty. A comparison of the refined atomic positions at 10 K with the values reported in Ref. [105] shows no significant difference. This confirms the good quality of the low-temperature PD refinements. For the XRD refinement at 300 K, the positions of the O and Ge atoms show a clear difference to the low-temperature values and a larger uncertainty whereas the coordinates of the Ba atom are similar. As discussed already in Sec. 7.2.1, this inferior performance of the laboratory XRD refinement may be traced back to the strong contributions of the heavy Ba atom overshadowing the light atoms and the distortion effects by the multiple spurious phases in the sample. As a result of these positional inaccuracies, only the Mn-O distance $d_{\text{Mn-O}}$ of the tetrahedral parameters shows consistent values between low-temperature and 300 K.

For the isotropic temperature factors U^{iso} listed in Table 7.4, there is again a systematic underestimation of the uncertainties due to correlations with the absolute value of the background level at high two theta angles as discussed in Sec. 7.2.1 for $Ba_2CuGe_2O_7$. An estimation analogous to the one in Sec. 7.2.1 provides a more realistic uncertainty of around 0.001 Å^2 for the refined U^{iso} values. Nevertheless, similar U^{iso} values are found for the low-temperature refinements and their order of magnitude is consistent with the values reported by Sazonov *et al.* [105]. In addition, anisotropic temperature factors and thermal displacement ellipsoids are precisely defined by ND in Ref. [105]. However, an attempt to refine (partially) anisotropic temperature factors from the presented low-temperature PD patterns did not lead to a satisfactory convergence. As expected, clearly larger U^{iso} values are refined for the 300 K measurement compared to the low-temperature results. Only for the U^{iso} value of the oxygen atoms, which had to be restricted to be equal to stabilize the refinement, no clear increase is found. This may again be attributed to the low sensitivity of the XRD refinement to the light and weakly contributing oxygen. Compared to the literature values in Ref. [105], the refined U^{iso} value for the oxygen is around a factor of two too small whereas the values for the Ba, Mn and Ge atoms are a factor of three too large. This demonstrates again the limits of the structure determination from the presented laboratory XRD measurements.

7.2.3. Structure of the $Ba_2Cu_{1-x}Mn_xGe_2O_7$ solid solution series

Like for the pure $Ba_2CuGe_2O_7$ (Sec. 7.2.1) and $Ba_2MnGe_2O_7$ (Sec. 7.2.2) powders, precise PD and laboratory XRD patterns were collected for the mixed samples of the $Ba_2Cu_{1-x}Mn_xGe_2O_7$ solid solution series at room and low temperature. Analyzing the measured powder data with the *Jana2006* software, some clear spurious peaks were found for almost all samples. These peaks, which could not be indexed by the $P\bar{4}2_1m$ symmetry, are similar to those indicated in Figs. 7.5 and 7.6 by small black arrows for the pure compounds. The most significant contamination is noticed in the $x = 0.10$ and $x = 1.00$ samples for the Cu- and Mn-rich side, respectively. Thus, the measured diffraction patterns of these two compositions were used for the identification and characterization of the spurious phases.

Potential candidate materials for the spurious phases can be found in the starting, intermediate or byproducts of the synthesis described in Ref. [98], in the sample envi-

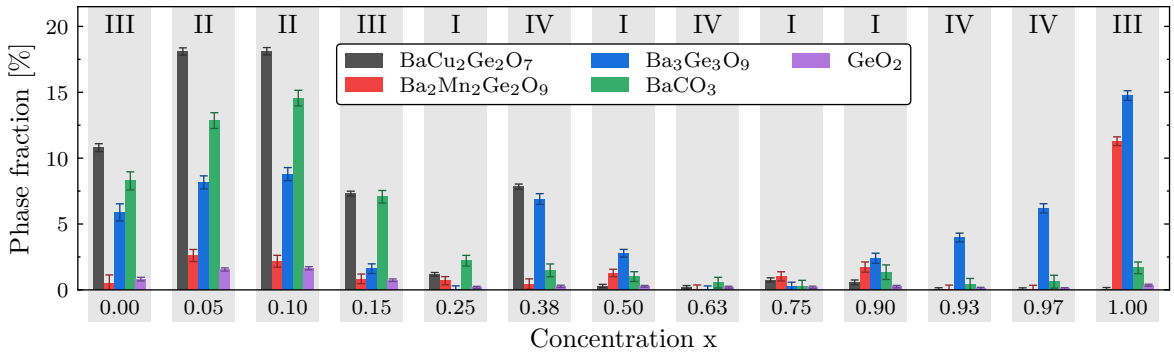

Figure 7.7.: Refined phase fractions of the spurious phases identified in the mixed $Ba_2Cu_{1-x}Mn_xGe_2O_7$ samples at 100 K. The samples were synthesized in four batches, indicated by the roman numerals.

ronment (e.g. vanadium sample can) and in the tools used for sample preparation (e.g. agate mortar). A list of these specific candidates is given in Tables 7.1 and 7.3. Using the *Jana2006* software and a custom *Python* script, an attempt was made to match the proposed materials to the spurious peak positions identified in the $x = 0.10$ and 1.00 PD patterns collected at 100 K at POWGEN (SNS) with the center of the wavelength bandwidth at 1.500 Å. In addition, 72 654 inorganic structures based on Ba, Ge, Cu, Mn, O, H and C were collected from the Inorganic Crystal Structure Database (ICSD), FIZ Karlsruhe GmbH, and compared with the spurious peak positions using the *Match!* software. With this exhaustive analysis, we were able to successfully identify the presence of five spurious phases, namely $BaCu_2Ge_2O_7$, $Ba_2Mn_2Ge_2O_9$, $Ba_3Ge_3O_9$, $BaCO_3$ and GeO_2 ($P3_121$ symmetry). Only this combination of phases could account for all observed significant spurious contributions without requiring additional non-observed peaks. Thus, the presence of further or other spurious phases is rather unlikely, however, cannot be entirely ruled out. Note that a spurious contribution of CuO as suggested in Ref. [100] for a similar polycrystalline $Ba_2CuGe_2O_7$ powder could not be evidenced. The structural parameters of the identified phases were specified at 10 K and 100 K by a combined Rietveld refinement of the $x = 0.10$ and 1.00 patterns using the *Jana2006* software. As the software suffered from allocation problems due to the large amount of reflections present for the multiple phase and pattern refinement, the intensities above 130° had to be excluded for both diffraction patterns. For the 300 K laboratory XRD data, the spurious peaks are less pronounced and more difficult to separate from the contributions of the primary $Ba_2Cu_{1-x}Mn_xGe_2O_7$ phase. Thus, only the lattice parameters of the spurious phases could be refined whereas other structural parameters were taken as determined from the 100 K neutron data refinement.

Selecting the structural parameters of the spurious phases as defined by the multi pattern refinement for the respective temperatures of 10 K, 100 K and 300 K, the phase fractions and the $Ba_2Cu_{1-x}Mn_xGe_2O_7$ structure were refined for all measurements of the mixed compounds. For the pure end compounds ($x = 0.00$ and 1.00) of the solid solution series, the results are discussed in detail in the previous Secs. 7.2.1 and 7.2.2. An overview of the determined phase fractions for the different PD samples is given in Fig. 7.7. The values are taken from the refinements at 100 K because at this temperature the

highest number of different $Ba_2Cu_{1-x}Mn_xGe_2O_7$ compounds were measured. Note that the combination of the refined phases must not necessarily represent the stoichiometric ratios of the $Ba_2Cu_{1-x}Mn_xGe_2O_7$ samples as the individual phases may not be homogeneously distributed over the raw $Ba_2Cu_{1-x}Mn_xGe_2O_7$ pellets and only a part of these pellets was used for the measurement (see Sec. 7.1.3).

Clear to see is a high concentration of $BaCu_2Ge_2O_7$ (black bars) for the Cu-rich compounds in Fig. 7.7, which is maximized in the $x = 0.05$ and 0.10 samples with a volume fraction of around 18%. As expected, no evidence for this Cu-bearing compound is found in the pure Mn ($x = 1.00$) sample. Likewise, $BaCO_3$ (green bars) and GeO_2 (purple bars) occur primarily in the Cu-rich compounds. They have their largest fractions with around 14% for $BaCO_3$ and 1.5% for GeO_2 also for the $x = 0.05$ and 0.10 samples, but they are to some extent additionally present in the Mn-rich compounds with almost 2% of $BaCO_3$ and around 0.3% of GeO_2 for $x = 0.90$ and 1.00. For the $Ba_2Mn_2Ge_2O_9$ phase (red bars), a large amount of around 11% is only detected in the $x = 1.00$ sample. Remarkably, a clear fraction of this Mn-bearing phase appears also in the Cu-rich $x = 0.05$ and 0.10 samples. However, this might be related to the high $BaCu_2Ge_2O_7$ concentration in these samples, which could lead to some excess of Mn ions, eventually forming the $Ba_2Mn_2Ge_2O_9$ phase or vice versa. In contrast, no significant evidence of $Ba_2Mn_2Ge_2O_9$ is found in the pure Cu ($x = 0.00$) sample, which fulfills the expectation. The final and most common spurious phase in the refinements is $Ba_3Ge_3O_9$ (blue bars). It is observed both in the Cu- and Mn-rich compounds with fractions up to around 15% for $x = 1.00$. A negligible concentration clearly below 1% is evident only for the three mixed compounds with $x = 0.25$, 0.63 and 0.75.

As the samples were synthesized in four different batches, which are indicated in Fig. 7.7 by the roman numerals, their correlation with the spurious phase fractions may provide useful information on the ideal synthesis conditions. Especially the samples of the first batch (I) show an almost negligible contamination by the spurious phases whereas the two compounds of batch II reveal a particularly large fraction for all spurious phases. Thus, potential differences in the synthesis conditions between batch I and II may be considered as impairing. Similarly for batch III, a significant contamination of all samples is observed. In contrast, batch IV achieves very good results for $x = 0.63$ and only a single phase contamination of the Mn-rich samples by $Ba_3Ge_3O_9$. Compared to batch III, it successfully suppresses a clear contamination by $Ba_2Mn_2Ge_2O_9$, $BaCO_3$ and GeO_2. In general, these results show that the synthesis procedure may need some further optimization to fully prevent the formation of spurious phases. However, this improvement of the $Ba_2Cu_{1-x}Mn_xGe_2O_7$ synthesis is out of the scope of this thesis and might be addressed elsewhere.

For characterizing the $Ba_2Cu_{1-x}Mn_xGe_2O_7$ structure, precise values for the atomic and lattice parameters are refined for all temperatures and available concentrations x. To illustrate the relative lattice change as function of x, the difference $\Delta a = a_x - a_{1.00}$ and $\Delta c = c_x - c_{1.00}$ of the lattice parameters to the pure Mn values $a_{1.00}$ and $c_{1.00}$ (see Table 7.4), normalized by $a_{1.00}$ and $c_{1.00}$, is shown in Fig. 7.8(a). Clear to see are consistent values for all temperatures and an almost linear change with x as expected by Vegard's law [281]. The overall expansion of the UC with increasing x can be attributed to the

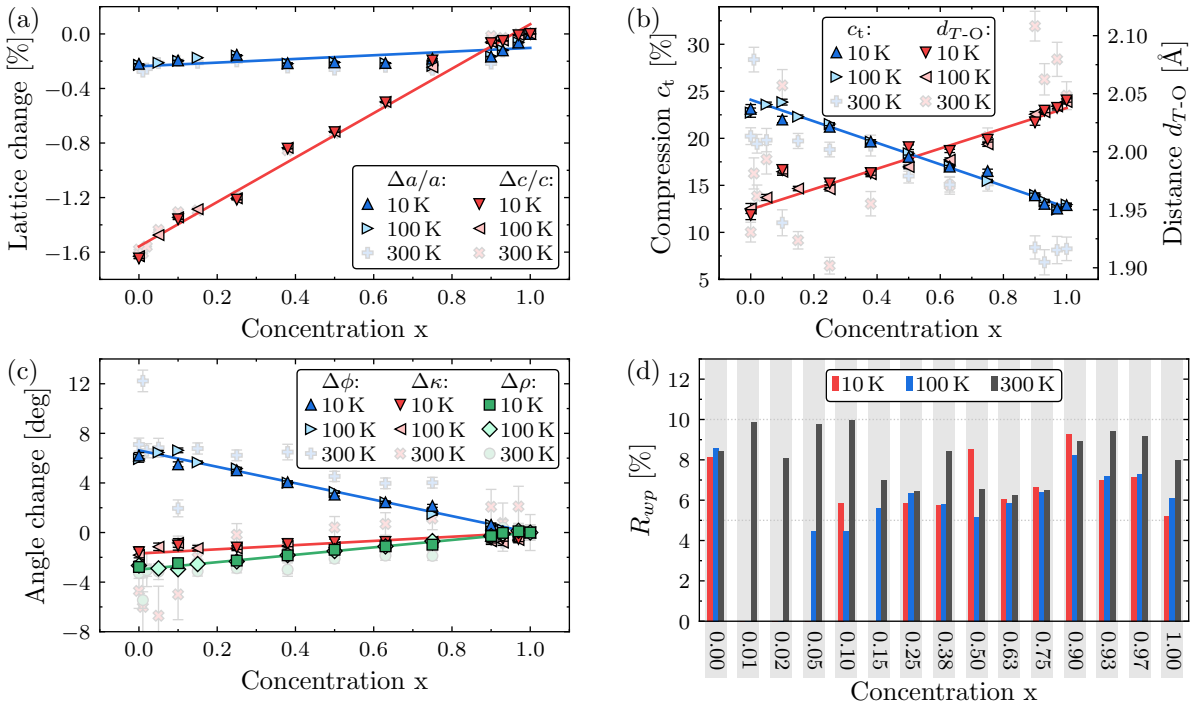

Figure 7.8.: Change in (a) the lattice constants and (b,c) the tetrahedral parameters as function of the concentration x, based on the refinement results of PD at 10 K and 100 K (bold symbols) and XRD at 300 K (light symbols). The tetrahedral parameters in (b,c) are defined in Sec. 2.1. (d) The weighted profile R-factors for the respective Rietveld refinements considering the identified spurious phases.

linear increase in the T-O bond distance $d_{T\text{-O}}$ (red symbols in Fig. 7.8(b)) due to the higher ionic radii of Mn compared to Cu [105]. However, the relative difference in c (red symbols in Fig. 7.8(a)) is with 1.6% about eight times higher than in a with around 0.2% (blue symbols in Fig. 7.8(a)). This significantly stronger expansion in c can be explained by an additional linear decline of the tetrahedral compression c_t (blue symbols in Fig. 7.8(b)) due to the continuous exchange of the JT active Cu (see Sec. 2.2.1) by Mn. This anisotropic expansion of the TO_4 tetrahedron with increasing x is also visible in Fig. 7.8(c) in the linear change of the tetrahedral angles with a decrease of around 7° in ϕ (blue symbols in Fig. 7.8(c)) and an incline of around 3° in ρ (green symbols in Fig. 7.8(c)). Moreover, a slight but linear rotation of the tetrahedron with x, characterized by the deviation angle κ (red symbols in Fig. 7.8(c)), could be evidenced. These x dependent distortions of the TO_4 tetrahedron indicated in Figs. 7.8(b) and 7.8(c) are consistent for the two PD measurements at 10 K and 100 K, shown by bold symbols. Although the results of the 300 K laboratory XRD measurements, shown by light symbols in Figs. 7.8(b) and 7.8(c), reflect the basic dependencies discussed above, they are polluted by clear deviations from the low-temperature values, large uncertainties and irregular jumps. However, these effects can be attributed to the imprecise determination of the O3 position, discussed in detail for the pure compounds in Secs. 7.2.1 and 7.2.2.

In general, a good match between the calculated and observed diffraction patterns could be achieved by the Rietveld refinement for all temperatures and mixed compounds.

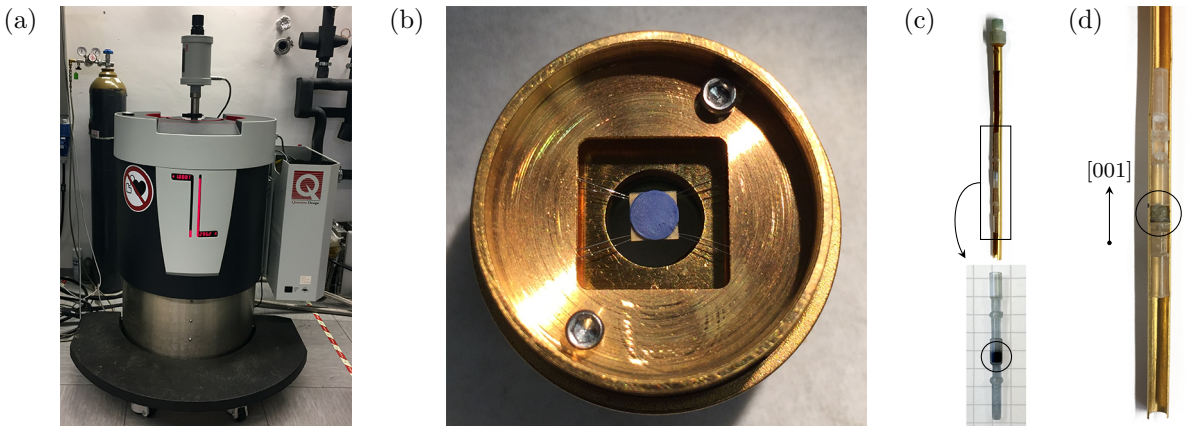

Figure 7.9.: (a) PPMS Dynacool at the JCNS in Jülich, Germany, equipped with the standard VSM option (see Sec. 7.3.2 for details). (b) HC puck for the PPMS Dynacool with an exemplary $Ba_2Cu_{1-x}Mn_xGe_2O_7$ pressed powder pellet (3 mm diameter, around 5 mg mass, $x = 1.00$) mounted to the sample platform. (c) The upper part shows the brass trough sample holder. The polycarbonate capsule, which is enlarged in the lower part of (c), contains around 30 mg of $Ba_2Cu_{1-x}Mn_xGe_2O_7$ powder (black circle) and is clamped in the lower region of the sample holder, indicated by the black rectangle. (d) N21 $Ba_2CuGe_2O_7$ single crystal (black circle) mounted with its c-direction parallel to the axis of the brass trough sample holder for the magnetization measurements in Sec. 7.3.2.

This is quantified by the reasonably good values for the profile R-factors visualized in Fig. 7.8(d). For the neutron measurements, an average R_{wp} value of 6.86% and 6.26% is reached for 10 K and 100 K, respectively. For the 300 K XRD refinements, the average R_{wp} value is with 8.22% slightly higher. Nevertheless, the precisely determined structural parameters of the $Ba_2Cu_{1-x}Mn_xGe_2O_7$ solid solution series, in particular, from the low-temperature neutron measurements, provide an excellent basis for the study of their magnetic properties in the subsequent sections.

7.3. Magnetic phase diagram

To reveal magnetic transition temperatures and investigate the low-temperature magnetic properties in the $Ba_2Cu_{1-x}Mn_xGe_2O_7$ compounds, HC and magnetization measurements were carried out using the commercially available Quantum Design physical property measurement system (PPMS) Dynacool at the JCNS in Jülich, Germany. A photograph of the PPMS Dynacool is shown in Fig. 7.9(a). As the ^{3}He insert for this setup was at the time of the measurements not available, the lowest available sample temperature was limited to around 1.8 K. Thus, additional PPMS specific heat measurements were performed at the Materials Growth and Measurement Laboratory (MGML) in Prague, Czech Republic, and at the Institute of Physics at the University of Augsburg in Augsburg, Germany, down to 0.4 K for some selected $Ba_2Cu_{1-x}Mn_xGe_2O_7$ polycrystalline samples.

7.3.1. Heat capacity

For the standard HC option of the PPMS Dynacool, the sample is mounted on the platform of the HC puck shown in Fig. 7.9(b). This platform is only suspended by eight thin wires such that a well-defined thermal conductance between the sample platform and the thermal bath, provided by the puck frame, is achieved. In addition, these wires serve as electrical connections to the heater and thermometer attached to the bottom side of the platform. To ensure a good thermal connection and adhesion between sample and platform, a thin layer of grease is used. The HC measurement is performed in high vacuum (around 0.01 μbar) to thermally isolate the platform expect for the well-defined thermal conductance by the thin wires. As the pressure remains unchanged during the measurement, the studied quantity is C_p, the pressure-constant molar HC.

The measurement of a single C_p value at a specific temperature T can be separated into three steps. First, the platform (T_P) and the puck temperature are stabilized at T. Then, the heater is activated for a certain timeframe to add a thermal energy ΔQ to the platform and sample, causing a rise of T_P. After the deactivation of the heater, the platform and sample temperature relax back to T. Throughout the whole process, T_P is monitored and can be described by a two-τ model to extract $C_p = dQ/dT$ [282]. This measurement method and analysis is fully automatized by the PPMS Dynacool control software.

Before placing the sample on the platform, typically a measurement with only grease, the so-called addenda measurement, is performed. Its values are considered as background and later on subtracted from the results with the mounted sample. Scanning the C_p over temperature, structural and magnetic phase transitions are usually visible as clear peaks or similar anomalies in an otherwise smooth curve.

To map out the magnetic phase diagram of the solid solution series, the HC of thin $Ba_2Cu_{1-x}Mn_xGe_2O_7$ plates pressed from the polycrystalline powders (see Sec. 7.1.3) was measured from the lowest available temperature up to around 20 K. As the available measurement time was strictly limited and the contribution of the grease very small compared to that of the sample, the addenda measurement was only performed once and used for all collections of data. To minimize systematical deviations, an effort was made to use about the same amount of grease for all samples.

The HC of $Ba_2Cu_{1-x}Mn_xGe_2O_7$ as function of the temperature is shown for the exemplary $x = 0.00$, 1.00 and 0.50 compounds in Figs. 7.10(a), 7.10(b) and 7.10(c), respectively. To highlight peaks or anomalies in the data, the second derivative $\partial^2 C_p/\partial^2 T$ is also depicted. It is calculated from the Akima spline interpolated measurement values and smoothed by the Savitzky-Golay method of quadratic order [283, 284]. Especially peak-like contributions with a shape similar to a Gaussian function lead to a clear negative peak in $\partial^2 C_p/\partial^2 T$. For the compounds with only a small admixture of the other TM ion (i.e. $x \leq 0.25$ and $x \geq 0.75$), such a negative peak in the second derivative and an anomaly in C_p is clearly visible. This unambiguously indicates a phase transition and is marked by the dashed line in Figs. 7.10(a) and 7.10(b). As no structural transition is expected at low temperatures (see also Secs. 7.5 and 7.4), it can be identified as magnetic and T_N determined. However, for the compounds with an almost equal mixture

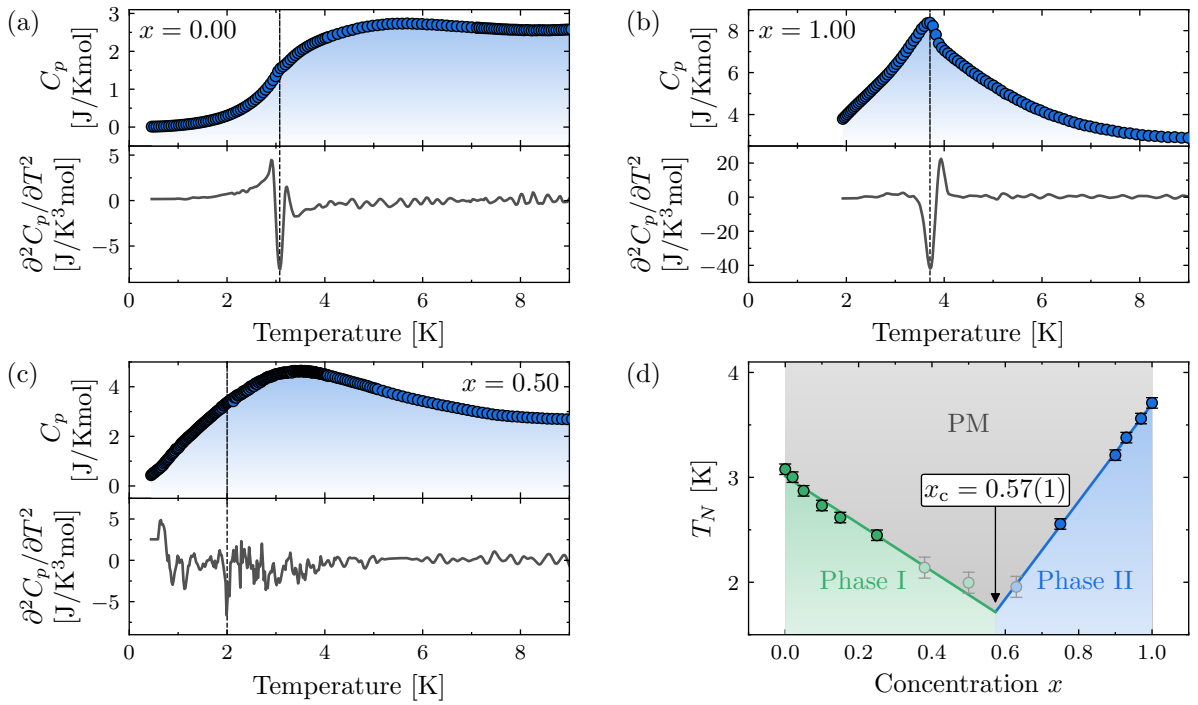

Figure 7.10.: (a-c) Measured HC (blue symbols) and its second derivative for different compounds of the $Ba_2Cu_{1-x}Mn_xGe_2O_7$ solid solution series. (a) and (c) were measured at the Institute of Physics at the University of Augsburg whereas (b) was measured at the JCNS in Jülich. The vertical dashed lines mark the center of the observed anomaly in C_p, implied by the negative peak in $\partial^2 C_p/\partial^2 T$ and indicating a magnetic phase transition. (d) The extracted magnetic phase transition temperatures T_N as function of x, suggesting two ordered magnetic phases as discussed in the text.

of Cu and Mn (i.e. $0.38 \leq x \leq 0.63$), the strength of the anomaly reduces significantly and makes the determination of T_N more difficult. For $x = 0.50$, which is shown in Fig. 7.10(c), the anomaly is barely visible in C_p, whereas a small negative peak can still be detected in $\partial^2 C_p/\partial^2 T$, and thus T_N roughly defined as indicated by the dotted line. However, this T_N value should be considered with caution.

The extracted T_N values as function of x are presented in Fig. 7.10(d). The uncertainty of T_N was estimated by 0.05 K, corresponding to the typical temperature step size as used in Figs. 7.10(a) and 7.10(b). For the three compounds with an almost equal mixture of Cu and Mn (light symbols in Fig. 7.10(d)), the uncertainty was doubled due to the discussed difficulties in determining T_N. For both Cu- and Mn-rich compounds, a mostly linear decrease of T_N with an increasing mixture is clear to see. This effect is maximized at a critical concentration of $x_c = 0.57(1)$ with an expected T_N of around 1.7 K and indicates the presence of two different magnetic phases for the Cu-rich (Phase I, $x < x_c$) and the Mn-rich (Phase II, $x > x_c$) side. This is not surprising, because the two end members of the solid solution series form a completely different ordered magnetic structure at low temperature (see Sec. 2.2). Taking these structures into account, the expected magnetic ordering in Phase I and II should be incommensurate AFM cycloidal and commensurate AFM, respectively.

Compared to the literature values of $T_N = 3.26\,\mathrm{K}$ for $Ba_2CuGe_2O_7$ and $4.0\,\mathrm{K}$ for $Ba_2MnGe_2O_7$ [15, 117], the presented transition temperatures are slightly smaller with $T_N = 3.08(5)\,\mathrm{K}$ and $3.71(5)\,\mathrm{K}$ for $x = 0.00$ and 1.00, respectively. However, this might be attributed to the different measurement method used in Refs. [15, 117], namely neutron diffraction. For this technique, T_N is typically selected as the temperature that shows first magnetic scattering contributions. Assuming again a peak shape similar to a Gaussian function for the phase transition in the HC, this onset of the magnetic contributions is represented by a smaller positive peak attached to the right-hand side of the primary negative peak in the second derivative of C_p. This positive secondary peak can be well identified for the $x = 0.00$ and $x = 1.00$ compounds in Figs. 7.10(a) and 7.10(b) and yields $T_N = 3.23(5)\,\mathrm{K}$ and 3.94(5), respectively. As expected, these slightly higher values for T_N are consistent with the literature values from neutron diffraction. Nevertheless, the position of the negative peak in $\partial^2 C_p/\partial^2 T$, and thus the center of the anomaly in C_p, was used as T_N definition to be in accordance with the common practice for HC measurements (e.g., see Ref. [285]). Moreover, it proofed to be more reliable and convenient for the almost equally mixed compounds, for which the position of the negative peak is already difficult to identify (see Fig. 7.10(c)).

In addition to the magnetic phase transition temperature, the HC results can be used to quantify the phonon contribution, which is commonly approximated by the Debye model and can be written as

$$C_V^{\Theta_D} = 9Rn_D \left(\frac{T}{\Theta_D}\right)^3 \int_0^{\frac{\Theta_D}{T}} \frac{x^4 e^x}{(e^x-1)^2} dx \cong \begin{cases} \frac{12\pi^4}{5} Rn_D \left(\frac{T}{\Theta_D}\right)^3 & \text{for } T \ll \Theta_D \\ 9Rn_D & \text{for } T \gg \Theta_D \end{cases} \tag{7.3}$$

with the Debye temperature Θ_D, the universal gas constant $R \approx 8.31\,\mathrm{J/Kmol}$ and the number n_D of atoms per formula unit [109]. For the low and high temperature limit, the integral can be analytically solved and the characteristic T^3 and constant behavior of $C_V^{\Theta_D}$ for $T \ll \Theta_D$ and $T \gg \Theta_D$ is derived. Note that the measured C_p value at constant pressure is always slightly larger than the C_V value expected at constant sample volume; however, this difference, which scales with the sample's bulk modulus and the square of the thermal expansion coefficient, is typically very small and is neglected in the following by assuming $C_V^{\Theta_D} = C_p^{\Theta_D}$ [109].

In Ref. [126], the phonon contribution in $Ba_2CuGe_2O_7$ was fitted between 10 K and 50 K to the Debye model, providing $\Theta_D = 177\,\mathrm{K}$ and an effective number of atoms of $n_D^{\mathrm{eff}} = 4.18$ per formula unit. A comparison between the observed and calculated C_p values is not shown. The lower limit of the fit was selected as magnetic contributions dominate close to T_N. As the primary purpose of our C_p measurements was to provide comprehensive values for T_N, only four $Ba_2Cu_{1-x}Mn_xGe_2O_7$ compounds with $x = 0.15$, 0.38, 0.90 and 0.97 were measured up to intermediate temperatures of around 100 K. Thus, the Debye fit of Ref. [126] could not be directly reproduced from our limited measurements of the $x = 0.00$ compound. Nevertheless, a comparable fit for the $x = 0.15$ compound yields similar values of $\Theta_D = 175(2)\,\mathrm{K}$ and $n_D^{\mathrm{eff}} = 4.21(7)$ as in Ref. [126] and is shown in Fig. 7.11(a). Clear to see is a significant mismatch between the calculated and observed values. Even an attempt to fit the low-temperature $x = 0.00$ data between

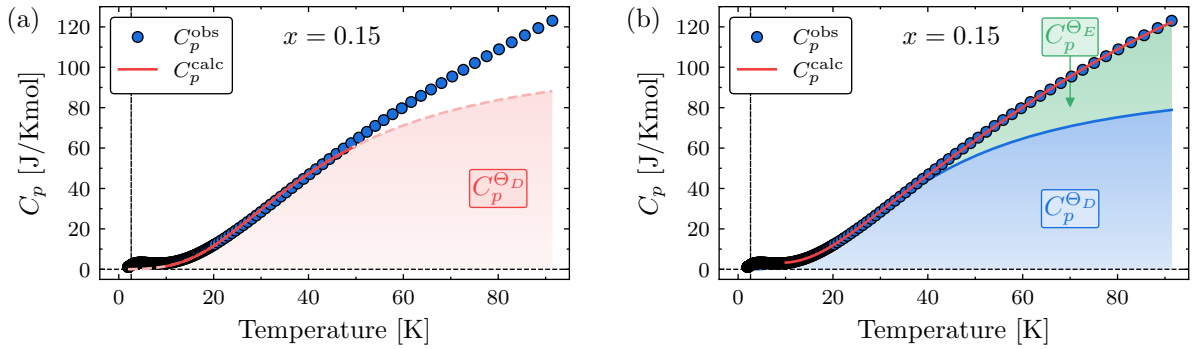

Figure 7.11.: Measured and fitted HC for the $Ba_2Cu_{1-x}Mn_xGe_2O_7$ compound with $x = 0.15$. For (a) Eq. (7.3) was used as fit function for temperatures between 10 K and 50 K (solid red line) whereas for (b) a magnetic (C_p^{mag}) and three different phonon ($C_p^{\Theta_{Di}}$) contributions were considered for the fit in the intermediate temperature range above 7.5 K. The individual contributions to the fit are marked by color. The dashed line in (a) illustrates the continuation of the fit function for the full measurement range. The magnetic contribution in (b) is only significant at low temperatures (see Fig. 7.12(a)) and thus not visible. The vertical dashed lines mark T_N.

10 K and 20 K to Eq. (7.3) did not lead to satisfactory results, clearly indicating an incomplete fitting model.

To improve the Debye HC model, an additional Einstein contribution is included, which is given by

$$C_p^{\Theta_E} = 3Rn_E^{\text{eff}} \left(\frac{\Theta_E}{T}\right)^2 \frac{e^{\frac{\Theta_E}{T}}}{\left(e^{\frac{\Theta_E}{T}} - 1\right)^2} \tag{7.4}$$

with Θ_E the characteristic Einstein temperature and n_E^{eff} the effective number of contributing atoms per formula unit [109]. As for the Einstein model the phonon density of states $D_E(\omega) \propto \delta(\omega - \omega_E)$ is a delta function centered at the frequency $\omega_E = \Theta_E k_B/\hbar$, it represents the contribution of optical phonon modes, having a typically flat dispersion. In contrast, the Debye model assumes a quadratic phonon density of state $D_D(\omega) \propto \omega^2$ that is cut off at the Debye frequency $\omega_D = \Theta_D k_B/\hbar$. Thus, Eq. (7.3) represents the contribution of acoustic phonon modes. Moreover, a magnetic contribution $C_p^{\text{M}} \propto T^{-2}$ is added, which accounts for the onset of the broad low-temperature peak in C_p (see Figs. 7.12(a) and 7.12(b) and discussion below) and clearly improves the fit quality close to T_N. This magnetic contribution is derived as highest order from a general high-temperature expansion ($T \gg T_N$) of the Heisenberg model in Ref. [286].

A fit of the extended Debye-Einstein model to the measured HC data above 10 K for the four $Ba_2Cu_{1-x}Mn_xGe_2O_7$ compounds that were measured up to intermediate temperatures of around 100 K was performed by a custom *Python* script and the resulting parameters are listed in Table 7.5. The good fit to the observed values, exemplified for the $x = 0.15$ compound in Fig. 7.11(b), emphasizes the necessity of both Debye and Einstein contributions. For the measured compounds, the total effective number of atoms $n_D^{\text{eff}} + n_E^{\text{eff}} \approx 8.0(1)$ is clearly lower than the expected value of 12, indicating another phonon mode at higher energies, not probed by the limited temperature range

Table 7.5.: Results of the HC fit with the extended Debye-Einstein model combining Eqs. (7.3) and (7.4) for the intermediate temperature range above 10 K up to around 100 K in four different $Ba_2Cu_{1-x}Mn_xGe_2O_7$ compounds. The magnetic contribution C_p^{M} to the fit is discussed in the main text as entropy S and shown in Fig. 7.12(d).

x	n_D^{eff}	Θ_D [K]	n_E^{eff}	Θ_E [K]
0.15	3.72(4)	167(1)	4.39(4)	318(3)
0.38	3.69(4)	170(1)	4.42(4)	334(4)
0.90	3.73(3)	188(1)	4.26(3)	402(4)
0.97	3.66(4)	176(1)	4.23(4)	348(4)

for the measurement ($T < 100$ K). This expectation is consistent with the specific heat results presented in Ref. [287] for the isomorphous $Ba_2FeSi_2O_7$ compound, displaying a high-energy optical phonon mode at $\Theta_{E2} \approx 1345$ K additional to the low-energy acoustic and optical modes at $\Theta_D \approx 237$ K and $\Theta_{E1} \approx 554$ K, respectively. Overall, an increase in the phonon energies of $Ba_2Cu_{1-x}Mn_xGe_2O_7$ is evident in Table 7.5 towards higher Mn concentrations. This can be attributed to the lower Mn mass (54.9 u) compared to Cu (63.5 u), which is also consistent with the significantly higher phonon energies reported for the $Ba_2FeSi_2O_7$ compound with the lightweight Si atoms (28.1 u) compared to Ge (72.6 u) [109]. In contrast, n_E^{eff} slightly reduces for higher x values whereas n_D^{eff} remains at an almost constant value of around 3.70(3). This shift towards the unobserved high-energy phonon mode might also be connected to the change in the molar mass or to differences in the atomic bond strengths.

Focusing only on the C_p measurements in the low-temperature range ($T < 20$ K), which are available for many concentrations x, the Einstein contributions $C_p^{\Theta_E}$ associated with the optical phonon modes can be neglected as clearly visible in Fig. 7.11(b). Thus, only the remaining $C_p^{\Theta_D}$ and C_p^{M} components are considered, assuming a constant $n_D^{\mathrm{eff}} = 3.70$ as found above. The determined Debye temperatures resulting from this reduced fit model to C_p in the low-temperature range between 10 K and 20 K are shown in Fig. 7.12(c) by bold blue circles and exemplified in Figs. 7.12(a) and 7.12(b) for $x = 0.15$ and 1.00, respectively. They confirm the suggested increase in $C_p^{\Theta_D}$ for higher concentrations x and closely reproduce the values extracted for the four compounds from the intermediate temperature region (light blue circles), demonstrating the reliability of the low-temperature fit.

Moreover, the broad magnetic contribution to C_p for temperatures close to T_N (gray areas in Figs. 7.12(a) and 7.12(b)) is clearly visible in the low-temperature HC measurements. Its high-temperature onset below around 15 K can be well described by the T^{-2} dependence predicted in Ref. [286]. Based on this broad magnetic contribution, a magnetic entropy S for the TM ions can be calculated by integration as

$$S = \int_0^\infty \frac{C_p^{\mathrm{M}}(T)}{T} \mathrm{d}T. \tag{7.5}$$

Using a linear extrapolation in C_p^{M} for low temperatures (indicated by the dashed gray

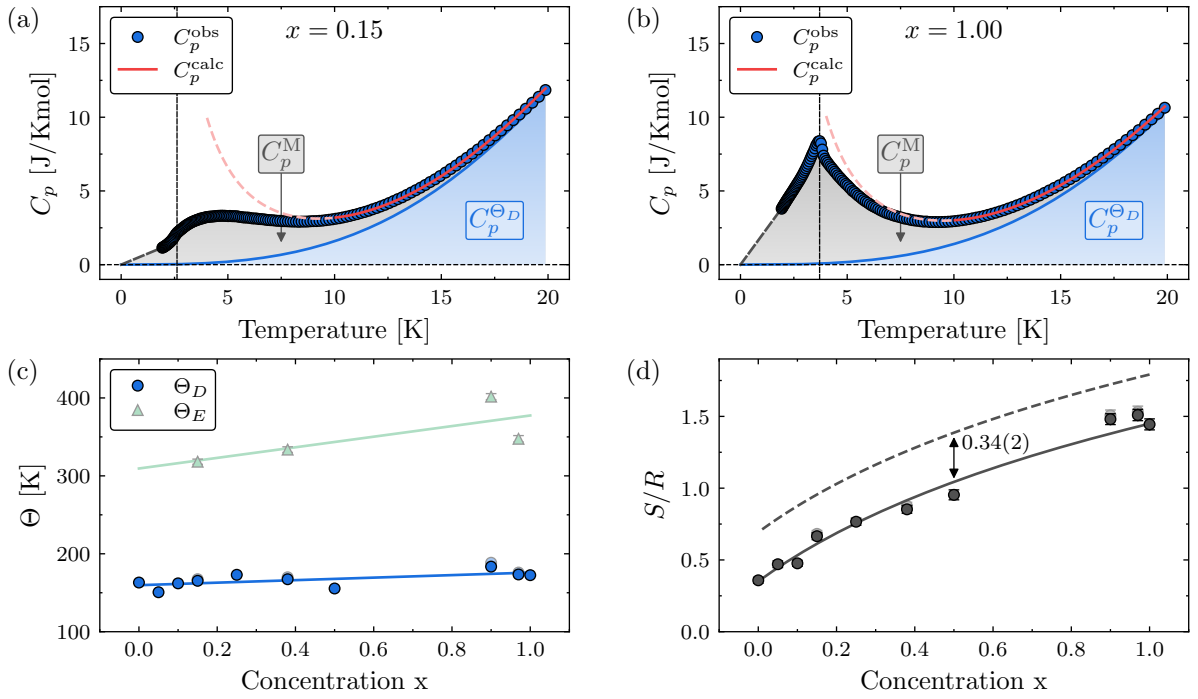

Figure 7.12.: (a,b) Measured and fitted HC for the $Ba_2Cu_{1-x}Mn_xGe_2O_7$ compound with (a) $x = 0.15$ and (b) $x = 1.00$. The used fit function is described in the text. The individual contributions to the fit are marked by color and T_N by vertical dashed lines. The red dashed line illustrates the continuation of the fit function to lower temperatures, pointing out the T^{-2} dependence assumed for the magnetic contribution. (c,d) Results of the HC fit for the low (bold symbols) and the intermediate (light symbols) temperature range, defined in the text. The lines in (c) are linear fits to the respectively colored symbols and serve as guide to the eye. The dashed and solid line in (d) are discussed in the text and represent the expected and shifted dependency of S on x, respectively.

line in Figs. 7.12(a) and 7.12(b)), normalized magnetic entropies S/R are determined for the different compounds and shown in Fig. 7.12(d). Clear to see is an increase of S towards higher Mn concentrations, which is also visually evident by comparing the magnetic contributions C_p^M for $x = 0.15$ and 1.00 in Figs. 7.12(a) and 7.12(b). Based on the total angular moment J, the magnetic entropy of the TM ion can be estimated as $S = R\ln(2J+1)$ [109]. Assuming spin only values of $J = 1/2$ and $5/2$ for Cu^{2+} and Mn^{2+}, respectively, the magnetic entropy for the $Ba_2Cu_{1-x}Mn_xGe_2O_7$ solid solution series can be calculated as indicated by the dashed line in Fig. 7.12(d), which is clearly higher than the measured values. However, shifting the curve for 0.34(2) (solid line in Fig. 7.12(d)) provides an excellent agreement with the measurement values. Typically, lower entropy values than the expectation indicate a magnetic ordering at higher temperatures but this is not expected from the macroscopic measurements presented in the subsequent Sec. 7.3.2 and from the literature reports on $Ba_2CuGe_2O_7$ and $Ba_2MnGe_2O_7$ addressed in Sec. 2.2. Likewise, another magnetic transition at lower temperatures is rather unlikely as, for example, the $x = 0.00$ and 0.50 compounds are measured down to 0.4 K and demonstrate a similar difference in S. Nevertheless, strong deviations from the linear extrapolations down to 0 K cannot be completely excluded and may cause

such difference. However, the more probable reason for this offset might be systematical uncertainties in the measurement or the determination of the phonon contributions to C_p. For example, for the first, the addenda measurement was not properly repeated for each measurement, whereas for the latter, the high-energy optical phonon mode could not be included in the fit model as no C_p values were measured above 100 K. As both of these uncertainties result from the strictly limited available measurement time as discussed before, they could be eliminated by a more careful repetition of the experiment up to higher temperatures (e.g. RT), potentially combined with a systematical variation of sample diameter, thickness and preparation method. However, this is out of the scope of this work, focusing mainly on outlining the magnetic phase diagram of $Ba_2Cu_{1-x}Mn_xGe_2O_7$ by macroscopic measurements and probing its microscopic magnetic properties by diffraction.

7.3.2. Magnetization

To characterize the macroscopic response of $Ba_2Cu_{1-x}Mn_xGe_2O_7$ to external magnetic fields, magnetization measurements were performed using the standard vibrating sample magnetometer (VSM) option of the PPMS Dynacool at JCNS in Jülich, Germany. As the name already suggest, the sample is connected for this option to a linear transport motor and sinusoidally oscillated in the center of two small pickup coils. In addition, a static magnetic field up to ±9 T, provided by large superconducting coils, can be applied along the vertical sample direction, which coincides with the direction of the sinusoidal motion and the axis of the pickup coils. Thus, any macroscopic magnetization of the sample in the field direction induces a sinusoidal voltage in the pickup coils according to Faraday's law of induction. As the amplitude of this voltage is directly proportional to the samples magnetization, VSM offers a reliable and straightforward method to macroscopically monitor even small changes in the magnetic structure as function of the sample temperature and the applied field.

For the magnetization measurements of the mixed $Ba_2Cu_{1-x}Mn_xGe_2O_7$ polycrystalline compounds, around 30 mg of powder was filled into a non-magnetic polycarbonate capsule and clamped in a brass trough sample holder, both exemplarily shown in Fig. 7.9(c). For an applied magnetic field of 1 T, the magnetization was continuously measured in a sweeping mode for temperatures from 300 K down to around 2.0 K, which was the lower limit that could be reliably reached with the VSM option at the time of the experiment. Afterwards, the sample was heated to around 100 K, clearly above T_N, and then measured again from 20 K to around 2.0 K with a different applied magnetic field value. This procedure was repeated for several selected field values to investigate the low-temperature region in more detail.

The raw measurement data was reduced using a custom *Python* script, correcting the applied magnetic field values B for the sample specific demagnetization field NM_V and interpolating the data points on a regular temperature grid by a linear fit model. The demagnetization factor N, scaling the measured volume magnetization M_V, was calculated analytically according to the model for short cylinders and weakly magnetic materials (susceptibility $\chi_V \to 0$) presented in Ref. [288]. The latter approximation ap-

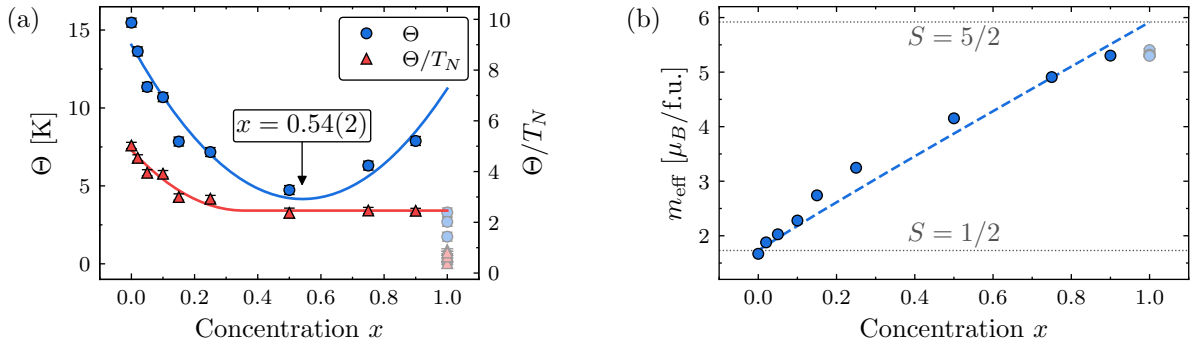

Figure 7.13.: CW parameters resulting from the 1 T field-cooled magnetization measurements on the polycrystalline $Ba_2Cu_{1-x}Mn_xGe_2O_7$ compounds with different concentrations x. Additional to the paramagnetic Néel temperature Θ (blue circles), its ratio to the T_N values from HC measurements (see Sec. 7.3.1) is shown in (a) as red triangles. The solid blue line is quadratic in x and serves together with the red solid line as guide to the eye. The m_{eff} values in (b) are calculated from the CW constant C using Eq. (7.6). The horizontal dotted lines indicate the expected spin-only values for Cu^{2+} ($S = 1/2$) and Mn^{2+} ($S = 5/2$) and the dashed blue line for their mixture Cu_xMn_{1-x}. As discussed in the text, the light symbols in (a) and (b) correspond to results from different $x = 1.00$ samples that are somewhat contaminated by $Ba_2Mn_2Ge_2O_9$.

plies as the maximal observed dimensionless magnetic volume susceptibility was around $\chi_V \approx 0.01$, and thus substantially smaller than for FM materials, indicating already a mainly AFM-type ordering at low temperatures. This low χ_V and a diameter to height ratio of the samples close to 1 finally lead to an overall negligible demagnetization correction, but it was still applied for completeness.

For temperatures clearly above T_N and small external fields B, the susceptibility in $Ba_2Cu_{1-x}Mn_xGe_2O_7$ is expected to comply with the Curie-Weiss (CW) law for antiferromagnets

$$\chi_V = \mu_0 \frac{\partial M_V}{\partial B} = \underbrace{\frac{n\mu_0 m_{\mathrm{eff}}^2}{3k_B}}_{C} \frac{1}{T + \Theta}, \tag{7.6}$$

with Θ the paramagnetic Néel temperature and C the Curie constant [109]. In the definition of the latter, n denotes the particle density of the magnetic atoms, μ_0 the magnetic permeability in vacuum, k_B the Boltzmann constant and m_{eff} the effective magnetic moment defined in Eq. (2.1). Assuming low fields in the PM state, the susceptibility can be approximated by $\chi_V = \mu_0 M_V / B$; thus, the inverse of the magnetization is expected to be linear for $T > T_N$.

Analysing the 1 T field-cooled measurements from 300 K to 2 K for the polycrystalline $Ba_2Cu_{1-x}Mn_xGe_2O_7$ compounds, a clearly linear behaviour is found in the inverse magnetization above around 50 K, which can be well described by the CW law as shown in Fig. G.6(a) in appendix G.3. The thereby arising Θ values are presented in Fig. 7.13(a) by blue circles. Their uncertainty takes the experimental precision into account that was estimated from the variance in the CW parameters resulting from multiple repetitions of the exact same measurement. The extracted Θ values are clearly lower for the mixed compounds and the overall behaviour can be roughly approximated by a parabola cen-

tered at around $x = 0.54(2)$ (solid blue line in Fig. 7.13(a)). Significant deviations from this trend are only visible for the $x = 1.00$ compound (light symbols in Fig. 7.13(a)), which showed, in addition, inconsistent results for samples prepared from different parts of the initial $Ba_2MnGe_2O_7$ pellet. This inconsistency indicates that the deviation might be caused by the presence of a spurious phase, which takes up a varying fraction in the different samples. This is supported by the neutron measurements in Sec. 7.2.3, identifying a comparably large volume fraction of $Ba_2Mn_2Ge_2O_9$ for the $x = 1.00$ sample (see Fig. 7.7), which could cause such deviations. Moreover, a field-direction averaged Θ value of around 12 K was measured in a high-quality $Ba_2MnGe_2O_7$ single crystal (see Table 7.6 and discussion below) that complies well with the trend suggested by the solid blue line in Fig. 7.13(a). Thus, the CW parameters for the $x = 1.00$ compounds can be confidently marked as corrupted by spurious phases and are mostly excluded from further discussions.

A comparison of the Θ values with T_N in Fig. 7.10(d) shows a similar behaviour and the x value associated with the minimum in Θ corresponds closely to the kink in T_N at the critical concentration of $x_c = 0.57(1)$, separating the two magnetic phases. This affinity between T_N and Θ is not surprising as, for example, in the mean-field (MF) approximation of a simple antiferromagnet with two sublattices A and B, the ratio between Θ and T_N is expected to be

$$\left(\frac{\Theta}{T_N}\right)^{\mathrm{MF}} = \left|\frac{\gamma_{AB} + \gamma_{AA}}{\gamma_{AB} - \gamma_{AA}}\right|. \tag{7.7}$$

Within this approximation, which might be somewhat suitable for the suggested AFM structure (Phase II) of the Mn-rich compounds, the MF constants γ_{AA} and γ_{AB} are directly connected to the exchange constants J_{AA} and J_{AB} for NNs within and between the magnetic sublattices, respectively [109]. Thus, the almost constant Θ/T_N ratios (red triangles in Fig. 7.13(a)) of 2.5(1) for high x values suggest no relative changes in the exchange constants and same signed γ_{AB} and γ_{AA} and thus J_{AB} and J_{AA} values in the frame of the simple AFM MF model. In contrast, towards lower x values, the ratio rises and suggests an increase of γ_{AA}/γ_{AB}. However, as an incommensurate and not a simple AFM structure is expected for the Cu-rich compounds (Phase I), Eq. (7.7) is most likely not applicable for $x \leq 0.50$.

Additional to Θ, the slope of the CW fit in Fig. G.6(a) yields the CW constant C, which is directly proportional to the square of the effective magnetization m_{eff} (see Eq. (7.6)), which is presented in Fig. 7.13(b). An additional systematical uncertainty of 1% was considered for the CW constant due to the limiting precision in determining the sample weight. As orbital momenta are assumed to be quenched in $Ba_2Cu_{1-x}Mn_xGe_2O_7$ (see Sec. 2.2), effective spin-only magnetic moments of 1.73 μ_B and 5.92 μ_B (dotted black lines in Fig. 7.13(b)) are expected for $x = 0.00$ and 1.00, respectively. Clear to see is a good conformity between the expected and measured value at $x = 0.00$, whereas for the $x = 1.00$ compounds (light symbols in Fig. 7.13(b)) reduced values, corresponding to $S \approx 2.25$, are found. This might again be attributed to the previously discussed presence of the $Ba_2Mn_2Ge_2O_9$ spurious phase, identified by neutron diffraction (see Sec. 7.2.3).

Although the magnetic structure of this compound is not reported in the literature, a detailed study of the isomorphous Si-based $Ba_2Mn_2Si_2O_9$ is presented in Ref. [289], indicating an oxidation state of 3+ rather than 2+ for the Mn ions. This lower oxidation state for some ions in the $x = 1.00$ samples, which is connected to a lower effective magnetic moment of $4.90\mu_B/Mn^{3+}$ due to $S = 2$, may cause the observed reduction in the measured m_{eff}. To account for these differences, a $Ba_2Mn_2Ge_2O_9$ phase fraction of roughly 20% is required, which is somewhat larger than the around 10% refined for the neutron sample but still of similar order. In contrast, a field-direction averaged value of around $S = 2.45(2)$ K is extracted from the CW results of the high-quality $Ba_2MnGe_2O_7$ single crystal (see Table 7.6 and discussion below), demonstrating a negligible difference to the expected value of $S = 5/2$, and thus endorsing again the assumption of spurious contributions in the polycrystalline $x = 1.00$ compounds.

The expected m_{eff} for the mixed compounds is depicted in Fig. 7.13(b) by the dashed blue line and coincides well with the measurement results for the Cu-rich and Mn-rich compounds. Only for the mixed compounds between $x = 0.15$ and 0.5, slightly higher values are measured. Although this difference could, for example, be associated with an incomplete quenching of orbital angular momenta or an increase in the g-factor due to an admixture of exited states by SOC as in the anisotropic g-tensor of single crystalline $Ba_2CuGe_2O_7$ (see Sec. 2.2.1 as well as Table 7.6 and discussion below), they are also likely to result from systematical and experimental inaccuracies. This might be the case since m_{eff} scales with the absolute values of the magnetization and is thus highly sensitive, for example, to a proper treatment of the raw VSM signal and to deviations in the sample weight, which might be larger than the 1% assumed above.

The magnetization measurements in the low-temperature region (2.0 K - 20 K) with different applied magnetic fields can be used to reveal field-dependent variations in the magnetic ordering temperature T_N. As proposed by Fisher [285], precise T_N values that are consistent with HC results can be identified in an AFM material as positive peaks in $\partial\chi_V T/\partial T$. To enhance these peaks in the first derivative, the third derivative $\partial^3\chi_V T/\partial T^3$ is calculated and smoothed by the Savitzky-Golay method of cubic order, like for the HC measurements in Sec. 7.3.1. Thus, T_N can be identified as the position of a negative peak in $\partial^3\chi_V T/\partial T^3$.

Using again the approximation $\chi_V = \mu_0 M_V/B$ for the applied magnetic fields B, the mass magnetization M, normalized to B, and the third derivative $\partial^3\chi_V T/\partial T^3$, normalized to the previously determined Curie constants C, are shown in Figs. 7.14(a) and 7.14(b) for the exemplary $x = 0.00$ and 1.00 polycrystalline $Ba_2Cu_{1-x}Mn_xGe_2O_7$ compounds, respectively. The centers of the negative peaks in the third derivative, corresponding to T_N, are marked by dashed lines. Clear to see is an additional FM contribution in the $x = 0.00$ compound for small fields of 0.01 T arising below a temperature of around $T_C = 8.76(5)$, which is characterised by a maximum in the third derivative and denoted by the dotted red line in Fig. 7.14(a). As this contribution is only barely visible at 0.1 T and invisible for $B \geq 1$ T, it might be of WFM-type, and thus overshadowed by the larger $Ba_2Cu_{1-x}Mn_xGe_2O_7$ contributions at higher fields. In general, no WFM moment is expected in $Ba_2Cu_{1-x}Mn_xGe_2O_7$. Therefore, it might be related to the spurious phases identified in Sec. 7.2.1 by neutron diffraction and indeed, the appearance of a

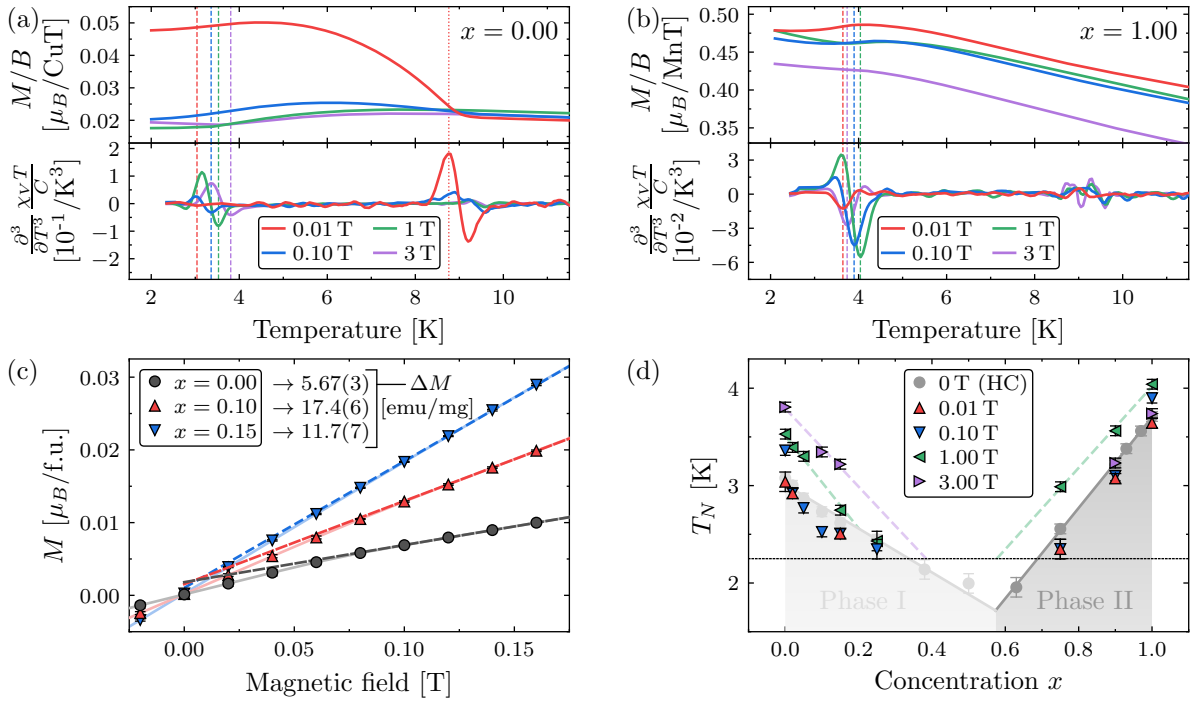

Figure 7.14.: (a,b) Normalized mass magnetization M and its third derivative $\partial^3\chi_V T/\partial T^3$ as function of the temperature for the $Ba_2Cu_{1-x}Mn_xGe_2O_7$ compounds with (a) $x = 0.00$ and (b) $x = 1.00$ and for different applied magnetic fields B. The third derivative for $B = 0.01$ T in (a) is scaled by a factor of 1/5 for clarity. The dashed vertical lines mark magnetic phase transitions indicated by a negative peak in $\partial^3\chi_V T/\partial T^3$. The dotted vertical line in (a) indicates the T_C of a FM contribution in M, defined by a positive peak in $\partial^3\chi_V T/\partial T^3$. (c) Mass magnetization M as function of the magnetic field at 3.5 K for $Ba_2Cu_{1-x}Mn_xGe_2O_7$ compounds with $x = 0.00$, 0.10 and 0.15. The values of $x = 0.00$ are scaled by a factor of 3 for clarity. The dashed lines result from a linear fit to the low field region (0.1 T$\leq B \leq$ 0.3 T). Their y-axis offsets ΔM are additionally listed. (d) Extracted magnetic phase transition temperatures T_N as function of x for different applied magnetic fields. The results and the suggested phase boundaries from the HC measurements in Fig. 7.10(d) are indicated in light gray. The dashed lines are linear fits to the respectively colored symbols and indicate the by magnetic field shifted phase boundaries. The dotted horizontal line represents the lower limit of the probed temperature range for the magnetization measurements.

WFM order is reported in $BaCu_2Ge_2O_7$ below 8.8 K, which suits well to the determined T_C value [290]. Note that similar WFM contributions at very low fields were observed for all measured samples with $x \leq 0.15$ that show also a significant $BaCu_2Ge_2O_7$ contamination in the neutron measurements. To characterize the WFM contributions in these compounds, the magnetization was measured as function of the field at a constant temperature of 3.5 K, which is between T_N and T_C. The results are shown in Fig. 7.14(c) and a linear fit (dashed lines in Fig. 7.14(c)) confirms the presence of a steep increase in the magnetization up to around 0.05 T, leading to an additional contribution of around 10 emu/mg ($\approx 10^{-3}\,\mu_B$/f.u.). This behaviour is similar to that found for $BaCu_2Ge_2O_7$ in Ref. [290]. Performing a powder averaging of the reported magnetization results, an additional contribution of around 100 emu/mg is expected for pure $BaCu_2Ge_2O_7$. Thus, phase fractions of 5.8(6)%, 18(2)% and 12(1)% can be estimated for the $x = 0.00$, 0.10

and 0.15 compounds, respectively. Although these values are somewhat different to the corresponding fractions of 10.8(3)%, 18.1(3)% and 7.3(2)% for the neutron diffraction samples (see Fig. 7.7), the spurious phases are on a comparable scale and similarly maximized for the $x = 0.10$ compound. For the $x = 1.00$ compound in Fig. 7.14(b), there are also some fluctuations in the third derivative close to 9 K visible. However, these are measurement artifacts caused by the PPMS Dynacool when it switches from the main flow mode to the low-temperature mode at around 10 K in cooling. Similar artifacts can be found at around 16 K in heating when the PPMS Dynacool switches back from the low-temperature to the main flow mode. As clearly visible, these fluctuations are not connected to any significant features in the interpolated M/B values.

In Fig. 7.14(c), the field and x dependent T_N values, identified from the positions of the negative peaks in $\partial^3\chi_V T/\partial T^3$, are added to the zero-field magnetic phase diagram outlined by HC measurements in Sec. 7.3.1. Based on the step size in temperature, an uncertainty of 0.05 K was estimated for T_N. This value was doubled for the barely visible 0.01 T transition in $x = 0.00$ (see red line in Fig. 7.14(a)) and for the T_N values very close to the lower limit of the probed temperature range at the PPMS Dynacool, indicated by the dotted black line in Fig. 7.14(c). As expected, there is a broad consistency between the resulting T_N values for the zero-field HC and the low field ($B \leq 0.1$ T) magnetization measurements. In contrast for magnetic fields of 1 T, systematically higher T_N values are found for the Cu- and Mn-rich compounds. This field-induced shift of the phase boundary is depicted in Fig. 7.14(d) by the dashed lines. For the Cu-rich compounds, even higher fields of 3 T suggest a further increase in T_N, whereas for the Mn-rich side T_N reduces again to the low-field value. These results are consistent with the findings in Ref. [86], reporting a transition temperature of 4.0 K for applied fields of 1 T in $Ba_2MnGe_2O_7$ and temperatures of 3.0 K, 3.3 K and 3.7 K for fields of 0 T, 1 T and 3 T in $Ba_2CuGe_2O_7$.

To complement these studies on the polycrystalline samples, the macroscopic magnetization was also measured on the N21 $Ba_2CuGe_2O_7$ and the 3E $Ba_2MnGe_2O_7$ single crystals, which were synthesized under similar conditions as the mixed powders and by the same group (see Sec. 7.1). As described in more detail in Secs. 7.1.1 and 7.1.2, the irregularly shaped single crystals were carefully oriented using the neutron Laue method and embedded in a matrix, providing specific surfaces and edges representing crystallographic planes and directions. Enabled by this well defined matrix, the crystals were precisely oriented in the brass trough sample holder using specifically customized non-magnetic polycarbonate capsules and GE vanish as low-temperature adhesive. Consequently, measurements at the PPMS Dynacool (JCNS, Jülich, Germany) with magnetic fields aligned in the [100], [110] and [001] directions for $Ba_2MnGe_2O_7$ and in the [100], [110], [001] and [203] directions for $Ba_2CuGe_2O_7$ could be realized. The latter direction, [203], corresponds to a field in the ac plane that encloses an angle of around 45° with the c axis. Although the sample orientation was carefully prepared, the final precision might be around ±5°, particularly for the diagonal [203] direction. A photograph of the N21 sample mounted for magnetic fields along the [001] direction is shown in Fig. 7.9(d).

Like for the polycrystalline powders, the magnetization of the oriented single crystals was measured in cooling from 300 K to 2 K with an applied magnetic field of 1 T. For some field orientations, the sample was afterwards heated to around 100 K, clearly above

Table 7.6.: Results of the CW fit for the $Ba_2CuGe_2O_7$ and $Ba_2MnGe_2O_7$ single crystals, which are shown in Fig. G.6(b) in appendix G.3. The average, denoted as Avg., is calculated from the values of the three principal magnetic field directions [100], [110] and [001]. Its uncertainty is estimated as the square root of the variance. The total spin S is calculated from m_{eff} using Eq. (2.1) and quenched orbital angular momenta. In addition, anisotropic g-factors are used for the calculation. These are $g_{\perp c} = 2.044$ and $g_{\parallel c} = 2.474$ for $Ba_2CuGe_2O_7$ (see Sec. 2.2.1) and result in $g_{[203]} = 2.269$ for the field direction denoted as [203]. For $Ba_2MnGe_2O_7$, these are $g_{\perp c} = 2.005$ and $g_{\parallel c} = 2.002$ (see Sec. 2.2.3).

	$Ba_2CuGe_2O_7$ (N21)					$Ba_2MnGe_2O_7$ (3E)			
B	[100]	[110]	[203]	[001]	Avg.	[100]	[110]	[001]	Avg.
Θ [K]	14.2(3)	12.7(3)	14.0(3)	14.5(3)	13.8(8)	13.4(3)	11.9(3)	9.7(3)	12(1)
m_{eff} $[\frac{\mu_B}{\text{f.u.}}]$	1.84(2)	1.84(2)	2.10(2)	2.28(2)	2.0(2)	5.88(3)	5.81(3)	5.77(3)	5.82(4)
S	0.55(1)	0.55(1)	0.56(1)	0.55(1)	0.55(1)	2.48(2)	2.45(2)	2.43(2)	2.45(2)

T_N, and then measured again from 20 K to around 2.0 K with different applied magnetic fields to investigate the low-temperature region in more detail. Finally, M was measured as function of B at the lowest available temperature of 1.8 K up to the maximal field of ± 9 T. The data was reduced as discussed for the polycrystalline samples; however, no demagnetization correction was performed due its previously demonstrated insignificance for these predominantly AFM materials. To account for the contributions of the matrix, consisting mainly of diamagnetic epoxy glue, a dummy matrix of similar composition and weight, but without sample, was prepared and analogously measured. In the low-temperature region ($T < 20$ K), the strength of this matrix contribution is at round 1% for $Ba_2CuGe_2O_7$ and 0.1% for $Ba_2MnGe_2O_7$, and was thus neglected. In contrast, for the high temperature region (20 K $< T <$ 300 K), it can lead to sizable effects, particularly for $Ba_2CuGe_2O_7$, and was thus carefully subtracted.

In a similar approach as for the polycrystalline compounds, the CW parameters were determined using Eq. (7.6) from the linear behaviour in the inverse magnetization above around 50 K for the field cooled measurements at 1.0 T. The individual CW fits for the different applied field directions and crystals are illustrated in Fig. G.6(b) in appendix G.3 and supplemented by further details about the fitting procedure. The resulting CW parameters are summarized in Table 7.6. Their uncertainty takes the experimental precision, discussed for the polycrystalline compounds, into account but might be somewhat underestimated due to a limited accuracy of the sample matrix correction and crystal alignment. In addition, average values are calculated from the three principal magnetic field directions.

For the resulting Θ values in $Ba_2CuGe_2O_7$, only small deviations emerge from the average value of around 14 K, which suits well to the results of the polycrystalline powders in Fig. 7.13(a). For $Ba_2MnGe_2O_7$, the average Θ value of around 12 K complies also well with the expectations of the powder results in Fig. 7.13(a) but the individual results for the different directions show some clear discrepancies. However, these discrepancies might be attributed to somewhat larger measurement uncertainties as discussed above. This assumption is also encouraged by a visual comparison between the inverse magnetization curves of the three field directions in Fig. G.6(b) for $Ba_2MnGe_2O_7$, revealing

no significant differences. In contrast, obviously different slopes of the inverse magnetization are observed for the field directions in the $Ba_2CuGe_2O_7$ crystal, which is also reflected in Table 7.6 by an increasing m_{eff} value for magnetic fields directed closer to the [001] axis. This clearly indicates an easy c axis anisotropy in the PM susceptibility, characterized by a ratio of $m_{\text{eff}}^{\perp[001]}/m_{\text{eff}}^{\parallel[001]} = 0.81(1)$. As discussed in Sec. 2.2.1, this characteristic can be directly attributed to an easy axis anisotropy $g_{\perp c}/g_{\parallel c} \approx 0.83$ in the g-tensor resulting from an admixture of exited states due to SOC. Thus, using the reported values for the g-tensor and assuming quenched orbital momenta ($L = 0$), a consistent S value of around 0.55, which is close to the expectation of 0.5 for Cu^{2+}, is found for all applied field directions as evident from Table 7.6.

For $Ba_2MnGe_2O_7$, only small deviations of m_{eff} from the average value of 5.82(4) μ_B are noticeable in Table 7.6. This is reflected in a ratio $m_{\text{eff}}^{\perp[001]}/m_{\text{eff}}^{\parallel[001]} = 1.013(5)$, indicating a very weak in-plane anisotropy for $Ba_2MnGe_2O_7$ as expected from the detailed discussion in Sec. 2.2.3. Note that the measured anisotropy in the effective moments is in agreement with the susceptibility results in Ref. [15], suggesting a ratio of $\chi_{11}/\chi_{33} = 1.02$. Using the slightly anisotropic values for the g-tensor reported in Ref. [15] and assuming quenched orbital momenta ($L = 0$), the average total spin of $S = 2.45(2)$ listed in Table 7.6 for $Ba_2MnGe_2O_7$ recovers almost perfectly the expected value of 2.5 for Mn^{2+}.

To highlight phase transitions in the field cooled measurements of $Ba_2CuGe_2O_7$ and $Ba_2MnGe_2O_7$ at low temperature, the third derivative $\partial^3\chi_V T/\partial T^3$ is calculated. The results for fields in the [203] and [001] directions in $Ba_2CuGe_2O_7$ and $Ba_2MnGe_2O_7$ are presented in Figs. 7.15(a) and 7.15(b), respectively. In addition, the normalized mass magnetizations M/B are shown and the T_N values, indicated by a negative peak in the third derivative, are marked by a dashed vertical line. Clear to see is an increase in T_N for increasing fields in $Ba_2CuGe_2O_7$, whereas a decrease in T_N becomes apparent in $Ba_2MnGe_2O_7$. This reproduces well the general field-dependent T_N behaviour of the Cu- and Mn-rich polycrystalline compounds for fields above 1 T, outlined in Fig. 7.14(d). Notably, no clear phase transition, and thus no negative peak in the third derivative can be identified for applied fields of 9 T. For $Ba_2CuGe_2O_7$ (Fig. 7.15(a)), this might be connected to the continuously decreasing negative peak amplitude in the third derivative, being simply below the measurement sensitivity at 9 T. This conclusion is supported by a broad feature at around 4 K in M, showing a AFM typical behaviour similar to that visible for lower fields. In contrast for $Ba_2MnGe_2O_7$ (Fig. 7.15(b)), the negative peak amplitude does not decrease with increasing fields and no feature is observed in M for an applied field of 9 T, confidently suggesting no magnetic phase transition in the measured temperature range.

In the field-dependent measurements at low temperatures of 1.8 K, phase transitions are typically represented by peak-like features in $\partial M/\partial B$ (see Refs. [86, 126]). To emphasize these transitions, the third derivative $\partial^3 M/\partial B^3$ is calculated and smoothed by the Savitzky-Golay method of cubic order, like for the temperature-dependent measurements. Both the magnetization and its third derivative are shown in Figs. 7.15(c) and 7.15(d) as function of B for different magnetic field directions in the $Ba_2CuGe_2O_7$ and $Ba_2MnGe_2O_7$ single crystals, respectively. The primary transitions, indicated by a large

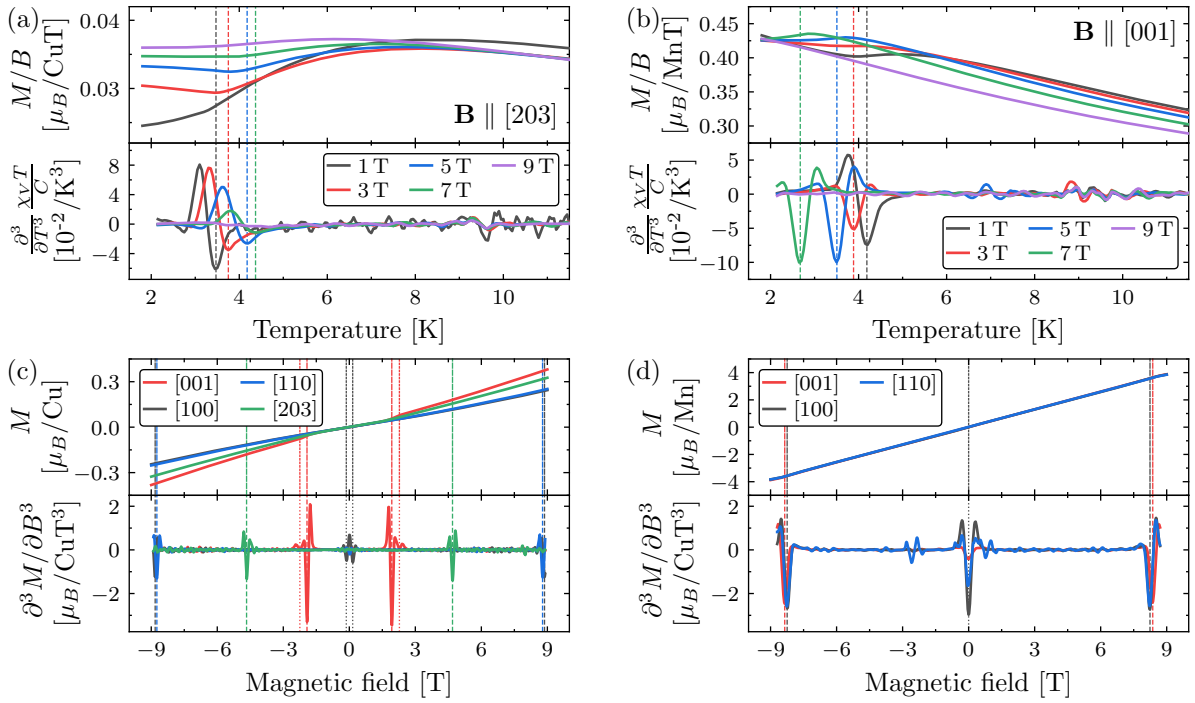

Figure 7.15.: (a,b) Normalized mass magnetization M and its third derivative $\partial^3\chi_V T/\partial T^3$ as function of the temperature for the (a) $Ba_2CuGe_2O_7$ and (b) $Ba_2MnGe_2O_7$ single crystals and different applied magnetic fields B in the [203] and [001] directions, respectively. (c,d) Mass magnetization M and its third derivative $\partial^3 M/\partial B^3$ as function of the field for the (c) $Ba_2CuGe_2O_7$ and (d) $Ba_2MnGe_2O_7$ single crystals and for different magnetic field directions at 1.8 K. In all panels, the dashed vertical lines mark magnetic phase transitions indicated by a negative peak in the third derivative. The dotted vertical lines in (c,d) highlight secondary features discussed in the text.

negative peak in $\partial^3 M/\partial B^3$, are marked by dashed vertical lines. For $Ba_2CuGe_2O_7$, these transitions appear for magnetic field directions closer to the *ab* plane at increasing field values. In contrast for $Ba_2MnGe_2O_7$, an almost direction independent field strength of around 8.3 T is evident for the transition. Secondary features, visible as weak negative peaks, are marked by dotted vertical lines. In $Ba_2CuGe_2O_7$ with magnetic field along [001] (red lines in Fig. 7.15(c)), the secondary feature at around 2.25 T indicates the transition from the narrow AFM cone phase, starting at around 1.90 T, to the commensurate AFM phase, introduced in Sec. 2.2.1. For fields in the [100] direction (black lines in Fig. 7.15(c)), the marked feature at around 0.15 T that indicates a reduced susceptibility at very low fields is similarly visible but not discussed in the results of Mühlbauer *et al.* [126]. As this feature appears only for magnetic field directions with a considerable deviation from the ⟨110⟩ directions, it can be attributed to a discontinuous alignment of the cycloidal spin plane perpendicular to the magnetic field direction. For fields below 0.15 T in the [100] direction, the normal of the spin plane remains aligned with the preferential ⟨110⟩ directions (see Sec. 2.2.1), and thus encloses a finite angle with the field direction. As the susceptibility of the AFM cycloid is anisotropic, favouring fields normal to the spin plane as evidenced in Ref. [87], this finite angle causes the

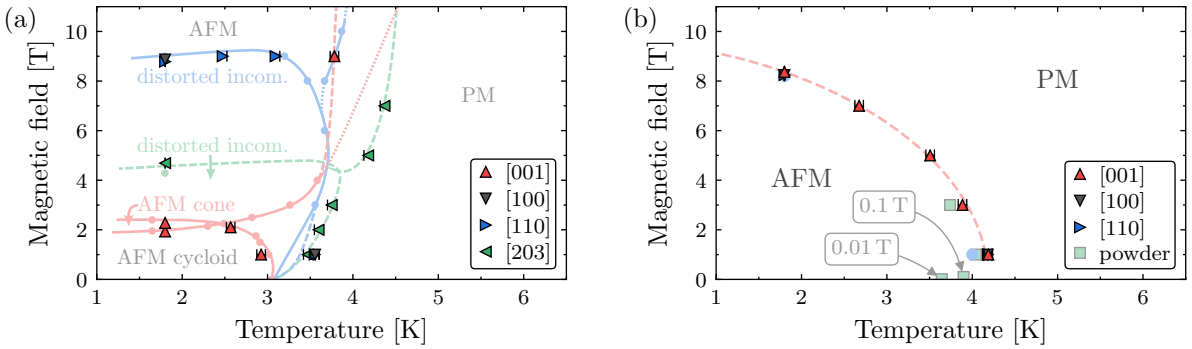

Figure 7.16.: Magnetic field- and temperature-dependent magnetic phase diagram in (a) $Ba_2CuGe_2O_7$ and (b) $Ba_2MnGe_2O_7$. The triangular symbols mark the T_N values identified in Fig. 7.15. The light circles and the phase boundaries, represented by solid and dotted lines, are taken from (a) Mühlbauer *et al.* [126] and (b) Murakawa *et al.* [86] and their color corresponds to the respective applied field direction. The dashed lines in (a) are phase boundaries suggested by our measurements and serve as guide to the eye. In (b), the dashed red line is a fit to the $\mathbf{B} \parallel [001]$ measurement based on Eq. (7.8) and is discussed in the text. The green square symbols indicate the results from the $Ba_2Cu_{1-x}Mn_xGe_2O_7$ polycrystalline powder measurements with $x = 1.00$, taken from Fig. 7.14(d).

observed reduced susceptibility at very low fields. For magnetic fields above 0.15 T, the spin planes are aligned normal to the field direction, and thus an increased susceptibility is measured. This behaviour is consistent with the results of Murakawa *et al.* [87], suggesting an alignment of the spin plane normal to B for fields between 0.1 T and 0.2 T. For $Ba_2MnGe_2O_7$, the secondary feature observed at 0 T, which is maximized for fields in the ab plane, indicates an increased susceptibility at very low fields. This feature may result from an alignment of the WFM moments in $Ba_2MnGe_2O_7$, which cancel out in zero field due to the AFM stacking in the [001] direction (see Sec. 2.2.1) but may provide a strong response to small fields that quickly saturates. The lower response of WFM moments for magnetic fields in c direction might be related to their restriction to the ab plane in the suggested high-symmetry magnetic space groups for $Ba_2MnGe_2O_7$ (blue groups in Fig. 2.8). The additional non-symmetric fluctuations for fields of around -3 T and 1 T in the [110] direction (blue lines in Fig. 7.15(d)) can be attributed to measurement artifacts, resulting from a four times faster magnetic field sweep rate selected for this measurement compared to the other directions for lack of time.

Extracting all T_N values indicated in the magnetization measurements, a rather complex field- and temperature-dependent magnetic phase diagram is revealed for single crystalline $Ba_2CuGe_2O_7$ as depicted by the triangular symbols in Fig. 7.16(a). For comparison, the phase boundaries and measurement results reported in Ref. [126] are additionally shown by the light solid lines and circles, respectively. For $\mathbf{B} \parallel [001]$, the determined T_N values (red triangular symbols) recover well the phase boundaries of the almost AFM cycloidal and the narrow AFM cone phase at low fields (red solid lines). For the high-field transition between the PM and the commensurate AFM structure, a lower T_N value than expected from the assumed continuation in Ref. [126] (dotted red line) is found; thus, we would suggest a steeper continuation that is indicated by the red dashed line. For the fields in [110] direction, the high-field values at around 9 T (blue triangular

symbols) confirm precisely the I/C phase boundary (horizontal blue solid line) reported in Ref. [126]. At fields of 1 T, we find a slightly higher $T_N \approx 3.5$ K than suggested by the phase boundary taken from Ref. [126]. Therefore, it might be adjusted for the low field region as indicated by the dashed blue line. No significant difference is observed between the T_N values resulting from the magnetization measurements with magnetic field in [110] and [100] direction, shown by blue and black symbols, respectively. For the fields in [203] direction, which corresponds to field angles of $\phi \approx 45°$ and $\alpha \approx 45°$ in the notation of Ref. [126], only the T_N point shown by the green circle at around 1.8 K and 4.2 T is reported, which coincides well with our results (green triangles). Following the somewhat related results with $\phi = 25°$ in Ref. [126], phase boundaries as indicated by the dashed green line are suggested for the [203] field direction. Below the I/C transition (horizontal dashed green line), a gradually increasing distortion of the AFM cycloidal structure is expected.

From the resulting T_N values of the $Ba_2MnGe_2O_7$ measurements shown in Fig. 7.16(b), no significant differences are apparent for the three magnetic field directions and a comparably simple phase diagram can be built. In addition, the T_N values at around 4 K and 1.8 K reported in Ref. [86] for magnetic fields in [110] direction are shown by light blue circles. Whereas the first value shows a slight difference to our findings, the latter one is perfectly reproduced.

For Ising antiferromagnets, the general variation of T_N with applied magnetic fields B was derived by Bienenstock [291] using a high-temperature expansions of the free energy and reduced to an expression of the form

$$\frac{T_N}{T_{N,0}} = \left(1 - \left(\frac{B}{B_0}\right)^2\right)^{\zeta}, \tag{7.8}$$

with zero-field transition temperature $T_{N,0}$, zero-temperature critical field B_0 and exponent ζ. The critical field $B_0 = -zJ/m$ is given by the coordination number z, the spin coupling energy J and the magnetic moment m. Using this approximation, the field dependency can be well fitted by $T_{N,0} = 4.18(4)$ K, $B_0 = 9.5(3)$ T and $\zeta = 0.58(8)$, as shown by the dashed red line in Fig. 7.16(b), representing additionally the boundary between the AFM and PM phase. As the exponent ζ reflects mainly the dimension of the system and is around 0.87 for a 2D square lattice and around 0.35 for a simple or body centered cubic 3D structure [291], the fitted result of 0.58(8) indicates the quasi-2D AFM characteristic for $Ba_2MnGe_2O_7$, resulting from its layered structure discussed in Sec. 2.1. The decrease of T_N for $B \geq 1$ T is also consistent with the T_N results for the $x = 1.00$ polycrystalline $Ba_2Cu_{1-x}Mn_xGe_2O_7$ powder, taken from Fig. 7.14(d) and shown by green squares in Fig. 7.16(b). However, the powder values at 0.01 T and 0.1 T indicate a reduction of T_N also towards low fields for $B < 1$ T, which is not expected for typical AFM systems and from Eq. (7.8). This unusual non-monotonic behaviour in the AFM phase boundary is similarly found in $Ba_2FeSi_2O_7$ and can be attributed to the quasi-2D character with weak interplane coupling [287]. Applying a magnetic field typically reduces the magnitude of the order parameter but also suppresses phase fluctuations by reducing the order parameter space. For quasi-2D systems, these phase fluctuation are

characteristically strong and drive the thermal suppression of the long-range magnetic ordering. Thus, applying a magnetic field results in a competing effect between the reduction of the order parameter magnitude and space. At low fields ($B < 1\,\mathrm{T}$), the latter dominates and T_N slightly increases with B whereas at higher fields ($B > 1\,\mathrm{T}$) the first effect is stronger and causes the usually observed decrease of T_N with B [292]. This striking non-monotonic behaviour demonstrates again the quasi-2D AFM characteristic for $Ba_2MnGe_2O_7$.

7.4. Magnetic structures of the Cu-rich compounds

As demonstrated by macroscopic measurements in Sec. 7.3, two somewhat different magnetic structures, denoted as phase I and II in Figs. 7.10(d) and 7.14(d), are expected for the Cu- and Mn-rich polycrystalline $Ba_2Cu_{1-x}Mn_xGe_2O_7$ compounds. Within this section, low-temperature PD is used to reveal the microscopic magnetic ordering of the Cu-rich phase I and to characterize its dependency on the concentration x. Prior to this, a detailed insight into the rich magnetic phase diagram of single crystalline $Ba_2CuGe_2O_7$ is provided by a comprehensive PND study, complementary to the results of Mühlbauer *et al.* [39, 126, 127, 129]. A similar study of the Mn-rich compounds is elaborated in Sec. 7.5.

7.4.1. Paramagnetic structure of $Ba_2CuGe_2O_7$

For a microscopic characterization of the field-induced magnetic moment in the PM phase of $Ba_2CuGe_2O_7$, polarized neutron FRs (see Sec. 3.3.1) were measured at 10 K on the VIP (LLB, Saclay, France) and D3 (ILL, Grenoble, France) diffractometers. The experimental setups and procedures were analogous to those described in Sec. 6.2.2 with D3 using a single counter detector like POLI (see Sec. 5.1). For the measurements, the large $Ba_2CuGe_2O_7$ single crystal shown in Fig. 7.1(a) and the smaller N27c crystal (see Sec. 7.1.1) were used at VIP and D3, respectively. They were mounted with the [100], [110], [112] and [113] direction almost parallel to the vertical axis of the instrument, and thus to the applied magnetic field direction. For each orientation and field strength, FR data was collected with a neutron wavelength of around 0.84 Å.

For the VIP measurements, the FR data was reduced as described for $Ba_2CoGe_2O_7$ in Sec. 6.2.2. Following a similar approach also for the reduction of the D3 measurement, 46 Bragg reflections were excluded that were either poorly centered or had an intensity below 2% of the maximal observed value, and thus a high uncertainty in the calculated asymmetry. This leaves in total 4813 Bragg reflections for the magnetic moment refinement with the structural parameters of $Ba_2CuGe_2O_7$ specified as listed in Table 7.2. As no extinction coefficients are provided by the PD measurements in Sec. 7.2.1, the isotropic extinction parameter x_{11} was refined for all FR datasets like in Sec. 6.3.2, yielding an average value of 0.26(7) and 0.29(6) for the large and the N27c single crystal. Based on their negligible difference, a combined value of $x_{11} = 0.27(5)$ was assumed for all subsequent refinements.

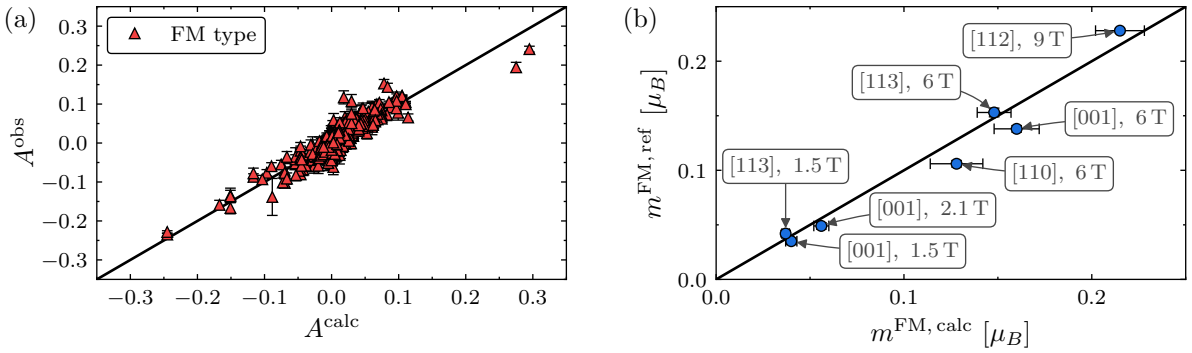

Figure 7.17.: (a) Observed and calculated asymmetry values for all FM-type reflections measured in $Ba_2CuGe_2O_7$ at 10 K with different field strengths and directions. The calculation is based on the refinement results in Table G.1. (b) Comparison between FM moments from the refinement ($m^{FM,\,ref}$ in Table G.1) and from the calculation ($m^{FM,\,calc}$) with $\chi_{11} = 0.021(2)\,\mu_B/T$ and $\chi_{33} = 0.027(2)\,\mu_B/T$. Each point is labeled by its respective magnetic field direction and value.

According to the discussion in Sec. 6.2.2, the magnetic moments of the Cu atoms can be separated into a FM and AFM moment, denoted as $\mathbf{m}^{FM}$ and $\mathbf{m}^{AFM}$. Again, their components are addressed in a field-dependent reference system, defined by $\mathbf{x} \parallel \mathbf{B}$, $\mathbf{y} \parallel (\mathbf{c} \times \mathbf{x})$ and $\mathbf{z} \parallel (\mathbf{x} \times \mathbf{y})$, where $\mathbf{c}$ denotes the lattice [001] direction. This leads to six parameters for the free magnetic moment refinement and only a non-zero m_x^{FM} component for the restricted refinement with magnetic moments in field direction. Note again that for the calculation of the reference system, the precise direction of $\mathbf{B}$ is taken from the crystal orientation matrix, which has in practice, even for fields denoted as $\mathbf{B} \parallel [001]$, a finite in-plane component defining the $\mathbf{y}$ axis.

The detailed results of the free and restricted magnetic moment refinements using *Mag2Pol* are listed in Table G.1 in the appendix. As expected, no significant contributions other than m_x^{FM} are found in the free refinement. Thus, the restricted refinement provides a comparable fit quality and negligible differences in the induced magnetic moments. Overall, a good agreement between the measured and calculated asymmetry values could be achieved, which is demonstrated in Fig. 7.17(a) by their visual comparison for the combined 2499 FM-type reflections of all FR datasets.

Like in Sec. 6.2.2, the resulting field-induced magnetic moments from the restricted refinements can be used to determine the magnetic susceptibility tensor χ, which is restricted by symmetry to $\chi_{11} = \chi_{22}$ and $\chi_{12} = \chi_{13} = \chi_{23} = 0$. Using a least squares procedure, the two independent tensor components can be determined to be $\chi_{11} = 0.021(2)\,\mu_B/T$ and $\chi_{33} = 0.027(4)\,\mu_B/T$ per Cu atom and a comparison between the calculated and refined magnetic moments is shown in Fig. 7.17(b). Although these χ values are somewhat lower than, for example, the reported macroscopic in-plane susceptibility of around $0.029\,\mu_B/T$ in Ref. [86], the indicated slight easy-axis anisotropy of $\chi_{11}/\chi_{33} = 0.8(1)$ along the c direction is consistent with the anisotropy in the spin g-factor of around 0.81, which is suggested in Ref. [121] (see Sec. 2.2.1) and reproduced by the CW results for $Ba_2CuGe_2O_7$ in Table 7.6. Note that this magnetic anisotropy is opposite to the strong easy plane found in Sec. 6.2.2 for $Ba_2CoGe_2O_7$.

Table 7.7.: Overview of the results of the restricted magnetic moment refinement for the FR measurements with different field values and directions in $Ba_2CuGe_2O_7$ at 2 K. The two datasets with **B** ∥ [112] that were measured at D3 using the N27c single crystal are labeled accordingly. The remaining datasets are measured at VIP using the large $Ba_2CuGe_2O_7$ single crystal shown in Fig. 7.1(a). The components of the magnetization refer to the field-dependent xyz reference system defined in the text. The results of the free refinement with unrestricted FM and AFM moments are listed in Table G.2 in the appendix.

Magnetic field		Phase	m_x^{FM} [μ_B]	m_y^{AFM} [μ_B]	m^{tot} [μ_B]	$\chi_r^{2,\,\mathrm{FM}}$	$\chi_r^{2,\,\mathrm{AFM}}$	χ_r^2
B ∥ [001]	1.5 T	AFM-Cycl.	0.022(3)	0.00(1)	0.022(3)	1.85	1.62	1.74
	2.1 T	AFM-Cone	0.040(3)	0.25(2)	0.25(2)	1.60	1.66	1.63
	6.0 T	AFM	0.138(3)	0.42(2)	0.44(2)	2.27	1.82	2.04
B ∥ [112]	2.0 T	Dis. Inc.	0.040(1)	0.03(1)	0.050(6)	2.49	0.88	2.36
(D3-ILL)	9.0 T	AFM	0.232(2)	0.44(1)	0.497(9)	4.14	2.68	3.44
B ∥ [112]	6.75 T	AFM	0.16(2)	0.56(8)	0.58(8)	1.27	1.30	1.28
B ∥ [113]	1.5 T	AFM-Cycl.	0.026(3)	0.02(2)	0.03(1)	1.68	1.50	1.59
	6.0 T	AFM	0.153(4)	0.46(2)	0.49(2)	2.02	1.84	1.93

7.4.2. Low- and high-field magnetic structures of $Ba_2CuGe_2O_7$

In addition to the measurements in the PM phase of $Ba_2CuGe_2O_7$, polarized neutron FRs were collected in the different long-range ordered magnetic phases at 2.0 K at the VIP and D3 diffractometers by applying magnetic fields up to 9 T in various crystal directions. As the FR method is based on contributions from the nuclear magnetic interference (see Sec. 3.3.1), no incommensurate magnetic Bragg reflections are measured. Thus, the measured FRs are only sensitive to commensurate magnetic structures with an integer modulation $\boldsymbol{\tau} = (uvw)$, particularly excluding contributions from the cycloidal spin structures at low fields with modulations $\boldsymbol{\tau} = (\zeta\zeta 0)$ and an incommensurability parameter of $\zeta \approx 0.027$. Nevertheless, these commensurate magnetic moments can be separated again into FM and AFM parts, representing integer modulations of $\boldsymbol{\tau} = (000)$ and (100), respectively. The components of the magnetic moments are addressed in the field-dependent reference system introduced in Sec. 7.4.1.

The results for an unrestricted magnetic moment refinement are listed in Table G.2 in the appendix. For the refinement, the structural parameters and the extinction coefficient were selected as for the PM phase in Sec. 7.4.1 and the FR data analogously reduced, providing the asymmetry of in total 4579 Bragg reflections. As expected, only a non-zero x component is found for $\mathbf{m}^{\mathrm{FM}}$, representing the induced magnetic moment in field direction. For the AFM part, a sizable contribution is only evident in y direction, which suggests for $Ba_2CuGe_2O_7$ an alignment of $\mathbf{m}^{\mathrm{AFM}}$ within the ab plane perpendicular to the applied magnetic field direction. Thus, the refinement can be restricted to only non-zero m_x^{FM} and m_y^{AFM} values, yielding similar results and a comparable fit quality as presented in Table 7.7. The good agreement between the observed and calculated asymmetry values for both the AFM and FM-type reflections of all FR datasets is demonstrated in Fig. 7.18(a).

For the low-field AFM cycloidal structures, probed by the FR measurements with

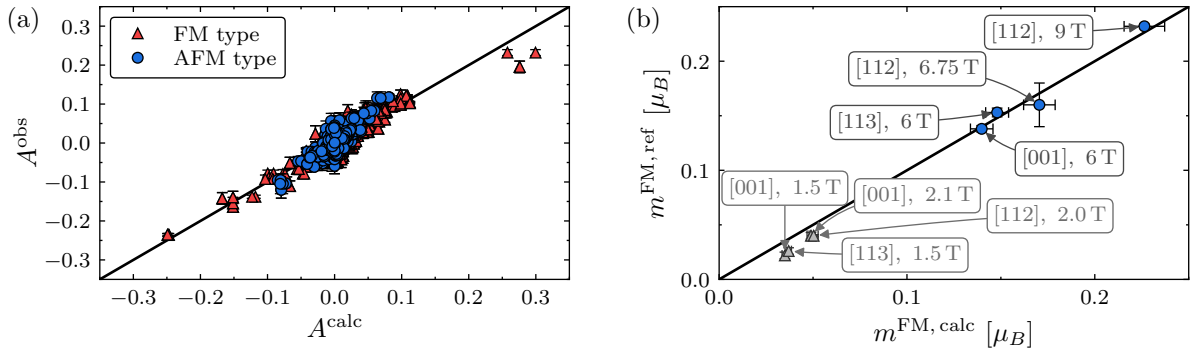

Figure 7.18.: (a) Observed and calculated asymmetry values for all FM and AFM-type reflections measured in $Ba_2CuGe_2O_7$ at 2 K with different field strengths and directions. The calculation is based on the refinement results in Table 7.7. (b) Comparison between FM moments from the refinement ($m^{\mathrm{FM,\ ref}}$ in Table 7.7) and from the calculation ($m^{\mathrm{FM,\ calc}}$) with $\chi_{11} = 0.027(2)\,\mu_B/\mathrm{T}$ and $\chi_{33} = 0.023(1)\,\mu_B/\mathrm{T}$. Each point is labeled by its respective magnetic field direction and value.

magnetic fields of 1.5 T in the [001] and [113] direction, no commensurate AFM moments are expected. This is met by the refinement results in Table 7.7, yielding zero m_y^{AFM} values within their uncertainty. A similar expectation holds for the distorted incommensurate structure, investigated by an applied magnetic field of 2.0 T in the [112] direction. Again, only an insignificant $m_y^{\mathrm{AFM}} = 0.03(1)\,\mu_B/\mathrm{Cu}$ is refined.

For the high-field AFM structure, which is similar to that in $Ba_2CoGe_2O_7$, a commensurate AFM moment is expected in the *ab* plane perpendicular to the field direction (see Sec. 2.2), represented by m_y^{AFM}. Typically, such an AFM structure is accompanied by two equally populated 180° domains with opposite m_y^{AFM} signs. However, each of the two domains is connected to a WFM moment caused by the DMI that lifts their degeneracy in an applied magnetic field (see discussion for $Ba_2CoGe_2O_7$ in Sec. 4.2.2). The resulting imbalance between the two 180° domains finally enables the measurement of a finite AFM moment by PND. Assuming a saturated single AFM domain state, m_y^{AFM} values of around $0.45\,\mu_B/\mathrm{Cu}$ and an total ordered moment of around $0.50\,\mu_B/\mathrm{Cu}$ are found as listed in Table 7.7 for the high-field measurements with **B** in the [001], [112] and [113] directions. Although no ordered moment is reported from the neutron studies on $Ba_2CuGe_2O_7$ in the literature so far, the macroscopic measurements of the electric polarization and magnetization in Ref. [86] can be used to estimate an upper limit of $0.65(3)\,\mu_B/\mathrm{Cu}$ on m^{tot} based on the implications of the pd-hybridization model as discussed in detail in the subsequent Sec. 7.4.3. This is clearly lower than the typically expected value of around $1\,\mu_B$ for the Cu^{2+} ions with $S = 1/2$ and somewhat supports the validity of the PND results. Nevertheless, the refined m_y^{AFM} values might be reduced due to not completely saturated single AFM domain states. This can be caused by a particularly small WFM moment implying a fairly weak energy splitting between the two domains in the applied magnetic field like reported for hematite (α-Fe_2O_3) in Ref. [21]. Note that the magnitude of the WFM moment in $Ba_2CuGe_2O_7$ has not yet been directly measured but it can be calculated from the estimation of D_z/J in Ref. [293] to be around $0.004\,\mu_B/\mathrm{Cu}^{2+}$, which is even lower than for $Ba_2CoGe_2O_7$. Setting the total

magnetic moment to the estimated upper limit of $0.65\,\mu_B$/Cu, all three refinements in the AFM phase provide a fraction of around 15% for an additional 180° domain without any significant difference in the fit quality. An attempt to refine both the domain population and the magnetic moment leads, however, to severe correlations between the parameters and diverging results. Note that the 180° AFM domains are indistinguishable by ND in, e.g., Refs. [119, 129] and are also invisible to the macroscopic studies in Ref. [86] as both AFM domains are connected to same signed electric polarizations.

With an applied magnetic field of 2.1 T close to the c axis (tilted for around 1.6° in [100] direction), FR data was collected in the narrow AFM cone phase of $Ba_2CuGe_2O_7$. According to Mühlbauer *et al.* [129], this phase is characterized by the combination of an commensurate AFM moment, aligned along the y direction, and an AFM cycloidal modulation in the xz plane. In total, this corresponds to a precession of the Cu spins around the y axis, forming the suggested AFM cones. Again, two 180° domains are possible with opposite m_y^{AFM} values. As the measured m_y^{AFM} in Table 7.7 is finite, this indicates the presence of a DMI-induced canting even in the AFM cone phase, causing the experimentally apparent imbalance between the two domains with applied magnetic fields. As expected, the total magnetic moment of $0.25\,\mu_B$/Cu revealed by PND is clearly smaller than in the AFM phase since the additional cycloidal part does not contribute. However, also the presence of 180° domains or even of tetrahedral domains (see Ref. [126]) due to the very small in-plane component of the magnetic field might be influential to the refinement results. Nevertheless, assuming a similar domain configuration and thus the same m^{tot} as for the corresponding 6 T measurement, a half apex angle $\rho = \cos^{-1}(m_y^{\mathrm{AFM}}/m^{\mathrm{tot}})$ of 55(3)° can be estimated for the AFM cones. Although precise magnetic amplitudes are measured in the AFM cone phase in Refs. [119, 129], no values are reported for ρ.

Like for the PM phase in Sec. 7.4.1, the induced magnetic moments m_x^{FM} in the high-field commensurate AFM phase are used to define a susceptibility tensor with components $\chi_{11} = 0.027(2)\,\mu_B$/T and $\chi_{33} = 0.023(1)\,\mu_B$/T. A comparison between the refined and calculated moments is shown in Fig. 7.18(b) with blue circles denoting the high-field datasets. The ratio $\chi_{11}/\chi_{33} = 1.1(1)$ indicates no significant anisotropy in the susceptibility tensor. However, this is in contrast to the easy-axis type anisotropy indicated for $Ba_2CuGe_2O_7$ by magnetization and PND measurements in Secs. 7.3.2 and 7.4.1 and can be attributed to the magnetic form factors, which are not isotropic as assumed for simplification in this PND refinement (see Sec. 8.2).

For the datasets in the different incommensurate phases at lower magnetic fields, shown as gray triangular symbols in Fig. 7.18(b), a consistently smaller refined than calculated FM moment is clear to see. This indicates a reduced susceptibility in the low field range, which is consistent with the non-linear behavior of the macroscopic magnetization in Fig. 7.15(c).

7.4.3. DMI sign of $Ba_2CuGe_2O_7$

As the imbalance between the 180° AFM domains in the high-field commensurate AFM phase of $Ba_2CuGe_2O_7$, clearly evident in the PND measurements of the preceding Sec.

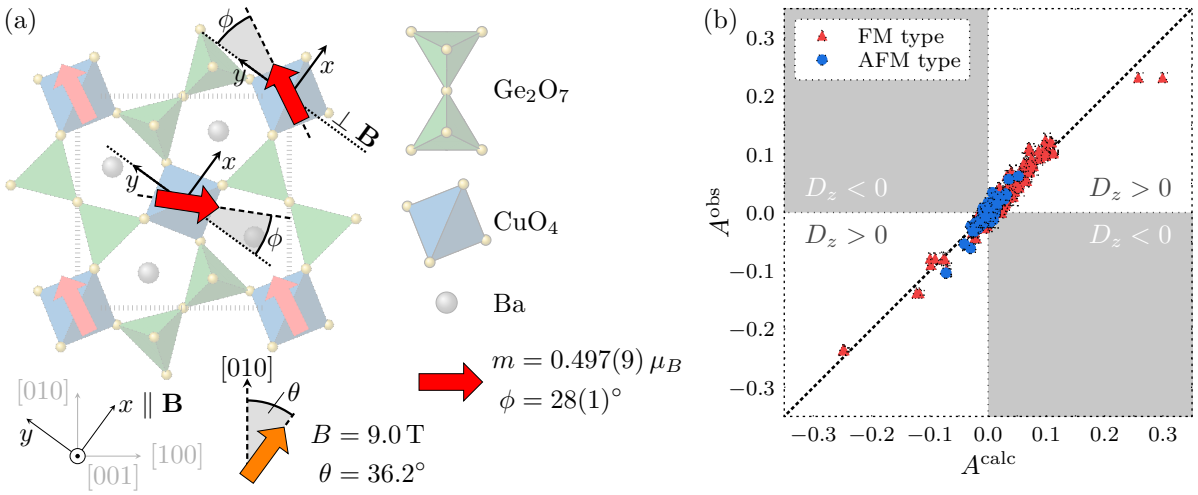

Figure 7.19.: Results of the magnetic moment refinement in $Ba_2CuGe_2O_7$ from Table 7.7 with an applied magnetic field of 9 T close to the [112] direction. The projection of the exact field direction (orange arrow) and the resulting magnetic moment configuration (red arrows) on the *ab* plane are visualized in (a). In addition, the x and y directions of the field-dependent reference system used for the refinement are illustrated. The comparison between the observed and calculated asymmetry values for the refinement, separately for FM-type and AFM-type reflections, is shown in (b).

7.4.2, is caused by an energetically favourable alignment of the WFM moment in field direction, the resulting spin configuration of the predominant domain allows to determine the DMI sign in $Ba_2CuGe_2O_7$. A detailed discussion about the connection between the D_z sign of the DMI vector and the alignment of the commensurate AFM and WFM moments in the $Ba_2TGe_2O_7$ compounds can be found in Sec. 4.2. As consistent conventions for the atomic parameters and the field-dependent reference system are used for all $Ba_2TGe_2O_7$ compounds within this work, Eq. (6.5) in Sec. 6.3.3 for the DMI energy in $Ba_2CoGe_2O_7$ is directly applicable also to the case of $Ba_2CuGe_2O_7$. Thus, D_z and m_y^{AFM} must be same signed for $Ba_2CuGe_2O_7$ in order to be energetically favorable. Based on the consistently positive m_y^{AFM} components in Table 7.7 for the commensurate AFM phase, a positive D_z sign can be unambiguously reported for the first time in $Ba_2CuGe_2O_7$. Note that the in Sec. 6.3.3 discussed simple verification method of $m_x^{FM} > 0$ for a correctly defined refinement model is clearly satisfied in Table 7.7.

The positive DMI sign can additionally be verified by a visual comparison between the refined magnetic moment arrangement and the theoretical expectations in Figs. 4.2(a) and 4.2(b). For this purpose, the projection of the refined magnetic moments to the *ab* plane is visualized in Fig. 7.19(a) for the exemplary measurement with a field of 9 T applied along the [112] direction. Although the in-plane component of the field is rotated by around 36.2° towards the *a* axis for this measurement compared to the theoretical consideration in Figs. 4.2(a) and 4.2(b), the displayed alignment of the AFM to WFM moment, which is the crucial characteristic for the DMI sign, can still serve as reference. The clear consistency between the magnetic moment alignments in Fig. 7.19(a) and Fig. 4.2(b) confirms again the positive D_z sign for $Ba_2CuGe_2O_7$.

In addition, the good agreement between the calculated and observed asymmetry

values for the exemplary 9 T measurement is demonstrated in Fig. 7.19(b). According to the discussion in Sec. 6.3.3, which is also directly applicable to the case of $Ba_2CuGe_2O_7$, the sign of the asymmetry of an AFM-type reflection is directly related to the sign of m_y^{AFM} (see Eq. (6.6)) and thus also to the sign of D_z. As the refined magnetic moment arrangement for the 9 T measurement refers to a positive D_z, the signs of the calculated asymmetries A^{calc} in Fig. 7.19(b) are the ones expected for $D_z > 0$. Thus, all the AFM-type asymmetries (blue circles in Fig. 7.19(b)) in the white areas confirm the positive D_z whereas those in the gray areas suggest a negative one. As all significant AFM-type asymmetries are located within the white areas; thus, $D_z > 0$ is clearly confirmed.

Finally, the implications of the determined DMI sign can be used to estimate the total ordered magnetic moment m^{tot} in the commensurate AFM phase of $Ba_2CuGe_2O_7$ by inspecting the macroscopic electric polarization (reproduced in Fig. 2.11(a)) and magnetization measurements with an applied magnetic field in [110] direction at 1.8 K reported in Ref. [86]. According to the *p-d* hybridization and the spin-nematic interaction model (see Secs. 2.3.1 and 2.3.3 and Table 2.2), the z component of the electric polarization is given by $P_z \propto \cos(2\kappa + 2\phi)$ for an applied magnetic field in the [110] direction and a positive D_z sign. Note the differently signed dependency on the canting angle ϕ in P_z compared to the discussion in Sec. 6.3.3 for $Ba_2CoGe_2O_7$ due to their opposite DMI signs. The distortion angle $\kappa = 21.4(5)$ is given in Table 7.2 from PD and $\phi \in [0°, 90°]$ can be estimated by the ratio between the field-induced FM and the total magnetic moment as $\phi = \sin^{-1}(m^{\mathrm{FM}}/m^{\mathrm{tot}})$. Based on its cosine dependency, a sign change at $\phi = 45° - \kappa$ and a maximum at $\phi = 90° - \kappa$ is expected in P_z [90]. In the reported macroscopic measurement, the commensurate AFM phase, present above in-plane fields of 8.7 T (dashed gray line in Fig. 2.11(a)), is studied up to 14 T. Within this magnetic field range, no sign change or extrema in P_z is observed. As the measured P_z at 1.8 K has the same sign as for higher temperatures in the PM phase, corresponding to $\phi = 90°$, the canting angle in the commensurate AFM phase should be within $45° - \kappa < \phi \leq 90° - \kappa$ for the probed field range. From the reported field-induced magnetization of around $0.26(1)\,\mu_B$/Cu and $0.45(1)\,\mu_B$/Cu at 8.7 T and 14 T, respectively, the total magnetic moment per Cu^{2+} atom can be estimated as $0.48(1)\,\mu_B \leq m^{\mathrm{tot}} < 0.65(3)\,\mu_B$, with the upper limit defined by the apparent absence of the sign change in P_z. This suggest a clearly lower ordered magnetic moment than typically expected for Cu^{2+} with $S = 1/2$ and supports the validity of the PND results discussed in Sec. 7.4.2. This reduction might be related to the low T_N value of around 3.2 K for $Ba_2CuGe_2O_7$, which is rather close to the measurement temperature of 1.8 K. Thus, the ordered moment may not be fully saturated as discussed in more detail for $Ba_2MnGe_2O_7$ in Sec. 7.5.2 below.

Note that for a negative D_z sign in $Ba_2CuGe_2O_7$, a dependency of $P_z \propto \cos(2\kappa - 2\phi)$ with a sign change at $\phi = 45° + \kappa$ would be expected like in $Ba_2CoGe_2O_7$. However, this implies the restriction of $\phi > 45° + \kappa$ for the induced magnetic moment of $0.26\,\mu_B$/Cu at 8.7 T, yielding $m^{\mathrm{tot}} < 0.28(1)\,\mu_B$/Cu that can be confidently refuted by the PND results in Table 7.7 and the measured induced magnetization up to $0.45\,\mu_B$/Cu at 14 T in Ref. [86]; thus, confirming again the positive D_z sign in $Ba_2CoGe_2O_7$ extracted above by PND.

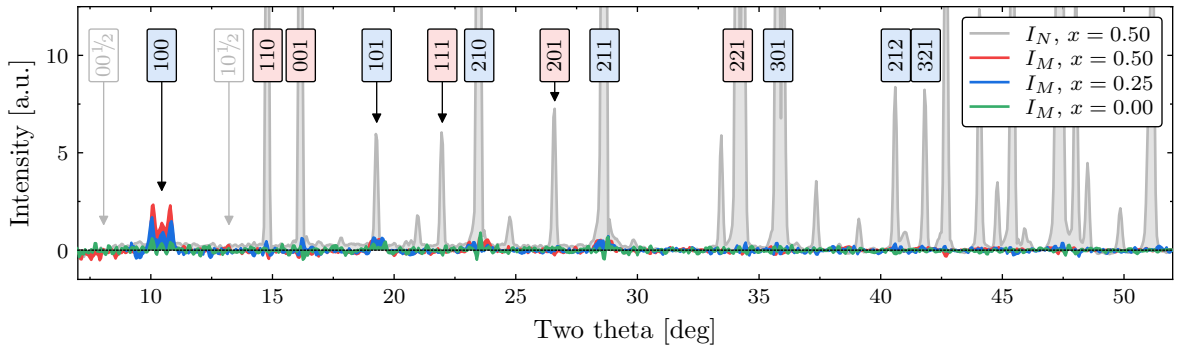

Figure 7.20.: Magnetic intensity I_M for different Cu-rich $Ba_2Cu_{1-x}Mn_xGe_2O_7$ polycrystalline compounds calculated as the difference between the diffraction patterns measured in the PM and magnetically ordered phase at 10 K and 1.5 K, respectively. In addition, the PM intensity I_N for the $x = 0.50$ compound at 10 K is shown as reference. The positions of AFM- and FM-type reflections are indicated by blue and red labels, respectively. The gray labels indicate the positions of the first reflection expected for a FM- and AFM-type ordering with a doubling of the magnetic UC in c direction. The latter corresponds to the magnetic order reported in Ref. [15] for single crystalline $Ba_2MnGe_2O_7$.

7.4.4. Zero-field magnetic structure of $Ba_2Cu_{1-x}Mn_xGe_2O_7$

In the frame of the PD experiments on the $Ba_2Cu_{1-x}Mn_xGe_2O_7$ polycrystalline compounds discussed in Sec. 7.2, additional diffraction patterns at low temperatures of around 1.5 K were collected for the Cu-rich compounds ($x \leq 0.50$) to microscopically characterize the macroscopically identified phase I in Sec. 7.3. Detailed information about the powder samples, the experimental procedure and the data reduction can is available in Sec. 7.2. All magnetic structure refinements presented in this section are conducted with the *Jana2006* software. They are based on the low-temperature nuclear structure parameters for the $Ba_2Cu_{1-x}Mn_xGe_2O_7$ compounds determined in Sec. 7.2.3 and consider all spurious phases previously identified. To visualize the magnetic contributions, the intensity difference between the PM (10 K) and the low-temperature (1.5 K) pattern is built and shown for some selected Cu-rich compounds in Fig. 7.20. Clear to see is a magnetic contribution at the commensurate AFM-type Bragg positions with a modulation vector $\boldsymbol{\tau} = (100)$ accompanied by two incommensurate satellites and a decreasing strength towards smaller x values. Note that these magnetic peaks cannot be indexed in a reasonable way by any of the spurious phases identified in Sec. 7.2.3, confirming their affiliation to the primary $Ba_2Cu_{1-x}Mn_xGe_2O_7$ phase. This is additionally endorsed by the high magnetic contributions for the $x = 0.50$ and $x = 0.25$ compounds (red and blue intensity in Fig. 7.20), showing both no significant contamination. At the $(10\frac{1}{2})$ Bragg positions, indicated by a gray label in Fig. 7.20, no magnetic intensity is evident, and thus an AFM-type ordering like in $Ba_2MnGe_2O_7$ can be excluded.

Based on the different low-temperature phases reported in $Ba_2CuGe_2O_7$, three potential candidates can be identified as long range ordered magnetic structure in the $Ba_2Cu_{1-x}Mn_xGe_2O_7$ compounds. The most obvious choice is certainly a pure AFM cycloidal structure. However, assuming a cycloidal propagation vector $\boldsymbol{\tau} = (\zeta\zeta 0)$ as reported for low and zero magnetic fields in single crystalline $Ba_2CuGe_2O_7$ and illustrated

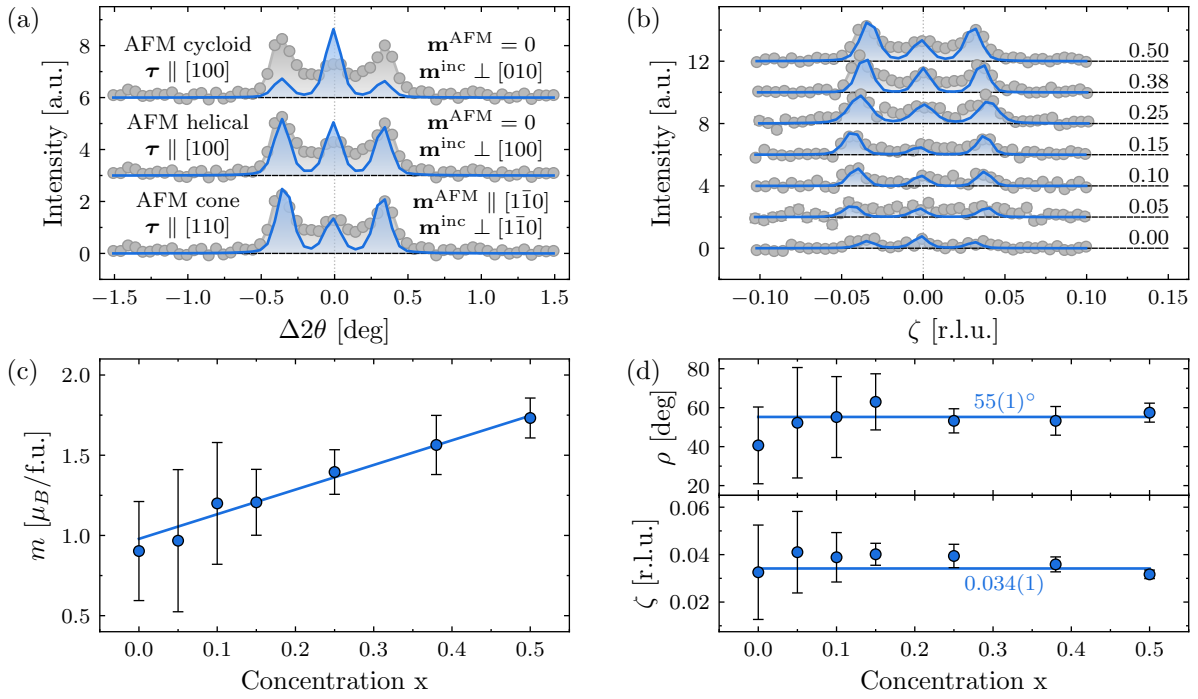

Figure 7.21.: (a) Comparison between the observed and refined intensity of the $x = 0.50$ compound for the different magnetic models discussed in the text. $\Delta 2\theta$ denotes the difference in two theta to the (100) reflection. (b) Comparison between the observed and refined intensity assuming an AFM cone magnetic model for different concentrations x, labeled on the right side of the figure. The curves in (a) and (b) have been shifted vertically by 3 and 2 for clarity, respectively. (c,d) Total magnetic moment m and half apex angle ρ of the refined AFM cone with incommensurability parameter ζ as function of the concentration x. The blue solid lines in (c) and (d) serve as a guide to the eye and are linear and constant fits to the data, respectively.

in Fig. 2.4(a), only contributions at the $(1 \pm \zeta, \zeta, 0)$ satellite positions in the powder diffraction pattern and not at (100) are expected. Thus, such a magnetic structure can be excluded. In contrast, for an AFM cycloid with $\boldsymbol{\tau} = (\zeta 00)$ propagation vector, satellite reflections are expected at the $(1 \pm \zeta, 0, 0)$ and $(1, \zeta, 0)$ positions due to the powder averaging with the latter almost indistinguishable from the (100) peak in the powder profile. Using this candidate structure as magnetic model for the refinement of the $x = 0.50$ pattern, the comparison between the observed and refined magnetic intensity close to the (100) position is shown in the upper panel of Fig. 7.21(a). Clear to see is a significantly higher expected intensity at the central position compared to the satellites at $(1 \pm \zeta, 0, 0)$. This results from the total scattering vector $\mathbf{q}$ being almost normal to the spin plane for the central $(1, \zeta, 0)$ reflection and within the spin plane for $(1 \pm \zeta, 0, 0)$. Since only the magnetic moments perpendicular to $\mathbf{q}$ contribute (see Eq. (3.7)), this clearly reduces the magnetic intensities of the satellites. Therefore, the expected intensity for the pure AFM cycloidal structure does clearly not coincide with the measurement results and can be excluded.

To maximize the intensity of the satellite reflections compared to the central contribution, a helical structure with a spin plane normal to the $(\zeta 00)$ propagation vector

can be assumed. The refined magnetic intensity for this helical model is shown in the central panel of Fig. 7.21(a). Although it demonstrates a certainly better agreement with the measurement results as for the AFM cycloid, a lower intensity of the central peak compared to the satellites is clearly evident in the measurement data and cannot be reproduced by the assumed helical magnetic model. Thus, it can also be excluded.

Another potential candidate of high magnetic symmetry is the AFM cone structure, which was experimentally evidenced in single crystalline $Ba_2CuGe_2O_7$ under applied magnetic fields (see Sec. 2.2.1) and is illustrated in Fig. 2.5(b). It is composed of an AFM cycloidal part with $\boldsymbol{\tau} = (\zeta\zeta 0)$ propagation vector, leading to $(1 \pm \zeta, \zeta, 0)$-type satellite reflections, and a commensurate AFM part with moments in the *ab* plane perpendicular to $\boldsymbol{\tau}$, resulting in a (100) contribution. A refinement of both incommensurate and commensurate magnetic moments results in a good agreement between the observed and calculated intensities for the $x = 0.50$ compound as shown in the lower panel of Fig. 7.21(a). Thus, the AFM cone phase can be reliably identified as the adopted high-symmetry magnetic structure at zero field in phase I of the $Ba_2Cu_{1-x}Mn_xGe_2O_7$ solid solution series. Note that the simultaneous presence of two AFM cycloids with $\boldsymbol{\tau} = (\zeta\zeta 0)$ and $(\zeta 00)$ could also reproduce the measured magnetic intensity but this corresponds to a magnetic configuration of clearly lower symmetry compared to the AFM cone structure. To completely exclude this possibility, single crystal measurements that allow to distinguish between (100) and $(1\zeta 0)$ contributions are required. However, no single crystals are available yet for the mixed $Ba_2Cu_{1-x}Mn_xGe_2O_7$ compounds.

Assuming the AFM cone structure, commensurate and incommensurate AFM moments are refined for all measured Cu-rich $Ba_2Cu_{1-x}Mn_xGe_2O_7$ compounds at 1.5 K. A comparison between the observed and refined intensities close to the magnetic (100) Bragg position is given in Fig. 7.21(b). Clear to see is a strong decrease in the magnetic intensity for lower x values, causing an almost linear behaviour in the total refined magnetic moment shown in Fig. 7.21(c). The suggested total moment of around 1 μ_B/f.u. for the $x = 0.00$ compound coincides well with the general expectation of $S = 1/2$ for Cu^{2+} ions. However, note that the magnetic intensity is only barely visible for the $x \leq 0.10$ compounds even in these high-resolution PD patterns collected at POWGEN, leading to the large uncertainties in the refined values. Particularly for the pure $Ba_2CuGe_2O_7$ compound ($x = 0.00$), the magnetic intensity is so low that it would be typically attributed to background effects. This might explain why Zheludev *et al.* [117] failed to detect any long-range magnetic ordering in $Ba_2CuGe_2O_7$ powders down to 1.4 K. For the incommensurability parameter ζ and the half apex angle ρ of the AFM cones, the refinement yields almost constant values of 0.034(1) and 55(1)°, displayed in the lower and upper panel of Fig. 7.21(d), respectively. This ζ value is close to the value of 0.027 reported for the $Ba_2CuGe_2O_7$ single crystals [117, 129]. Although no values for ρ are reported from the single crystalline $Ba_2CuGe_2O_7$ measurements in the literature, the determined value coincides with the value of the half apex angle estimated by PND measurements in the AFM cone phase in Sec. 7.4.2.

B (6 T)	m^{FM} [μ_B]	$\chi_r^{2,\mathrm{FM}}$	$\chi_r^{2,\mathrm{AFM}}$	χ_r^2
[001]	1.912(8)	3.68	3.08	3.37
[100]	1.957(3)	3.92	3.40	3.64
[110]	2.005(3)	3.80	1.90	2.81
Avg.	1.96(4)			

Table 7.8.: Overview of the results of the restricted magnetic moment refinement ($\mathbf{m}^{\mathrm{FM}} \parallel \mathbf{B}$ and $\mathbf{m}^{\mathrm{AFM}} = 0$) for the FR measurements with different field directions in $Ba_2MnGe_2O_7$ at 10 K. The results of the free refinement with unrestricted FM and AFM moments are listed in Table G.3 in the appendix.

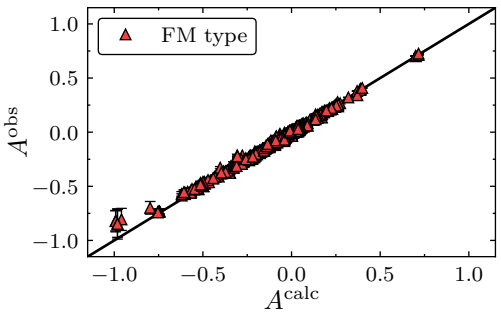

Figure 7.22.: Observed and calculated asymmetry values for all FM-type reflections measured in $Ba_2MnGe_2O_7$ at 10 K with different field directions. The calculation is based on the refinement results in Table 7.8.

7.5. Magnetic structures of the Mn-rich compounds

Like for the Cu-rich compounds in the preceding Sec. 7.4, low-temperature neutron diffraction is used to study microscopically the magnetic structure properties in single crystalline $Ba_2MnGe_2O_7$ and the mixed Mn-rich $Ba_2Cu_{1-x}Mn_xGe_2O_7$ polycrystalline compounds. Based on these measurements, the magnetic ordering is revealed for the phase II, identified by macroscopic measurements in Sec. 7.3 for the Mn-rich compounds.

7.5.1. Paramagnetic structure of $Ba_2MnGe_2O_7$

Polarized neutron FRs (see Sec. 3.3.1) were measured at 10 K in the PM phase of $Ba_2MnGe_2O_7$ on the VIP (LLB, Saclay, France) diffractometer with an analogous experimental setup as described in Sec. 6.2.2. A photograph of the used $Ba_2MnGe_2O_7$ single crystal is shown in Fig. 7.2(a). The crystal was mounted with the three high-symmetry directions [001], [100] and [110] close to the vertical axis of the instrument, and thus parallel to the direction of the applied field of 6 T. For each orientation, PND data was collected with a neutron wavelength of 0.84 Å and reduced like in Sec. 6.2.2.

For the magnetic moment refinements, the atomic parameters of $Ba_2MnGe_2O_7$ were specified as listed for 10 K in Table 7.4. In addition, an average isotropic extinction parameter of $x_{11} = 0.023(8)$ was used, which was determined from the FR measurements as in Sec. 7.4.1 for $Ba_2CuGe_2O_7$. The results of the refinement with the induced magnetization $\mathbf{m}^{\mathrm{FM}}$ restricted parallel to **B** are listed in Table 7.8 and the very good agreement between the measured and calculated asymmetry values for the FM-type reflections of all datasets is demonstrated in Fig. 7.22. The corresponding results with free FM and AFM moments are given in Table G.3 in the appendix for completeness but indicate no significant changes in the refined magnetic moments or the fit quality. For all three high-symmetry field directions, a similar induced magnetic moment is refined, yielding almost equal susceptibility components of $\chi_{11} = 0.330(4)$ and $\chi_{33} = 0.32(2)$. This results in a negligible anisotropy of $\chi_{11}/\chi_{33} = 1.04(5)$, which is in agreement with the expectation

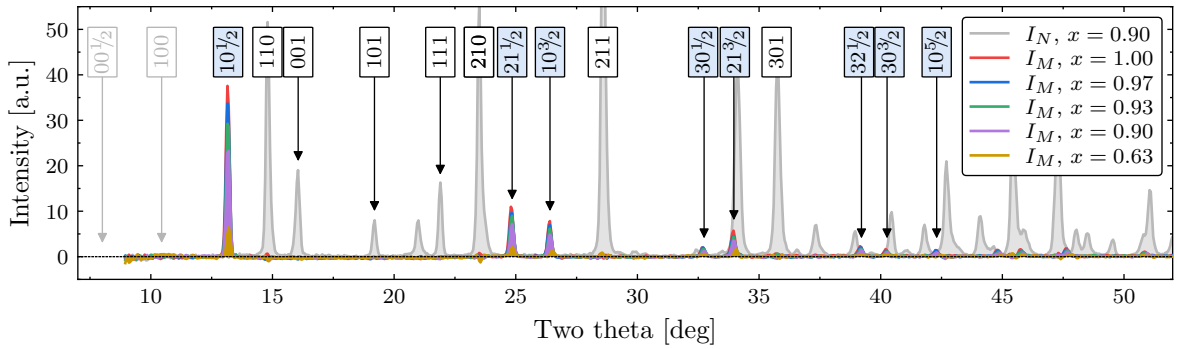

Figure 7.23.: Magnetic intensity I_M for different Mn-rich $Ba_2Cu_{1-x}Mn_xGe_2O_7$ polycrystalline compounds calculated as the difference between the diffraction patterns measured in the PM and magnetically ordered phase at 10 K and 1.5 K, respectively. In addition, the PM intensity I_N for the $x = 0.90$ compound at 10 K is shown as reference. The indices of some magnetic and nuclear reflections are indicated by blue and white labels, respectively. The gray labels indicate the positions of the first reflection expected for a FM- and AFM-type in-plane ordering with and without a doubling of the magnetic UC in c direction, respectively. The latter corresponds to the magnetic order reported for $Ba_2CoGe_2O_7$.

discussed in Sec. 2.2.3 and the macroscopic results presented in Sec. 7.3.2. However, the average value of $1.96(4)\mu_B$/Mn for an applied field of 6 T at 10 K in $Ba_2MnGe_2O_7$ is slightly lower than the reported value of around $2.3\,\mu_B$/Mn in Ref. [86], measured by magnetization with $\mathbf{B} \parallel [110]$. Note that no PND was measured in $Ba_2MnGe_2O_7$ below T_N within this work as the ordered AFM moments cannot be probed by the FR method due to the doubling of the magnetic UC in c direction.

7.5.2. Antiferromagnetic structure of $Ba_2Cu_{1-x}Mn_xGe_2O_7$

In the same way as for the Cu-rich $Ba_2Cu_{1-x}Mn_xGe_2O_7$ compounds discussed in Sec. 7.4.4, neutron powder diffraction patterns were collected for the Mn-rich polycrystalline compounds ($x \geq 0.63$) at low temperatures of around 1.5 K to study the magnetic ordering of phase II, which is outlined in Sec. 7.3 by macroscopic measurements. As these patterns are measured as part of the experiments at POWGEN (SNS) and BT-1 (NCNR), detailed information to the powder samples, the experimental procedure and the data reduction is available in Sec. 7.2.

For a clear visualization of the magnetic contributions in the diffraction pattern, the intensity difference between the PM (10 K) and the low-temperature (1.5 K) measurement is calculated and shown in Fig. 7.23 for the Mn-rich compounds measured with high resolution at POWGEN. This difference reveals several sharp peaks with increasing amplitude for higher x values. The peak positions can be unambiguously indexed by a magnetic UC that is doubled in c direction (see labels in Fig. 7.23). Note that no reasonable indexing of the observed magnetic reflections is possible by any spurious phase identified in Sec. 7.2.3, confirming their affiliation to the primary $Ba_2Cu_{1-x}Mn_xGe_2O_7$ phase. As $h + k$ is odd for all magnetic peaks, this suggests an AFM arrangement for the magnetic moments in the ab plane. Combining this conclusion with the doubling of the magnetic UC in c direction, a magnetic structure as reported for $Ba_2MnGe_2O_7$ (see

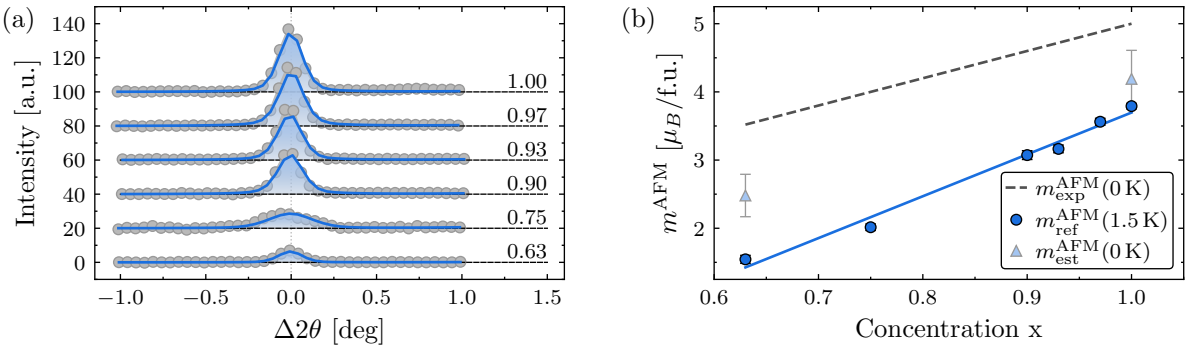

Figure 7.24.: (a) Comparison between the observed (gray circles) and refined (blue lines) magnetic intensities from PD measurements on $Ba_2Cu_{1-x}Mn_xGe_2O_7$ at 1.5 K assuming an AFM model as discussed in the text. The different concentrations x are labeled on the right side of the figure. The curves are shifted vertically by 20 for clarity. $\Delta 2\theta$ denotes the difference in two theta to the $(10\frac{1}{2})$ reflection. (b) The refined AFM moment ($m_{\mathrm{ref}}^{\mathrm{AFM}}$) as function of x at 1.5 K. The blue solid line serves as a guide to the eye and is a linear fit to the data. The gray dashed line indicates the $T = 0$ K expectation ($m_{\mathrm{exp}}^{\mathrm{AFM}}$) resulting from the corresponding mixture of Cu^{2+} and Mn^{2+} ions with spin-only moments of $1\,\mu_B$ and $5\,\mu_B$, respectively. The triangular symbols indicate the estimation of the saturated $T = 0$ K moment ($m_{\mathrm{exp}}^{\mathrm{AFM}}$) from the extrapolation in Fig. 7.25 discussed in the text.

Sec. 2.2.3) can be clearly identified for the Mn-rich $Ba_2Cu_{1-x}Mn_xGe_2O_7$ compounds.

A refinement of the low-temperature patterns using the *Jana2006* software and a corresponding AFM model provides a satisfactory agreement with the measured magnetic contributions. This is exemplified for the Mn-rich compounds in Fig. 7.24(a) by the comparison between the observed and calculated magnetic intensity of the strong $(10\frac{1}{2})$ magnetic Bragg reflection. Note that the refined structural parameters at 1.5 K show no significant differences to those presented and discussed in Sec. 7.2.3 for 10 K. The refined AFM moments at 1.5 K are illustrated in Fig. 7.24(b) and linearly increase for higher Mn concentrations. Although this linear dependency complies with a x dependent mixture of Cu^{2+} and Mn^{2+} moments with the latter being larger, the refined values are clearly lower than expected from the spin-only moments of $1\,\mu_B$ for Cu^{2+} and $5\,\mu_B$ for Mn^{2+} (dashed line in Fig. 7.24(b)), and thus require a closer inspection.

Comparing the refined ($m_{\mathrm{ref}}^{\mathrm{AFM}}$) and expected ($m_{\mathrm{exp}}^{\mathrm{AFM}}$) AFM moments in Fig. 7.24(b), an increase in their difference is clearly evident towards smaller x values, which can also be expressed by their ratio $m_{\mathrm{ref}}^{\mathrm{AFM}}/m_{\mathrm{exp}}^{\mathrm{AFM}}$, decreasing from around 75% for $x = 1.00$ to only 45% for $x = 0.63$. The reason for this might be connected to the x dependent T_N values, showing a similar reduction towards the equally mixed compounds from HC measurements in Fig. 7.10(d). Thus, the ratio $\Delta T/T_N$ decreases likewise from around 60% for $x = 1.00$ to only 25% for $x = 0.63$, with ΔT the difference between T_N and the measurement temperature of 1.5 K. In particular for the latter compound, this implies that the measurement temperature is very close to T_N and the ordered magnetic moment might not yet be saturated as assumed for $m_{\mathrm{exp}}^{\mathrm{AFM}}$ in Fig. 7.24(b).

To investigate the temperature dependence of the ordered magnetic moment in the $x = 0.63$ and 1.00 samples in the frame of the PD experiment at POWGEN, the temperature was slowly increased from 1.5 K to 8 K and the diffraction patterns continuously

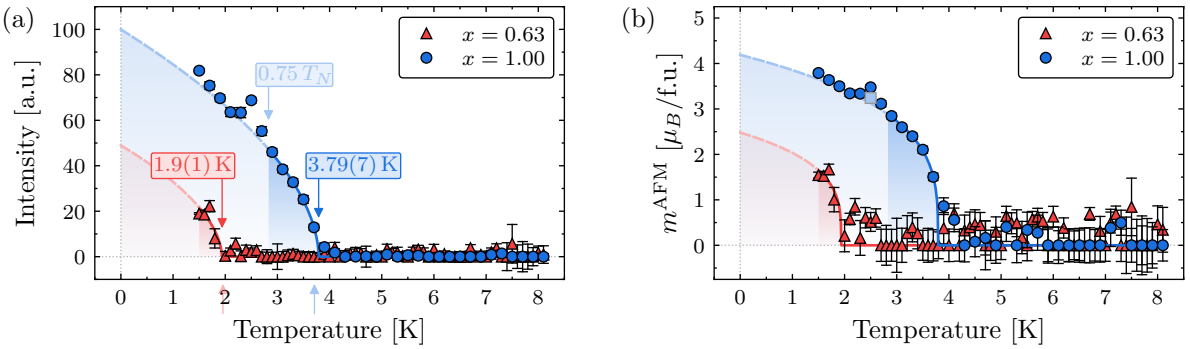

Figure 7.25.: (a) Intensity for the purely magnetic $(10\frac{1}{2})$ reflection as function of the temperature from PD on $Ba_2Cu_{1-x}Mn_xGe_2O_7$ compounds with $x = 1.00$ (blue circles) and 0.63 (red triangles). The solid lines are critical exponent fits according to Eq. (7.9) as discussed in the text. The determined T_N values are indicated and labeled. The light upward pointing arrows below the x-axis indicated the corresponding T_N values determined by HC in Sec. 7.3.1. (b) AFM moment estimated as function of the temperature in the two $Ba_2Cu_{1-x}Mn_xGe_2O_7$ compounds, denoted by respective colors and symbols as in (a). The estimation is based on the connection $m \propto \sqrt{I_M}$ and scaled by the corresponding AFM moment values for 1.5 K given in Fig. 7.24(b). The light blue rectangular symbol at 2.5 K represents the AFM moment determined by unpublished neutron diffraction measurements of Sazonov *et al.* on the same $Ba_2MnGe_2O_7$ single crystal as used in Sec. 7.5.1.

measured in event-driven TOF mode. Using the *Mantid* software, the resulting data was binned in 0.1 K and 0.2 K steps (around 5% of T_N) for the $x = 0.63$ and 1.00 sample, respectively. For each temperature step, the intensity I_M at the position of the magnetic $(10\frac{1}{2})$ reflection was fitted to a Gaussian function and is shown for both compounds in Fig. 7.25(a). Clear to see is a significant increase of I_M with decreasing temperature below T_N that is typically described close to T_N by a power law dependency

$$I_M = I_0 \left(\frac{T_N - T}{T_N} \right)^{2\beta} \tag{7.9}$$

where I_0 is the magnetic intensity at 0 K and β the critical exponent of the magnetic moment $m \propto \sqrt{I_M}$ [294]. A corresponding fit to the measured intensities close to the transition temperature (shown as solid blue line in Fig. 7.25(a) with $T/T_N > 0.75$) reveals $T_N = 3.79(7)$ K and $\beta = 0.27(4)$ for $x = 1.00$. This transition temperature is consistent with the value of 3.71(5) determined from HC measurements in Sec. 7.3.1. The critical exponent is somewhat lower than the expected value of 0.345 for a three dimensional system from the XY model [294]. This reduced β value indicates a two dimensional AFM characteristic for $Ba_2MnGe_2O_7$, resulting from its layered structure discussed in Secs. 2.1 and 7.3.2, and is similar to the $\beta = 0.21(4)$ reported for $Ba_2CoGe_2O_7$ in Ref. [112]. Note that a continuation of the fitted critical exponent curve (dashed blue line in Fig. 7.25(a)) provides a good estimation for the low-temperature values.

For the $x = 0.63$ compound, only the onset of the magnetic intensity emerging at low temperatures is probed; thus, only a strongly limited number of datapoints with a significant magnetic intensity are measured. In addition, they have a larger uncertainty compared to the $x = 1.00$ intensities due to the required finer binning for the around two

times smaller T_N value. Although the values can be utilized for a rough estimate of I_0 and T_N from Eq. (7.9), a refinement of β is not possible. Thus, β was assumed as refined for $x = 1.00$. The fit curve, shown as red line in Fig. 7.25(a), results in $T_N = 1.9(1)$, which is consistent with the value of 2.0(1) determined from HC in Sec. 7.3.1.

As the magnetic moment is proportional to the square root of I_M, the results in Fig. 7.25(a) can be used to estimate the ordered AFM moment value at low temperatures as shown in Fig. 7.25(b) based on the refinement results presented in Fig. 7.24(b) for 1.5 K. In addition, the curves of the critical exponent fit and their continuation are shown by solid and dashed lines, respectively. This continuation provides an estimation for the AFM moment at 0 K of $m_{\text{est}}^{\text{AFM}} = 2.5(3)\,\mu_B$ for the $x = 0.63$ and $4.2(4)\,\mu_B$ for the $x = 1.00$ compound. These 0 K values are indicated in Fig. 7.24(b) by triangular symbols and are clearly closer to the expectation given by the dashed line. It is important to note that the uncertainty of $m_{\text{est}}^{\text{AFM}}$ for $x = 0.63$ should be even larger because the available number of data points with a significant magnetic intensity for this compound is very low and β was not refined but only approximated from $x = 1.00$.

Calculating the ratio $m_{\text{est}}^{\text{AFM}}/m_{\text{exp}}^{\text{AFM}}$ indicates that $m_{\text{est}}^{\text{AFM}}$ is reduced by 29(9)% and 16(8)% compared to the theoretical spin-only value at 0 K for the $x = 0.68$ and 1.00 compound, respectively. Taking into account the large additional uncertainty of $m_{\text{est}}^{\text{AFM}}$ for $x = 0.68$ discussed above, these values are somewhat close to the reduction of almost 10% evidenced in the sister compound $Ba_2CoGe_2O_7$ by temperature-dependent ND in Ref. [112]. For this compound, the smaller ordered AFM moment compared to the high-field saturation magnetization is attributed to single ion anisotropy (SIA) effects, causing an energy gap between the $S_z = 1/2$ ground state of Co^{2+} and the $S_z = \pm 3/2$ spin states. Similar effects might occur in Mn-rich $Ba_2Cu_{1-x}Mn_xGe_2O_7$ as SIA proved to be present in $Ba_2MnGe_2O_7$ (see Sec. 2.2.3). The temperature-dependent results on the $x = 1.00$ compound are additionally supported by unpublished neutron diffraction measurements of Sazonov *et al.* on the same $Ba_2MnGe_2O_7$ single crystal as used in Sec. 7.5.1. These measurements revealed an AFM moment of around $3.2\,\mu_B$/Mn at 2.5 K, which is consistent with the results on the $x = 1.00$ powder sample as visible in Fig. 7.24(b) by the light blue rectangular symbol. Interestingly, Masuda *et al.* [15] report a value of of $4.66(6)\,\mu_B$/Mn from their neutron measurements down to 1.7 K, whereas our results in Fig. 7.24(b) indicate only a moment of around $3.6\,\mu_B$/Mn at that temperature. However, as no refinement details are given and only a temperature-dependent intensity of the $(10\frac{1}{2})$ reflection is presented, this magnetic moment value might also be an estimate for $T = 0$ K rather than a result at the lowest measurement temperature of 1.7 K. In this case, a somewhat reasonable correspondence with our estimation of $4.2(4)\,\mu_B$/Mn at 0 K can be noticed.

7.6. Conclusions

The nuclear and magnetic structure of the $Ba_2Cu_{1-x}Mn_xGe_2O_7$ solid solution series in the PM and long-range ordered phases has been comprehensively studied by macroscopic measurements and diffraction. In the PM phase, laboratory X-ray and high-resolution

neutron powder diffraction, conducted on a series of polycrystalline $Ba_2Cu_{1-x}Mn_xGe_2O_7$ compounds in Sec. 7.2, provided precise structural parameters and revealed their temperature and x dependency. Contributions from spurious phases were successfully identified and characterized in a multi-pattern Rietveld refinement. The phonon contribution to the specific heat in $Ba_2Cu_{1-x}Mn_xGe_2O_7$ was analyzed in Sec. 7.3.1 and precise x dependent Curie-Weiss parameters provided in Sec. 7.3.2. Additional magnetization measurements for single crystals of the end compounds revealed an easy-axis type anisotropy in the susceptibility for $Ba_2CuGe_2O_7$, which could be confirmed by PND measurements at 10 K in Sec. 7.4.1. In $Ba_2MnGe_2O_7$, no clear anisotropy was found for the susceptibility by the magnetization and PND measurements in Secs. 7.3.2 and 7.5.1, respectively. These results are consistent with reports in the literature and the expectation from the discussions in Secs. 2.2.1 and 2.2.3.

Based on the low-temperature heat capacity and magnetization measurements in Sec. 7.3, the concentration x and temperature-dependent magnetic phase diagram of the $Ba_2Cu_{1-x}Mn_xGe_2O_7$ solid solution series and its magnetic field dependency were carefully outlined for the first time. This indicated two different ordered magnetic phases for the Cu- and Mn-rich sides with transition temperatures between 2 K and 4 K. Applying high-resolution neutron powder diffraction at low temperatures of 1.5 K, an incommensurate AFM cone (see Fig. 2.5(b)) and a commensurate AFM structure (see Fig. 2.7) were identified and characterized for the Cu- and Mn-rich compounds in Secs. 7.4.4 and 7.5.2, respectively. For the latter, the temperature dependency of the magnetic contribution was additionally studied, revealing a reduced critical exponent that suggest a 2D-like behaviour as reported, e.g., in $Ba_2CoGe_2O_7$. This detailed information about the nuclear and magnetic structure of the $Ba_2Cu_{1-x}Mn_xGe_2O_7$ solid solution series will serve as a valuable reference for further experimental and theoretical studies. In particular, the presence of the strong AFM cone structure in the mixed $Ba_2Cu_{1-x}Mn_xGe_2O_7$ compound with $x = 0.50$ provides promising characteristics towards novel magnetic structures like the stable skyrmion phase suggested for $Ba_2CuGe_2O_7$ in Ref. [37]. In addition, we could identify $x_c = 0.57(1)$ as critical concentration between the two ordered phases and a compound of that composition might emerge a novel phase coexistence or even a quantum critical behavior. Thus, we anticipate a high potential in synthesizing and studying Cu-rich mixed $Ba_2Cu_{1-x}Mn_xGe_2O_7$ single crystals and further powders of critical ($x \approx 0.57$) composition; however, this is beyond the scope of this thesis.

Complementary to the exhaustive studies of the incommensurate magnetic structure in the literature, a detailed insight of the commensurate magnetic ordering in the different phases of $Ba_2CuGe_2O_7$ was provided in Sec. 7.4.2 by PND measurements. The evidenced imbalance between 180° domains confirms the presence of a WFM moment in all $Ba_2CuGe_2O_7$ phases with a commensurate AFM moment. Based on the alignment of this WFM to AFM moment, the sign of the D_z component of the DMI vector in $Ba_2CuGe_2O_7$ was unambiguously revealed in Sec. 7.4.3 for the first time and proves to be opposite to the one determined in $Ba_2CoGe_2O_7$. The implications of this DMI sign on the macroscopic properties were shown to be consistent with the electric polarization measurements reported in Ref. [86] and might serve as basis for theoretical models, numerical simulations and further experiments.

8. Magnetization density distribution in $Ba_2TGe_2O_7$

For the refinements of neutron diffraction data on $Ba_2TGe_2O_7$ (T = Cu, Co, Mn) in the previous Chaps. 6 and 7, the magnetic form factor was approximated by exponential functions based on the magnitude q of the scattering vector as proposed in Ref. [150] and applied in Eqs. (3.9) to (3.12). However, this assumption implies a spherical magnetization density distribution, which may not be fulfilled for the TM ions in some crystal field environment as, for example, shown in the pioneer works with PND on systems like Fe_3Al [295], Mn_2Sb [296], iron [297], $MnCO_3$ [204], $CoCO_3$ [298] and Fe_2B [299].

To identify potential deviations from the assumed spherical magnetization density distributions for $Ba_2TGe_2O_7$, the magnetic form factor is directly calculated from the measured asymmetry values in the PM phase for all three compounds. As their space group $P\bar{4}2_1m$ is noncentrosymmetric, Eq. (D.3) for the magnetic Fourier components in the PM phase needs to be modified for this calculation to

$$\begin{aligned} F_{\mathrm{M}} &= \left(\frac{2\mu_B}{\gamma_N r_0}\right) \frac{P\,\mathrm{Re}[N]}{A} \left(1 \pm \sqrt{1 - \Bigg(\underbrace{\frac{A}{P\sin(\rho)}\frac{|N|}{\mathrm{Re}[N]}}_{x}\Bigg)^2}\right) \\ &\overset{x\ll 1}{=} \left(\frac{2\mu_B}{\gamma_N r_0}\right) \frac{A}{2P\sin^2(\rho)} \frac{|N|^2}{\mathrm{Re}[N]} \left(1 + \mathcal{O}\left(x^2\right)\right). \end{aligned} \tag{8.1}$$

Note that directly solving for F_{M} in this noncentrosymmetric system is only possible as the magnetic ions form a centrosymmetric structure, and thus F_{M} is always real, whereas N is generally complex. Evaluating the magnetic Fourier components for FM-type reflections in the field-dependent reference system with $\mathbf{x} \parallel \mathbf{B}$ provides

$$F_{\mathrm{M}}^{\mathrm{FM}} = 2m_x^{\mathrm{FM}} e^{-W_T} f(\mathbf{q}), \tag{8.2}$$

which can be directly solved for the observed magnetic form factors by assuming the TM ions Debye-Waller factor W_T as given by U^{iso} (see Eq. (3.5)) and m_x^{FM} according to the restricted refinement results listed in Tables G.1, 6.2 and 7.8 for T = Cu, Co and Mn, respectively. It is important to note that these calculated $f(\mathbf{q})$ values for the different measured reflections $\mathbf{q}$ should collapse into one line $f(q)$ for a spherical magnetization density distribution, regardless of its particular radial dependence (see Chap. 3).

The magnetic form factors calculated from Eqs. (8.1) and (8.2) as function of q for the FM-type reflections measured at 10 K are visualized for all three studied compounds in

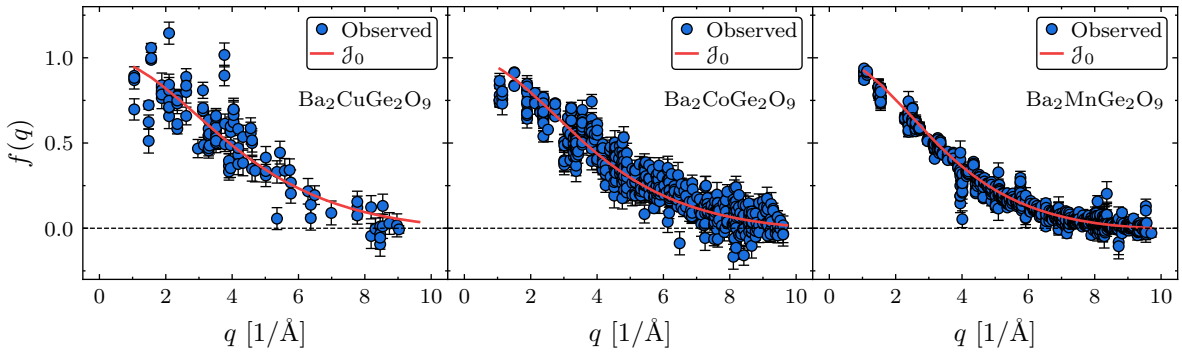

Figure 8.1.: Comparison between the magnetic form factor of $Ba_2TGe_2O_7$ (T = Cu, Co and Mn) calculated directly from the at 10 K measured FR data using Eq. (8.1) (blue circles) and the expectation from the spherical model in Eq. (3.11) with a radial function as described by the empirical coefficients provided in Ref. [150] (red solid line). For clarity, only the calculated magnetic form factors with an uncertainty $\Delta f \leq 7.5\%$ are displayed in the figure.

Fig. 8.1. In addition, the expected spin-only magnetic form factor $\mathcal{J}_0$ for a spherical density distribution (see Eq. (3.9)) is shown as red line, calculated from the approximation given by Eq. (3.11) with the coefficients as listed in Ref. [150]. It is clear to see that the observed $f(\mathbf{q})$ values accumulate largely on a single line for $Ba_2MnGe_2O_7$ (right panel in Fig. 8.1) and show wide consistency with $\mathcal{J}_0$, suggesting a spherical character of the magnetization density as discussed above. Only at q around 4 Å^{-1} larger deviations from the expected $\mathcal{J}_0$ line are evident, which might be attributed to irregularities in the background for the measurements at VIP due to scattering from the sample environment as clearly visible by powder rings in Ref. [250]. In contrast for $Ba_2CoGe_2O_7$ (central panel in Fig. 8.1), a large fraction of the measured form factors shows a strong deviation from the expected $\mathcal{J}_0$ line, particularly for higher q values. Although the overall fit could be increased by including an orbital magnetic moment that provides an additional $\mathcal{J}_2$ contribution at high q (see discussion in Sec. 6.2.2), the significant spread of the observed $f(\mathbf{q})$ values, apparently not accumulating in a well defined line as for $Ba_2MnGe_2O_7$, clearly hints towards aspherical deformations. An even higher spread, most evident at lower q values, is also found in $Ba_2CuGe_2O_7$ (left panel in Fig. 8.1) and indicates similar aspherical deformations of the local magnetization density. Note that due to the very low susceptibility in $Ba_2CuGe_2O_7$, only a very limited fraction of the measured FM-type reflections allow to extract $f(\mathbf{q})$ values with an uncertainty $\Delta f \leq 7.5\%$, which was selected as upper limit for the visualization in Fig. 8.1 for clarity.

8.1. Paramagnetic density

Encouraged by the hints in Fig. 8.1 regarding an anisotropic magnetic form factor in the $Ba_2TGe_2O_7$ compounds, an attempt was made to reconstruct a high-resolution 3D magnetization density in the UC directly from the FR measurements in the PM phase using the MEM. However, this reconstruction faces two main challenges. First, the space group is noncentrosymmetric, preventing the straightforward usage of the conventional

MEM (see Sec. 3.5.2) and, second, the resolution of a typical magnetization density reconstructed from a single FR measurement is very limited in the direction of the vertically applied magnetic field (**q** almost perpendicular to **B** for all experimentally available reflections) and thus commonly reduced to a 2D map instead of a 3D density by integration along **B**. The latter can be solved by a reconstruction of a combined 3D density distribution from multiple FR measurements with different applied magnetic field directions but no software capable of such a combined reconstruction was available.

8.1.1. Reconstruction by the advanced maximum entropy method

Within this work, a new and advanced 3D MEM for the reconstruction of magnetization densities was developed and implemented in the *AdvEnt* software package. A detailed overview of the used formalism and algorithms within this novel approach is given in Secs. 3.5.3 and D.3. By reconstructing the magnetization density directly from the measured asymmetry values, the *AdvEnt* software can be applied to noncentrosymmetric structures and thus overcomes the first challenge identified above. Moreover, the possibility to treat non-collinear densities by the magnetic base vector approach (see Eq. (3.45)) in the advanced MEM allows to combine FR datasets with different magnetic field directions and values, overcoming also the second challenge discussed above. For this purpose, the magnetization density distribution $\mathbf{m}(\mathbf{r})$, depending clearly on the applied field value and direction, is rewritten in terms of a susceptibility tensor density $\chi(\mathbf{r})$ that is based on two independent components $\chi_{11}(\mathbf{r})$ and $\chi_{33}(\mathbf{r})$ for the in-plane and out-of-plane fields, respectively. As the susceptibility represents an intrinsic magnetic property, $\chi_{11}(\mathbf{r})$ and $\chi_{33}(\mathbf{r})$ are assumed to be independent from the applied magnetic field direction and value. This assumption is the minimal requirement for the reconstruction of a combined 3D density distribution and was confirmed by reconstructing individual susceptibility densities from the FR measurements, showing the same features as the combined one but with a certainly lower resolution. Thus, the magnetization density $\mathbf{m}_n(\mathbf{r}_i)$ at grid point $\mathbf{r}_i$ can be expressed for the FR dataset n with applied magnetic field $\mathbf{B}_n$ as

$$\mathbf{m}_n(\mathbf{r}_i) = \underbrace{\chi_{11}(\mathbf{r}_i)}_{f_{i,1}} \underbrace{\mathbf{B}_n^{\perp[001]}}_{\mathbf{b}_1} + \underbrace{\chi_{33}(\mathbf{r}_i)}_{f_{i,2}} \underbrace{\mathbf{B}_n^{\parallel[001]}}_{\mathbf{b}_2} \tag{8.3}$$

with magnetic field components $\mathbf{B}_n^{\perp[001]} = \hat{\mathbf{c}} \times (\mathbf{B}_n \times \hat{\mathbf{c}})$ and $\mathbf{B}_n^{\parallel[001]} = (\hat{\mathbf{c}} \cdot \mathbf{B}_n)\hat{\mathbf{c}}$, which can be identified with the orthogonal magnetic base vectors $\mathbf{b}_1$ and $\mathbf{b}_2$, respectively. Note that these base vectors for the magnetization are not normalized, but as the reconstructed image was redefined in terms of the susceptibility, the definition of the image entropy S in Eq. (3.48) is still applicable with $f_{i,1} = \chi_{11}(\mathbf{r}_i)$ and $f_{i,2} = \chi_{33}(\mathbf{r}_i)$. The total fit quality C was selected as an average of the C_n values for the individual FR datasets, defined according to Eq. (3.44). This ensures an equal weight for the different density projections represented by the directions of the applied magnetic fields.

Introducing the magnetic field-dependent base vectors for each FR dataset and selecting the MEM control parameters as suggested in Sec. 3.5.3, the *AdvEnt* software was used to reconstruct the two combined susceptibility density distributions $\chi_{11}(\mathbf{r})$

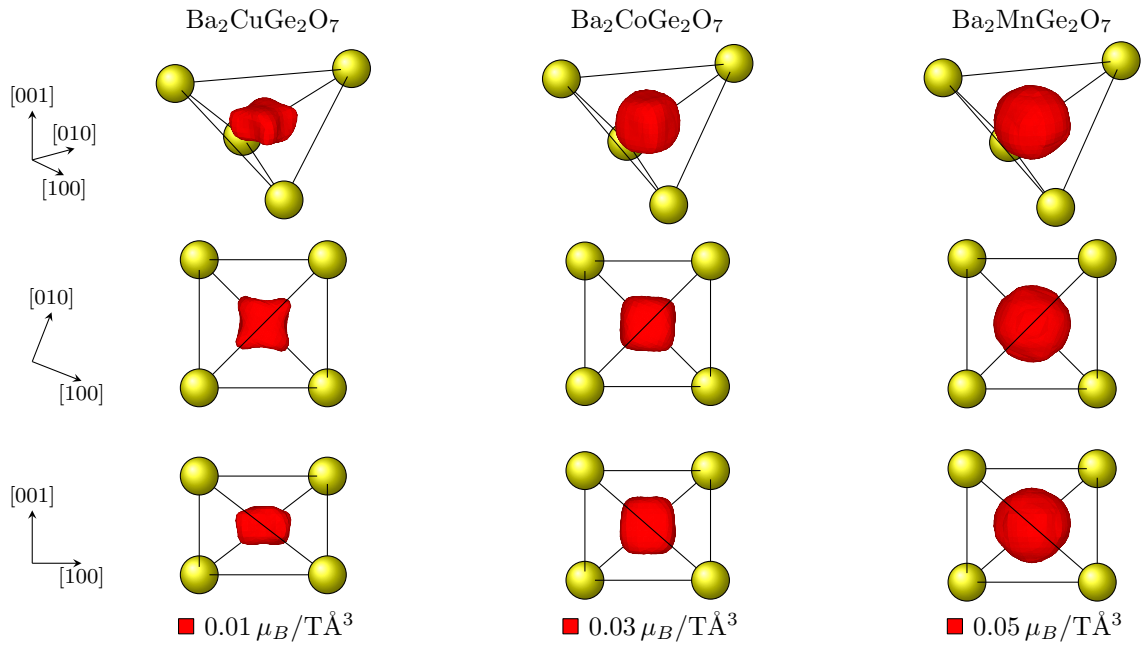

Figure 8.2.: Perspective views on the isosurface of the in-plane susceptibility density $\chi_{11}(\mathbf{r})$ in the $Ba_2TGe_2O_7$ compounds at 10 K, reconstructed by the advanced MEM approach using the *AdvEnt* software. The left, middle and right column refers to the results for T = Cu, Co and Mn, respectively. The solid black lines, connecting the oxygen atoms (yellow spheres), indicate the tetrahedral environment of the TM ions. For the reconstruction, the magnetization densities for the two T sites are assumed to be equal in the local tetrahedral environment; thus, only the one centered at the origin is shown. No density higher than the denoted isosurface value (around 10% of the maximal density) is found outside of the shown tetrahedral environment.

and $\chi_{33}(\mathbf{r})$ on a $84 \times 84 \times 54$ grid, corresponding to a grid-spacing of around 0.1 Å, for all three $Ba_2TGe_2O_7$ compounds. The χ_{11} density is displayed as isosurfaces in Fig. 8.2, which are drawn at a level corresponding to around 10% of the maximal density located at the central TM ion. For this reconstruction in the PM phase, equal susceptibility densities within the local tetrahedral environment are assumed for the two TM ion sites as they belong to the same Wyckoff position. In addition, the point group symmetry $\bar{4}$ of the T-sites is applied to the densities. This is a typical symmetry restriction also used in multipole expansions as the magnetization density is based on the atomic wave-functions that should conform to this local point-group symmetry (see Refs. [200, 298, 300] and the subsequent discussion in Sec. 8.1.2). These two basic constraints on the density, introduced by assigning the same susceptibility values to grid points related by $(\bar{x}+\frac{1}{2}, y+\frac{1}{2}, \bar{z})$ and $(\bar{y}, x, \bar{z})$, are beneficial to reduce artifacts caused by the incomplete covering of q-space and systematical uncertainties in the measurement results. A comparison between densities reconstructed with and without these constraints is given in the discussion of the $Ba_2CoGe_2O_7$ results below, emphasizing their advantage and validity.

For $Ba_2MnGe_2O_7$ (right panels in Fig. 8.2), the in-plane and out-of-plane susceptibility densities are reconstructed from the combination of the three FR measurements listed in

Table 7.8 with $C_{\mathrm{aim}} = 2$. This somewhat larger associated C_{min} value of around 1.8 can be attributed to the very strong Bragg intensities for the high mosaic $Ba_2MnGe_2O_7$ crystal measured at VIP, resulting in a clear underestimation of the measurement uncertainties by the data reduction script not considering systematic deviations. This is also evident in the consistently higher χ^2_r values in Table 7.8 compared, e.g., to those for $Ba_2CuGe_2O_7$ in Table G.1. In the displayed isosurface of χ_{11} in Fig. 8.2 for $Ba_2MnGe_2O_7$, an almost spherical shape of the density distribution is clearly evident. This agrees well with the expectation from the magnetic form factor discussed above.

In contrast for $Ba_2CoGe_2O_7$ (central panels in Fig. 8.2), a somewhat cubic shape is found in the isosurface of the χ_{11} density with its corners pointing towards the oxygen atoms in the tetrahedral Co^{2+} environments. This density is reconstructed from the FR measurements listed in Table 6.2 with $C_{\mathrm{aim}} = 1.2$. To confirm that this cubic shape is evident in the data and not a result of the assumed local $\bar{4}$ symmetry in the tetrahedral environment, a reconstruction of the susceptibility density without this symmetry constraint is given in Fig. H.1. The resulting isosurface resembles well the cubic shape of the symmetry restricted reconstruction but with slight deformations resulting from the limited q-space coverage of the measurements. This confirms the consistency of the reconstructed susceptibility densities with the expected $\bar{4}$ symmetry and validates the shape of the revealed aspherical density distribution in $Ba_2CoGe_2O_7$, which was also suggested by the strong variations in the magnetic form factor discussed above. An attempt to reconstruct the density without any constraints ($P1$), which allows also independent distributions for the two equivalent TM ion sites, yields a similar shape in the isosurfaces of the susceptibility for both Co^{2+} ions but with clearly larger deformations caused by the discussed limitations in the number of measured Bragg reflections and the measurement precision.

A similar shape but with an additional compression along the [001] direction and particularly pronounced corners is visible in the χ_{11} isosurface for $Ba_2CuGe_2O_7$ (left panels in Fig. 8.2), which was reconstructed from the VIP FR measurements listed in Table G.1 with $C_{\mathrm{aim}} = 1.5$. The additional two measurements at D3-ILL with the smaller N21 $Ba_2CuGe_2O_7$ single crystal were excluded from the combined reconstruction for consistency. This strongly non-spherical density in $Ba_2CuGe_2O_7$ represents well the severe variations found in the magnetic form factor in the left panel of Fig. 8.1.

Notably, the χ_{33} densities for all three compounds are shown in Fig. H.2 and have a similar shape to those displayed for χ_{11} in Fig. 8.2; however, the absolute scales of the densities might differ, reflecting an easy-axis ($\chi_{11} < \chi_{33}$) or an easy-plane ($\chi_{11} > \chi_{33}$) anisotropy. By integrating the susceptibility enclosed in the isosurfaces drawn at a level of 10% of the respective maximal density for χ_{11} and χ_{33}, anisotropy ratios χ_{11}/χ_{33} of around 0.75(2), 2.19(2) and 1.040(4) are calculated for T = Cu, Co and Mn, respectively. The uncertainty is estimated from the variance in the calculated ratio by changing the surface level for ±25%. These results are consistent with the expectations discussed in Secs. 2.2.1, 2.2.2 and 2.2.3 and previous refinement results in Secs. 7.4.1, 6.2.2 and 7.5.1 for T = Cu, Co and Mn, respectively.

8.1.2. Reconstruction by multipole refinement

To independently confirm the peculiar shapes of the susceptibility densities reconstructed for $Ba_2TGe_2O_7$ (T = Cu, Co and Mn) by the advanced MEM approach in the previous section, multipole (MP) refinements are applied to the FR measurements. Within this approach, implemented, for example, in the *MAG2POL* software [200], the local scalar magnetization density $m(\mathbf{r})$ is expanded in terms of the real spherical harmonics y_l^m combined with a Slater-type radial function R_n [301]. As the name already suggest, the latter describes the radial dependency of the atoms magnetization distribution in local spherical coordinates (r, θ, ϕ) and is defined as

$$R_{n_l,\zeta_l}(r) = \frac{{\zeta_l}^{n_l+3}}{(n_l+2)!} r^{n_l} e^{-\zeta_l r} \tag{8.4}$$

with the principal quantum number coefficient $n_l \geq l$, Slater parameter ζ_l, typically given in inverse units of the Bohr radius $a_0 \simeq 0.529\,\text{Å}$, and normalization

$$\int_0^\infty R_{n_l,\zeta_l}(r) r^2 \mathrm{d}r = 1. \tag{8.5}$$

In contrast, the real spherical harmonics, which form a complete set of orthogonal functions, describe the angular dependency of the local magnetization distribution and can be expressed as

$$y_l^m = \begin{cases} \frac{(-1)^m}{\sqrt{2}} \left(Y_l^m + Y_l^{-m}\right) & \text{for } m > 0 \\ Y_l^0 & \text{for } m = 0 \\ \frac{(-1)^m}{\sqrt{2}i} \left(Y_l^m - Y_l^{-m}\right) & \text{for } m < 0 \end{cases} \tag{8.6}$$

with $Y_l^m(\theta, \phi)$ the standard complex spherical harmonics, which employ the Condon-Shortley phase factor. These functions depend on the quantum numbers l and m and are commonly known as the angular dependency of the hydrogen orbitals. Explicit forms of y_l^m can be found, for example, in [301]. As the square of of y_l^m is a probability distribution, it obeys

$$\int |y_l^m|^2 \mathrm{d}\Omega = 1. \tag{8.7}$$

For the expansion of the magnetization density, however, the charge density-normalized real spherical harmonics $d_l^m \propto y_l^m$ are preferred whose normalization is given according to

$$\int |d_l^m| \mathrm{d}\Theta = \begin{cases} 1 & \text{for } l = 0 \\ 2 & \text{for } l > 0 \end{cases}. \tag{8.8}$$

Thus, the scalar magnetization density can be finally expressed as

$$m(r, \theta, \phi) = \sum_l R_{n_l,\zeta_l}(r) \sum_{m=-l}^{l} C_l^m d_l^m(\theta, \phi) \tag{8.9}$$

with non-zero coefficients C_l^m based on the local symmetry [300, 301]. For the TM ion sites in $Ba_2TGe_2O_7$ with point group symmetry $\bar{4}$ and a local XYZ reference system

as shown in Fig. 2.14(a), the allowed coefficients up to $l = 4$ are C_0^0, C_2^0, $C_3^{\pm 2}$, C_4^0 and $C_4^{\pm 4}$. By Fourier transformation for a Bragg reflection $\mathbf{q}$ expressed in the local spherical coordinates, the scalar magnetic scattering amplitude

$$mf(q,\, \theta_q,\, \phi_q) = \sum_l i^l \left\langle j_l(q) \right\rangle \sum_{m=-l}^{l} C_l^m d_l^m(\theta_q,\, \phi_q) \tag{8.10}$$

can be directly calculated from the coefficients of the MP expansion with $m = C_0^0$ and the Fourier-Bessel transform of the radial density

$$\left\langle j_l(q) \right\rangle = \int_0^\infty R_{n_l,\zeta_l}(r) j_l(qr) 4\pi r^2 \mathrm{d}r, \tag{8.11}$$

defined as the integration of the Slater-type radial functions scaled by the well known spherical Bessel functions j_l [301]. Analytical closed-form expressions for $\langle j_l(q) \rangle$ are given in Ref. [301] up to $l = 7$ and $n_l = 6$.

In MP refinement, the limited resolution provided by a single FR dataset discussed in Sec. 8.1.1 is typically less critical as the reconstruction of the magnetization density is reduced to the refinement of only a few parameters but the lack of spatial information in some directions might lead to strong correlations between individual parameters. However, to extract very precise values for all allowed coefficients C_l^m and the Slater parameter ζ_l, a combined refinement of the different datasets is clearly beneficial, but this option is so far not provided by any commonly available refinement software applicable to polarized neutrons. Thus, we have extended the *AdvEnt* software by an additional least squares refinement option for $\boldsymbol{\tau} = 0$ structures, which is based on somewhat similar functions already available from the MEM algorithm. This option is capable of refining all typical parameters used in the description of the nuclear and magnetic structure, including MP coefficients and extinction parameters, from a combined set of PND measurements (e.g. FR and SNP). The implemented least squares solver is based on the trust-region reflective algorithm provided in the *optimize.least_squares* function of the *SciPy* package [259] and uses the *Eigen* library [302] for the singular value decomposition. The uncertainty estimation of the refined parameters is based on the square root of the diagonal entries of the covariance matrix, scaled by the χ_r^2 value. Although this option was carefully tested by comparison with results provided by the MP refinement in *Mag2Pol*, it is, compared to the MEM option, still in a rather experimental stage with an only preliminary designed GUI. Nevertheless, it could be successfully applied to the FR measurements in $Ba_2TGe_2O_7$ to refine values for the in-plane and out-of-plane susceptibility and the MP parameters.

The results of the combined magnetic moment refinements, using the same FR datasets and atomic parameters as for the MEM reconstructions in the PM phase of $Ba_2TGe_2O_7$ in the previous section, are listed in Table 8.1. Prior to the MP refinement and for validation purposes, the *AdvEnt* software was used to reproduce the magnetic moment refinements with isotropic form factor directly on the combined datasets. For this case, the magnetic Fourier components are given for the FR measurement n by

$$\mathbf{F}_{\mathrm{M},n}^{\mathrm{iso}}(\mathbf{q}) \propto \left(\chi_{11} \mathbf{B}_n^{\perp[001]} + \chi_{33} \mathbf{B}_n^{\parallel[001]} \right) \mathcal{J}_0(q) \tag{8.12}$$

Table 8.1.: Results of the isotropic and multipolar magnetic moment refinements in $Ba_2TGe_2O_7$ using the *AdvEnt* software applied to the combined FR datasets measured at 10 K. As discussed in the text, the double-ζ model in Eq. (8.14) was used as radial function in the multipolar refinement of $Ba_2MnGe_2O_7$, marked by (*), with additional parameters $\lambda = 47(2)\%$ and $\zeta_\lambda = 4.70(9)/a_0$.

	Isotropic			Multipolar		
T	Cu	Co	Mn	Cu	Co	Mn
χ_{11} [μ_B/T/f.u.]	0.0194(6)	0.133(1)	0.3305(8)	0.0165(6)	0.120(1)	0.334(1)
χ_{33} [μ_B/T/f.u.]	0.0250(7)	0.0587(5)	0.318(2)	0.0231(7)	0.0545(5)	0.330(2)
χ_{11}/χ_{33}	0.78(3)	2.27(3)	1.039(7)	0.72(3)	2.21(3)	1.011(8)
ζ [$1/a_0$]				9.8(2)	8.53(5)	8.8(1)*
C_0^0				1	1	1
C_2^0				−0.13(2)	0.006(6)	−0.006(2)
C_3^{-2}				−0.01(4)	−0.01(1)	0.001(3)
C_3^2				−0.02(4)	0.00(1)	0.004(3)
C_4^{-4}				−0.05(4)	0.01(2)	0.005(3)
C_4^0				−0.13(6)	−0.08(2)	0.001(4)
C_4^4				−0.20(4)	−0.08(1)	0.002(3)
$x_{11} = \frac{c^2}{a^2}x_{33}$	0.7(2)	0.95(8)	0.050(8)	0.9(3)	1.07(9)	0.062(9)
χ_r^2	1.78	2.04	3.43	1.73	1.87	3.27

with the in-plane $\mathbf{B}_n^{\perp[001]}$ and out-of-plane $\mathbf{B}_n^{\parallel[001]}$ field components defined in the previous section and the spin-only magnetic form factor $\mathcal{J}_0(q)$, calculated by the empirical approximation provided in Ref. [150]. For $Ba_2CuGe_2O_7$ and $Ba_2MnGe_2O_7$, the combined refinement results on χ_{11} and χ_{33}, listed in the first column in Table 8.1, coincide within their uncertainty with the individually refined *Mag2Pol* results presented in Secs. 7.4.1 and 7.5.1, respectively. Note that the uncertainties for the susceptibilities are significantly smaller for the combined refinements, suggesting a higher precision. For $Ba_2CoGe_2O_7$, slightly larger susceptibilities are found compared to Sec. 6.2.2, which can be attributed to the significantly larger refined isotropic extinction parameter x_{11} that was selected to be 0.073(8) in Sec. 6.2.2 as determined by ND in Table 6.2. For the $T =$ Cu and Mn compounds, the refined x_{11} values are also larger than the ones assumed for the individual refinements in Secs. 7.4.1 and 7.5.1, but are on a similar scale. In summary, *AdvEnt* provides consistent results, validating its combined refinement option and confirming the individual refinement results of *Mag2Pol* presented above.

For the case of MP refinements (right column in Table 8.1), the magnetic Fourier components are given for the FR dataset n with applied magnetic field $\mathbf{B}_n$ by

$$\mathbf{F}_{\mathrm{M},n}^{\mathrm{mult}}(\mathbf{q}) \propto \left(\chi_{11}\mathbf{B}_n^{\perp[001]} + \chi_{33}\mathbf{B}_n^{\parallel[001]}\right) \sum_l i^l \langle j_l(q)\rangle \sum_{m=-l}^{l} C_l^m d_l^m(\theta_q, \phi_q) \tag{8.13}$$

with non-zero coefficients C_l^m up to $l = 4$ according to the local $\bar{4}$ symmetry listed above and $C_0^0 = 1$ for normalization. As only the unpaired electrons of the $3d$ orbitals should

contribute to the magnetic density (see Sec. 8.1.3), equal radial Slater-type functions are used for the multipoles ($\zeta_l = \zeta$) and $n_l = 4$ is selected based on the suggestion for first-row TM ions in Ref. [301]. Compared to the isotropic refinement, a slight improvement in the fit quality, indicated by a decrease of χ^2_r, is noticeable for the T = Cu and Co compounds. This improvement is associated with significant contributions by the C^2_0, C^4_0 and C^4_4 multipoles for both compounds, emphasizing their anisotropic density characteristic. Their radial parameters ζ are slightly higher than the expected values of around $8.8/a_0$ and $7.9/a_0$ for the ground states of the $3d$ subshells of the isolated Cu and Co atoms, respectively [301]. This increase, denoting a slight compression of the magnetization density, might be associated with the influence of the negatively charged ligands on the electron density of the TM ions in the tetrahedral crystal field environment. For the susceptibilities, a slight reduction of the in-plane and out-of-plane components is noticeable for both compounds, whereas the anisotropy ratio χ_{11}/χ_{33} remains constant within the uncertainty.

In contrast for $Ba_2MnGe_2O_7$, the assumed simple Slater-type radial function was insufficient to properly describe the Mn^{2+} magnetization density, resulting in $\chi^2_r = 7.27$, which is significantly higher than for the isotropic model ($\chi^2_r = 3.43$). To permit a somewhat higher complexity in $R(r)$, the radial dependence for T = Mn is modified to a double-ζ Slater-type function that is given by

$$R(r) = (1 - \lambda)R_{n_l,\zeta}(r) + \lambda R_{n_l,\zeta_\lambda}(r) \tag{8.14}$$

with mixing parameter $0 \leq \lambda \leq 1$ and normalization like in Eq. (8.5) [301]. As listed in Table 8.1, this significantly improved the fit quality to $\chi^2_r = 3.27$ with radial parameters $\lambda = 47(2)\%$, $\zeta = 8.8(1)/a_0$ and $\zeta_\lambda = 4.70(9)/a_0$. Note that the radial parameters are defined such that $\zeta > \zeta_\lambda$, and thus ζ reflects a compressed contribution to the radial function, whereas ζ_λ reflects an extended one. A theoretical estimation of these radial parameters in the double-ζ model is given by Ema *et al.* [303] based on Roothaan-Hartree-Fock (RHF) calculations for isolated atoms in the ground state. These calculations provide for the the compressed and extended contribution of the double-ζ radial function for isolated Mn atoms a mixing of $\lambda^{\text{exp}} = 65\%$ and Slater parameters of $\zeta^{\text{exp}} = 11.51/a_0$ and $\zeta^{\text{exp}}_\lambda = 5.00/a_0$, respectively. Thus, the refined ζ_λ is close to the expected value whereas ζ is somewhat lower than ζ^{exp}, suggesting a slight expansion of the compressed contribution compared to the expectation. However, this expansion is compensated by a strong enhancement of the compressed contribution in the MP refinement results, indicated by the clearly smaller value for λ than for λ^{exp}. This eventually leads to an overall compression of the MP density in $Ba_2MnGe_2O_7$ compared to the expected one for isolated Mn atoms, like it was found in $Ba_2CuGe_2O_7$ and $Ba_2CoGe_2O_7$ as well. Thus, it might be analogously attributed to the influence of the tetrahedral crystal environment as discussed above. Note that an attempt to refine a double-ζ model analogously for the $Ba_2CuGe_2O_7$ and $Ba_2CoGe_2O_7$ compounds led to unstable results with no significant improvement in χ^2_r. For the Mn susceptibilities in the MP refinement, there are only slight difference to the values of the isotropic one and the resulting ratio χ_{11}/χ_{33} very close to 1 supports the expected almost isotropic χ tensor. Moreover, the allowed MP parameters C^m_l with $l > 0$ differ only insignificantly from zero, confirming the mostly

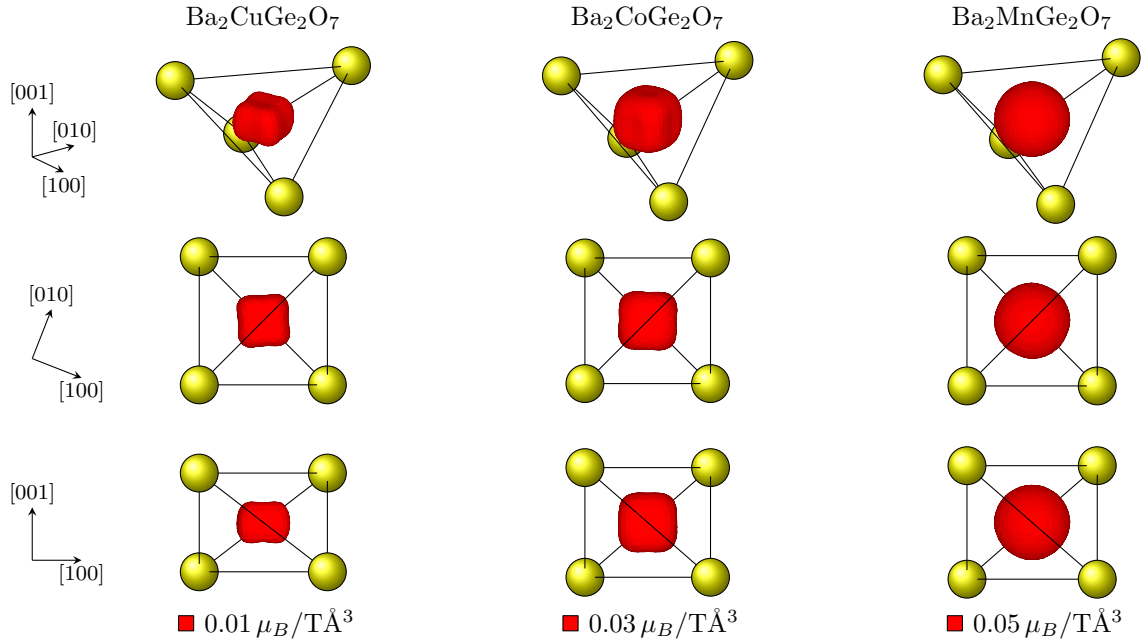

Figure 8.3.: Perspective views on the isosurface of the in-plane susceptibility density $\chi_{11}(\mathbf{r})$ in the $Ba_2TGe_2O_7$ compounds calculated from the multipole refinement results at 10 K listed in Table 8.1. The layout is analogous to that described in Fig. 8.2 with the same values for the isosurface levels. No significant density is associated with grid points outside of the shown tetrahedral environment.

spherical density distribution in $Ba_2MnGe_2O_7$, previously suggested by the calculation of the magnetic form factors in Fig. 8.1 and the MEM reconstruction in Fig. 8.2.

A visualization of the expected susceptibility density distributions for the in-plane χ_{11} components, numerically calculated from the results of the MP refinement on a $84 \times 84 \times 54$ grid in the UC, is given in Fig. 8.3 for all three $Ba_2TGe_2O_7$ compounds. Clear to see is a strong aspherical deformation of the density distribution for $T =$ Cu and Co, corresponding closely to the results identified by the advanced MEM reconstruction in Fig. 8.2, which uses the same isosurface levels. For $Ba_2MnGe_2O_7$, only a very weak deformation along c is suggested by the MP refinement resulting from the finite C_2^0 component, which is, however, too small to be visible in the illustration.

For a quantitative comparison between the results of the MEM and MP reconstruction, the presented susceptibility densities were averaged over spherical surfaces with radius r centered at the position of the TM ion. These averaged densities $\overline{\chi}_{ii}(r)$, normalized to the central value $\overline{\chi}_{ii}(0)$, are shown in Fig. 8.4 by solid lines to illustrate the radial dependency. The stepsize of 0.1 Å in r was selected to be consistent with the grid-spacing. In addition, the variance $\sigma^2_{ii}(r)$ of the susceptibility density over these surfaces was calculated and provides a good measure for aspherical deformations. The square-root of this variance, normalized also by $\overline{\chi}_{ii}(0)$, is shown in Fig. 8.4 by dotted lines. As the MEM provides two completely independent densities for the in-plane and out-of-plane susceptibility, visualized in Figs. 8.2 and H.2, they are separately analyzed and shown in Fig. 8.4 by black and red triangular symbols, respectively. In contrast for

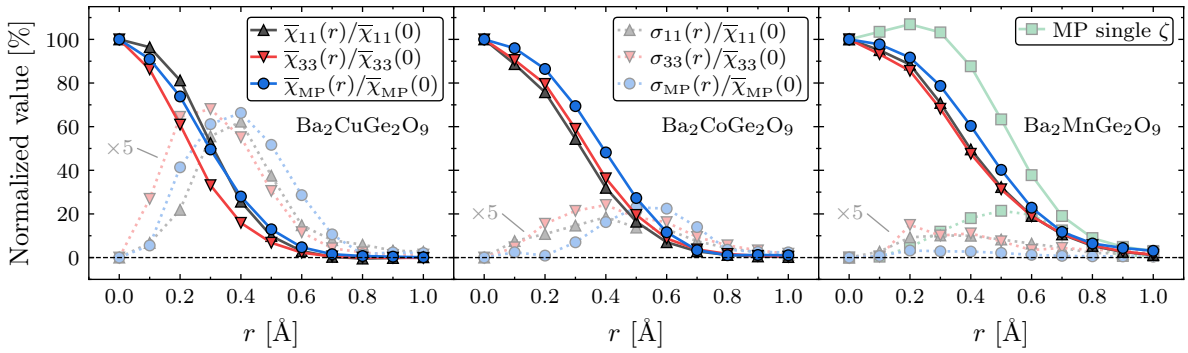

Figure 8.4.: The spherically averaged susceptibility densities (solid lines) and the square-root of their variance (dotted lines), normalized to the central density value at the TM ion position, for the different methods in the $Ba_2TGe_2O_7$ compounds at 10 K. The $\overline{\chi}_{11}$ and $\overline{\chi}_{33}$ values and their variances σ_{11} and σ_{33} (black and blue triangular symbols) are calculated from the MEM susceptibility densities displayed in Figs. 8.2 and H.2, respectively. In contrast, $\overline{\chi}_{\mathrm{MP}}$ and σ_{MP} (blue circular symbols) are based on the susceptibility density of the MP refinement, visualized in Fig. 8.3. The spherically averaged density and variance of the MP refinement with single-ζ radial function and large residuals (see discussion in the text) are shown for completeness (right panel, green squares). Note that the normalized variances are scaled by a factor of five for visibility.

the MP refinement, the in-plane and out-of-plane susceptibility densities differ only by the scaling factors χ_{11} and χ_{33} listed in Table 8.1 that cancel out by the normalization. Thus, $\overline{\chi}_{\mathrm{MP}}(r)$ and $\sigma_{\mathrm{MP}}(r)$ are representative for both MP densities and are illustrated in Fig. 8.4 by blue circular symbols.

For $Ba_2MnGe_2O_7$ (right panel of Fig. 8.4), there is no significant difference between the normalized $\overline{\chi}_{11}$ and $\overline{\chi}_{33}$ values of the MEM reconstruction as expected from the visual comparison of Figs. 8.2 and H.2. Both densities show a continuous decrease of the average value with r that reaches the half maximum (i.e. $\overline{\chi}(r_{\mathrm{HM}})/\chi(0) = \frac{1}{2}$) at $r_{\mathrm{HM}} = 0.39(1)$ Å. This radius is determined by a linear interpolation and the uncertainty is estimated by the variance in r_{HM} if the desired value for $\overline{\chi}(r_{\mathrm{HM}})/\chi(0)$ is changed by ±5%. The average $\overline{\chi}_{\mathrm{MP}}$ of the MP density has a similar radial dependency but with a somewhat increased radius of $r_{\mathrm{HM}} = 0.45(1)$ Å. This indicates a minor expansion of the MP density compared to the MEM results and might be directly attributed to the nature of the MEM algorithm, selecting the lowest possible image values, and thus the most compressed density, compatible with the FR data. However, also the restrictions in the MP density introduced by assuming a particular radial and angular function (see Eq. (8.9)) might cause such differences to the MEM results, which are only restricted by the crystal symmetry. This is clearly evident in the discussed MP refinement with a single-ζ Slater-type radial function that was rejected for $Ba_2MnGe_2O_7$ due to its high residuals. The radial dependency of its spherically averaged susceptibility density is shown in Fig. 8.4 by green squares and as expected from its bad fit quality, a strong deviation from the MEM results is clear to see. Remarkably enough, this strong deviation almost vanishes for the double-ζ model (blue circular symbols), including only one additional parameter in the radial function, and thus emphasizing the importance of a proper MP model. The calculated variance σ_{MP} of the susceptibility density from the MP refinement with

double-ζ radial function (blue circles connected by dotted line) has a consistently low value as expected from the very weak deformations identified in the discussion above. For the MEM density, this variance is only slightly higher, indicating aspherical deformations on a similar level. Note that there is inherently a finite background noise present in the reconstructed MEM density, which is absent in the calculated MP density and might cause an additional low-level contribution to σ_{ii}.

For $Ba_2CoGe_2O_7$ (central panel of Fig. 8.4), there is a small difference between the normalized $\overline{\chi}_{11}$ and $\overline{\chi}_{33}$ values of the MEM reconstruction, with the latter being slightly higher. This difference might be attributed to the strong in-plane anisotropy in $Ba_2CoGe_2O_7$ (see Sec. 2.2.2), which could induce some deformations in the suppressed χ_{33} density. However, the discrepancy between the two spherically averaged susceptibility densities is so small that they are both characterized by the same $r_{\mathrm{HM}} = 0.33(2)$ Å. Compared to the larger r_{HM} in $Ba_2MnGe_2O_7$, this suggests a more compact $Ba_2CoGe_2O_7$ density, which is consistent with the expectation of a larger ζ value in the radial dependency of isolated Co atoms than for Mn atoms in Ref. [301]. Like for $Ba_2MnGe_2O_7$, the density of the MP refinement is slightly enlarged with $r_{\mathrm{HM}} = 0.39(1)$ Å, which might again be attributed to the nature of the MEM algorithm or to restrictions in the MP density caused by the particular choice of radial and angular function as discussed before. In the variance, there is a broad maximum visible for all $Ba_2CoGe_2O_7$ densities, clearly indicating aspherical deformations as visually evident in Figs. 8.2, H.2 and 8.3. Although the relative variance of up to around 5% for these deformations is similar for both the MP and MEM density, the maxima is centered at around 0.40 Å for the MEM results, whereas it is at a slightly larger radius of around 0.55 Å for the MP refinement. This shift might be attributed to the overall compression of the MEM density compared to the MP one.

In the case of $Ba_2CuGe_2O_7$ (left panel of Fig. 8.4), there are more significant differences between the normalized $\overline{\chi}_{11}$ and $\overline{\chi}_{33}$ values of the MEM reconstruction. Like in $Ba_2CoGe_2O_7$, the suppressed component, which is $\overline{\chi}_{11}$ for the easy-axis anisotropy in $Ba_2CuGe_2O_7$ (see Sec. 2.2.1), has a more extended density shape with $r_{\mathrm{HM}} = 0.31(1)$ Å than the enhanced one with $r_{\mathrm{HM}} = 0.24(1)$ Å. This is also faintly visible in a close comparison of the isosurfaces of the χ_{11} and χ_{33} density in Figs. 8.2 and H.2, respectively. Although both densities have the same basic shape as pointed out in Sec. 8.1.1, the corners are less pronounced in the latter, indicating the more compact radial dependency. However, it is important to note that $Ba_2CuGe_2O_7$ has the smallest susceptibility in the $Ba_2TGe_2O_7$ (T = Cu, Co and Mn) series, which leads to a comparably high relative uncertainty in the measured asymmetries. Thus, differences between $\overline{\chi}_{11}$ and $\overline{\chi}_{33}$ might also be enhanced in $Ba_2CuGe_2O_7$ due to the limited data precision. For the density of the MP model refinement, the calculated radial dependency of $\overline{\chi}_{\mathrm{MP}}$ is similar to that of $\overline{\chi}_{11}$ and the radius at half maximum is $r_{\mathrm{HM}} = 0.30(1)$ Å. Thus, the spherically averaged densities in $Ba_2CuGe_2O_7$ indicate an even higher compression than in $Ba_2CoGe_2O_7$, which is in agreement with the expectations of a larger ζ value for isolated Cu atoms than for Co atoms in Ref. [301]. With regard to the variance of the spherically averaged density, a strong maximum with normalized values up to around 15% is clear to see for all models. This suggests the most pronounced aspherical deformations within the

$Ba_2TGe_2O_7$ series for T = Cu, confirming the expectation from the isosurfaces visualized in Figs. 8.2, H.2 and 8.3. The maximum of this deformation is at a radius of around 0.3 Å for $\overline{\chi}_{33}$ and at around 0.4 Å for $\overline{\chi}_{11}$ and $\overline{\chi}_{\mathrm{MP}}$. This difference is most likely connected to the higher overall compression of the out-of-plane susceptibility density compared to the in-plane and MP one.

To summarize, we could reveal unconventional shapes for the susceptibility densities in $Ba_2TGe_2O_7$ (T = Cu, Co and Mn) at 10 K by applying our novel MEM approach in Sec. 8.1.1 and could confirm these shapes by their consistency with the results from MP refinement. This certainly raises the question of their origin, which is addressed in the subsequent section.

8.1.3. Calculation by the electronic configuration

For spin-only magnetism, which is justified due to largely quenched orbital momenta in the $Ba_2TGe_2O_7$ (T = Cu, Co and Mn) compounds (see Sec. 2.2), the magnetization density is directly proportional to the density $\rho(\mathbf{r})$ of the unpaired electrons [148]. Thus, it can be written as a sum of the absolute squares of the atomic wave functions $\Phi^m_{n,l}(\mathbf{r})$ for the unpaired electrons in states n, l and m as

$$\rho(\mathbf{r}) = \sum_{n,l,m} \left|\Phi^m_{n,l}(\mathbf{r})\right|^2 \tag{8.15}$$

with normalization

$$\int \left|\Phi^m_{n,l}(\mathbf{r})\right|^2 \mathrm{d}\,V = 1. \tag{8.16}$$

For isolated atoms in local spherical coordinates with r, θ and ϕ, the angular distribution of these atomic wave functions can be expressed by the complex spherical harmonics $Y^m_l(\theta,\,\phi)$. For the TM ions $3d$ electrons, these $Y^m_l(\theta,\,\phi)$ functions with $l = 2$ and $-l \leq m \leq l$ are illustrated in the upper half of Fig. 8.5 and suggest a rotationally symmetric density $\rho(r\,\theta) \propto |Y^m_l(\theta,\,\phi)|^2$. However, in the presence of the tetrahedral crystal environment in the $Ba_2TGe_2O_7$ compounds with oxygens at the local $(\pm a_\mathrm{O}, \pm a_\mathrm{O}, c_\mathrm{O})$ and $(\pm a_\mathrm{O}, \mp a_\mathrm{O}, -c_\mathrm{O})$ positions, the angular part of these atomic wave functions collapses to the real spherical harmonics y^m_l, which are defined in Eq. (8.6) and visualized for $l = 2$ in the lower half of Fig. 8.5. The three atomic wave functions proportional to y^1_2, y^{-1}_2 and y^{-2}_2, typically denoted as triplet (t_2) states d_{xz}, d_{yz} and d_{xy}, form an electron density with lobes mostly towards the ligand positions and are thus higher in energy. In contrast, the singlet (e) states d_{z^2} and $d_{x^2-y^2}$, proportional to y^0_2 and y^2_2, form lobes between the ligand positions, reducing their energy. This effect of the tetrahedral environment on the orbital functions is visualized by the crystal field splitting in Fig. 2.2 and is further refined by a compression of the tetrahedron ($c_\mathrm{O}/a_\mathrm{O} < 1$), slightly increasing the energy of the d_{xy} and $d_{x^2-y^2}$ states, whereas the others are lowered. Thus, the expected spin-only magnetization density for the TM ions in the $Ba_2TGe_2O_7$ compounds, having a total magnetic moment of $\mathbf{m}^\mathrm{tot}$, is given by

$$\mathbf{m}(r,\,\theta,\,\phi) = \frac{\mathbf{m}^\mathrm{tot}}{n_e} \sum_m \tilde{C}^m_2 R(r) |y^m_2(\theta,\,\phi)|^2, \tag{8.17}$$

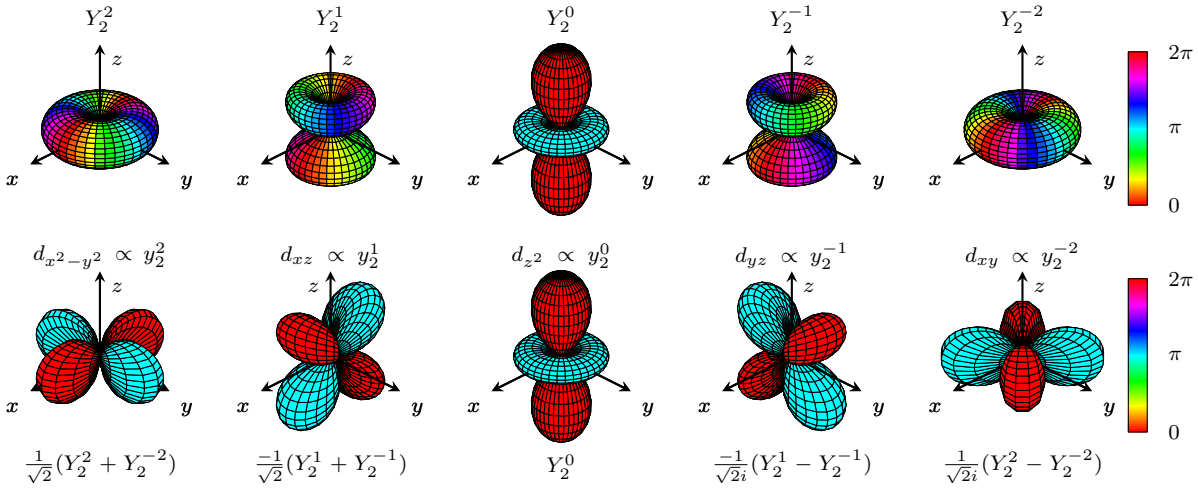

Figure 8.5.: Visualization of the angular dependency of the complex and real spherical harmonics Y_l^m (upper half) and Y_l^m (lower half) for $l = 2$, respectively. The color represents the complex phase as labeled in the color bar on the right. For the real spherical harmonics, the name of the corresponding $3d$ orbital and its relation to Y_l^m according to Eq. (8.6) is provided. The figure was created using the *tikz-3dplot* LaTeX package [304].

with a common radial distribution $R(r)$ and occupations $\tilde{C}_2^m = 1$ if there is an unpaired electron in state m and $\tilde{C}_2^m = 0$ otherwise. Thus, the total number of unpaired electrons n_e is given by $\sum_m \tilde{C}_2^m$. Note that the squared real spherical harmonics $|y_l^m(\theta, \phi)|^2$ are expandable in terms of the $d_{l'}^{m'}$ functions ($l' \leq 2l$) for simplification, which are introduced for the MP refinements in Sec. 8.1.2. For the $3d$ orbitals ($l = 2$), this relation is given in Ref. [301] by

$$\begin{pmatrix} |y_2^0|^2 \\ |y_2^{\pm 1}|^2 \\ |y_2^2|^2 \\ |y_2^{-2}|^2 \end{pmatrix} = \underbrace{\begin{pmatrix} 1 & 0.27493 & 0.36848 & 0 \\ 1 & 0.13747 & -0.24565 & 0 \\ 1 & -0.27493 & 0.061413 & 0.31831 \\ 1 & -0.27493 & 0.061413 & -0.31831 \end{pmatrix}}_{A} \cdot \underbrace{\begin{pmatrix} d_0^0 \\ d_2^0 \\ d_4^0 \\ d_4^4 \end{pmatrix}}_{\mathbf{d}(\theta,\phi)}. \tag{8.18}$$

Applying this approximation and rewriting the density in terms of the two independent susceptibility components χ_{ii} with $i \in \{1, 3\}$ yields finally

$$\chi_{ii}(r, \theta, \phi) = \chi_{ii} R(r) \mathbf{C}^\mathsf{T} \cdot A \cdot \mathbf{d}(\theta, \phi) \tag{8.19}$$

with relative orbital contributions $\mathbf{C}^\mathsf{T} = (C_{z^2}, C_{xz} + C_{yz}, C_{x^2-y^2}, C_{xy})$, which are normalized by the number of unpaired electrons compared to the occupations $\tilde{C}_2^m$ such that $\sum_i C_i = 1$. As radial distribution $R(r)$, the Slater-type functions defined in the MP refinements in Sec. 8.1.2 provide a reasonable approximation, particularly as the refined values for the ζ parameters are close to the ones theoretically expected [301, 303].

For the case of $Ba_2MnGe_2O_7$ with an electronic configuration of $[Ar]3d^5$, all $3d$ orbitals are occupied by an unpaired electron such that $\mathbf{C}_{Mn^{2+}}^\mathsf{T} = (1, 2, 1, 1)/5$. In contrast,

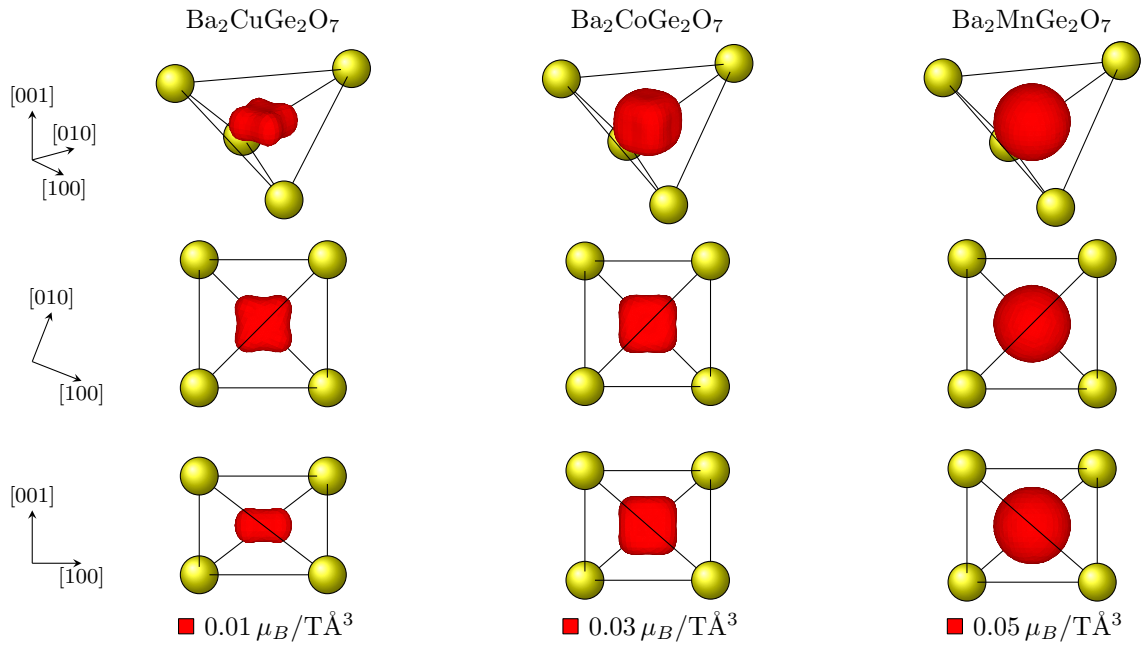

Figure 8.6.: Perspective views on the isosurface of the in-plane susceptibility density $\chi_{11}(\mathbf{r})$ in the $Ba_2TGe_2O_7$ compounds calculated according to Eq. (8.19) from the theoretical occupations of the $3d$ orbitals resulting from the electron configuration of the respective TM ion. The χ_{11} value and the parameters for the radial dependency $R(r)$, which do not influence the angular shape, are estimated by the MP refinement results listed in Table 8.1. The layout of the figure is analogous to that described in Fig. 8.7 with the same values for the isosurface levels. No significant density is associated with grid points outside of the shown tetrahedral environment.

for $Ba_2CoGe_2O_7$ ($[Ar]3d^3$) and $Ba_2CuGe_2O_7$ ($[Ar]3d^1$), only t_2 orbitals are occupied by unpaired electrons, resulting in $\mathbf{C}^{\mathsf{T}}_{Co^{2+}} = (0, 2, 0, 1)/3$ and $\mathbf{C}^{\mathsf{T}}_{Cu^{2+}} = (0, 0, 0, 1)$, respectively. Plugging the susceptibility values χ_{ii} and the parameters for the radial function as listed in Table 8.1 in Eq. (8.19), the theoretically expected susceptibility densities for all three $Ba_2TGe_2O_7$ compounds can be calculated and are shown for $\chi_{11}(\mathbf{r})$ in Fig. 8.6. Clear to see is a spherical shape of the isosurface for $T = Mn$, a cubic shape for $T = Co$ and a compressed cubic shape with pronounced corners for $T = Cu$. By comparison with the experimentally determined densities from the advanced MEM reconstruction and the MP refinement in Figs. 8.2 and 8.3, respectively, a very good agreement between the theoretical expectation and the experimental findings is evident. This clearly demonstrates that the unconventional density shapes in the $Ba_2TGe_2O_7$ compounds revealed by PND are of physical origin and can be unambiguously attributed to the TM ions electronic configuration, and thus to the crystal field effects of their compressed tetrahedral environment on the $3d$ orbitals.

To quantitatively compare the results of the MP refinement with the expected orbital configurations, the transformation matrix A from Eq. (8.18) can be used to calculate the suggested relative orbital contributions $\mathbf{C}^{\mathrm{MP}}$ from the refined MP parameters C^l_m.

Table 8.2.: Relative 3*d* orbital populations $\mathbf{C}^{\text{mult}}$ for the $Ba_2TGe_2O_7$ compounds calculated from the results of the MP refinements on the combined FR datasets at 10 K. The theoretically expected values from the electronic configurations of the respective TM ions are given in the text.

	C_{z^2} [%]	$C_{x^2-y^2}$ [%]	$C_{xz} = C_{yz}$ [%]	C_{xy} [%]
$Ba_2CuGe_2O_7$	-11(9)	-1(6)	25(6)	61(6)
$Ba_2CoGe_2O_7$	9(3)	5(3)	28(2)	30(2)
$Ba_2MnGe_2O_7$	19.6(6)	21.0(5)	19.5(4)	20.3(5)

This connection is given by

$$\mathbf{C}^{\text{MP}} = (A^{\mathsf{T}})^{-1} \cdot \begin{pmatrix} C_0^0 \\ C_2^0 \\ C_4^0 \\ C_4^4 \end{pmatrix}. \tag{8.20}$$

Note that local symmetry allowed multipoles C_3^2, C_3^{-2} and C_4^{-4} are not represented by the orbital density and are thus expected to be zero. This agrees with the MP refinement results listed in Table 8.1, showing C_l^m values close to zero for these multipoles in all compounds. Thus, a revision of the MP refinements for the three $Ba_2TGe_2O_7$ compounds with only non-zero values for the four C_l^m parameters listed in Eq. (8.20) causes no noticeable change in the refinement results and the same χ_r^2 values. The estimations of the relative orbital contributions $\mathbf{C}^{\text{MP}}$, which are calculated from the revised four orbital C_l^m parameters using Eq. (8.20), are listed in Table 8.2. The same values for C_{xz} and C_{yz} are assumed as their respective orbitals are energetically degenerate.

For $Ba_2MnGe_2O_7$, almost equal contributions of around 20% are suggested for all 3*d* orbitals from the refinement results in Table 8.2, which coincides with the expected electronic configuration discussed above. The very weak deviations from 20% indicate a slight reduction for C_{z^2}, C_{xz} and C_{yz} and an equivalent increase for $C_{x^2-y^2}$ and C_{yz}. As all orbitals with reduced population are elongated in z direction and the others are almost confined to the xy plane (see Fig. 8.5), these deviations reflect a compression of the density in c direction, which might be connected to the corresponding compression of the tetrahedral environment (see Sec. 2.1).

In $Ba_2CoGe_2O_7$, relative populations of 33% are expected for the C_{xz}, C_{yz} and C_{xy} orbitals. This is almost met by the refinement results in Table 8.2 but the differences to the expected values are slightly larger than for $Ba_2MnGe_2O_7$. As $Ba_2CoGe_2O_7$ has a similar tetrahedral compression as $Ba_2MnGe_2O_7$ (see Table 2.1), the higher discrepancies might be connected to effects additional to the compression. In particular, the *p*-*d* hybridization proved to be exceptionally strong in $Ba_2CoGe_2O_7$ and $Ba_2CuGe_2O_7$ and is directly mediated by the TM ions t_2 orbitals in these compounds and not by the e orbitals as in $Ba_2MnGe_2O_7$ (see Sec. 2.3.1 and Refs. [86, 89]). This might cause a stronger deformation of the unpaired electron density as in $Ba_2MnGe_2O_7$, and thus the enhanced differences between the refined and expected values for the orbital populations. However, also the restrictions of the MP density, induced by the particular choice of radial and angular model as discussed in Sec. 8.1.2, might be accountable for these differences.

For $Ba_2CuGe_2O_7$, only C_{xy} should be populated, which is fulfilled by the negligible C_{z^2} and $C_{x^2-y^2}$ values in Table 8.2 but not by the significant $C_{xz} = C_{yz}$. This additional $C_{xz,yz}$ contribution in the MP refinement is clearly visible in Fig. 8.3 by an elongation of the $Ba_2CuGe_2O_7$ density in [001] direction compared to the expected density in Fig. 8.6. Again, this difference to the expected shape might be attributed to hybridization effects, favouring a delocalization of the unpaired electron density. However, as this particular elongation is almost absent in the visualization of the MEM reconstruction in Figs. 8.2 and H.2, it is also likely to result from an insufficiently good approximation of the radial and angular dependency by the MP model discussed in Sec. 8.1.2. Thus, it might be worthwhile to revise and optimize the used radial and angular functions, potentially based on the 3D results of our MEM reconstructions and its spherical average in Fig. 8.4. These new functions could be implemented in the state-of-the-art PND refinement software packages, like *Mag2Pol* or *AdvEnt*, and provide more reliable orbital populations. However, this elaborate and complex process to generally improve the multipole refinement capabilities is beyond the scope of this thesis.

8.2. Antiferromagnetic density

As the advanced MEM and its implementation in the *AdvEnt* software are capable of treating non-collinear densities, an attempt was made to simultaneously reconstruct both the field-induced FM and the ordered AFM magnetization densities from the combined FR measurements in the commensurate WFM phases of $Ba_2TGe_2O_7$ with T = Cu and Co at 2 K. Note that the AFM structure in $Ba_2MnGe_2O_7$ has $\boldsymbol{\tau} = (10\frac{1}{2})$ such that FR measurements of the AFM moment are not applicable.

8.2.1. Reconstruction by the advanced maximum entropy method

To treat the commensurate AFM moments, which were confirmed to be parallel to $\mathbf{y}_n \parallel \mathbf{B}_n \times \hat{\mathbf{c}}$ for each FR dataset n in Secs. 6.3.2 and 7.4.2, Eq. (8.3) needs to be extended for an additional base vector to

$$\mathbf{m}_n(\mathbf{r}_i) = \underbrace{\chi_{11}(\mathbf{r}_i)}_{f_{i,1}} \underbrace{\mathbf{B}_n^{\perp[001]}}_{\mathbf{b}_1} + \underbrace{\chi_{33}(\mathbf{r}_i)}_{f_{i,2}} \underbrace{\mathbf{B}_n^{\parallel[001]}}_{\mathbf{b}_2} + m_{y,n}^{\mathrm{AFM}} \underbrace{\rho^{\mathrm{AFM}}(\mathbf{r}_i)}_{f_{i,3}} \underbrace{\mathbf{y}_n}_{\mathbf{b}_3} . \tag{8.21}$$

Thus, the reconstructed AFM magnetization density distribution $m_{y,n}^{\mathrm{AFM}}(\mathbf{r})$ is assumed to be given by a common density distribution $\rho^{\mathrm{AFM}}(\mathbf{r})$ scaled by the $m_{y,n}^{\mathrm{AFM}}$ value of the magnetic moment refinement for each FR dataset n in Tables 6.4 and 7.7. Although this assumption on the AFM density might be a significant simplification, it is typically used in MP refinements and required in order to combine different FR datasets. Like for the susceptibility density in Sec. 8.1.1, the local $\bar{4}$ point group symmetry and the AFM coupling between the two equal TM ion sites are applied to the scalar AFM density distribution by assigning equal and sign inverted ρ^{AFM} values to grid points related by $(\bar{y}, x, \bar{z})$ and $(\bar{x} + \frac{1}{2}, y + \frac{1}{2}, \bar{z})$, respectively.

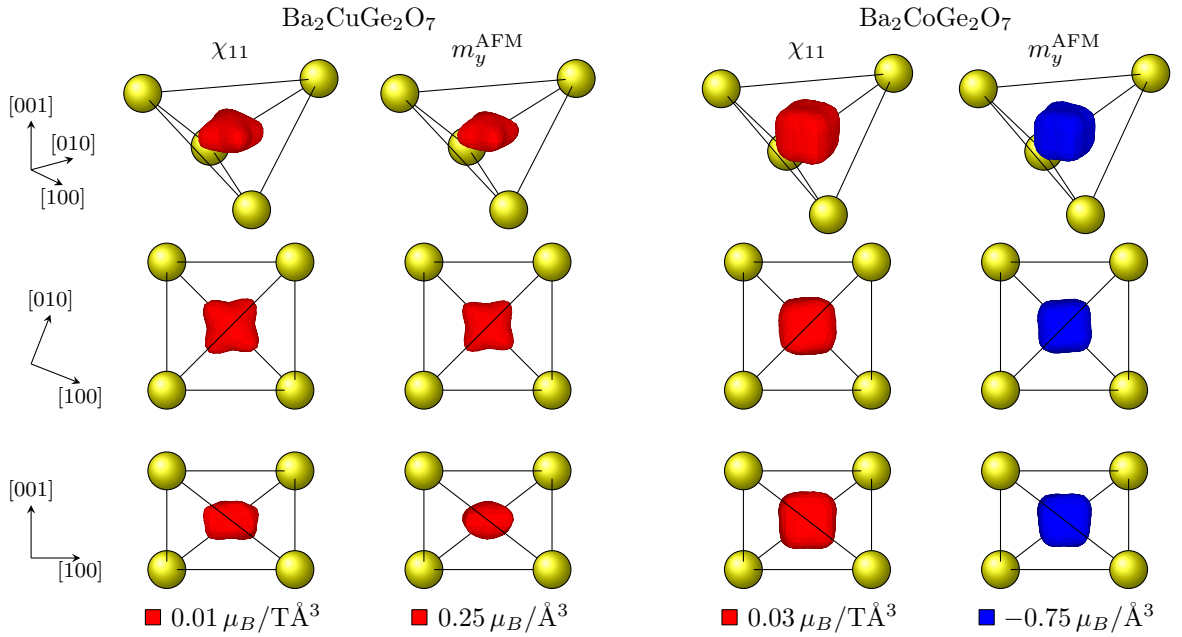

Figure 8.7.: Perspective views on the isosurface of the in-plane susceptibility density $\chi_{11}(\mathbf{r})$ and the AFM density $m_y^{\mathrm{AFM}}(\mathbf{r})$ in the $Ba_2TGe_2O_7$ compounds (T = Cu and Co) at 2 K, reconstructed with the *AdvEnt* software as discussed in the text. The shown tetrahedral environment corresponds to the TM ions located at the origin. The layout of the figure is similar to that described in Fig. 8.7 with the same values for the isosurface levels of $\chi_{11}(\mathbf{r})$. The levels for the AFM density are similarly selected at around 10% of the maximal observed value. No significant densities are associated with grid points outside of the shown tetrahedral environment.

Applying Eq. (8.21) to reconstruct the common χ_{11}, χ_{33} and ρ^{AFM} densities from the FR measurements, reasonable low C_{min} values could be reached. For this reason, no larger systematical uncertainties or inappropriate density restrictions are indicated in the reconstruction and values of $C_{\mathrm{aim}} = 1.4$ and 1.8 are selected for $Ba_2CuGe_2O_7$ and $Ba_2CoGe_2O_7$, respectively. For the latter compound, all datasets listed in Table 6.4 are used for the reconstruction and the structural parameters are assumed as listed in Table 6.3. The isotropic extinction coefficients of $x_{11} = 1.8(3)$ is taken from the FR refinements in Sec. 6.3.2. For $Ba_2CuGe_2O_7$, only the FR measurements collected in the commensurate high-field structure, denoted as AFM phase in Table 7.7, can be considered in the combined reconstruction. Of these, the FR dataset measured at D3 (ILL) with the smaller N21 $Ba_2CuGe_2O_7$ single crystal is again excluded for consistency. The structural parameters are selected as listed in Table 7.2 for 10 K and the isotropic extinction parameter of $x_{11} = 0.27(5)$ is taken from Sec. 7.4.1.

The resulting in-plane susceptibility densities $\chi_{11}(\mathbf{r})$ and the AFM densities $m_y^{\mathrm{AFM}}(\mathbf{r})$ are illustrated in Fig. 8.7 for the two $Ba_2TGe_2O_7$ compounds. For visualization purposes, the reconstructed ρ^{AFM} densities are scaled by $m_y^{\mathrm{AFM}} = 0.46\,\mu_B$ and $-2.63\,\mu_B$ for the T = Cu and Co compounds, corresponding to the refined values for the 6 T FR measurements with $\mathbf{B} \parallel [113]$ and [110], respectively. Note that the different AFM density signs for $Ba_2CuGe_2O_7$ and $Ba_2CoGe_2O_7$ reflect the different absolute directions of the

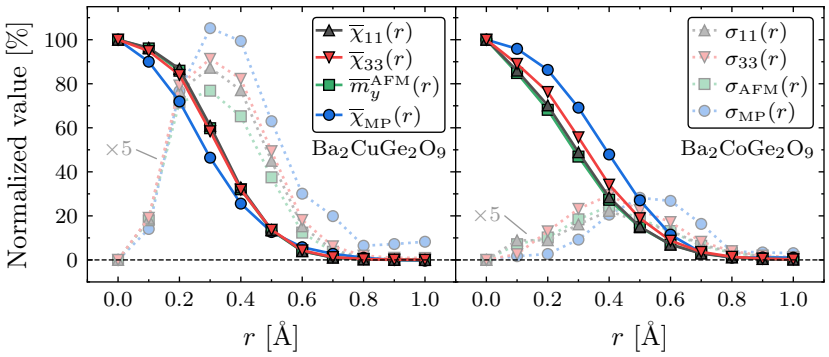

Figure 8.8.: The spherically averaged susceptibility and AFM densities (solid lines) and the square-root of their variance (dotted lines), normalized to the central density value at the TM ion position ($r = 0$), for the different methods in the $Ba_2TGe_2O_7$ (T = Cu and Co) compounds at 2 K. The $\overline{\chi}_{11}$, $\overline{\chi}_{33}$ and $\overline{m}_y^{\mathrm{AFM}}$ values and their variances σ_{11}, σ_{33} and σ_{AFM} (black, blue and green symbols) are calculated from the MEM susceptibility densities displayed in Figs. 8.7 and H.3. In contrast, $\overline{\chi}_{\mathrm{MP}}$ and σ_{MP} (blue circular symbols) are based on the susceptibility density of the MP refinement discussed in the text. Note that the normalized variances are scaled by a factor of five for visibility.

D_z component of the DMI vector, discussed in Secs. 6.3.3 and 7.4.3. The out-of-plane susceptibility densities $\chi_{33}(\mathbf{r})$ are shown for completeness in Fig. H.3 but reveal very similar shapes as $\chi_{11}(\mathbf{r})$ displayed in Fig. 8.7. By integrating the $\chi_{11}(\mathbf{r})$ and $\chi_{33}(\mathbf{r})$ densities as described in Sec. 8.1.1, an anisotropy ratio of $\chi_{11}/\chi_{33} = 0.72(1)$ and 2.27(2) can be estimated for $Ba_2CuGe_2O_7$ and $Ba_2CoGe_2O_7$ at 2 K, respectively. These values reproduce closely the results of the PM phase (see Sec. 8.1.1) and the expectations discussed in Secs. 2.2.1 and 2.2.2. In particular, they clearly recover the easy-axis anisotropy in $Ba_2CuGe_2O_7$, which could not be evidenced by the regular magnetic moment refinement of the FR data with isotropic form factor in Sec. 7.4.2.

Visually comparing the densities in Figs. 8.7 and H.3 from the low-temperature MEM reconstruction in $Ba_2CuGe_2O_7$ and $Ba_2CoGe_2O_7$, quite the same density shapes are apparent for all three components (χ_{11}, χ_{33} and m_y^{AFM}) for each compound. Moreover, no fundamental differences are evident in the susceptibility densities at 2 K compared to the 10 K results in Figs. 8.2 and H.2. This is not surprising as all the density distributions for the field-induced and ordered spin-only magnetic moments, independent on their direction and magnitude, are based on the same scalar density distribution of the unpaired electrons. As this density distribution is mainly defined by the crystal field effects on the electronic configuration (see Sec. 8.1.3), it is also not expected to fundamentally change between the measurements in the WFM and PM phase at 2 K and 10 K, respectively. However, to analyze and compare the densities from the MEM reconstruction in the low-temperature WFM phase in more detail, their spherically averaged value and its variance have been calculated like in Fig. 8.4 for the PM phase.

The normalized result of the averaging according to the procedure described in Sec. 8.1.2 is shown in Fig. 8.8 by triangular and square symbols for the MEM susceptibility and AFM density, respectively. For $Ba_2CoGe_2O_7$, an almost identical radial dependency is clear to see for $\overline{\chi}_{11}$ and $\overline{m}_y^{\mathrm{AFM}}$, which is characterized by a radius of $r_{\mathrm{HM}} = 0.29(2)$ Å

at half maximum. This radius is slightly higher for $\overline{\chi}_{33}$ with $r_{\mathrm{HM}} = 0.33(1)$ Å, which indicates a weak expansion and might be attributed to the influence of the easy-plane anisotropy as discussed in Sec. 8.1.2. Nevertheless, both radii are somewhat consistent with the MEM results at 10 K and also the broad maximum in the relative variances σ_{11}, σ_{33} and σ_{AFM} is on a similar scale ($\approx 5\%$) and at an equal position (≈ 0.40 Å) as at 10 K. Thus, no significant differences are evident between the density shapes of $Ba_2CoGe_2O_7$ in the WFM and PM phase. In contrast for $Ba_2CuGe_2O_7$, the almost identical radial dependency for $\overline{\chi}_{11}$, $\overline{\chi}_{33}$ and $\overline{m}_y^{\mathrm{AFM}}$ with $r_{\mathrm{HM}} = 0.34(1)$ Å reflects an overall expansion of the MEM densities at 2 K compared to those at 10 K. In addition, the relative strength of the maxima in the variance ($\approx 18\%$) is also visibly increased compared to the 10 K results in Fig. 8.4, whereas the center remains almost constant at around 0.3 Å. These differences, particular prominent in $\overline{\chi}_{11}$, could indicate a slight delocalization of the unpaired electron density, which might be associated with a change in the hybridization between the Cu^{2+} ion and its ligands upon cooling to low temperature. As this change is only evident for $Ba_2CuGe_2O_7$, it might also be somewhat connected to the magnetic field-induced I/C transition of the AFM structure in $Ba_2CuGe_2O_7$ (see Sec. 2.2.1), required to apply the FR technique. However, it should be emphasized that the AFM and induced moments in $Ba_2CuGe_2O_7$ are rather small, which results in a reduced precision of the combined FR datasets consisting of only three measurements. This lack of accuracy could also cause some distortions of the reconstructed densities.

8.2.2. Reconstruction by multipole refinement

To complement the MEM results, a MP refinement of the combined FR datasets in $Ba_2CuGe_2O_7$ and $Ba_2CoGe_2O_7$ at 2 K was carried out using the *AdvEnt* software. For the MP model, Eq. (8.13) is extended based on Eq. (8.21) for an AFM contribution $\propto m_{y,n}^{\mathrm{AFM}}\mathbf{y}_n$, defined for each FR dataset n by the direction $\mathbf{y}_n \parallel \mathbf{B}_n \times \hat{\mathbf{c}}$ and the AFM moment $m_{y,n}^{\mathrm{AFM}}$. The single-ζ Slater-type function is selected as radial distribution. For the angular dependency, only the $3d$ orbital coefficients C_2^0, C_4^0 and C_4^4 (see Sec. 8.1.3) are refined and $C_0^0 = 1$ is chosen for normalization. Note that there is no improvement in χ_r^2 if the additional symmetry-allowed coefficients $C_3^{\pm 2}$ and C_4^{-4} are included in the refinement. The detailed MP refinement results are listed in Table H.1. The refined susceptibilities and AFM moments are similar to those provided and discussed in Secs. 7.4.2 and 6.3.2 for an isotropic form factor. Therefore, the MP refinement for $Ba_2CuGe_2O_7$ indicates, just like the isotropic one, no easy-axis anisotropy ($\chi_{11}/\chi_{33} < 1$), which is expected from theory (see Sec. 2.2.1) and confirmed by magnetization measurements and the integration of the MEM density discussed above. This discrepancy in the anisotropy between the MP and MEM approach in $Ba_2CuGe_2O_7$ discloses a superior quality of the latter one. Similar findings can be made for the MP coefficients C_l^m and ζ. For $Ba_2CoGe_2O_7$, they agree within their uncertainty with the PM results in Table 8.1. In contrast for $Ba_2CuGe_2O_7$, the magnitude of C_2^0 and the uncertainty for C_4^0 are clearly increased compared to the 10 K results. In particular, the large uncertainty of C_4^0 suggests that some density cannot be properly described by the assumed MP model but might be correctly reproduced by the less restrictive MEM reconstruction.

Table 8.3.: Relative 3*d* orbital populations $\mathbf{C}^{\text{mult}}$ for the $Ba_2TGe_2O_7$ compounds calculated from the results of the MP refinements on the combined FR datasets at 2 K in Table H.1. The theoretically expected values from the electronic configurations of the respective TM ions are discussed in the text.

	C_{z^2} [%]	$C_{x^2-y^2}$ [%]	$C_{xz} = C_{yz}$ [%]	C_{xy} [%]
$Ba_2CuGe_2O_7$	33(20)	13(10)	-19(13)	92(10)
$Ba_2CoGe_2O_7$	6(2)	3(2)	30(1)	32(2)

For a more detailed comparison between the resulting densities of the MEM and the MP approach, the spherically averaged density value and its variance are also calculated for the results of the MP refinement and shown in Fig. 8.8 by blue circles. As discussed in Sec. 8.1.2, $\overline{\chi}_{\text{MP}}$ and σ_{MP} represent all MP density components as they are based on the same radial and angular functions (see Eq. (8.13)). For $Ba_2CoGe_2O_7$, there is a slight expansion of the average density compared to the MEM results that leads to $r_{\text{HM}} = 0.39(1)$ Å, which is consistent with the PM results discussed in Sec. 8.1.2. The broad maximum in σ_{MP} has also a similar value and center as in Fig. 8.4 for 10 K, indicating no sizable differences to the PM density shapes as already emphasized for the MEM results above. For $Ba_2CuGe_2O_7$, $\overline{\chi}_{\text{MP}}$ shows a more compressed radial dependency as the MEM results and a radius of $r_{\text{HM}} = 0.29(1)$ Å. Although this radius agrees with the MP results at 10 K (see Sec. 8.1.2), it does not reflect the expansion of the density upon cooling to 2 K that is evident in the MEM results. This might again be attributed to the selection of a particular model for the MP density, not capable of describing deformations in the reconstructed density that go beyond the approximation in Eq. (8.13) and might occur due to hybridization effects. Remarkably, the maximum in the variance of the MP density with values up to around 20% for $Ba_2CuGe_2O_7$ is even larger than for the MEM results but it is similarly centered at around 0.3 Å.

Finally, the coefficients C_l^m listed in Table H.1 for the MP refinement of the 2 K measurements are used to calculated the populations of the 3*d* orbitals in the commensurate AFM phase according to the procedure presented in Sec. 8.1.3. The results are listed in Table 8.3. For $Ba_2CoGe_2O_7$, they show no significant differences to the PM populations in Table 8.2, and thus confirm the slight deviations from the expected populations of around 33% in C_{xz}, C_{yz} and C_{xy}, discussed in Sec. 8.1.3. For $Ba_2CuGe_2O_7$, the calculation provides a large C_{xy} population and rather insignificant values for the remaining coefficients. Although this complies with the expectation of only C_{xy} being present, the large uncertainties in the calculated populations might indicate an insufficient MP refinement model as discussed above.

8.3. Conclusions

Applying the proposed advanced maximum entropy approach, implemented in the novel *AdvEnt* software, we could reconstruct in Sec. 8.1.1 for the first time high-resolution magnetization densities in the PM phase of the noncentrosymmetric $Ba_2TGe_2O_7$ compounds from combined FR datasets. These density distributions revealed unconventional

shapes for the different transition metal ions and could be confirmed by multipole refinements in Sec. 8.1.2. By calculating the expected orbital configurations and their associated densities in Sec. 8.1.3, a clear connection between the electronic configuration and the reconstructed densities could be established. This demonstrates that PND, combined with proper analysis software, is a powerful and reliable tool to experimentally visualize magnetization densities at the unit cell level and to provide direct evidence for the basic crystal field effects defining the orbital configuration.

Utilizing the connection between the electronic orbitals and the functions of the multipole expansion, we successfully demonstrated in Sec. 8.1.3 the calculation of the $3d$ orbital populations from the PND refinement results. These extracted populations disclosed only minor differences to the expected values from the theoretical configuration. Nevertheless, it might be of particular interest to clarify in further studies whether these differences are of physical origin, like hybridization effects and tetrahedral compression, or are solely due to distortions arising from an insufficient multipole model or from limitations in the data quality. In this regard, density functional theory (DFT) simulations of the magnetization density in the $Ba_2TGe_2O_7$ series are already in progress and first results show a promising consistency with the density from the maximum entropy reconstruction. This comparison between the maximum entropy and DFT density might provide an exceptional insight into the transition metal ion's hybridization mechanism and could help to improve both data analysis and simulation.

Driven by the new *AdvEnt* software's capabilities for treating non-collinear density distributions, we were also able to reconstruct for the first time simultaneously the field-induced susceptibility and AFM density from the combined FR datasets collected in the commensurate WFM phases of $Ba_2CuGe_2O_7$ and $Ba_2CoGe_2O_7$. These densities showed consistent aspherical shapes with the ones observed in the PM phase, emphasizing their connection to the electronic configuration. However, a slight deformation of the $Ba_2CuGe_2O_7$ density upon cooling from the PM to the AFM phase could be identified, which might be connected to delocalization effects or the field-induced I/C magnetic phase transition, and thus provides particularly high potential for further experimental studies and simulations.

The successful reconstruction of magnetization densities in the $Ba_2TGe_2O_7$ compounds proves the proper functioning of the advanced maximum entropy approach and the associated *AdvEnt* software. It also demonstrates their superior performance compared to conventional maximum entropy software, incapable of treating noncentrosymmetric structures or non-collinear magnetizations. Moreover, this is the first study comprehensively reporting and analyzing aspherical density distributions in a series of transition metal ion based compounds and revealing their direct connection to the crystal field effects in the manner of a textbook example. Thus, the new approach and software are now ready to be used as an efficient and straightforward standard analysis tool in single crystal PND and we anticipate a timely application in many more compounds with compelling results. The presented methods and applications might also be of particular interest for the study and understanding of transition-metal-containing molecules and serve as a valuable reference for results of DFT and other numerical simulations.

9. Summary and outlook

In the frame of this thesis, the atomic and magnetic structure in the $Ba_2TGe_2O_7$ (T = Cu, Co and Mn) compounds and the $Ba_2Cu_{1-x}Mn_xGe_2O_7$ solid solution series was studied in detail by neutron diffraction and macroscopic measurements. These melilite-type compounds are of particular interest in the current condensed matter research as they exhibit a strong magnetoelectric coupling that could not be explained by the conventional models of spin-driven multiferroicity but might be of high potential for spintronic applications. Thus, new mechanisms have been recently proposed to account for these peculiar effects in $Ba_2TGe_2O_7$ [89, 91, 92, 94]. These mechanisms were briefly introduced, discussed and compared in this thesis.

In particular for the mixed compounds of the $Ba_2Cu_{1-x}Mn_xGe_2O_7$ solid solution series, no structural and magnetic details have been reported in the literature yet. Thus, $Ba_2Cu_{1-x}Mn_xGe_2O_7$ polycrystalline samples with, in total, 14 different concentrations x have been synthesized and provided by the Department of Physics, University of Salerno, Italy [98]. Using laboratory X-ray and high-resolution neutron powder diffraction, detailed structural parameters were refined as function of x and related to deformations of the transition metal ion's tetrahedral oxygen environment. Moreover, spurious phases in the polycrystalline compounds were successfully identified and their phase fraction revealed. This helped to conclusively explain unexpected weak ferromagnetic (WFM) contributions in the magnetization measurements and may be a valuable reference to optimize the synthesis procedure, which could be an essential step towards the realization of mixed $Ba_2Cu_{1-x}Mn_xGe_2O_7$ single crystals for further studies.

Based on macroscopic measurements of the $Ba_2Cu_{1-x}Mn_xGe_2O_7$ solid solution series, the magnetic phase diagram was carefully mapped out for the first time. Zero-field heat capacity showed the presence of two magnetically ordered phases, one for the Cu-rich and one for the Mn-rich side, separated by a critical concentration of $x_c = 0.57(1)$. Both phases showed transition temperatures T_N consistent with the values reported for single crystals of $Ba_2CuGe_2O_7$ ($x = 0.00$) and $Ba_2MnGe_2O_7$ ($x = 1.00$) and a linear decrease in T_N towards x_c. In addition, an extended Debye-Einstein model was applied to the heat capacity measurements to characterize phonon contributions and to calculate the magnetic entropy. Magnetization measurements on $Ba_2Cu_{1-x}Mn_xGe_2O_7$ revealed for the Cu-rich phase a clear increase in T_N for an increasing magnetic field strength, which is consistent with the reports on single crystalline $Ba_2CuGe_2O_7$ [126]. In contrast for the Mn-rich phase, the T_N values increased only for magnetic field strengths up to 1 T and then decreased again for even higher fields. This exceptional behavior was successfully attributed to the 2D characteristics in the melilite-type structure. Furthermore, applying the Curie-Weiss law for antiferromagnets to the field-cooled magnetization, precise and x-dependent values for the paramagnetic Néel temperature and the transition metal

ion's effective magnetic moment are revealed. Additional magnetization measurements as function of the temperature and the magnetic field in $Ba_2CuGe_2O_7$ and $Ba_2MnGe_2O_7$ single crystals confirmed and complemented both the polycrystalline and literature results [86, 126]. In particular, a significant easy-axis anisotropy in $Ba_2CuGe_2O_7$ and an almost isotropic behavior in $Ba_2MnGe_2O_7$ was clearly evidenced.

Applying high-resolution neutron powder diffraction to the $Ba_2Cu_{1-x}Mn_xGe_2O_7$ compounds in zero magnetic field at low temperature, an antiferromagnetic (AFM) cone-like ground state structure that is composed of a cycloidal and a commensurate AFM moment was identified and analyzed as function of x for the Cu-rich phase. This AFM cone structure is similar to that evidenced in $Ba_2CuGe_2O_7$ single crystals for an applied magnetic field in c direction [126], and thus might be of high interest for further studies as it provides promising characteristics towards a stable skyrmion phase as suggested for $Ba_2CuGe_2O_7$ in Ref. [37]. For the Mn-rich phase, the magnetic structure was shown to be commensurate AFM like reported for $Ba_2MnGe_2O_7$ single crystals [15]. The AFM moment was studied as function of the temperature and revealed a reduced critical exponent, which confirms the 2D-like characteristic that is generally present in the mellilte-type compounds. Although both phases were analyzed in detail, further studies could address compounds with critical composition ($x \approx 0.57$) as there might emerge a novel phase coexistence or even a quantum critical behavior. Nevertheless, also the synthesis of mixed $Ba_2Cu_{1-x}Mn_xGe_2O_7$ single crystals might be of high scientific value as their investigation could shed light on anisotropy effects and their change with x.

In preparation for the neutron diffraction measurements on the $Ba_2TGe_2O_7$ compounds, the flipping ratio (FR) setup option of the single crystal diffractometer POLI at the Heinz Maier-Leibnitz Zentrum (MLZ) in Garching, Germany, was successfully extended for a new high-field superconducting magnet with dedicated solid state supermirror bender and Mezei-type flipper. All components were numerically simulated and optimized. In a dedicated test experiment, the constant and high degree of polarization, transport and flip efficiency of the new setup could be demonstrated for the entire available field range up to 8 T. However, due to operational issues of the neutron source (FRM-II) at MLZ, the majority of the neutron diffraction experiments within this work had to be performed at other facilities, including the Institut Laue-Langevin (ILL, France), the Spallation Neutron Source (SNS, USA), and the Laboratoire Léon Brillouin (LLB, France). Nevertheless, we anticipate a high potential of this new FR option for the user community at POLI, which might be further extended by a 2D detector and novel sample environments for multi-parameter studies in the near future.

Performing FR measurements on single crystals of all three $Ba_2TGe_2O_7$ (T = Cu, Co and Mn) compounds in the paramagnetic (PM) phase, precise values for the field-induced magnetic moments and the local susceptibility tensors were determined. They disclosed a clear easy-axis anisotropy in $Ba_2CuGe_2O_7$, an easy-plane anisotropy in $Ba_2CoGe_2O_7$ and a negligible anisotropy in $Ba_2MnGe_2O_7$, which is in agreement with results from electron spin resonance spectroscopy [15, 114, 119] and theoretical considerations based on single-ion anisotropy and spin-orbit coupling effects. Similar FR measurements in the commensurate AFM structures of $Ba_2CuGe_2O_7$ and $Ba_2CoGe_2O_7$ provided precise values for the ordered moment in addition to the field-induced one. These results were success-

fully related to particular features in the electric polarization reported in the literature [86] using the predictions of the novel spin-nematic and p-d hybridization mechanisms; thus, confirming their validity on a microscopic scale. Moreover, the refined magnetic moment arrangement in $Ba_2CuGe_2O_7$ and $Ba_2CoGe_2O_7$ was used to reveal their absolute sign of the out-of-plane component of the Dzyaloshinskii-Moriya interaction (DMI) vector parameter, based on a detailed symmetry analysis in the $Ba_2TGe_2O_7$ compounds. This DMI component proved to be of opposite sign for both compounds, which is in agreement with theoretical considerations in Ref. [90]. Because of its straightforward and elegant application, requiring the FR value of only one suitable Bragg reflection, this novel approach to determine the DMI sign by polarized neutron diffraction (PND) is expected to be applied to many more WFM compounds in the near future.

In addition to FR measurements, spherical neutron polarimetry (SNP) was applied to unambiguously determine the magnetic ground state structure in $Ba_2CoGe_2O_7$ to be $P2_1'2_12'$, which contradicts earlier results in Ref. [112] but coincides with the theoretical study in Ref. [90]. Based on this $P2_1'2_12'$ ground state symmetry and the revealed sign of the DMI, spherical neutron polarimetry (SNP) was used to monitor the remnant tetragonal domain configuration as function of the applied magnetic field. These measurements demonstrated that the domain distribution can be saturated by applied in-plane magnetic fields as small as 1 G during cooling and that the domains can be completely switched by fields above 250 G at low temperature. This high sensitivity to small magnetic fields in $Ba_2CoGe_2O_7$ combined with the novel mechanisms of multiferroicity might be interesting in terms of new materials for spintronic applications.

Finally, a new and advanced maximum entropy approach for the reconstruction of magnetization density maps at the unit cell level from PND data was developed and implemented in the new software tool *AdvEnt*. It was successfully applied to the FR measurements in the PM and commensurate AFM phase of the $Ba_2TGe_2O_7$ (T = Cu, Co and Mn) compounds and revealed clearly aspherical density distributions for the Cu^{2+} and Co^{2+} ions. These unconventional shapes are consistent with aspherical deformations evident in the magnetic form factor and were confirmed by multipolar expansion. Analyzing the electronic configuration defined by the crystal field effects in the tetrahedral environment, these shapes were directly attributed to the unpaired electron density of the 3d ions. In addition, the results of the multipolar expansion was used to calculate the respective 3d orbital populations. These revealed only slight differences to the expected values, mainly for the $Ba_2CuGe_2O_7$ and $Ba_2CoGe_2O_7$ compounds, with the differences being related to either hybridization effects, to an insufficient multipolar model or to limitations in the data quality. To clarify this, a more detailed PND experiment, for example, using the new FR setup option at POLI, or a comparison with DFT density simulations is required. For the latter, preparations are already ongoing and show promising first results. Nevertheless, PND combined with the new *AdvEnt* software proved to be a powerful tool to reconstruct model-free magnetization densities at the unit cell level, providing an exceptional insight in the electronic configuration and crystal field effects and serving as valuable reference for theoretical calculations and simulations. Thus, a timely application of the new software to PND measurements in many more compounds is anticipated.

Appendix

A. Magnetic space groups and symmetry

This part of the appendix provides an introduction to the symmetry transformations of magnetic moments, followed by a brief overview of the symmetry operations of the melilite-type parent space group $P\bar{4}2_1m$. Moreover, it presents the magnetic space groups derived from $P\bar{4}2_1m$ for different propagation vectors and in-plane magnetic moments.

A.1. Symmetry transformation of magnetic moments

Magnetic moments $\mathbf{m}$ transform as axial vectors such that $\mathbf{m}_S$, resulting from symmetry operation $\mathcal{S}$ with point group symmetry part $\mathcal{R}$, is given by

$$\mathbf{m}_{S^{(\prime)}} = (-)\det(\mathcal{R})\,\mathcal{R}\mathbf{m} \tag{A.1}$$

with $(-)$ if $\mathcal{S}$ is additionally combined with time-inversion $1'$. The symmetry transformation of a vector product of magnetizations $\mathbf{m}_1$ and $\mathbf{m}_2$ obeys the conventional rules for a vector product under a matrix transformation and is given by

$$\mathbf{m}_{S1} \times \mathbf{m}_{S2} = \underbrace{\det(\mathcal{R})^2}_{=1}(\mathcal{R}\mathbf{m_1}) \times (\mathcal{R}\mathbf{m_1}) = \det(\mathcal{R})\,\underbrace{(\mathcal{R}^{-1})^{\mathsf{T}}}_{=\mathcal{R}}(\mathbf{m}_1 \times \mathbf{m}_2). \tag{A.2}$$

For all points group symmetries $\mathcal{R}$, the inversion and transpose are equivalent (i.e. $\mathcal{R}^{-1} = \mathcal{R}^{\mathsf{T}}$). Thus, the vector product $\mathbf{m}_1 \times \mathbf{m}_2$ transforms as an axial vector. Note that also a vector product of polar vectors transform as an axial vector.

A.2. Symmetry operation of the parent space group

For the tetragonal nuclear space group $P\bar{4}2_1m$ (# 113), there are three types of symmetry operations in addition to the lattice translations (see also illustration in Fig. 4.1(a)):

- **Four-fold inversion axis ($\bar{4}$):** The nuclear space group contains a four-fold inversion axis in [001] direction, which can be expressed as $y, \bar{x}, \bar{z}$ with multiples $\bar{x}, \bar{y}, z$ (two-fold rotation around [001]) and $\bar{y}, x, \bar{z}$.
- **Two-fold screw axis (2_1):** There are two-fold screw axes along the [100] and [010] directions, expressed as $\frac{1}{2} + x, \frac{1}{2} - y, \bar{z}$ and $\frac{1}{2} - x, \frac{1}{2} + y, \bar{z}$, respectively.
- **Mirror plane (m):** There are mirror planes normal to the diagonal [110] and [1$\bar{1}$0] directions, which can be expressed as $\frac{1}{2} - y, \frac{1}{2} - x, z$ and $\frac{1}{2} + y, \frac{1}{2} + x, z$, respectively.

A.3. Magnetic space groups for in-plane AFM ordering and $\tau = 0$

The four-fold inversion axis $y, \bar{x}, \bar{z}$ transforms magnetic moments (uvw) to $(\bar{v}uw)$ or $(v\bar{u}\bar{w})$ if combined with time-inversion $1'$. As the $\bar{4}$ and $\bar{4}'$ operations keep the positions of the magnetic TM ions T in $Ba_2TGe_2O_7$ invariant, the respective eigenvectors with eigenvalue $+1$ represent the allowed magnetic moment directions, which is [001] for $\bar{4}$ and none for $\bar{4}'$ (i.e. does not allow any magnetic moment at the $2a$ Wyckoff Position of group $P\bar{4}2_1m$). Thus, neither $\bar{4}$ nor $\bar{4}'$ can be conserved by the magnetic space group describing an in-plane AFM structure in $Ba_2TGe_2O_7$. Because the combination of any two-fold rotation axis with any mirror plane listed above recovers the four-fold inversion symmetry, at least one of the two must be excluded as well. This gives rise to two possible high-symmetry magnetic space groups, which will be discussed in more detail in the following. An overview of all possible magnetic space groups consistent with the $P\bar{4}2_1m$ parent space group is given in Fig. 2.6.

Magnetic space group conserving the two-fold screw axis

The two-fold screw axis along the [100] direction transforms magnetic moments (uvw) to $(u\bar{v}\bar{w})$ or if combined with $1'$ to $(\bar{u}vw)$. Analogously, a transformation to $(u\bar{v}\bar{w})$ or $(\bar{u}vw)$ results from the screw axis in [010] direction with or without $1'$, respectively. As both symmetry operations relate the TM ion at (000) with the central one at $(\frac{1}{2}\frac{1}{2}0)$, they must have an equal magnetic transformation to allow an in-plane moment. Thus, exactly one of the two has to host $1'$.

For the first pair, namely $2'_1$ in [100] and 2_1 in [010], the magnetic moment of the central ion is given by $(\bar{u}vw)$, leading to an AFM order in [100] direction and a FM order in [010] direction. The combination of both screw axes leads to $\bar{x}\bar{y}z$ combined with $1'$, denoting a two-fold rotation axis $2'$ along [001]. As $2'$ transforms magnetic moments (uvw) to $(uv\bar{w})$ and keeps the positions of the magnetic TM ions invariant, it restricts the magnetic moments to the ab plane. To summarize, the first symmetry operation pair forms the orthorhombic magnetic space group $P2'_12_12'$ and has an AFM order in [100] direction and a FM order in [010] direction. For the second pair, an analogous consideration leads to the equivalent magnetic space group $P2_12'_12'$ with AFM order in [010] direction and FM order in [100] direction.

The excluded symmetry operations of the parent space groups, optionally combined with time reversal, form the set of possible magnetic domains. Thus, four tetragonal domains, related by a 90° rotation of the in-plane magnetic moment, compensate the exclusion of the four-fold inversion and mirror plane symmetry in the magnetic space group. These four domains keep the alignment of the FM to AFM moment (i.e. the vector product of the AFM and FM moment) constant. This is in agreement with the expectation that the DMI energy, which is proportional to $D_z \left(\boldsymbol{m}^{\mathrm{AFM}} \times \boldsymbol{m}^{\mathrm{FM}}\right)_z$ as discussed in Chap. 4, should be the same for all magnetic domains.

Magnetic space group conserving the mirror plane

Likewise, a magnetic space group can be built using only the diagonal mirror planes. The one normal to the [110] direction transforms magnetic moments (uvw) to $(vu\bar{w})$ or if combined with time-inversion $1'$ to $(\bar{v}\bar{u}w)$. Analogously, the mirror plane with normal to $[1\bar{1}0]$ transforms magnetic moments to $(\bar{v}\bar{u}w)$ or if combined with $1'$ to $(vu\bar{w})$. Thus, exactly one of the two operations must be combined with $1'$ to allow an magnetic moment for the TM ions in $Ba_2TGe_2O_7$. Combining the two operations leads again to a $2'$ symmetry in [001] direction, confining the magnetic moment to the ab plane. For the first operation pair, namely m' normal to [110] and m normal to $[1\bar{1}0]$, the magnetic moment of the central ion is given by $(\bar{v}\bar{u}w)$ and results in an AFM order in [110] direction and a FM order in $[1\bar{1}0]$ direction. The corresponding orthorhombic magnetic space group is $Cm'm2'$, which is related to the parent setting by the transformation $a' = a+b$, $b' = b-a$ and $c' = c$. This transformation aligns the high-symmetry directions with the orthorhombic axes and changes the centering from primitive to C centered. The second pair of magnetic symmetry operations forms the equivalent magnetic space group $Cmm'2'$, which has an FM and a AFM order in the [110] and $[1\bar{1}0]$ direction of the parent setting, respectively. A similar consideration as in the previous section leads to four possible tetragonal domains with uniform alignment of the FM to AFM moment.

Magnetic space group conserving the vertical two-fold rotation axis

If the four-fold inversion axis, the two-fold screw axes and the diagonal mirror planes of the parent space group $P\bar{4}2_1m$ are dismissed, the remaining symmetry is the two-fold rotation, originally contained in the four-fold inversion axis. This symmetry operation transforms magnetic moments (uvw) to $(\bar{u}\bar{v}w)$ or if combined with $1'$ to $(uv\bar{w})$. As the positions of the TM ions are kept invariant by the two-fold rotation axis, only $2'$ is consistent with an in-plane magnetic moment, as 2 restricts the magnetic moments to the c direction. If equal magnetic moment values for both TM ions are assumed, an arbitrary in-plane direction for the AFM ordering with perpendicular FM ordering can be realized in the resulting orthorhombic magnetic space group $P112'$. We denote the angle between the AFM ordering direction and the a axis as ρ (illustrated in Fig. 2.7(c)). From the omission of the four-fold inversion symmetry in the magnetic space group, four tetragonal domains with uniform alignment of the FM to AFM moment are expected. In addition, the exclusion of the two-fold screw axes and the diagonal mirror planes results in another set of four tetragonal domains, having the same alignment of the FM to AFM moment; however, enclosing an angle of $-\rho$ to the a axis.

A.4. Magnetic space groups for $\boldsymbol{\tau} = (00½)$

To get a $\boldsymbol{\tau} = (00½)$ propagation vector as a result of an AFM ordering in c direction, the UC needs to be enlarged in c direction and the symmetry operator extended by the so-called *antitranslation*, which is in this case a regular c-translation for ½ in the enlarged UC combined with time reversal $1'$. If a, b and c denote the original lattice

parameters, $a' = a$, $b' = b'$ and $c' = 2c$ denote the ones of the enlarged UC. Accordingly, the relative lattice positions (xyz) of the atoms transform to $(x'y'z')$ with $x' = x$, $y' = y$ and $z' = z/2$. The upper half of the UC ($z \geq \frac{1}{2}$) is populated by the antitranslation. Interestingly, a combination of the primed mirror plane m' and the antitranslation leads to the non-primed glide plane c. Thus, the mirror plane can simply be replaced by a non-primed glide plane instead of priming it. Accordingly, the primed two-fold rotation axis $2'$ in c direction is equivalent to a non-primed screw axis 2_1. However, it is less straightforward for the screw axes in the $\langle 100 \rangle$ directions. An additional c-shift of $\frac{1}{2}$ during the transformation from abc to $a'b'c'$ is equivalent to priming both [100] and [010] screw axes. This is indicated by a $*$ in Fig. 2.8. For differently primed [100] and [010] screw axes, implicating a $2'$ rotation or a 2_1 screw axis in c direction, the abc to $a'b'c'$ transformation must have an additional $\frac{1}{4}$ shift in [100] or [010] to the $\frac{1}{2}$ shift in c, leading to a primed [100] or [010] screw axis, respectively. Following these relations, the discussion in appendix A.3 still holds and the magnetic space groups for the $\boldsymbol{\tau} = (00\frac{1}{2})$ propagation vector (illustrated in Fig. 2.8) can be extracted from those with $\boldsymbol{\tau} = (000)$ (illustrated in Fig. 2.6).

B. Polarized neutron diffraction

In this part of the appendix, mathematical details to PND, some neutron polarizers and the complete equations for SNP are presented.

B.1. Density matrix formalism for polarized neutron scattering

Properties of Pauli spin matrices

For Pauli spin matrices, the following identities hold [154].

$$\hat{\sigma}_x = \begin{pmatrix} 0 & 1 \\ 1 & 0 \end{pmatrix} \quad \hat{\sigma}_y = \begin{pmatrix} 0 & -i \\ i & 0 \end{pmatrix} \quad \hat{\sigma}_z = \begin{pmatrix} 1 & 0 \\ 0 & -1 \end{pmatrix} \quad |+\rangle = \begin{pmatrix} 1 \\ 0 \end{pmatrix} \quad |-\rangle = \begin{pmatrix} 0 \\ 1 \end{pmatrix}$$

$$\begin{aligned} \hat{\sigma}_\alpha \hat{\sigma}_\beta &= \delta_{\alpha\beta} + i\epsilon_{\alpha\beta\gamma}\hat{\sigma}_\gamma \\ \mathrm{Tr}(\hat{\sigma}_\alpha) &= 0 \\ \mathrm{Tr}(\hat{\sigma}_\alpha \hat{\sigma}_\beta) &= 2\delta_{\alpha\beta} \\ \mathrm{Tr}(\hat{\sigma}_\alpha \hat{\sigma}_\beta \hat{\sigma}_\gamma) &= 2i\epsilon_{\alpha\beta\gamma} \\ \mathrm{Tr}(\hat{\sigma}_\alpha \hat{\sigma}_\beta \hat{\sigma}_\gamma \hat{\sigma}_\delta) &= 2(\delta_{\alpha\beta}\delta_{\gamma\delta} - \delta_{\alpha\gamma}\delta_{\beta\delta} + \delta_{\alpha\delta}\delta_{\beta\gamma}) \\ (\mathbf{a}\cdot\hat{\boldsymbol{\sigma}})(\mathbf{b}\cdot\hat{\boldsymbol{\sigma}}) &= (\mathbf{a}\cdot\mathbf{b})\mathbb{1} + i\hat{\boldsymbol{\sigma}}\cdot(\mathbf{a}\times\mathbf{b}) \end{aligned}$$

Note that the trace is invariant for cyclic permutations

$$\mathrm{Tr}\big(\hat{A}\hat{B}\hat{C}\big) = \mathrm{Tr}\big(\hat{C}\hat{A}\hat{B}\big) = \mathrm{Tr}\big(\hat{B}\hat{C}\hat{A}\big).$$

Total scattering cross-section

The total scattering cross-section σ for a scattering matrix $\hat{V}$ from a neutron spin state χ, defining the density matrix $\hat{\rho} = |\chi\rangle\langle\chi^\dagger|$, is given by

$$\frac{\mathrm{d}\sigma}{\mathrm{d}\Omega} = \sum_i \left| \langle\phi_i|\hat{V}|\chi\rangle \right|^2,$$

with $|\phi_i\rangle$ the pure spin states $|+\rangle$ and $|-\rangle$. This can be rewritten as

$$\sum_i \left| \langle\phi_i|\hat{V}|\chi\rangle \right|^2 = \sum_i \langle\phi_i|\,\hat{V}\,\underbrace{|\chi\rangle\langle\chi^\dagger|}_{\hat{\rho}}\,\hat{V}^\dagger\,|\phi_i\rangle = \sum_i \langle\phi_i|\hat{V}\hat{\rho}\hat{V}^\dagger|\phi_i\rangle = \mathrm{Tr}\left(\hat{\rho}\hat{V}^\dagger\hat{V}\right),$$

which finally provides

$$\sigma = \mathrm{Tr}\left(\hat{\rho}\hat{V}^\dagger\hat{V}\right) = \left\langle \hat{V}^\dagger\hat{V} \right\rangle_{\hat{\rho}}.$$

B.2. Devices for polarized neutron diffraction

This section provides a brief overview of the basic functionality of some common PND devices, used for polarizing and analyzing the neutron beam.

Ferromagnetic single crystal polarizers

For FM single crystal polarizers in a magnetic field with direction $\hat{\mathbf{B}}$, the polarizing efficiency P^{Pol} for an non-polarized neutron beam can be directly defined by combining Eqs. (3.22) and (3.23) and selecting the incoming polarization $\mathbf{P}$ as zero

$$P^{\mathrm{Pol}} = \mathbf{P}^{\mathrm{sc}} \cdot \hat{\mathbf{B}} = \frac{2\,\mathrm{Re}[\mathbf{M}N^*] \cdot \hat{\mathbf{B}}}{NN^* + \mathbf{M}\cdot\mathbf{M}^*}. \tag{B.1}$$

Note that chiral contributions are omitted as they cannot be present in pure FM systems. An almost perfect beam polarization results from the (111) reflection of a Heusler (Cu_2MnAl) single crystal with $P^{\mathrm{Pol}} \approx -0.95$ [305].

^{3}He spin filter cells (SFCs)

For ^{3}He SFCs, the polarized ^{3}He gas has different absorption cross-sections for neutrons in the up and down state. This results in a finite neutron polarization P^{Pol} of the transmitted beam given by

$$P^{\mathrm{Pol}} = \tanh\left(\Omega P^{\mathrm{He}}\right), \tag{B.2}$$

with the opacity $\Omega = 0.0732\,p[\mathrm{bar}]\,l[\mathrm{cm}]\,\lambda[\text{Å}]$, defined by the used neutron wavelength λ, the cell length l and the ^{3}He pressure p [244]. As the ^{3}He spin polarization $P^{\mathrm{He}} = P_0^{\mathrm{He}}\exp(-t/T_1)$ relaxes exponentially with a time constant T_1 of around 100 h, also the polarization efficiency is time dependent, and thus requires particular consideration during the data analysis as explicitly discussed in Ref. [244]. Note that also the SFC's

transmission T for an incoming non-polarized neutron beam is time dependent and should be considered during the analysis. It is given by

$$T = T_0 \exp(-\Omega) \cosh\left(\Omega P^{\mathrm{He}}\right), \tag{B.3}$$

with T_0 the neutron transmission of the evacuated cell.

Supermirrors

Neutron supermirrors are thin-film multilayer structures with alternating layers of a FM and a non-magnetic material. The materials are chosen such that the neutron scattering density for the FM and non-magnetic material are equal for one of the two spin states. Thus, the supermirror has a uniform refractive index for this spin state, resulting in pure transmission. For the other spin state, the refractive index has a periodic structure that gives rise to Bragg reflection. Thus, a very high polarization of the reflected beam (P^{Pol} typically above 99%) is achieved. To provide a good reflectively for all angles of the incoming neutrons up to a preferably high cutoff angle $\theta^{\max}$, the supermirrors are designed to have a gradual change in their layer thickness [168, 306]. The cutoff angle for the neutron wavelength λ is defined by the characteristic m-value of the supermirror as $\theta^{\max} \approx 0.1 m \lambda \frac{\mathrm{deg}}{\mathrm{\AA}}$. The supermirror is typically situated in a strong magnetic field ($> 500\,\mathrm{G}$) produced by permanent magnets to saturate its FM layers and to serve as guide field for the neutron polarization.

B.3. Cross-sections for polarized neutron diffraction

The 36 individual cross-sections of SNP, resulting from all the combinations of the polarization and analysis axis aligned along the $\pm x$, $\pm y$ and $\pm z$ axes of the scattering reference system with $x \parallel \mathbf{q}$, $z \parallel \mathbf{k}_i \times \mathbf{k}_f$ and y making up a right-handed set, are listed in Table B.1.

B.4. Polarization matrix elements

The polarization matrix elements of SNP, defined in Eq. (3.31), can be evaluated for a polarization and analysis axis along the xyz-directions of the scattering reference system defined in Sec. 3.3.2 using Eq. (3.30). This leads to nine distinct matrix elements $\mathcal{P}_{ij}$ with finite polarization and analysis efficiencies P and P', which can be written as

$$\begin{aligned}
\mathcal{P}_{xx} &= P' \frac{P\left(NN^* - M_y M_y^* - M_z M_z^*\right) - 2\,\mathrm{Im}[M_y M_z^*]}{NN^* + M_y M_y^* + M_z M_z^* + 2P\,\mathrm{Im}[M_y M_z^*]} \\
\mathcal{P}_{yy} &= P' \frac{P\left(NN^* + M_y M_y^* - M_z M_z^*\right) - 2\,\mathrm{Re}[M_y N^*]}{NN^* + M_y M_y^* + M_z M_z^* + 2P\,\mathrm{Re}[M_y N^*]} \\
\mathcal{P}_{zz} &= P' \frac{P\left(NN^* - M_y M_y^* + M_z M_z^*\right) - 2\,\mathrm{Re}[M_z N^*]}{NN^* + M_y M_y^* + M_z M_z^* + 2P\,\mathrm{Re}[M_z N^*]}
\end{aligned}$$

Table B.1.: Scattering cross-sections for all 36 possible spin channels in SNP with finite P and $P^{'}$. Suppressed contributions are grayed out.

σ_{ij}			nuclear	magnetic	chiral	nuclear magnetic interference	
xx	=	½ (	$\left(1+PP^{'}\right)NN^{*}$	$+\left(1-PP^{'}\right)\left(M_yM_y^{*}+M_zM_z^{*}\right)$	$+2\left(P-P^{'}\right)\mathrm{Im}[M_yM_z^{*}]$		)
$x\bar{x}$	=	½ (	$\left(1-PP^{'}\right)NN^{*}$	$+\left(1+PP^{'}\right)\left(M_yM_y^{*}+M_zM_z^{*}\right)$	$+2\left(P+P^{'}\right)\mathrm{Im}[M_yM_z^{*}]$		)
$\bar{x}x$	=	½ (	$\left(1-PP^{'}\right)NN^{*}$	$+\left(1+PP^{'}\right)\left(M_yM_y^{*}+M_zM_z^{*}\right)$	$-2\left(P+P^{'}\right)\mathrm{Im}[M_yM_z^{*}]$		)
$\bar{x}\bar{x}$	=	½ (	$\left(1+PP^{'}\right)NN^{*}$	$+\left(1-PP^{'}\right)\left(M_yM_y^{*}+M_zM_z^{*}\right)$	$-2\left(P-P^{'}\right)\mathrm{Im}[M_yM_z^{*}]$		)
yy	=	½ (	$\left(1+PP^{'}\right)NN^{*}$	$+\left(1+PP^{'}\right)M_yM_y^{*}+\left(1-PP^{'}\right)M_zM_z^{*}$		$+2\left(P+P^{'}\right)\mathrm{Re}[M_yN^{*}]$	)
$y\bar{y}$	=	½ (	$\left(1-PP^{'}\right)NN^{*}$	$+\left(1-PP^{'}\right)M_yM_y^{*}+\left(1+PP^{'}\right)M_zM_z^{*}$		$+2\left(P-P^{'}\right)\mathrm{Re}[M_yN^{*}]$	)
$\bar{y}y$	=	½ (	$\left(1-PP^{'}\right)NN^{*}$	$+\left(1-PP^{'}\right)M_yM_y^{*}+\left(1+PP^{'}\right)M_zM_z^{*}$		$-2\left(P-P^{'}\right)\mathrm{Re}[M_yN^{*}]$	)
$\bar{y}\bar{y}$	=	½ (	$\left(1+PP^{'}\right)NN^{*}$	$+\left(1+PP^{'}\right)M_yM_y^{*}+\left(1-PP^{'}\right)M_zM_z^{*}$		$-2\left(P+P^{'}\right)\mathrm{Re}[M_yN^{*}]$	)
zz	=	½ (	$\left(1+PP^{'}\right)NN^{*}$	$+\left(1-PP^{'}\right)M_yM_y^{*}+\left(1+PP^{'}\right)M_zM_z^{*}$		$+2\left(P+P^{'}\right)\mathrm{Re}[M_zN^{*}]$	)
$z\bar{z}$	=	½ (	$\left(1-PP^{'}\right)NN^{*}$	$+\left(1+PP^{'}\right)M_yM_y^{*}+\left(1-PP^{'}\right)M_zM_z^{*}$		$+2\left(P-P^{'}\right)\mathrm{Re}[M_zN^{*}]$	)
$\bar{z}z$	=	½ (	$\left(1-PP^{'}\right)NN^{*}$	$+\left(1+PP^{'}\right)M_yM_y^{*}+\left(1-PP^{'}\right)M_zM_z^{*}$		$-2\left(P-P^{'}\right)\mathrm{Re}[M_zN^{*}]$	)
$\bar{z}\bar{z}$	=	½ (	$\left(1+PP^{'}\right)NN^{*}$	$+\left(1-PP^{'}\right)M_yM_y^{*}+\left(1+PP^{'}\right)M_zM_z^{*}$		$-2\left(P+P^{'}\right)\mathrm{Re}[M_zN^{*}]$	)
$xy=y\bar{x}^{\dagger}$	=	½ (	NN^{*}	$+M_yM_y^{*}+M_zM_z^{*}$	$+2P\mathrm{Im}[M_yM_z^{*}]$	$+2P^{'}\mathrm{Re}[M_yN^{*}]-2PP^{'}\mathrm{Im}[M_zN^{*}]$	)
$x\bar{y}=\bar{y}\bar{x}^{\dagger}$	=	½ (	NN^{*}	$+M_yM_y^{*}+M_zM_z^{*}$	$+2P\mathrm{Im}[M_yM_z^{*}]$	$-2P^{'}\mathrm{Re}[M_yN^{*}]+2PP^{'}\mathrm{Im}[M_zN^{*}]$	)
$\bar{x}y=yx^{\dagger}$	=	½ (	NN^{*}	$+M_yM_y^{*}+M_zM_z^{*}$	$-2P\mathrm{Im}[M_yM_z^{*}]$	$+2P^{'}\mathrm{Re}[M_yN^{*}]+2PP^{'}\mathrm{Im}[M_zN^{*}]$	)
$\bar{x}\bar{y}=\bar{y}x^{\dagger}$	=	½ (	NN^{*}	$+M_yM_y^{*}+M_zM_z^{*}$	$-2P\mathrm{Im}[M_yM_z^{*}]$	$-2P^{'}\mathrm{Re}[M_yN^{*}]-2PP^{'}\mathrm{Im}[M_zN^{*}]$	)
$xz=z\bar{x}^{\dagger}$	=	½ (	NN^{*}	$+M_yM_y^{*}+M_zM_z^{*}$	$+2P\mathrm{Im}[M_yM_z^{*}]$	$+2P^{'}\mathrm{Re}[M_zN^{*}]+2PP^{'}\mathrm{Im}[M_yN^{*}]$	)
$x\bar{z}=\bar{z}\bar{x}^{\dagger}$	=	½ (	NN^{*}	$+M_yM_y^{*}+M_zM_z^{*}$	$+2P\mathrm{Im}[M_yM_z^{*}]$	$-2P^{'}\mathrm{Re}[M_zN^{*}]-2PP^{'}\mathrm{Im}[M_yN^{*}]$	)
$\bar{x}z=zx^{\dagger}$	=	½ (	NN^{*}	$+M_yM_y^{*}+M_zM_z^{*}$	$-2P\mathrm{Im}[M_yM_z^{*}]$	$+2P^{'}\mathrm{Re}[M_zN^{*}]-2PP^{'}\mathrm{Im}[M_yN^{*}]$	)
$\bar{x}\bar{z}=\bar{z}x^{\dagger}$	=	½ (	NN^{*}	$+M_yM_y^{*}+M_zM_z^{*}$	$-2P\mathrm{Im}[M_yM_z^{*}]$	$-2P^{'}\mathrm{Re}[M_zN^{*}]+2PP^{'}\mathrm{Im}[M_yN^{*}]$	)
$yz=zy^{\dagger}$	=	½ (	NN^{*}	$+M_yM_y^{*}+M_zM_z^{*}+2PP^{'}\mathrm{Re}[M_yM_z^{*}]$		$+2P\mathrm{Re}[M_yN^{*}]+2P^{'}\mathrm{Re}[M_zN^{*}]$	)
$y\bar{z}=\bar{z}y^{\dagger}$	=	½ (	NN^{*}	$+M_yM_y^{*}+M_zM_z^{*}-2PP^{'}\mathrm{Re}[M_yM_z^{*}]$		$+2P\mathrm{Re}[M_yN^{*}]-2P^{'}\mathrm{Re}[M_zN^{*}]$	)
$\bar{y}z=z\bar{y}^{\dagger}$	=	½ (	NN^{*}	$+M_yM_y^{*}+M_zM_z^{*}-2PP^{'}\mathrm{Re}[M_yM_z^{*}]$		$-2P\mathrm{Re}[M_yN^{*}]+2P^{'}\mathrm{Re}[M_zN^{*}]$	)
$\bar{y}\bar{z}=\bar{z}\bar{y}^{\dagger}$	=	½ (	NN^{*}	$+M_yM_y^{*}+M_zM_z^{*}+2PP^{'}\mathrm{Re}[M_yM_z^{*}]$		$-2P\mathrm{Re}[M_yN^{*}]-2P^{'}\mathrm{Re}[M_zN^{*}]$	)

N : Nuclear scattering factor (see Eq. (3.4))
M_i : Components of the vectorial magnetic scattering factor $\mathbf{M}\perp\mathbf{q}$ (see Eq. (3.7))
σ_{ij} : Scattering cross-section for polarization axis i and analysis axis j (see general Eq. (3.30))
$ij^{\dagger}$: These scattering cross-sections result from the given equation by exchanging the efficiencies P and $P^{'}$ such that $P^{\dagger}=P^{'}$ and $P^{'\dagger}=P$

P : Polarizing efficiency
$P^{'}$: Analyzing efficiency
x,y,z : Reference system defined in Sec. 3.3.2

$$
\begin{aligned}
\mathcal{P}_{xy} &= P' \frac{2\,\mathrm{Re}[M_y N^*] - 2P\,\mathrm{Im}[M_z N^*]}{NN^* + M_y M_y^* + M_z M_z^* + 2P\,\mathrm{Im}[M_y M_z^*]} \\
\mathcal{P}_{yx} &= P' \frac{-2\,\mathrm{Im}[M_y M_z^*] + 2P\,\mathrm{Im}[M_z N^*]}{NN^* + M_y M_y^* + M_z M_z^* + 2P\,\mathrm{Re}[M_y N^*]}
\end{aligned}
$$

$$
\begin{aligned}
\mathcal{P}_{xz} &= P' \frac{2\,\mathrm{Re}[M_z N^*] + 2P\,\mathrm{Im}[M_y N^*]}{NN^* + M_y M_y^* + M_z M_z^* + 2P\,\mathrm{Im}[M_y M_z^*]} \\
\mathcal{P}_{zx} &= P' \frac{-2\,\mathrm{Im}[M_y M_z^*] - 2P\,\mathrm{Im}[M_y N^*]}{NN^* + M_y M_y^* + M_z M_z^* + 2P\,\mathrm{Re}[M_z N^*]}
\end{aligned}
$$

$$
\begin{aligned}
\mathcal{P}_{yz} &= P' \frac{2\,\mathrm{Re}[M_z N^*] + 2P\,\mathrm{Re}[M_y M_z^*]}{NN^* + M_y M_y^* + M_z M_z^* + 2P\,\mathrm{Re}[M_y N^*]} \\
\mathcal{P}_{zy} &= P' \frac{2\,\mathrm{Re}[M_y N^*] + 2P\,\mathrm{Re}[M_y M_z^*]}{NN^* + M_y M_y^* + M_z M_z^* + 2P\,\mathrm{Re}[M_z N^*]}.
\end{aligned}
$$

Notably, the denominator of the $\mathcal{P}_{ij}$ elements reflects the total scattering cross-section for an incoming polarization in i direction.

C. Extinction correction

Starting from the kinematic theory, Becker and Coppens [195] derived a model for primary and secondary extinction within the limit of the validity of the Darwin transfer equations [307]. This model provides a correction factor y for the theoretical integrated intensity I^{calc} such that the measured intensity I^{mes} is given by

$$
I^{\mathrm{mes}} = y I^{\mathrm{calc}}. \tag{C.1}
$$

C.1. Primary extinction

For primary extinction, the correction factor y_p for a reflection $|\mathbf{q}| = 4\pi \sin(\theta)/\lambda$ with Bragg angle θ and neutron wavelength λ is given by

$$
y_p = \frac{1}{\sqrt{1 + 2x_p + \frac{A_p x_p^2}{1 + B_p x_p}}} \tag{C.2}
$$

with A_p, B_p and x_p defined as

$$
\begin{aligned}
A_p &= 0.20 + 0.45\cos(2\theta) \\
B_p &= 0.22 - 0.12\,(0.5 - \cos(2\theta))^2 \\
x_p &= \frac{2}{3}\frac{\sigma \lambda^3 \bar{\alpha}_p \bar{t}}{V_{\mathrm{UC}}^2 \sin(2\theta)}.
\end{aligned} \tag{C.3}
$$

The scattering cross-section and the UC volume are denoted as σ and V_{UC}, respectively. $\bar{t}$ indicates the mean path length through the crystal and is, for example, in a spherical crystal with radius r given by $\bar{t} = \frac{3}{2}r$. The local thickness l of the crystal parallel to the diffracted beam defines $\bar{\alpha}_p$ by an average over the crystal volume V_{C} as

$$\bar{\alpha}_p = \frac{1}{V_{\mathrm{C}}} \int_{\mathrm{C}} \frac{l \sin(2\theta)}{\lambda} \, \mathrm{d}V \, . \tag{C.4}$$

For a sphere of radius r, it is given by $\bar{\alpha}_p = \frac{3}{2} r \sin(2\theta)/\lambda$.

C.2. Secondary extinction

For secondary extinction in a mosaic crystal with idealized spherical domains with radius r_{dom} and Gaussian (G) or Lorentzian (L) mosaic spread g in inverse radians, the correction factors can be analogously expressed as

$$\begin{aligned} y_{s,G} &= \frac{1}{\sqrt{1 + 2.12 x_{s,G} + \frac{A_{s,G} x_{s,G}^2}{1 + B_{s,G} x_{s,G}}}} \\ y_{s,L} &= \frac{1}{\sqrt{1 + 2.00 x_{s,L} + \frac{A_{s,L} x_{s,L}^2}{1 + B_{s,L} x_{s,L}}}} \end{aligned} \tag{C.5}$$

with A_s, B_s and x_s defined as

$$\begin{aligned} A_{s,G} &= 0.58 + 0.48 \cos(2\theta) + 0.24 \cos^2(2\theta) \\ A_{s,L} &= 0.025 + 0.285 \cos(2\theta) \\ B_{s,G} &= 0.02 - 0.025 \cos(2\theta) \\ B_{s,L} &= \begin{cases} 0.15 - 0.2 \left(0.75 - \cos(2\theta)\right)^2 & \text{if } \cos(2\theta) > 0 \\ -0.45 \cos(2\theta) & \text{if } \cos(2\theta) < 0 \end{cases} \\ x_{s,G} &= \frac{\sigma \lambda^3 \bar{t}}{V_{\mathrm{UC}}^2 \sin(2\theta)} \frac{1}{\sqrt{\left(\frac{\lambda}{\sin(2\theta) r_{\mathrm{dom}}}\right)^2 + \frac{9}{8g^2}}} \\ x_{s,L} &= \frac{\sigma \lambda^3 \bar{t}}{V_{\mathrm{UC}}^2 \sin(2\theta)} \frac{1}{\frac{\lambda}{\sin(2\theta) r_{\mathrm{dom}}} + \frac{1}{g}} . \end{aligned} \tag{C.6}$$

The total correction parameter y can be approximated as

$$y \approx y_p[x_p] y_s[y_p x_s] \tag{C.7}$$

and extended for anisotropy in the crystal shape and the mosaicity (see Ref. [308]).

D. Reconstruction of magnetization densities

Within this section of the appendix, some additional details about the reconstruction of magnetization densities are provided.

D.1. Inverse Fourier transformation from classical FR data

For the classical case of a field-induced magnetic moment in centrosymmetric structures (e.g. in the PM phase), the magnetization density $\mathbf{m}(\mathbf{r}) = m(\mathbf{r})\hat{\mathbf{B}}$ and the Fourier coefficients $\mathbf{F}_\mathrm{M} = F_\mathrm{M}\hat{\mathbf{B}}$ in Eq. (3.40) are assumed to be parallel to the applied field direction $\hat{\mathbf{B}}$ and the nuclear and magnetic structure factors are real (i.e. $\mathrm{Im}[N] = 0$ and $\mathrm{Im}[\mathbf{M}] = 0$). As the incoming beam polarization $\mathbf{P}$ is also in field direction (see Sec. 3.3.1), the measured asymmetry from Eq. (3.26) is given by

$$A = P\frac{2N\mathbf{M}\cdot\hat{\mathbf{B}}}{|N|^2 + \mathbf{M}\cdot\mathbf{M}}. \tag{D.1}$$

The projections of the magnetic structure factor are given by

$$\begin{aligned}\mathbf{M}\cdot\hat{\mathbf{B}} &= \left(\frac{\gamma_N r_0}{2\mu_B}\right) F_\mathrm{M}\sin^2(\rho)\\ \mathbf{M}\cdot\mathbf{M} &= \left(\frac{\gamma_N r_0}{2\mu_B}\right)^2 |F_\mathrm{M}|^2\sin^2(\rho).\end{aligned} \tag{D.2}$$

with ρ the angle enclosed by $\hat{\mathbf{B}}$ and $\mathbf{q}$. As a result, Eq. (D.1) can solved for the Fourier coefficients F_M and simplified assuming a small asymmetry A and $|N| > |\mathbf{M}|$ to

$$\begin{aligned}F_\mathrm{M} &= \left(\frac{2\mu_B}{\gamma_N r_0}\right)\frac{NP}{A}\left(1 \pm \sqrt{1 - \left(\underbrace{\frac{A}{P\sin(\rho)}}_{x}\right)^2}\right)\\ &\overset{x\ll 1}{=} \left(\frac{2\mu_B}{\gamma_N r_0}\right)\frac{NA}{2P\sin^2(\rho)}\left(1 + \mathcal{O}\left(x^2\right)\right).\end{aligned} \tag{D.3}$$

Using this direct connection between the measured asymmetry and the Fourier coefficients F_M, the magnetization density in the UC can be reconstructed using Eq. (3.41). However, for more complex magnetic arrangements or noncentrosymmetric structures, the direct connection between F_M and A in Eq. (D.3) is no longer valid.

D.2. The Skilling and Bryan maximum entropy algorithm

For the maximal entropy solution according to the Skilling-Bryan (SB) algorithm [207], the two main properties, namely the entropy S and the fit quality C, are defined in Eqs. (3.42) and (3.43) in Sec. 3.5.2. In this regard, the scalar magnetization density at grid point $\mathbf{r}_i$ in the UC is given by the positive images points $f_i^\pm$, representing the positive and negative part of the density as $m_i = f_i^+ - f_i^-$. Note that without any data constraints, the entropy is maximized by $f_i^\pm = A$ corresponding to a vanishing density $m_i = A - A = 0$. The magnetic Fourier coefficients F_k, defined in Eq. (3.6), can be expressed as

$$F_k = \left(\frac{\gamma_N r_0}{2\mu_B}\right)\frac{V_\mathrm{UC}}{N_i}\sum_i\left(f_i^+ - f_i^-\right)e^{-i\mathbf{q}_k\cdot\mathbf{r}_i}. \tag{D.4}$$

The purpose of the SB algorithm is to maximize S to the constraint of $C \leq C_{\text{aim}}$ with C_{aim} typically selected close to 1. This is usually done by maximizing an objective function Q combining S and C, controlled by the Lagrange multiplier λ.

$$Q = S - \lambda C \tag{D.5}$$

However, the iterative SB algorithm is characterized by not using λ explicitly [309]. Since this algorithm is presented in detail in Ref. [207], only the basic procedure is outlined in the following.

Concerning, for example, a $50\times50\times50$ grid in the UC, thus in total $N = 2N_i = 2.5\cdot10^5$ image points, it is not reasonable to optimize every grid point individually. Therefore, the optimization process is broken down into search directions (SDs) $\mathbf{e}_\mu^{\text{SD}} \in \mathbb{R}^N$ in the image space. The key to a fast converging and robust algorithm is the proper definition of these search directions. In the SB algorithm, the first three search directions for each iteration are defined as

$$(\mathbf{e}_1^{\text{SD}})_i = f_i \tag{D.6}$$

$$(\mathbf{e}_2^{\text{SD}})_i = \sum_j \left(-\frac{\partial^2 S}{\partial f_i \partial f_j}\right)^{-1} \frac{\partial S}{\partial f_j} \tag{D.7}$$

$$(\mathbf{e}_3^{\text{SD}})_i = \sum_j \left(-\frac{\partial^2 S}{\partial f_i \partial f_j}\right)^{-1} \frac{\partial C}{\partial f_j}, \tag{D.8}$$

with $f_{2i} = f_i^+$ and $f_{2i+1} = f_i^-$ shortened for clarity. These $N_{\text{SD}} = 3$ search directions $\mathbf{e}_\mu^{\text{SD}}$ are used for a quadratic approximation of the change of S and C by

$$S(\mathbf{x}) = S_0 + \mathbf{S}\cdot\mathbf{x} + \frac{1}{2}\mathbf{x}^\mathsf{T}\mathcal{S}\mathbf{x} \tag{D.9}$$

$$C(\mathbf{x}) = C_0 + \mathbf{C}\cdot\mathbf{x} + \frac{1}{2}\mathbf{x}^\mathsf{T}\mathcal{C}\mathbf{x}, \tag{D.10}$$

resulting from a small variation $\mathrm{d}\mathbf{f} = \sum_\mu^{N_{\text{SD}}} x_\mu \mathbf{e}_\mu^{\text{SD}}$ of the image. S_0 and C_0 denote the entropy and the fit quality for the current image $\mathbf{f}$, respectively. The vectors $\mathbf{S}$ and $\mathbf{C}$ and the matrices $\mathcal{S}$ and $\mathcal{C}$ are given by

$$(\mathbf{S})_\mu = \sum_i \frac{\partial S}{\partial f_i}\left(\mathbf{e}_\mu^{\text{SD}}\right)_i \tag{D.11}$$

$$(\mathbf{C})_\mu = \sum_i \frac{\partial C}{\partial f_i}\left(\mathbf{e}_\mu^{\text{SD}}\right)_i \tag{D.12}$$

$$(\mathcal{S})_{\mu\nu} = (\mathcal{S})_{\nu\mu} = \sum_{i,j} \frac{\partial^2 S}{\partial f_i \partial f_j}\left(\mathbf{e}_\mu^{\text{SD}}\right)_i (\mathbf{e}_\nu^{\text{SD}})_j \tag{D.13}$$

$$(\mathcal{C})_{\mu\nu} = (\mathcal{C})_{\nu\mu} = \sum_{i,j} \frac{\partial^2 C}{\partial f_i \partial f_j}\left(\mathbf{e}_\mu^{\text{SD}}\right)_i (\mathbf{e}_\nu^{\text{SD}})_j, \tag{D.14}$$

with $\mu, \nu \in \{1, 2, ..., N_{\mathrm{SD}}\}$. A basic control algorithm, described in detail by Skilling and Bryan [207] and summarized by Wu [309], is used to find the optimal solution $\mathbf{x}$ for maximizing S and minimizing the constrained C. In order to converge smoothly to the maximum entropy solution, the increments x_μ along the search directions are limited according to $\sum_{\nu\mu} x_\nu(\mathcal{S})_{\mu\nu}x_\mu \leq l_0^2 S_0$ with the step size l_0 and the entropy $S_0 = NA$ for a zero image ($f_i = 0$), given by the total image points N and the default image value A. The solution $\mathbf{x}^3$ for these search directions corresponds to the image variation $\mathrm{d}\mathbf{f}^3 = \sum_\mu^3 (\mathbf{x}^3)_\mu \mathbf{e}_\mu^{\mathrm{SD}}$ and is used to define a new search direction

$$(\mathbf{e}_4^{\mathrm{SD}})_i = \sum_l \underbrace{\sum_j \left(-\frac{\partial^2 S}{\partial f_i \partial f_j}\right)^{-1} \frac{\partial^2 C}{\partial f_j \partial f_l}}_{A_{il}} df_l^3, \tag{D.15}$$

shortened as $\mathbf{e}_4^{\mathrm{SD}} = \mathcal{A}\mathrm{d}\mathbf{f}^3$. With this additional search direction, the components of the quadratic model in Eqs. (D.9) and (D.10) are revised and the basic control algorithm used to find a new solution $\mathbf{x}^4$, resulting in an improved image variation $\mathrm{d}\mathbf{f}^4 = \sum_\mu^4 x_\mu \mathbf{e}_\mu^{\mathrm{SD}}$. This solution defines the fifth search direction as $\mathbf{e}_5^{\mathrm{SD}} = \mathcal{A}\mathrm{d}\mathbf{f}^4$, leading analogously to a solution $\mathbf{x}^5$ and image variation $\mathrm{d}\mathbf{f}^5$. The proposed image variation might be further improved in an iterative process, by continuously replacing $\mathbf{e}_4^{\mathrm{SD}}$ and $\mathbf{e}_5^{\mathrm{SD}}$ with

$$\mathbf{e}_4^{\mathrm{SD}} = \mathrm{d}\mathbf{f}^5 \quad \mathbf{e}_5^{\mathrm{SD}} = \mathcal{A}\mathrm{d}\mathbf{f}^5 \tag{D.16}$$

and recalculating the solution $\mathbf{x}^5$ with a revised quadratic model, until the image variation $\mathrm{d}\mathbf{f}^5$ is accepted. This acceptance criteria is based on the step size of $\mathbf{x}$ and the expected variation in C. After the image is updated to $\mathbf{f}' = \mathbf{f} + \mathrm{d}\mathbf{f}^5$, a new iteration starts, beginning with the definition of a new set of search directions according to Eqs. (D.6) and (D.8).

The convergence criteria for the algorithm can be based either on a lower limit of the image variation $\mathrm{d}\mathbf{f}^5$ or on the degree of non-parallelism ϕ between $\boldsymbol{\nabla}_f S$ and $\boldsymbol{\nabla}_f C$, which is zero for a true maximum entropy image. This angle is defined as

$$\cos(\phi) = \frac{\sum_{i,j} \frac{\partial S}{\partial f_i}\left(-\frac{\partial^2 S}{\partial f_i \partial f_j}\right)^{-1}\frac{\partial C}{\partial f_j}}{\sqrt{\left(\sum_{i,j} \frac{\partial S}{\partial f_i}\left(-\frac{\partial^2 S}{\partial f_i \partial f_j}\right)^{-1}\frac{\partial S}{\partial f_j}\right)\left(\sum_{i,j} \frac{\partial C}{\partial f_i}\left(-\frac{\partial^2 S}{\partial f_i \partial f_j}\right)^{-1}\frac{\partial C}{\partial f_j}\right)}}. \tag{D.17}$$

Note that the partial derivatives of S and C, which are defined in Eqs. (3.42) and (3.43), are given by

$$\frac{\partial S}{\partial f_i^\pm} = -\log\left(\frac{f_i^\pm}{A}\right) \tag{D.18}$$

$$\frac{\partial^2 S}{\partial f_i^\pm \partial f_j^\pm} = -\frac{1}{f_i^\pm}\delta_{ij} \tag{D.19}$$

$$\frac{\partial C}{\partial f_i^\pm} = \pm\left(\frac{\gamma_N r_0}{2\mu_B}\right)\frac{2V_{\mathrm{UC}}}{N_i N_k}\sum_k \frac{F_k^{\mathrm{calc}} - F_k^{\mathrm{obs}}}{\left(dF_k^{\mathrm{obs}}\right)^2} e^{-i\mathbf{q}_k\cdot\mathbf{r}_i} \tag{D.20}$$

$$\frac{\partial^2 C}{\partial f_i^{\pm}\partial f_j^{\pm}} = -\frac{\partial^2 C}{\partial f_i^{\pm}\partial f_j^{\mp}} = \left(\frac{\gamma_N r_0}{2\mu_B}\right)^2 \frac{2V_{\mathrm{UC}}}{N_i N_k} \sum_k \frac{1}{\left(dF_k^{\mathrm{obs}}\right)^2} e^{-i\mathbf{q}_k\cdot(\mathbf{r}_i+\mathbf{r}_j)} \tag{D.21}$$

with $f_i^+ = f_{2i}$ and $f_i^- = f_{2i+1}$ as defined above. This results in $(-\partial^2 S/\partial f_i \partial f_j)^{-1} = f_i \delta_{ij}$, clearly simplifying the presented equations for the conventional MEM.

D.3. Advanced maximum entropy algorithm

As discussed in Sec. 3.5.3, the conventional entropy S in Eq. (3.42) needs to be adjusted for the advanced MEM approach. To allow positive and negative values for the image points, f_i can be replaced by $|f_i| + A$, leading to

$$S^{\mathrm{adv}} = -\sum_i (|f_i| + A)\left(\log\left(\frac{|f_i| + A}{A}\right) - 1\right). \tag{D.22}$$

with continuous partial derivatives

$$\frac{\partial S^{\mathrm{adv}}}{\partial f_i} = -\log\left(\frac{|f_i| + A}{A}\right)\mathrm{sgn}(f_i) \tag{D.23}$$

$$\frac{\partial^2 S^{\mathrm{adv}}}{\partial f_i \partial f_j} = -\frac{1}{|f_i| + A}\delta_{ij}, \tag{D.24}$$

where $\mathrm{sgn}(x)$ is the sign function ($\mathrm{sgn}(x) = 1$ for $x \geq 0$ and -1 otherwise). For a collinear alignment, the scalar magnetization density is directly given by the image points as $m_i = f_i$. As shown by Gull and Skilling [212], also the conventional entropy, defined in Eq. (3.42) with m_i split into a positive and negative image point $f_i^{\pm}$, can be rewritten as functional of m_i alone, leading to

$$S^{\mathrm{conv}} = \sum_i \sqrt{\frac{m_i^2}{4} + A^2} - \frac{m_i}{2}\log\left(\frac{\sqrt{\frac{m_i^2}{4} + A^2} + \frac{m_i}{2}}{A}\right) \tag{D.25}$$

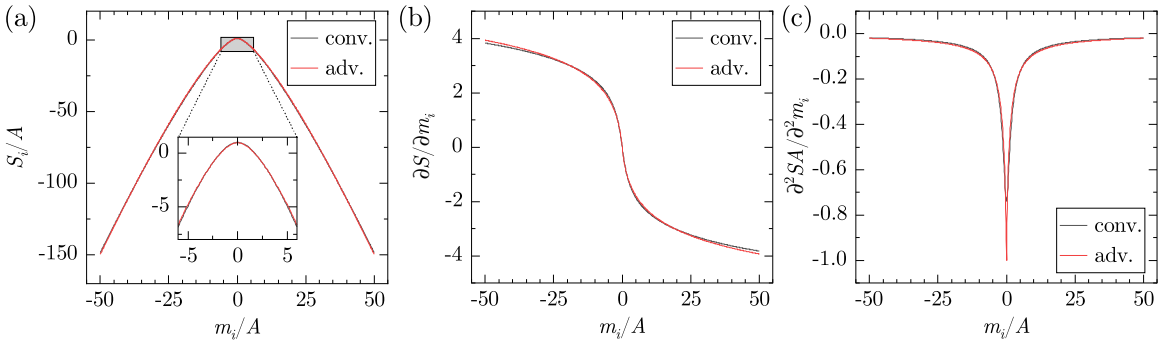

Figure D.1.: Graphical comparison between the dependence of (a) the normalized entropy S_i for a single magnetization m_i and (b,c) its partial derivatives on m_i/A for the conventional (black line) and advanced (red line) MEM definition, presented in Eqs. (D.25) to (D.26) and Eqs. (D.22) to (D.24), respectively. The background level A for the conventional definition was scaled by $(e-1)^{-1}$ for consistency between the models.

with partial derivatives

$$\frac{\partial S^{\text{conv}}}{\partial m_i} = -\frac{1}{2}\log\left(\frac{\sqrt{\frac{m_i^2}{4}+A^2}+\frac{m_i}{2}}{A}\right) \qquad \frac{\partial^2 S^{\text{conv}}}{\partial m_i \partial m_j} = -\frac{1}{4\sqrt{\frac{m_i^2}{4}+A^2}}\delta_{ij}. \tag{D.26}$$

Comparing the dependency of S on the normalized magnetization density m_i/A, the novel advanced approach reproduces well the behaviour of the conventional entropy as illustrated in Fig. D.1(a). Clear to see is a maximum in the entropy located at $m_i = 0$ for both models, which is adopted if no data constraints are present. Furthermore, only slight differences are observed in the first (Fig. D.1(b)) and second (Fig. D.1(c)) partial derivatives, which are not significant for any practical usage. In particular, the resulting constant entropy surfaces will also be convex for the advanced entropy definition, which is an important perquisite for the uniqueness of the reconstructed density map [207]. Thus, the selected novel function for the advanced approach in Eq. (D.22) serves as a valid approximation for the entropy S.

For the extension of the entropy to the non-collinear case in Eq. (3.48), the partial derivatives are given by

$$\frac{\partial S}{\partial f_{i,b}} = -\log\left(\frac{|\mathbf{f}_i|+A}{A}\right)\frac{f_{i,b}}{|\mathbf{f}_i|} \tag{D.27}$$

$$\frac{\partial^2 S}{\partial f_{i,b}\partial f_{j,b'}} = -\left(\frac{1}{|\mathbf{f}_i|+A}-\frac{1}{|\mathbf{f}_i|}\log\left(\frac{|\mathbf{f}_i|+A}{A}\right)\right)\frac{f_{i,b}f_{j,b'}}{|\mathbf{f}_i|^2}\delta_{ij} - \frac{1}{|\mathbf{f}_i|}\log\left(\frac{|\mathbf{f}_i|+A}{A}\right)\delta_{ij}\delta_{bb'} \tag{D.28}$$

Note that Eq. (D.27) ensures a gradient in S only for non-zero image points $f_{i,b}$.

The fit quality C for the advanced MEM is defined by Eq. (3.44) and based on the general scattering cross-section σ_k given in Eq. (3.46). The parameters for the quadratic dependency of this cross-section on the image points $\mathbf{f}_i$ can be determined from Eq. (3.29) as

$$\begin{aligned}
u_k &= \frac{1+\mathbf{P}_k\cdot\mathbf{P}'_k}{2}NN^* \\
\mathbf{v}_{i,k} &= \operatorname{Re}[\mathcal{A}^{\mathsf{T}}_{i,k}]\left(\left(\mathbf{P}_k+\mathbf{P}'_k\right)\operatorname{Re}[N_k]+\left(\mathbf{P}_k\times\mathbf{P}'_k\right)\operatorname{Im}[N_k]\right) \\
&\quad+\operatorname{Im}[\mathcal{A}^{\mathsf{T}}_{i,k}]\left(\left(\mathbf{P}_k+\mathbf{P}'_k\right)\operatorname{Im}[N_k]-\left(\mathbf{P}_k\times\mathbf{P}'_k\right)\operatorname{Re}[N_k]\right) \\
\mathcal{W}_{i,j,k} &= \frac{1-\mathbf{P}_k\cdot\mathbf{P}'_k}{2}\left(\operatorname{Re}[\mathcal{A}^{\mathsf{T}}_{j,k}]\operatorname{Re}[\mathcal{A}_{i,k}]+\operatorname{Im}[\mathcal{A}^{\mathsf{T}}_{j,k}]\operatorname{Im}[\mathcal{A}_{i,k}]\right) \\
&\quad+\operatorname{Re}[\mathcal{A}^{\mathsf{T}}_{j,k}]\left(\mathbf{P}'_k\cdot\mathbf{P}^{\mathsf{T}}_k\right)\operatorname{Re}[\mathcal{A}_{i,k}]+\operatorname{Im}[\mathcal{A}^{\mathsf{T}}_{j,k}]\left(\mathbf{P}'_k\cdot\mathbf{P}^{\mathsf{T}}_k\right)\operatorname{Im}[\mathcal{A}_{i,k}] \\
&\quad+\operatorname{Re}[\mathcal{A}^{\mathsf{T}}_{j,k}]\begin{pmatrix} 0 & -\left(\mathbf{P}_k-\mathbf{P}'_k\right)_z & \left(\mathbf{P}_k-\mathbf{P}'_k\right)_y \\ \left(\mathbf{P}_k-\mathbf{P}'_k\right)_z & 0 & -\left(\mathbf{P}_k-\mathbf{P}'_k\right)_x \\ -\left(\mathbf{P}_k-\mathbf{P}'_k\right)_y & \left(\mathbf{P}_k-\mathbf{P}'_k\right)_x & 0 \end{pmatrix}\operatorname{Im}[\mathcal{A}_{i,k}]
\end{aligned} \tag{D.29}$$

with Fourier matrices $\mathcal{A}_{i,k} \in \mathbb{C}^{3\times N_b}$ defined as

$$\mathcal{A}_{i,k} = \left(\frac{\gamma_N r_0}{2\mu_B}\right) \frac{V_{\mathrm{UC}}}{N_i} e^{-i\mathbf{q}_k\cdot\mathbf{r}_i} \mathcal{B}_k^{\perp}. \tag{D.30}$$

The columns of the matrix $\mathcal{B}_k^{\perp}$ are formed by the to $\mathbf{q}_k$ perpendicular parts of the N_b base vectors $\mathbf{b}_{b,k}^{\perp} = \hat{\mathbf{q}}_k \times (\mathbf{b}_b \times \hat{\mathbf{q}}_k)$. The partial derivatives of C are given by the partial derivatives of the calculated asymmetry A_k^{calc} as

$$\frac{\partial C}{\partial f_{i,b}} = \frac{2}{N_k} \sum_k \frac{A_k^{\mathrm{calc}} - A_k^{\mathrm{obs}}}{(dA_k^{\mathrm{obs}})^2} \frac{\partial A_k^{\mathrm{calc}}}{\partial f_{i,b}} \tag{D.31}$$

$$\frac{\partial^2 C}{\partial f_{i,b}\partial f_{j,b'}} = \frac{2}{N_k} \sum_k \left(\frac{A_k^{\mathrm{calc}} - A_k^{\mathrm{obs}}}{(dA_k^{\mathrm{obs}})^2} \frac{\partial^2 A_k^{\mathrm{calc}}}{\partial f_{i,b}\partial f_{j,b'}} + \frac{1}{(dA_k^{\mathrm{obs}})^2} \frac{\partial A_k^{\mathrm{calc}}}{\partial f_{i,b}} \frac{\partial A_k^{\mathrm{calc}}}{\partial f_{j,b'}} \right). \tag{D.32}$$

Accordingly, the partial derivatives of the calculated asymmetry, defined in Eq. (3.47), are given by the partial derivatives of the general scattering cross-section $\sigma_k^{\pm}$ for the measurement with and without spin flipping as

$$\frac{\partial A_k^{\mathrm{calc}}}{\partial f_{i,b}} = \frac{1}{\sigma_k^+ + \sigma_k^-} \left((1 - A_k^{\mathrm{calc}}) \frac{\partial \sigma_k^+}{\partial f_{i,b}} - (1 + A_k^{\mathrm{calc}}) \frac{\partial \sigma_k^-}{\partial f_{i,b}} \right) \tag{D.33}$$

$$\begin{aligned} \frac{\partial^2 A_k^{\mathrm{calc}}}{\partial f_{i,b}\partial f_{j,b'}} = {} & \frac{1}{\sigma_k^+ + \sigma_k^-} \left((1 - A_k^{\mathrm{calc}}) \frac{\partial^2 \sigma_k^+}{\partial f_{i,b}\partial f_{j,b'}} - (1 + A_k^{\mathrm{calc}}) \frac{\partial^2 \sigma_k^-}{\partial f_{i,b}\partial f_{j,b'}} \right) \\ & - \frac{1 - A_k^{\mathrm{calc}}}{(\sigma_k^+ + \sigma_k^-)^2} \left(2 \frac{\partial \sigma_k^+}{\partial f_{i,b}} \frac{\partial \sigma_k^+}{\partial f_{j,b'}} + \frac{\partial \sigma_k^+}{\partial f_{i,b}} \frac{\partial \sigma_k^-}{\partial f_{j,b'}} + \frac{\partial \sigma_k^-}{\partial f_{i,b}} \frac{\partial \sigma_k^+}{\partial f_{j,b'}} \right) \\ & + \frac{1 + A_k^{\mathrm{calc}}}{(\sigma_k^+ + \sigma_k^-)^2} \left(2 \frac{\partial \sigma_k^-}{\partial f_{i,b}} \frac{\partial \sigma_k^-}{\partial f_{j,b'}} + \frac{\partial \sigma_k^+}{\partial f_{i,b}} \frac{\partial \sigma_k^-}{\partial f_{j,b'}} + \frac{\partial \sigma_k^-}{\partial f_{i,b}} \frac{\partial \sigma_k^+}{\partial f_{j,b'}} \right). \end{aligned} \tag{D.34}$$

Finally, the partial derivatives of the scattering cross-sections are given by

$$\frac{\partial \sigma_k^{\pm}}{\partial f_{i,b}} = \left(\mathbf{v}_{i,k}^{\pm}\right)_b + \sum_{j,b'} \left(\left(\mathcal{W}_{i,j,k}^{\pm}\right)_{b'b} + \left(\mathcal{W}_{j,i,k}^{\pm}\right)_{bb'} \right) f_{j,b'} \tag{D.35}$$

$$\frac{\partial^2 \sigma_k^{\pm}}{\partial f_{i,b}\partial f_{j,b'}} = \left(\mathcal{W}_{i,j,k}^{\pm}\right)_{b'b} + \left(\mathcal{W}_{j,i,k}^{\pm}\right)_{bb'} \tag{D.36}$$

Note that it is usually impossible to store $\mathcal{W}_{i,j,k}$ explicitly, as it has for a typical $50 \times 50 \times 50$ grid with $N_b = 3$ base vectors and $N_k = 500$ measured data points around $7 \cdot 10^{13}$ elements. Assuming the entries to be of 32 bit float type, the static construction of such a matrix would require around 280 TB of RAM. Even the static construction of the complex $\mathcal{A}_{i,k}$ matrix, which would require around 4.5 GB of RAM, is not very beneficial and even impossible in a 32 bit system, where the total RAM is limited to around 4.3 GB. In contrast, for example, the complex magnetic scattering factors $\mathbf{M}_k = \sum_i \mathcal{A}_{i,k}\mathbf{f}_i$, which are composed of around 3000 individual entries of float type, require only around 12 kB of RAM and are thus easily storable.

E. Hamilton test

A typical problem in data refinement is the proper selection of model parameters. If we have, for example, a measurement with n observations, the refinement by a model with m free parameters may yield a certain generalized weighted R-factor R_m defining the fit quality. If we now apply d constraints ($0 < d < m$) to the model, which is then defined by a smaller set of $m - d$ free parameters, the refinement may provide a R-Factor R_{m-d}, which is typically larger than R_m. This inevitably leads to the question whether the d constraints are reasonable or if the resulting difference in the R-factor is too significant. This issue is addressed by the so-called Hamilton test [248]. It provides for the ratio $\mathcal{R} = R_{m-d}/R_m$ tabulated values $\mathcal{R}_{d,n-m,s}$, which can be used to reject the hypothesis (i.e. the constraints) at a significance level s, if $\mathcal{R} \geq \mathcal{R}_{d,n-m,s}$. The significance level denotes in this case the probability for wrongly rejecting the hypothesis. Note that $\mathcal{R}_{d,n-m,s'} > \mathcal{R}_{d,n-m,s}$ if $s' < s$.

In conventional crystallography, the weighted R-factor is typically defined as

$$R'_{\mathrm{F}} = \sqrt{\frac{\sum_{\mathbf{q}} \frac{1}{|dF^{\mathrm{obs}}(\mathbf{q})|^2} \left(|F^{\mathrm{obs}}(\mathbf{q})| - |F^{\mathrm{calc}}_{\mathrm{N}}(\mathbf{q})|\right)^2}{\sum_{\mathbf{q}} \frac{1}{|dF^{\mathrm{obs}}(\mathbf{q})|^2} |F^{\mathrm{obs}}(\mathbf{q})|^2}} \tag{E.1}$$

with F^{calc}, F^{obs} the calculated and observed total scattering factors, respectively, and dF^{obs} the uncertainty at standard deviation level [248]. For integrated intensities I, the total scattering factor can be expressed as $F = c\sqrt{I}$ with uncertainty $dF = c\frac{dI}{2\sqrt{I}}$ and scaling constant c.

F. Supplemental results on $Ba_2CoGe_2O_7$

This part of the appendix provides additional results for the non-polarized and polarized neutron diffraction studies on $Ba_2CoGe_2O_7$ discussed in Chap. 6.

F.1. Extinction-free refinement of non-polarized neutron diffraction data

To validate the new *Mag2Pol* software, the refinement of the non-polarized neutron diffraction data on $Ba_2CoGe_2O_7$, given in Ref. [30], was reproduced. The resulting structural parameters are compared to the literature values for $T = 10.4\,\mathrm{K}$ in Table F.1 and for $T = 2.2\,\mathrm{K}$ in Table F.2, both showing a good agreement. The slight differences, which are mostly within the uncertainty, may be attributed to a marginally different selection of reflections and a potentially different choice of minimization parameter for the least squares refinement (χ^2 for *Mag2Pol*, whereas the modulus of the structure factor is the default option for *CCSL*).

Table F.1.: Comparison between the structural parameters of $Ba_2CoGe_2O_7$ at 10.4 K refined by the *Mag2Pol* software (left) and taken from Ref. [30]. Both refinements are performed within space group $P\bar{4}2_1m$ and without extinction correction using the HEiDi ND data presented in Ref. [30].

	Mag2Pol refinement ($R_F = 4.72$, 517 reflections, $T = 10.4$ K)				*CCSL* refinement in Ref. [30] ($R_F = 4.7$, 525 reflections, $T = 10.4$ K)			
	x	y	z	U^{iso} [Å^2]	x	y	z	U^{iso} [Å^2]
Ba	0.3345(2)	$0.5-x$	0.4924(3)	0.0000(4)	0.3347(1)	$0.5-x$	0.4924(3)	0.0010(3)
Co	0	0	0	0.003(2)	0	0	0	0.0023(9)
Ge	0.1405(1)	$0.5-x$	0.0407(2)	0.0009(3)	0.1409(1)	$0.5-x$	0.0403(2)	0.0027(2)
O1	0	0.5	0.1597(5)	0.0019(5)	0	0.5	0.1600(4)	0.0044(4)
O2	0.1382(2)	$0.5-x$	0.7300(3)	0.0033(4)	0.1380(2)	$0.5-x$	0.7296(3)	0.0044(3)
O3	0.0793(2)	0.1852(2)	0.1884(2)	0.0030(3)	0.0791(2)	0.1845(1)	0.1883(2)	0.0043(2)

Table F.2.: Comparison between the structural parameters and the ordered AFM moment (denoted as m) of $Ba_2CoGe_2O_7$ at 2.2 K refined by the *Mag2Pol* software (left) and taken from Ref. [30]. Both refinements are performed within the nuclear space group $P\bar{4}2_1m$ and without extinction correction using the HEiDi ND data presented in Ref. [30].

	Mag2Pol refinement ($R_F = 4.53$, 559 reflections, $T = 2.2$ K)				*CCSL* refinement in Ref. [30] ($R_F = 4.5$, 522 reflections, $T = 2.2$ K)			
	x	y	z	U^{iso} [Å^2]	x	y	z	U^{iso} [Å^2]
Ba	0.3348(2)	$0.5-x$	0.4928(4)	0.0010(4)	0.3347(2)	$0.5-x$	0.4924(3)	0.0009(3)
Co	0	0	0	0.002(1)	0	0	0	0.0017(9)
Ge	0.1406(1)	$0.5-x$	0.0404(2)	0.0023(3)	0.1407(1)	$0.5-x$	0.0402(2)	0.0023(2)
O1	0	0.5	0.1596(5)	0.0047(6)	0	0.5	0.1594(4)	0.0040(5)
O2	0.1380(2)	$0.5-x$	0.7297(3)	0.0044(4)	0.1379(2)	$0.5-x$	0.7296(3)	0.0041(3)
O3	0.0794(2)	0.1848(2)	0.1883(2)	0.0043(3)	0.0791(2)	0.1845(2)	0.1886(2)	0.0042(2)
m	$2.9(2)\,\mu_B/Co^{2+}$				$2.9(1)\,\mu_B/Co^{2+}$			

F.2. Restriction-free FR refinement

Complementary to the restricted magnetic moment refinement in Sec. 6.3.2 with only m_x^{FM} and m_y^{AFM} non-zero, the unrestricted results for all three FM and AFM vector components are given in Table F.3. For this free refinement, comparable fit qualities and no significant changes for the FM moments are observed. For some measurements, the refinement indicates an additional small contribution in the m_z^{AFM} component, which suggests a slight out-of-plane angle for the AFM moment. However, this tilt angle is with up to 4° comparably small and may result from uncertainties in the crystal orientation, and thus in the applied field direction. Moreover, the neglected anisotropic character of the extinction may also distort the refinement results on such a small scale.

Table F.3.: Overview of the results of the free magnetic moment refinement for the FR measurements with different field values and directions in $Ba_2CoGe_2O_7$ at 2 K. The components of the magnetization refer to the field-dependent xyz reference system defined in Sec. 6.2.2. The results of the restricted refinement with $\mathbf{m}^{\mathrm{FM}} \parallel \mathbf{B}$ and $\mathbf{c} \perp \mathbf{m}^{\mathrm{AFM}} \perp \mathbf{B}$ are listed in Table 6.4.

Magnetic field		Component	m_x [μ_B]	m_y [μ_B]	m_z [μ_B]	χ^2_r	
B ∥ [100]	1 T	$\mathbf{m}^{\mathrm{FM}}$	0.150(6)	0.00(2)	0.00(3)	1.77	1.91
		$\mathbf{m}^{\mathrm{AFM}}$	0.01(1)	−2.56(3)	−0.04(3)	2.04	
	3 T	$\mathbf{m}^{\mathrm{FM}}$	0.423(7)	0.02(3)	0.03(3)	1.97	2.11
		$\mathbf{m}^{\mathrm{AFM}}$	0.02(1)	−2.60(4)	−0.00(3)	2.24	
	6 T	$\mathbf{m}^{\mathrm{FM}}$	0.93(1)	−0.02(5)	0.05(4)	2.06	1.88
		$\mathbf{m}^{\mathrm{AFM}}$	0.01(2)	−2.42(6)	−0.12(6)	1.70	
B ∥ [110]	1 T	$\mathbf{m}^{\mathrm{FM}}$	0.136(7)	0.03(2)	−0.00(3)	1.61	1.69
		$\mathbf{m}^{\mathrm{AFM}}$	−0.049(8)	−2.61(4)	0.17(3)	1.77	
	3 T	$\mathbf{m}^{\mathrm{FM}}$	0.419(8)	0.01(3)	−0.04(3)	1.79	1.77
		$\mathbf{m}^{\mathrm{AFM}}$	−0.02(1)	−2.66(5)	0.17(3)	1.75	
	6 T	$\mathbf{m}^{\mathrm{FM}}$	0.941(9)	−0.09(4)	0.01(3)	2.10	1.81
		$\mathbf{m}^{\mathrm{AFM}}$	−0.03(1)	−2.62(6)	0.03(4)	1.56	
B ∥ [001]	1 T	$\mathbf{m}^{\mathrm{FM}}$	0.074(6)	−0.02(4)	−0.01(4)	1.75	1.82
		$\mathbf{m}^{\mathrm{AFM}}$	−0.011(7)	−1.93(3)	−0.10(3)	1.88	
	3 T	$\mathbf{m}^{\mathrm{FM}}$	0.209(7)	0.08(4)	0.01(4)	1.94	2.43
		$\mathbf{m}^{\mathrm{AFM}}$	−0.02(1)	−2.39(4)	−0.14(3)	2.86	
	6 T	$\mathbf{m}^{\mathrm{FM}}$	0.424(8)	−0.05(4)	−0.10(5)	1.81	1.94
		$\mathbf{m}^{\mathrm{AFM}}$	0.01(1)	−2.64(5)	−0.15(4)	2.05	

G. Supplemental results on $Ba_2Cu_{1-x}Mn_xGe_2O_7$

In this part of the appendix, additional figures and tables for the diffraction and macroscopic study on the $Ba_2Cu_{1-x}Mn_xGe_2O_7$ solid solution line are listed. The corresponding discussion of the presented results can be found in Chap. 7.

G.1. Powder diffraction on $Ba_2CuGe_2O_7$

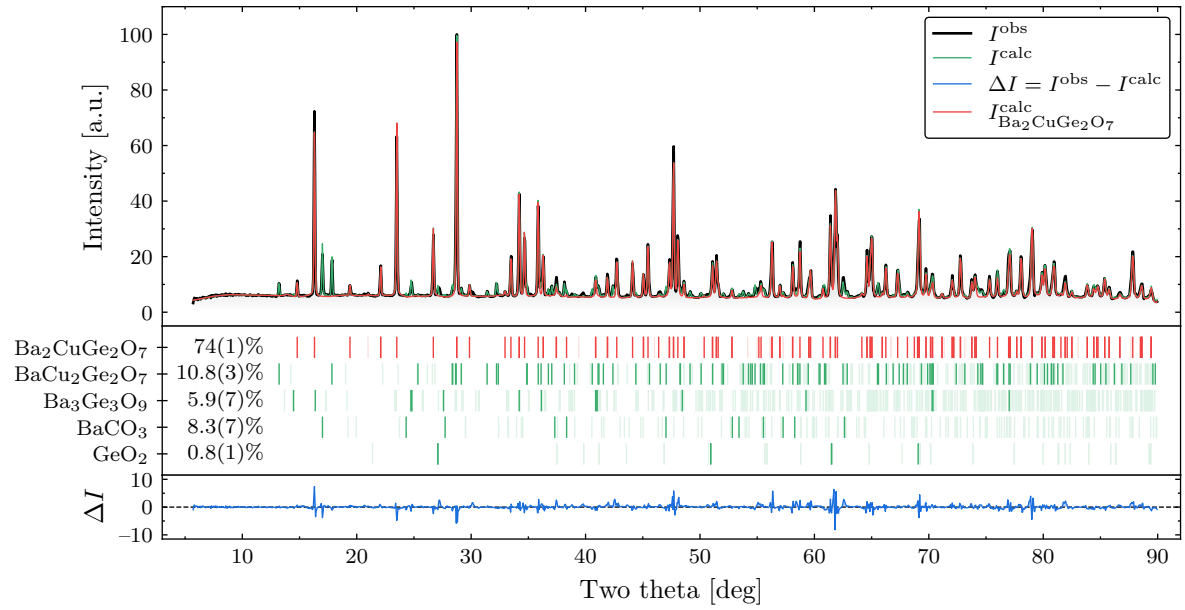

Figure G.1.: Neutron powder diffraction pattern of $Ba_2CuGe_2O_7$ reduced from the TOF measurement at 100 K at POWGEN (SNS) with the center of the wavelength bandwidth at 2.665 Å. For details about the layout refer to the related Fig. 7.5 and Sec. 7.2.1.

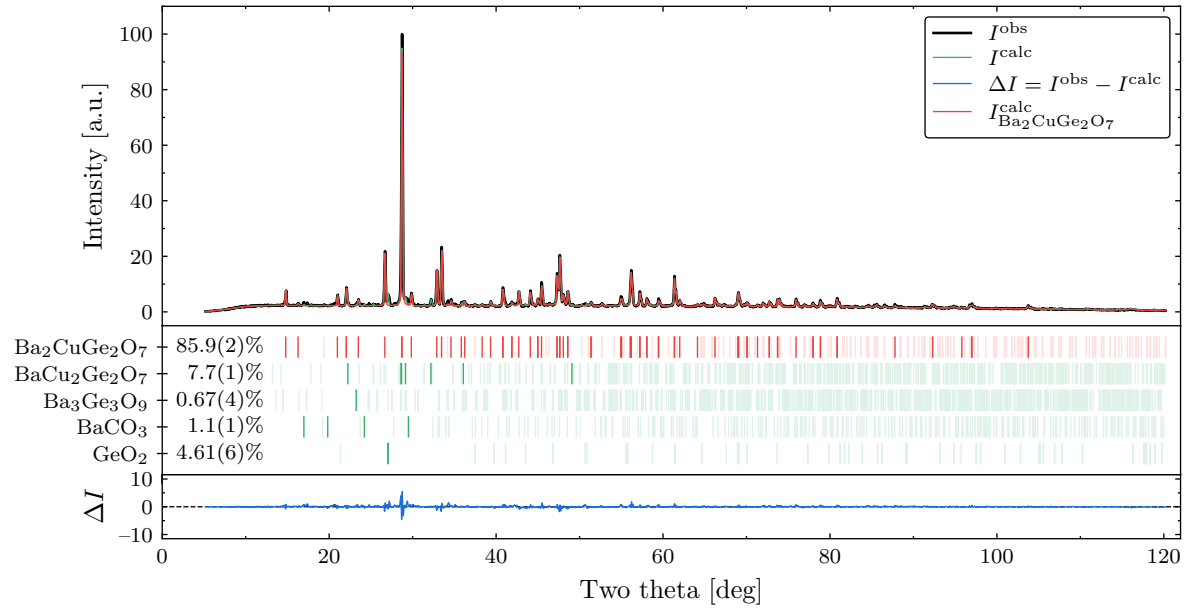

Figure G.2.: Laboratory XRD pattern of $Ba_2CuGe_2O_7$ measured with the Cu $K\alpha 1$ and $K\alpha 2$ lines using the Bruker D2 PHASER at RT. For details about the layout refer to the related Fig. 7.5 and Sec. 7.2.1.

G.2. Powder diffraction on $Ba_2MnGe_2O_7$

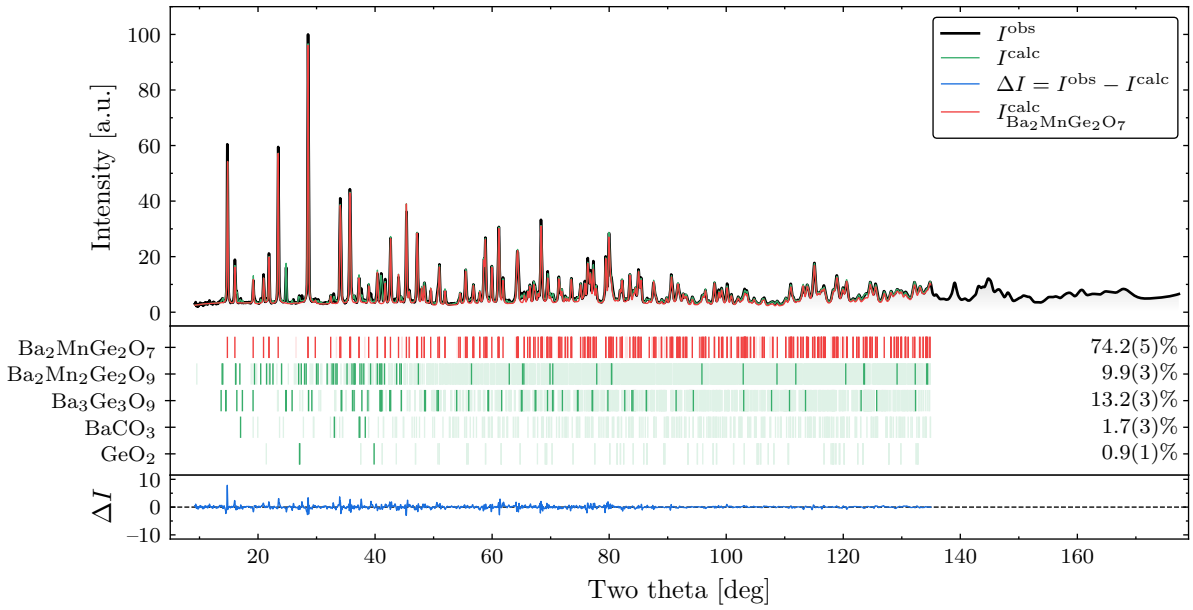

Figure G.3.: Complete neutron powder diffraction pattern of $Ba_2MnGe_2O_7$ reduced from the TOF measurement at 10 K at POWGEN (SNS) with the center of the wavelength bandwidth at 1.500 Å. For details about the layout and the limits in I^{calc} refer to the related Fig. 7.6 and Sec. 7.2.2.

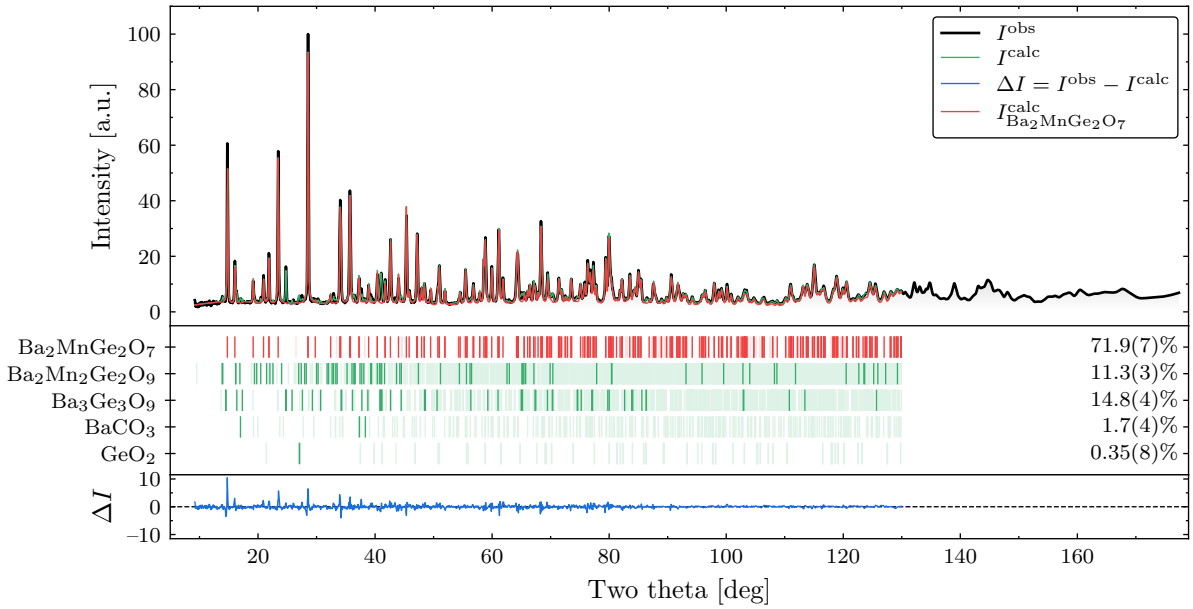

Figure G.4.: Complete neutron powder diffraction pattern of $Ba_2MnGe_2O_7$ reduced from the TOF measurement at 100 K at POWGEN (SNS) with the center of the wavelength bandwidth at 1.500 Å. For details about the layout and the limits in I^{calc} refer to the related Fig. 7.6 and Sec. 7.2.2.

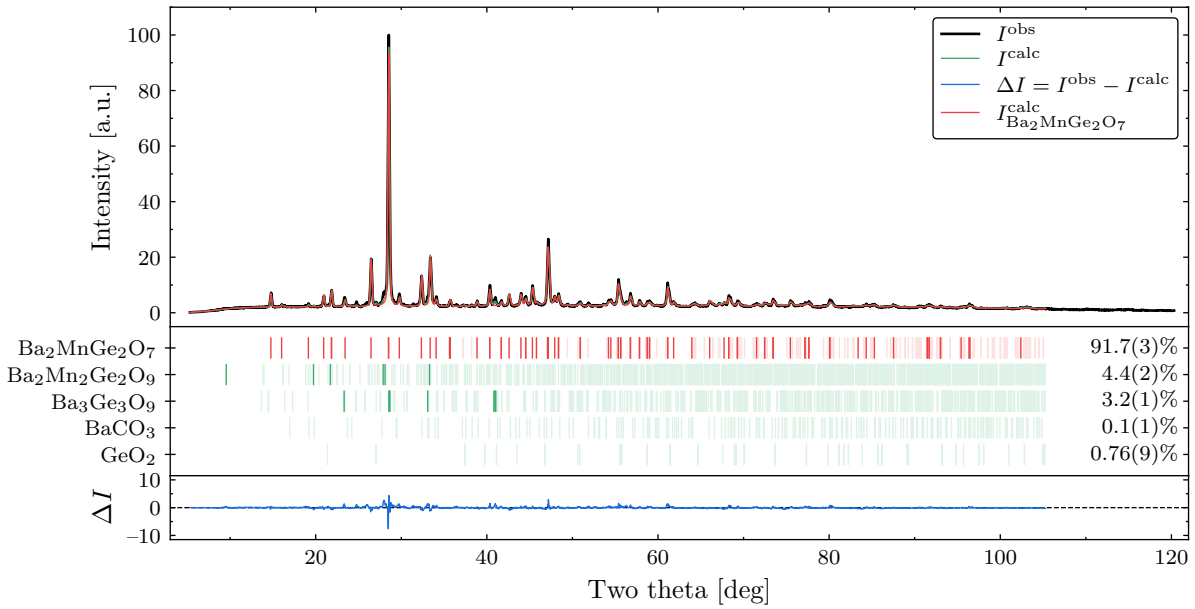

Figure G.5.: Laboratory XRD pattern of $Ba_2MnGe_2O_7$ measured with the Cu $K\alpha 1$ and $K\alpha 2$ lines using the Bruker D2 PHASER at RT. For details about the layout and the limits in I^{calc} refer to the related Fig. 7.6 and Sec. 7.2.2.

G.3. Curie-Weiss law in $Ba_2Cu_{1-x}Mn_xGe_2O_7$

The CW fits for the polycrystalline $Ba_2Cu_{1-x}Mn_xGe_2O_7$ powders and single crystals of $Ba_2CuGe_2O_7$ and $Ba_2MnGe_2O_7$ according to Eq. (7.6) are illustrated in Figs. G.6(a) and G.6(b), respectively. For the measurements on the single crystal compounds in

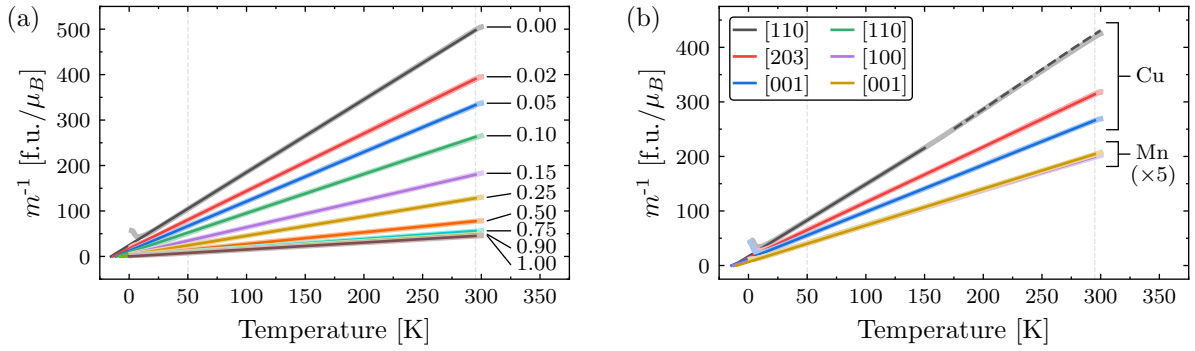

Figure G.6.: Inverse mass magnetization as function of the temperature measured in field cooling at 1 T for (a) polycrystalline $Ba_2Cu_{1-x}Mn_xGe_2O_7$ powders (x values are labeled in the figure) and (b) single crystals of $Ba_2CuGe_2O_7$ and $Ba_2MnGe_2O_7$. The values for $Ba_2MnGe_2O_7$ in (b) are scaled by a factor of 5 to be visible. The measurement values are shown by thick lines with light color whereas the thinner lines represent CW fits to the data according to Eq. (7.6). For the fit, a temperature range between 50 K and 295 K, indicated by the vertical dotted lines, was selected. Only for the [110] direction of $Ba_2CuGe_2O_7$ (black line) in (b), the fit range was limited to 150 K as for higher temperatures diamagnetic contributions play a significant role. The dashed black line in (b) above 175 K shows the measurement data uncorrected for the diamagnetic effects.

Fig. G.6(b), the diamagnetic contributions from the epoxy glue matrix used for alignment of the crystal (see Sec. 7.1) were subtracted from the measurement data. These contributions caused a particularly strong influence for temperatures above 150 K on the measurements in $Ba_2CuGe_2O_7$ with magnetic field along [110] direction, having the lowest observed magnetization values with around $0.002\,\mu_B/Cu^{2+}T$ at 300 K. This is illustrated in Fig. G.6(b) by the dashed black line, representing the uncorrected measurement data, showing a slightly higher slope at high temperatures. As the estimation of the diamagnetic contributions from the measurement of the dummy matrix may have a limited precision, this particularly strong influenced measurement region above 150 K was excluded from the CW fit.

G.4. FR refinement results in $Ba_2CuGe_2O_7$

The results of the free and restricted magnetic moment refinement in $Ba_2CuGe_2O_7$ in the PM phase at 10 K for the different applied magnetic field directions are listed in Table G.1 and discussed in Sec. 7.4.1. The results of the free magnetic moment refinement in the AFM phase at 2 K are listed in Table G.2 and correspond to the discussion in Sec. 7.4.2.

Table G.1.: Overview of the results of the free and symmetry restricted magnetic moment refinement for the FR datasets in $Ba_2CuGe_2O_7$ at 10 K. The two datasets with **B** ∥ [112] that were measured at D3 using the N27c single crystal are labeled accordingly. The remaining datasets are measured at VIP using the large $Ba_2CuGe_2O_7$ single crystal shown in Fig. 7.1(a). The components of the magnetization refer to the *xyz* directions defined in Sec. 7.4.1. For the 9 T measurement with **B** ∥ [112] at D3 (ILL), no AFM-type reflections were collected; thus, no AFM moment could be refined.

Magnetic field		Component	Restriction	m_x [μ_B]	m_y [μ_B]	m_z [μ_B]	χ^2_r	
B ∥ [001]	1.5 T	$\mathbf{m}^{\mathrm{FM}}$	free	0.035(3)	−0.00(1)	−0.01(1)	1.48	1.47
		$\mathbf{m}^{\mathrm{AFM}}$	free	0.004(4)	0.03(2)	0.00(2)	1.45	
		$\mathbf{m}^{\mathrm{FM}}$	∥ **B**	0.035(3)	0	0	1.48	1.47
		$\mathbf{m}^{\mathrm{AFM}}$	= 0	0	0	0	1.45	
	2.1 T	$\mathbf{m}^{\mathrm{FM}}$	free	0.049(3)	0.01(2)	0.00(1)	1.55	1.63
		$\mathbf{m}^{\mathrm{AFM}}$	free	−0.002(4)	0.01(2)	0.01(2)	1.72	
		$\mathbf{m}^{\mathrm{FM}}$	∥ **B**	0.049(3)	0	0	1.54	1.62
		$\mathbf{m}^{\mathrm{AFM}}$	= 0	0	0	0	1.70	
	6.0 T	$\mathbf{m}^{\mathrm{FM}}$	free	0.137(3)	0.03(2)	0.00(2)	2.10	1.81
		$\mathbf{m}^{\mathrm{AFM}}$	free	0.000(1)	0.03(2)	−0.01(3)	1.52	
		$\mathbf{m}^{\mathrm{FM}}$	∥ **B**	0.138(3)	0	0	2.10	1.81
		$\mathbf{m}^{\mathrm{AFM}}$	= 0	0	0	0	1.52	
B ∥ [110]	6.0 T	$\mathbf{m}^{\mathrm{FM}}$	free	0.108(3)	0.03(1)	−0.01(1)	2.03	1.93
		$\mathbf{m}^{\mathrm{AFM}}$	free	0.004(4)	0.01(2)	−0.01(2)	1.84	
		$\mathbf{m}^{\mathrm{FM}}$	∥ **B**	0.106(3)	0	0	2.08	1.95
		$\mathbf{m}^{\mathrm{AFM}}$	= 0	0	0	0	1.83	
B ∥ [112] (D3-ILL)	9.0 T	$\mathbf{m}^{\mathrm{FM}}$	free	0.232(3)	−0.04(1)	−0.05(2)	3.76	3.76
		$\mathbf{m}^{\mathrm{AFM}}$	free	-	-	-	-	
		$\mathbf{m}^{\mathrm{FM}}$	∥ **B**	0.228(2)	0	0	4.37	4.37
		$\mathbf{m}^{\mathrm{AFM}}$	= 0	0	0	0	-	
B ∥ [113]	1.5 T	$\mathbf{m}^{\mathrm{FM}}$	free	0.042(3)	−0.00(1)	−0.03(1)	1.66	1.67
		$\mathbf{m}^{\mathrm{AFM}}$	free	−0.004(4)	−0.01(2)	0.00(1)	1.68	
		$\mathbf{m}^{\mathrm{FM}}$	∥ **B**	0.042(3)	0	0	1.68	1.68
		$\mathbf{m}^{\mathrm{AFM}}$	= 0	0	0	0	1.67	
	6.0 T	$\mathbf{m}^{\mathrm{FM}}$	free	0.154(4)	0.01(2)	−0.03(1)	2.26	1.96
		$\mathbf{m}^{\mathrm{AFM}}$	free	0.005(5)	−0.00(2)	0.00(2)	1.66	
		$\mathbf{m}^{\mathrm{FM}}$	∥ **B**	0.153(4)	0	0	2.29	1.97
		$\mathbf{m}^{\mathrm{AFM}}$	= 0	0	0	0	1.66	

Table G.2.: Overview of the results of the free magnetic moment refinement for the FR measurements in $Ba_2CoGe_2O_7$ at 2 K.The two datasets with $\mathbf{B} \parallel [112]$ that were measured at D3 using the N27c single crystal are labeled accordingly. The remaining datasets are measured at VIP using the large $Ba_2CuGe_2O_7$ single crystal shown in Fig. 7.1(a). The components of the magnetization refer to the field-dependent xyz reference system defined in Sec. 6.2.2. The results of the restricted refinement with $\mathbf{m}^{\mathrm{FM}} \parallel \mathbf{B}$ and $\mathbf{c} \perp \mathbf{m}^{\mathrm{AFM}} \perp \mathbf{B}$ are listed in Table 7.7

Magnetic field		Component	m_x [μ_B]	m_y [μ_B]	m_z [μ_B]	χ^2_r	
$\mathbf{B} \parallel [001]$	1.5 T	$\mathbf{m}^{\mathrm{FM}}$	0.022(3)	0.01(2)	0.01(1)	1.86	1.74
		$\mathbf{m}^{\mathrm{AFM}}$	−0.004(4)	−0.02(2)	−0.02(2)	1.62	
	2.1 T	$\mathbf{m}^{\mathrm{FM}}$	0.039(3)	0.02(2)	−0.00(1)	1.60	1.63
		$\mathbf{m}^{\mathrm{AFM}}$	0.005(4)	0.25(2)	0.00(2)	1.66	
	6.0 T	$\mathbf{m}^{\mathrm{FM}}$	0.138(3)	−0.01(2)	−0.01(2)	2.28	2.05
		$\mathbf{m}^{\mathrm{AFM}}$	0.004(5)	0.41(3)	0.03(3)	1.81	
$\mathbf{B} \parallel [112]$ (D3-ILL)	2.0 T	$\mathbf{m}^{\mathrm{FM}}$	0.041(1)	−0.003(6)	−0.007(5)	2.50	2.38
		$\mathbf{m}^{\mathrm{AFM}}$	−0.001(3)	0.03(1)	−0.01(2)	0.97	
	9.0 T	$\mathbf{m}^{\mathrm{FM}}$	0.236(2)	−0.05(1)	−0.02(1)	3.64	3.20
		$\mathbf{m}^{\mathrm{AFM}}$	−0.000(3)	0.44(1)	0.00(1)	2.71	
$\mathbf{B} \parallel [112]$	6.75 T	$\mathbf{m}^{\mathrm{FM}}$	0.16(2)	0.17(9)	0.06(8)	1.25	1.27
		$\mathbf{m}^{\mathrm{AFM}}$	0.03(2)	0.56(8)	−0.11(7)	1.28	
$\mathbf{B} \parallel [113]$	1.5 T	$\mathbf{m}^{\mathrm{FM}}$	0.026(3)	−0.00(1)	−0.02(1)	1.68	1.59
		$\mathbf{m}^{\mathrm{AFM}}$	0.002(4)	0.02(2)	0.00(2)	1.51	
	6.0 T	$\mathbf{m}^{\mathrm{FM}}$	0.153(4)	−0.01(2)	−0.02(1)	2.01	1.92
		$\mathbf{m}^{\mathrm{AFM}}$	0.004(5)	0.46(2)	0.04(2)	1.83	

G.5. FR refinement results in $Ba_2MnGe_2O_7$

The results of the free magnetic moment refinement in $Ba_2MnGe_2O_7$ in the PM phase at 10 K for different field directions are listed in Table G.3 and discussed in Sec. 7.5.1.

Table G.3.: Overview of the results of the free magnetic moment refinement for the FR measurements in $Ba_2MnGe_2O_7$ at 10 K. The components of the magnetization refer to the field-dependent xyz reference system defined in Sec. 6.2.2. The results of the restricted refinement with $\mathbf{m}^{\mathrm{FM}} \parallel \mathbf{B}$ and $\mathbf{m}^{\mathrm{AFM}} = 0$ are listed in Table 7.8.

Magnetic field		Component	m_x [μ_B]	m_y [μ_B]	m_z [μ_B]	χ^2_r	
$\mathbf{B} \parallel [001]$	6 T	$\mathbf{m}^{\mathrm{FM}}$	1.912(8)	0.00(3)	−0.01(3)	3.70	3.39
		$\mathbf{m}^{\mathrm{AFM}}$	0.003(5)	−0.00(2)	0.01(2)	3.10	
$\mathbf{B} \parallel [100]$	6 T	$\mathbf{m}^{\mathrm{FM}}$	1.948(4)	−0.03(2)	−0.11(3)	3.76	3.58
		$\mathbf{m}^{\mathrm{AFM}}$	−0.002(5)	−0.01(2)	0.00(2)	3.42	
$\mathbf{B} \parallel [110]$	6 T	$\mathbf{m}^{\mathrm{FM}}$	2.001(3)	0.01(3)	−0.09(2)	3.69	2.75
		$\mathbf{m}^{\mathrm{AFM}}$	−0.002(4)	0.02(1)	−0.01(1)	1.88	

H. Supplemental results on $Ba_2TGe_2O_7$ magnetization densities

This part of the appendix lists additional figures and tables for the magnetization densities in the $Ba_2TGe_2O_7$ (T = Cu, Co and Mn) compounds. The corresponding discussion of the presented results can be found in Chap. 8.

H.1. Density results in the paramagnetic phase at 10 K

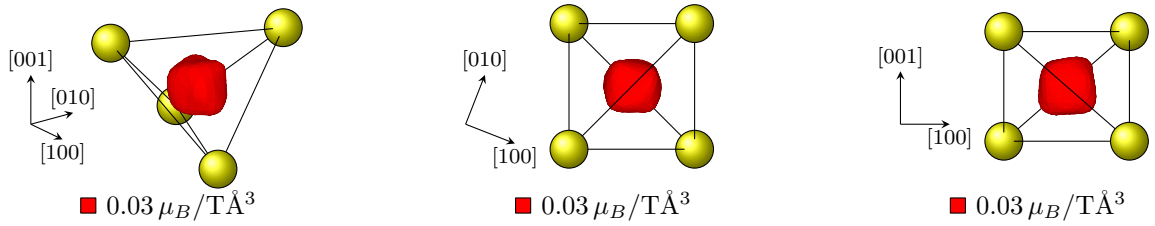

Figure H.1.: Perspective views on the isosurface of the in-plane susceptibility density $\chi_{11}(\mathbf{r})$ in $Ba_2CoGe_2O_7$ at 10 K, reconstructed by the advanced MEM approach discussed in Sec. 8.1.1 with the AdvEnt software. For the reconstruction, equal magnetization densities for the two Co sites within the frame of the tetrahedral environment are assumed but no local symmetry restrictions are applied. The layout elements are analogous to those described in Fig. 8.2.

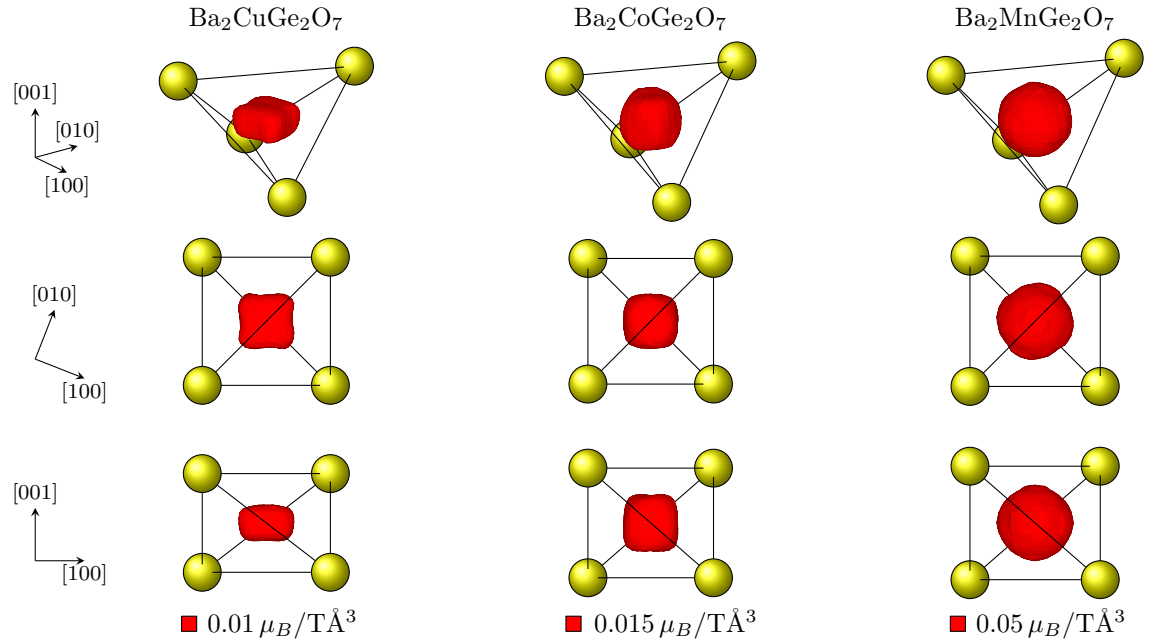

Figure H.2.: Perspective views on the isosurface of the out-of-plane susceptibility density $\chi_{33}(\mathbf{r})$ in the $Ba_2TGe_2O_7$ compounds at 10 K, reconstructed by the advanced MEM approach using the AdvEnt software. The layout is analogous to that described in Fig. 8.2 illustrating $\chi_{11}(\mathbf{r})$, only the surface level for T = Co was modified to account for the strong in-plane anisotropy of $\chi_{11}/\chi_{33} \approx 2$. No significant density is associated with grid points outside of the shown tetrahedral environment.

H.2. Density results in the antiferromagnetic phase at 2 K

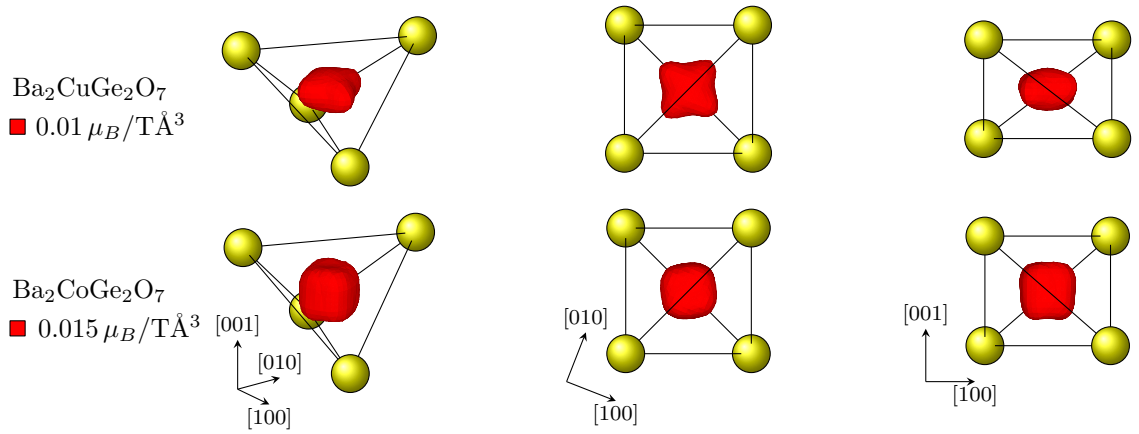

Figure H.3.: Perspective views on the isosurface of the out-of-plane susceptibility density $\chi_{33}(\mathbf{r})$ in the $Ba_2TGe_2O_7$ compounds at 2 K reconstructed by the advanced MEM approach using the AdvEnt software. The top and bottom row refers to the results for T = Cu and Co, respectively. The layout elements are analogous to those described in Fig. 8.7, only the surface level for T = Co was modified to account for the strong in-plane anisotropy of $\chi_{11}/\chi_{33} \approx 2$. No significant density is associated with grid points outside of the shown tetrahedral environment.

Table H.1.: Results of the MP magnetic moment refinements in $Ba_2TGe_2O_7$ (T = Cu and Co) using the AdvEnt software applied to the combined FR datasets measured at 2 K. The magnetic scattering amplitudes for the respective refinements are calculated according to Eqs. (8.12) and (8.13), extended by Eq. (8.21). For the MP refinement, the single-ζ model was used as radial function.

T	Cu			Co			
χ_{11} [μ_B/T/f.u.]	0.024(2)			0.140(2)			
χ_{33} [μ_B/T/f.u.]	0.023(1)			0.064(1)			
χ_{11}/χ_{33}	1.0(1)			2.20(6)			
m_y^{AFM} [μ_B]		6 T	6.75 T		1 T	3 T	6 T
	B ∥ [001]	0.41(3)		**B** ∥ [001]			-2.50(7)
	B ∥ [112]		0.54(9)	**B** ∥ [100]	-2.34(6)	-2.35(6)	-2.32(7)
	B ∥ [113]	0.45(3)		**B** ∥ [110]	-2.41(6)	-2.50(7)	-2.46(6)
ζ [$1/a_0$]	9.7(3)			8.6(4)			
C_0^0	1			1			
C_2^0	-0.25(6)			0.001(4)			
C_4^0	0.3(2)			-0.10(1)			
C_4^4	-0.25(4)			-0.10(1)			
$x_{11} = \frac{c^2}{a^2} x_{33}$	0.9(3)			6.2(5)			
χ_r^2	1.74			1.90			

Acknowledgment

Of course, this thesis would not have been possible without the help of others. Although the following list might not be exhaustive, I want to thank all the colleagues and friends who significantly contributed to the outcome of this work.

First of all, I want to express my sincere gratitude to **Prof. Dr. Georg Roth**, **Prof. Dr. Thomas Brückel** and **Prof. Dr. Mirijam Zobel** for providing me the opportunity to conduct my thesis as bridge-student between the RWTH Aachen, the FZ Jülich and the JCNS in Garching and giving me a lot of freedom in choosing my topics and methods. I also want to thank **Dr. Stefan Mattauch** for providing me hospitality and support at the JCNS in Garching and giving me the opportunity to present my work at many conferences.

Next, I want to thank **Prof. Dr. Peter Böni** who kindly agreed to take the second revision of this thesis.

A special gratitude goes also to my supervisors **Dr. Valdimir Hutanu** and **Prof. Dr. Manuel Angst** for their guidance, advice and support throughout my PhD work. You were always open and available for fruitful discussions, provided excellent suggestions and critics and showed endless patience with me. In particular, I want to thank Manuel for taking the time to carefully reading and profoundly reviewing my work and Vladimir for the many years of successfully working together at POLI and for the countless hours we spent together at beamlines all over the world. During my time at the MLZ, you taught me all about (polarized) neutron diffraction and everything else one needs to know in science. It was always a pleasure to work with each of you and I miss it already!

I also want to thank **Wolfgang Luberstetter** for all your technical support and dedication to the POLI instrument. You always had an open door and I really appreciate your expertise and kindness.

Moreover, I want to thank the **colleagues** from the University of Salerno (Department of Physics), in particular, **Dr. Veronica Granata** and **Dr. Rosalba Fittipaldi**, for their efforts in providing me this large number of different $Ba_2Cu_{1-x}Mn_xGe_2O_7$ compounds for my studies. Also I want to thank **Dr. Sebastian Mühlbauer** and the **colleagues** from the RIKEN Center for Emergent Matter Science and the Yokohama City University (International Graduate School of Arts and Sciences) for lending me large single crystals of $Ba_2TGe_2O_7$ (T = Cu, Co and Mn).

Next, I want to thank all former and current **colleagues** of the **POLI** and **HEiDi group**, I really enjoyed working with you for many years and it was always nice to spent time with you both in the office and at the instruments during the cycle. In particular, I want to thank **Dr. Martin Meven** for his constant support and for reading through this thesis.

In addition, I want to thank **Dr. Arsen Gukasov** and **Dr. Iurii Kibalin** for their

support with the measurements at LLB and the fruitful discussions about maximum entropy reconstructions.

I also want to thank all **colleagues** of the JCNS in Jülich and Garching for their good collaboration. In particular, I want to thank **Dr. Oleg Petracic**, **Dr. Shibabrata Nandi** and **Berthold Schmitz** for their help with the macroscopic measurements and **Dr. Yixi Su** for letting me use the laboratory X-ray machine.

Many thanks also to **Dr. Anne Stunault**, **Dr. Thomas Hansen**, **Dr. Jeffrey W. Lynn** and **Dr. Qiang Zhang** for their help and scientific support during my diffraction experiments at their facility.

Finally, I want to thank my parents **Achim & Martina**, my brother **Jan** and my girlfriend **Maximiliane** for all your love, constant support, encouragement and for always believing in me. I am very grateful to have you in my life and to share so many beautiful memories with you. I am also thankful to all my **friends** who have accompanied me during my studies and made this time so unique and wonderful.

Bibliography

[1] B. Fegley, Phase Equilibria of Binary Systems, in *Practical Chemical Thermodynamics for Geoscientists*, edited by B. Fegley (Elsevier, 2013) pp. 585–622.

[2] E. F. Osborn and J. F. Schairer, The ternary system pseudowollastonite-akermanite-gehlenite, Am. J. Sci. **239**, 715 (1941).

[3] G. MacPherson, Calcium–Aluminum-Rich Inclusions in Chondritic Meteorites, in *Treatise on Geochemistry*, Vol. 1 (Elsevier, 2014) 2nd ed., pp. 139–179.

[4] B. E. Warren, XV. The Structure of Melilite (Ca, Na)$_2$(Mg, Al)$_1$(Si, Al)$_2$O$_7$, Z. Kristallogr. Cryst. Mater. **74**, 131 (1930).

[5] M. Ardit, M. Dondi, M. Merlini, and G. Cruciani, Melilite-type and melilite-related compounds: structural variations along the join $Sr_{2-x}B_xMgSi_2O_7$ ($0 \leq x \leq 2$) and high-pressure behavior of the two end-members, Phys. Chem. Miner. **39**, 199 (2012).

[6] T. Armbruster, F. Rothlisberger, and F. Seifert, Layer topology, stacking variation, and site distortion in melilite- related compounds in the system CaO-ZnO-GeO$_2$-SiO$_2$, Am. Mineral. **75**, 847 (1990).

[7] M. Alam, K. H. Gooen, B. D. Bartolo, A. Linz, E. Sharp, L. Gillespie, and G. Janney, Optical Spectra and Laser Action of Neodymium in a Crystal $Ba_2MgGe_2O_7$, J. Appl. Phys. **39**, 4728 (1968).

[8] P. Becker, L. Bohatý, J. Liebertz, H.-J. Kleebe, M. Müller, H. Eichler, H. Rhee, J. Hanuza, and A. Kaminskii, Non-centrosymmetric tetragonal $Sr_2ZnGe_2O_7$ - a novel melilite-type nonlinear-laser crystal offering $\chi^{(2)}$-, $\chi^{(3)}$-, and cascaded $\chi^{(3)} \leftrightarrow \chi^{(2)}$-interactions, Laser Phys. Lett. **7**, 367 (2010).

[9] A. Kaminskii, H. Rhee, O. Lux, H. Eichler, L. Bohatý, P. Becker, J. Liebertz, K. Ueda, A. Shirakawa, V. Koltashev, J. Hanuza, J. Dong, and D. Stavrovskii, Many-phonon stimulated Raman scattering and related cascaded and cross-cascaded $\chi(3)$-nonlinear optical effects in melilite-type crystal $Ca_2ZnSi_2O_7$, Laser Phys. Lett. **8**, 859 (2011).

[10] A. Kaminskii, L. Bohati, P. Becker, J. Liebertz, H. Eichler, H. Rhee, and J. Hanuza, Cascaded nonlinear-laser interactions in melilite-type crystals of $Sr_2MgGe_2O_7$ and $Ba_2ZnGe_2O_7$, Laser Phys. Lett. **7**, 528 (2010).

[11] A. Kaminskii, L. Bohatý, P. Becker, J. Liebertz, P. Held, H. Eichler, H. Rhee, and J. Hanuza, Tetragonal $Ba_2MgGe_2O_7$ - a novel multifunctional optical crystal with numerous manifestations of nonlinear-laser effects: almost sesqui-octave Stokes and anti-Stokes combs and cascaded $\chi^{(3)} \leftrightarrow \chi^{(2)}$ lasing with involved second and third harmonic generation, Laser Phys. Lett. **5**, 845 (2008).

[12] A. A. Kaminskii, L. Bohatý, H. J. Eichler, O. Lux, H. Rhee, M. Burianek, and P. Becker, Stimulated Raman Scattering in Melilite-Type Crystals $Ca_2MgSi_2O_7$ and $Ca_2Ga_2SiO_7$, Cryst. Res. Technol. **55**, 2000038 (2020).

[13] T. Endo, Y. Doi, M. Wakeshima, K. Suzuki, Y. Matsuo, K. Tezuka, T. Ohtsuki, Y. J. Shan, and Y. Hinatsu, Magnetic Properties of the Melilite-Type Oxysulfide $Sr_2MnGe_2S_6O$: Magnetic Interactions Enhanced by Anion Substitution, Inorg. Chem. **56**, 2459 (2017).

[14] T. Endo, Y. Doi, Y. Hinatsu, and K. Ohoyama, Magnetic and Neutron Diffraction Study on Melilite-Type Oxides $Sr_2MGe_2O_7$ (M = Mn, Co), Inorg. Chem. **51**, 3572 (2012).

[15] T. Masuda, S. Kitaoka, S. Takamizawa, N. Metoki, K. Kaneko, K. C. Rule, K. Kiefer, H. Manaka, and H. Nojiri, Instability of magnons in two-dimensional antiferromagnets at high magnetic fields, Phys. Rev. B **81**, 100402 (2010).

[16] M. Matsumoto, M. Soda, and T. Masuda, Quantum-Phase-Transition-Induced Multiferroics and Higgs Mode in Integer Spin Systems in Noncentrosymmetric Lattice with Strong Single-Ion Anisotropy, J. Phys. Soc. Jpn. **82**, 093703 (2013).

[17] I. Dzyaloshinskii, Thermodynamic Theory of "Weak" Ferromagnetism In Antiferromagnetic Substances, Sov. Phys. JETP **5**, 1259 (1957).

[18] I. Dzyaloshinsky, A thermodynamic theory of "weak" ferromagnetism of antiferromagnetics, J. Phys. Chem. Solids **4**, 241 (1958).

[19] T. Moriya, New Mechanism of Anisotropic Superexchange Interaction, Phys. Rev. Lett. **4**, 228 (1960).

[20] T. Moriya, Anisotropic superexchange interaction and weak ferromagnetism, Phys. Rev. **120**, 91 (1960).

[21] H. Thoma, V. Hutanu, H. Deng, V. E. Dmitrienko, P. J. Brown, A. Gukasov, G. Roth, and M. Angst, Revealing the Absolute Direction of the Dzyaloshinskii-Moriya Interaction in Prototypical Weak Ferromagnets by Polarized Neutrons, Phys. Rev. X **11**, 011060 (2021).

[22] J. Chovan and N. Papanicolaou, Commensurate and Incommensurate Magnetism in Layered Antiferromagnets, in *Front. Magn. Mater.*, edited by A. V. Narlikar (Springer-Verlag, Berlin, Heidelberg, 2005) pp. 347–384.

[23] S.-W. Cheong and M. Mostovoy, Multiferroics: a magnetic twist for ferroelectricity, Nat. Mater. **6**, 13 (2007).

[24] M. Shiranzaei, J. Fransson, H. Cheraghchi, and F. Parhizgar, Nonlinear spin susceptibility in topological insulators, Phys. Rev. B **97**, 180402 (2018).

[25] R. Cheng, M. W. Daniels, J.-G. Zhu, and D. Xiao, Antiferromagnetic Spin Wave Field-Effect Transistor, Sci. Rep. **6**, 24223 (2016).

[26] M. Bode, M. Heide, K. von Bergmann, P. Ferriani, S. Heinze, G. Bihlmayer, A. Kubetzka, O. Pietzsch, S. Blügel, and R. Wiesendanger, Chiral magnetic order at surfaces driven by inversion asymmetry, Nature **447**, 190 (2007).

[27] S. Heinze, K. von Bergmann, M. Menzel, J. Brede, A. Kubetzka, R. Wiesendanger, G. Bihlmayer, and S. Blügel, Spontaneous atomic-scale magnetic skyrmion lattice in two dimensions, Nat. Phys. **7**, 713 (2011).

[28] Y. Togawa, T. Koyama, K. Takayanagi, S. Mori, Y. Kousaka, J. Akimitsu, S. Nishihara, K. Inoue, A. S. Ovchinnikov, and J. Kishine, Chiral Magnetic Soliton Lattice on a Chiral Helimagnet, Phys. Rev. Lett. **108**, 107202 (2012).

[29] A. Zheludev, T. Sato, T. Masuda, K. Uchinokura, G. Shirane, and B. Roessli, Spin waves and the origin of commensurate magnetism in $Ba_2CoGe_2O_7$, Phys. Rev. B **68**, 024428 (2003).

[30] V. Hutanu, A. Sazonov, M. Meven, H. Murakawa, Y. Tokura, S. Bordács, I. Kézsmárki, and B. Náfrádi, Determination of the magnetic order and the crystal symmetry in the multiferroic ground state of $Ba_2CoGe_2O_7$, Phys. Rev. B **86**, 104401 (2012).

[31] A. Sazonov, V. Hutanu, M. Meven, G. Roth, H. Murakawa, Y. Tokura, V. K. Guduru, L. C. J. M. Peters, U. Zeitler, L. F. Kiss, D. Szaller, B. Náfrádi, and I. Kézsmárki, Magnetic structure of the magnetoelectric material $Ca_2CoSi_2O_7$, Phys. Rev. B **95**, 174431 (2017).

[32] M. Soda, S. Hayashida, T. Yoshida, M. Akaki, M. Hagiwara, M. Avdeev, O. Zaharko, and T. Masuda, Magnetic Structure and Dielectric State in the Multiferroic $Ca_2CoSi_2O_7$, J. Phys. Soc. Jpn. **86**, 064703 (2017).

[33] S. Hayashida and T. Masuda, *Activity Report on Neutron Scattering Research: Experimental Reports*, Tech. Rep. (The Institute for Solid State Physics, The University of Tokyo, Kashiwa, Japan, 2014).

[34] T. Endo, Y. Doi, M. Wakeshima, and Y. Hinatsu, Crystal Structures and Magnetic Properties of New Europium Melilites $Eu_2MSi_2O_7$ (M = Mg, Mn) and Their Strontium Analogues, Inorg. Chem. **49**, 10809 (2010).

[35] G. A. Petrakovskiĭ, L. N. Bezmaternykh, I. A. Gudim, O. A. Bayukov, A. M. Vorotynov, A. F. Bovina, R. Szymczak, M. Baran, and C. Ritter, Spin glass state in crystals of barium ferrigermanate $Ba_2Fe_2GeO_7$, Phys. Solid State **48**, 1906 (2006).

[36] A. Zheludev, S. Maslov, G. Shirane, Y. Sasago, N. Koide, and K. Uchinokura, Field-induced Commensurate-Incommensurate phase transition in a Dzyaloshinskii-Moriya spiral antiferromagnet, Phys. Rev. Lett. **78**, 4857 (1997).

[37] A. N. Bogdanov, U. K. Rößler, M. Wolf, and K.-H. Müller, Magnetic structures and reorientation transitions in noncentrosymmetric uniaxial antiferromagnets, Phys. Rev. B **66**, 214410 (2002).

[38] U. K. Rößler, A. N. Bogdanov, and C. Pfleiderer, Spontaneous skyrmion ground states in magnetic metals, Nature **442**, 797 (2006).

[39] S. Mühlbauer, B. Binz, F. Jonietz, C. Pfleiderer, A. Rosch, A. Neubauer, R. Georgii, and P. Boni, Skyrmion Lattice in a Chiral Magnet, Science **323**, 915 (2009).

[40] N. S. Kiselev, A. N. Bogdanov, R. Schäfer, and U. K. Rößler, Chiral skyrmions in thin magnetic films: new objects for magnetic storage technologies?, J. Phys. D: Appl. Phys. **44**, 392001 (2011).

[41] J. Sampaio, V. Cros, S. Rohart, A. Thiaville, and A. Fert, Nucleation, stability and current-induced motion of isolated magnetic skyrmions in nanostructures, Nat. Nanotechnol. **8**, 839 (2013).

[42] A. Fert, V. Cros, and J. Sampaio, Skyrmions on the track, Nat. Nanotechnol. **8**, 152 (2013).

[43] H. T. Yi, Y. J. Choi, S. Lee, and S. W. Cheong, Multiferroicity in the square-lattice antiferromagnet of $Ba_2CoGe_2O_7$, Appl. Phys. Lett. **92**, 212904 (2008).

[44] P. Curie, Sur la symétrie dans les phénomènes physiques, symétrie d'un champ électrique et d'un champ magnétique, J. Phys. Theor. Appl. **3**, 393 (1894).

[45] L. D. Landau and E. M. Lifshitz, *Electrodynamics of continuous media*, 1st ed., edited by J. B. Sykes and J. S. Bell, Course of Theoretical Physics Volume 8 (Pergamon, Oxford, 1960).

[46] I. E. Dzyaloshinskii, On the magneto-electrical effect in antiferromagnets, Sov. Phys. JETP **10**, 628 (1960).

[47] Y. Tokura, S. Seki, and N. Nagaosa, Multiferroics of spin origin, Rep. Prog. Phys. **77**, 076501 (2014).

[48] J. Stein, M. Baum, S. Holbein, T. Cronert, V. Hutanu, A. C. Komarek, and M. Braden, Control of multiferroic domains by external electric fields in $TbMnO_3$, J. Phys.: Condens. Matter **27**, 446001 (2015).

[49] W. Eerenstein, N. D. Mathur, and J. F. Scott, Multiferroic and magnetoelectric materials, Nature **442**, 759 (2006).

[50] N. A. Hill, Why Are There so Few Magnetic Ferroelectrics?, J. Phys. Chem. B **104**, 6694 (2000).

[51] A. Moreira dos Santos, S. Parashar, A. Raju, Y. Zhao, A. Cheetham, and C. Rao, Evidence for the likely occurrence of magnetoferroelectricity in the simple perovskite, $BiMnO_3$, Solid State Commun. **122**, 49 (2002).

[52] T. Kimura, S. Kawamoto, I. Yamada, M. Azuma, M. Takano, and Y. Tokura, Magnetocapacitance effect in multiferroic $BiMnO_3$, Phys. Rev. B **67**, 180401 (2003).

[53] J. Wang, Epitaxial $BiFeO_3$ Multiferroic Thin Film Heterostructures, Science **299**, 1719 (2003).

[54] T. Kimura, T. Goto, H. Shintani, K. Ishizaka, T. Arima, and Y. Tokura, Magnetic control of ferroelectric polarization, Nature **426**, 55 (2003).

[55] M. Mostovoy, Ferroelectricity in Spiral Magnets, Phys. Rev. Lett. **96**, 067601 (2006).

[56] M. Kenzelmann, A. B. Harris, S. Jonas, C. Broholm, J. Schefer, S. B. Kim, C. L. Zhang, S.-W. Cheong, O. P. Vajk, and J. W. Lynn, Magnetic Inversion Symmetry Breaking and Ferroelectricity in $TbMnO_3$, Phys. Rev. Lett. **95**, 087206 (2005).

[57] T. Arima, A. Tokunaga, T. Goto, H. Kimura, Y. Noda, and Y. Tokura, Collinear to Spiral Spin Transformation without Changing the Modulation Wavelength upon Ferroelectric Transition in $Tb_{1-x}Dy_xMnO_3$, Phys. Rev. Lett. **96**, 097202 (2006).

[58] T. Goto, T. Kimura, G. Lawes, A. P. Ramirez, and Y. Tokura, Ferroelectricity and Giant Magnetocapacitance in Perovskite Rare-Earth Manganites, Phys. Rev. Lett. **92**, 257201 (2004).

[59] J. Hemberger, F. Schrettle, A. Pimenov, P. Lunkenheimer, V. Y. Ivanov, A. A. Mukhin, A. M. Balbashov, and A. Loidl, Multiferroic phases of $Eu_{1-x}Y_xMnO_3$, Phys. Rev. B **75**, 035118 (2007).

[60] Y. J. Choi, C. L. Zhang, N. Lee, and S.-W. Cheong, Cross-Control of Magnetization and Polarization by Electric and Magnetic Fields with Competing Multiferroic and Weak-Ferromagnetic Phases, Phys. Rev. Lett. **105**, 097201 (2010).

[61] S. Seki, T. Kurumaji, S. Ishiwata, H. Matsui, H. Murakawa, Y. Tokunaga, Y. Kaneko, T. Hasegawa, and Y. Tokura, Cupric chloride $CuCl_2$ as an $S=\frac{1}{2}$ chain multiferroic, Phys. Rev. B **82**, 064424 (2010).

[62] L. Zhao, T.-L. Hung, C.-C. Li, Y.-Y. Chen, M.-K. Wu, R. K. Kremer, M. G. Banks, A. Simon, M.-H. Whangbo, C. Lee, J. S. Kim, I. Kim, and K. H. Kim, $CuBr_2$ - A New Multiferroic Material with High Critical Temperature, Adv. Mater. **24**, 2469 (2012).

[63] S. Park, Y. J. Choi, C. L. Zhang, and S.-W. Cheong, Ferroelectricity in an S=$\frac{1}{2}$ Chain Cuprate, Phys. Rev. Lett. **98**, 057601 (2007).

[64] Y. Naito, K. Sato, Y. Yasui, Y. Kobayashi, Y. Kobayashi, and M. Sato, Ferroelectric Transition Induced by the Incommensurate Magnetic Ordering in $LiCuVO_4$, J. Phys. Soc. Jpn. **76**, 023708 (2007).

[65] G. Lawes, M. Kenzelmann, N. Rogado, K. H. Kim, G. A. Jorge, R. J. Cava, A. Aharony, O. Entin-Wohlman, A. B. Harris, T. Yildirim, Q. Z. Huang, S. Park, C. Broholm, and A. P. Ramirez, Competing Magnetic Phases on a Kagomé Staircase, Phys. Rev. Lett. **93**, 247201 (2004).

[66] G. Lawes, A. B. Harris, T. Kimura, N. Rogado, R. J. Cava, A. Aharony, O. Entin-Wohlman, T. Yildirim, M. Kenzelmann, C. Broholm, and A. P. Ramirez, Magnetically Driven Ferroelectric Order in $Ni_3V_2O_8$, Phys. Rev. Lett. **95**, 087205 (2005).

[67] T.-h. Arima, Spin-Driven Ferroelectricity and Magneto-Electric Effects in Frustrated Magnetic Systems, J. Phys. Soc. Jpn. **80**, 052001 (2011).

[68] H. Katsura, N. Nagaosa, and A. V. Balatsky, Spin Current and Magnetoelectric Effect in Non-collinear Magnets, Phys. Rev. Lett. **95**, 057205 (2005).

[69] I. A. Sergienko and E. Dagotto, Role of the Dzyaloshinskii-Moriya interaction in multiferroic perovskites, Phys. Rev. B **73**, 094434 (2006).

[70] B. Lorenz, Y.-Q. Wang, and C.-W. Chu, Ferroelectricity in perovskite $HoMnO_3$ and $YMnO_3$, Phys. Rev. B **76**, 104405 (2007).

[71] V. Yu Pomjakushin, M. Kenzelmann, A. Dönni, A. B. Harris, T. Nakajima, S. Mitsuda, M. Tachibana, L. Keller, J. Mesot, H. Kitazawa, and E. Takayama-Muromachi, Evidence for large electric polarization from collinear magnetism in $TmMnO_3$, New J. Phys. **11**, 043019 (2009).

[72] S. Ishiwata, Y. Kaneko, Y. Tokunaga, Y. Taguchi, T.-h. Arima, and Y. Tokura, Perovskite manganites hosting versatile multiferroic phases with symmetric and antisymmetric exchange strictions, Phys. Rev. B **81**, 100411 (2010).

[73] Y. J. Choi, H. T. Yi, S. Lee, Q. Huang, V. Kiryukhin, and S.-W. Cheong, Ferroelectricity in an Ising Chain Magnet, Phys. Rev. Lett. **100**, 047601 (2008).

[74] Y. Tokunaga, N. Furukawa, H. Sakai, Y. Taguchi, T.-h. Arima, and Y. Tokura, Composite domain walls in a multiferroic perovskite ferrite, Nat. Mater. **8**, 558 (2009).

[75] J. Kanamori, Superexchange interaction and symmetry properties of electron orbitals, J. Phys. Chem. Solids **10**, 87 (1959).

[76] Y. Koyata, H. Nakamura, N. Iwata, A. Inomata, and K. Kohn, Electric and Magnetic Low-Temperature Phase Transitions of $YbMn_2O_5$, J. Phys. Soc. Jpn. **65**, 1383 (1996).

[77] N. Iwata, M. Uga, and K. Kohn, Magnetic-field-induced transition of thulium manganese oxide $TmMn_2O_5$, Ferroelectrics **204**, 97 (1997).

[78] M. Uga, N. Iwata, and K. Kohn, Magnetoelectric effect of $TmMn_2O_5$, Ferroelectrics **219**, 55 (1998).

[79] Y. Koyata and K. Kohn, Low-temperature phase transition in $ErMn_2O_5$, Ferroelectrics **204**, 115 (1997).

[80] Y. F. Popov, A. M. Kadomtseva, S. S. Krotov, G. P. Vorob'ev, K. I. Kamilov, M. M. Lukina, and M. M. Tegranchi, Magnetic and structural phase transitions in YMn_2O_5 ferromagnetoelectric crystals induced by a strong magnetic field, J. Exp. Theor. Phys. **96**, 961 (2003).

[81] N. Hur, S. Park, P. A. Sharma, J. S. Ahn, S. Guha, and S.-W. Cheong, Electric polarization reversal and memory in a multiferroic material induced by magnetic fields, Nature **429**, 392 (2004).

[82] N. Hur, S. Park, P. A. Sharma, S. Guha, and S.-W. Cheong, Colossal Magnetodielectric Effects in $DyMn_2O_5$, Phys. Rev. Lett. **93**, 107207 (2004).

[83] Y. Noda, H. Kimura, M. Fukunaga, S. Kobayashi, I. Kagomiya, and K. Kohn, Magnetic and ferroelectric properties of multiferroic RMn_2O_5, J. Phys.: Condens. Matter **20**, 434206 (2008).

[84] M. Akaki, J. Tozawa, D. Akahoshi, and H. Kuwahara, Gigantic magnetoelectric effect caused by magnetic-field-induced canted antiferromagnetic-paramagnetic transition in quasi-two-dimensional $Ca_2CoSi_2O_7$ crystal, Appl. Phys. Lett. **94**, 212904 (2009).

[85] M. Akaki, H. Iwamoto, T. Kihara, M. Tokunaga, and H. Kuwahara, Multiferroic properties of an akermanite $Sr_2CoSi_2O_7$ single crystal in high magnetic fields, Phys. Rev. B **86**, 060413 (2012).

[86] H. Murakawa, Y. Onose, S. Miyahara, N. Furukawa, and Y. Tokura, Comprehensive study of the ferroelectricity induced by the spin-dependent d-p hybridization mechanism in $Ba_2XGe_2O_7$ (X = Mn, Co, and Cu), Phys. Rev. B **85**, 174106 (2012).

[87] H. Murakawa, Y. Onose, and Y. Tokura, Electric-Field Switching of a Magnetic Propagation Vector in a Helimagnet, Phys. Rev. Lett. **103**, 147201 (2009).

[88] T.-h. Arima, Ferroelectricity Induced by Proper-Screw Type Magnetic Order, J. Phys. Soc. Jpn. **76**, 073702 (2007).

[89] H. Murakawa, Y. Onose, S. Miyahara, N. Furukawa, and Y. Tokura, Ferroelectricity induced by spin-dependent metal-ligand hybridization in $Ba_2CoGe_2O_7$, Phys. Rev. Lett. **105**, 137202 (2010).

[90] J. Romhányi, M. Lajkó, and K. Penc, Zero- and finite-temperature mean field study of magnetic field induced electric polarization in $Ba_2CoGe_2O_7$, Phys. Rev. B **84**, 224419 (2011).

[91] P. Toledano, D. D. Khalyavin, and L. C. Chapon, Spontaneous toroidal moment and field-induced magnetotoroidic effects in $Ba_2CoGe_2O_7$, Phys. Rev. B **84**, 094421 (2011).

[92] M. Soda, M. Matsumoto, M. Månsson, S. Ohira-Kawamura, K. Nakajima, R. Shiina, and T. Masuda, Spin-Nematic Interaction in the Multiferroic Compound $Ba_2CoGe_2O_7$, Phys. Rev. Lett. **112**, 127205 (2014).

[93] A. Andreev and I. Grishchuk, Spin nematics, Sov. Phys. JETP **60**, 267 (1984).

[94] P. Barone, K. Yamauchi, and S. Picozzi, Jahn-Teller distortions as a novel source of multiferroicity, Phys. Rev. B **92**, 014116 (2015).

[95] I. Kézsmárki, D. Szaller, S. Bordács, V. Kocsis, Y. Tokunaga, Y. Taguchi, H. Murakawa, Y. Tokura, H. Engelkamp, T. Rõõm, and U. Nagel, One-way transparency of four-coloured spin-wave excitations in multiferroic materials, Nat. Commun. **5**, 3203 (2014).

[96] I. Kézsmárki, N. Kida, H. Murakawa, S. Bordács, Y. Onose, and Y. Tokura, Enhanced Directional Dichroism of Terahertz Light in Resonance with Magnetic Excitations of the Multiferroic $Ba_2CoGe_2O_7$ Oxide Compound, Phys. Rev. Lett. **106**, 057403 (2011).

[97] S. Bordács, I. Kézsmárki, D. Szaller, L. Demkó, N. Kida, H. Murakawa, Y. Onose, R. Shimano, T. Rõõm, U. Nagel, S. Miyahara, N. Furukawa, and Y. Tokura, Chirality of matter shows up via spin excitations, Nat. Phys. **8**, 734 (2012).

[98] V. Granata, A. Ubaldini, R. Fittipaldi, L. Rocco, S. Pace, and A. Vecchione, Synthesis and characterization of mixed melilite-type oxides, J. Cryst. Growth **457**, 128 (2017).

[99] T. Sato, T. Masuda, and K. Uchinokura, Magnetic property of $Ba_2CoGe_2O_7$, Physica B Condens. Matter **329-333**, 880 (2003).

[100] R. Fittipaldi, L. Rocco, M. Ciomaga Hatnean, V. Granata, M. R. Lees, G. Balakrishnan, and A. Vecchione, Crystal growth and characterization of the non-centrosymmetric antiferromagnet $Ba_2CuGe_2O_7$, J. Cryst. Growth **404**, 223 (2014).

[101] Y. Malinovskii, E. Pobedimskaya, and N. Belov, Synthesis and X-Ray analysis of two new iron-containing barium germanates $Ba_2Fe(Ge_2O_7)$ and $Fe_2NaBa_6Ge_8O_24(OH, H_2O)_4$, Sov. Phys. Crystallogr. **21**, 698 (1976).

[102] J. Liebertz and S. Stähr, Kristalle der Melilith-Reihe, Z. Kristallogr. Cryst. Mater. **159**, 271 (1982).

[103] M. Tovar, R. E. Dinnebier, and W. Eysel, The $Cu(II)O_4$ Tetrahedron in the Åkermanite Structure, Mater. Sci. Forum **278-281**, 750 (1998).

[104] A. Sazonov, M. Meven, G. Roth, R. Georgii, I. Kézsmárki, V. Kocsis, Y. Tokunaga, Y. Taguchi, Y. Tokura, and V. Hutanu, Origin of forbidden reflections in multiferroic $Ba_2CoGe_2O_7$ by neutron diffraction: symmetry lowering or Renninger effect?, J. Appl. Crystallogr. **49**, 556 (2016).

[105] A. Sazonov, V. Hutanu, M. Meven, G. Roth, R. Georgii, T. Masuda, and B. Náfrádi, Crystal Structure of Magnetoelectric $Ba_2MnGe_2O_7$ at Room and Low Temperatures by Neutron Diffraction, Inorg. Chem. **57**, 5089 (2018).

[106] T. Nakajima, Y. Tokunaga, V. Kocsis, Y. Taguchi, Y. Tokura, and T.-h. Arima, Uniaxial-Stress Control of Spin-Driven Ferroelectricity in Multiferroic $Ba_2CoGe_2O_7$, Phys. Rev. Lett. **114**, 067201 (2015).

[107] M. Gerloch, The sense of Jahn-Teller distortions in octahedral copper(II) and other transition-metal complexes, Inorg. Chem. **20**, 638 (1981).

[108] H. A. Jahn and E. Teller, Stability of polyatomic molecules in degenerate electronic states - I-Orbital degeneracy, Proc. R. Soc. Lond. A **161**, 220 (1937).

[109] R. Gross and A. Marx, *Festkörperphysik*, 2nd ed. (De Gruyter Oldenbourg, Munich, 2014).

[110] R. Dutta, H. Thoma, I. Radelytskyi, A. Schneidewind, V. Kocsis, Y. Tokunaga, Y. Taguchi, Y. Tokura, and V. Hutanu, Spin dynamics study and experimental realization of tunable single-ion anisotropy in multiferroic $Ba_2CoGe_2O_7$ under external magnetic field, Phys. Rev. B **104**, L020403 (2021).

[111] K. Penc, J. Romhányi, T. Rõõm, U. Nagel, Á. Antal, T. Fehér, A. Jánossy, H. Engelkamp, H. Murakawa, Y. Tokura, D. Szaller, S. Bordács, and I. Kézsmárki, Spin-stretching modes in anisotropic magnets: spin-wave excitations in the multiferroic $Ba_2CoGe_2O_7$, Phys. Rev. Lett. **108**, 257203 (2012).

[112] V. Hutanu, A. P. Sazonov, M. Meven, G. Roth, A. Gukasov, H. Murakawa, Y. Tokura, D. Szaller, S. Bordács, I. Kézsmárki, V. K. Guduru, L. C. J. M. Peters, U. Zeitler, J. Romhányi, and B. Náfrádi, Evolution of two-dimensional antiferromagnetism with temperature and magnetic field in multiferroic $Ba_2CoGe_2O_7$, Phys. Rev. B **89**, 064403 (2014).

[113] M. Akaki, H. Kuwahara, A. Matsuo, K. Kindo, and M. Tokunaga, Successive Magnetic Transitions of $Ca_2CoSi_2O_7$ in High Magnetic Fields, J. Phys. Soc. Japan **83**, 093704 (2014).

[114] M. Akaki, D. Yoshizawa, A. Okutani, T. Kida, J. Romhányi, K. Penc, and M. Hagiwara, Direct observation of spin-quadrupolar excitations in $Sr_2CoGe_2O_7$ by high-field electron spin resonance, Phys. Rev. B **96**, 214406 (2017).

[115] D. Piwowarska, P. Gnutek, and C. Rudowicz, Origin of the Ground Kramers Doublets for Co2+(3d7) Ions with the Effective Spin $\frac{3}{2}$ Versus the Fictitious 'Spin' $\frac{1}{2}$, Appl. Magn. Reson. **50**, 797 (2019).

[116] S.-D. Jiang, B.-W. Wang, and S. Gao, Single-Ion Anisotropy: An Insight to Complicated Magnetic Molecules, in *Topics in Organometallic Chemistry*, Vol. 64 (Springer, Cham, 2018) pp. 227–252.

[117] A. Zheludev, G. Shirane, Y. Sasago, N. Kiode, and K. Uchinokura, Spiral phase and spin waves in the quasi-two-dimensional antiferromagnet $Ba_2CuGe_2O_7$, Phys. Rev. B **54**, 15163 (1996).

[118] A. Carrington and A. McLachlan, *Introduction to Magnetic Resonance*, A Harper international edition (Harper & Row, New York, 1967).

[119] A. Zheludev, S. Maslov, and G. Shirane, Field-induced incommensurate-to-commensurate transition in $Ba_2CuGe_2O_7$, Phys. Rev. B **57**, 2968 (1998).

[120] C. A. Bates and P. E. Chandler, The Jahn-Teller interaction and $3d^9$ ions at tetrahedral sites. II. Tetragonal distortions, J. Phys. C: Solid State Phys. **6**, 1975 (1973).

[121] A. Zheludev, S. Maslov, G. Shirane, I. Tsukada, T. Masuda, K. Uchinokura, I. Zaliznyak, R. Erwin, and L. P. Regnault, Magnetic anisotropy and low-energy spin waves in the Dzyaloshinskii-Moriya spiral magnet $Ba_2CuGe_2O_7$, Phys. Rev. B **59**, 11432 (1999).

[122] A. Zheludev, G. Shirane, Y. Sasago, N. Koide, and K. Uchinokura, Spiral order in $Ba_2CuGe_2O_7$, Physica B Condens. Matter **234-236**, 546 (1997).

[123] A. Zheludev, S. Maslov, I. Tsukada, I. Zaliznyak, L. P. Regnault, T. Masuda, K. Uchinokura, R. Erwin, and G. Shirane, Experimental Evidence for Kaplan–Shekhtman–Entin-Wohlman–Aharony Interactions in $Ba_2CuGe_2O_7$, Phys. Rev. Lett. **81**, 5410 (1998).

[124] T. A. Kaplan, Single-band Hubbard model with spin-orbit coupling, Z. Phys. B **49**, 313 (1983).

[125] L. Shekhtman, O. Entin-Wohlman, and A. Aharony, Moriya's anisotropic superexchange interaction, frustration, and Dzyaloshinsky's weak ferromagnetism, Phys. Rev. Lett. **69**, 836 (1992).

[126] S. Mühlbauer, S. Gvasaliya, E. Pomjakushina, and A. Zheludev, Phase Diagram of the Dzyaloshinskii-Moriya Helimagnet $Ba_2CuGe_2O_7$ in Canted Magnetic Fields, Phys. Rev. B **86**, 024417 (2012).

[127] S. Mühlbauer, G. Brandl, M. Månsson, and M. Garst, Formation of incommensurate long-range magnetic order in the Dzyaloshinskii-Moriya antiferromagnet $Ba_2CuGe_2O_7$ studied by neutron diffraction, Phys. Rev. B **96**, 134409 (2017).

[128] A. Zheludev, S. Maslov, G. Shirane, Y. Sasago, N. Koide, K. Uchinokura, D. A. Tennant, and S. E. Nagler, Square-lattice spiral magnet $Ba_2CuGe_2O_7$ in an in-plane magnetic field, Phys. Rev. B **56**, 14006 (1997).

[129] S. Mühlbauer, S. N. Gvasaliya, E. Pomjakushina, and A. Zheludev, Double-k phase of the Dzyaloshinskii-Moriya helimagnet $Ba_2CuGe_2O_7$, Phys. Rev. B **84**, 5 (2011).

[130] J. Chovan, N. Papanicolaou, and S. Komineas, Intermediate phase in the spiral antiferromagnet $Ba_2CuGe_2O_7$, Phys. Rev. B **65**, 064433 (2002).

[131] D. B. Litvin, *Magnetic Group Tables* (International Union of Crystallography, Chester, England, 2013).

[132] N. V. Belov, N. N. Neronova, , and T. S. Smirnova, Shubnikov groups, Sov. Phys. Crystallogr. **2**, 311 (1957).

[133] E. R. Gansner and S. C. North, An open graph visualization system and its applications to software engineering, Softw. Pract. Exper. **30**, 1203 (2000).

[134] J. Perez-Mato, S. Gallego, E. Tasci, L. Elcoro, G. de la Flor, and M. Aroyo, Symmetry-Based Computational Tools for Magnetic Crystallography, Annu. Rev. Mater. Res. **45**, 217 (2015).

[135] S. Miyahara and N. Furukawa, Theory of Magnetoelectric Resonance in Two-Dimensional S $=\frac{3}{2}$ Antiferromagnet $Ba_2CoGe_2O_7$ via Spin-Dependent Metal-Ligand Hybridization Mechanism, J. Phys. Soc. Jpn. **80**, 073708 (2011).

[136] Y. Xu and J. Yao, *Electron Magnetic Resonance Principles* (De Gruyter, Berlin, Boston, 2019).

[137] P. Fabrykiewicz, R. Przeniosło, and I. Sosnowska, Magnetic modes compatible with the symmetry of crystals, Acta Cryst. **A77**, 327 (2021).

[138] S. Hasegawa, S. Hayashida, S. Asai, M. Matsuura, Z. Igor, and T. Masuda, Nontrivial temperature dependence of magnetic anisotropy in multiferroic $Ba_2MnGe_2O_7$, Phys. Rev. Res. **3**, L032023 (2021).

[139] J. M. Perez-Mato and J. L. Ribeiro, On the symmetry and the signature of atomic mechanisms in multiferroics: The example of $Ba_2CoGe_2O_7$, Acta Cryst. **A67**, 264 (2011).

[140] C. Jia, S. Onoda, N. Nagaosa, and J. H. Han, Bond electronic polarization induced by spin, Phys. Rev. B **74**, 224444 (2006).

[141] C. Jia, S. Onoda, N. Nagaosa, and J. H. Han, Microscopic theory of spin-polarization coupling in multiferroic transition metal oxides, Phys. Rev. B **76**, 144424 (2007).

[142] N. A. Spaldin, M. Fiebig, and M. Mostovoy, The toroidal moment in condensed-matter physics and its relation to the magnetoelectric effect, J. Phys. Condens. Matter **20**, 434203 (2008).

[143] C. Ederer and N. A. Spaldin, Towards a microscopic theory of toroidal moments in bulk periodic crystals, Phys. Rev. B **76**, 214404 (2007).

[144] M. Soda, S. Hayashida, B. Roessli, M. Månsson, J. S. White, M. Matsumoto, R. Shiina, and T. Masuda, Continuous control of local magnetic moment by applied electric field in multiferroics $Ba_2CoGe_2O_7$, Phys. Rev. B **94**, 094418 (2016).

[145] G. L. Squires, *Introduction to the Theory of Thermal Neutron Scattering* (Cambridge University Press, Cambridge, 2012).

[146] K. N. Trueblood, H. B. Bürgi, H. Burzlaff, J. D. Dunitz, C. M. Gramaccioli, H. H. Schulz, U. Shmueli, and S. C. Abrahams, Atomic Dispacement Parameter Nomenclature. Report of a Subcommittee on Atomic Displacement Parameter Nomenclature, Acta Cryst. **A52**, 770 (1996).

[147] W. F. Kuhs, Atomic displacement parameters, in *International Tables for Crystallography*, Vol. D, edited by A. Authier (International Union of Crystallography, Chester, England, 2006) pp. 228–242.

[148] O. Halpern and M. H. Johnson, On the Magnetic Scattering of Neutrons, Phys. Rev. **55**, 898 (1939).

[149] E. Balcar and S. W. Lovesey, *Theory of Magnetic Neutron and Photon Scattering*, Oxford Series on Neutron Scattering in Condensed Matter (Clarendon Press, Oxford, 1989).

[150] P. J. Brown, Magnetic form factors, in *International Tables for Crystallography Volume C: Mathematical, physical and chemical tables*, edited by E. Prince (Wiley, Chichester, 2006) Chap. 4.4.5., pp. 454–461.

[151] U. Fano, Description of States in Quantum Mechanics by Density Matrix and Operator Techniques, Rev. Mod. Phys. **29**, 74 (1957).

[152] D. T. Haar, Theory and applications of the density matrix, Rep. Prog. Phys. **24**, 307 (1961).

[153] B. Roessli and P. Böni, Polarised Neutron Scattering, in *Scattering*, edited by R. Pike and P. Sabatier (Academic Press, London, 2002) Chap. 2.8.5, pp. 1242–1263.

[154] O. Schärpf, Polarization Elements, in *Polarized neutron scattering*, edited by T. Brückel and W. Schweika (Forschungszentrum Jülich GmbH, Jülich, 2002) Chap. 2, pp. 31–98.

[155] M. Blume, Polarization Effects in the Magnetic Elastic Scattering of Slow Neutrons, Phys. Rev. **130**, 1670 (1963).

[156] S. V. Maleev, V. G. Bar'yakhtar, and R. A. Suris, The Scattering of Slow Neutrons by Complex Magnetic Structures, Sov. Phys. Solid State **12**, 2533 (1963).

[157] M. Meven and A. Sazonov, HEiDi: Single crystal diffractometer at hot source, Journal of large-scale research facilities **1**, A7 (2015).

[158] M. Hoelzel, A. Senyshyn, and O. Dolotko, SPODI: High resolution powder diffractometer, Journal of large-scale research facilities **1**, A5 (2015).

[159] V. Hutanu, POLI: Polarised hot neutron diffractometer, Journal of large-scale research facilities **1**, A16 (2015).

[160] P. Debye and P. Scherrer, Interferenz an regellos orientierten Teilchen im Röntgenlicht, Nachr. Ges. Wiss. Göttingen, Math.-Phys. Kl. , 1 (1916).

[161] H. M. Rietveld, A profile refinement method for nuclear and magnetic structures, J. Appl. Crystallogr. **2**, 65 (1969).

[162] V. K. Pecharsky and P. Y. Zavalij, The Powder Diffraction Pattern, in *Fundamentals of Powder Diffraction and Structural Characterization of Materials* (Springer US, Boston, MA, 2005) Chap. 8, pp. 151–202.

[163] R. A. Young, ed., *The Rietveld Method*, IUCr monographs on crystallography (Oxford University Press, 1995).

[164] F. Mezei, Neutron spin echo: A new concept in polarized thermal neutron techniques, Z. Physik **255**, 146 (1972).

[165] S. Parnell, A. Washington, H. Kaiser, F. Li, T. Wang, W. Hamilton, D. Baxter, and R. Pynn, Performance of a polarised neutron cryo-flipper using a high-T_c YBCO film, Nucl. Instrum. Methods Phys. Res. A **722**, 20 (2013).

[166] P. J. Brown, J. B. Forsyth, and F. Tasset, Neutron Polarimetry, Proc. R. Soc. Lond. A **442**, 147 (1993).

[167] C. G. Shull, E. O. Wollan, and W. C. Koehler, Neutron Scattering and Polarization by Ferromagnetic Materials, Phys. Rev. **84**, 912 (1951).

[168] F. Mezei, Novel polarized neutron devices: supermirror and spin component amplifier, Commun. Phys **1**, 81 (1976).

[169] K. Coulter, T. Chupp, A. McDonald, C. Bowman, J. Bowman, J. Szymanski, V. Yuan, G. Cates, D. Benton, and E. Earle, Neutron polarization with a polarized ^{3}He spin filter, Nucl. Instrum. Methods Phys. Res. A **288**, 463 (1990).

[170] A. Gukasov and P. J. Brown, Determination of atomic site susceptibility tensors from polarized neutron diffraction data, J. Phys.: Condens. Matter **14**, 8831 (2002).

[171] P. J. Brown and C. Wilkinson, A method of determining a set of experimental spherically symmetrical form factors from X-ray or neutron-diffraction measurements, Acta Cryst. **18**, 398 (1965).

[172] H. Stanley, P. Brown, K. McEwen, and B. Rainford, Magnetic form factor and susceptibility of neodymium, Physica B+C **136**, 400 (1986).

[173] F. A. Wedgwood, Electron-spin transfer due to covalent bonding in the $(CrF_6)_3$-group of K_2NaCrF_6, Proc. R. Soc. Lond. A **349**, 447 (1976).

[174] B. Gillon and J. Schweizer, Study of Chemical Bonding in Molecules: The Interest of Polarised Neutron Diffraction, in *Molecules in Physics, Chemistry, and Biology: Electronic Structure and Chemical Reactivity*, edited by J. Maruani (Springer Netherlands, Dordrecht, 1989) pp. 111–147.

[175] R. J. Papoular and B. Gillon, Maximum Entropy Reconstruction of Spin Density Maps in Crystals from Polarized Neutron Diffraction Data, EPL **13**, 429 (1990).

[176] V. Hutanu, W. Luberstetter, E. Bourgeat-Lami, M. Meven, A. Sazonov, A. Steffen, G. Heger, G. Roth, and E. Lelièvre-Berna, Implementation of a new Cryopad on the diffractometer POLI at MLZ, Rev. Sci. Instrum. **87**, 105108 (2016).

[177] F. Tasset, Zero field neutron polarimetry, Physica B Condens. Matter **156-157**, 627 (1989).

[178] V. Hutanu, M. Meven, E. Lelièvre-Berna, and G. Heger, POLI-HEiDi: The new polarised neutron diffractometer at the hot source (SR9) at the FRM II-Project status, Phys. B Condens. Matter **404**, 2633 (2009).

[179] H. Thoma, W. Luberstetter, J. Peters, and V. Hutanu, Polarized neutron diffraction using a novel high-T_c superconducting magnet on the single-crystal diffractometer POLI at MLZ, J. Appl. Crystallogr. **51**, 17 (2018).

[180] Y. Kousaka, T. Koyama, K. Ohishi, K. Kakurai, V. Hutanu, H. Ohsumi, T. Arima, A. Tokuda, M. Suzuki, N. Kawamura, A. Nakao, T. Hanashima, J. Suzuki, J. Campo, Y. Miyamoto, A. Sera, K. Inoue, and J. Akimitsu, Monochiral helimagnetism in homochiral crystals of $CsCuCl_3$, Phys. Rev. Materials **1**, 071402 (2017).

[181] F. Tasset, P. J. Brown, and J. B. Forsyth, Determination of the absolute magnetic moment direction in Cr_2O_3 using generalized polarization analysis, J. Appl. Phys. **63**, 3606 (1988).

[182] P. J. Brown, J. B. Forsyth, and F. Tasset, A study of magnetoelectric domain formation in Cr_2O_3, J. Phys.: Condens. Matter **10**, 663 (1998).

[183] P. Brown, J. Forsyth, and F. Tasset, Precision determination of antiferromagnetic form factors, Physica B Condens. Matter **267-268**, 215 (1999).

[184] N. Terada, N. Qureshi, L. C. Chapon, and T. Osakabe, Spherical neutron polarimetry under high pressure for a multiferroic delafossite ferrite, Nat. Commun. **9**, 4368 (2018).

[185] J. A. Rodríguez-Velamazán, O. Fabelo, J. Campo, J. Rodríguez-Carvajal, N. Qureshi, and L. C. Chapon, Switching of the Chiral Magnetic Domains in the Hybrid Molecular/Inorganic Multiferroic $(ND_4)_2[FeCl_5(D_2O)]$, Sci. Rep. **8**, 10665 (2018).

[186] I. A. Zobkalo, A. N. Matveeva, A. Sazonov, S. N. Barilo, S. V. Shiryaev, B. Pedersen, and V. Hutanu, Direct control of magnetic chirality in $NdMn_2O_5$ by external electric field, Phys. Rev. B **101**, 064425 (2020).

[187] T. Honda, J. S. White, A. B. Harris, L. C. Chapon, A. Fennell, B. Roessli, O. Zaharko, Y. Murakami, M. Kenzelmann, and T. Kimura, Coupled multiferroic domain switching in the canted conical spin spiral system Mn_2GeO_4, Nat. Commun. **8**, 15457 (2017).

[188] M. Janoschek, S. Klimko, R. Gähler, B. Roessli, and P. Böni, Spherical neutron polarimetry with MuPAD, Physica B Condens. Matter **397**, 125 (2007).

[189] R. Georgii and K. Seemann, MIRA: Dual wavelength band instrument, Journal of large-scale research facilities **1**, A3 (2015).

[190] K. D. Rouse, M. J. Cooper, E. J. York, and A. Chakera, Absorption corrections for neutron diffraction, Acta Cryst. **A26**, 682 (1970).

[191] H.-C. Hu, C. Yang, and K. Zhao, Absorption correction A^* for cylindrical and spherical samples with extended range and high accuracy calculated by the Thorkildsen and Larsen analytical method, Acta Cryst. **A68**, 778 (2012).

[192] W. R. Busing and H. A. Levy, High-speed computation of the absorption correction for single-crystal diffraction measurements, Acta Cryst. **10**, 180 (1957).

[193] M. Renninger, "Umweganregung", eine bisher unbeachtete Wechselwirkungserscheinung bei Raumgitterinterferenzen, Z. Physik **106**, 141 (1937).

[194] J. C. Speakman, The Renninger effect – an example and its implication, Acta Cryst. **18**, 570 (1965).

[195] P. J. Becker and P. Coppens, Extinction within the limit of validity of the Darwin transfer equations. I. General formalism for primary and secondary extinction and their applications to spherical crystals, Acta Cryst. **A30**, 129 (1974).

[196] K. Lonsdale, Extinction in X-ray crystallography, Mineral. Mag. J. Mineral. Soc. **28**, 14 (1947).

[197] M. Bonnet, A. Delapalme, P. Becker, and H. Fuess, Polarized neutron diffraction – a tool for testing extinction models: application to yttrium iron garnet, Acta Cryst. **A32**, 945 (1976).

[198] J. C. Matthewman, P. Thompson, and P. J. Brown, The Cambridge Crystallography Subroutine Library, J. Appl. Crystallogr. **15**, 167 (1982).

[199] V. Petříček, M. Dušek, and L. Palatinus, Crystallographic Computing System JANA2006: General features, Z. Kristallogr. Cryst. Mater. **229**, 345 (2014).

[200] N. Qureshi, Mag2Pol : a program for the analysis of spherical neutron polarimetry, flipping ratio and integrated intensity data, J. Appl. Crystallogr. **52**, 175 (2019).

[201] J. Rodríguez-Carvajal, Recent advances in magnetic structure determination by neutron powder diffraction, Physica B Condens. Matter **192**, 55 (1993).

[202] G. M. Sheldrick, A short history of SHELX, Acta Cryst. **A64**, 112 (2008).

[203] R. Nathans, H. A. Alperin, S. J. Pickart, and P. J. Brown, Measurement of the Covalent Spin Distribution in Manganous Fluoride using Polarized Neutrons, J. Appl. Phys. **34**, 1182 (1963).

[204] P. J. Brown and J. B. Forsyth, The spatial distribution of ferromagnetic moment in $MnCO_3$, Proc. Phys. Soc. **92**, 125 (1967).

[205] A. Balandin and A. Kaneko, Maximum entropy method for sign-altering functions, Inverse Probl. **15**, 445 (1999).

[206] G. Minerbo, MENT: A maximum entropy algorithm for reconstructing a source from projection data, Comput. Graph. Image Process. **10**, 48 (1979).

[207] J. Skilling and R. K. Bryan, Maximum entropy image reconstruction: general algorithm, Mon. Not. R. Astron. Soc. **211**, 111 (1984).

[208] J. Schweizer, Polarized Neutrons and Polarization Analysis, in *Neutron Scattering from Magnetic Materials*, edited by T. Chatterji (Elsevier Science, Amsterdam, 2006) Chap. 4, pp. 153–213.

[209] E. Ressouche, Polarized neutron diffraction, Collection SFN **13**, 02002 (2014).

[210] M. Sakata, T. Uno, M. Takata, and C. J. Howard, Maximum-entropy-method analysis of neutron diffraction data, J. Appl. Crystallogr. **26**, 159 (1993).

[211] P. Schleger, A. Puig-Molina, E. Ressouche, O. Rutty, and J. Schweizer, A General Maximum-Entropy Method for Model-Free Reconstructions of Magnetization Densities from Polarized Neutron Diffraction Data, Acta Cryst. **A53**, 426 (1997).

[212] S. Gull and J. Skilling, *Quantified Maximum Entropy. MEMSYS5 User's Manual* (M.E.D.C, 33 North End, Royston, SG8 6NR, England, 1991).

[213] T. R. Marsh, *C++ maximum entropy code* (2000). Available at: `https://www.github.com/trmrsh/cpp-mem`, accessed on: 01.07.2022.

[214] I. A. Kibalin and A. Gukasov, Asphericity of magnetization density and anisotropy in rare-earth pyrochlores via polarized neutron diffraction and iterative entropy maximization, Phys. Rev. B **105**, 104411 (2022).

[215] P. W. Anderson, New Approach to the Theory of Superexchange Interactions, Phys. Rev. **115**, 2 (1959).

[216] C. D. Hu, Giving directions, Nat. Phys. **10**, 180 (2014).

[217] J. Cho, N.-H. Kim, S. K. Kang, H.-K. Hwang, J. Jung, H. J. M. Swagten, J.-S. Kim, and C.-Y. You, The sign of the interfacial Dzyaloshinskii–Moriya interaction in ultrathin amorphous and polycrystalline magnetic films, J. Phys. D: Appl. Phys. **50**, 425004 (2017).

[218] S. S. P. Parkin, M. Hayashi, and L. Thomas, Magnetic Domain-Wall Racetrack Memory, Science **320**, 190 (2008).

[219] S. Emori, U. Bauer, S. M. Ahn, E. Martinez, and G. S. Beach, Current-driven dynamics of chiral ferromagnetic domain walls, Nat. Mater. **12**, 611 (2013).

[220] J. Torrejon, J. Kim, J. Sinha, S. Mitani, M. Hayashi, M. Yamanouchi, and H. Ohno, Interface control of the magnetic chirality in CoFeB/MgO heterostructures with heavy-metal underlayers, Nat. Commun. **5**, 4655 (2014).

[221] C. Moreau-Luchaire, C. Moutafis, N. Reyren, J. Sampaio, C. A. F. Vaz, N. Van Horne, K. Bouzehouane, K. Garcia, C. Deranlot, P. Warnicke, P. Wohlhüter, J.-M. George, M. Weigand, J. Raabe, V. Cros, and A. Fert, Additive interfacial chiral interaction in multilayers for stabilization of small individual skyrmions at room temperature, Nat. Nanotechnol. **11**, 444 (2016).

[222] X. Zhang, Y. Zhou, and M. Ezawa, Magnetic bilayer-skyrmions without skyrmion Hall effect, Nat. Commun. **7**, 10293 (2016).

[223] K.-W. Kim, K.-W. Moon, N. Kerber, J. Nothhelfer, and K. Everschor-Sitte, Asymmetric skyrmion Hall effect in systems with a hybrid Dzyaloshinskii-Moriya interaction, Phys. Rev. B **97**, 224427 (2018).

[224] V. E. Dmitrienko, E. N. Ovchinnikova, J. Kokubun, and K. Ishida, Dzyaloshinskii–Moriya interaction: How to measure its sign in weak ferromagnets?, Jetp Lett. **92**, 383 (2010).

[225] G. Beutier, S. P. Collins, O. V. Dimitrova, V. E. Dmitrienko, M. I. Katsnelson, Y. O. Kvashnin, A. I. Lichtenstein, V. V. Mazurenko, A. G. A. Nisbet, E. N. Ovchinnikova, and D. Pincini, Band Filling Control of the Dzyaloshinskii-Moriya Interaction in Weakly Ferromagnetic Insulators, Phys. Rev. Lett. **119**, 167201 (2017).

[226] H. Thoma, V. Hutanu, R. Dutta, A. Gukasov, V. Kocsis, Y. Tokunaga, Y. Taguchi, Y. Tokura, I. Kezsmarki, G. Roth, and M. Angst, Magnetic Order and Sign of the Dzyaloshinskii–Moriya Interaction in 2-D Antiferromagnet $Ba_2CoGe_2O_7$ Under Applied Magnetic Field, IEEE Trans. Magn. **58**, 1 (2022).

[227] A. Bogdanov, U. Rößler, M. Wolf, and K.-H. Müller, Modulated and localized structures in chiral antiferromagnets with weak ferromagnetism, J. Magn. Magn. Mater. **272-276**, 332 (2004).

[228] M. Belmeguenai, M. S. Gabor, Y. Roussigné, T. Petrisor, R. B. Mos, A. Stashkevich, S. M. Chérif, and C. Tiusan, Interfacial Dzyaloshinskii-Moriya interaction sign in Ir/Co_2FeAl systems investigated by Brillouin light scattering, Phys. Rev. B **97**, 054425 (2018).

[229] S. V. Grigoriev, N. M. Potapova, S.-A. Siegfried, V. A. Dyadkin, E. V. Moskvin, V. Dmitriev, D. Menzel, C. D. Dewhurst, D. Chernyshov, R. A. Sadykov, L. N. Fomicheva, and A. V. Tsvyashchenko, Chiral Properties of Structure and Magnetism in $Mn_{1-x}Fe_xGe$ Compounds: When the Left and the Right are Fighting, Who Wins?, Phys. Rev. Lett. **110**, 207201 (2013).

[230] S.-A. Siegfried, E. V. Altynbaev, N. M. Chubova, V. Dyadkin, D. Chernyshov, E. V. Moskvin, D. Menzel, A. Heinemann, A. Schreyer, and S. V. Grigoriev, Controlling the Dzyaloshinskii-Moriya interaction to alter the chiral link between structure and magnetism for $Fe_{1-x}Co_xSi$, Phys. Rev. B **91**, 184406 (2015).

[231] V. E. Dmitrienko, E. N. Ovchinnikova, S. P. Collins, G. Nisbet, G. Beutier, Y. O. Kvashnin, V. V. Mazurenko, A. I. Lichtenstein, and M. I. Katsnelson, Measuring the Dzyaloshinskii-Moriya interaction in a weak ferromagnet, Nat. Phys. **10**, 202 (2014).

[232] F. de Bergevin and M. Brunel, Diffraction of X-rays by magnetic materials. I. General formulae and measurements on ferro- and ferrimagnetic compounds, Acta Cryst. **A37**, 314 (1981).

[233] M. Blume, Magnetic effects in anomalous dispersion, in *Resonant Anomalous X-ray Scattering: Theory and Applications*, edited by G. Materlik, C. Sparks, and K. Fischer (Elsevier Science, Amsterdam, 1994) Chap. 5, p. 495.

[234] D. Pincini, F. Fabrizi, G. Beutier, G. Nisbet, H. Elnaggar, V. E. Dmitrienko, M. I. Katsnelson, Y. O. Kvashnin, A. I. Lichtenstein, V. V. Mazurenko, E. N. Ovchinnikova, O. V. Dimitrova, and S. P. Collins, Role of the orbital moment in a series of isostructural weak ferromagnets, Phys. Rev. B **98**, 104424 (2018).

[235] A. Ovsianikov, H. Thoma, O. Usmanov, P. J. Brown, T. Chatterji, A. Sazonov, S. Barilo, L. Peters, and V. Hutanu, Breaking the Magnetic Symmetry by Reorientation Transition Near 50 K in Multiferroic Magnetocaloric $HoFeO_3$, IEEE Trans. Magn. **58**, 1 (2022).

[236] H. Thoma, H. Deng, G. Roth, and V. Hutanu, Setup for polarized neutron diffraction using a high-T_c superconducting magnet on the instrument POLI at MLZ and its applications, J. Phys. Conf. Ser. **1316**, 012016 (2019).

[237] Y. B. Ke, S. Lan, Y. Wu, H. H. Wu, V. Hutanu, H. Deng, A. Pramanick, Y. Ren, and X.-L. Wang, Unraveling magneto-structural coupling of Ni_2MnGa alloy under the application of stress and magnetic field using in situ polarized neutron diffraction, Appl. Phys. Lett. **117**, 081905 (2020).

[238] J. Jeong, B. Lenz, A. Gukasov, X. Fabrèges, A. Sazonov, V. Hutanu, A. Louat, D. Bounoua, C. Martins, S. Biermann, V. Brouet, Y. Sidis, and P. Bourges, Magnetization Density Distribution of Sr_2IrO_4 : Deviation from a Local $j_{eff} = \frac{1}{2}$ Picture, Phys. Rev. Lett. **125**, 097202 (2020).

[239] V. Hutanu, H. Thoma, H. Deng, G. Brandl, A. Weber, V. Rubanskyi, J. Peters, W. Luberstetter, T. Krist, G. Roth, L. Peters, T. Bruckel, and S. Mattauch, New Polarized Neutron Diffraction Setup for Precise High-Field Investigations of Magnetic Structures up to 8 T at MLZ, IEEE Trans. Magn. **58**, 1 (2022).

[240] A. Eich, M. Hölzle, Y. Su, V. Hutanu, R. Georgii, L. Beddrich, and A. Grzechnik, Clamp cells for high pressure neutron scattering at low temperatures and high magnetic fields at Heinz Maier-Leibnitz Zentrum (MLZ), High Press. Res. **41**, 88 (2021).

[241] Oxford Instruments, *Leading provider of high technology products and services for research and industry.* (2022). Available at: `https://www.oxinst.com`, accessed on: 01.07.2022.

[242] COMSOL Multiphysics, *Software for Multiphysics Simulation.* (2022). Available at: https://www.comsol.com, accessed on: 01.07.2022.

[243] T. Krist and F. Mezei, Neutron optics made in berlin, Neutron News **12**, 10 (2001).

[244] V. Hutanu, M. Meven, S. Masalovich, G. Heger, and G. Roth, ^{3}He spin filters for spherical neutron polarimetry at the hot neutrons single crystal diffractometer POLI-HEiDi, J. Phys. Conf. Ser. **294**, 012012 (2011).

[245] F. Tasset and E. Ressouche, Optimum transmission for a ^{3}He neutron polarizer, Nucl. Instrum. Methods Phys. Res. A **359**, 537 (1995).

[246] V. Hutanu, A. Sazonov, H. Murakawa, Y. Tokura, B. Náfrádi, and D. Chernyshov, Symmetry and structure of multiferroic $Ba_2CoGe_2O_7$, Phys. Rev. B **84**, 212101 (2011).

[247] S. R. Parnell, E. B. Woolley, S. Boag, and C. D. Frost, Digital pulsed NMR spectrometer for nuclear spin-polarized ^{3}He and other hyperpolarized gases, Meas. Sci. Technol. **19**, 045601 (2008).

[248] W. C. Hamilton, Significance tests on the crystallographic R factor, Acta Cryst. **18**, 502 (1965).

[249] A. Gukasov, A. Goujon, J. L. Meuriot, C. Person, G. Exil, and G. Koskas, Super-6T2, a new position-sensitive detector polarized neutron diffractometer, Phys. B Condens. Matter **397**, 131 (2007).

[250] A. Gukasov, S. Rodrigues, J.-L. Meuriot, T. Robillard, A. Sazonov, B. Gillon, A. Laverdunt, F. Prunes, and F. Coneggo, Very Intense Polarized (VIP) Neutron Diffractometer at the ORPHEE Reactor in Saclay, Phys. Procedia **42**, 150 (2013).

[251] A. Sazonov, *Davinci - A Scientific Software for the Visualization and Processing of Single-Crystal Diffraction Data Measured with a Point Detector* (2018). Available at: https://www.davinci.sazonov.org, accessed on: 01.07.2022.

[252] I. V. Solovyev, Magnetization-induced local electric dipoles and multiferroic properties of $Ba_2CoGe_2O_7$, Phys. Rev. B **91**, 224423 (2015).

[253] K. Yamauchi, P. Barone, and S. Picozzi, Theoretical investigation of magnetoelectric effects in $Ba_2CoGe_2O_7$, Phys. Rev. B **84**, 165137 (2011).

[254] G. H. Lander, Spin and orbital magnetic moments in actinide compounds, Phys. Scr. **44**, 33 (1991).

[255] R. M. Moon, W. C. Koehler, J. W. Cable, and H. R. Child, Distribution of Magnetic Moment in Metallic Gadolinium, Phys. Rev. B **5**, 997 (1972).

[256] V. Granata, L. Rocco, A. Ubaldini, M. R. Lees, R. Fittipaldi, M. Ciomaga Hatnean, S. Pace, G. Balakrishnan, and A. Vecchione, Effect of different atmospheres on the synthesis of $Ba_2CuGe_2O_7$ single crystals, Eur. Phys. J. Special Topics **228**, 703 (2019).

[257] Bruker, *D2 PHASER - Benchtop X-ray Powder Diffraction* (2014). Available at: https://www.bruker.com, accessed on: 01.07.2022.

[258] A. Huq, M. Kirkham, P. F. Peterson, J. P. Hodges, P. S. Whitfield, K. Page, T. Hűgle, E. B. Iverson, A. Parizzi, and G. Rennich, POWGEN: rebuild of a third-generation powder diffractometer at the Spallation Neutron Source, J. Appl. Crystallogr. **52**, 1189 (2019).

[259] P. Virtanen, R. Gommers, T. E. Oliphant, M. Haberland, T. Reddy, *et al.*, SciPy 1.0: fundamental algorithms for scientific computing in Python, Nat. Methods **17**, 261 (2020).

[260] A. March, Mathematische Theorie der Regelung nach der Korngestah bei affiner Deformation, Z. Kristallogr. Cryst. Mater. **81**, 285 (1932).

[261] W. A. Dollase, Correction of intensities for preferred orientation in powder diffractometry: application of the March model, J. Appl. Crystallogr. **19**, 267 (1986).

[262] W. Pitschke, N. Mattern, and H. Hermann, Incorporation of microabsorption corrections into Rietveid analysis, Powder Diffraction **8**, 223 (1993).

[263] S. M. Antao and I. Hassan, $BaCO_3$: high-temperature crystal structures and the Pmcn→R3m phase transition at 811 °C, Phys. Chem. Miner. **34**, 573 (2007).

[264] J. Glinnemann, H. E. King, H. Schulz, T. Hahn, S. J. L. Placa, and F. Dacol, Crystal structures of the low-temperature quartz-type phases of SiO_2 and GeO_2 at elevated pressure, Z. Krist. **198**, 177 (1992).

[265] A. A. Bolzan, C. Fong, B. J. Kennedy, and C. J. Howard, Structural Studies of Rutile-Type Metal Dioxides, Acta Cryst. **B53**, 373 (1997).

[266] N. Brese, M. O'Keeffe, B. Ramakrishna, and R. Von Dreele, Low-temperature structures of CuO and AgO and their relationships to those of MgO and PdO, J. Solid State Chem. **89**, 184 (1990).

[267] W. Hilmer, Die Struktur der Hochtemperaturform des Bariumgermanates $BaGeO_3$(h), Acta Cryst. **15**, 1101 (1962).

[268] D. M. Többens, V. Kahlenberg, C. Gspan, and G. Kothleitner, Atomic and domain structure of the low-temperature phase of barium metagermanate ($BaGeO_3$), Acta Cryst. **B62**, 1002 (2006).

[269] W. K. Wong-Ng, K. Davis, and R. S. Roth, X-ray Powder Study of 2BaO·CuO, J. Am. Ceram. Soc. **71**, C (1988).

[270] M. T. Weller and D. R. Lines, Structure and oxygen stoicheiometry in $BaCuO_{2+x}$, J. Chem. Soc., Chem. Commun. **2772**, 484 (1989).

[271] M. Braden, G. Wilkendorf, J. Lorenzana, M. Aïn, G. J. McIntyre, M. Behruzi, G. Heger, G. Dhalenne, and A. Revcolevschi, Structural analysis of $CuGeO_3$: Relation between nuclear structure and magnetic interaction, Phys. Rev. B **54**, 1105 (1996).

[272] T. Yamada, Z. Hiroi, and M. Takano, Spin-$\frac{1}{2}$ Quantum Antiferromagnetic Chains with Tunable Superexchange Interactions Found in $BaCu_2(Si_{1-x}Ge_x)_2O_7$, J. Solid State Chem. **156**, 101 (2001).

[273] J. Oliveira, B. Klockow, and W. Eysel, Compounds and Solid Solutions in the System CuO-BaO-SiO2-GeO2, Mater. Sci. Forum **133-136**, 621 (1993).

[274] W. Liang, L. Li, R. Li, Y. Yin, Z. Li, X. Liu, S. Shan, Y. He, Y. Meng, Z. Li, and H. Li, Crystal structure of impurity-free rhodochrosite ($MnCO_3$) and thermal expansion properties, Phys. Chem. Miner. **47**, 10.1007/s00269-019-01078-2 (2020).

[275] K. Sander and H. Müller-Buschbaum, Synthese und Aufbau von Ba_2MnO_3, Z. anorg. allg. Chem. **478**, 52 (1981).

[276] J. Hadermann, A. M. Abakumov, J. J. Adkin, and M. A. Hayward, Topotactic Reduction As a Route to New Close-Packed Anion Deficient Perovskites: Structure and Magnetism of 4H-$BaMnO_{2+x}$, J. Am. Chem. Soc. **131**, 10598 (2009).

[277] G. J. Redhammer, C. Vorberg, and G. Tippelt, Crystal structure and high temperature phase relations of monoclinic and orthorhombic pyroxene-compounds $MnGeO_3$: a comparison, N. Jb. Miner. Abh. **189**, 103 (2012).

[278] S. Sasaki, K. Fujino, and Y. Takéuchi, X-ray determination of electron-density distributions in oxides, MgO, MnO, CoO, and NiO, and atomic scattering factors of their constituent atoms., Proc. Japan Acad. Ser. B **55**, 43 (1979).

[279] J. W. Kaiser and W. Jeitschko, Crystal structure of dibarium dimanganese disilicium nonaoxide $Ba_2Mn_2Si_2O_9$, Z. Kristallogr. NCS **215**, 313 (2000).

[280] L. D. Sanjeewa, A. S. Sefat, M. Smart, M. A. McGuire, C. D. McMillen, and J. W. Kolis, Synthesis, structure and magnetic properties of $Ba_3M_2Ge_4O_14$ (M = Mn and Fe): Quasi-one-dimensional zigzag chain compounds, J. Solid State Chem. **283**, 121090 (2020).

[281] L. Vegard, Die Konstitution der Mischkristalle und die Raumfüllung der Atome, Z. Physik **5**, 17 (1921).

[282] J. S. Hwang, K. J. Lin, and C. Tien, Measurement of heat capacity by fitting the whole temperature response of a heat-pulse calorimeter, Rev. Sci. Instrum. **68**, 94 (1997).

[283] H. Akima, A New Method of Interpolation and Smooth Curve Fitting Based on Local Procedures, J. ACM **17**, 589 (1970).

[284] A. Savitzky and M. J. E. Golay, Smoothing and Differentiation of Data by Simplified Least Squares Procedures., Anal. Chem. **36**, 1627 (1964).

[285] M. E. Fisher, Relation between the specific heat and susceptibility of an antiferromagnet, Philos. Mag. **7**, 1731 (1962).

[286] H.-J. Schmidt, A. Lohmann, and J. Richter, Eighth-order high-temperature expansion for general Heisenberg Hamiltonians, Phys. Rev. B **84**, 104443 (2011).

[287] T.-h. Jang, S.-h. Do, M. Lee, H. Wu, C. M. Brown, A. D. Christianson, S.-w. Cheong, and J.-h. Park, Physical properties of the quasi-two-dimensional square lattice antiferromagnet $Ba_2FeSi_2O_7$, Phys. Rev. B **104**, 214434 (2021).

[288] D.-X. Chen, J. Brug, and R. Goldfarb, Demagnetizing factors for cylinders, IEEE Trans. Magn. **27**, 3601 (1991).

[289] Z. He, M.-H. Wangbo, Y. Ueda, Y. Narumi, K. Kindo, T. Taniyama, M. Itoh, and W. Cheng, Synthesis and Magnetic Properties of $Ba_2Mn_2Si_2O_9$: the First Example of S=2 Spin-Dimer with Spin-Singlet Ground State, Chemistry - An Asian Journal **4**, 1530 (2009).

[290] I. Tsukada, J. Takeya, T. Masuda, and K. Uchinokura, Weak ferromagnetism of quasi-one-dimensional S=$\frac{1}{2}$ antiferromagnet $BaCu_2Ge_2O_7$, Phys. Rev. B **62**, R6061 (2000).

[291] A. Bienenstock, Variation of the Critical Temperatures of Ising Antiferromagnets with Applied Magnetic Field, J. Appl. Phys. **37**, 1459 (1966).

[292] P. Sengupta, C. D. Batista, R. D. McDonald, S. Cox, J. Singleton, L. Huang, T. P. Papageorgiou, O. Ignatchik, T. Herrmannsdörfer, J. L. Manson, J. A. Schlueter, K. A. Funk, and J. Wosnitza, Nonmonotonic field dependence of the Néel temperature in the quasi-two-dimensional magnet $[Cu(HF_2)(pyz)_2]BF_4$, Phys. Rev. B **79**, 060409 (2009).

[293] J. Chovan, M. Marder, and N. Papanicolaou, Field-induced phase transitions in the helimagnet $Ba_2CuGe_2O_7$, Phys. Rev. B **88**, 064421 (2013).

[294] T. Chatterji, Paramagnetic and Critical Scattering, in *Neutron Scattering from Magnetic Materials*, edited by T. Chatterji (Elsevier Science, Amsterdam, 2006) Chap. 7, pp. 333–361.

[295] S. J. Pickart and R. Nathans, Unpaired Spin Density in Ordered Fe_3Al, Phys. Rev. **123**, 1163 (1961).

[296] H. A. Alperin, P. J. Brown, and R. Nathans, Aspherical Spin Density in the Ferrimagnetic Compound Mn_2Sb, J. Appl. Phys. **34**, 1201 (1963).

[297] C. G. Shull and H. A. Mook, Distribution of Internal Magnetization in Iron, Phys. Rev. Lett. **16**, 184 (1966).

[298] P. J. Brown, P. J. Welford, and J. B. Forsyth, Magnetization density and the magnetic structure of cobalt carbonate, J. Phys. C: Solid State Phys. **6**, 1405 (1973).

[299] P. J. Brown and J. L. Cox, Charge and spin density distributions in the ferromagnetic alloy Fe_2B, Philos. Mag. **23**, 705 (1971).

[300] M. Kara and K. Kurki-Suonio, Symmetrized multipole analysis of orientational distributions, Acta Cryst. **A37**, 201 (1981).

[301] P. Coppens, *X-Ray Charge Densities and Chemical Bonding* (Oxford University Press, 1997).

[302] G. Guennebaud, B. Jacob, *et al.*, *Eigen v3* (2010). Available at: `https://www.eigen.tuxfamily.org`, accessed on: 01.07.2022.

[303] I. Ema, J. M. De La Vega, B. Miguel, J. Dotterweich, H. Meißner, and E. Steinborn, Exponential-Type Basis Functions: Single- and Double-Zeta $\mathcal{B}$ Function Basis Sets for the Ground States of Neutral Aatoms from Z = 2 to Z = 36, At. Data Nucl. Data Tables **72**, 57 (1999).

[304] J. Hein, *tikz-3dplot - development notes on a LaTeX package which extends tikz/PGF to draw 3D diagrams* (2012). Available at: `https://www.tikz3dplot.wordpress.com`, accessed on: 01.07.2022.

[305] P. Courtois, Characterization of Heusler crystals for polarized neutrons monochromators, Physica B Condens. Matter **267-268**, 363 (1999).

[306] J. B. Hayter and H. A. Mook, Discrete thin-film multilayer design for X-ray and neutron supermirrors, J. Appl. Crystallogr. **22**, 35 (1989).

[307] C. Darwin, XCII. The reflexion of X-rays from imperfect crystals, London, Edinburgh, Dublin Philos. Mag. J. Sci. **43**, 800 (1922).

[308] P. J. Becker and P. Coppens, Extinction within the limit of validity of the Darwin transfer equations. III. Non-spherical crystals and anisotropy of extinction, Acta Cryst. **A31**, 417 (1975).

[309] N. Wu, Maximum Entropy Method MEM2 and its Application in Image Restoration, in *The Maximum Entropy Method* (Springer, Berlin, Heidelberg, 1997) Chap. 3, pp. 109–190.

List of Figures

List of Tables

List of Abbreviations

AFM antiferromagnetic
BNS Belov-Neronova-Smirnova
CW Curie-Weiss
DAQ data acquisition
DFT density functional theory
DMI Dzyaloshinskii-Moriya interaction
ESR electron spin resonance
FR flipping ratio
FM ferromagnetic
GUI graphical user interface
HC heat capacity
I/C incommensurate to commensurate
JT Jahn-Teller
MEM maximum entropy method
MF mean-field
MP multipole
ND non-polarized neutron single crystal diffraction
NMR nuclear magnetic resonance
NN nearest neighbor
PA uniaxial polarization analysis
PD neutron powder diffraction
PM paramagnetic
PND polarized neutron diffraction
PPMS physical property measurement system
RT room-temperature
SANS small-angle neutron scattering
SD search direction
SFC spin filter cell
SIA single ion anisotropy
SNP spherical neutron polarimetry
SOC spin-orbit coupling
TM transition metal
TOF time-of-flight
UC unit cell
VSM vibrating sample magnetometer
WFM weak ferromagnetic
XRD X-ray powder diffraction